Final Technical Report

Marine Renewable Energy Center
DOE Award Number: DE-EE0000299
Project Period: December 2009 – March 31, 2013 (Extended to October 8, 2013)
Principal Investigator: Paul Vigeant (PI at the time of this report), John Miller, former Executive Director of MREC was the earlier PI.
New England MREC, UMass Dartmouth 285 Old Westport Road Dartmouth, MA 02747
Names of other project team member organizations (see below)
October 8, 2013

Working Partners:

University of Massachusetts Dartmouth School of Marine Science and Technology (SMAST)
University of Massachusetts Amherst
University of New Hampshire
University of Rhode Island
Massachusetts Institute of Technology (Dropped out)
Woods Hole Oceanographic Institution

Cost-Sharing Partners and Contacts

University of Massachusetts Dartmouth SMAST
Dr. Brian Howes, bhowes@umassd.edu, 508.910.6316

University of Massachusetts Amherst
Dr. Jon G. McGowan; jgmcgowa@ecs.umass.edu; 413.545.2756

University of New Hampshire
Dr. Kenneth Baldwin, Kenneth.Baldwin@unh.edu, 603.862.1898

University of Rhode Island
Dr. Annette Grilli, agrilli@egr.uri.edu, 401.874.6139

Woods Hole Oceanographic Institution
Dr. Eugene Terray, eterray@whoi.edu, 774.392.0070

Acknowledgment, Disclaimer and Proprietary Data Notice –

Acknowledgment: "This report is based upon work supported by the U. S. Department of Energy under Award No.DE-EE0000299".

Disclaimer: "Any findings, opinions, and conclusions or recommendations expressed in this report are those of the author(s) and do not necessarily reflect the views of the Department of Energy"

Proprietary Data Notice: If there is any patentable material or protected data in the report, the recipient, consistent with the data protection provisions of the award, must mark the appropriate block in Section K of the DOE F 241.3, clearly specify it here, and identify them on appropriate pages of the report. Other than patentable material or protected data, reports must not contain any proprietary data (limited rights data), classified information, information subject to export control classification, or other information not subject to release. Protected data is specific technical data, first produced in the performance of the award, which is protected from public release for a period of time by the terms of the award agreement. Reports delivered without such notice may be deemed to have been furnished with unlimited rights, and the Government assumes no liability for the disclosure, reproduction or use of such reports.

Table of Contents

Lists of Figures

List of Tables

Executive Summary

The push to research and then develop economically feasible, sustainable and environmentally sound methods of obtaining useful power from ocean processes has had resurgence in the last 10 years. Where once there were only millionaires, hobbyists and surf board manufacturers involved in developing devices to get power from ocean waves, tides and currents, now there are a host of small to medium sized companies engaging in preliminary research comparing long term and multiple unit deployments of various ocean energy generation devices.

Recognizing that New England is home to one of the most dense population centers and the highest concentration of world class marine science and technology research and development institutions, government agencies and manufacturing companies, standing up a center for marine renewable energy research was a sensible goal.

Obtaining data about the possible areas in New England waters that might be suitable for testing and evaluation of ocean energy devices was the first task. A parallel effort was underway on the part of the MA Ocean Management planning task force to conduct a state wide inventory of all the different uses and users of coastal waters. (Massachusetts Ocean Management Plan, 2009) The Massachusetts Clean Energy Center bravely lead the charge by proving seed funding to New England MREC which enabled the organization to pull together a consortium of stakeholders and universities to collaborate to characterize several potential test sites through funded research, support potential high value research and engage in public and industry outreach to obtain input about the research and types of generating devices that would be suitable for the region.

Tasks 1.1 to 1.4 are basically five different and distinct research projects that were partially funded through this award. Each participating organization provided either or both funding from their home institution or in-kind services to complete their specific projects. In several cases graduate students were able to utilize some or all of the data collected during the project to complete their thesis work. Task 1 was to identify and characterize three specific test sites and recommend optimal test site design concepts. Additionally, the wind and wave climatology for one of these areas was modeled and reported for future offshore wind and or wave testing purposes

Task 2 was designed to fund two projects addressing a topic of high potential, a new technology or new method of energy extraction. Initially an MIT modeling team led by C.C.Mei proposed applying various mathematical models to assess the resource but that project was withdrawn soon after due to institutional administrative issues. A second project, Linear Electric Generator, directed by Dr. Annette Grilli of the University of Rhode Island resulted in a successful project from which a master's thesis was granted. The final report is included as part of this report.

Task 3, Project Management was performed by John Miller, former executive director of New England MREC. The results of that work were reported in great detail in the quarterly reports submitted by J. Miller to the DOE project team. These reports represent a rich body of knowledge and commentary about how to conceive of where ocean energy devices could be placed in the ocean. The process of discovery and on site logistics were both challenging and rewarding. The research completed under this DOE award will inform many of the wind, wave, tidal resource potential in the proposed National Offshore Renewable Energy Innovation Zone (NOREIZ) test

zone as well as near the Governor Sullivan Bridge in New Hampshire. That data will enable follow on researchers and eventually device developers to make informed decisions about working in those key energy areas.

The technical community engaged in developing ocean energy devices hail from many disciplines including hydrodynamics, physical oceanography, marine biology, structural engineering, materials science, policy, planning, and marketing to mention just a few. It was clear in the at the start of the New England Marine Renewable Energy Center (NE MREC) that the many stakeholders would benefit from workshops and conferences designed to introduce them to the devices as well as their impacts both negative and positive on the environment and on the other users of the water space. New England MREC hosted and produced two such conferences in two consecutive falls. (Ocean Energy for New England Conferences; 2008, 2009) As a result of those events it was determined that the technical community needed a forum to exchange research results and ideas about devices. It was because of this need that NE MREC launched the Annual Marine Renewable Energy Technical Conference series. After 4 of these successful events, industry and university colleagues suggested the next step for this conference was to move it to a place that brought together more professionals, offered a peer reviewed journal and speaking opportunities. The technical team decided to collaborate with the Marine Technology Society and the IEEE/Oceanic Engineering Society to enhance the ocean energy sessions at the Oceans 2013 Conference taking place in San Diego, CA. Sept. 22-27, 2013. Additionally, the MTS Journal Special Issue on Marine Renewable Energy was co-edited by guest editors from the MREC University Consortium, resulting in 22 peer reviewed papers. (MTS Journal; Marine Renewable Energy Technologies, 2013)

The executive summaries of the final reports submitted by the individual research partners included within the body of this report have been excerpted and they are included as appendices. The Quarterly Reports Quarter 1—Quarter 14 can be accessed by contacting the DOE Contract Manager.

The networking and outreach that New England MREC has undertaken has positioned MREC as the go-to organization for information about what's happening with regards to ocean wind, wave, tide and current energy power development in New England. Many speaking engagements too numerous to record have positioned MREC with a strong foundation on which to build. The collegial nature of the research funded here has shown the partners that one can accomplish more together than alone.

Project Objective: The New England Marine Renewable Energy Center (MREC) promotes the development of ocean energy (wave, tidal and offshore wind) through academic research, development of test sites, and involvement of all stakeholders, including government, industry, academia, public interest grouping and the public. MREC has defined two strategic objectives: 1. To develop a world class university consortium to promote marine renewable energy and 2. To develop a suite of pre-permitted and closely monitored test sites for marine renewable devices.

Project Background: MREC was initially established in 2008 with $400,000 in Massachusetts funding and $160,000 in University of Massachusetts funding, and was then allocated an additional $951,500 for FY09 and $750,000 for FY10 from the DOE for this Congressionally Directed Project. The current federal funding, combined FY09 and FY10, was used to support the MREC administration, maintain

its University Research Consortium (URC), provide small research grants for research at coalition universities, and to begin feasibility studies for ocean test sites. MREC's University Research Consortium continued its annual technical conferences, as well as other technology sharing activities. NE MREC also created several public outreach meetings for other stakeholders, including governmental agencies, public interest groups, and the general public. Developing one or more test sites in the proposed National Offshore Renewable Energy Innovation Zone (NOREIZ) is of particular interest to MREC, however funding for build-out of the test bed has not yet been secured and was not part of this award. Resource and environmental surveys will continue in that area and the required permitting activities will be pursued.

Project Goals: The funding provided by this contract supported the following activities:
A) Test Site Development; B) Seed Grant Funded Technology Development; C) Stakeholder Activities

The first year of funding was dedicated to the formation of the NE MREC University Consortium which was comprised of University of Massachusetts Dartmouth (UMD) and Amherst (UMA), Massachusetts Institute of Technology (MIT), Woods Hole Oceanographic Institution (WHOI), University of New Hampshire (UNH), and the University of Rhode Island (URI). The consortium worked together to encourage research and promote benefits of obtaining energy from ocean wind, waves, tides and currents.

In addition, NE MREC's goal was to fund projects aimed at potential test sites with the first year funding going to studies of the potential for tidal device testing in Muskeget Channel, at the General Sullivan Bridge in New Hampshire, and for wave device testing at the proposed National Offshore Renewable Energy Innovation Zone (NOREIZ) located off the Massachusetts coast. The project spanned 4.5 years and addressed three specific tasks that are interrelated but also served as independent investigations.

Project Coordination and Leveraging:

Grant funds from the Massachusetts Clean Energy Center (MACEC) and the National Oceanographic Partnership Program (NOPP) were used in concurrent investigations within Muskeget Channel and the NOREIZ lease blocks to increase the impacts of the work detailed in this report and to synergistically increase the overall value of all three projects.

Work for MACEC focused upon barge deployments of MHK technology in Muskeget Channel (August 2011 and July 2012) to assess performance of two types of tidal turbines and to collect data on ecological response to turbine presence. Of specific concern were the near and far field impacts of acoustic noise generated by the turbines and the potential for both fish and planktonic animal strikes by the rotating blade. Support and logistics were provided by the Massachusetts Maritime Academy during 2011 and they have become regular project partners. The 2012 demonstration was spearheaded by UNH partners who utilized many lessons learned through work at General Sullivan Bridge to ensure success while building upon knowledge base for Muskeget Channel.
The NOPP grant entitled "Roadmap: Technologies for Cost Effective, Spatial Resource Assessments for Offshore Renewable Energy" included many field related components that were conducted within Muskeget Channel and the NOREIZ. The most important of those were the construction of a radar array to assess wind potential at the NOREIZ site and to test a variety of instruments and methodologies to forecast wave energy. This work, performed by Eugene Terray at the Woods Hole

Oceanographic Institution, was informed in part by work done under this grant. The weather buoy deployed by SMAST provided a point source measure for comparison to the radar data. And the radar data was to provide a large scale picture of local wave conditions to support a pilot deployment of a wave energy conversion device monitored by SMAST. In addition autonomous underwater vehicles, equipped with bottom mapping sensors were deployed in Muskeget Channel to further refine bottom characteristics at the most promising locations defined by the additional surveying under this grant.

Thus, inter-institutional cooperation and collaboration and careful planning and coordination of activities has given all three of these projects the ability to leverage the funds to not only answer the awardees' specific hypotheses but to complement and supplement other consortium member's research.

Results and Discussion

Task 1. Initial Test Site Development and Assessments

The MREC University Research Consortium identified three sites for consideration as potential test infrastructure. Site #1, the waters between Martha's Vineyard and Muskeget Island were surveyed by UMD's School for Marine Science and Technology (SMAST) researchers to assess the physical and biological elements present in order to understand the tidal resource in the area. Sediment surveys were completed to determine the impacts of tidal turbines on the seafloor. Biotic habitats were documented in order to project the environmental impacts of testing tidal devices. These data were provided to the MA Office of Coastal Zone Management for inclusion in the MA Ocean Management Plan. (MA Ocean Management Plan, 2009)

Once a test site was established, conceptual studies were performed to determine the different options for test infrastructure that could be installed at a later date when funding becomes available. Bottom mounting hardware will be assessed and cable runs determined. Again, if funding is available, an initial grid connection study will be made.

Task 1.1 Muskeget Channel Survey: UMD Project

" Follow-on Data Collection and Synthesis of Muskeget Channel Hydrokinetic Potential and NOREIZ Wave & Wind Energy Potential", Dr. Brian L. Howes, Dr. Roland Samimy, Dr. David Schlezinger, Mr. Michael Bartlett, Ms. Jennifer Benson, M.S., Dr. David White. Coastal Systems Program, School of Marine Science and Technology, University of Massachusetts Dartmouth, Submitted September 20, 2013. (Appendix 1)

The intent of the partnership between the New England Marine Renewable Energy Center (MREC) situated within the University of Massachusetts-Dartmouth and the Coastal Systems Program (CSP) situated within the University of Massachusetts-Dartmouth School for Marine Science and Technology (SMAST) was the completion of specific data collection tasks aimed at further characterizing the hydrokinetic and environmental resource of Muskeget Channel, located between Martha's Vineyard and Nantucket. Funding for completion of the data collection tasks was garnered by MREC from the United States Department of Energy (USDOE). The data collection undertaken by the CSP and summarized in this report supplements an earlier investigation of the hydrokinetic

energy potential of Muskeget Channel that was funded by a grant from the Massachusetts Technology Collaborative. Data summarized herein has been developed specifically to meet the needs of the UMASS Marine Renewable Energy Center in its effort to establish a National Offshore Renewable Energy Innovation Zone (NOREIZ) to serve as a marine renewable energy technology test bed as well as satisfy the needs of the Town of Edgartown (Martha's Vineyard) which holds a preliminary permit from the Federal Energy Regulatory Commission (FERC) for the development of a tidal energy pilot project in Muskeget Channel.

Based upon the determinations of the velocity field within Muskeget Channel in 2008-09 (as funded by the grant from the Massachusetts Technology Collaborative), it was clear that hydrokinetic energy generation potential using underwater turbines presently exists within a very specific portion of Muskeget Channel (the southern region of the Town of Edgartown FERC permit area). The initial investigation into the hydrokinetic energy potential of Muskeget Channel also revealed that further surveying of currents would be required to refine the best location for tidal energy generation technologies. In addition, data collection on the environmental characteristics of the area would be necessary to begin to ascertain the potential impacts resulting from tidal energy generation in Muskeget Channel, specifically the routing of cables to bring tidal power ashore to Martha's Vineyard. These data would further support the Town of Edgartown in its development of a pilot scale tidal energy project while also yielding valuable baseline data sets useful in the establishment of the NOREIZ by MREC.

Building on baseline data previously collected by the SMAST-Coastal Studies Program in Muskeget Channel under the Massachusetts Technology Collaborative grant, the Coastal Studies Program team continued data collection with support from the DOE during the period September 1, 2009 to December 31, 2010. The field work undertaken focused on two elements as follows:

Element 1 - Time-series current and wave field within the Muskeget Channel FERC and initial studies in the NORIEZ (including wind potential).

Element 2 – Town of Edgartown FERC Permit Perimeter Area Investigation to Support Power Transmission to Upland Grid.

Each element had specific data collection tasks aimed at further characterizing the hydrokinetics and environment of Muskeget Channel and waters south (the upper portion of NOREIZ).

Element 1 - Time-series current and wave field within the Muskeget Channel FERC and initial studies in the NORIEZ (including wind potential).

Under this data collection element were six specific tasks:

1. Current measurements in the FERC Permit Site.
2. Current Measurements in Northern Portion of NOREIZ.
3. Measurement of wave heights and frequency in FERC Permit Site
4. Measurement of wave heights and frequency in NOREIZ
5. Initial data gathering on wind energy potential associated with NOREIZ
6. Sediment sampling in NOREIZ in a variety of locations potentially supportive of wind

Element 2 – Town of Edgartown FERC Permit Perimeter Area Investigation to Support Power Transmission to Upland Grid.

Under this data collection element were eight specific tasks:

1. Seasonal Benthic infauna characterization (2 cable routes) in test areas under both disturbed and undisturbed conditions
2. Sediment sampling to go along with Benthic Infauna Sampling
3. Eelgrass surveying along potential cable routes
4. Bottom mounted ADCP to measure along shore currents in vicinity of potential cable routes
5. Surficial sediments sampled and mapped along potential cable routes
6. Assess coastal resources in area of proposed cable route (beach survey)
7. Assess coastal resources in area of proposed cable route (dunes)
8. Assess coastal resources in area of proposed cable route (wetlands)

Overall Results: Element 1

- Detailed ship board ADCP profile transects identified an area within Muskeget Channel that is of sufficient depth for current in-stream tidal turbines to operate on a commercial scale and narrowed the search area for velocities for viable commercialization. Focused, lunar period, bottom moored ADCP deployments supported this contention. The long-term studies indicated higher current velocities than expected from transect surveys. These long term velocities were in excess of 4 knots, generally considered a threshold for commercial viability.
- Wave measurements, made concurrent with long term velocity profiles, showed that the wave fields were bi-modal and temporally inconsistent. The data suggests that local bathymetry, characterized by large expanses of shoals, creates short steep waves, while the deep water swells from the open ocean to the south create waves of comparatively long periods. The combination of wave types are influenced by changes in tidal direction and wind stresses which are both parallel to the wave fronts. The resulting wave environment appears chaotic and is not believed to be commercially viable with current technology, despite the relatively large amount of potential wave energy.
- Within the northern portion of the NOREIZ examined current velocities are uniformly low (<1m/s) and extremely consistent showing only moderate changes through lunar cycles.
- Wave measurements at the NOREIZ site were dominated by long period waves with monthly average energy ranging from 36 to52 kW/m during January and February, respectively.
- Initial data gathering on wind energy potential associated with NOREIZ indicates that the wind fields are energetic and consistent. Though the buoy mast was only 2 meters high wind velocities ranged from 6-8.5 m/s. This data is consistent with other work beginning in the area which utilizes radar arrays for wind and wave prediction. In general the NOREIZ site should be conducive to both wind and wave power extraction.
- Sediment sampling in the vicinity of the NOREIZ buoy showed medium to coarse sand dominates the benthic environment. The sediment appears to be seasonally stable, however, infauna samples suggest that there if frequent reworking of the surficial sediment which limits both the density of animals and the diversity of taxa present.

Overall Results: Element 2

- Benthic infauna communities along both proposed cable routes had extremely low densities and concomitantly low diversity. Markers were removed by vandals making comparison of disturbed and undisturbed conditions impossible. However, visual inspection of the disturbance sites showed no discernible effect of disturbance. Furthermore, statistical analysis of the samples (triplicate at each of the 8 sites) showed that given the low numbers of individuals and variability between replicates that even if the population were decimated the difference would not reach a level of significance in over half the locations.
- Sediment sampling and grain size analysis performed in conjunction with the infaunal analysis showed medium to coarse sand dominates the benthic environment along the Pochet transect. The sediment appears was seasonally stable, however, infauna samples suggest that there if frequent reworking of the superficial sediment which limits both the density of animals and the diversity of taxa present. Results from the Katama transect indicated the presence of glacial clay deposits underlying coarse to medium sand that regularly emerged to the sediment surface. The presence of surface clay deposits, increased infauna densities and diversity while decreasing submerged aquatic vegetation. Clay deposits also complicate cable placement. Final decisions for the cable installation will need to weigh all of these competing factors.
- Beach, dune and wetland surveys where proposed cable installations transition to shore present no immediate obstacles. Both Pochet and Katama cable landings will require review and permitting by Massachusetts Department of Environmental Protection, local conservation commission and Massachusetts Natural Heritage & Endangered Species Program. Portions of both landings are adjacent to wetlands and priority habitat for rare species, however, both locations also have public rights of way and access that could mediate any potential impacts.

The work funded under this grant is descriptive in its nature; however, it has been widely disseminated and has been the basis for much academic work within the field of renewable energy. Publications and presentations using the data set, whole or in part, collected under this grant are listed in Appendix 1a. Further publications are expected.

Task 1.2 Muskeget Tidal Test Site Concept Designs: **UNH Project**

A final report was submitted to New England MREC in May 2013 entitled; Muskeget Channel Tidal Energy Test Facility, M. Robinson Swift, K. Baldwin, M. Wosnik, B.Celikkol, Graduate Student, T. Dewhurst. This project was completed by UNH CORE researchers and graduate student. A copy of that report is included in Appendix: 2

Conceptual designs were investigated for a tidal hydrokinetic device test facility at Muskeget Channel, MA. Muskeget Channel runs north-south between Martha's Vineyard and Nantucket islands. Peak tidal currents of approximately 2.5 m/s (5 knots) combined with depth on the order of 30m (100 ft.) make the site ideal for testing large hydrokinetic systems.(Robinson,R.,2013)

Six platform concepts were investigated for devices of various sizes. A fixed, bottom gravity foundation would be below surface wave activity and marine traffic, thereby favoring a long-term deployment, but there would challenges in mounting and recovering turbines for the subsurface platform. A telescoping, bottom gravity foundation would allow surface mounting and retrieval of devices at the expense of mechanical complexity. A fixed, four-pile supported mid-water platform would have advantages and disadvantages similar to the gravity foundation. A two-pile surface-piercing structure that could raise and lower a device would be accessible and maintain a permanent surface presence. All permanent hard structure systems were found to have considerable construction and installation costs and be subject to sedimentation and or scour processes. A submerged buoyant platform held against the current by a flexible mooring system could also be arranged to surface for turbine attachment ad retrieval. A floating platform would use a decked, twin-hulled configuration. The platform would be anchored in place during actual testing and brought to a shore base between on-site test programs. A natural berth option was also considered. The instrumented natural berth concept would allow developers to evaluate complete systems incorporating the mounting structure and generator, as well as the tidal turbine itself. The current environment would be measured by bottom secured ADCPs and the power output to a grid tie-in on Martha's Vineyard would be monitored.

Designs of each concept mentioned above were developed for structural soundless, dynamic response, vibration, scour, corrosion, bio-fouling, electrical connection, monitoring, operating limits, ease of turbine installation and access, and cost. The floating platform, and the two -pile platform were found to be the most practical. A floating platform would require less installation work and would be easier to remove at the end of its service life, but would need to be towed to port for extreme weather events. A two-pile, surface piercing platform would constitute a more significant infrastructure investment.

The research included six design alternatives for a test platform that were considered for technical and economic feasibility, in addition to a natural berth test bed concept. Neither the four-pile platform nor the fixed gravity foundation platform provided convenient access for developers. The submerged buoyant platform and the telescoping gravity foundation platform both provided access for developers but would require extensive proof-of-concept work and further development before being implemented. Since developer-friendliness and reliability were crucial factors in comparing design alternatives, all four of these concepts were rated lower after the preliminary engineering calculations and costing were completed.

Both the floating platform and the two-pile, surface piercing platform were analyzed in detail. This analysis focused on platforms capable of testing a maximum turbine diameter of 9 m (29 ft.) because the core of the maximum tidal current extends vertically over this range in the upper portion of the water column.

The floating platform would incur lower construction and installation costs (approximately $1 million) than the two-pile platform. It could be easily removed from the site when necessary, which could be very useful as the test site and testing procedures are being developed. As for a floating platform's performance in Muskeget's wave environment, it was found that a floating platform could typically operate for more than 90% of the year.

The two-pile, surface piercing platform would require more capital for construction and installation (approximately $2 million). However, testing from a fixed platform can be very beneficial to the developer and a permanent presence in the Muskeget Channel could be advantageous.

Furthermore, a natural berth would be necessary for developers wishing to evaluate complete systems (including mounting structure). Thus, it is recommended that natural berth be incorporated in addition to a testing platform.

The floating platform, the two-pile platform, and the natural berth were presented to the U.S. Coast Guard Waterways Management Division for comment. It was indicated that either option could be implemented in the Muskeget Channel (E.G. LeBlanc, *personal communication*). It was noted that the two-pile platform could even be used as an aid to navigation.

Given the lower cost of the floating platform and the present experience with such platforms, it is recommended that the Muskeget Channel tidal energy facility implement a floating platform as the near-term testing solution. Then, as the tidal energy industry grows, demand for the facility increases, experience with the testing site is gained, and funding becomes available, a two-pile, surface piercing platform could be implemented. Details of the analysis of the different test site options are explained in the final report which is included as Appendix 2.

Task 1.3 Wave Observations and Modeling in the NOREIZ- WHOI Project

Dr. E. Terray; Department of Applied Ocean Physics and Engineering; Woods Hole Oceanographic Institution submitted the final report for this part of the work in September 2013. The report is entitled, Wave observations and Modeling in the NOREIZ and is included in Appendix 3.

This project supplemented the acquisition of a Datawell MK-III Directional Waverider (DWR) by the New England Marine Renewable Energy Center (MREC) at the University of Massachusetts Dartmouth. Because high-quality, stand-alone measurements of waves is not a readily-available capability, it was understood that in addition to using the DWR in connection with this project, insofar as possible we would coordinate with other MREC activities in order to support them with wave measurements. A brief description of those supporting activities is presented here.

The original motivation for this project was to develop an operational capability to use the DWR, in terms of its mooring, telemetry, and data recovery, and to use the buoy measurements to validate a wave prediction model for MREC's proposed National Offshore Renewable Energy Innovation Zone (NOREIZ). This region, which was proposed as a testbed for wind and hydrokinetic power generation technology, is shown in Figure 1. The Commonwealth of Massachusetts and the Department of the Interior have announced Requests for Interest (RFIs) to lease blocks for wind power development in an area that abuts the western boundary of the NOREIZ region. For hydrokinetics, the main area of interest is the Muskeget Channel, which is located just to the east of Martha's Vineyard and lies at the northern edge of the NOREIZ. There is a strong tidal flow in this channel and MREC investigators were involved in a study commissioned by Edgartown to investigate the feasibility of installing tidal turbines there to provide supplemental power to the town. For the development and operation of both wind and tidal power generation facilities, knowledge of the wave climate is important mostly in relation to construction and maintenance since the waves are the primary limiting factor for

operations at sea. Consequently, the availability of reliable forecasts of the likely sea state (in terms of the heights, periods and directions of the most energetic waves) is an important capability.

These quantities are measured very well by the DWR system. A more detailed, spectral, description of the waves is required for the efficient operation of wave power generation devices. But since this is not a good region for wave power generation, we have not considered that application as a strong motivating factor.

At the start of this project, there was general consensus in the wave community that the SWAN spectral wave model (developed at the Delft University of Technology) was the leading model for predicting wave evolution in intermediate- and shallow-depth water. Although the project team started implementing that model, personnel changes prevented them from completing the work. However, over the life of the project, the performance of the NOAA wave model Wavewatch-III in intermediate and shallow water has improved considerably to the point where it is equivalent to SWAN in terms of suitability for the project requirements. A major advantage of Wavewatch-III is that as an operational model run by NOAA, its predictions are available on-line.

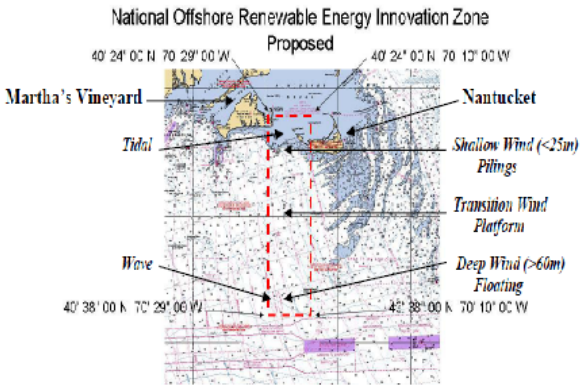

Figure 1 The proposed MREC NOREIZ region

The project task had several goals in this deployment:

1) to gain additional experience mooring (deploying/recovering) the DWR-III in deeper water, and to see if HF telemetry could be used reliably to distances of over 30 km,

2) to support HF radar measurements in a region covering the "area of interest" by both Massachusetts and the Department if the Interior for leasing to offshore wind power developers, and

3) to collect a high quality data set that can be used to test wave models to predict the wave climate in the lease region.

The project task addressed each of these goals as described below:

1) As discussed earlier in this section, we were successful in using a new HF antenna having substantially greater directivity to extend the useful range of the HF telemetry from the buoy. This will greatly facilitate future buoy deployments in this general region.

2) The goal of the HF radar work is to improve the ability of direction-finding (DF) HF radars to obtain information about the waves in the footprint of the radar. It is known that the backscattered power measured by a phased-array (PA) HF radar can be inverted to estimate the frequency-direction spectrum of the waves. However, such radars must employ relatively large arrays of antennas. For example, a 30 MHz radar has a 10 m wavelength. So a 16 element linear array with a half-wavelength spacing would be 75 m long. A longer-range radar operating at, say, 15 MHz would need an array over 150 m in extent. For this reason, people have preferred HF radars that make use of compact antennas (such as crossed dipoles) which require much less space to deploy. Such radars measure currents using direction-finding algorithms, but the wave signal is averaged over an annular region in azimuth and range, and cannot be obtained directly by inversion. Consequently, to test new ideas of how to extract wave information it is critical to have high quality wave measurements within the radar footprint. We recently recovered the buoy and were successful in obtaining a 3 month record of wave height and direction, contemporaneous with the radar, that can be used for this purpose.

3) The third goal was to obtain a relatively long record of wave observations in intermediate water depth, both to compare with wave models, and to see if the in-situ data could be used to initialize a simple wave model that would permit us to propagate waves kinematically over relatively short distances past he buoy. Although the potential DOI offshore lease area extends to much deeper water, our feeling is that 30-40 m is likely to be an upper limit for developers for the foreseeable future because the cost of the turbine support structures rises rapidly with increasing water depth. Consequently the buoy was just seaward of the regions that are likely to receive serious consideration by developers.

Task 1.3a Development of a Low-Cost Lidar for Wind Profiling in the Marine Atmospheric Boundary Layer

The goal of this project was to improve the performance of vertically-profiling wind Lidars using a pulse-compression technique borrowed from HF radar, and to demonstrate the feasibility of the approach by constructing a single beam profiling Lidar. The WHOI team from the Applied Pysics laboratory carried out the design study for a demonstration Lidar (in terms of the required optical and electrical engineering) before the realized that the basic idea was flawed. Although the believe they now have a different way to achieve their original goal, unfortunately they did not work it out until close to the end of the project period, and so were unable to acquire the necessary optical components (which differed from those required by our original proposal) required to demonstrate the approach.

The report which is included in Appendix 3a, includes a review and discussion of the technical underpinnings of the approach universally adopted (with small variations) by the vendors of the currently commercially-available Lidar vertical wind profilers. This will be followed by a recap of their original proposal and a discussion of what was flawed. They conclude with an analysis of the expected performance of a new method (at least when applied to Lidar) to reduce the velocity error. This method is widely used to improve the performance of Doppler sonar for measuring water velocity, and we find it somewhat ironic that a method borrowed from radar was not appropriate in the

optical domain, despite the equality of the propagation speeds, whereas a technique from acoustics likely will work. Results of those "lessons learned" can be found in the Appendix 3a.

Task 1.4 NOREIZ Wind Climate Assessments for Testing of Offshore Wind Generation Devices- UMA Project

NOREIZ Wind Climate Assessment was performed by University of Massachusetts Amherst researchers; Frederick Letson and James Manwell. They modeled the wind field and provided results in a final report that was submitted to New England MREC October 20, 2011. The report was included in totality with the Quarterly Report for Q9. The report is entitled, "Wind Resource Assessment for the National Offshore Renewable Energy Zone," (Appendix 4)

A wind resource assessment for the National Offshore Renewable Energy Innovation Zone (NOREIZ) was performed by the Wind Energy Center (WEC) at The University of Massachusetts, Amherst. This resource assessment was based primarily on re-analysis data from the Modern Era Retrospective-Analysis for Research and Applications (MERRA) project by the NASA Goddard Earth Sciences center.

Based on nine years of re-analysis data, the long-term mean wind speed representative of the NOREIZ area was calculated to be 8.33 m/s (18.6 mph*). The 50-year maximum expected hourly average wind speed was calculated to be 30.3 m/s (67.8 mph*).

Prevailing winds in the NOREIZ area are from westerly directions: generally Northwest in the winter and Southwest in the summer.

Additional information about interpreting the data presented in this report can be found in the Fact Sheet, "Interpreting Your Wind Resource Data," produced by the WEC and the Massachusetts Technology Collaborative (MTC). This document is found through the WEC website: http://www.umass.edu/windenergy/publications/published/communityWindFactSheets/RERL_Fact_Sheet_6_Wind_resource_interpretation.pdf. (Reference 6 Executive Summary Appendix 4)

Offshore Wind Economic and Environmental Impacts UMA Project

A Review and Comparison of The Environmental Impacts of Construction of Offshore Wind Farms: Nearshore Bottom Mounted VS Farshore Floating", Final Project Report, NOREIZ Sub-Contract University of Massachusetts Dartmouth and University of Massachusetts Amherst, by Micah Brewer, Jon McGowen, James Manwell. Wind Energy Center at the Dept. of Mechanical and Industrial Engineering at UMass Amherst, December 2011. (Appendix 5)

A primary focus of the report is a review of the available literature on the environmental impacts of offshore wind turbines, both fixed and floating. A majority of the environmental studies have been out of Europe, but there have been important environmental impact assessments performed in the United States.

Detailed comparisons of the relative environmental impacts of the commonly used offshore wind foundations and support structures is explored. (Appendix 5)

.

"Similar to onshore wind systems, the environmental effects of offshore wind farms are expected to

play an important part of the development of future large-scale wind energy systems. This report presents a detailed review of the status of, and recent developments in, research on the environmental impacts of fixed and floating offshore wind turbine systems. A significant amount of information that has been reviewed has come from European sources where a large number of offshore installations have been installed, but some work on this subject has been carried out recently in the United States. By synthesizing available information on the environmental impacts of benthic organisms, fish, marine mammals, avian species and bats, an extensive review of the effects of fixed and floating offshore wind turbines is presented". (Brewer,M., 2011)

The environmental impacts between floating and fixed systems are anticipated to be highly variable due to multiple parameters that need to be taken into account when identifying environmental impacts, however general patterns are identified. Additionally, these impacts varied throughout the lifecycle of the offshore wind system. The focus was narrowed down to analyze the environmental impacts through the scope of barrier and habitat impacts in addition to the rate of mortality for avian species and bats. In addition a noise propagation model was used to determine the extent of effects due to the installation of fixed and floating support structures using piling installation methods. Finally, a summary of progress in all the major environmental impact areas is given along with recommendations for future research on this important subject. (Appendix 5)

Task 1.5 General Sullivan Bridge Tidal Assessments UNH Project

The final report for this part of the project was submitted as part of the Quarter 10 Report in January 2012. It is included in its entirely in Appendix 6, Final Report UNH/CORE MHK Sites' Resource Assessment Preliminary Results.

"To support emerging technologies in the ocean renewable energy field, the University of New Hampshire established two in-situ test sites located in the coastal waters of New Hampshire. A marine hydrokinetic turbine test site was found in the Great Bay Estuary (adjacent to the General Sullivan Bridge) to allow testing of up to ½ scale commercial devices. The wave testing site is 10km southeast of Portsmouth, NH. This is the former Open Ocean Aquaculture site which was established in 1996. " (UNH CORE, 2012)

To support this effort UNH started measuring tidal current velocities at this site. The tidal energy site required an examination of tidal currents as a function of depth, across the channel as a function of position and time. This measurement regime will provide a more detailed perspective on the structure of the tidal currents in space and how this varies with time. These types of measurements are best done via ADCP transects across the site. For the wave site that is further offshore, it was important to have an understanding of the significant wave heights and dominant periods broken down by mouth to optimize best deployment windows.

The tidal velocities at the General Sullivan Tidal Test site can approach 6 knots. Further the GSB test site tidal resource was most recently tested using an ADCP mounted on a CBASS jet-ski which provided high maneuverability and enabling multiple transects across the site. The currents have been assessed in that same site over the years in preparation for it being used as a tidal energy test site however those data were only collected for one point in the tidal cycle. The data for these transects are included in Appendix 6.

Offshore Wave Site, in 1999 UNH established an open ocean aquaculture site in 52 meters of water approximately 10 km from the New Hampshire coast in the gulf of Maine. For 10 years the site was utilized to test the engineering and biological feasibility of offshore aquaculture including the deployment of fish cages, moorings, surface buoys. During this time UNH also deployed an environmental buoy to measure waves at the site. In 2010 the aquaculture gear was decommissioned due to funding issues. It turns out that UNH had collected wave data for almost all ten years of the aquaculture projects. A few years ago it became clear that UNH had the expertise to re-purpose the open ocean aquaculture site to use for testing wave energy devices. UNH focused on permitting the site for wave energy applications

The first task was to organize all the wave data obtained over the years. Although the buoy was out there for 60-70% of the time, the data stream was not continuous. In addition UNH personnel wanted data in a format that was similar to that employed by the National Data Buoy Center, so wave data could be easily compared across the country and other test sites.

Data were obtained from the NDBC #44005. According to the final report, Appendix 6, this buoy was found to have similar wave characteristics as the UNH site. The wave data presentation was done using MatLab code to perform the requisite spectral analysis and present the significant wave height and period and statistical values on a daily basis. These results provide a potential developer with an easily understandable view of what to expect at the site during specific times of the year. The data are included in the report and will be posted to the UNH/CORE Server/website for developers and others.

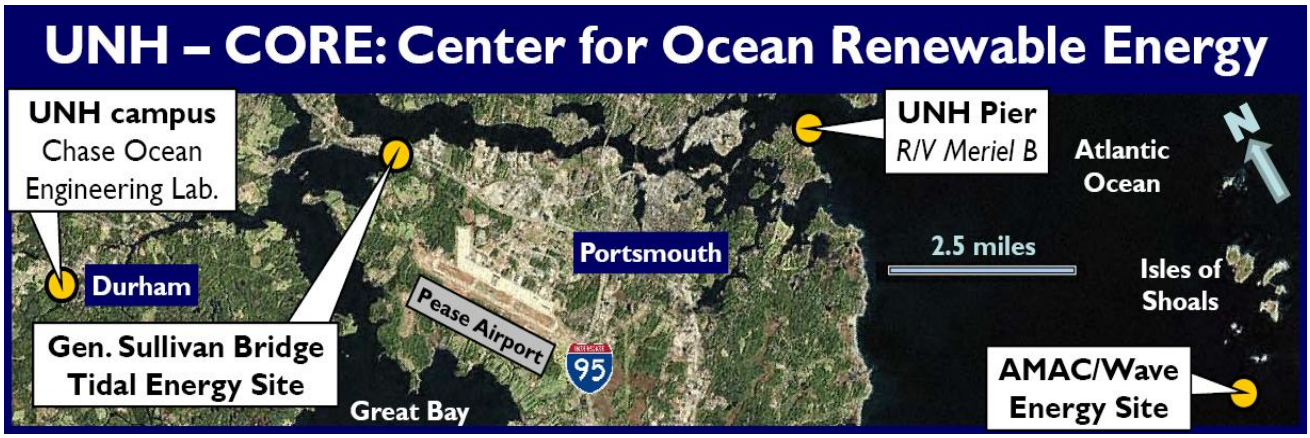

The map above shows key sites of the Center for Ocean Renewable Energy (CORE), University of New Hampshire: Ocean Engineering Laboratory, Tidal and Wave Energy Test Sites, UNH Pier (staging, support vessels). Note the geographic proximity (horizontal bar = 2.5 miles).
Figure 2: (Source: www.unh.edu/core)

Tidal Energy Test Site: The UNH tidal energy test site is at the General Sullivan Bridge where the Lower Piscataqua enters Little Bay through a constriction. The tidal range is nominally 8.2 ft (2.5 m), and approximately 40 percent of the volume of Great Bay flows under the bridge every tidal cycle. This results in peak current speeds of greater than 4 knots (2 m/s), as well as relatively short periods of slack water and a steep current speed ramp-up. UNH-CORE faculty have modeled the dynamics of this tidal system in several studies. This site is considered a full-scale test site for vertical axis

turbines, while it can be considered a “large-scale” test site (geometric scale 1:3-1:5) for large diameter horizontal axis turbines.

Wave Energy Test Site: The wave energy test site is located at the UNH Atlantic Marine Aquaculture (AMAC) site, which covers an area of 30 acres in 170 ft (52 m) of water approximately 6 miles from the New Hampshire coast. It has been successfully deployed under extreme New England winter conditions as a demonstration site for open ocean aquaculture for the past 10 years. The site has a subsurface mooring system and a large feed buoy (AMAC) is available as a useable platform and a potential end user load for any wave energy extraction device. The site comes with a dedicated 50 ft research vessel (Meriel B). Available environmental data consisting of wave monitoring, benthic and water column environmental data, and bathymetry obtained by the UNH Center for Coastal and Ocean Mapping (C-COM) will be essential for the quick successful deployment of a given energy extraction device, and makes this a cost effective wave energy test site. (www.unh.edu/core)

Task 2 High Potential Research

At the outset of this project MREC proposed addressing two high potential research areas that were both needed by the industry and that matched the interests of researchers in the Consortium. One of the projects proposed modeling wave energy conversion buoys laid out in arrays. MIT professor C.C. Mei initially was on board to do this work but had to withdraw his proposal and therefore his award. In addition Dr. Annette Grilli of University of Rhode Island and a graduate student, Taylor Asher completed their proposed work to develop a design tool to analyze the performance of wave energy systems.

Task 2.1 Array Wave Modeling Modeling performance of buoys design for wave extraction is a critical element in design. MIT’s Chiang C. Mei, has extensively modeled the hydrodynamics of buoys with regard to power extraction. As stated earlier, this project was not started. Funds were reallocated.

Task 2.2 Linear Electric Generator (LEG) Design Tool URI Project (Appendix 7)
Linear Electric Generators (LEGs) are the primary energy conversion devices in many wave Energy Conversion devices. URI has developed several WEC devices and determined that modeling of the LEG was a critical need for in the industry. URI will develop and validate a fully integrated design tool, that will include the ability to simulate heave (or even roll) dominated wave energy conversion devices. In addition the availability to simulate buoy motion the tool will include the mechanical, electric control system responses of the LEG, for both regular and random seas, as a function of the many parameters governing the design. The tool will also feature an ability to animate system response to assist in presenting data to scientific and lay audiences.

Professor Annette Grilli, of University of Rhode Island and her graduate student, Taylor Asher teamed up with Electro Standards Laboratories a RI manufacturer on this project. Funding came from a combined set of sources including: ONR, the State of RI (STAT Alliance), URI and MREC. The project addressed the design, numerical simulation, and scale model and field testing of a small buoy system for multi-directional wave energy harvesting. The actual application for these systems is to develop fairly simple, easily deployable, and storm resilient systems to generate wave energy (about 1kW) for distributed marine surveillance and instrumentation systems (underwater sensors, target recognition devices, tracking and identification of vessels and miniature sensor networks). Several buoy designs

were evaluated through a combination of theoretical analysis and numerical simulations for periodic and irregular waves. Those studies lead the researchers to choose two specific buoy configurations DC2 and DC3. (See Figure 1 page 3 final report in Appendix 7) According the aforementioned report, both systems produce energy by using the kinetic energy created by wave motion which produces electricity via induced coupled oscillation of a Linear Electric Generator (LEG) located in a central spar (cylinder) buoy. Scale models were built for both buoy types and tests were performed at the URI wave tank. These successful tests then lead to upping the size of both buoys to 1:4 scale which were slated to be field tested. The DC3 was in fact tested out in Narragansett Bay, RI. The data and a detailed accounting of the all tests is included in the final report in Appendix 7.

Since the final report was submitted, the research has been either presented at or published in several conference proceedings. Also at least one master's thesis resulted from the project, Taylor Asher, (OCE-MS) Autonomous Ocean Wave Energy Conversion Systems, URI, Spring 2011.

Task 3 Project Management and Public Outreach

Task 3.1 Project Management and Reporting

Project technical and financial status was reported on a quarterly basis by the New England MREC personnel from Award start through Q-13. After that time, there was a personnel change, Q-14 report was waived by DOE Project Manager to facilitate preparation of this final report. All documentation is located at UMass Dartmouth and was shared with the MREC Consortium, as required by the contract or agreed upon by the appropriate project manager.

Task 3.2 Public Outreach and Technical Exchange

MREC made all reasonable efforts to sponsor conferences and exchanges to involve all stakeholders in the development of marine renewable energy. Technical exchanges and other appropriate conference attendance, as approved by the Consortium, were supported, and the information was disseminated widely. Information exchange was encouraged between the SuperGen Marine Consortium in the UK, the Ocean Renewable Energy Group in Canada, as well as with numerous ocean energy industry organizations, government agencies and non-profits with interest in ocean renewable energy monitoring and development. Workforce training groups were also included as a way to explore the readiness of skilled workers when ocean energy devices come on stream for testing, evaluation and eventual commercial use.

Stakeholder Outreach Activities

New England MREC was established in 2008 by bringing together the many stakeholders who would care about ocean energy system being deployed in NE waters. The first stakeholder conference was held at the UMass Dartmouth, Advanced Technology and Manufacturing Center in Fall River, MA. Funding for that event was provided by the MA Clean Energy Center as a way to test the waters so to speak to understand what the issues would be relative to introducing wind, wave, or tidal power to the region. That first event was very well attended and laid the foundation for subsequent stakeholder and then technical conferences that followed on and are listed in the table below.

In the non-profit field, where budgets and staff time is at a premium, trade agreements are made between like-minded groups to help each other get the word out about one another's events and news items. New England MREC has partnership agreements with the Ocean Renewable Energy

Group in Canada; (recently rebranded Marine Renewables Canada; the Ocean Renewable Energy Coalition in Washington, DC; New England Clean Energy Council of Boston, Maine Wind Industry Alliance, the International Network of Ocean Renewable Energy students (INORE), and the Oregon Wave Energy Trust. There is strength in numbers and in collaborations. By working together these organizations have been able to leverage precious resources to accomplish much more together than if anyone would be able to alone.

While New England MREC has partnered with groups to assist with their events, MREC has created and executed many events specifically targeted to local, regional, national and international audiences. The stakeholder events that were held early on convened regulators, fishermen, policy makers, developers to educate one another about the complications of putting ocean energy devices in in new England waters. Federal regulators from FERC and Minerals Management Service, now, BOEM attended a these forums regularly as way to meet people in the area to establish relationships with key stakeholder groups. This work has paid off well, in their subsequent work to scope out areas of the ocean that would be better suited to developing ocean energy, specifically offshore wind before the leasing process went forward.

Representatives of the New England MREC have served in various capacities on several non-profit and/or non- governmental organizations (boards, committees, advisory councils) such as the Massachusetts Ocean Partnership, Environmental Business Council of New England, Marine and Oceanographic Technology Network, others. Having a “seat at the table” so to speak has facilitated open communication about ocean energy technologies and their social, environmental, technical as well as economic impacts.

Exhibiting, speaking or attending industry conferences and trade shows has been an effective method for networking to meet the key players in the ocean energy industry as well as illustrating that New England MREC is “open for business”. It was via conferences such as Energy Ocean where New England MREC made many international connections with device developers seeking US locations to potentially test their equipment.

Table 1 New England MREC Stakeholder and Technical Conferences

Event & Location	Date	Attendees / Reach	
Energy Ocean 2013, Warwick RI	June 10-12, 2013,	300	
MA Dept. Transportation Energy Expo. , Boston, MA	22-May-13	800	
Canadian Consulate General Marine Tech. Event, New Bedford, MA	4/30/2013,	60	
4th Tech Conf. Warwick, RI	Jan. 10, 2013	122	
4th Tech. Conf. Webinars	Jan. 8-9, 2013	35	
4th Tech. Conf. Warwick, RI (cancelled by hurricaine)	Oct. 31, 2012		
Muskeget Test Open House, Marthas Vineyard	Aug.22. 2012	80	
Wind, Wave, Tidal Power Open House, Fairhaven, MA	July 13,2012	80	
Energy Ocean 2012 Danvers, MA; Speaker, exhibitor, co-sponsor	June 19-21, 2012	400	
Ocean Energy Workforce Summit; Portland, ME	May-12	95	
Global Marine Renewable Energy Conf. (Wash.DC) - Exhibitor	April, 2012	290	
3rd Annual Tech. Conf. MREC (Cambridge, MA)	Nov. 7-8 2011	125	
Muskeget Channel Tidal Demos (Edgartown, MA)	Aug. 10-15, 2011	30	

Table 1 – Continued

Event & Location	Date	Attendees / Reach	
Global Marine Renewable Energy Conf. (Seattle, WA); Speaker, exhibitor	April, 2011	300	
Nortek USA Symposium Speaker (Newport, RI)	March 16-17, 2011	100	
6th Conf. on Clean Energy (Boston, MA) Ocean Energy	Nov. 3-4, 2010	120	
2nd Annual Tech. Conf. MREC (Cambridge, MA)	Nov. 2, 2010	135	
1st Annual Tech. Conf. MREC (Fall River, MA)	Oct. 15, 2009	88	
2nd Annual Ocean Energy for NE Stakeholders Conf.-(Hyannis, MA)	Sept. 17, 2009	150	
1st Annual Ocean Energy for NE Stakeholder Conf. - Fall River, MA	Oct. 6, 2008	185	
Total direct contacts made		**3,937**	
Additional reach due to partnerships, co-sponsorships, co-promotions		**23,000**	
Persistent publicity via energy and marine trade communications outlets			
Main stream media placements (New Bedford Standard Times, WGBH Radio; Boston Globe, local television coverage of open houses			

Products (Publications, Presentations, Conferences) Resulting From This Contract

Numerous publications, presentations, abstracts, and conferences were organized as a direct result of this contract. A list of those products is included here. Links to web sites where more detailed information and in some cases actual presentations are also included for quick reference.

Publications

Asher, T., (OCE-MS). *Autonomous Ocean Wave Energy Conversion Systems*. *Non thesis option*. Ocean Engineering, Master's Thesis, University of Rhode Island. Spring 2011.

Barrett, Stephen, The Muskeget Channel Tidal Energy Project: A Unique Case Study in the Licensing and Permitting of a Tidal Energy Project in Massachusetts, *Marine Technology Society Journal,* Marine Renewable Energy Technologies; Vol. 47, No. 4, July/August 2013.

Dewhurst, T.,Swift, R, Wosnik, M, Baldwin, K, DeCew, J, Rowell, M. "Dynamics of a Floating Platform Mounting a Hydrokinetic Turbine", *Marine Technology Society Journal*, Marine Renewable Energy Technologies; Vo. 47, No.4, July/August 2013.

Grilli, A.R. and T. Asher 2011.Development of an Integrated Design Tool for Wave Energy Conversion Devices used to Power Coastal Surveillance Systems. *Final Technical Report* for DOE-MREC grant. Ocean Engineering, University of Rhode Island, 44 pps.

Hakim, A, Cowles, G, Churchill, J. The Impact of Tidal Stream Turbines on Circulation and Sediment Transport in Muskeget Channel, MA, *Marine Technology Society Journal*: Marine Renewable Energy Technologies; Vo. 47, No.4, July/August 2013. Hakim, A., Cowles, G., & Churchill, J. (2013). The Impact of Tidal Stream Turbines on Circulation and Sediment Transport in Muskeget Channel, MA. *Marine Technology Society Journal* 47(4), 122-136.

***Hakim, A**., Cowles, G., & Churchill, J. (in preparation). A high resolution numerical model for tidal energy resource assessment in Massachusetts.*

Kirincich,A, Toward Real-time, Remote Observations of the Coastal Wind Resource Using High-Frequency Radar*, Marine Technology Society Journal*: Marine Renewable Energy Technologies; Vo. 47, No.4, July/August 2013.

Miller, J., "The Return of NEMED", Marine Technology Reporter, May 17, 2012 (http://www.seadiscovery.com/mtStories.aspx?ShowStory=106229)

Merrill, M.," Test Sites Needed to Launch US Ocean Energy Industry", Sea Technology Magazine, April 2010.

Rowell, M, Wosnik, M, Barnes, J, King, J. Experimental Evaluation of a Mixer-Ejector Marine Hydrokinetic Turbine at Two Open-Water Tidal Energy Test Sites in NH and MA. *Marine Technology Society Journa*l: Marine Renewable Energy Technologies; Vo. 47, No.4, July/August 2013.

Schlezinger,D, Taylor, C, Howes, B. Assessment of Zooplankton Injury and Mortality Associated with Underwater Turbines for Tidal Energy Production. *Marine Technology Society Journal*: Marine Renewable Energy Technologies; Vo. 47, No.4, July/August 2013.

Presentations

Gemme, D., Bastien, S.,Sepe, R., Montgomery, J., Grilli, S., Grilli,,A.,2013. Experimental Testing and Model Validation for Ocean Wave Energy Harvesting Buoys.In Proc. Energy Conversion

Congress and Exposition (ECCE) *conf*. (Denver, CO, September 16 -20, 2013.

Grilli A., 2013. Marine Hydrokinetic Energy. Part 1: Wave Power, sustainable? Presentation for the Metcalf Institute program, Peter B. Lord Seminars series, GSO, URI, March 15 2013.

Hakim, A., Cowles, G., & Churchill, J. "A High Resolution Model for the Resource Assessment of Tidal Kinetic Energy and Evaluation of Impacts." **January 2013,** 4th Annual New England Marine Renewable Energy Center Technical Conference.

Howes, B. L., R. Samimy, D. Schlezinger. "**Oceanographic Data Collection in Muskeget Channel for Siting to Maximize Power." October 2009,** 1st Annual New England Marine Renewable Energy Center Technical Conference.

Howes, B.L., Samimy, R.I., Schlezinger, D.R., Bartlett, M. A , Benson, J.L., White, D. "Macro to Micro: Finding the sweet spot for marine hydrokinetic technology deployments, Muskeget Channel Case Study." November 2010, 2nd Annual New England Marine Renewable Energy Center Technical Conference.

Howes, B. L. Schlezinger, D. R. Samimy, R. I. "Field Investigations to Project Near Field Environmental Responses to Installation and Operation of Marine HydroKinetic Energy Generators: Muskeget Channel Case Study" November 2011, 3rd Annual New England Marine Renewable Energy Center Technical Conference.

Samimy, R.I. "Characterization of Muskeget Channel In-Stream Tidal Resources." July 2011. Marine Energy Workshop Pontificia Universidad Catolica de Chile

Samimy, R.I. "Tidal Resources of Muskeget Channel." October 2012. Chilean Delegation FIU - UMASS Miami, Florida

Schlezinger, D.R., Howes, B.L., Samimy, R.I., Bartlett, M. A. "Environmental Effects of Sediment Transport Alteration and Impacts on Protected Species: Edgartown Tidal Project Topic Area II: Marine Science and Hydrokinetic Site Specific Environmental Studies University of Massachusetts-Dartmouth, SMAST. February 2012. Department of Energy Webinar.

Schlezinger, D. R., Samimy, R. I., Howes, B. L. "In situ testing of tidal turbines in Muskeget Channel." June 2012, EnergyOcean International 10th Annual Conference.

Schlezinger, D. R., Singh, S., **Howes, B. L. "**Using AUVs to Survey Potential Hydrokinetic Energy Sites." **November 2011,** 3rd Annual New England Marine Renewable Energy Center Technical Conference.

Wosnik M; Baldwin K; Celikkol B; Swift R; Gress D; Carter M; Tsukrov I; White C (2010) "Ocean Renewable Energy Research and Infrastructure Development at the University of New Hampshire", presentation to DOE program manager A. Moreno and colleagues, 7 August 2010

Wosnik M; Bachant P; Nedyalkov I; Rowell M; Dufresne N; Lyon V; "Marine Hydrokinetic (MHK) Energy Conversion Research at UNH: From Fundamental Studies of Hydrofoil Sections, to Moderate Reynolds Number Turbine Tests in a Tow Tank, to Open Water Deployments at Tidal Energy Test Sites." *Invited Lecture* in Ocean Sciences at Fall Meeting of American Geophysical Union (AGU) in San Francisco, CA, 12 Dec 2013.

Conference Proceedings:

Grilli, S.T., Grilli, A.R., Bastien, S.P., Sepe, Jr., R.B., and M.L. Spaulding 2011. Small Buoys for Energy Harvesting: Experimental and Numerical Modeling Studies. In *Proceedings 21st Offshore and Polar Engineering Conference* (ISOPE11, Maui, HI, USA, June 19-24, 2011), 598-605, Intl. Society of Offshore and Polar Engineering.

Wosnik, M; Swift MR; Baldwin KC; Despins R; Celikkol B (2010) Infrastructure Development towards a Calibrated Tidal Energy Test Site at the University of New Hampshire. *Proceedings of First*

European Congress of the Int'l Association of Hydraulic Research (IAHR), Edinburgh, Scotland, May 4-6, 2010.

Published abstracts:

Byrne J; Swift MR; Wosnik M; Baldwin K; Celikkol B (2012) Design of the Next Generation Tidal Energy Test Platform at UNH-CORE. Extended abstract for *4th Annual NE-MREC Technical Conference,* New England Marine Renewable Energy Center, Providence/Warwick, RI, 7-8 & 10 January 2013.

Byrne J; Swift R; Wosnik M; Celikkol B; Baldwin K (2011) Test Platform for Evaluation of Large Scale Hydrokinetic Turbines at UNH-CORE Tidal Energy Test Site. *3rd Annual NE-MREC Technical Conference,* New England Marine Renewable Energy Center (NE-MREC), Cambridge, MA, 7-8 November 2011.

Byrne J; Swift R, Wosnik M (2010) Second Generation Tidal Energy Test Platform for UNH-CORE Tidal Energy Test Site. *2nd Annual NE-MREC Technical Conference,* New England Marine Renewable Energy Center (NE-MREC), Cambridge, MA, 2 November 2010.

Dewhurst T; Rowell M; DeCew J; Baldwin K; Swift MR; Wosnik M (2012) Turbulent inflow and wake of a marine hydrokinetic turbine, including effects of wave motion. 65th Annual Meeting of the APS Division of Fluid Dynamics, 18-20 Nov, San Diego, CA. *Bull. Amer. Phys. Soc.*, Vol.57. No.17, p.146.

Rowell M; Wosnik M (2013) Experimental Evaluation of Mixer Ejector Hydrokinetic Turbine (MEHT). Extended abstract for *4th Annual NE-MREC Technical Conference,* New England Marine Renewable Energy Center (NE-MREC), Providence/Warwick, RI, 7-8 & 10 January 2013.

Wosnik M; Baldwin K; Celikkol B; Swift R (2010) Marine Hydrokinetic (MHK) Testing Infrastructure Development. *2nd Annual NE-MREC Technical Conference,* New England Marine Renewable Energy Center (NE-MREC), Cambridge, MA, 2 November 2010.

Conference Poster Presentations:

Bachant P; Dewhurst T; Johnston A; Byrne J; Wosnik M; Swift R; Baldwin K; Celikkol B (2010) Works in progress - An overview of ongoing research at the UNH Center for Ocean Renewable Energy. *2nd Annual NE-MREC Technical Conference,* New England Marine Renewable Energy Center (NE-MREC), Cambridge, MA, 2 November 2010.

Byrne J; Rowell M; Dewhurst T; Wosnik M; Swift R; Baldwin K; Celikkol B (2011) Second Generation Tidal Energy Test Platform for UNH-CORE Tidal Energy Test Site. 4th Global Marine Renewable Energy Conference (GMREC) in Washington, DC, 28-29 April 2011.

Dewhurst T; Byrne J; Rowell M; Swift R; Wosnik M; Baldwin K; Celikkol B; Miller J (2011) Development of Tidal Energy Deployment Platforms for the Muskeget Channel Test Site – a Joint Project Between UMASS and UNH. 4th Global Marine Renewable Energy Conference (GMREC) in Washington, DC, 28-29 April 2011.

Rowell M; Johnston A; Byrne J; Bachant P; Dewhurst T; Wosnik M; Swift R; Baldwin K; Celikkol B (2011) Progress report on ongoing research at the UNH Center for Ocean Renewable Energy. 4th Global Marine Renewable Energy Conference (GMREC) in Washington, DC, 28-29 April 2011.

Wosnik M; Baldwin K; Celikkol B; Swift R (2011) Infrastructure and Test Sites at Center for Ocean Renewable Energy (CORE) at University of New Hampshire. 4th Global Marine Renewable Energy Conference (GMREC) in Washington, DC, 28-29 April 2011.

Wosnik M; Baldwin K; Celikkol B; Swift R (2010) Infrastructure and Test Sites at Center for Ocean Renewable Energy (CORE) at University of New Hampshire. *2nd Annual NE-MREC Technical Conference,* New England Marine Renewable Energy Center (NE-MREC), Cambridge, MA, 2 November 2010.

Wosnik M; Baldwin K; Celikkol B; Swift R (2010) Infrastructure and Test Sites at Center for Ocean Renewable Energy (CORE) at University of New Hampshire. 3rd Global Marine Renewable Energy Conference (GMREC) in Seattle, WA, 14-15 April 2010.

Sponsored Conferences:

New England MREC Stakeholder and Technical Conferences
www.mrec.umassd.edu/conference
1st Annual Ocean Energy for New England, October 6, 2008, Fall River, MA http://www.mrec.umassd.edu/agendasandpresentations/oceanenergyfornewenglandconference2008/
2nd Annual Ocean Energy for New England Conference, September 17, 2009, Hyannis, MA http://www.mrec.umassd.edu/agendasandpresentations/oceanenergyfornewenglandconference2009/
1st Annual New England MREC Technical Conference; October 15, 2009, Fall River, MA http://www.mrec.umassd.edu/agendasandpresentations/1stannualmrectechnicalconference/
2nd Annual New England MREC Technical Conference; November 2, 2010, Cambridge, MA http://www.mrec.umassd.edu/agendasandpresentations/2ndannualmrectechnicalconference/
3rd Annual New England MREC Technical Conference; November 7, 2011, Cambridge, MA http://www.mrec.umassd.edu/agendasandpresentations/3rdannualmrectechnicalconference/
Ocean Energy Workforce Development Summit, May 4, 2012, New Bedford, MA http://www.mrec.umassd.edu/agendasandpresentations/oceanenergyworkforcesummit2012/
4th Annual Marine Renewable Energy Technical Webinars and Conference; January 7, 8 & 10, 2013; Warwick, RI http://www.mrec.umassd.edu/agendasandpresentations/4thannualtechnicalconference/
Ocean Energy Technical Sessions @ Oceans13MTSIEEE San Diego; September 26, 2013. New England MREC coordinated four 90 minute sessions. http://www.oceans13mtsieeesandiego.org/searchprogram.cfm?trID=36

Conclusions:

1. Based upon the determinations of the velocity field within Muskeget Channel in 2008-09 (as funded by the grant from the Massachusetts Technology Collaborative), it was clear that hydrokinetic energy generation potential using underwater turbines presently exists within a very specific portion of Muskeget Channel (the southern region of the Town of Edgartown FERC permit area). The initial investigation into the hydrokinetic energy potential of Muskeget Channel also revealed that further surveying of currents would be required to refine the best location for tidal energy generation technologies. In addition, data collection on the environmental characteristics of the area would be necessary to begin to ascertain the potential impacts resulting from tidal energy generation in Muskeget Channel, specifically the routing of cables to bring tidal power ashore to Martha's Vineyard. These data would further support the Town of Edgartown in its development of a pilot scale tidal energy project while also yielding valuable baseline data sets useful in the establishment of the NOREIZ by MREC.

2. The floating platform, the two-pile platform, and the natural berth were presented to the U.S. Coast Guard Waterways Management Division for comment. It was indicated that either option could be implemented in the Muskeget Channel (E.G. LeBlanc, *personal communication*). It was noted that the two-pile platform could even be used as an aid to navigation. Given the lower cost of the floating platform and the present experience with such platforms, it is recommended that the Muskeget Channel tidal energy facility implement a floating platform as the near-term testing solution. Then, as the tidal energy industry grows, demand for the facility 103 increases, experience with the testing site is gained, and funding becomes available, a two-pile, surface piercing platform could be implemented.

3. Using a new HF antenna having substantially greater directivity to extend the useful range of the HF telemetry from the buoy. This will greatly facilitate future buoy deployments in this general region.

4. It is recommended that collecting on-site wind data for the NOREIZ. Measured data, either from conventional anemometry or remote sensing would increase confidence in the wind climate characterization described in this report. Ideally, wind data would be collected with anemometry on an offshore tower and a LIDAR would be used as well to better assess the wind speeds at greater heights. In addition, wave data should be taken simultaneously so that joint probability of occurrences of wind and waves could be ascertained. Simultaneous wind and wave date would also facilitate better understanding of the variation of wind speed with height under various climatic conditions.

Recommendations for Future Work

The work described herein is the culmination of 5 years of collaboration between research partners. One partner that was not officially included in this particular project, but factored crucially, for related projects funded by NOPP and MCEC, was the operations and management department at the Massachusetts Maritime Academy located in Buzzards Bay, Massachusetts. As a full scale maritime training and degree granting institution, MMA engages in applied research as it relates to existing courses on power generation, renewable systems engineering, tidal energy power take off design and more. Located at the west entrance to the commercially accessible Cape Cod Canal, MMA is perfectly situated to provide all manner of waterfront and maritime support activities. In 2010 MMA took delivery of a test barge that was built for Verdant Power of New York. That barge was renovated to accommodate at least two tidal turbines that were tested in Muskeget Channel by UNH and a private company. Those demonstrations could not have been performed if not for the advance work of the DOE Task 1 scientific characterization work. Additionally, having MMA's expertise in naval architecture, propulsion systems, mechanical engineering, marine engineering, welding, and electric power generation was extremely valuable to the outcome of the demonstrations.

As a direct result of the relationships created doing those demonstrations, MMA administration and UMD are discussing the creation of an informal partnership to build a dockside MHK device test site for research, industry and for student educational purposes. Funding for the proposed test platform is in the process of being secured and plans are to have it operational in the Spring 2014. This collaboration will build upon the groundwork done by the MREC research team and the MMA operational staff. MMA has the people and the capabilities to continue to provide field support for continued work in Muskeget Channel and further off in the BOEM approved tracks within the NOREIZ area and beyond if needed. The SMAST scientific team has the expertise to provide the analytical work on the immediate environment and on the device performance overall.

Bureau of Ocean Energy Management (BOEM) approval of the three lease blocks located within the proposed NOREIZ is a tangible result that will enable that area to be considered by industry or researchers in the future to test larger scale offshore wind, wave or tidal devices. Working in the waters near Nantucket can be supported by pre-positioned small research vessels located in Nantucket, Edgartown, New Bedford or in Falmouth, MA. This support can be provided by MMA and or by private contractors skilled in deploying marine instrumentation and conducting oceanographic and marine environmental monitoring services. There is a skilled maritime workforce located throughout Southern New England to provide support to these test sites and equipment demonstrations.

Federal Energy Regulatory Commission (FERC) approval of the operational site within Muskeget Channel will last three years from date of issue. Currently the Town of Edgartown is at a stand still on making any progress in terms of placing a turbine in the approved site due to lack of funding. If funding were to materialize, or an industrial partner, a concerted effort would result to choose and install a small scale tidal turbine for consideration to produce electricity into the Martha's Vineyard municipal grid.

The project described in this report helped characterize and suggest infrastructure to support the operations of 4 ocean related test sites (Martha's Vineyard, NOREIZ, General Sullivan Bridge, and the

re-purposed Offshore Wave Test site off New Hampshire. These sites can all be supported by a local workforce housed in universities, government agencies and private industry.

Next steps include identifying several device developers who want to test their units in one of these ocean sites. In order to accomplish this, additional funding would be required.

References (In order of appearance in text)

MA Ocean Plan; Oceans Act: June 30, 2009, MA Office of Energy and Environmental Affairs http://www.mass.gov/eea/ocean-coastal-management/mass-ocean-plan/

1st and 2nd Ocean Energy for New England Stakeholder Conferences; Sept. 17, 2009 and October 6, 2008 respectively.

Co-Editors; MTS Journal Marine Renewable Energy Technologies; Vol.47, No,4, July/August 2013.

National Ocean Renewable Energy Innovation Zone (NORIEZ) Flier, http://www.mrec.umassd.edu/resourcecenter/noreizandmarineplatform/

Appendix 1; Howes. B, Samimy,R., Schlezinger,D., Bartlett,M., Benson,J., White,D., Follow-on Data Collection and Synthesis of Muskeget Channel Hydrokinetic Potential and NOREIZ Wave & Wind Energy Potential", Coastal Systems Program, School of Marine Science and Technology, University of Massachusetts Dartmouth, Submitted September 20, 2013.

Appendix 2; Executive Summary, Swift, R., Baldwin, K., Wosnik,M., Celikkol,C., Dewhurst,T., "Muskeget Channel Tidal Energy Test Facility Design Concepts", Final Report for New England MREC Project. May 2013.

Appendix 3; Terray,E., Wave Observations and Modeling in the NOREIZ, Woods Hole Oceanographic Institution, Spring 2013.

Appendix 3a; Terray, E.,Sonnichsen,F., Development of a Low-Cost Lidar for Wind Profiling in the Marine Atmospheric Boundary Layer, Final Report, Submitted to New England MREC. October 2013.

Appendix 4: Letson, F., Manwell, J.,Wind Resource Assessment for the National Offshore Renewable Energy Zone, Final Report, Submtted to New England MREC. October 2011.

Appendix 5: Abstract, Brewer, M., McGowan, J., Manwell, J., A Review and Comparison of the Environmental Impacts of Construction of Offshore Wind Farms: Nearshore Bottom Mounted vs. Farshore Floating, Prepared for Marine Renewable Energy Center, December 30, 2011.

Appendix 6: Executive Summary, UNH Center for Renewable Energy, Chase Engineering Laboratory, UNH., "UNH/CORE MHK Sites' Resource Assessment Preliminary Results", Final Report Marine Renewable Energy Center, New Bedford, MA (January, 2011)

Appendix 7: Grilli, A., Asher,T., Development of an Integrated Design Tool for Wave Energy Conversion Devices used to Power Coastal Surveillance Systems, University of Rhode Island, Dept. of Ocean Engineering, April 2011.

Follow-on Data Collection and Synthesis of Muskeget Channel Hydrokinetic Potential and NOREIZ Wave & Wind Energy Potential

A UMASS Dartmouth Partnership Project between SMAST - Coastal Systems Program (CSP) and the UMASS Marine Renewable Energy Center (MREC)

Submitted by:

Dr. Brian L. Howes
Dr. Roland Samimy
Dr. David Schlezinger
Mr. Michael Bartlett
Ms. Jennifer Benson, M.S.
Dr. David White

Coastal Systems Program
School of Marine Science and Technology
University of Massachusetts Dartmouth

Submitted to:

Mr. John Miller, Director

New England Marine Renewable Energy Center (UMASS-Dartmouth)

September 20, 2013

EXECUTIVE SUMMARY

The intent of the partnership between the New England Marine Renewable Energy Center (MREC) situated within the University of Massachusetts-Dartmouth and the Coastal Systems Program (CSP) situated within the University of Massachusetts-Dartmouth School for Marine Science and Technology (SMAST) was the completion of specific data collection tasks aimed at further characterizing the hydrokinetic and environmental resource of Muskeget Channel, located between Martha's Vineyard and Nantucket. Funding for completion of the data collection tasks was garnered by MREC from the United States Department of Energy (USDOE). The data collection undertaken by the CSP and summarized in this report supplements an earlier investigation of the hydrokinetic energy potential of Muskeget Channel that was funded by a grant from the Massachusetts Technology Collaborative. Data summarized herein has been developed specifically to meet the needs of the UMASS Marine Renewable Energy Center in its effort to establish a National Offshore Renewable Energy Innovation Zone (NOREIZ) to serve as a marine renewable energy technology test bed as well as satisfy the needs of the Town of Edgartown (Martha's Vineyard) which holds a preliminary permit from the Federal Energy Regulatory Commission (FERC) for the development of a tidal energy pilot project in Muskeget Channel.

Based upon the determinations of the velocity field within Muskeget Channel in 2008-09 (as funded by the grant from the Massachusetts Technology Collaborative), it was clear that hydrokinetic energy generation potential using underwater turbines presently exists within a very specific portion of Muskeget Channel (the southern region of the Town of Edgartown FERC permit area). The initial investigation into the hydrokinetic energy potential of Muskeget Channel also revealed that further surveying of currents would be required to refine the best location for tidal energy generation technologies. In addition, data collection on the environmental characteristics of the area would be necessary to begin to ascertain the potential impacts resulting from tidal energy generation in Muskeget Channel, specifically the routing of cables to bring tidal power ashore to Martha's Vineyard. These data would further support the Town of Edgartown in its development of a pilot scale tidal energy project while also yielding valuable baseline data sets useful in the establishment of the NOREIZ by MREC.

Building on baseline data previously collected by the SMAST-CSP in Muskeget Channel under the MTC grant, the CSP continued data collection with support from the DOE during the period September 1, 2009 to December 31, 2010. The field work undertaken focused on two elements as follows:

Element 1 - Time-series current and wave field within the Muskeget Channel FERC and initial studies in the NORIEZ (including wind potential).

Element 2 – Town of Edgartown FERC Permit Perimeter Area Investigation to Support Power Transmission to Upland Grid.

Each element had specific data collection tasks aimed at further characterizing the hydrokinetics and environment of Muskeget Channel and waters south (the upper portion of NOREIZ).

Element 1 - Time-series current and wave field within the Muskeget Channel FERC and initial studies in the NORIEZ (including wind potential).

Under this data collection element were six specific tasks:

1. Current measurements in the FERC Permit Site.
2. Current Measurements in Northern Portion of NOREIZ.
3. Measurement of wave heights and frequency in FERC Permit Site
4. Measurement of wave heights and frequency in NOREIZ
5. Initial data gathering on wind energy potential associated with NOREIZ
6. Sediment sampling in NOREIZ in a variety of locations potentially supportive of wind

Element 2 – Town of Edgartown FERC Permit Perimeter Area Investigation to Support Power Transmission to Upland Grid.

Under this data collection element were eight specific tasks:

1. Seasonal Benthic infauna characterization (2 cable routes) in test areas under both disturbed and undisturbed conditions
2. Sediment sampling to go along with Benthic Infauna Sampling
3. Eelgrass surveying along potential cable routes
4. Bottom mounted ADCP to measure along shore currents in vicinity of potential cable routes
5. Surficial sediments sampled and mapped along potential cable routes
6. Assess coastal resources in area of proposed cable route (beach survey)
7. Assess coastal resources in area of proposed cable route (dunes)
8. Assess coastal resources in area of proposed cable route (wetlands)

Overall Results: Element 1

- Detailed ship board ADCP profile transects identified an area within Muskeget Channel that is of sufficient depth for current in-stream tidal turbines to operate on a commercial scale and narrowed the search area for velocities for viable commercialization. Focused, lunar period, bottom moored ADCP deployments supported this contention. The long-term studies indicated higher current velocities than expected from transect surveys. These long term velocities were in excess of 4knts, generally considered a threshold for commercial viability.
- Wave measurements, made concurrent with long term velocity profiles, showed that the wave fields were bi-modal and temporally inconsistent. The data suggests that local bathymetry, characterized by large expanses of shoals, creates short steep waves, while the deep water swells from the open ocean to the south create waves of comparatively long periods. The combination of wave types are influenced by changes in tidal direction and wind stresses which are both parallel to the wave fronts. The resulting wave environment appears chaotic and is not believed to be commercially viable with current technology, despite the relatively large amount of

potential wave energy.

- Within the northern portion of the NOREIZ examined current velocities are uniformly low (<1m/s) and extremely consistent showing only moderate changes through lunar cycles.
- Wave measurements at the NOREIZ site were dominated by long period waves with monthly average energy ranging from 36 to52 kW/m during January and February, respectively.
- Initial data gathering on wind energy potential associated with NOREIZ indicates that the wind fields are energetic and consistent. Though the buoy mast was only 2 meters high wind velocities ranged from 6-8.5 m/s. This data is consistent with other work beginning in the area which utilizes radar arrays for wind and wave prediction. In general the NOREIZ site should be conducive to both wind and wave power extraction.
- Sediment sampling in the vicinity of the NOREIZ buoy showed medium to coarse sand dominates the benthic environment. The sediment appears to be seasonally stable, however, infauna samples suggest that there if frequent reworking of the surficial sediment which limits both the density of animals and the diversity of taxa present.

Overall Results: Element 2

- Benthic infauna communities along both proposed cable routes had extremely low densities and concomitantly low diversity. Markers were removed by vandals making comparison of disturbed and undisturbed conditions impossible. However, visual inspection of the disturbance sites showed no discernible effect of disturbance. Furthermore, statistical analysis of the samples (triplicate at each of the 8 sites) showed that given the low numbers of individuals and variability between replicates that even if the population were decimated the difference would not reach a level of significance in over half the locations.
- Sediment sampling and grain size analysis performed in conjunction with the infaunal analysis showed medium to coarse sand dominates the benthic environment along the Pochet transect. The sediment appears was seasonally stable, however, infauna samples suggest that there if frequent reworking of the surficial sediment which limits both the density of animals and the diversity of taxa present. Results from the Katama transect indicated the presence of glacial clay deposits underlying coarse to medium sand that regularly emerged to the sediment surface. The presence of surface clay deposits, increased infauna densities and diversity while decreasing submerged aquatic vegetation. Clay deposits also complicate cable placement. Final decisions for the cable installation will need to weigh all of these competing factors.
- Beach, dune and wetland surveys where proposed cable installations transition to shore present no immediate obstacles. Both Pochet and Katama cable landings will require review and permitting by Massachusetts Department of Environmental Protection, local conservation commission and Massachusetts Natural Heritage & Endangered Species Program. Portions of both landings are adjacent to wetlands and priority habitat for rare species, however, both locations also have public rights of way and access that could mediate any potential impacts.

Table of Contents

List of Figures

List of Tables

1.0 Introduction

The work summarized herein is in satisfaction of funding received by the Coastal Systems Program (CSP) within the school for Marine Science and Technology at the University of Massachusetts-Dartmouth. Funding for this data collection was received by the CSP from the US Department of Energy via the UMASS Marine Renewable Energy Center (MREC). This work builds upon data collection efforts initiated by the CSP in Muskeget Channel in 2008 and 2009 as supported by a Massachusetts Technology Collaborative grant received jointly by the University of Massachusetts-Dartmouth, Advanced Technology Manufacturing Center and the Coastal Systems Program. We are providing this summary of findings from field surveys undertaken in 2010 of Muskeget Channel to support deployment of hydrokinetic energy generation technologies by the Town of Edgartown under an existing preliminary permit from the Federal Energy Regulatory Commission (FERC). Additionally, this data collection work was planned to help advance the establishment of a National Offshore Renewable Energy Innovation Zone (NOREIZ) as conceived by UMASS-MREC.

All data previously collected under the MTC grant, as well as new data collected using the DOE funds and summarized herein, is being shared with the Town of Edgartown to meet specific requirements of their preliminary permit from the FERC to investigate the viability of a tidal energy project in the waters between Martha's Vineyard and Nantucket (specifically Muskeget Channel and surrounding waters). Finally, this more advanced data collection effort was designed to be begin generating information on biological and ecological characteristics of the Muskeget Channel area and was planned to be part of baseline data collection for the establishment of NOREIZ by the UMASS Marine Renewable Energy Center (MREC) with the goal of accelerating the deployment of marine renewable energy technologies in an environmentally sound manner within U.S. waters.

Background: The intent of the partnership between the UMASS-MREC and SMAST-CSP was to (a) determine if Muskeget Channel generally has sufficient tidal velocities to support hydrokinetic power generation, (b) more specifically to identify the most energetic zone within Muskeget Channel to guide deployment of a pilot scale tidally driven generating unit and (c) begin to determine potential environmental impacts of deployment of generators and associated infrastructure (moorings, cables, etc). The initial phases of this on-going effort were conducted with the support from the MTC, specifically baseline surveys (physical) of the Muskeget Channel area in Nantucket Sound and the greater region between Muskeget Island and Martha's Vineyard. These surveys included the use of both shipboard and moored instrumentation to measure current velocity, tide stage, and bathymetry and sampling of sediment characteristics. Using funds garnered from the US DOE, data collection in 2010 was focused more specifically on further understanding the current velocity characteristics in the most energetic zone of Muskeget Channel over a complete lunar cycles, quantifying the wave field of the area to inform the design of the barge mounted pilot scale tidal energy project, quantify the wind conditions during both summer and winter seasons and conduct preliminary surveying of benthic characteristics in the near shore waters along two proposed cable routes, one located along the eastern shore of Martha's Vineyard and the other situated in waters south of the Island.

Muskeget Channel extends approximately from Muskeget Island (western most island in

Nantucket County) to the easternmost shore of Chappaquiddick Island on Martha's Vineyard (Dukes County) as depicted in Figure 1. The main channel generally runs north-south near Chappaquiddick Island adjacent the Town of Edgartown, MA. While oceanographic surveys assessed the whole of Muskeget Channel relative to hydrokinetic generation potential, the thrust of this data collection effort focused on the higher flow region, at the southern end of the channel, the nearshore waters along Martha's Vineyard and waters south of the Channel that comprise the upper region of the proposed NOREIZ.

Figure 1 – General Location of Muskeget Channel and the survey area (circled area), which was the focus of baseline data collection as originally supported by a grant from the MTC with follow on data collection funded by DOE via MREC.

The UMASS-MREC served as the overall leader of the project with the ultimate goal of establishing an Ocean Energy Test site in the Muskeget Channel area and waters south (NOREIZ) and also supporting the deployment of a pilot scale tidal energy generating unit. The SMAST-Coastal Systems Group (CSP) served as the oceanographic survey leader in this effort. The baseline survey utilized the field and laboratory resources of the SMAST-CSP group and its collaborators, which simplified logistics and provided an efficient means for maximum data collection. Available resources included a variety of oceanographic instruments for field data collection on ocean physics and biological habitats, water quality and biologic resources, in addition to the resources of a full analytical facility. This joint effort between the Coastal Systems Program – UMASS-SMAST and the UMASS Marine Renewable Energy Center (MREC) fulfills one of the primary missions of the University of Massachusetts-Dartmouth, the bringing together of key research and technology groups for sustainable socioeconomic development of the region.

Data Collected by Field Program: The data collection effort was conducted over approximately a one year period including the 2010 summer field seasons. Due to weather limitations during the summer of 2010, the field data collection period was extended into the fall and winter of 2010. The analysis of data collected was under the direction of Dr. Brian L. Howes, Director of the Coastal Systems Program at SMAST-UMD with the assistance of CSP Research Coordinators, Mr. Roland Samimy and Dr. David Schlezinger. SMAST-CSP through the UMASS-MREC served as the lead for the data collection effort while a limited number of technical specialists with proven capabilities and experience within the region were integrated into the effort to assist with some high end data processing, primarily related to the benthic infaunal analysis.

2.0 Description of Data Collection Program

Element 1 - Time-series current and wave field within the Muskeget Channel FERC and Initial studies in the NORIEZ (including wind potential).

Time-series current and wave data were collected within both the Muskeget Channel FERC permit area and within the NOREIZ. The Muskeget Channel deployments of an upward looking trawl resistant bottom mounted acoustic doppler current profiler (ADCP) was guided by ship based ADCP surveys to identify areas of optimum current fields for deployment of hydrokinetic technologies. Shipboard current profiling surveys were continue within the FERC site and single point current profiling was undertaken in the northern portion of the NOREIZ in the vicinity of a weather buoy deployed as part of this effort. The additional ship based surveying as well as the time series current surveying is being undertaken to gain the necessary spatial data on high velocity areas to better define the areal extent of the previously identified "hot spot" for potential energy production in Muskeget Channel. This will also serve to inform the future design of a large tidal turbine array assuming successful results from an initial barge based pilot scale tidal energy generation project. The fine scale time series current profiling of currents over complete lunar cycles at a single point was undertaken to assist future energy developers quantitatively estimate the power production potential of the site over a broad range of current velocity conditions.

In addition to quantifying the velocity field, the time-series data collection included measurements of wave heights and frequency. These data were collected both within the Town of Edgartown FERC permit area and in the MREC proposed NOREIZ. This DOE funded data collection program also included initial data gathering on wind profiles for evaluation of wind energy potential associated with the NOREIZ. This was achieved through the deployment of a weather buoy approximately 8 nautical miles south of Muskeget Channel. The weather buoy was programmed to collect data on wind direction and intensity, barometric pressure, temperature and solar radiation.

In concert with the field surveys of current velocity and wind direction and intensity within the NOREIZ, mapping of surficial sediments in the vicinity of the NOREIZ weather buoy was

completed as well. Sediment characteristics and sediment transport are critical to understanding the physics of water movement and particularly the potential for structures to influence sediment transport (e.g. deposition, erosion, scour). As such, ongoing data collection in Muskeget Channel was extended southward into the NOREIZ to characterize surficial sediment types in a variety of locations that maybe supportive of future offshore wind development. Sub-bottom profiling will be conducted in the future as funding becomes available for future consideration of wind tower design, should there be a suitable wind resource south of the islands. Furthermore, determination of the composition of the sediment in specific areas was undertaken as would be applicable for testing of future wind technologies. Assessment of the sediment characteristics of the sea bed will not only elucidate the engineering challenges associated with mooring or construction of energy devices but also clarify the degree to which benthic animal communities may be affected by shifts in sediment transport.

Element 2 – Town of Edgartown FERC Permit Perimeter Area Investigation to Support Power Transmission to Upland Grid.

While associated work is underway to determine the most feasible and economic paths for installing a power cable from the exisiting electrical grid on Chappaquiddick Island grid to the shore, the present data collection effort focused on both an upland and underwater survey of the biota along two proposed cable routes. The upland survey was undertaken to assess the presence of environmentally protected areas or areas requiring special permits that stand between the terminus of existing electrical infrastructure and the high potential hydrokinetic energy generation sites within the Muskeget Channel FERC permit area. At present, this is a "data gap" as regards the installation of cables associated with power generation at this site. This upland survey work entailed nearshore evaluation of wetlands, dunes and beach environments that will need to be identified and addressed in planning/implementation of any tidal project with shore side connection to the electrical infrastructure. Similarly, assessment of eelgrass beds and assessment of benthic infaunal animal communities and sediments along the two proposed offshore cable routes was undertaken.

Establishing the existing biological/ecological baseline for the area and how this baseline could be affected by power transmission via submarine cables will be a critical component of the permitting process that the Town of Edgartown, as holder of the FERC Permit for this resource, will have to satisfy. Presently, very little data has been collected in the Muskeget Channel area to answer questions related to power transmission via cables from an offshore array of tidal generating units.

At present two (2) cable routes are being considered by the Town of Edgartown to bring power to shore (Figure 2). Engineering and permitting activities to support the burial of cables require:

(a) evaluation of the biotic resources to be impacted during construction, primarily benthic infaunal communities and eelgrass beds.
(b) sediment type
(c) coastal resources above MLW (i.e. beach, dune, wetland)

Evaluation of the resources:

Benthic Communities - Trenching activities to bury cables create acute disturbance to benthic communities through burial, with subsequent recovery of benthic communities post-construction. Determination of the infaunal community along the 2 potential cable routes being considered by the Town of Edgartown will allow assessment of the likely rate of recovery post-construction. The benthic animal communities and the surface sediments were assessed utilizing benthic grab samples and sediment core tubes to establish a baseline for the types of organisms and sediments present prior to deployment of a transmission cable. To gauge likely rates of recovery from cable installation, test areas were created (disturbed and undisturbed) and communities monitored through time. In addition, community recovery rates determined from other cable projects that have been monitored were captured and used in this assessment. However, the high current velocities within the Channel appear to be outside of velocities at these other sites and pose a potentially unique area for this determination (indicating the need for post-construction monitoring).

Eelgrass - A critical marine habitat in the shallow waters of Martha's Vineyard is the submerged aquatic plant, *Zostera marina*. General practice is to avoid, whenever possible, disturbance of these communities. Therefore, a detailed site-specific survey of eelgrass along each cable route was conducted to guide future cable placement. A combination of diver performed visual surveys and a review of aerial photography and video surveys by the Massachusetts Department of Environmental Protection (Mass DEP) Eelgrass Mapping Program was used to produce the summary of submerged aquatic vegetation along the proposed cable routes. Note that the Mass DEP eelgrass distribution data in this region is relatively coarse for the purpose of cable route planning and therefore was augmented by the site specific visual survey completed by the project divers.

Bottom Mounted Single Point Current Meter – Energetics (tidal, wind driven, waves) along the shore was measured to augment the understanding of the interaction between the environment and the transmission cables in two specific cable locations under consideration by the Town of Edgartown. The near bottom alongshore current velocity was measured using a downward looking single point current meter.

Sediment Type.

Surficial sediment types were identified along the cable route using standard grain size analysis techniques. Sediment samples were collected by divers every 50 meters along the 600 meters of transect surveyed in total at each of the two proposed cable route locations. Sediment sampling was completed in concert with the infaunal community monitoring. Infaunal samples were collected using a Van Veen grab sampler lowered from a boat positioned along a given transect. Infaunal grabs were obtained every 200 meters along both transects (0m, 200m, 400m, 600m). Once a definitive cable route is selected and as future funds become available, sub-bottom profiling will be conducted in order to characterize the deeper sediments down to a depth of approximately 1.5m to 2.0m below the surface of the seabed and will extend into the deeper waters where a future array of tidal turbines may be deployed.

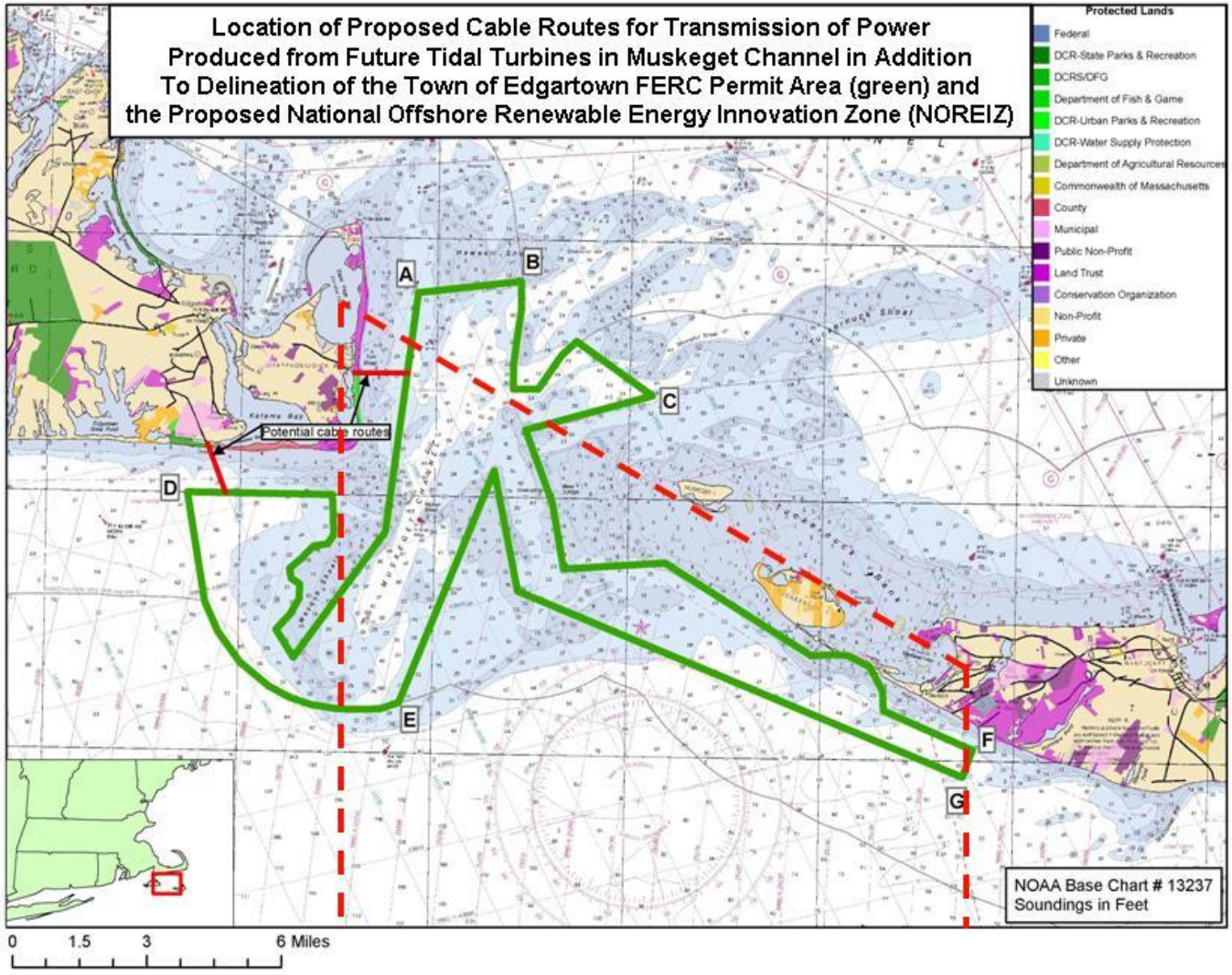

Figure 2 – Location of the Town of Edgartown Muskeget Channel FERC Permit Area relative to the proposed NOREIZ Area. Data collection efforts focused on proposed cable routes (Pochet Transect-north and Katama Transect-south), Muskeget Channel and waters south of the channel.

Coastal Resources above MLW (i.e. beach, dune, wetland).
Cable route construction will also affect upland resources and also must fit coastal regulatory frameworks. It is critical to evaluate the coastal resources that may trigger environmental permits, in order to assess the cost/benefit of alternative cable routes and to minimize regulatory issues. This effort is required as part of both design and implementation and can be used to avoid sensitive areas and accelerate technology deployment.

3.0 Summary of Results

Element 1 - Time-series current and wave field within the Muskeget Channel FERC and Initial studies in the NORIEZ (including wind potential).

Ship-based ADCP Data Collection on Current Velocities along Additional Transect in the High Energy Zone of Muskeget Channel in the Edgartown FERC Permit Area

Previous hydrokinetic surveying to characterize the current velocities in Muskeget Channel, completed under a grant from the Massachusetts Technology Collaborative in 2008/2009, revealed a clear zone of high current velocities suitable for tidal energy production using existing technologies. Current velocity surveying was achieved using both bottom mounted single point current meters as well as acoustic doppler current profiling (ADCP) technology. Current velocity measurements were made at ten different transect locations and the strongest current velocities were found along transects 6, 7, 8 and 9 in the narrowest section of Muskeget Channel in an area generally demarcated by the 15-20 meter depth contour (Figure 3). More specifically, the strongest current velocities measured using ADCP during the initial survey work were found along both transect 6 and 7 (Figures 4, 5) with a clear indication that the greatest current velocity was found in approximately the top half of the water column from the surface to approximately 15 meters.

Cross-sectional profiles of currents and volumetric flow were measured along multiple transects throughout the Muskeget Channel study area using a ship mounted Acoustic Doppler Current Profiler (ADCP). Seven (7) survey transects were completed through both the ebbing and flooding portions of a tidal cycle (approximately 14 hours in duration) three days preceeding a neap phase of the lunar cycle. The measurements were made to determine the flow velocities throughout the water column to allow determination of the depths and timing of maximum and minimum velocities (i.e. determine differences in velocity with depth over the tidal cycle) and provide a finer scale characterization of the currents in the high velocity zone of Muskeget Channel. The ADCP surveying undertaken in partial fulfillment of this grant builds upon previous current velocity measurements that were undertaken in 2008 and 2009 along three main transects referred to as Transect 6, Transect 7 and Transect 8. In this effort, Transect 6, 7 and 8 were resurveyed, however, additional transects (2 transects {6.1 and 6.2} located between Transect 6 and 7 and 2 transects {7.1 and 7.2} between Transect 7 and 8) were surveyed as well

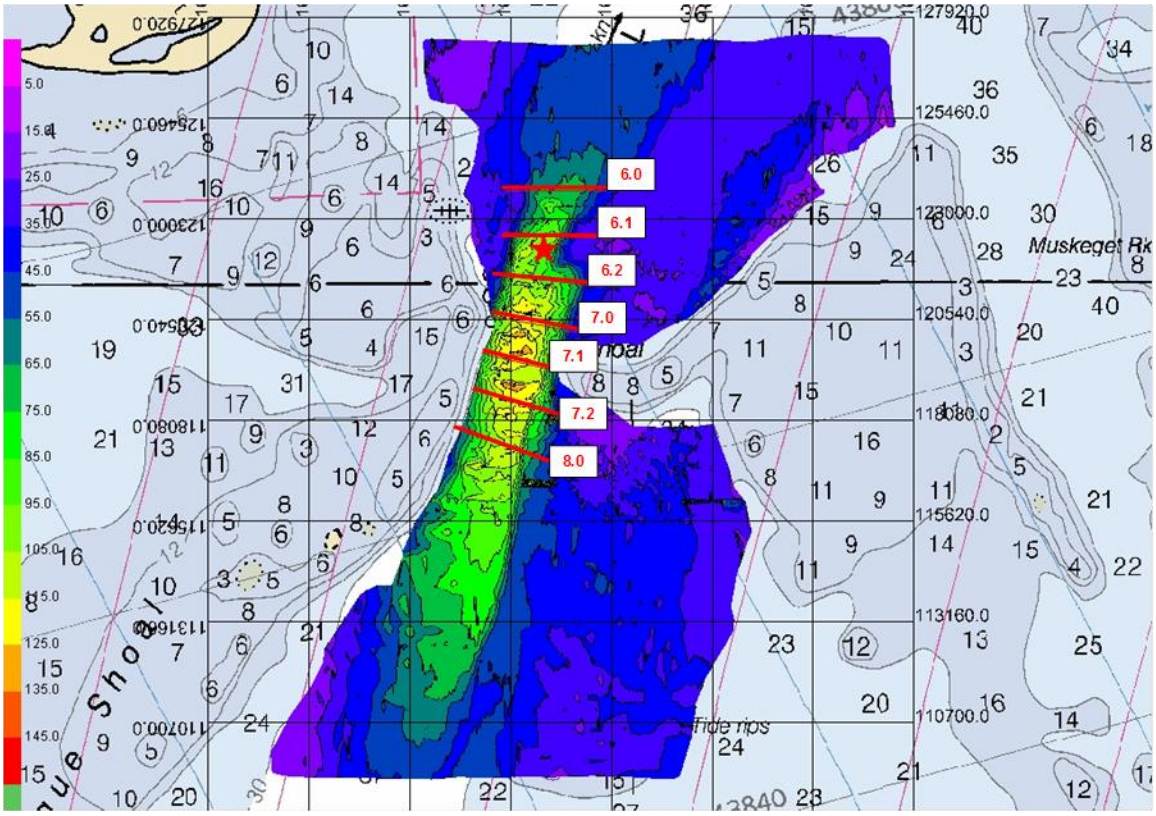

Figure 3 – Location of additional ship based ADCP surveying undertaken in the high velocity zone. Location of the TRBM is denoted with a red star.

(Figure 4 and 5; also see Appendix A). The finer scale ADCP surveying data has been important for the Town of Edgartown, energy developers and the UMASS-MREC as a way of further screening the Town of Edgartown FERC permit area and refine the demarcation of areas of high energy generation potential for more optimal siting of future tidal turbine arrays. Current profiles were completed along transects situated strategically across Muskeget Channel (Figure 3), such that currents throughout the area could be measured in greater detail. The information was also collected to validate future hydrodynamic models related to the site. These additional survey lines allowed for the most advantageous placement of the TRBM.

The original ADCP surveying completed along transects 6 and 7 in 2008 and 2009 in the most energetic zone of Muskeget Channel being considered for tidal energy development were further refined using an upward looking trawl resistant bottom mounted (TRBM) ADCP at a single point situated between both transect 6 and 7. This velocity measurement effort was a longer term deployment aimed at capturing a fine scale time series record of current velocities through the entire water column over a complete lunar cycle. This would provide potential energy developers an accurate measure of the degree of variation in current velocities over both hourly periods under both ebb and flood tide conditions as well as differing lunar phases (Spring, Neap, Quadrature and in between). This time series data is intended for use by developers to make accurate estimates of power production under the broadest range possible of current velocity conditions.

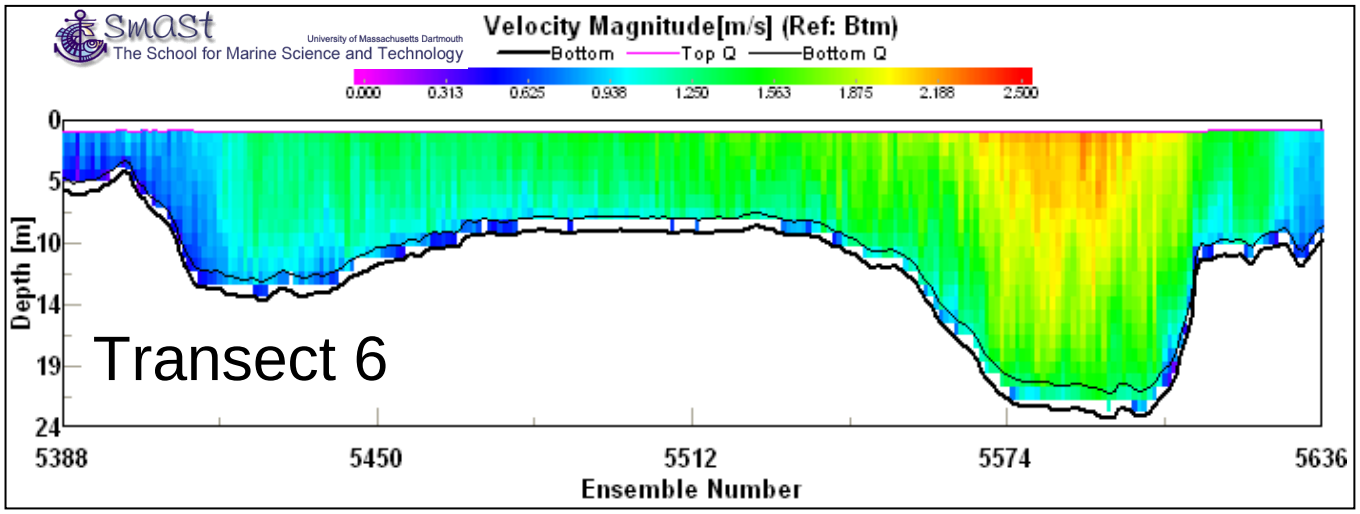

Figure 4A – Results of ADCP survey along Transect 6 depicting maximum current velocities under spring tide conditions, mid-FLOOD cycle (August 29, 2008).

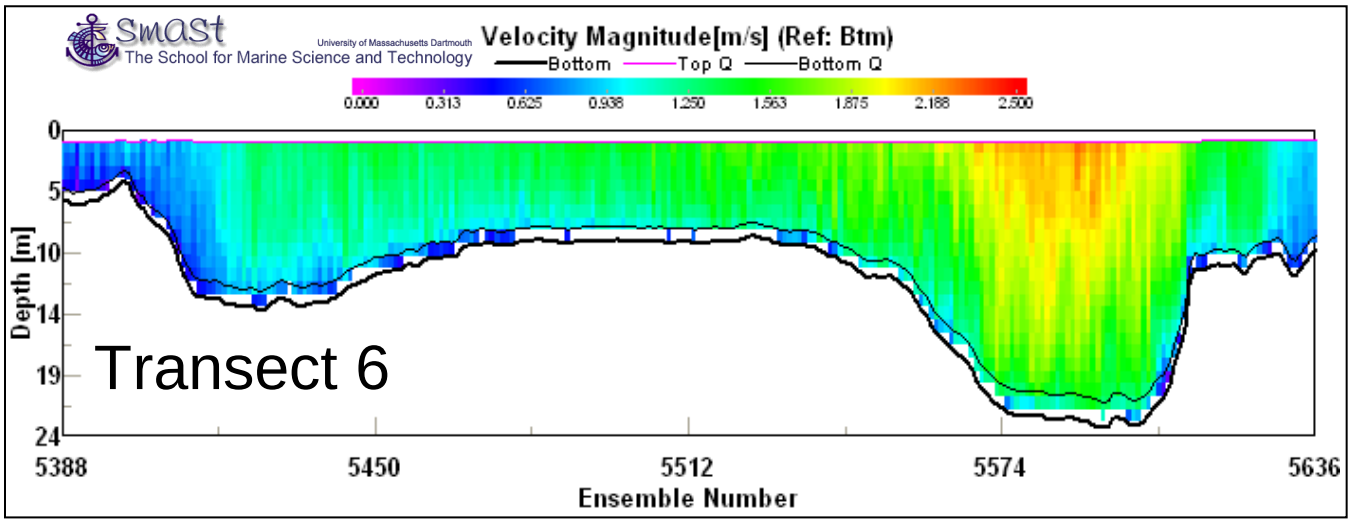

Figure 4B – Results of ADCP survey along Transect 6 depicting maximum current velocities along Transect 6 under spring tide conditions and an EBBING tide (June 25, 2009).

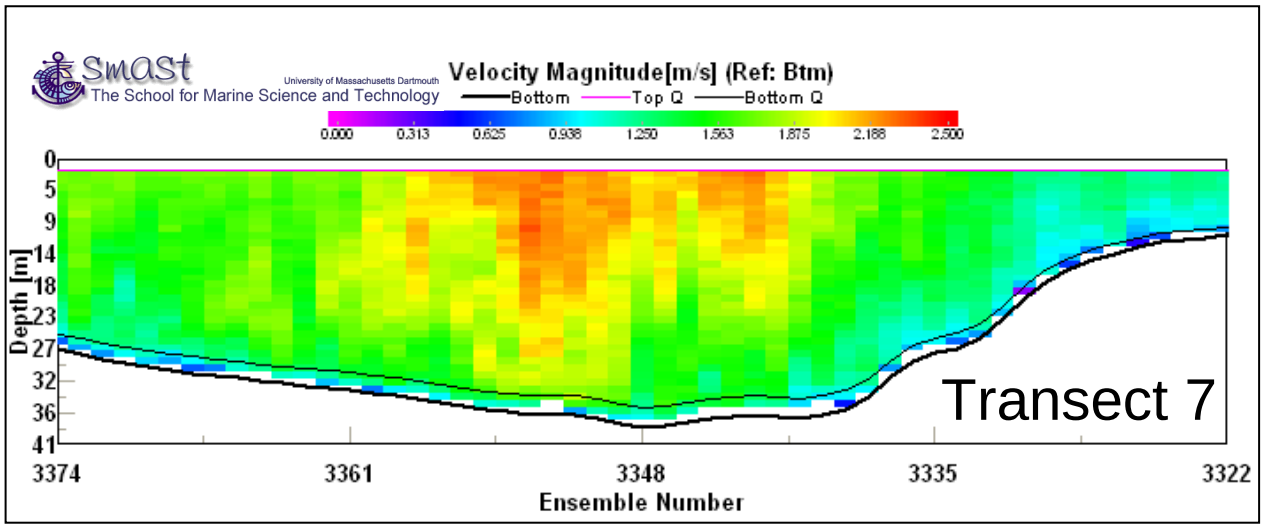

Figure 5A – ADCP survey results for current velocities along Transect 7 under spring tide conditions and a FLOODING tide (June 25, 2009).

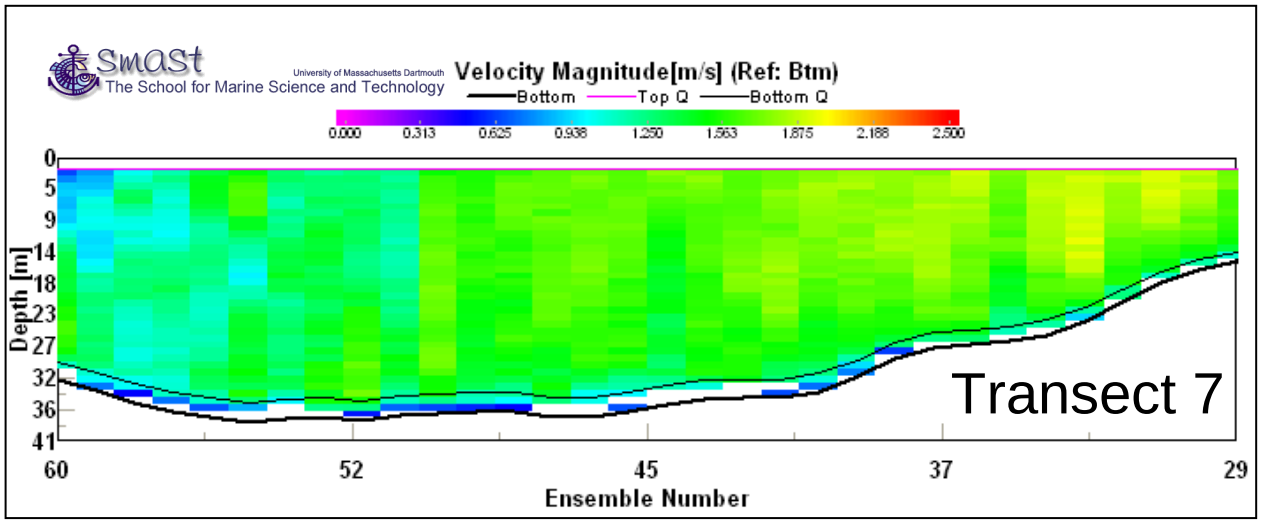

Figure 5B – ADCP survey results for current velocities along Transect 7 under spring tide conditions and an EBBING tide (June 25, 2009).

Time Series Data Collection on Current Velocities using Bottom Mounted, Upward Looking Acoustic Doppler Current Profiler (ADCP) in the Edgartown FERC Permit Area over a Complete Lunar Cycle.

In conjunction with the previously discussed ship-based ADCP surveying along individual transects (6.0, 6.1, 6.2, 7.0, 7.1, 7.2, 8.0) a bottom mounted upward looking ADCP was deployed to capture near continuous current measurements through a portion of the water column in the area that showed the strongest currents based on data collection along the transects (Figure 4,5 and Appendix A). This instrument was deployed on November 22, 2010 and was retrieved on January 6, 2011 (Figure 6). Deployment duration was focused to cover at least one full lunar cycle such that variations in the velocity field could be quantified as a function of changing phases of the moon. The deployment of the bottom mounted ADCP also served as a validation of velocity measurements obtained during the ADCP surveying of transect 6.2. The overall objective was to capture the average, maximum and minimum velocities and flows for evaluating the number of locations that can be utilized for deployment of tidal generating units and how the monthly fluctuations in current intensity might affect future power generation in this area.

Figure 6 – ADCP deployed November 2010 to measure current velocity over a complete lunar cycle in the high velocity zone of Muskeget Channel.

The bottom mounted ADCP record was mostly complete with occasional gaps resulting from sand wave movement over the bottom mount and by turbulence that prevented reconciliation of the 4 beam data (Figure 7). Current directions were consistently North-South. As expected, periodic variation in velocity was seen with respect to diurnal tides and lunar cycles. Subsets of the entire deployment are shown in Figures 8-11. Figure 8 shows the time series velocity magnitude during the period that the shipboard ADCP transects were being measured. The remaining figures 9-11 show the velocity magnitudes recorded for Neap, Quadrature, and Spring tides, respectively. December 10 velocities were among the lowest observed (Figure 8),

exceeding 1.6 m/s in the surface waters only during ebb tides. These results are consistent with those collected during the transect measurements.

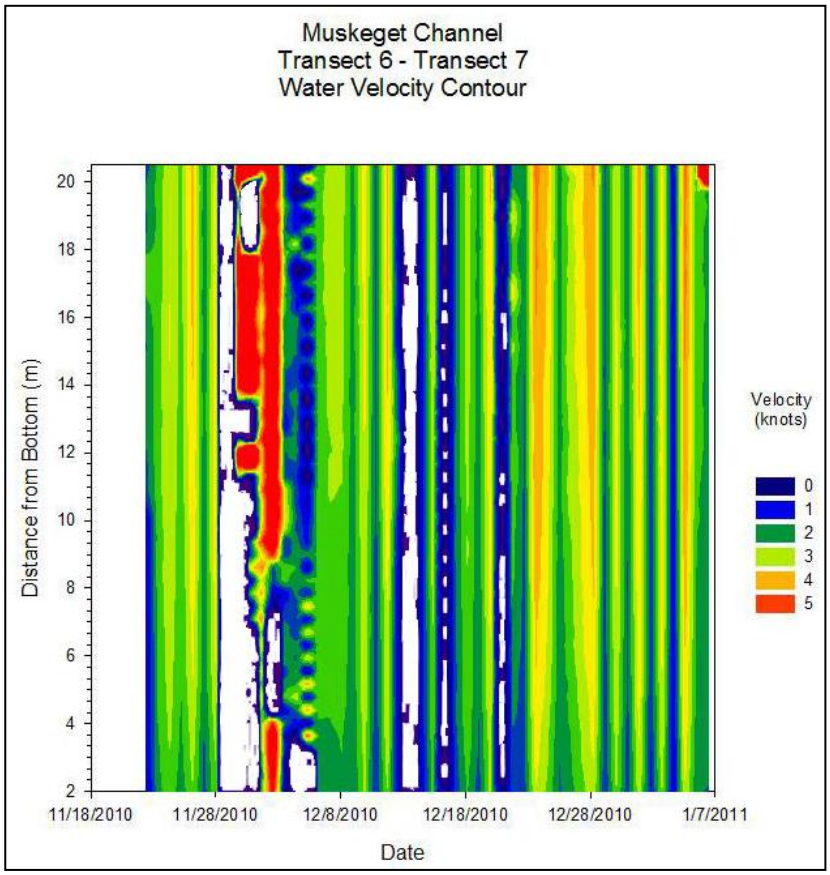

Figure 7 – Contour plot of current velocity for the bottom 20 m of the water column over the deployment period at a single point along Transect 6.2. Data was collected using the bottom mounted ADCP logging once every 15 minutes between November 22, 2010 and January 6, 2011. Areas in white represent times when data quality was poor due to fouling or extreme turbulence.

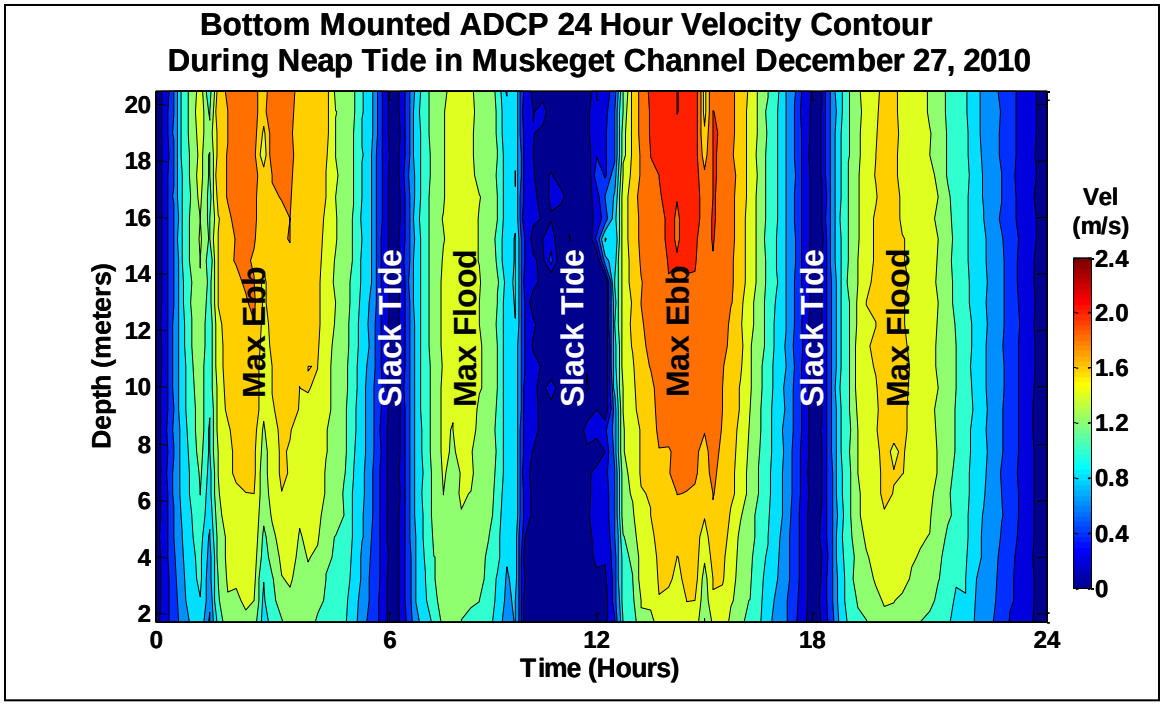

Figure 8 - Hour Velocity Contour Plot of the current velocities within the high velocity zone of Muskeget Channel three days prior to a first quarter lunar (Neap tide) cycle. The highest velocities occurred during the ebb tides. These measurements support the shipboard ADCP surveys that were conducted on December 10, 2010.

The Neap tide velocities were expected to be the lowest recorded, however the velocity magnitudes during one ebb tide were significantly higher than seen in Figure 9. Wind forcing of water through the channel is believed to account for this behavior with support provided by the truncated flood tide and extended slack tide immediately prior. Diurnal asymmetries in the ebb and flood tide velocities were small with a difference of 15-20% (1.8m/s vs. 2.2 m/s) (Figure 9). Similar differences were observed between successive flood tides.

Under quadrature conditions (Figure 10) velocity magnitudes were similar, but slack tide intervals were symmetric as compared to neap tide conditions. The main difference was in the depth to which the maximum velocity zone extends from the surface down into the water column. Although the maximum velocities were similar, the average velocity for the water column increased as the surface high velocity zone extended further down in the water column.

Spring tide conditions (Figure 11) demonstrated similar velocities and symmetry as Quadrature conditions with a further increase in depth of the high velocity zone extending down from the surface. Thus maximum velocities recorded were similar throughout the lunar cycle, yet mean water column velocity increased from neap to spring tides by involving a greater portion of the total water column. While the vertical differences in velocity magnitude may create challenges for some turbine designs, the upper velocity threshold remains relatively constant simplifying the engineering required to meet maximum velocities

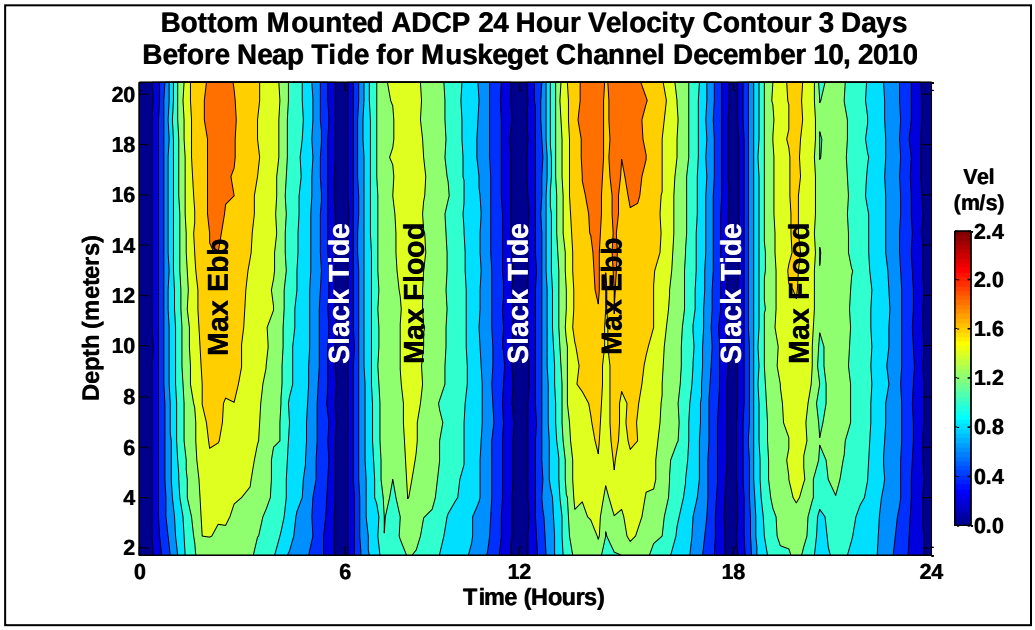

Figure 9 - 24 Hour Velocity contour plot during a true Neap tide in the high velocity zone of Muskeget Channel. Current velocities are at a maximum during the ebb tide conditions. Maximum velocities ranged from 1.6 to 2.3 m/s (~3.1-4.5 knots).

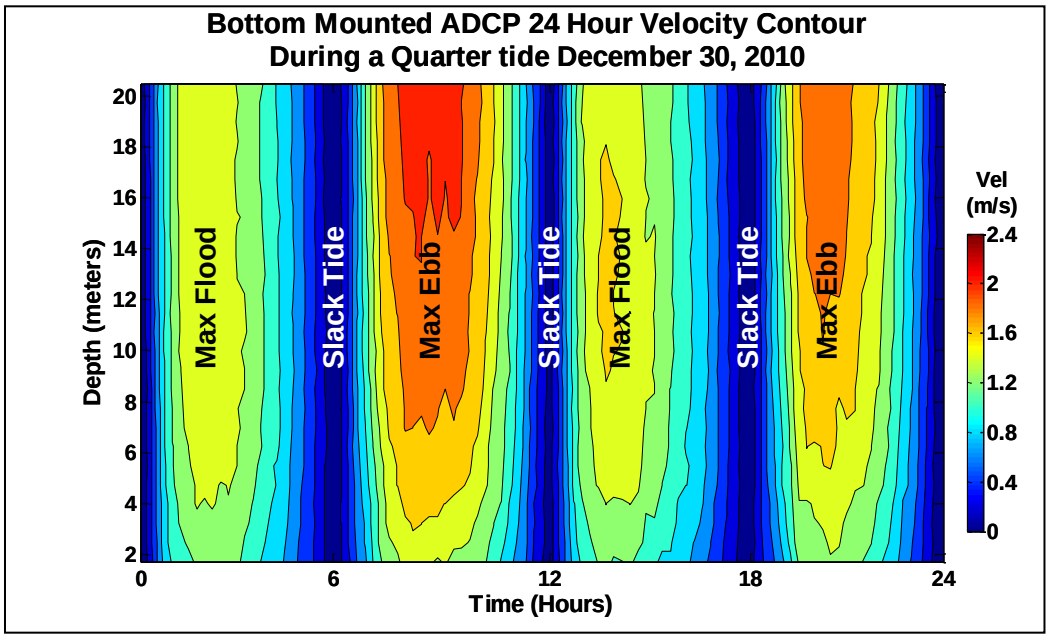

Figure 10 - 24 hour velocity contour plot displaying current velocities during a quadrature between the Neap and Spring lunar tide cycles. Maximum velocities ranged between 1.6 to 2.3 m/s (~3.1-4.5 knots) from the surface to 16 meter depth during the ebb tides.

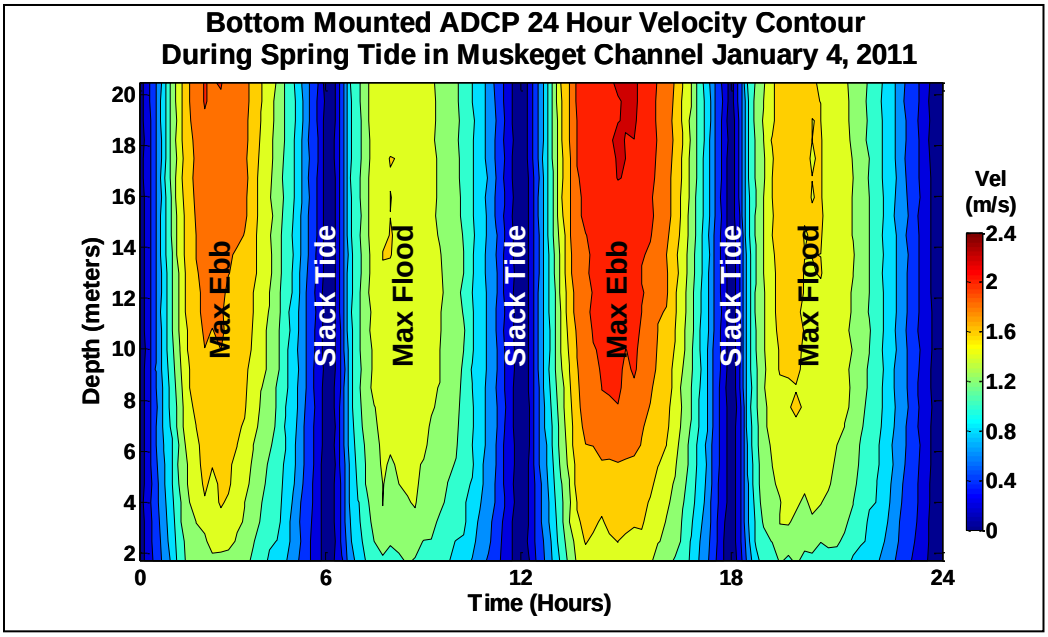

Figure 11 - Spring tide velocity contour plot for a 24 hour period from the bottom mounted ADCP deployed within the high velocity zone in Muskeget Channel. Maximum current velocities ranged between 1.7 to 2.4 m/s (~3.3-4.7 knots) through the first 16 meters of the water column.

Time Series Data Collection on Wave Frequency and Direction in the Muskeget Channel portion of the Edgartown FERC Permit Area

The upward looking ADCP was also configured to evaluate the wave field with periodic high frequency sampling bursts including depth and surface tracking of wave generated orbital velocities. Both wave amplitude and direction are affected by a combination of wind forcing and current velocity and direction. In the case of Muskeget Channel which is surrounded by shoals (Figure 3) the wave period displayed a bi-modal character with a distinct split between long period swell from the open waters to the south and short period waves resulting from influence of nearby shoals. Interactions between currents and wind also contribute to the bi-modal character (Figure 12). On flood tides coincident with the dominant wind direction wave periods are longer, but when currents and wind are in opposition shorter, steeper, waves predominate. When examining the daily averages the power diminishes considerably (Figure 12). Examining wave height and period as a function of directional heading (Figure 13) a clear trend emerged. Maximum wave height and period were coincident with the long offshore swell coming from the south. While there are significant wave heights in excess of 3 meters from other headings the majority of wave periods associated with those waves were quite short; the majority was at the detection limit of ~1.9-2.1 seconds. These tall steep waves are indicative of longer waves piling up on the adjacent shoals.

A comparison with nearby monitoring locations Martha's Vineyard Coastal Observatory (MVCO) to the west and NOAA Buoy 44020 (Nantucket Sound) to the north show similar

patterns in wave height and period, however the local variables within Muskeget Channel create much more variability (Figure 14) for the reasons given above.

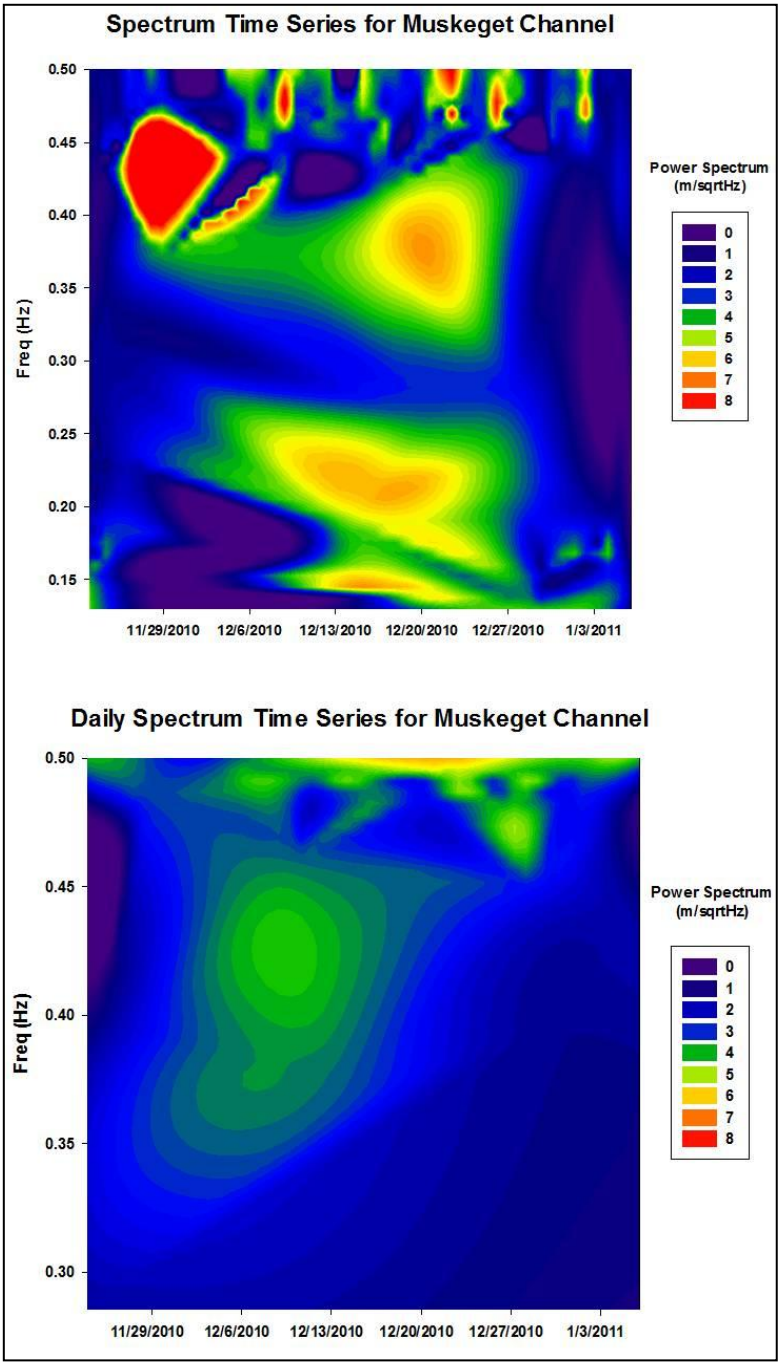

Figure 12 - Time series power spectrums showing instantaneous and daily averaged data for the entire deployment period.

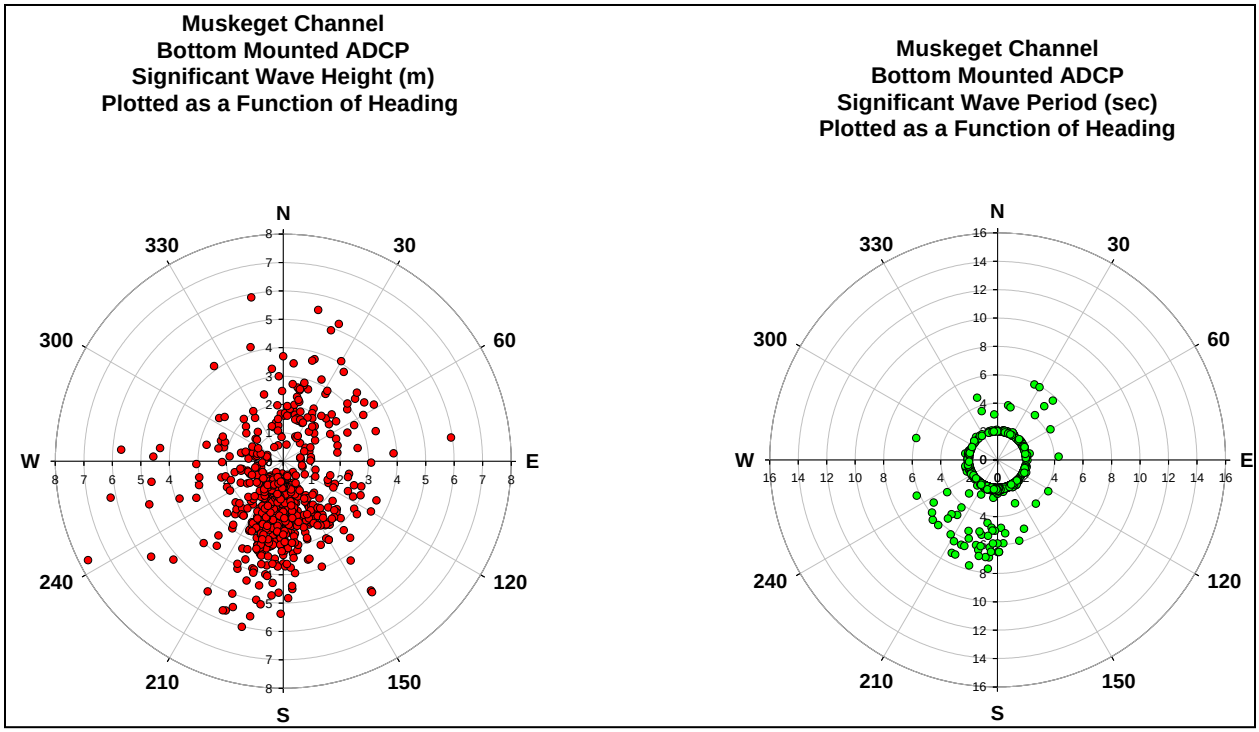

Figure 13 – Significant wave heights and wave periods plotted as a function of heading for the entire deployment duration at the Muskeget Channel site.

In general wave periods appear to be a function of surrounding shoals, while wave heights reflect local wind forcing and other weather related variables. Figure 15 demonstrates that wave period and height were independent throughout most of the deployment duration.

Any wave energy conversion device would need to be able to utilize a wide range of wave frequencies over short time spans. That said, the potential energy available is substantial and may make a substantial contribution in the future as technology improves (Figure 16). Average wave power available for extraction during the deployment was 133kW/m; during December the average power was ~15% higher.

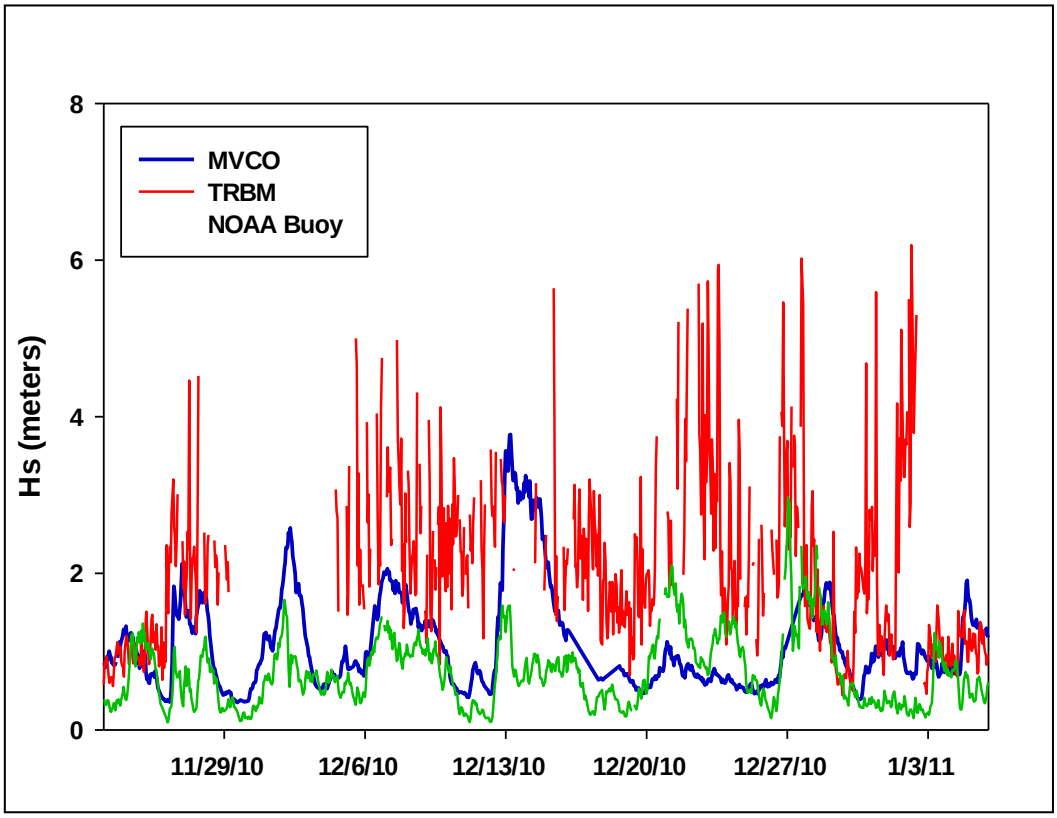

Figure 14 - Significant wave height (Hs, meters) record for the Muskeget Channel deployment location compared to the Martha's Vineyard Coastal Observatory (MVCO), and NOAA observation buoy 44020 (Nantucket Sound). During the deployment period a similar observed wave climate is observed between the MVCO and NOAA buoy 44020. The significant wave height at the Muskeget site showed a high variability which can be attributed to the combination of tidal (high current velocity) and weather conditions (wind) that affected the test area over the deployment period. These in-situ variables caused a highly variable wave field or sea state.

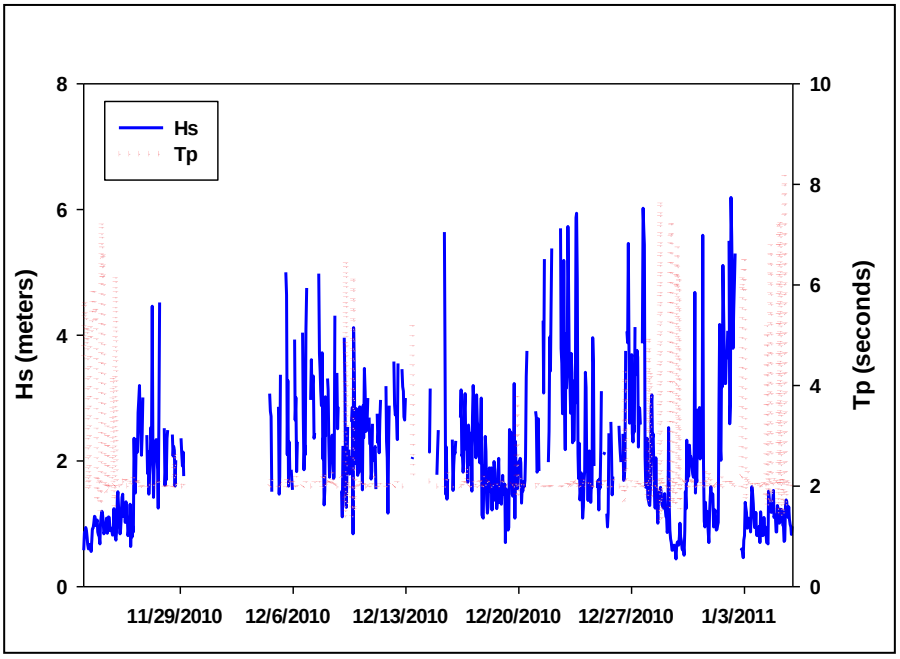

Figure 15 - Wave climate summary (Hs, meters) for Muskeget Channel test site over the 48 day deployment period. A high degree of variability in significant wave height (Hs) was observed due to localized tidal and weather conditions. Tidal and wind forces dominated in-situ conditions causing a variable wave climate over a relatively short time period (hours). These physical forces create erratic wave fields within Muskeget Channel as displayed in the above plot. Gaps in the data record are due to the burial of the TRBM from shifting sand waves

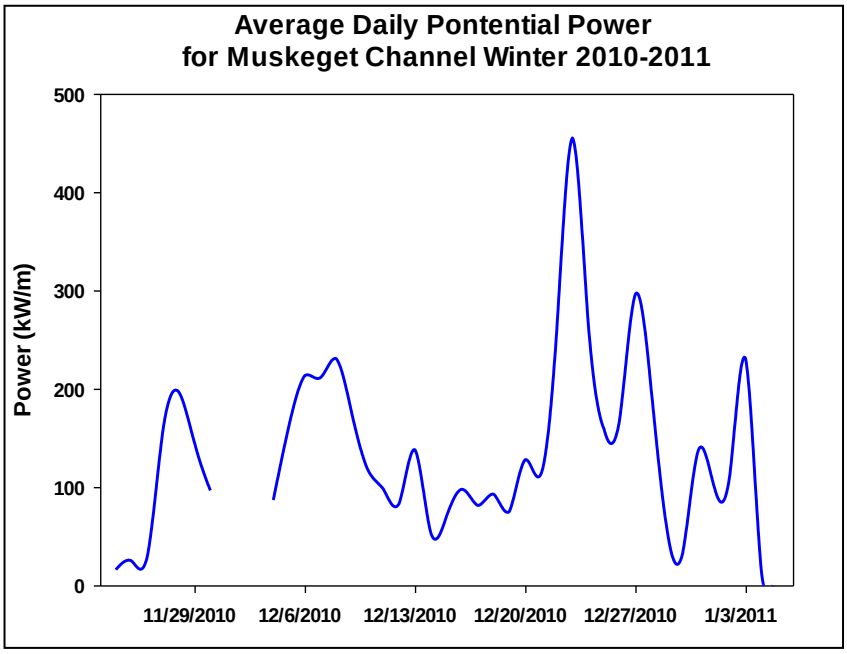

Figure 16 - Temporal display of the average daily potential power for Muskeget Channel over the 48 day deployment period. A mean power of 133 kW/m was calculated for the entire deployment period while a mean power of 152 kW/m was calculated for the month of December.

Time Series Data Collection on Current Velocities using Bottom Mounted, Upward Looking Acoustic Doppler Current Profiler (ADCP) in the NOREIZ, Waters South of Muskeget Channel

The NOREIZ site was chosen from many possible lease blocks to ensure mid depth wave and wind potential without interference from variable bathymetry or the possibility of entanglement with the numerous wrecks in the region (Figure 17). Following the deployment in Muskeget Channel the bottom mounted ADCP was refitted and deployed at the NOREIZ site south of Nantucket. The goal of the deployment was to determine the general current parameters in the area and whether there was any contra indication for siting a mid-water depth experimental wind platform at the location.

Current velocities were less than 1 m/s throughout the deployment period. Snap shots of consecutive Neap and Spring tides are shown in Figures 18-21. Highest velocities occurred near the surface and diminished with depth to less than 0.5 m/s near the sediment surface. Spring tides showed both higher velocities and greater penetration of contours into the bottom of the water column. The tidal currents were generally symmetrical showing similar durations and intensities regardless of whether the tide was ebbing or flooding. Currents at the site were unremarkable and should pose no obstacle to future utilization of the site for renewable energy research, including the establishment of a test platform if permitted.

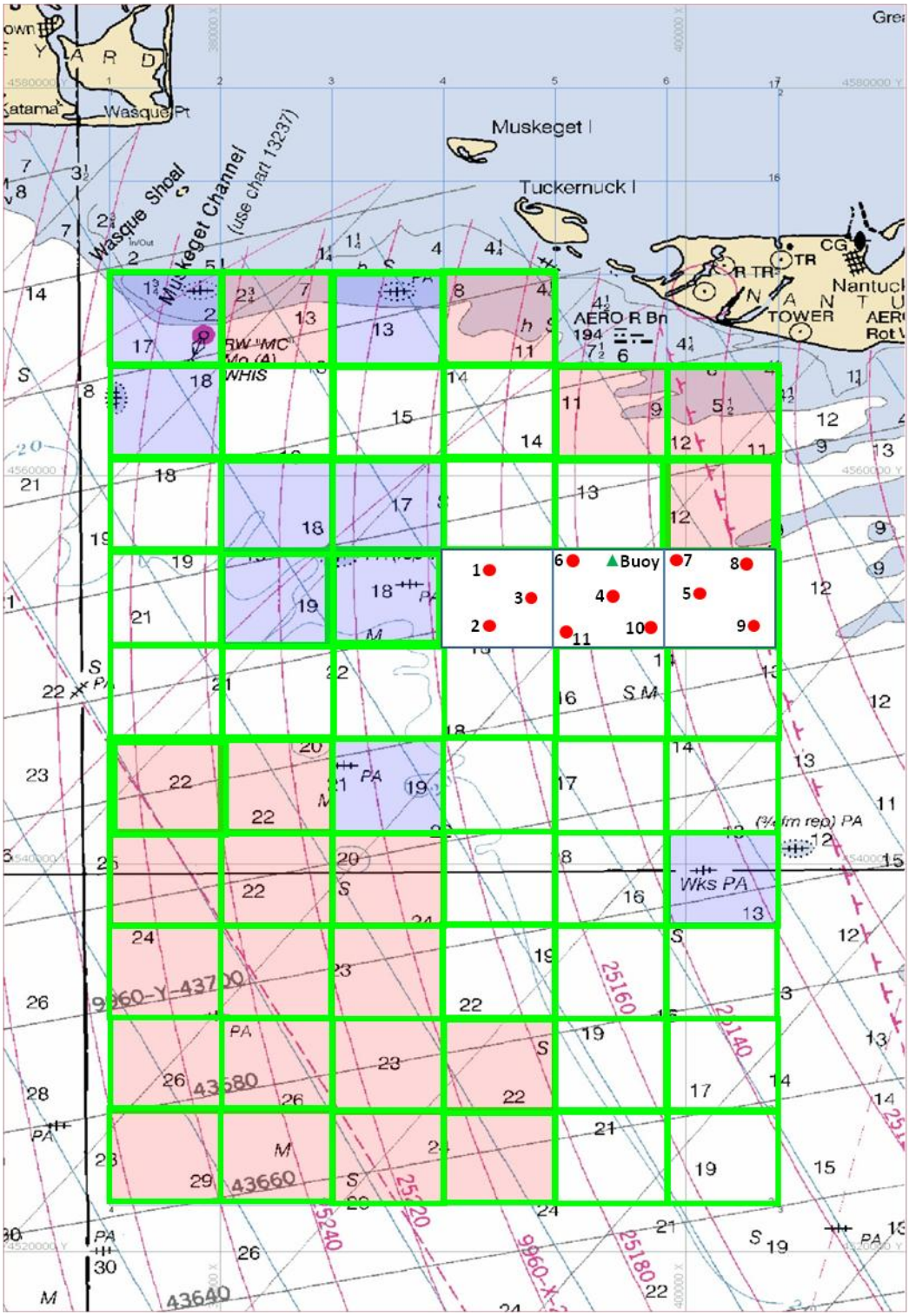

Figure 17 – Potential lease blocks available in the proposed NOREIZ region. Three contiguous blocks were selected. Locations of weather buoy and sediment samples are labelled. Blocks in blue were excluded due to the presence of wrecks. Red blocks were excluded because of bathymetry.

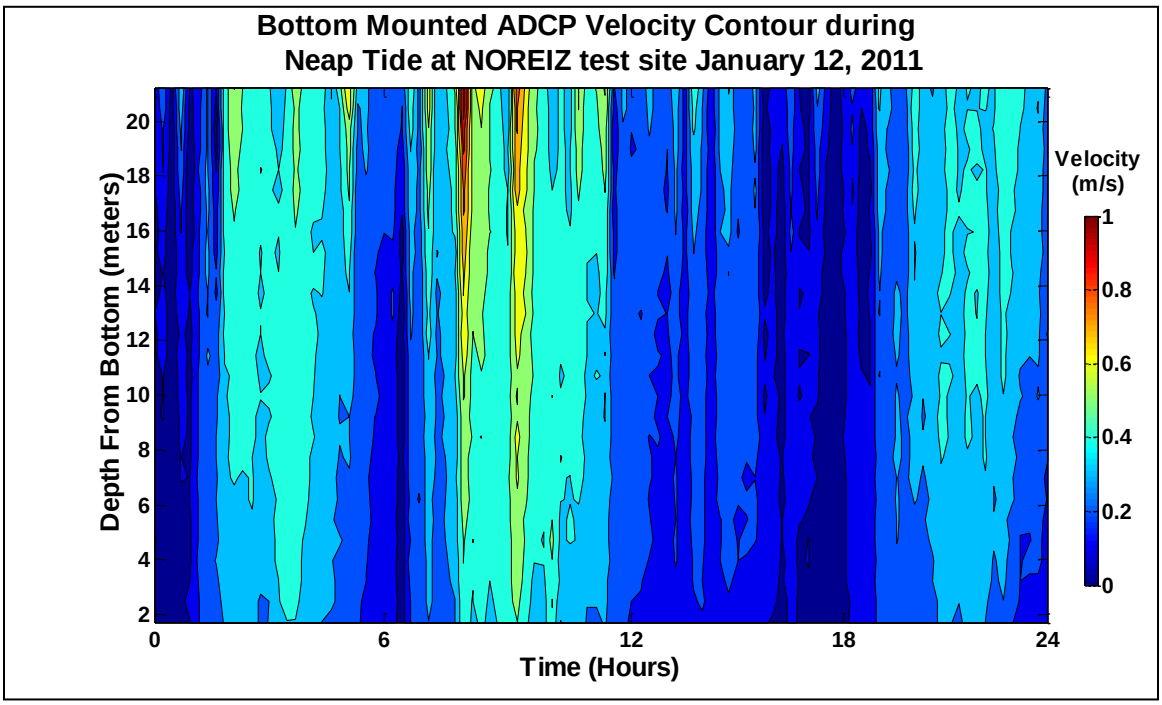

Figure 18 - Velocity magnitude contour plot for the NOREIZ test site during a neap tide moon phase. Current velocities ranged from a maximum of 1.0 m/s to a minimum of 0.15 m/s over a 24 hour period.

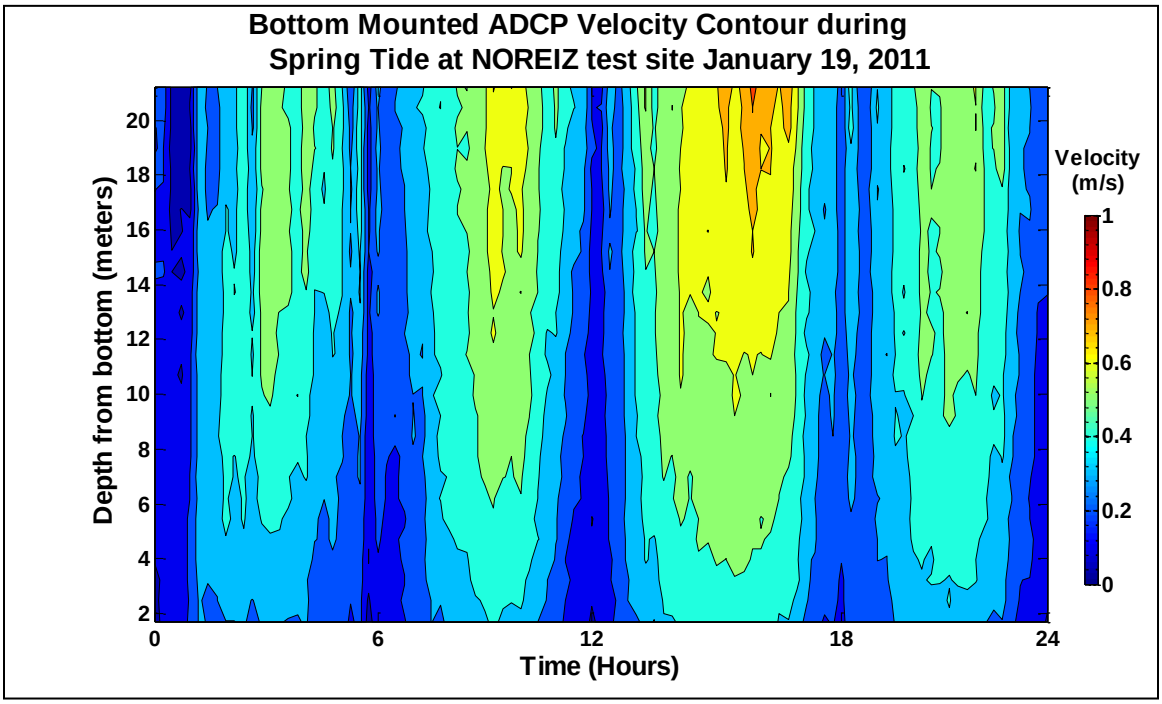

Figure 19 - Velocity magnitude contour plot for the NOREIZ test site during a Spring tide moon phase. Current velocities ranged from maximum of 0.8 m/s to a minimum of 0.2. m/s.

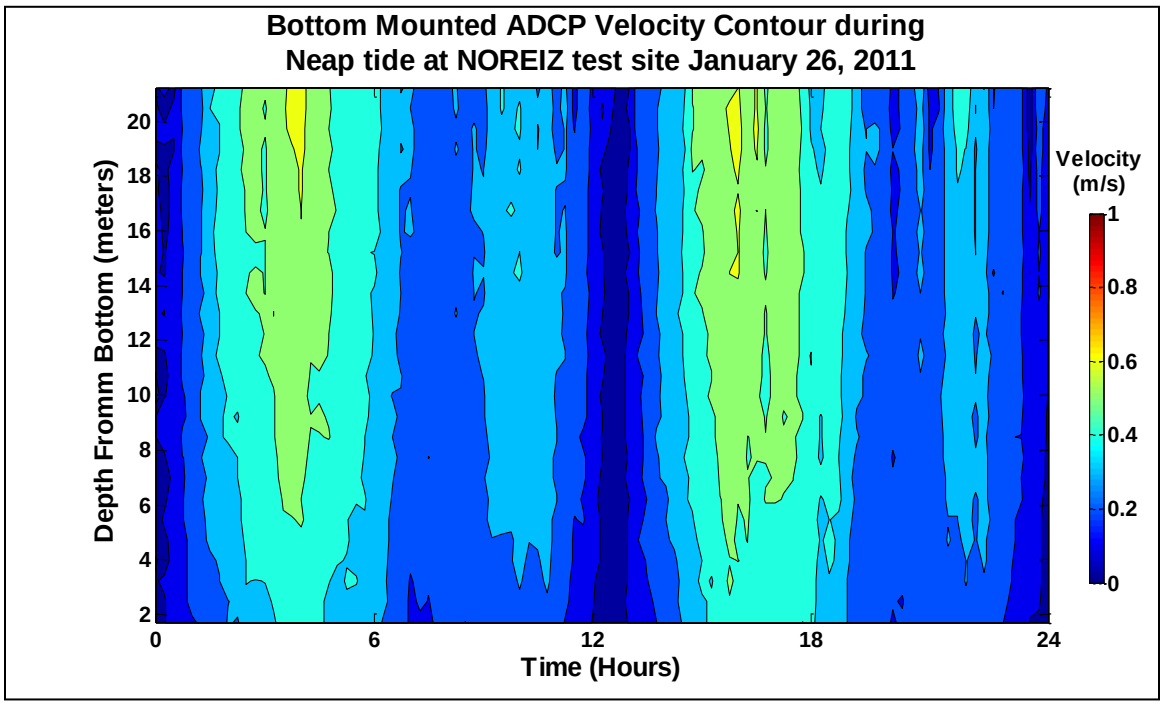

Figure 20 - Velocity magnitude contour plot for the NOREIZ test site during a neap tide moon phase. Current velocities ranged from a maximum of 0.7 m/s to a minimum of 0.15 m/s over a 24 hour period.

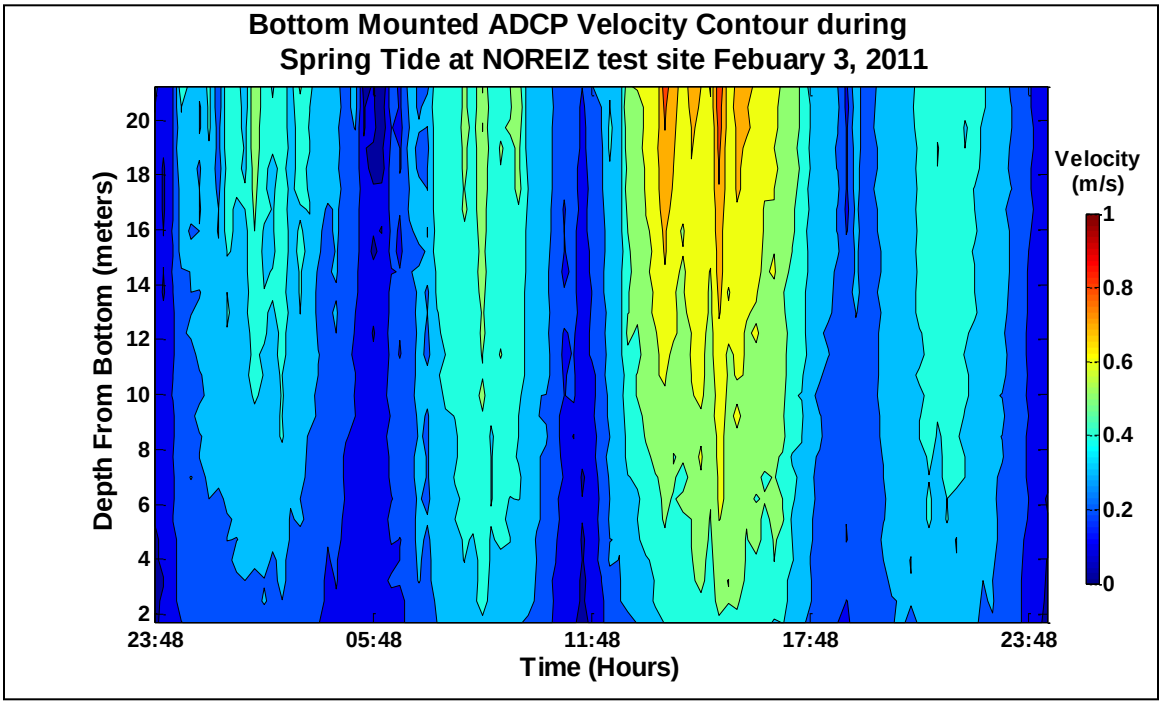

Figure 21 - Velocity magnitude contour plot for the NOREIZ test site during a Spring tide moon phase. Current velocities ranged from maximum of 0.9 m/s to a minimum of 0.2. m/s.

Time Series Data Collection on Wave Frequency and Direction in the NOREIZ, Waters South of Muskeget Channel

The establishment of the NOREIZ test site would if constructed provide a working platform for testing off shore wind technology. However, the possibility of providing a test bed for emerging wave energy conversion devices would complement the wind testing. Wave measurements were conducted using the same equipment as for Muskeget Channel. Time series power spectrums of wave frequency (Figure 22) shows primarily long swells arriving from off shore with few perturbations due to local conditions. Wave direction was consistently from the south-southwest and wave height and wave period appeared to vary together (Figure 23).

Perhaps most importantly, comparisons with nearby buoys show a strong similarity in the magnitude of significant wave heights (Figure 24). If the mathematical relationship for this 6 week record is found to be statistically significant then the long-term buoy record may be used to provide a more robust estimate of the wave climate. In addition, given the spatial relationship between the NOREIZ site and the buoys, if a test platform is constructed the buoys could provide valuable redundancy of key measures as well as a small time window of prediction in case of potentially damaging conditions.

Unlike the Muskeget Channel site wave period and height co-vary supporting the inference drawn from the power spectrum data that the wave field primarily reflects off-shore conditions (Figure 25). The rapidly changing weather experienced in the northeast during the winter months can be seen in the regular spikes in significant wave height recorded during the deployment (note significant wave heights in excess of 6m near the beginning of the record).

Potential power that could be used by wave conversion devices deployed at the NOREIZ site was estimated from the wave data to be 36.3 kW/m for the month of January and 52.3 kW/m for the month of February (Figure 26). Year round estimates based upon buoy data will provide a better estimate for commercial viability.

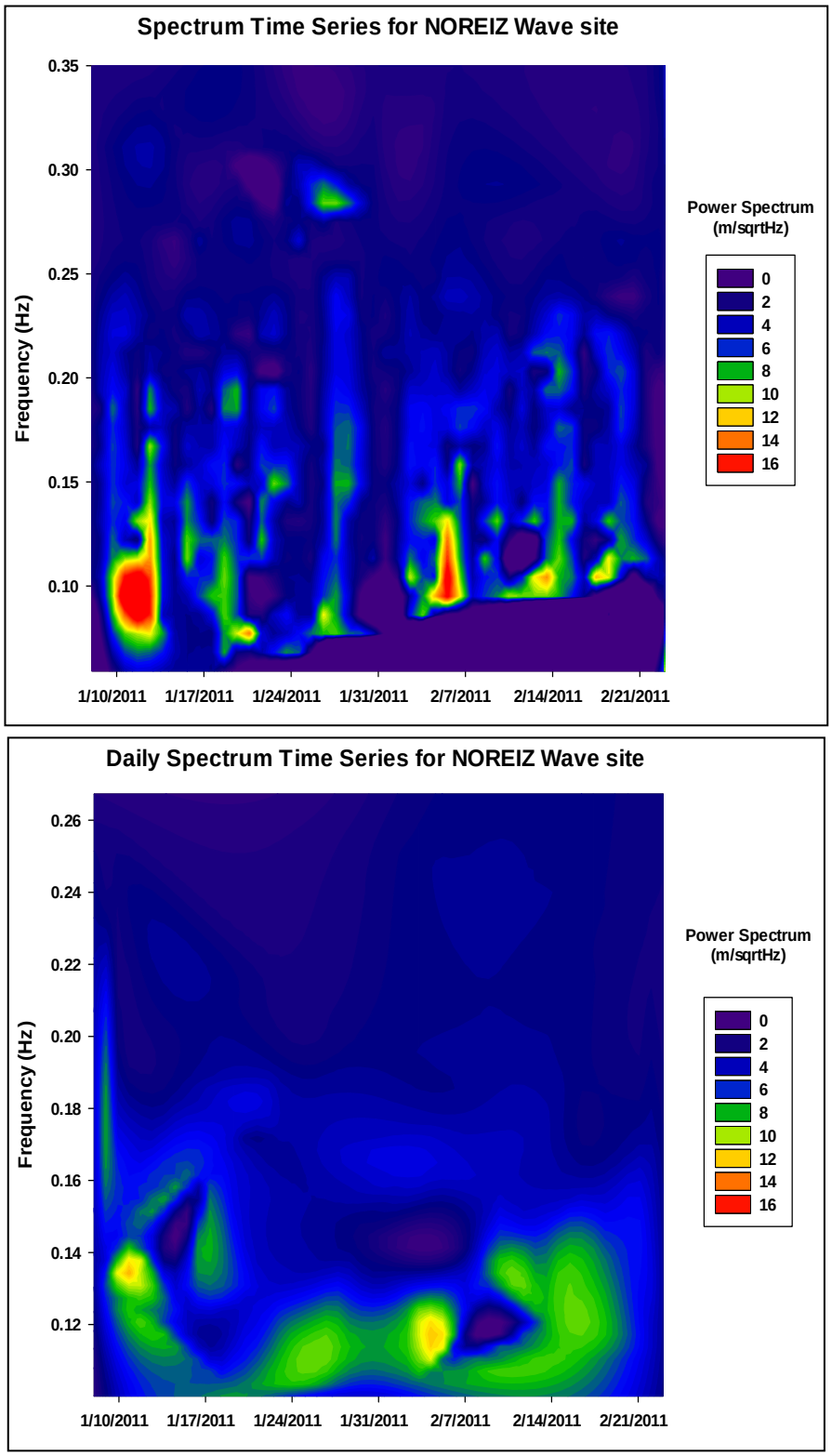

Figure 22 - Time series power spectrums showing instantaneous and daily averaged data for the entire deployment period.

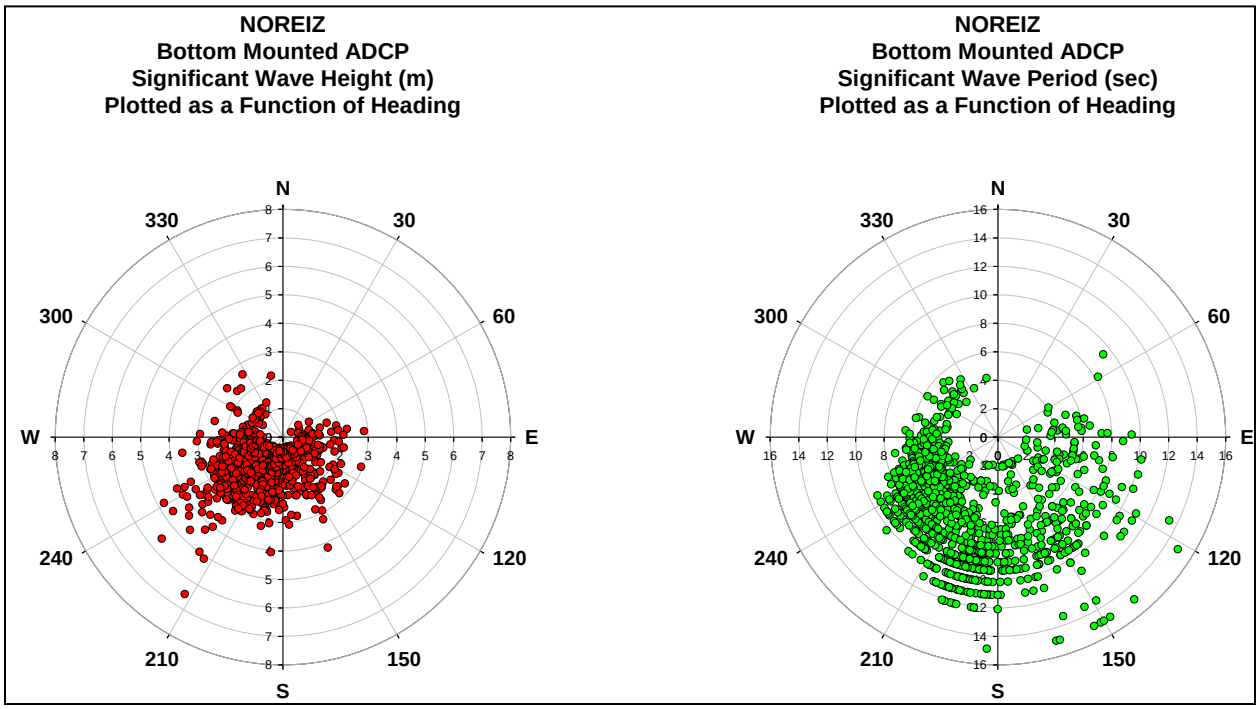

Figure 23 – Significant wave heights and wave periods plotted as a function of heading for the entire deployment duration at the NOREIZ site.

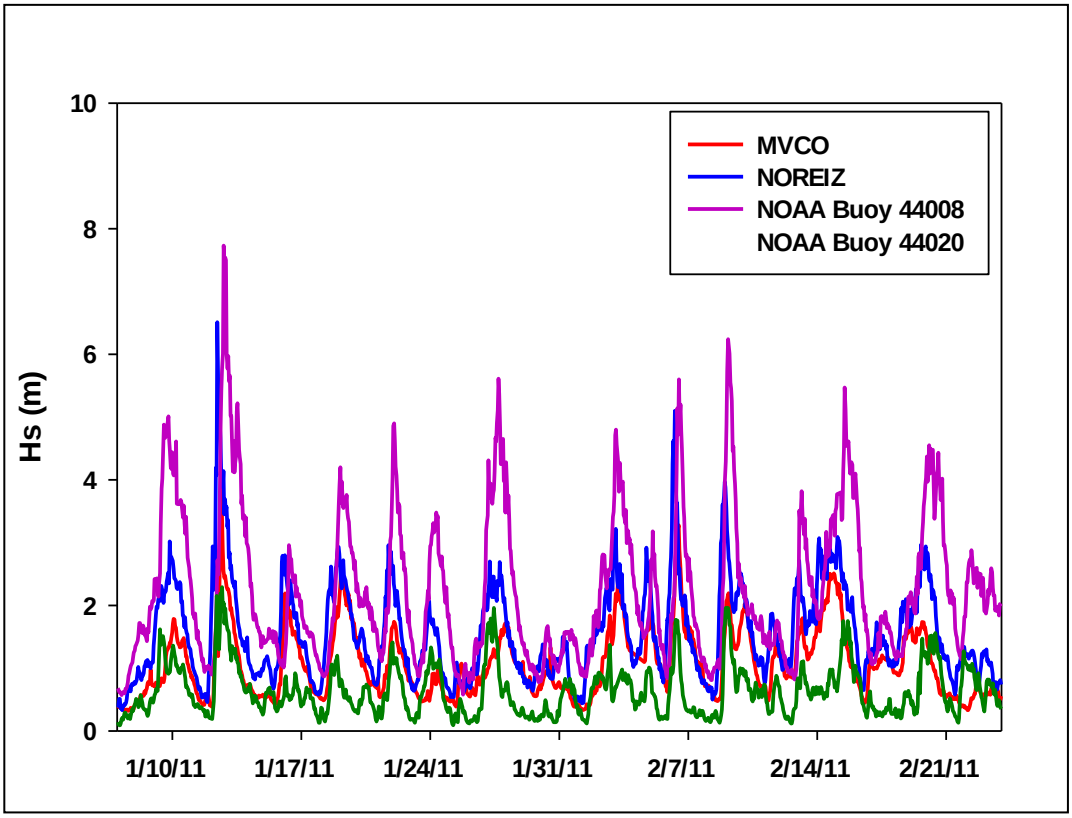

Figure 24 - Significant wave height (Hs, meters) record for the NOREIZ deployment location compared to the Martha's Vineyard Coastal Observatory (MVCO), NOAA observational buoy 44008 (54 nm south of Nantucket), and NOAA observation buoy 44020 (Nantucket Sound). During the deployment period a similar wave climate can be seen between all four locations with the largest significant wave heights observed at the NOREIZ site and NOAA buoy 44008. Mean Hs for the NOREIZ site was 1.55 (+/- 0.79) meters and 2.23 (+/- 1.20) meters for NOAA buoy 44008.

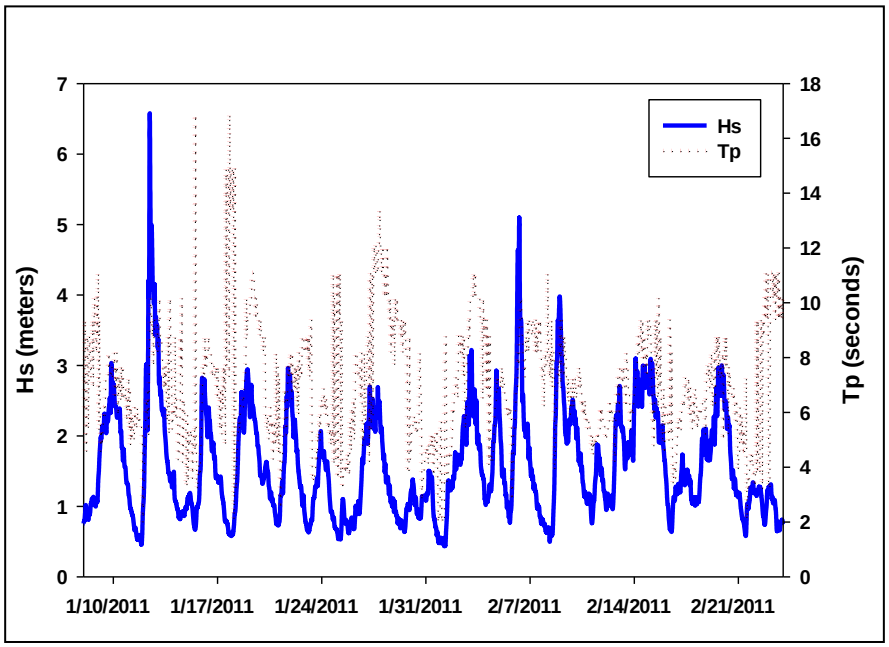

Figure 25 -. Wave climate summary displaying the temporal variation in wave conditions for the 48 day deployment period at the NOREIZ site (8 nautical miles south of Madaket Harbor, Nantucket MA). The largest peaks in significant wave height may be attributed to winter storms affecting the area.

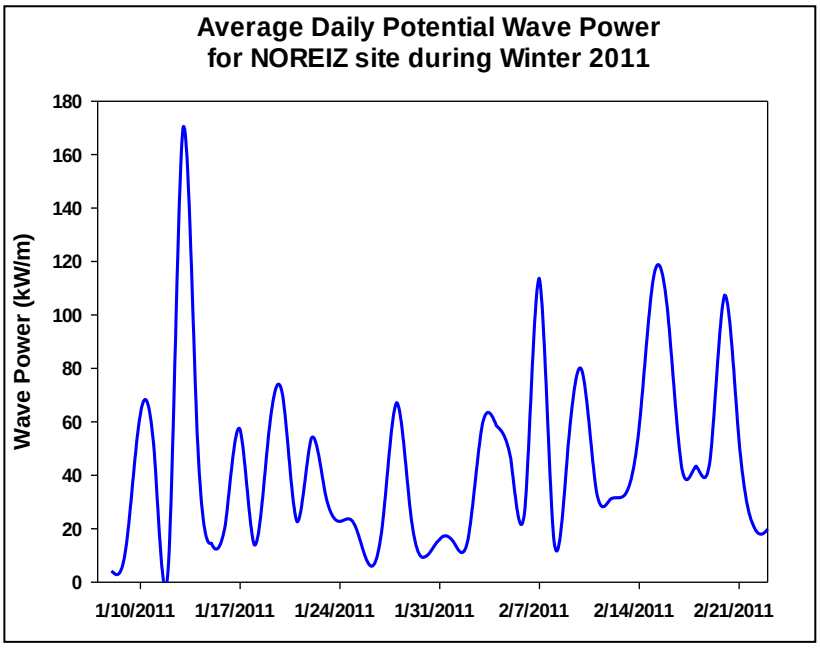

Figure 26 - Temporal display of the average daily potential wave power for the NOREIZ test site during the 48 day deployment period. A mean power of 36.3 kW/m was calculated for the month of January while the mean wave power increased during the month of February to 52.3 kW/m.

Time Series Data Collection on Wind Velocity and Direction in the NOREIZ, Waters South of Muskeget Channel

The weather buoy, configured to collect wind direction and velocity, temperature, relative humidity, solar radiation and precipitation was deployed August 2010 at the NOREIZ site (Figure 27). Primary importance was placed on wind data which will be used to assess the site potential for mid-depth wind turbine testing.

Figure 27 – Deployment of weather buoy at NOREIZ site.

Records of barometric pressure, temperature, relative humidity, and precipitation were collected and archived. There were no significant deviations from Nantucket Airport approximately 10 nautical miles to the north. The exceptions were temperature and relative humidity, with the

former reflecting surface water temperatures and the latter rarely deviating from 100%.

Wind data, on the other hand, showed significant differences, presumably because the buoy was outside the influence Nantucket Island. Histogram of wind direction (Figure 28) shows a fairly uniform distribution of wind directions with bi-modal peak durations occurring at 180-240^{o} and 70-90^{o}. These peaks coincident with regionally recognized dominant wind directions and are the same as nearly every primary airport runway within 50 nautical miles. A wind velocity histogram (Figure 29) displays peak duration of 8 days for wind speeds of 7 ms^{-} and peak velocity of 20ms^{-}. The composite distribution seen in Figure 30 demonstrates that the dominant local wind field was very constrained in direction with variable velocity.

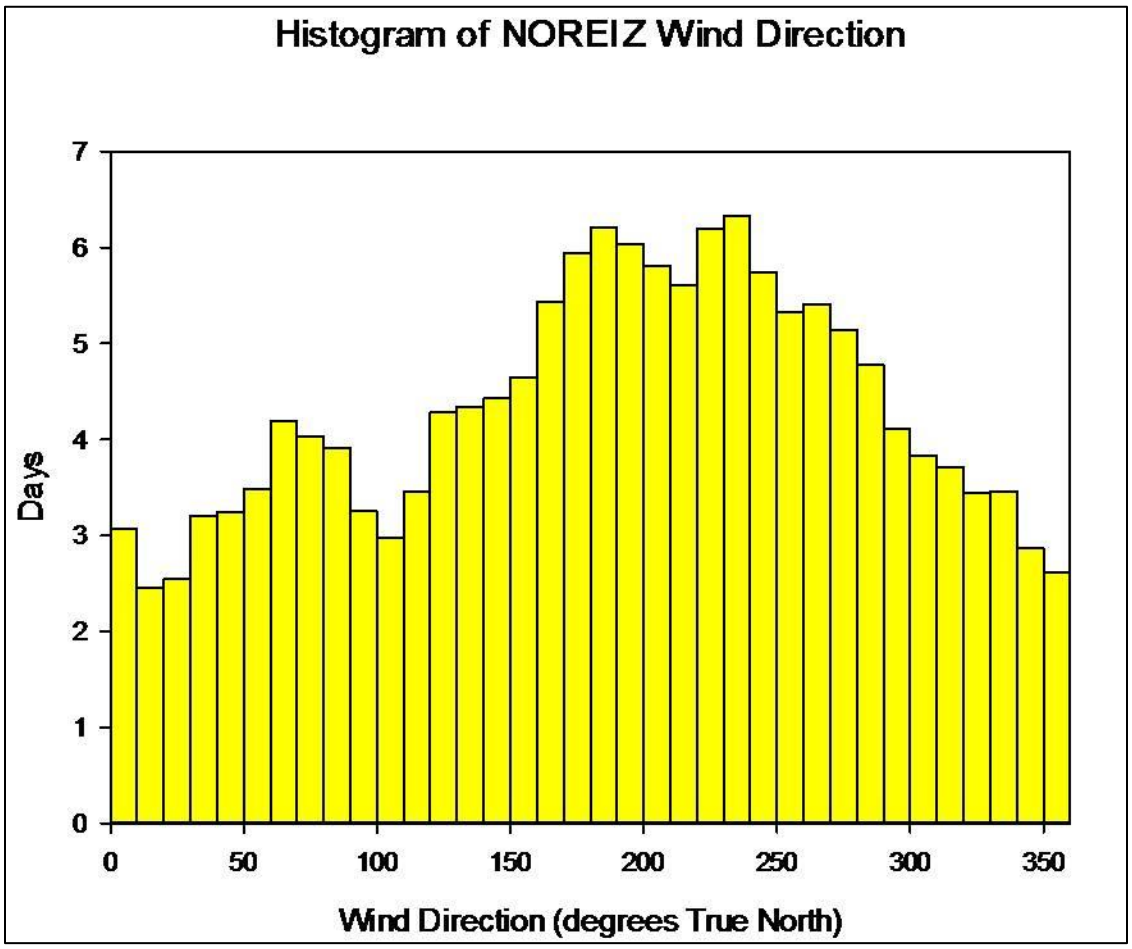

Figure 28 - Histogram showing the cumulative time during the deployment during which the wind came from a particular heading.

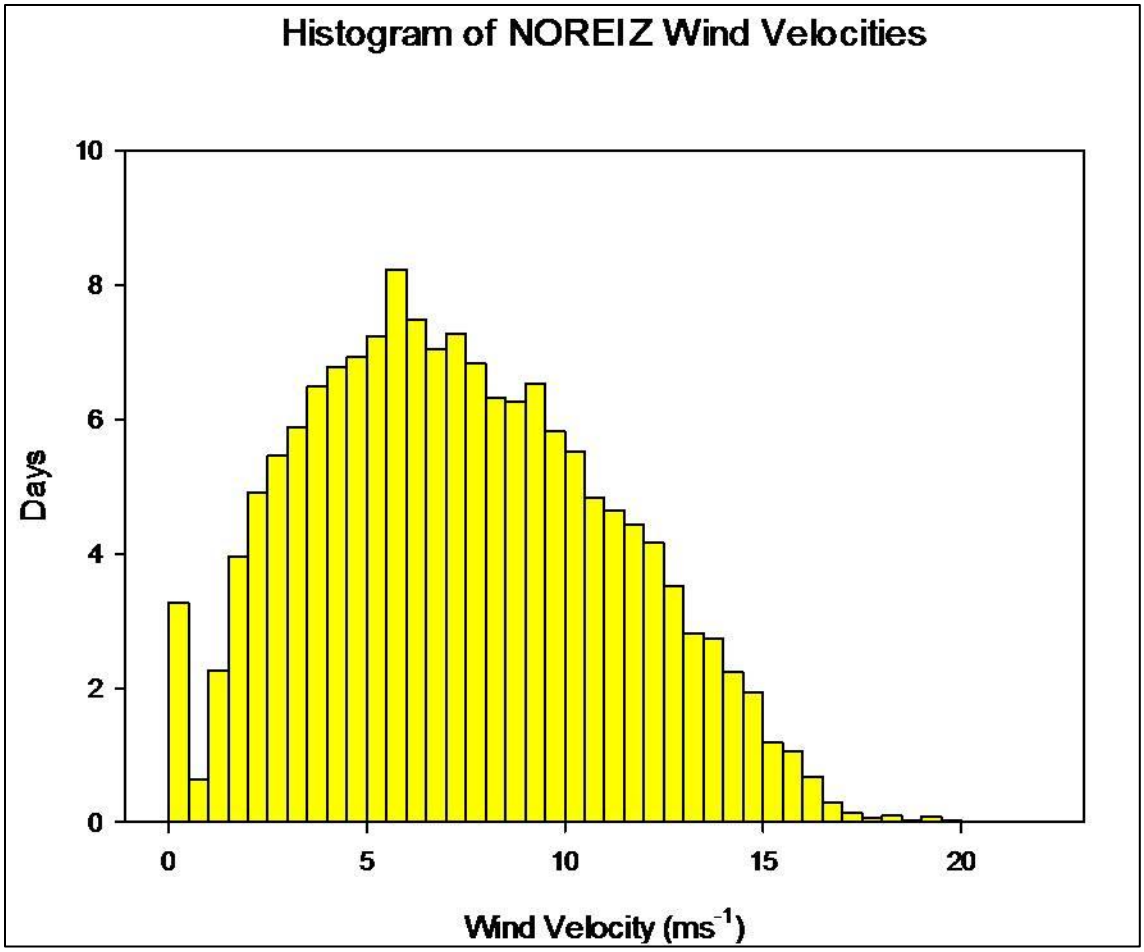

Figure 29 - Histogram showing the cumulative time during the deployment during which wind velocity reached as specific speed.

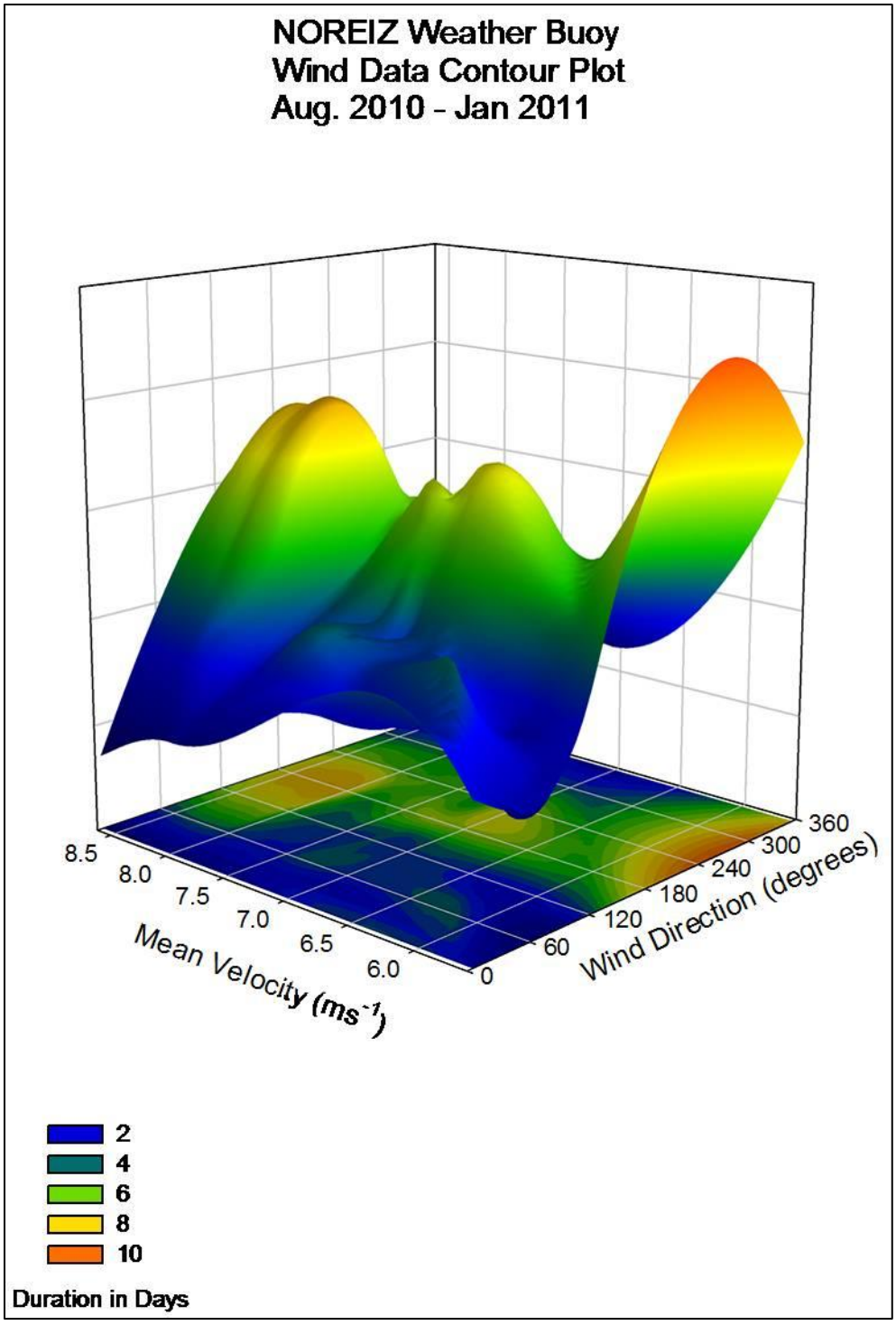

Figure 30 –Three dimensional plot combining wind velocity and direction for the NOREIZ site.

Characterization of Surficial Sediments in Vicinity of Buoy Deployed for Wind Measurements Associated with NOREIZ in Waters South of Muskeget Channel

Eleven sediment samples were collected within the NOREIZ blocks to assess seabed stability and infauna community structure (Figure 17). Sediments were collected with a Van Veen grab and were fairly uniform throughout the area sampled. Grain size distributions (Appendix XX) showed a large percentage of fine to medium sand and lesser quantities of fines and coarse grains suggesting an environment with low to moderate currents and a constant reworking of surficial sediments. Greater quantities of fine material were found in shallower waters in the eastern and northern regions of the NOREIZ site whereas greater quantities of coarse material were found in the southern and western region of the NOREIZ site.

The variability seen in the sediments was correlated with the highly variable infauna populations (Table 1). The largest numbers of individuals were found in the shallow finer sediments, while the smallest numbers of individuals were found in the coarsest sediments. Predictable the highest diversity was found at locations intermediate in character.

Location	Total Actual Species	Total Actual Individuals	Species Calculated @75 Indiv.	Weiner Diversity (H')	Evenness (E)
NOREIZ 1	13	2822	6	1.52	0.41
NOREIZ 2	24	953	9	1.45	0.32
NOREIZ 3	23	1324	10	2.35	0.52
NOREIZ 4	17	499	10	2.51	0.61
NOREIZ 5	12	55	N/A	2.67	0.74
NOREIZ 6	14	3077	6	1.24	0.33
NOREIZ 7	10	48	N/A	2.71	0.82
NOREIZ 8	15	66	N/A	2.68	0.69
NOREIZ 9	12	52	N/A	2.57	0.72
NOREIZ 10	16	208	10	1.96	0.49
NOREIZ 11	17	135	15	3.68	0.90

Table 1- Results of infaunal analysis at selected sites within the NOREIZ blocks.

Element 2 – Town of Edgartown FERC Permit Perimeter Area Investigation to Support Power Transmission to Upland Grid.

At present two (2) cable routes are being considered by the Town of Edgartown to bring power to shore (Figure 2). Engineering and permitting activities to support the burial of cables require:

(a) evaluation of the biotic resources to be impacted during construction, primarily benthic infaunal communities
(b) sediment type, eelgrass presence and near bottom current velocities
(c) coastal resources above MLW (i.e. beach, dune, wetland)

Evaluation of Biotic Resources (Infauna) along Proposed Cable Routes (Pochet / Katama)

Benthic animals are a critical feature of coastal systems, including the overall Nantucket Sound ecosystem and the Muskeget Channel sub system. Benthic communities provide the base of food webs for pelagic fisheries as well as being an economically important shellfish fishery. In addition, changes in benthic communities are excellent indicators of environmental change. Therefore, it is important to establish a baseline benthic community characterization to monitor potential future changes to benthic communities as a result of both natural agents of change as well as those resulting from the deployment of tidal energy generating technologies.

Trenching activities to bury cables create acute disturbance to benthic communities through burial, with subsequent recovery of benthic communities post-construction. Determination of the infaunal community along the 2 potential cable routes being considered by the Town of Edgartown for its tidal energy pilot project will allow assessment of the likely rate of recovery post-construction by establishing a baseline for the types of infauna populating the sediments in the absence of disturbance. Quantitative sediment sampling for infauna was conducted at 4 locations along each of the two transects (Figure 31 and 32). Sediment sampling for infauna community characterization was achieved using a Van Veen Grab Sampler (surface area = 0.0625 m^2).

Analysis of the evenness and diversity of the benthic animal communities at each of the four sampling locations on each transect was used to support density data and natural history information. The evenness statistic can range from 0-1 (one being most even), while the diversity index does not have a theoretical upper limit. The highest quality habitat areas, typically in areas with stable bottom sediments and high oxygen conditions, have the highest diversity (generally >3) and evenness (~0.7). The converse is also true, with poorest habitat

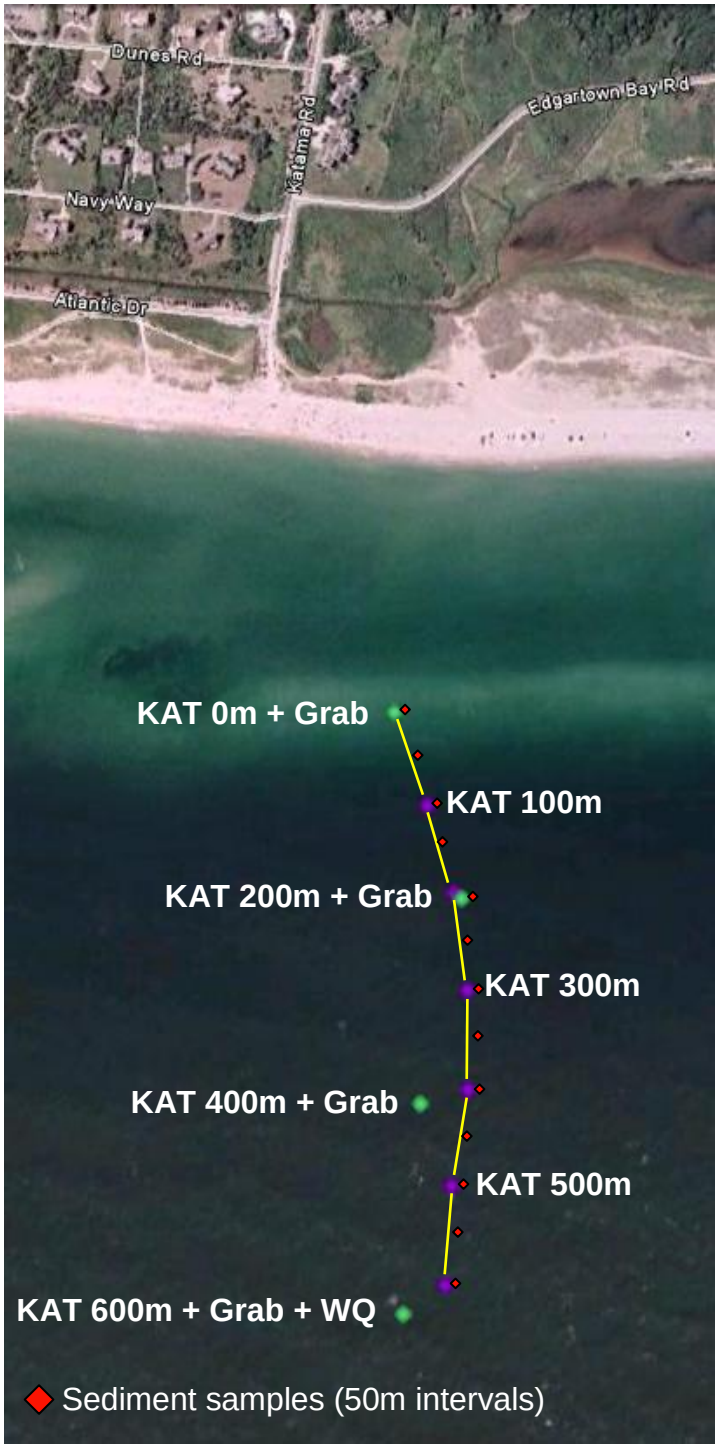

Figure 31 – Katama Transect, Martha's Vineyard south shore. Infaunal grab samples retrieved at 200 meter intervals (green symbols) with associated disturbance plots. Sediment samples retrieved at 50 meter intervals (red symbols). Underwater surveying completed by diver observation for eelgrass and bottom characteristics the length of transect.

Figure 32 – Pochet Transect, Martha's Vineyard eastern shore. Infaunal grab samples retrieved at 200 meter intervals (green symbols) with associated disturbance plots. Sediment samples retrieved at 50 meter intervals (red symbols). Underwater surveying completed by diver observation for eelgrass and bottom characteristics the length of transect. Water quality sampling was undertaken at 600 meter point and a downward looking single point current meter was deployed at 400 meters to measure near bottom current velocities for sediment transport modeling.

quality (unstable sediments) found where diversity is <1 and evenness is <0.5. Estimates of the number of species adjusted to the number of individuals and diversity (H') and Evenness (E) of the community allow comparison between locations.

Sub-Embayment	Location	Total Actual Species	Total Actual Individuals	Species Calculated @75 Indiv.	Weiner Diversity (H')	Evenness (E)
MUSKEGET ADULTS						
Pochet1	0M	8	44	N/A	2.59	0.86
Pochet2	0M	9	18	N/A	2.82	0.89
Pochet3	0M	8	26	N/A	2.21	0.74
Pochet1	200M	25	72	N/A	4.11	0.89
Pochet2	200M	31	68	N/A	4.65	0.94
Pochet3	200M	30	74	N/A	4.55	0.93
Pochet1	400M	14	32	N/A	3.35	0.88
Pochet2	400M	7	19	N/A	2.18	0.78
Pochet3	400M	6	10	N/A	2.16	0.84
PochetA	600M	1	1	N/A	0.00	N/A
PochetB	600M	5	7	N/A	2.24	0.96
PochetC	600M	3	11	N/A	1.10	0.69
Katama A	0M	4	201	3	0.94	0.47
Katama B	0M	4	102	4	1.16	0.58
Katama C	0M	8	200	6	1.46	0.49
Katama A	200M	23	106	20	3.82	0.84
Katama B	200M	12	38	N/A	2.54	0.71
Katama C	200M	18	141	15	3.42	0.82
Katama A	400M	9	103	7	0.84	0.27
Katama B	400M	14	77	14	2.62	0.69
Katama C	400M	11	35	N/A	2.41	0.70
Katama A	600M	12	31	N/A	2.82	0.79
Katama B	600M	15	32	N/A	3.52	0.90
Katama C	600M	9	21	N/A	2.49	0.79

Table 2 – Summary of total actual species and individuals identified at 4 stations (0m, 200m, 400m, 600m) along each transect representing the two proposed cable routes (Pochet and Katama). Each station along the two transects was sampled in triplicate. This summary table is limited to ADULTS.

Sub-Embayment	Location	Total Actual Species	Total Actual Individuals	Species Calculated @75 Indiv.	Weiner Diversity (H')	Evenness (E)
MUSKEGET JUVENILES						
Pochet1	0M	2	17	N/A	0.32	0.32
Pochet2	0M	6	19	N/A	2.21	0.85
Pochet3	0M	4	15	N/A	1.69	0.84
Pochet1	200M	2	32	N/A	0.81	0.81
Pochet2	200M	1	8	N/A	0.00	N/A
Pochet3	200M	3	72	N/A	1.53	0.97
Pochet1	400M	0	0	N/A	N/A	N/A
Pochet2	400M	2	24	N/A	0.92	0.92
Pochet3	400M	0	0	N/A	N/A	N/A
PochetA	600M	1	1	N/A	0.00	N/A
PochetB	600M	1	1	N/A	0.00	N/A
PochetC	600M	2	3	N/A	0.92	0.92
Katama A	0M	2	72	N/A	0.50	0.50
Katama B	0M	1	40	N/A	0.00	N/A
Katama C	0M	1	72	N/A	0.00	N/A
Katama A	200M	5	48	N/A	2.25	0.97
Katama B	200M	4	64	N/A	1.75	0.88
Katama C	200M	2	16	N/A	1.00	1.00
Katama A	400M	2	16	N/A	1.00	1.00
Katama B	400M	6	20	N/A	2.32	0.90
Katama C	400M	1	8	N/A	0.00	N/A
Katama A	600M	1	48	N/A	0.00	N/A
Katama B	600M	4	7	N/A	1.84	0.92
Katama C	600M	7	27	N/A	2.66	0.95

Table 3 – Summary of total actual species and individuals identified at 4 stations (0m, 200m, 400m, 600m) along each transect representing the two proposed cable routes (Pochet and Katama). Each station along the two transects was sampled in triplicate. This summary table is limited to JUVENILES.

Divers also created disturbance plots at 0m, 200m, 400m and 600m. These plots were established to understand the degree to which cable laying could affect bottom communities and how quickly these infaunal communities recover from disturbance. Sediment grab samples were collected to establish a control and were sieved and sorted for infauna identification. Both surface and subsurface markers for the disturbance plots could not be located following the initial disturbance event; locals suggested vandalism as likely, however, seasonal storm intensity was also greater than normal. Statistical analysis of the infauna samples indicates that there were so few individuals that it would be impossible to see a significant decrease in population size or diversity in over half the sites sampled. This conclusion is supported by a wide range of studies cited in the United Nation Environmental Protection publication*. In general these studies show low numbers of individuals in dynamic coarse sediments and recovery times in the range of weeks or months.

*Carter L., Burnett D., Drew S., Marle G., Hagadorn L., Bartlett-McNeil D., and Irvine N. (2009). Submarine Cables and the Oceans – Connecting the World. UNEP-WCMC Biodiversity Series No. 31. ICPC/UNEP/UNEP-WCMC.

Characterization of Surficial Sediment, Eelgrass Presence and along Proposed Cable Routes (Pochet / Katama)

Surficial Sediment Characterization and Eelgrass Presence – Sediment characterization is a critical aspect of preliminary planning for routing of electrical transmission cables. Characterization is typically needed for both the surficial sediments as well as slightly deeper sediments as these sediment characteristics define the effectiveness of the burial of the transmission cable (typically 1.0-1.5 meters below the seabed) as well as the degree to which the cable could become unburied over time. While the characteristics of the deeper sediments are obtained using acoustic instruments like side-scan sonar and multi-beam sensors, the surficial sediments were characterized using traditional sediment sampling and standard grain size analysis using dry and wet sieving methods as appropriate. As funding for sediment characterization was limited, the initial surveying was undertaken in the nearshore water portion of the proposed cable routes such that divers could collect sediment samples using core tubes while at the same time completing a visual survey of bedforms, submerged aquatic vegetation (eelgrass and macroalgae) and macrofauna. The use of side scan sonar and multi-beam instruments for characterizing the deeper sediments is being considered as future funding becomes available and will encompass the deeper water areas of Muskeget Channel all the way out to the future pilot project deployment location.

Grain size characterization was performed on samples collected at all sites along the Pochet and Katama transects (Appendix 3). With few exceptions the sites were dominated by medium sand characteristic of moderate currents and ground swell constantly reworking the surficial sediments. Katama sediments were patchy with surface expression of glacial clay lenses colonized with more diverse infauna owing to the greater stability of the substrate. Occurrence was most pronounced in shallow waters near the beginning of the transect (0m), but persistent out to 400 m. While both possible cable routes present regulatory hurdles once reaching landfall, the sediment variability seen in the Katama route presents additional logistical challenges in addition to significantly longer cabling distance.

Prior to conducting the underwater surveys of the two proposed cable routes, the CSP completed a brief search of background work on sediments and eelgrass distribution in the areas to be surveyed. Prior eelgrass survey work completed by the Massachusetts Department of Environmental Protection (MassDEP) Eelgrass Mapping Program (C. Costello) was helpful for anticipating the possible presence of eelgrass in the area to be surveyed (Figure 33 and 34). Eelgrass is a fundamentally important specie in the ecology of shallow coastal systems, providing both habitat structure and sediment stabilization. As such, it is important to know where eelgrass may occur within a given system such that those SAV resources can be safeguarded against impairment from anthropogenic activities like mooring of tidal energy generating units or the deployment of submarine transmission cables to shore.

Eelgrass (*Zostera marina*) is the most common seagrass present on the Massachusetts coastline. The two principal human disturbances affecting eelgrass growth is declining water quality and physical disturbance. Based on the MassDEP eelgrass surveys and as would be expected in highly energized environments such as the overall Muskeget Channel system, eelgrass is

primarily situated along the eastern shore of Chappiquiddick Island where the current velocities are low (< 1.0 knots) and the water is generally shallow (< 5.0 meters). Based on the MassDEP surveying, the eelgrass beds that are present exist as patches of eelgrass as opposed to a long continuous bed the length of the shoreline. While the eelgrass does generally appear consistently present along the shoreline, the areal extent of the eelgrass as depicted in the 1995 survey does seem to have shifted when compared to the 2001 distribution. That may simply be due to the natural variation associated with shifting beach sediments during winter storms but should be taken into consideration relative to the laying of submarine transmission cables from tidal energy generating units.

CSP divers did confirm the presence of eelgrass in the area mapped by the MassDEP, however, it was much more sparse then anticipated based on the MassDEP map reviewed in advance of the underwater survey in the summer of 2010.

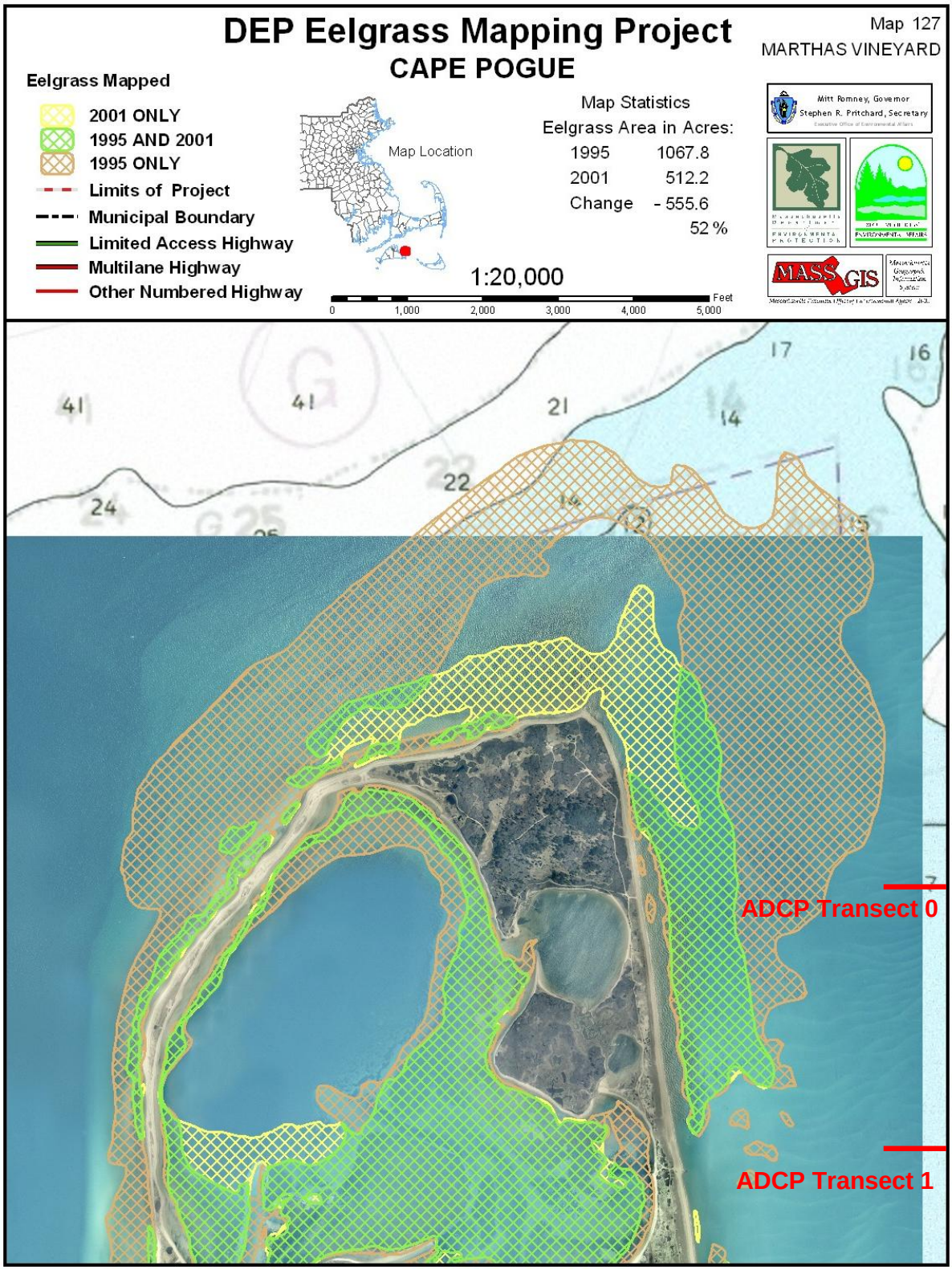

Figure 33- Eelgrass presence in the nearshore region of the northern reach of Muskeget Channel. The western ends of Transects 0 and 1 (low velocity areas) are shown for reference. Eelgrass was not observed at sediment sampling sites within the main channel along Transects 0 and 1.

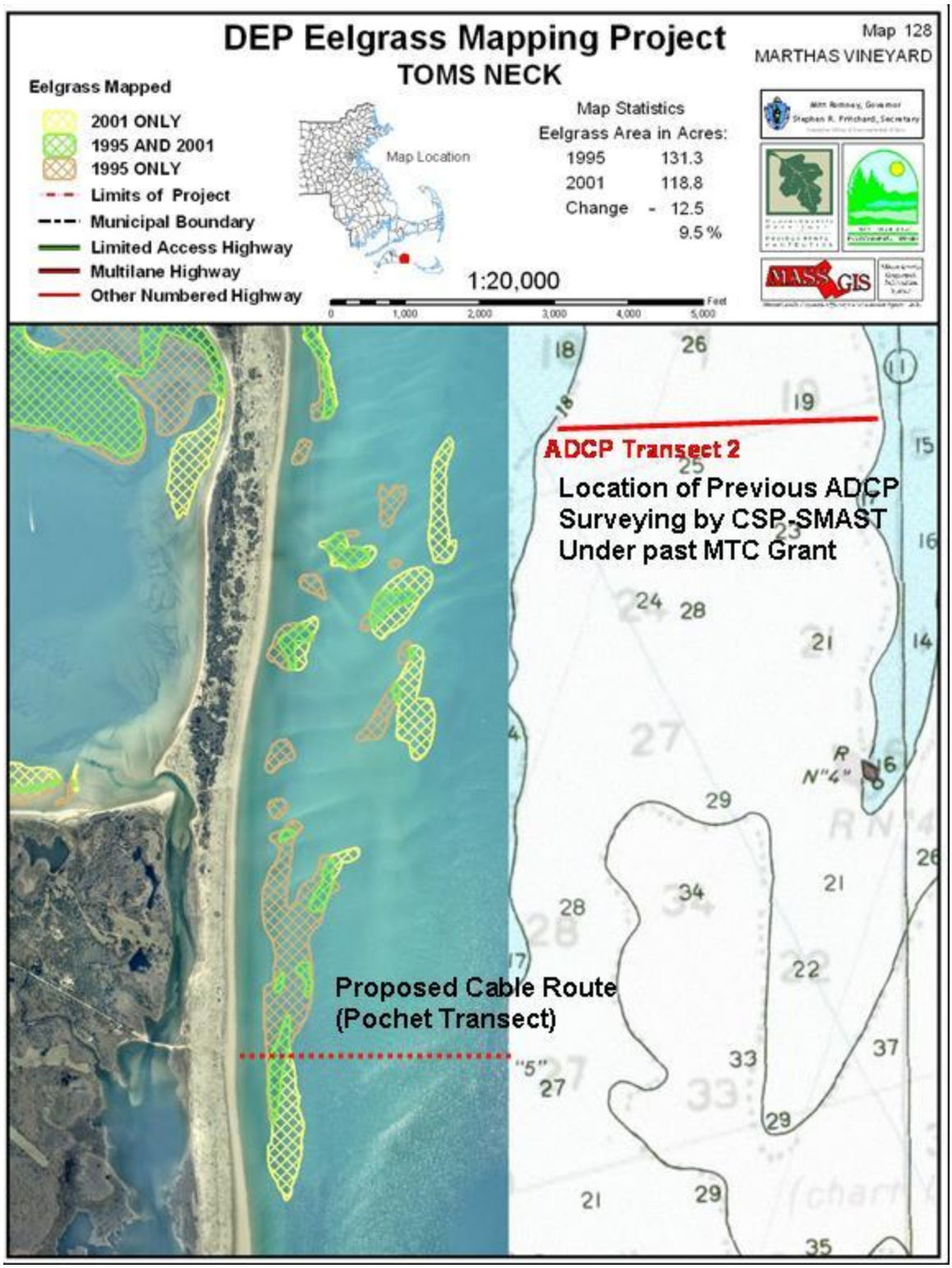

Figure 34- Eelgrass beds in the shallower waters in the western nearshore region of Muskeget Channel south of Transect 2 and in vicinity of proposed cable route. Eelgrass was not observed at sediment sampling sites within the main channel along Transect 2.

Survey transects were established in two different locations being considered as potential cable routes for bringing power ashore from a future tidal energy system. The first transect (Pochet) location extends out from the eastern shore of Martha's Vineyard (Chappaquiddick Island) between Cape Pogue to the north and Wasque Point to the south. The transect location was selected relative to the position of landside electrical infrastructure that terminates in the vicinity of the dike bridge. The second transect (Katama) extends out from the south shore of Martha's Vineyard, westward of the recently formed breach of the barrier beach separating Katama Bay from the Atlantic Ocean. Similar to the Pochet transect, the location of the Katama transect was dictated by the existing landside electrical infrastructure that terminates at the intersection of Katama Road and Navy Way. Underwater surveying was completed during the 2010 summer field season.

Each transect was limited to 600 meters in length and the near shore end of the Pochet and Katama transects was established at approximately 100 meters and 300 meters respectively. The near shore end of each transect was not established closer to shore given the degree to which the shallow waters are disturbed by the action of breaking waves. The near shore end of the Katama transect was set further out then the Pochet Transect because of the ground swell, depth constraints on the vessel and the safety of the divers subjected to the strong surging experienced underwater due to the ground swell. Both of the transects were visually surveyed by diver for bottom characteristics and bedforms, presence of eelgrass or other submerged aquatic vegetation and macrofauna. During the surveying, divers collected sediment samples at 50 meter intervals for the length of each transect. The sediment cores were obtained by hammering a polycarbonate core tube into the seabed. Sediments were collected from approximately the top 6 to 8 inches of the seabed. The samples were returned to the CSP Laboratory at UMASS-Dartmouth, SMAST and were dry sieved for grain size analysis.

Pochet Transect

The bottom sediments along the Pochet transect were uniformly sandy with sparse benthic macrofauna given the extremely dynamic nature of this location. Between 0m and 100m along the transect, divers observed a welk (large marine gastropod mollusk) as well as a small patch (~3 meter diameter) of sparse eelgrass. Along this section of the transect the sediments were mostly fine to medium grained sand mixed with shell hash. Between 100m and 200m along the transect the sediment became a mix of medium grained sand mixed with pebbles and cobbles as well as a few large rocks. A patch of sparse eelgrass was observed at approximately 110 meters along the transect and sparse attached macroalgae was observed as well. Small crabs were observed by the divers along with evidence of work tubes. Between 200m and 300m the surficial sediments were a mix of medium sand mixed with pebbles and shell hash. Macrofauna observed was limited to several spider crabs. From 300m to 400m the surficial sediments were mostly a medium sand mixed with pebbles and cobbles. In a few areas the sediment appeared compacted, mostly in between large sand waves comprised of unconsolidated medium sand. The large sand waves were observed rising approximately 1.0-1.5 meters off the bottom. Divers observed both spider crabs and hermit crabs in this section along the transect. Between 400m and 600m the surficial sediments were similar, mostly medium sand mixed with pebbles and shell has, compacted at the toe of large sand waves which were comprised of unconsolidated medium sand. No macrofauna was observed between 400m and 600m.

As described by the divers, bottom currents are strong and the sandy bottom is very dynamic to the point that sand particles could be observed moving along the bottom. The sand movement and the presence of large sand waves indicates that keeping a cable buried along this shoreline may be challenging. However, infaunal communities along the Pochet transect are relatively depauperate and similar to bottom communities observed and sampled in other dynamic and high current velocity areas such as the inlet to Chatham Harbors on Cape Cod as well as the inlet to Plymouth Harbor on Cape Cod Bay. Additionally, the sparse eelgrass habitat indicates that it may be possible to shift the cable route slightly and avoid eelgrass habitat altogether. Appendix 3 presents the results of the grain size analysis conducted on sediment samples retrieved from the Pochet transect.

Katama Transect

The seabed surficial sediments along the Katama transect were observably different than the surficial sediments observed along the Pochet Transect. The sediments were not uniformly sandy as was observed along the Pochet transect. Generally, surficial sediments along the Katama transect varied from a clay-like and sticky material to fine sand along the length of the transect and the surficial sediment appeared more compacted. Patches of clay were present unburied by sand and supporting macrofaunal communities of crabs and hermit crabs. More specifically, divers reported sediments between 0m and 100m to be a mix of medium to fine sand overlaying rock and cobble (0m-30m medium sand, 30m-50m fine sand, 50m-80m clay-like mud mixed with sand, 80-100m patch of cobbles). Below the rock and cobble appeared to be a base of more fine sand. From 100m to 200m the surficial sediments appeared to change to a mix of medium sand mixed with clay-like material (100-150m med sand/clay, sticky mud below (3 patches at approximately 15-20m intervals), 175m-200m large patch of clay/mud). According to the diver observations of the 100m to 200m section of the transect, there appeared to be more macro fauna than the 0m-100m section of the transect and there was also drift macroalgae. Along the 100m to 200m section of the transect divers observed 1 live clam, spider crabs, hermit crabs, many small crabs, horseshoe crabs and worm tubes. The 200m to 300m section surveyed by the divers did not appear significantly different than the previous 100m to 200m section (200m-250m was composed of fine sand with patches of clay, 250m-300m med to coarse sand over clayey mud) however they did report more infauna present between 200m and 300m (horseshoe crabs, surf clams, large crabs and snails). Between 300m and 400m surficial sediments appear to be a mix of medium to coarse grained sand interspersed with patches of fine grained sand. From 500m to 600m the sediments appeared to be more coarse grained sand. Macro-fauna observed included spider crabs, horseshoe crabs and snails.

Compared to the extremely dynamic nature of the Pochet transect location, there was much more observable benthic macro-fauna along the Katama transect, presumably due to the more stable surface sediments. The sandy sediments were generally more consolidated and mostly medium to fine grained sand mixed with clay like material. No large sand waves were observed, however, small sand waves were present given the strong surging felt by the divers on the bottom resulting from the ground swell on the south shore of Martha's Vineyard. No attached submerged aquatic vegetation was observed along this transect be it macroalgae or eelgrass. Bottom currents were strong but less so compared to the Pochet Transect. The main force experienced by the divers during the survey was the surging of water near the bottom resulting from the ground swell.

Along the Katama transect the sandy bottom interspersed with patches of clay like sediments seems more stable and less dynamic than the sediments along the Pochet transect, however, the significant surging action driven by the energetic wave environment along the south shore of Martha's Vineyard may also create difficulties for keeping a cable buried in this area. Additionally, the more abundant macrofauna in this area will have to be taken into consideration during site selection. Disturbance of the seabed during trenching and burial is likely to be longer lasting given the type of clayey sediments observed.

Near Bottom Current Velocity Measurements – In conjunction with the diver performed visual surveys of the Pochet and Katama transects and associated sediment sampling, a downward looking single point current meter was deployed on the Pochet Transect to measure near bottom current velocities integrated over a meter off the bottom. The instrument was deployed at the 600 meter station along the transect in order to more accurately measure tidal current velocity along shore with as little effect possible from the surge of passing surface waves. The along shore tidal current velocity measurements were conducted in order to better understand the sediment transport dynamics which would affect the burial of transmission cable from a tidal turbine pilot project in Muskeget Channel. Given the funding constraints, this initial near bottom current velocity survey was limited to the near shore waters of the proposed cable route. Similar measurements will be undertaken in the near future to characterize the near bottom current velocity in the deeper water areas of the proposed cable route. Ground swell disturbance of the mooring cable and float system limited the utility of the data, but did confirm the presence of long shore current eddies predicted by modelers studying sediment transport (G. Cowles, SMAST, personal communication).

Survey of Coastal Resources (e.g. beach, dune, wetland) above MLW (Pochet / Katama)

The upland vegetation surveys at Cape Pogue and Katama were conducted on April 30, 2010 to determine the types of upland coastal resources (beach, dune and wetland habitats) and the associated major vegetation in the vicinity of 2 potential sites for routing a power cable from Muskeget Channel to Martha's Vineyard. The 2 sites are: 1)East Beach at Cape Pogue, Chappaquiddick Island in the vicinity of Dike Bridge (associated with the Pochet proposed cable route), and 2) South Beach at Katama (associated with the Katama proposed cable route).

Cape Pogue

For the Cape Pogue upland survey area 6 transects were established, 3 on either side of Dike Bridge Rd. at approximately 50 ft. intervals (Figure 35). Transects extended from the Mean High Water mark at East Beach landward through the wetlands to the Upland border on the other side of the creek connecting Cape Pogue Bay with Pocha Pond. Their geographic positions were determined with a Trimble Geo XH Hand Held GPS/Data Logger. Habitats and major plant species along the length of each were identified and documented.

Katama

For the Katama survey area 6 transects were also established, 3 on either side of Katama Road at approximately 50 ft. intervals (Figure 36). Transects extended from the Mean High Water mark at South Beach landward through the wetlands into the adjacent upland as far as Navy Way on the west and Edgartown Bay Rd. on the east. Their geographic positions were also determined with a Trimble Geo XH Hand Held GPS/Data Logger and habitats and major plant species along the length of each were identified and documented.

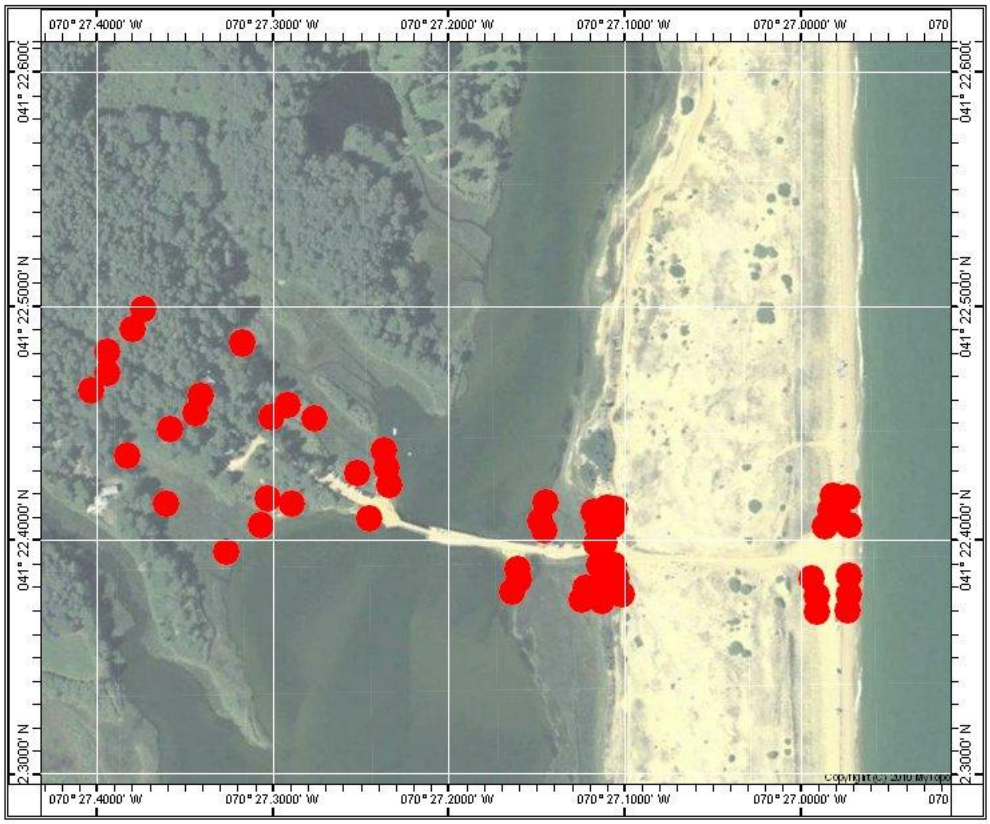

Figure 35 – Location of observations taken during survey of shore and upland environments for the East Beach at Cape Pogue location, Chappaquiddick Island in the vicinity of Dike Bridge (associated with Pochet proposed cable route).

Figure 36 – Location of observations taken during survey of shore and upland environments for the South Beach at Katama location (associated with the Katama proposed cable route).

Results

Cape Pogue

The locations of the 6 transects are shown on Figures 37 and 38. Each point along a transect represents the transition from one type of habitat to another documented with the Trimble GPS/Data Logger. The habitat and associated major vegetation for each documented interval between these points along the transect are shown superimposed on wetlands maps from the Massachusetts Department of Environmental Protection (DEP) on Figures 39 and 40 and described in Table 4. In addition to the 6 transects, the Upland locations of 2 potential sites for the hub are documented with surrounding habitat and associated major vegetation (Figures 38 and 40, Table 4). Results of the transect survey show that there is a transition from east to west along all 6 transects from Barrier Beach (East Beach) to Coastal Beach/Dune to Salt Marsh to open water, to Salt Marsh to Upland (Figures 37 and 39, Table 4). Barrier Beach habitat extends

approximately 45 and 66 ft. from Mean High Water on East Beach to the transition to Coastal Beach and associated Dune habitat (Table 4). Coastal Beach/Dune habitat extends west from the Barrier Beach border anywhere from approximately 509 to 579 ft. to the transition to Salt Marsh habitat (Table 4). These Coastal Dunes are typically vegetated by the dune grass *Ammophila breviligulata* (Table 4).

In transects T2, T4, T5, and T6 there is a small length, approximately 21-55 ft., of Maritime Shrub habitat between the dune and Salt Marsh (Figure 39, Table 4) characterized by low-lying shrubs such as beach rose (*Rosa rugosa*) and bayberry (*Myrica pensylvanica*).
Salt marsh is the major wetland type in all 6 transects. There is a short border area characterized by a mix of Salt Marsh grasses (*Spartina spp*.) and marsh elder (*Iva frutescens*) which varies in length between 21 and 55 ft. (Figure 39, Table 4). The Salt Marsh extends from this border area to the creek that connects Cape Pogue Bay to Pocha Pond (Figure 39) and then from the far shore of the creek to the Upland border (Figure 40). Salt marsh habitat varies in total length from 225-593 ft. along transects (Table 4). The width of the open water in the creek varies from 408-755 ft. (Figures 39 and 40, Table 4). At the Upland edge of the marsh in transects 1 and 3 there is another border area of mixed *Spartina* and *Iva* with a larger area of shrub swamp ranging between 85 and 303 ft. (Figure 40, Table 4). Plants typical of these shrub swamp habitats include arrowwood (*Viburnum dentatu*) and red chokeberry (*Photinia pyrifolia*). In the rest of the transects the marsh transitions directly into Upland with little to no border area (Figure 40, Table 4).

The locations of Hub 112 and a utility pole 58/111 were marked along Dike Road (Figures 38 and 40). The Upland habitat adjacent to these sites and the Salt Marsh habitat were characterized as pitch pine woodland with pitch pine (*Pinus rigida*) and species of oak (*Quercus spp*.) as the dominant vegetation (Figure 40, Table 4).

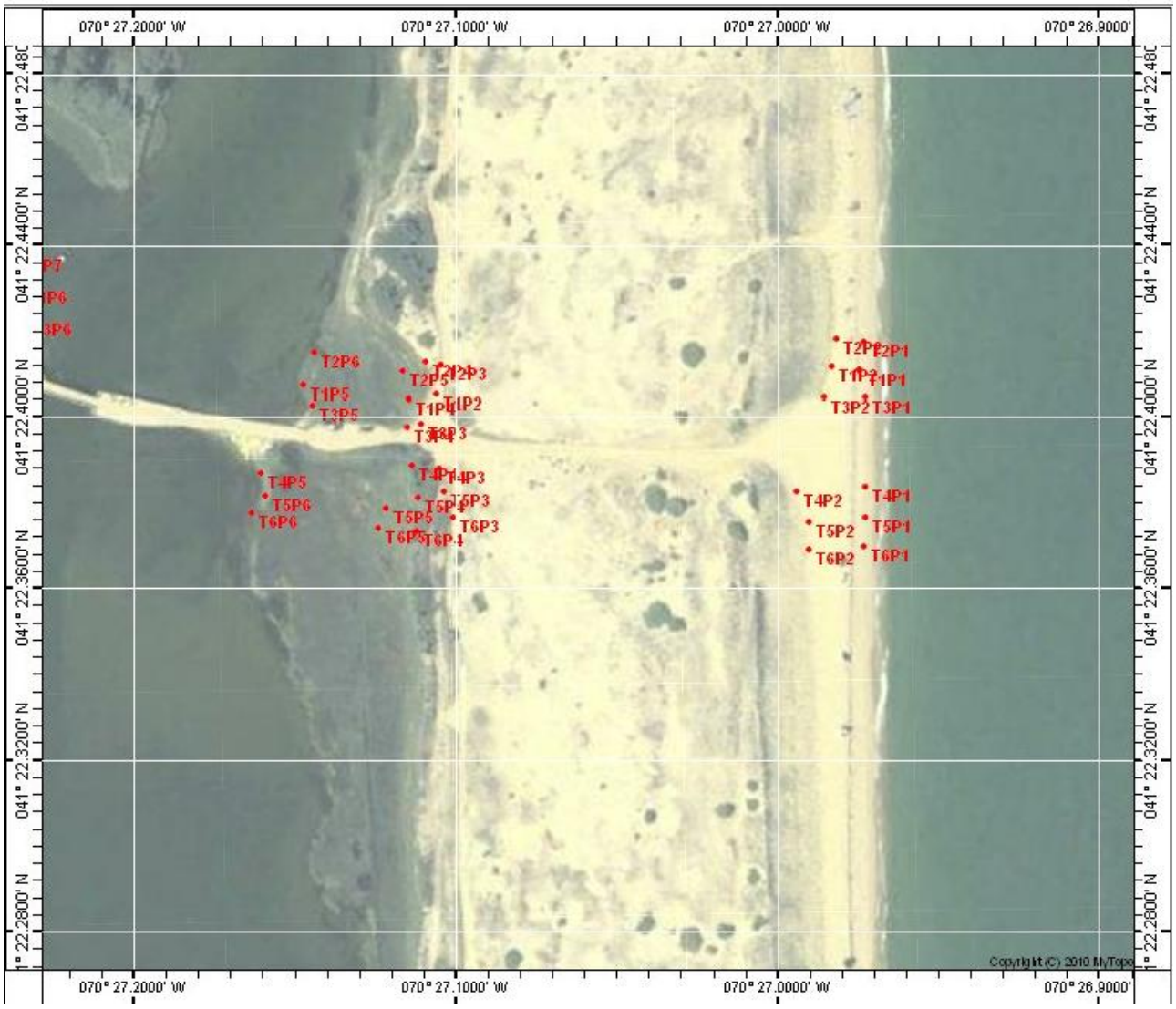

Figure 37 - The locations of the 6 Pocha transects. Each point along transect represents the transition from one type of habitat to another.

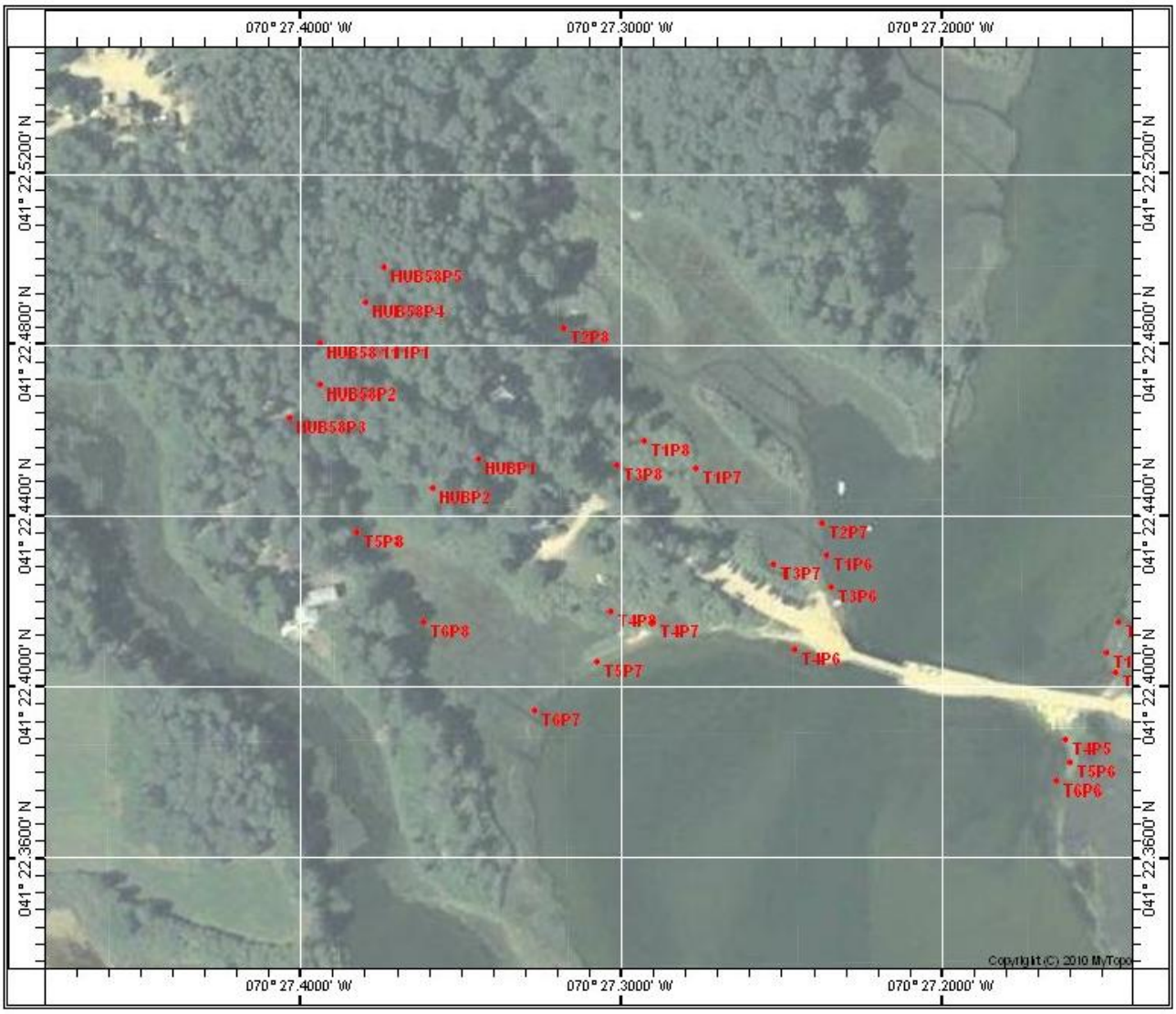

Figure 38 - The locations of the 6 Pocha upland transects. Each point along transect represents the transition from one type of habitat to another.

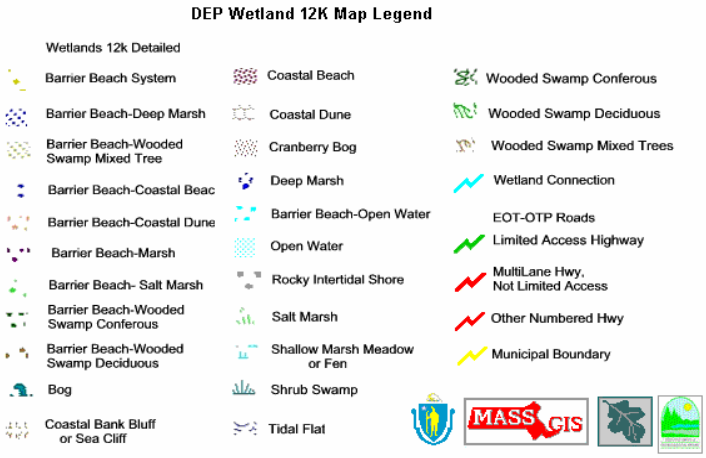

Figure 39 – Pocha transect habitat and associated major vegetation for each documented interval between points along the transect shown superimposed on wetlands maps from the Massachusetts Department of Environmental Protection (DEP).

Figure 40 - Pocha transect habitat and associated major vegetation for each documented interval between points along the transect shown superimposed on wetlands maps from the Massachusetts Department of Environmental Protection (DEP).

Table 4. Cape Pogue Vegetation Survey April 30, 2010

Transect	Point	North Latitude	West Longitude	Point Description	Interval Number	Habitat	Major Vegetation	Interval Length (feet)
T1	P1	41 22 24.694	70 26 58.389	MHW				
	P2	41 22 24.732	70 26 58.946	end beach begin dune grass	T1a	Barrier Beach		42.6
	P3	41 22 24.343	70 27 06.394	end dune begin SM/Iva mix	T1b	Coastal Beach/Dune	Ammophila breviligulata	567.9
	P4	41 22 24.297	70 27 06.884	end SM/Iva mix start SM	T1c	Salt Marsh/Border	Spartina patens./Iva frutescens	37.7
	P5	41 22 24.486	70 27 08.878	waters edge	T1d	Salt Marsh	Spartina spp.	153.0
	P6	41 22 25.827	70 27 14.123	waters edge	None	Open Water		421.5
	P7	41 22 27.087	70 27 16.572	end SM begin SM/Iva border mix/shrub swamp	T1e	Salt Marsh	Spartina spp.	225.7
	P8	41 22 27.486	70 27 17.550	end SM border/shrub swamp begin upland	T1f	Salt Marsh/Border/shrub swamp	Spartina/Iva frutescens/ arrowwoods (*Viburnum dentatu)* red chokeberry (*Photinia pyrifolia*)	85.0
T2	P1	41 22 25.079	70 26 58.336	MHW				
	P2	41 22 25.128	70 26 58.884	end beach begin dune grass	T2a	Barrier Beach		42.1
	P3	41 22 24.763	70 27 06.294	end dune grass begin dune shrub/pine	T2b	Coastal Beach/Dune	Ammophila breviligulata	566.7
	P4	41 22 24.793	70 27 06.574	end dune shrub/pine begin SM/Iva mix	T2c	Maritime Shrub	Myrica pensylvanica, Rosa rugosa	21.5
	P5	41 22 24.693	70 27 07.022	end SM/Iva mix start SM	T2d	Salt Marsh/Border	Spartina patens./Iva frutescens	35.5
	P6	41 22 24.924	70 27 08.662	waters edge	T2e	Salt Marsh	Spartina spp.	127.0
	P7	41 22 26.288	70 27 14.227	waters edge	None	Open Water		444.7
	P8	41 22 29.089	70 27 19.094	end SM begin upland	T2f	Salt Marsh	Spartina spp.	466.6
T3	P1	41 22 24.332	70 26 58.304	MHW				
	P2	41 22 24.308	70 26 59.110	end beach begin dune grass	T3a	Barrier Beach		61.4
	P3	41 22 23.944	70 27 06.694	end dune grass begin SM/Iva mix	T3b	Coastal Beach/Dune	Ammophila breviligulata	578.6
	P4	41 22 23.887	70 27 06.915	end SM/Iva mix start SM	T3c	Salt Marsh/Border	Spartina patens./Iva frutescens	17.7
	P5	41 22 24.202	70 27 08.706	waters edge	T3d	Salt Marsh	Spartina spp.	139.7
	P6	41 22 25.383	70 27 14.050	waters edge	None	Open Water		423.2
	P7	41 22 25.697	70 27 15.103	end SM begin SM/Iva border mix/shrub swamp	T3e	Salt Marsh	Spartina spp.	86.2
	P8	41 22 27.127	70 27 18.056	end SM border/shrub swamp begin upland	T3f	Salt Marsh/Border/shrub swamp	Spartina patens./Iva frutescens/ arrowwoods (*Viburnum dentatu)* red chokeberry (*Photinia pyrifolia*)	302.8
T4	P1	41 22 23.055	70 26 58.306	MHW				
	P2	41 22 22.978	70 26 59.617	end beach begin dune grass	T4a	Barrier Beach		100.3
	P3	41 22 23.326	70 27 06.324	end dune grass begin dune shrub/pine	T4b	Coastal Beach/Dune	Ammophila breviligulata	510.8
	P4	41 22 23.336	70 27 06.842	end dune shrub/pine begin SM (very small Iva border)	T4c	Maritime Shrub	Myrica pensylvanica, Rosa rugosa	39.3
	P5	41 22 23.242	70 27 09.638	water's edge	T4d	Salt Marsh	Spartina spp.	213.3

	P6	41 22 24.534	70 27 14.719	water's edge	None	Open Water		408.1
	P7	41 22 24.900	70 27 17.349	end SM begin SM/border	T4e	Salt Marsh	Spartina spp.	203.5
	P8	41 22 25.066	70 27 18.165	end SM/border begin upland	T4f	Salt Marsh	Spartina patens./Iva frutescens	64.3

Table 4. cont'd. Cape Pogue Vegetation Survey April 30, 2010

Transect	Point	North Latitude	West Longitude	Point Description	Interval Number	Habitat	Major Vegetation	Interval Length (feet)
T5	P1	41 22 22.604	70 26 58.325	MHW				
	P2	41 22 22.544	70 26 59.403	end beach begin dune grass	T5a	Barrier Beach		82.3
	P3	41 22 23.003	70 27 06.231	end dune grass begin dune shrub/pine	T5b	Coastal Beach/Dune	Ammophila breviligulata	521.6
	P4	41 22 22.887	70 27 06.719	end dune shrub/pine begin SM/Iva mix	T5c	Maritime Shrub	Myrica pensylvanica, Rosa rugosa	39.0
	P5	41 22 22.772	70 27 07.297	end mix begin SM	T5d	Salt Marsh	Spartina patens./Iva frutescens	45.4
	P6	41 22 22.942	70 27 09.565	water's edge	T5e	Salt Marsh	Spartina spp.	173.4
	P7	41 22 24.372	70 27 18.424	water's edge	None	Open Water		688.9
	P8	41 22 26.149	70 27 22.964	end SM begin upland	T5f	Salt Marsh	Spartina spp.	390.6
T6	P1	41 22 22.188	70 26 58.344	MHW				
	P2	41 22 22.148	70 26 59.384	end beach begin dune grass	T6a	Barrier Beach		79.4
	P3	41 22 22.598	70 27 06.054	end dune grass begin dune shrub/pine	T6b	Coastal Beach/Dune	Ammophila breviligulata	509.4
	P4	41 22 22.424	70 27 06.741	end dune shrub/pine begin SM/Iva mix	T6c	Maritime Shrub	Myrica pensylvanica, Rosa rugosa	55.2
	P5	41 22 22.453	70 27 07.444	end mix begin SM	T6d	Salt Marsh	Spartina patens./Iva frutescens	53.7
	P6	41 22 22.662	70 27 09.795	water's edge	T6e	Salt Marsh	Spartina spp.	180.7
	P7	41 22 23.676	70 27 19.622	water's edge	None	Open Water		755.9
	P8	41 22 24.905	70 27 21.689	end SM begin upland	T6f	Salt Marsh	Spartina spp.	200.6
	Hub # 112	41 22 27.696	70 27 20.447	in front of house along dirt road	None	Hub Location		
	Hub 1	41 22 27.231	70 27 20.661	Southwest of Hub # 112	None	Pitch Pine Woodland	Pinus rigida, Quercus spp.	49.6
	Hub 2	41 22 26.822	70 27 21.520	Southwest of Hub 1	None	Pitch Pine Woodland	Pinus rigida, Quercus spp.	76.8
	Pole # 58/111	41 22 28.848	70 27 23.627	along dirt road		Power Line Pole		
	Pole 2	41 22 28.280	70 27 23.654	Southwest of Pole # 58/111	None	Pitch Pine Woodland	Pinus rigida, Quercus spp.	57.0
	Pole 3	41 22 27.826	70 27 24.207	Southwest of Pole 2	None	Pitch Pine Woodland	Pinus rigida, Quercus spp.	62.1
	Pole 4	41 22 29.430	70 27 22.781	Northeast of Pole # 58/111	None	Pitch Pine Woodland	Pinus rigida, Quercus spp.	87.2
	Pole 5	41 22 29.933	70 27 22.447	Northeast of Pole 4	None	Pitch Pine Woodland	Pinus rigida, Quercus spp.	56.6

Katama

The locations of the 6 transects are shown on Figure 41. As was the case with the Cape Pogue data, each point along a transect represents the transition from one type of habitat to another with the location documented with the Trimble GPS/Data Logger. The habitat and associated major vegetation for each documented interval between these points along the transect are shown superimposed on wetlands maps from the Massachusetts Department of Environmental Protection (DEP) on Figure 42 and described in Table 5.

Results of the survey show that east of Katama Road there is a transition from south to north along all 3 transects (T1, T2, T3) from Barrier Beach to Coastal Beach/Dune to Salt Marsh (including a small pool of open water along T2 and T3) to Upland habitat (Figure 42, Table 5). Barrier Beach habitat extends approximately 48-55 ft. from Mean High Water (MHW) on South Beach to the transition to Coastal Dune habitat which is characterized by the dune grass *Ammophila breviligulata* (Table 5). In T1, Coastal Dune habitat extends approximately 218 ft. from the Barrier Beach to a transition from dune grass to a more low-lying shrub habitat (Table 5). This shrub habitat persists along the edge of Katama Rd. (T1c) approximately 417 ft. north to Edgartown Bay Rd. The transect intersects the edge of the Salt Marsh for a part of its length on the north side of the canal (connecting Katama Bay to Crackatuxet Cove) (Figure 42). This shrub habitat consists of low lying shrub plants such as bayberry (*Myrica pensylvanica*) and beach rose (*Rosa rugosa*).

In T2 and T3, the Coastal Dune covers approximately 133-153 ft. from the edge of the Barrier Beach to the Salt Marsh (Figure 42, Table 5). The Salt Marsh habitat along T2 and T3, including the open water pool and canal covers approximately 294-341 ft. (Figure 42, Table 5). There is a small Salt Marsh border area along T3 (T3e) of approximately 62 ft. (Table 5) before the Upland begins.

The Upland portion of T2 and T3 extends from the edge of the Salt Marsh to Edgartown Bay Rd. approximately 147-159 ft. (Figure 42, Table 5). As is the case with the Upland in T1, it is characterized by low lying Maritime Shrub habitat with plants such as beach rose and bayberry. West of Katama Rd. there is a transition from south to north along T4, T5 and T6 from Barrier Beach to Coastal Dune to Upland, primarily low lying Maritime Shrub habitat interspersed with developed areas (housing, roadway and parking area (Figure 42, Table 5). The Barrier Beach extends from Mean High Water (MHW) anywhere from 62-66 ft. to the border with Coastal Dune habitat which is dominated by dune grass *Ammophila breviligulata*. In T4 and T5, the Coastal Dune extends from the Barrier Beach approximately 191-192 ft. to Atlantic Drive (Figure 7, Table 2). In T6, the Coastal Dune extends approximately 66 ft. to a transition to low lying shrub habitat (Figure 42, Table 5). This shrub habitat is also associated with the Coastal Dune according to the DEP wetlands map, but the vegetation shifts from dune grass to shrub. Atlantic Drive marks the end of this dune/shrub habitat. North of the road along all 3 transects there is a mixture of low lying shrub habitat with developed areas that extend anywhere from approximately 365-435 ft. to Navy Way (Figure 42, Table 5).

Figure 41 - The locations of the 6 Katama upland transects. Each point along transect represents the transition from one type of habitat to another.

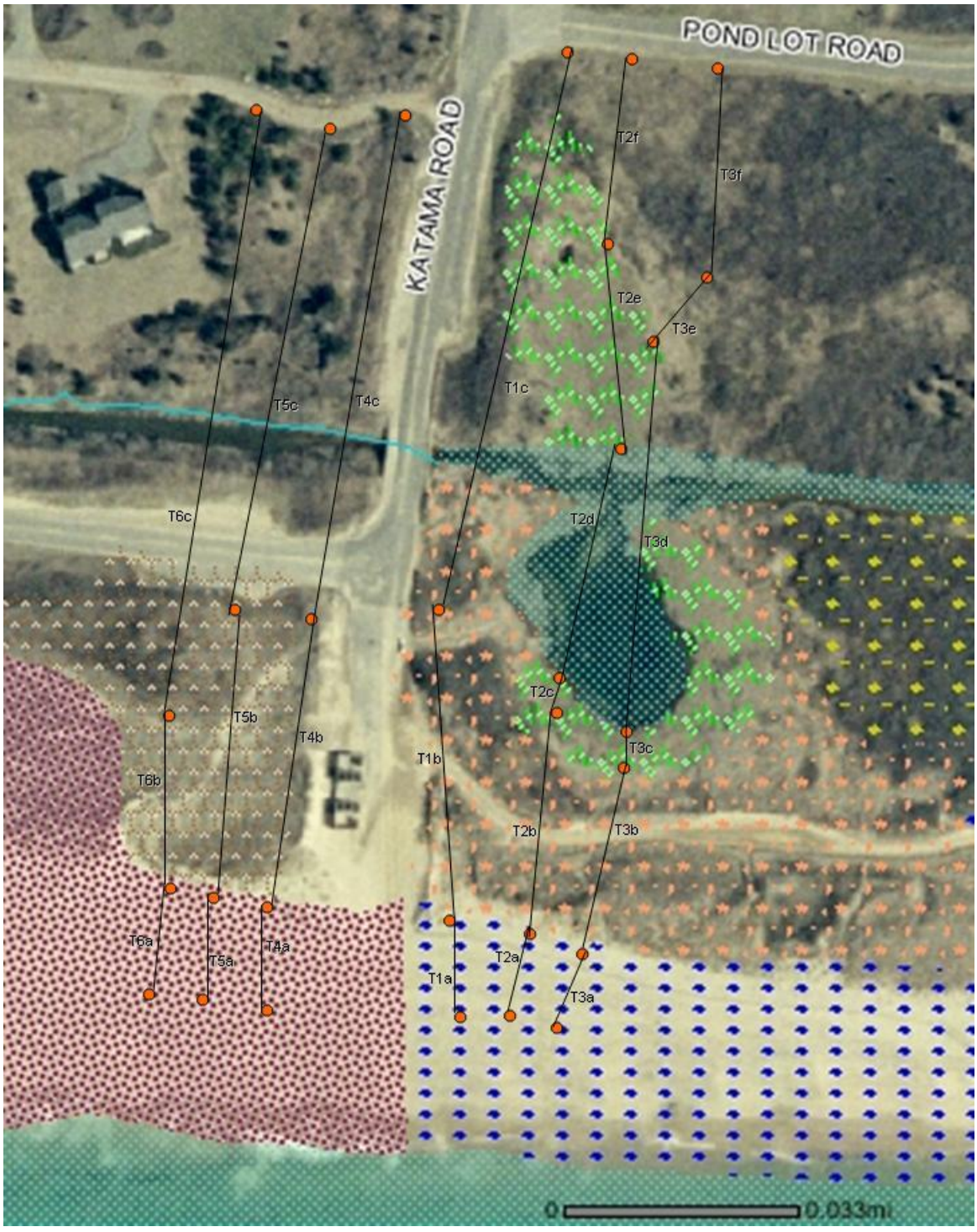

Figure 42 - Katama transect habitat and associated major vegetation for each documented interval between points along transect shown superimposed on wetlands maps from the Massachusetts Department of Environmental Protection (DEP).

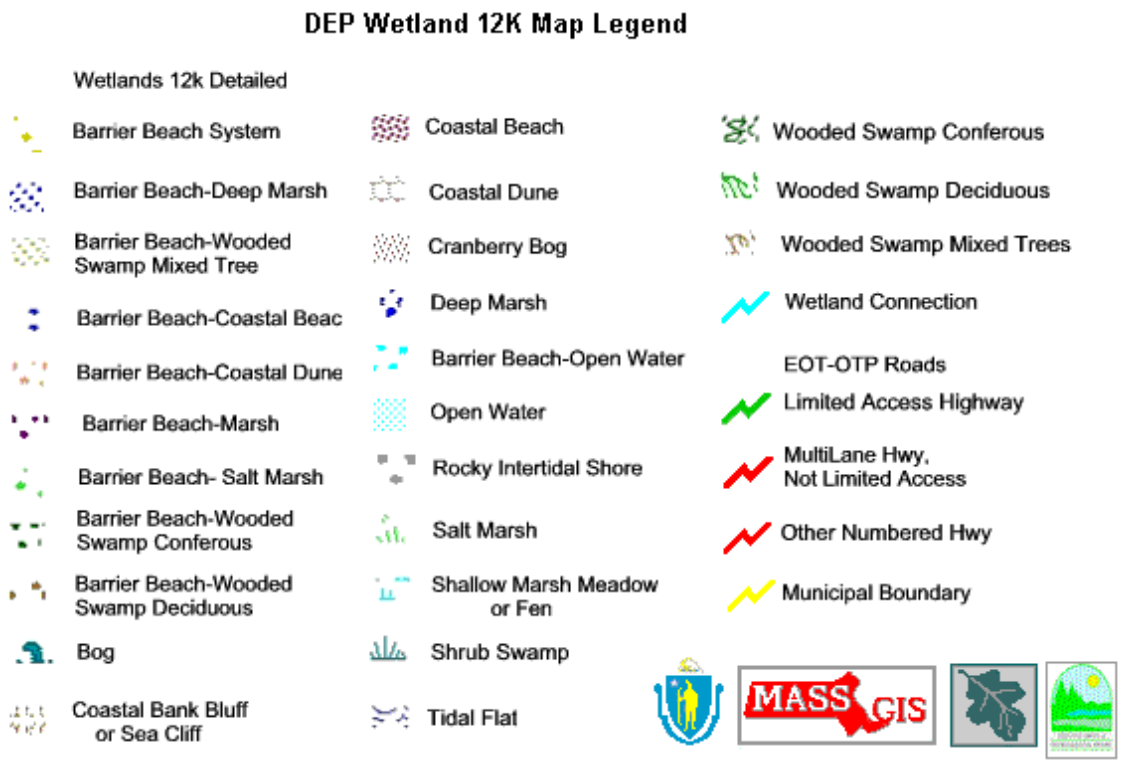

Figure 42 – Continued.

Table 5. Katama Vegetation Survey April 30, 2010 Summary of observed habitat types, locations and major vegetation types

Transect	Point	North Latitude	West Longitude	Point Description	Interval Number	Habitat	Major Vegetation	Interval Length (feet)
T1	P1	41 20.9147	70 30.6916	MHW				
	P2	41 20.9235	70 30.6950	begin coastal dune	T1a	Barrier Beach		55.64
	P4	41 20.9595	70 30.6963	end dune begin upland	T1b	Coastal Dune	Ammophila breviligulata	218.5
	P3	41 21.0262	70 30.6753	road/developed area	T1c	Maritime Shrub	Myrica pensylvanica, Rosa rugosa	417.1
T2	P1	41 20.9139	70 30.6814	MHW				
	P2	41 20.9220	70 30.6780	begin coastal dune	T2a	Barrier Beach		52.21
	P3	41 20.9473	70 30.6778	end dune begin SM	T2b	Coastal Dune	Ammophila breviligulata	153.13
	P4	41 20.9507	70 30.6782	water's edge	T2c	Salt Marsh	Spartina spp.	21.04
	P5	41 20.9774	70 30.6666	edge of creek/pool	T2d	Open Water		170.07
	P6	41 21.0021	70 30.66567	end SM/Border begin upland	T2e	Salt Marsh	Spartina spp.	150.25
	P7	41 21.0250	70 30.6642	road/developed area	T2f	Maritime Shrub	Myrica pensylvanica, Rosa rugosa	146.9
T3	P1	41 20.9131	70 30.6737	MHW				
	P2	41 20.9207	70 30.6702	begin coastal dune	T3a	Barrier Beach		48.56
	P3	41 20.9427	70 30.6663	end dune begin SM	T3b	Coastal Dune	Ammophila breviligulata	133.79
	P4	41 20.9470	70 30.6663	water's edge	T3c	Salt Marsh	Spartina spp.	26.22
	P5	41 20.9911	70 30.6625	end SM begin SM/Border	T3d	Open Water/Salt Marsh	Spartina spp.	268.09
	P6	41 20.9983	70 30.6525	end SM/Border begin upland	T3e	Salt Marsh/Border	Spartina patens./Iva frutescens	62.25
	P7	41 21.0245	70 30.6536	road/developed area	T3f	Maritime Shrub	Myrica pensylvanica, Rosa rugosa	159.18
T4	P1	41 20.9154	70 30.7175	MHW				
	P2	41 20.9263	70 30.7194	begin coastal dune	T4a	Barrier Beach		66.51
	P3	41 20.9580	70 30.7177	end dune begin upland	T4b	Coastal Dune	Ammophila breviligulata	192.28
	P4	41 21.0201	70 30.6991	road/developed area	T4c	Maritime Shrub	Myrica pensylvanica, Rosa rugosa	387.19
	P5							
T5	P1	41 20.9167	70 30.7299	MHW				
	P2	41 20.9270	70 30.7291	begin coastal dune	T5a	Barrier Beach		62.52
	P3	41 20.9586	70 30.7283	end dune begin upland	T5b	Coastal Dune	Ammophila breviligulata	191.53
	P4	41 21.0176	70 30.7101	road/developed area	T5c	Maritime Shrub	Myrica pensylvanica, Rosa rugosa	365.96
T6	P1	41 20.9175	70 30.7398	MHW				
	P2	41 20.9283	70 30.7379	begin coastal dune	T6a	Barrier Beach		66.3
	P3	41 20.9484	70 30.7365	end dune begin upland	T6b	Coastal Dune	Ammophila breviligulata	122.14
	P4	41 21.0200	70 30.7255	road/developed area	T6c	Maritime Shrub	Myrica pensylvanica, Rosa rugosa	435.78

Priority Habitat for Rare Species

According to the Massachusetts Natural Heritage & Endangered Species Program of the Division of Fish and Game, Priority Habitat is a geographic area of the known habitat for all state-listed rare species, both plants and animals. Habitat alteration within Priority Habitats is subject to regulatory review by NHESP. Priority Habitat maps are used for determining whether or not a proposed project must be reviewed by the NHESP for the Massachusetts Endangered Species Act (MESA) compliance.

Both Cape Pogue and Katama in the vicinity of the proposed project contain NHESP habitat (Figures 43 and 44). Table 6 contains a list of all rare and endangered species, plants and animals, known to exist within the town of Edgartown.

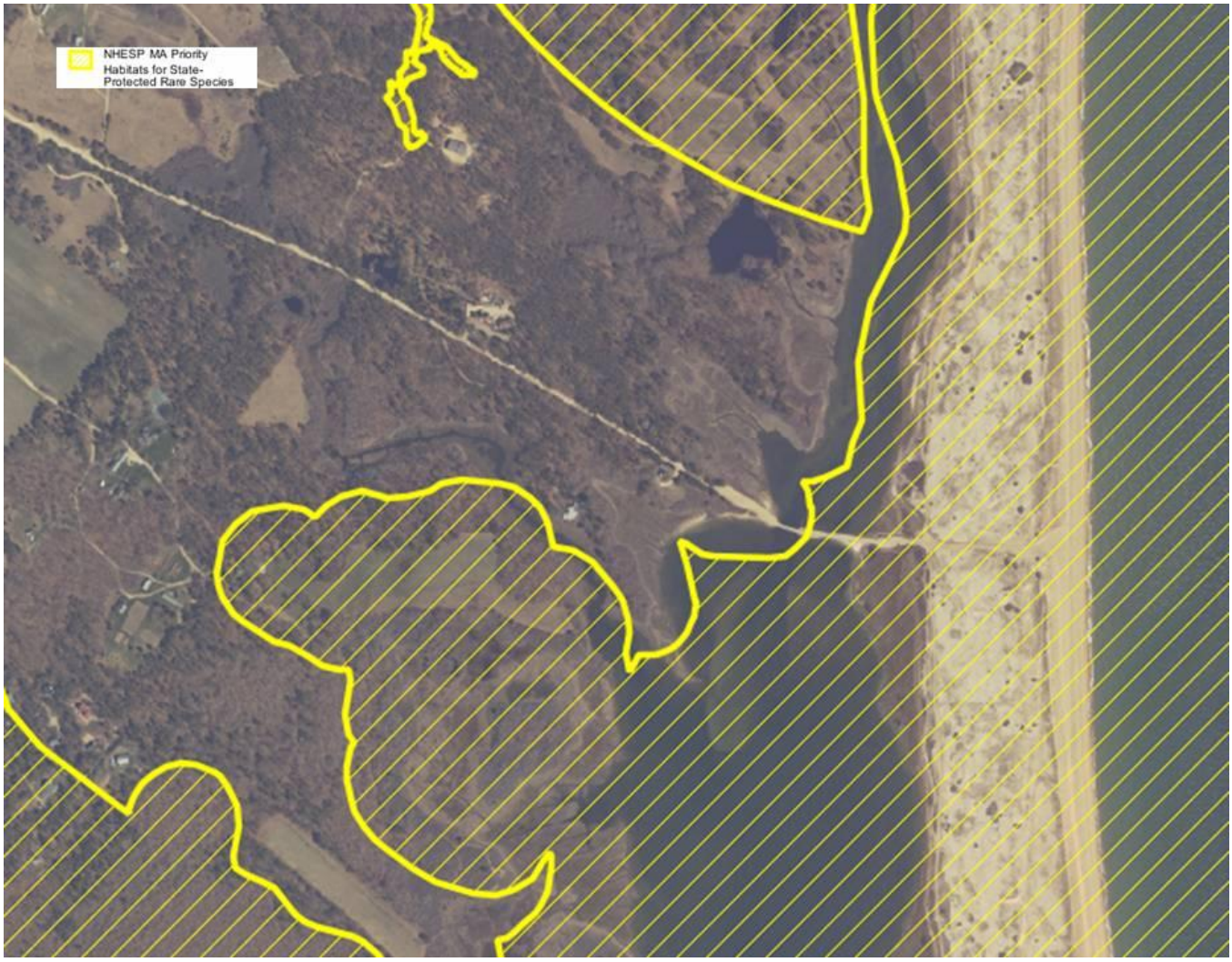

Figure 43 - Massachusetts Natural Heritage map of Priority Habitats for State Protected Rare Species, in the vicinity of Dike Bridge, Chappaquiddick Island, Edgartown, Martha's Vineyard, MA. (Town of Edgartown, eastern shore of Chappaquiddick Island).

Figure 44 - Massachusetts Natural Heritage map of Priority Habitats for State Protected Rare Species, in the vicinity of Katama, Edgartown, Martha's Vineyard, MA (Town of Edgartown, southern shore of Martha's Vineyard Island, South Beach).

Table 6. Massachusetts Natural Heritage List of State Protected Rare and Endangered Species, Edgartown, MA.

Town	Taxonomic Group	Scientific Name	Common Name	MESA Status	Federal Status	Most Recent Observation
EDGARTOWN	Amphibian	Scaphiopus holbrookii	Eastern Spadefoot	T		2000
EDGARTOWN	Beetle	Cicindela purpurea	Purple Tiger Beetle	SC		2008
EDGARTOWN	Bird	Ammodramus savannarum	Grasshopper Sparrow	T		2003
EDGARTOWN	Bird	Asio flammeus	Short-eared Owl	E		1997
EDGARTOWN	Bird	Asio otus	Long-eared Owl	SC		1979
EDGARTOWN	Bird	Bartramia longicauda	Upland Sandpiper	E		1957
EDGARTOWN	Bird	Charadrius melodus	Piping Plover	T	T	2006
EDGARTOWN	Bird	Circus cyaneus	Northern Harrier	T		2004
EDGARTOWN	Bird	Sterna dougallii	Roseate Tern	E	E	2008
EDGARTOWN	Bird	Sterna hirundo	Common Tern	SC		2008
EDGARTOWN	Bird	Sterna paradisaea	Arctic Tern	SC		1982
EDGARTOWN	Bird	Sternula antillarum	Least Tern	SC		2007
EDGARTOWN	Bird	Tyto alba	Barn Owl	SC		2007
EDGARTOWN	Butterfly/Moth	Abagrotis nefascia	Coastal Heathland Cutworm	SC		2008
EDGARTOWN	Butterfly/Moth	Acronicta albarufa	Barrens Daggermoth	T		2007
EDGARTOWN	Butterfly/Moth	Bagisara rectifascia	Straight Lined Mallow Moth	SC		2007
EDGARTOWN	Butterfly/Moth	Catocala herodias gerhardi	Gerhard's Underwing Moth	SC		2008
EDGARTOWN	Butterfly/Moth	Cicinnus melsheimeri	Melsheimer's Sack Bearer	T		2008
EDGARTOWN	Butterfly/Moth	Cingilia catenaria	Chain Dot Geometer	SC		2006
EDGARTOWN	Butterfly/Moth	Cycnia inopinatus	Unexpected Cycnia	T		2008
EDGARTOWN	Butterfly/Moth	Digrammia eremiata	Three-lined Angle Moth	T		1983
EDGARTOWN	Butterfly/Moth	Eacles imperialis	Imperial Moth	T		2008
EDGARTOWN	Butterfly/Moth	Euchlaena madusaria	Sandplain Euchlaena	SC		2008

Table 6 cont'd. Massachusetts Natural Heritage List of State Protected Rare and Endangered Species, Edgartown, MA.

Town	Taxonomic Group	Scientific Name	Common Name	MESA Status	Federal Status	Most Recent Observation
EDGARTOWN	Butterfly/Moth	Faronta rubripennis	The Pink Streak	T		2006
EDGARTOWN	Butterfly/Moth	Hemileuca maia	Barrens Buckmoth	SC		2004
EDGARTOWN	Butterfly/Moth	Itame sp. 1 nr. inextricata	Pine Barrens Itame	SC		2005
EDGARTOWN	Butterfly/Moth	Lycia ypsilon	Pine Barrens Lycia	T		2008
EDGARTOWN	Butterfly/Moth	Metarranthis apiciaria	Barrens Metarranthis Moth	E		1999
EDGARTOWN	Butterfly/Moth	Metarranthis pilosaria	Coastal Swamp Metarranthis Moth	SC		1993
EDGARTOWN	Butterfly/Moth	Oncocnemis riparia	Dune Noctuid Moth	SC		2008
EDGARTOWN	Butterfly/Moth	Papaipema sulphurata	Water-willow Stem Borer	T		1988
EDGARTOWN	Butterfly/Moth	Psectraglaea carnosa	Pink Sallow	SC		2008
EDGARTOWN	Butterfly/Moth	Ptichodis bistrigata	Southern Ptichodis	T		2005
EDGARTOWN	Butterfly/Moth	Stenoporpia polygrammaria	Faded Gray Geometer	T		2006
EDGARTOWN	Butterfly/Moth	Zale sp. 1 nr. lunifera	Pine Barrens Zale	SC		2006
EDGARTOWN	Vascular Plant	Ageratina aromatica	Lesser Snakeroot	E		1913
EDGARTOWN	Vascular Plant	Amelanchier nantucketensis	Nantucket Shadbush	SC		2008
EDGARTOWN	Vascular Plant	Aristida purpurascens	Purple Needlegrass	T		2008
EDGARTOWN	Vascular Plant	Asclepias verticillata	Linear-leaved Milkweed	T		1915
EDGARTOWN	Vascular Plant	Crocanthemum dumosum	Bushy Rockrose	SC		1999
EDGARTOWN	Vascular Plant	Gamochaeta purpurea	Purple Cudweed	E		1913
EDGARTOWN	Vascular Plant	Hydrocotyle verticillata	Saltpond Pennywort	T		1984
EDGARTOWN	Vascular Plant	Liatris scariosa var. novae-angliae	New England Blazing Star	SC		2006

Table 6 cont'd. Massachusetts Natural Heritage List of State Protected Rare and Endangered Species, Edgartown, MA.

Town	Taxonomic Group	Scientific Name	Common Name	MESA Status	Federal Status	Most Recent Observation
EDGARTOWN	Vascular Plant	Linum intercursum	Sandplain Flax	SC		2006
EDGARTOWN	Vascular Plant	Nabalus serpentarius	Lion's Foot	E		2004
EDGARTOWN	Vascular Plant	Ophioglossum pusillum	Adder's-tongue Fern	T		1917
EDGARTOWN	Vascular Plant	Polygonum glaucum	Sea-beach Knotweed	SC		2007
EDGARTOWN	Vascular Plant	Scleria pauciflora	Papillose Nut Sedge	E		2006
EDGARTOWN	Vascular Plant	Setaria parviflora	Bristly Foxtail	SC		2005
EDGARTOWN	Vascular Plant	Sisyrinchium fuscatum	Sandplain Blue-eyed Grass	SC		2006
EDGARTOWN	Vascular Plant	Spiranthes vernalis	Grass-leaved Ladies'-tresses	T		2001
EDGARTOWN	Vascular Plant	Symphyotrichum concolor	Eastern Silvery Aster	E		1929

Coastal Rivers and the Massachusetts Rivers Protection Act

The Rivers Protection Act (RPA), Chapter 258 of the Acts of 1996, protects nearly 9,000 miles of riparian habitats along the riverbanks of designated rivers and streams within the State, including coastal waterways. The law creates a 200-foot riverfront area that extends on both sides of rivers and streams out to the designated mouth of river or stream. Figures 45 and 46 show 2 designated coastal rivers that fall within the jurisdiction of the RPA, one each at Cape Pogue and Katama (Mattakessett Herring Creek - the canal connecting Katama Bay and Crackatuxet Cove). Any project conducted in their vicinity may be subject to review for compliance with the RPA by the local Conservation Commission and Massachusetts Department of Environmental Protection (DEP).

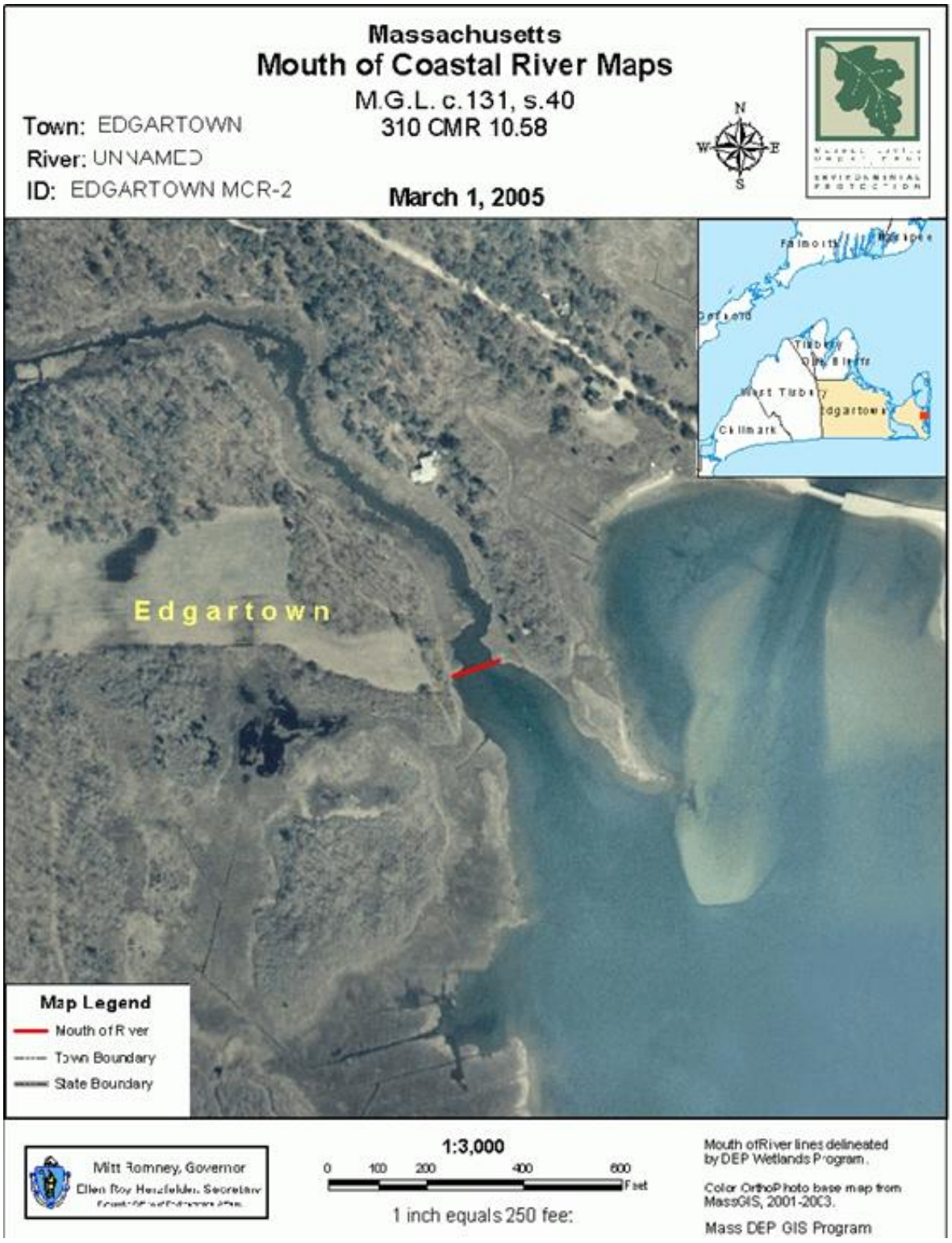

Figure 45 - Massachusetts Department of Environmental Protection designated Mouth of River (MOR) in the vicinity of Dike Bridge, Chappaquiddick Island, Edgartown, Martha's Vineyard, MA.

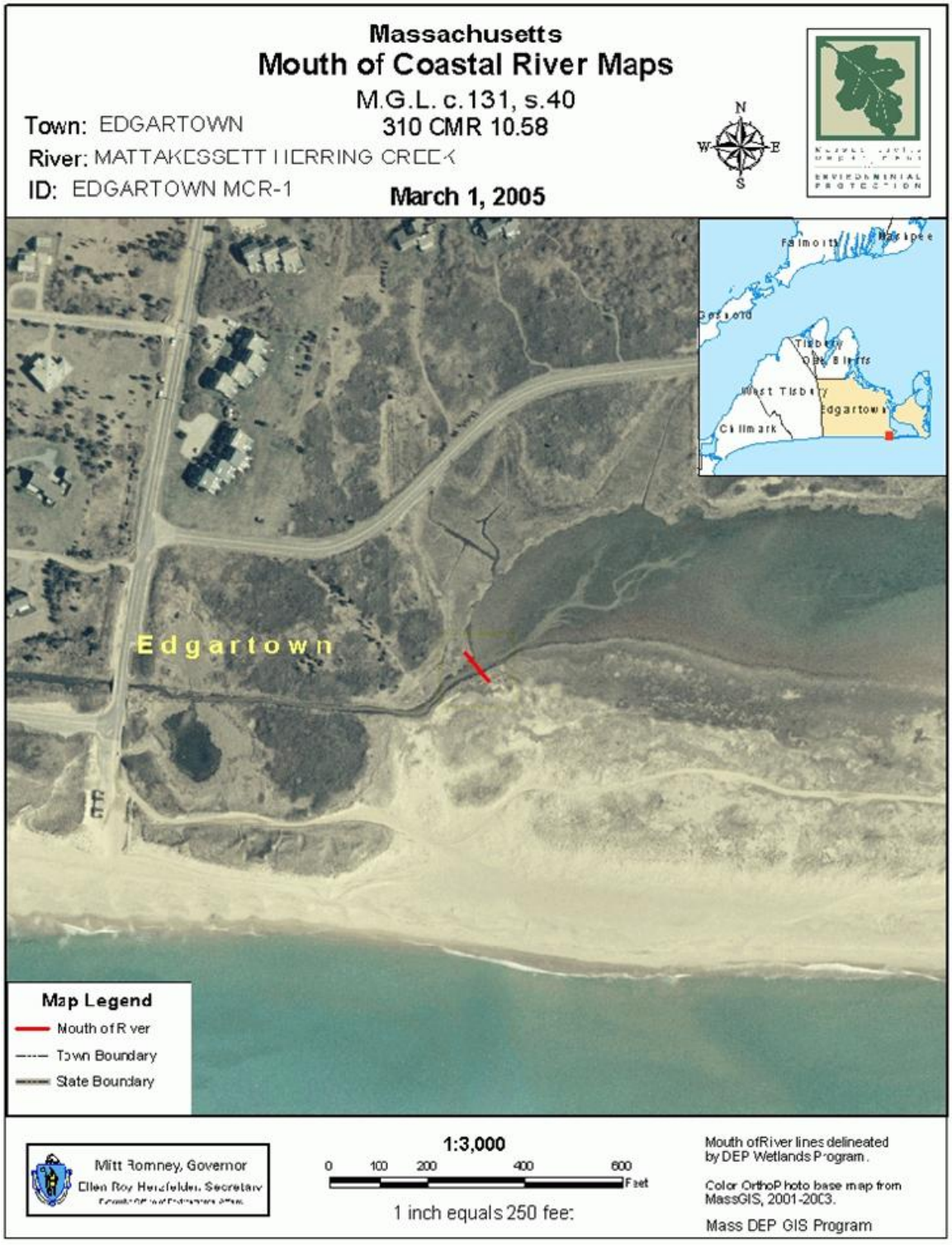

Figure 46 - Massachusetts Department of Environmental Protection designated Mouth of River (MOR) in the vicinity of Katama, Edgartown, Martha's Vineyard, MA.

4.0 Conclusions and Recommendations

Muskeget Channel and the surrounding waters is clearly a very dynamic system with relatively strong currents and large areas of shifting shoals. While there are several clear channels passing through shoal areas that move water into the main stem of Muskeget Channel from Nantucket Sound on the ebb tide, current velocities in these shallow channels are not sufficient to support tidal power development. Similarly, water flowing into the main north-south channel of Muskeget from the north (Nantucket Sound) or from the South (Atlantic Ocean) has low velocities (1.0-1.5 knots) relative to that which is needed by Tidal energy developers (> 4.0 knots). Additionally, these areas are too shallow to meet the depth criteria of existing turbine generating technologies, most of which require 30-40 feet of clearance to ensure the navigability of the area in which turbine deployments would be undertaken.

Detailed ship board ADCP profile transects identified an area within Muskeget Channel that is of sufficient depth for current in-stream tidal turbines to operate on a commercial scale and narrowed the search area for velocities for viable commercialization. Focused, lunar period, bottom moored ADCP deployments supported this contention. The long-term studies indicated higher current velocities than expected from transect surveys. These long term velocities were in excess of 4knts, generally considered a threshold for commercial viability. This level of nearly continuous velocity measurement at a single point along a transect, but through the entire water column was obtained to provide sufficient data for energy developers to make daily, weekly, monthly and annual projections of power production.

Wave measurements, made concurrent with long term velocity profiles, showed that the wave fields were bi-modal and temporally inconsistent. The data suggests that local bathymetry, characterized by large expanses of shoals, creates short steep waves, while the deep water swells from the open ocean to the south create waves of comparatively long periods. The combination of wave types are influenced by changes in tidal direction and wind stresses which are both parallel to the wave fronts. The resulting wave environment appears chaotic and is not believed to be commercially viable with current technology, despite the relatively large amount of potential wave energy.

Within the northern portion of the NOREIZ examined current velocities are uniformly low (<1m/s) and extremely consistent showing only moderate changes through lunar cycles. The conditions suggest no obvious impediment to the creation of a wind test platform.

Wave measurements at the NOREIZ site were dominated by long period waves with monthly average energy ranging from 36 to52 kW/m during January and February, respectively. The wave field was fairly consistent with regards to direction throughout the deployment which should allow parallel testing of wave power generators, thus significantly enhancing the utility of the wind testing platform.

Initial data gathering on wind energy potential associated with NOREIZ indicates that the wind

fields are energetic and consistent. Though the buoy mast was only 2 meters high wind velocities ranged from 6-8.5 m/s. This data is consistent with other work beginning in the area which utilizes radar arrays for wind and wave prediction. In general the NOREIZ site should be conducive to both wind and wave power extraction.

Sediment sampling in the vicinity of the NOREIZ buoy showed medium to coarse sand dominates the benthic environment. The sediment appears to be seasonally stable; however, infauna samples suggest that there is frequent reworking of the surficial sediment which limits both the density of animals and the diversity of taxa present. There was no contraindication for erecting a wind test platform based upon the benthic ecology.

Near shore, beach and upland survey transects along the two possible cable routes proposed for bringing power generated in Muskeget Channel to shore were analyzed extensively to determine whether any significant barriers to construction existed. This work specifically addressed issues that form the basis for typical environmental impact studies.

Benthic infauna communities along both proposed cable routes had extremely low densities and concomitantly low diversity. Markers were removed by vandals making comparison of disturbed and undisturbed conditions impossible. However, visual inspection of the disturbance sites showed no discernible effect of disturbance. Furthermore, statistical analysis of the samples (triplicate at each of the 8 sites) showed that given the low numbers of individuals and variability between replicates that even if the population were decimated the difference would not reach a level of significance in over half the locations.

Sediment sampling and grain size analysis performed in conjunction with the infaunal analysis showed medium to coarse sand dominates the benthic environment along the Pochet transect. The sediment appears was seasonally stable, however, infauna samples suggest that there if frequent reworking of the surficial sediment which limits both the density of animals and the diversity of taxa present. Results from the Katama transect indicated the presence of glacial clay deposits underlying coarse to medium sand that regularly emerged to the sediment surface. The presence of surface clay deposits, increased infauna densities and diversity while decreasing submerged aquatic vegetation. Clay deposits also complicate cable placement. Final decisions for the cable installation will need to weigh all of these competing factors.

Beach, dune and wetland surveys where proposed cable installations transition to shore present no immediate obstacles. Both Pochet and Katama cable landings will require review and permitting by Massachusetts Department of Environmental Protection, local conservation commission and Massachusetts Natural Heritage & Endangered Species Program. Portions of both landings are adjacent to wetlands and priority habitat for rare species; however, both locations also have public rights of way and access that could mediate any potential impacts.

\

Appendix 1
Supplementary ADCP Transects

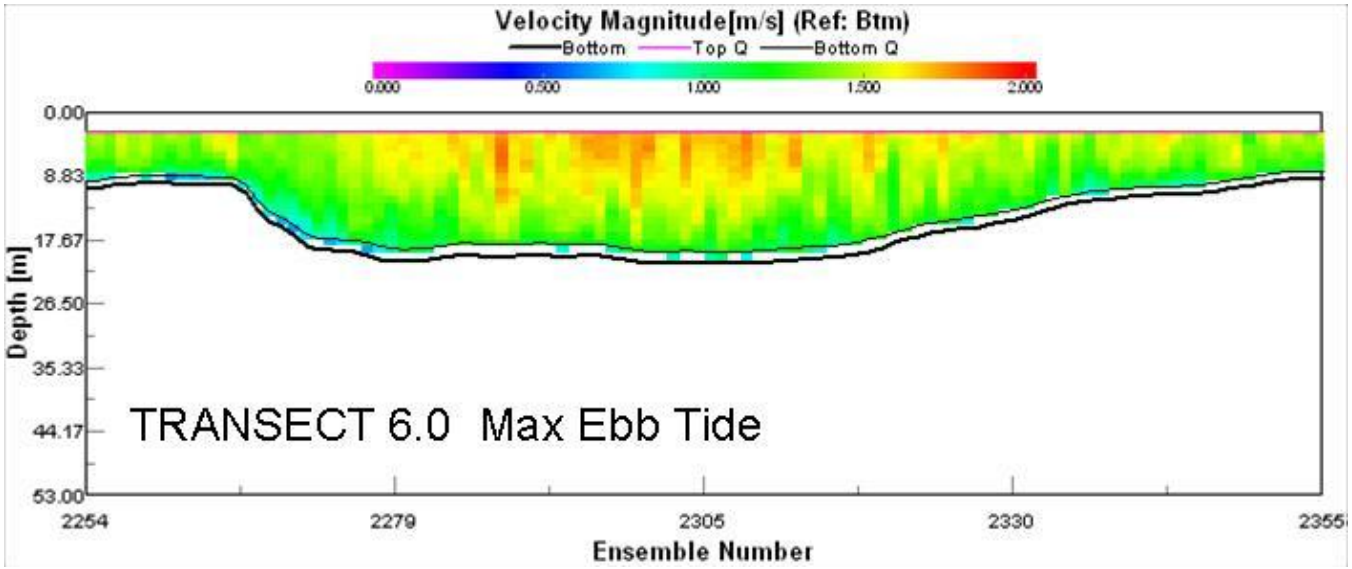
Velocity Magnitude[m/s] (Ref: Btm)
Bottom
Top Q
Bottom Q
0.000
0.500
1.000
1.500
2.000
0.00
8.83
17.67
26.50
35.33
44.17
53.00
Depth [m]
TRANSECT 6.0 Max Ebb Tide
2254
2279
2305
2330
2355
Ensemble Number

Figure –

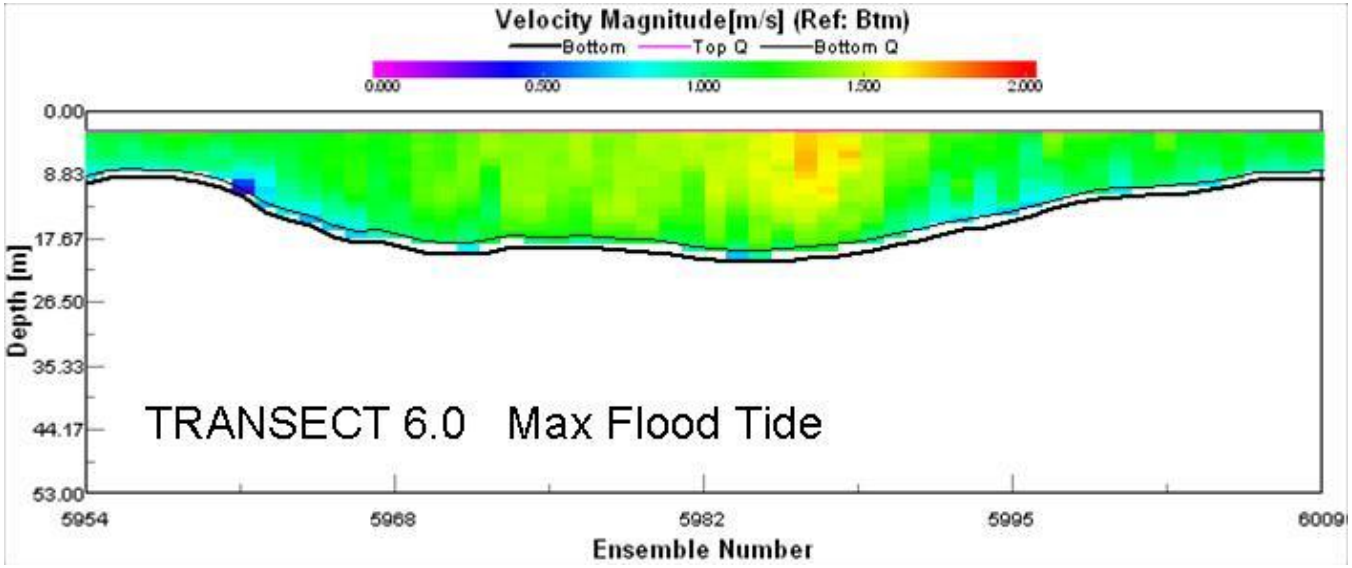
Velocity Magnitude[m/s] (Ref: Btm)
Bottom
Top Q
Bottom Q
0.000
0.500
1.000
1.500
2.000
0.00
8.83
17.67
26.50
35.33
44.17
53.00
Depth [m]
TRANSECT 6.0 Max Flood Tide
5954
5968
5982
5995
Ensemble Number

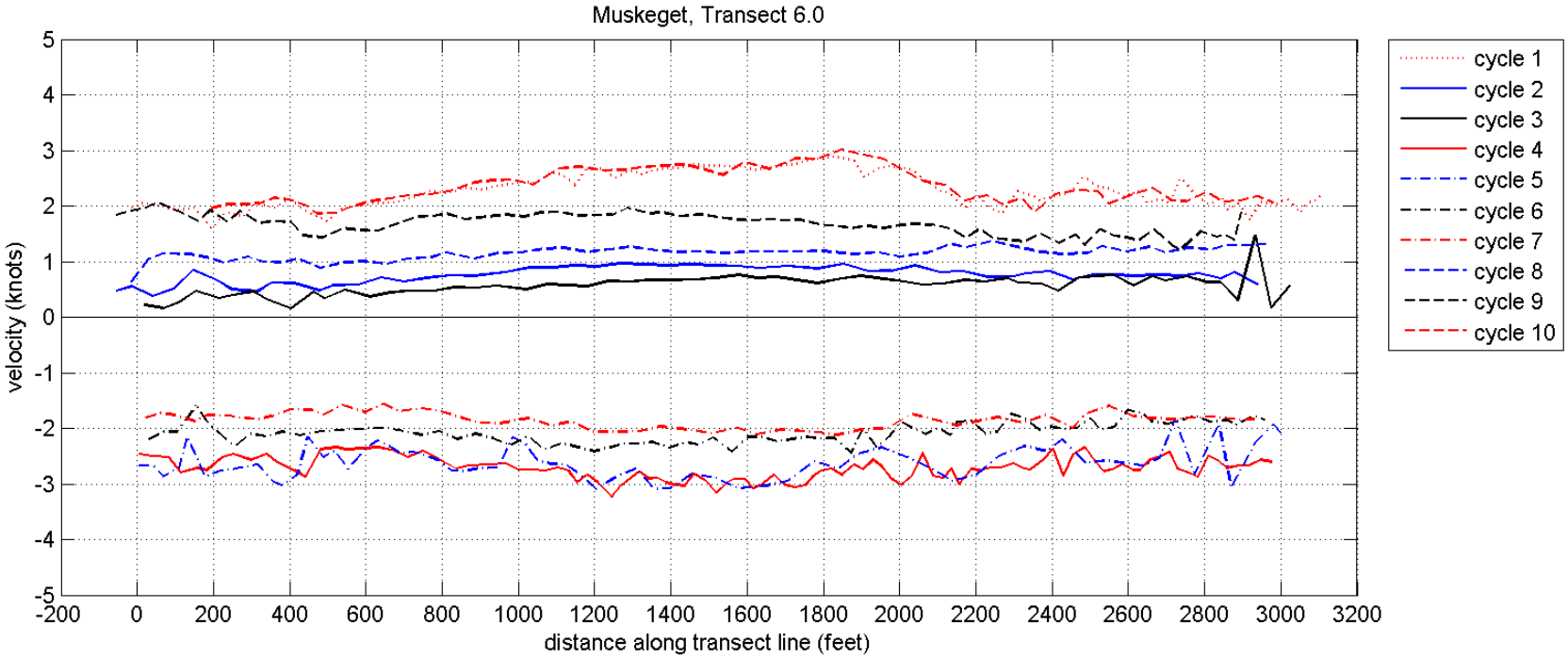
Muskeget, Transect 6.0
velocity (knots)
distance along transect line (feet)
cycle 1
cycle 2
cycle 3
cycle 4
cycle 5
cycle 6
cycle 7
cycle 8
cycle 9
cycle 10

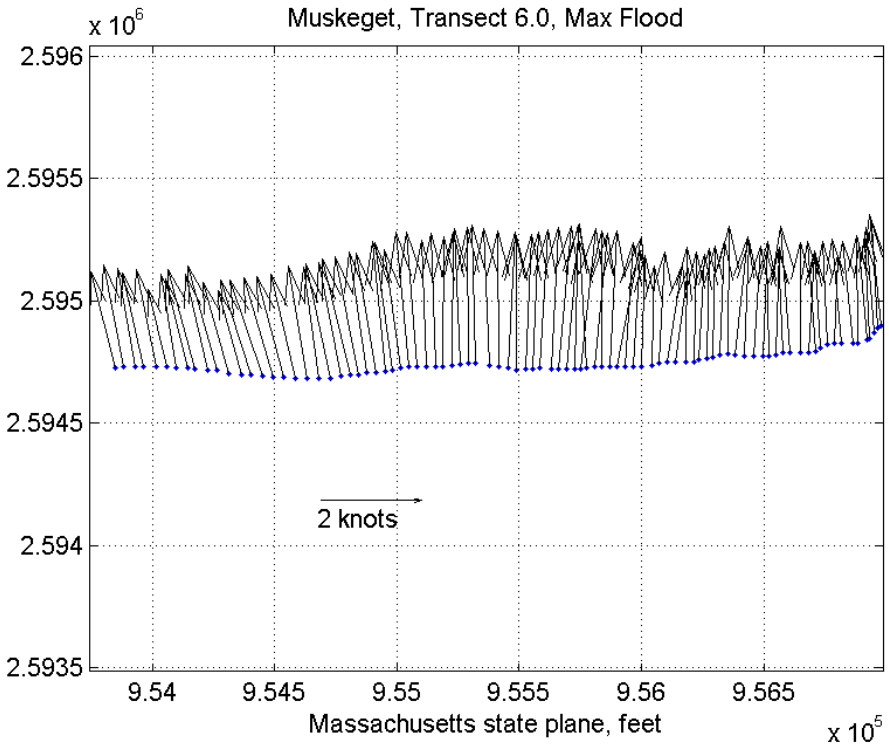
Muskeget, Transect 6.0, Max Flood
x 10^6
2.596
2.5955
2.595
2.5945
2.594
2.5935
2 knots
9.54
9.545
9.55
9.555
9.56
9.565
Massachusetts state plane, feet
x 10^5

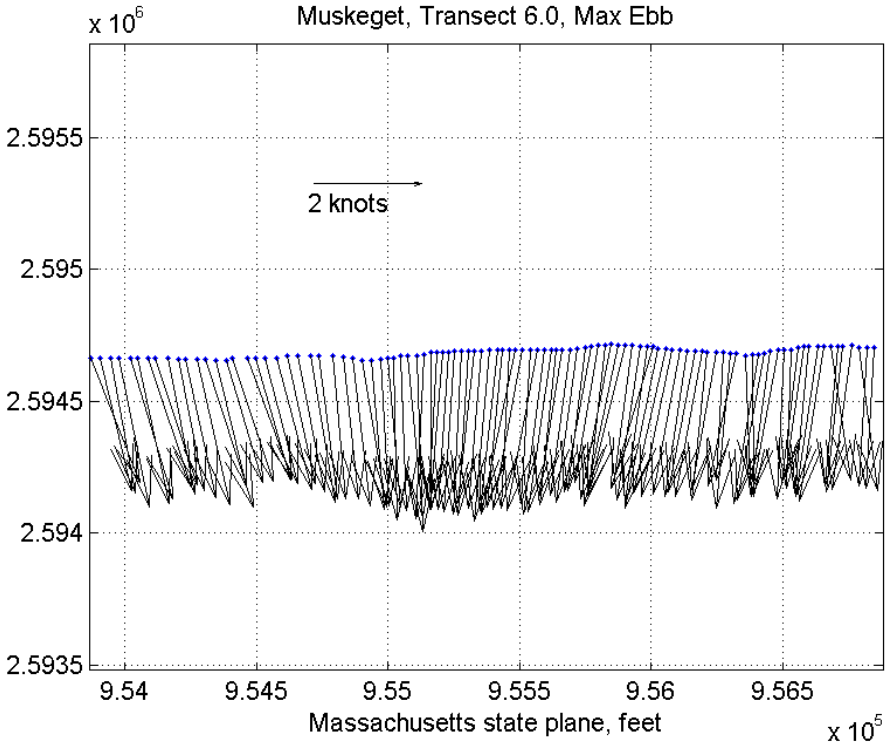
Muskeget, Transect 6.0, Max Ebb
x 10^6
2.5955
2.595
2.5945
2.594
2.5935
2 knots
9.54
9.545
9.55
9.555
9.56
9.565
Massachusetts state plane, feet
x 10^5

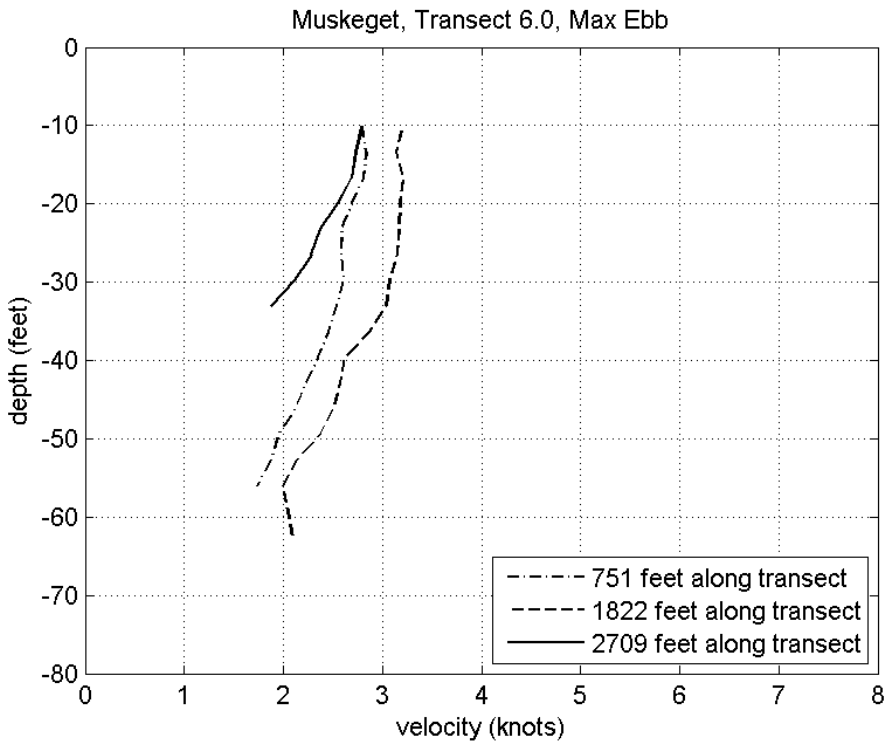
Muskeget, Transect 6.0, Max Ebb
depth (feet)
velocity (knots)
751 feet along transect
1822 feet along transect
2709 feet along transect

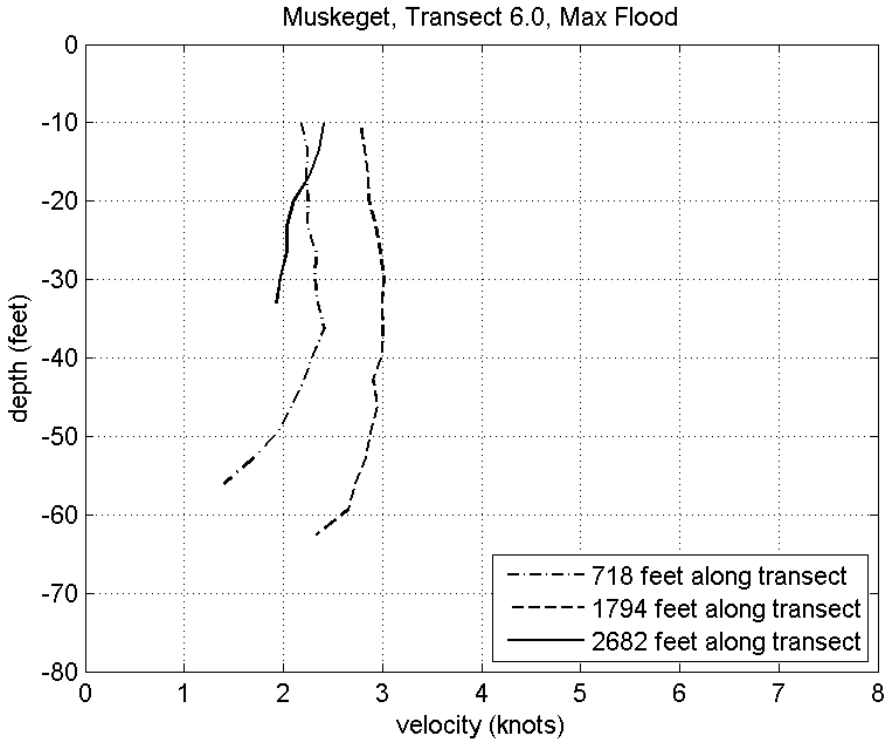
Muskeget, Transect 6.0, Max Flood
depth (feet)
velocity (knots)
718 feet along transect
1794 feet along transect
2682 feet along transect

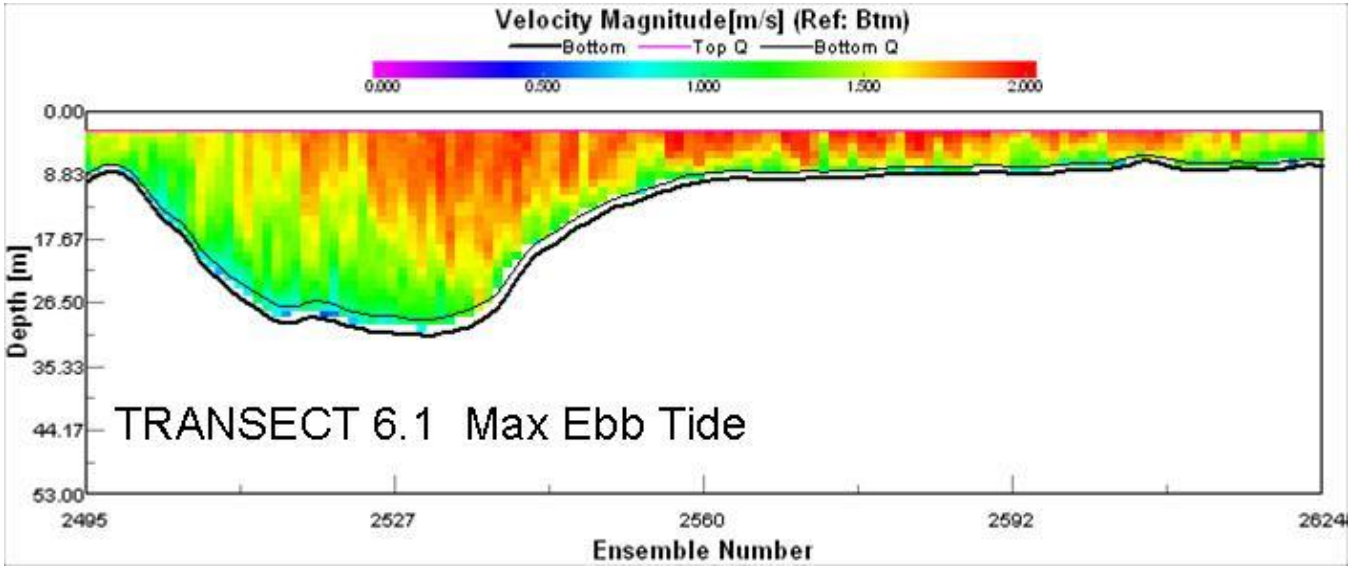
Velocity Magnitude[m/s] (Ref: Btm)
Bottom
Top Q
Bottom Q
0.000
0.500
1.000
1.500
2.000
0.00
8.83
17.67
26.50
35.33
44.17
53.00
Depth [m]
TRANSECT 6.1 Max Ebb Tide
2495
2527
2560
2592
Ensemble Number

Figure –

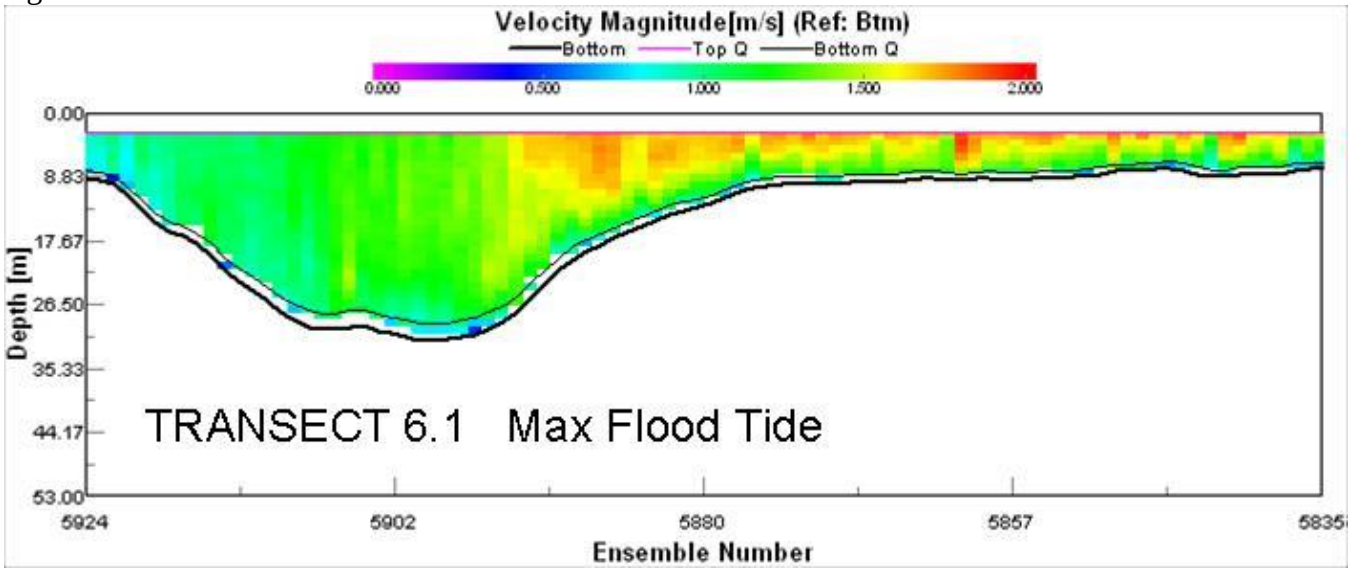
Velocity Magnitude[m/s] (Ref: Btm)
Bottom
Top Q
Bottom Q
0.000
0.500
1.000
1.500
2.000
0.00
8.83
17.67
26.50
35.33
44.17
53.00
Depth [m]
TRANSECT 6.1 Max Flood Tide
5924
5902
5880
5857
Ensemble Number

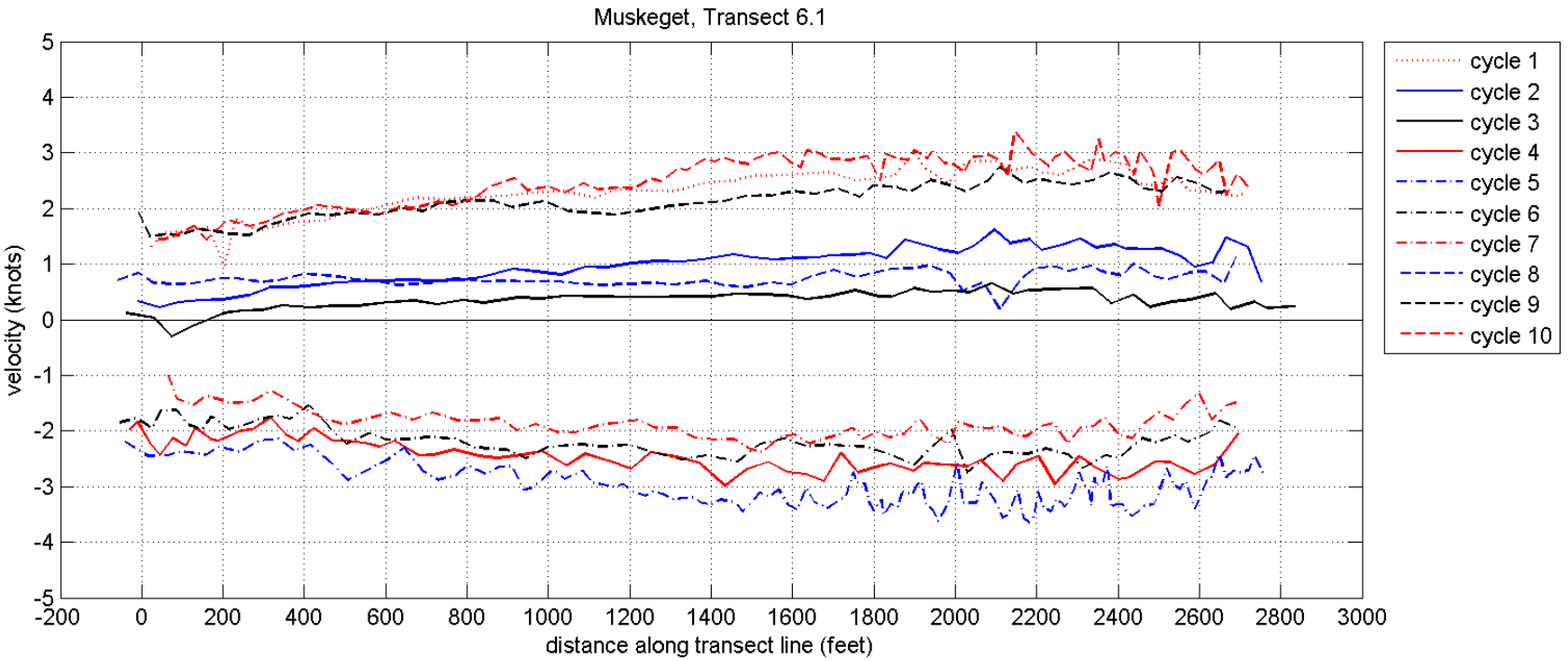
Muskeget, Transect 6.1
velocity (knots)
distance along transect line (feet)
cycle 1
cycle 2
cycle 3
cycle 4
cycle 5
cycle 6
cycle 7
cycle 8
cycle 9
cycle 10

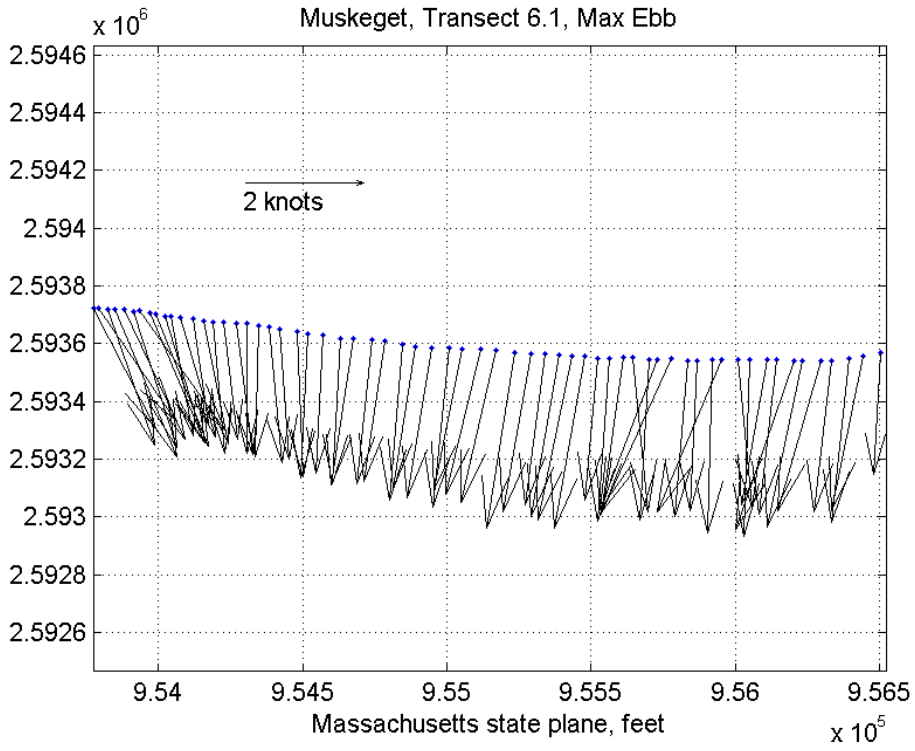
Muskeget, Transect 6.1, Max Ebb
x 10^6
2.5946
2.5944
2.5942
2.594
2.5938
2.5936
2.5934
2.5932
2.593
2.5928
2.5926
2 knots
9.54
9.545
9.55
9.555
9.56
9.565
Massachusetts state plane, feet
x 10^5

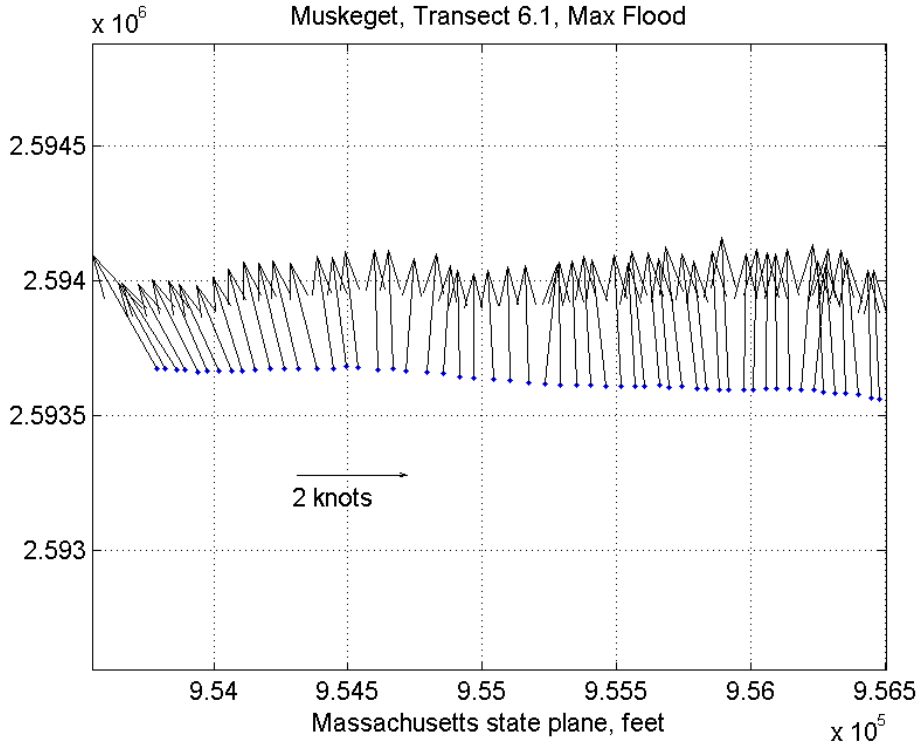
Muskeget, Transect 6.1, Max Flood
x 10^6
2.5945
2.594
2.5935
2.593
2 knots
9.54
9.545
9.55
9.555
9.56
9.565
Massachusetts state plane, feet
x 10^5

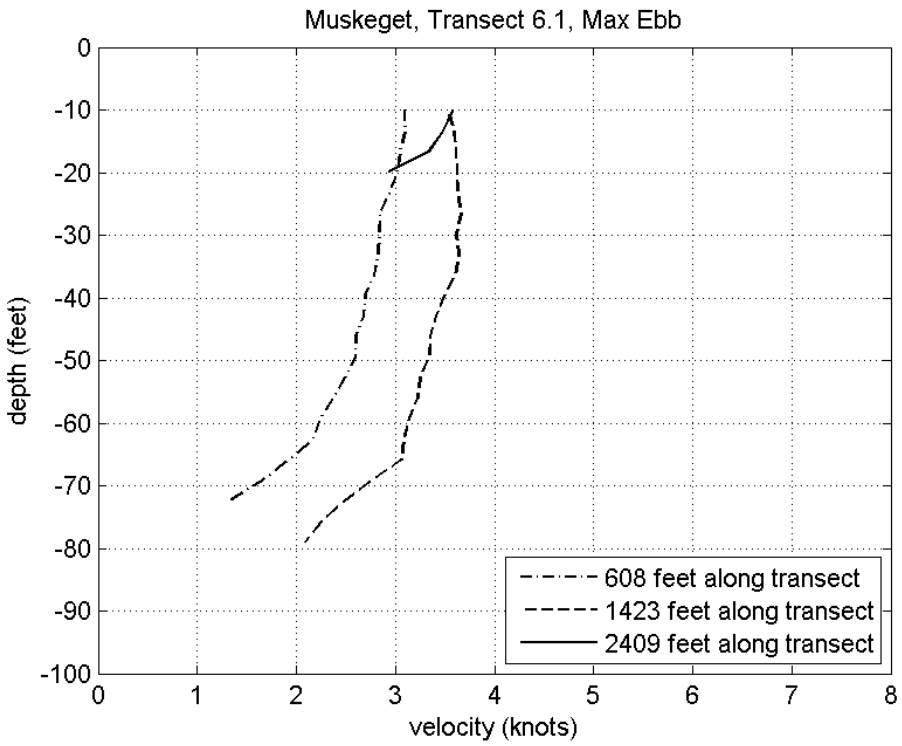
Muskeget, Transect 6.1, Max Ebb
depth (feet)
velocity (knots)
608 feet along transect
1423 feet along transect
2409 feet along transect

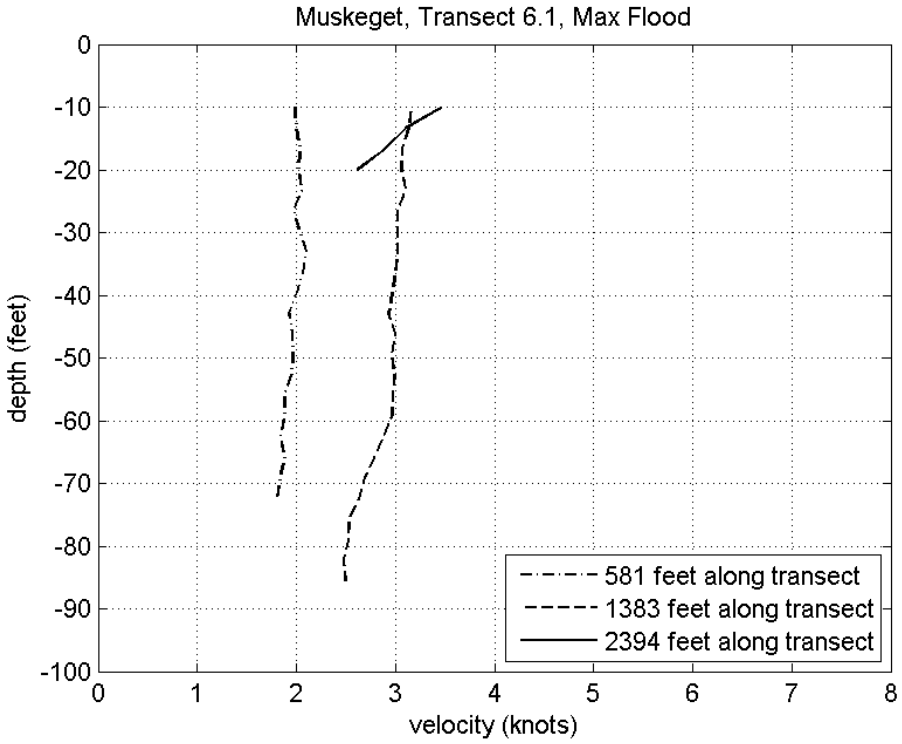
Muskeget, Transect 6.1, Max Flood
depth (feet)
velocity (knots)
581 feet along transect
1383 feet along transect
2394 feet along transect

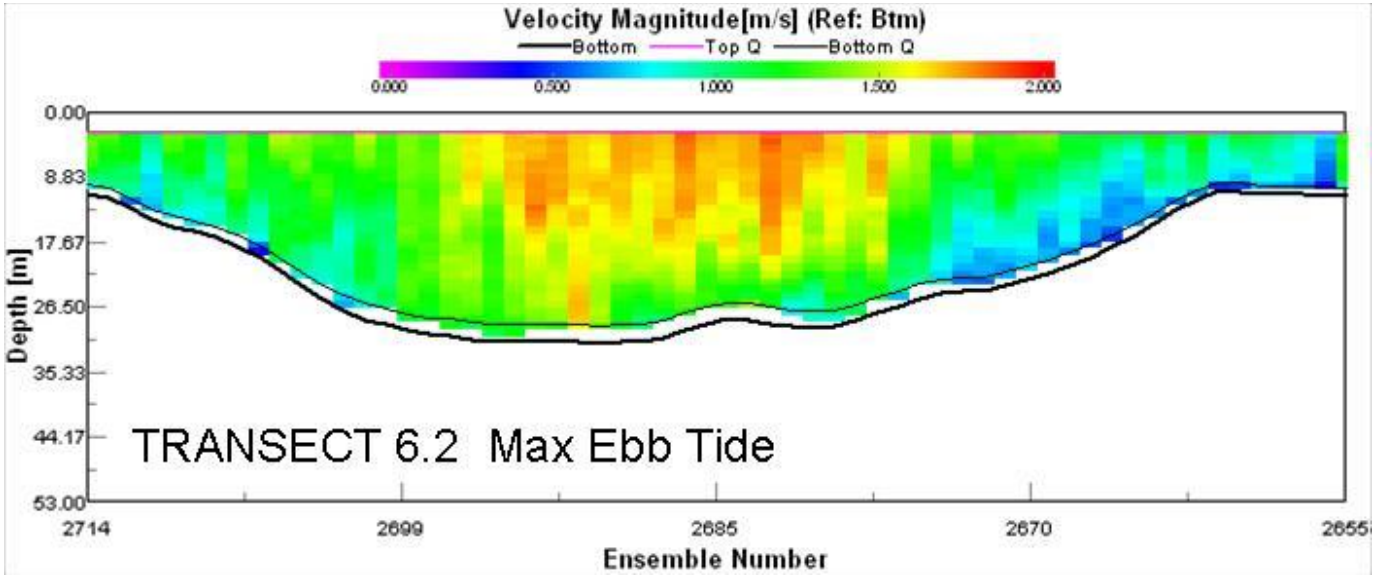
Velocity Magnitude[m/s] (Ref: Btm)
Bottom
Top Q
Bottom Q
0.000
0.500
1.000
1.500
2.000
0.00
8.83
17.67
26.50
35.33
44.17
53.00
Depth [m]
TRANSECT 6.2 Max Ebb Tide
2714
2699
2685
2670
Ensemble Number

Figure --

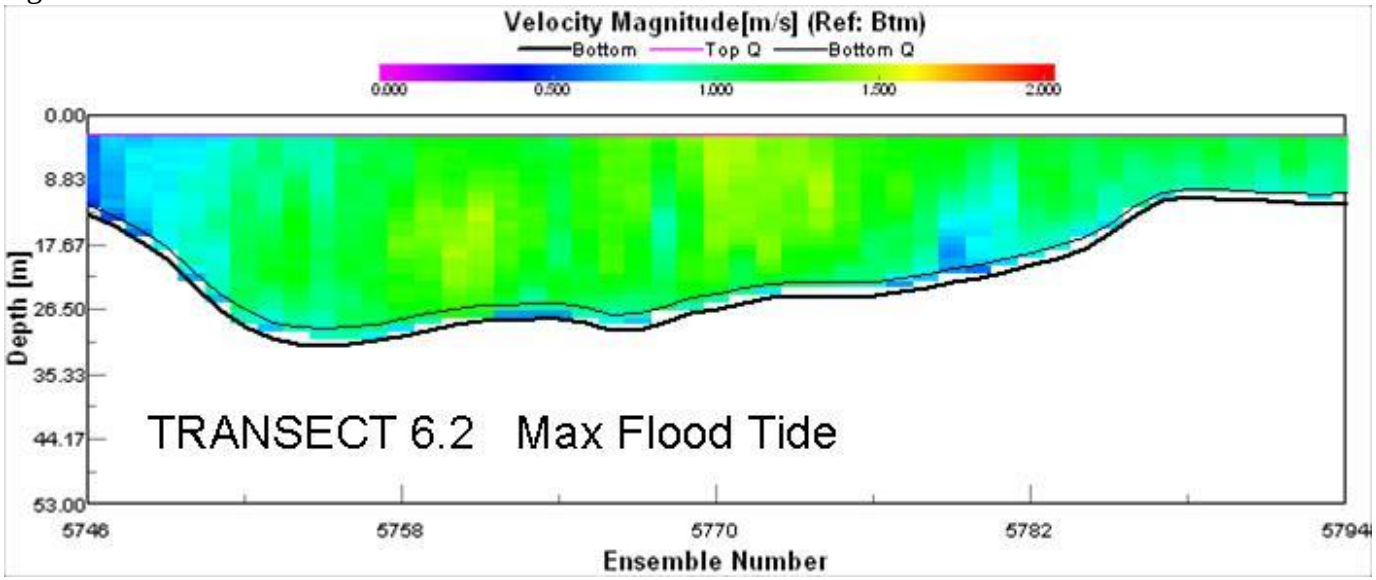
Velocity Magnitude[m/s] (Ref: Btm)
Bottom
Top Q
Bottom Q
0.000
0.500
1.000
1.500
2.000
0.00
8.83
17.67
26.50
35.33
44.17
53.00
Depth [m]
TRANSECT 6.2 Max Flood Tide
5746
5758
5770
5782
Ensemble Number

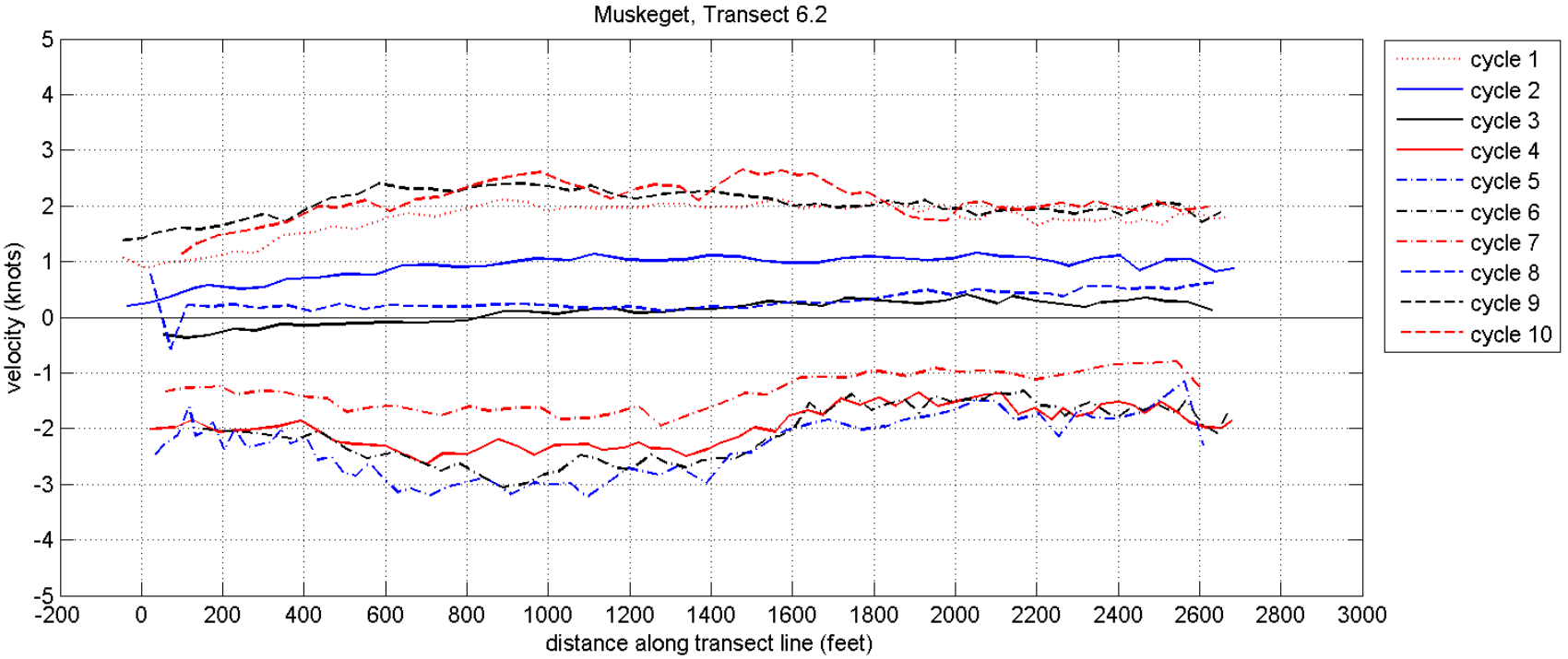
Muskeget, Transect 6.2
velocity (knots)
distance along transect line (feet)
cycle 1
cycle 2
cycle 3
cycle 4
cycle 5
cycle 6
cycle 7
cycle 8
cycle 9
cycle 10

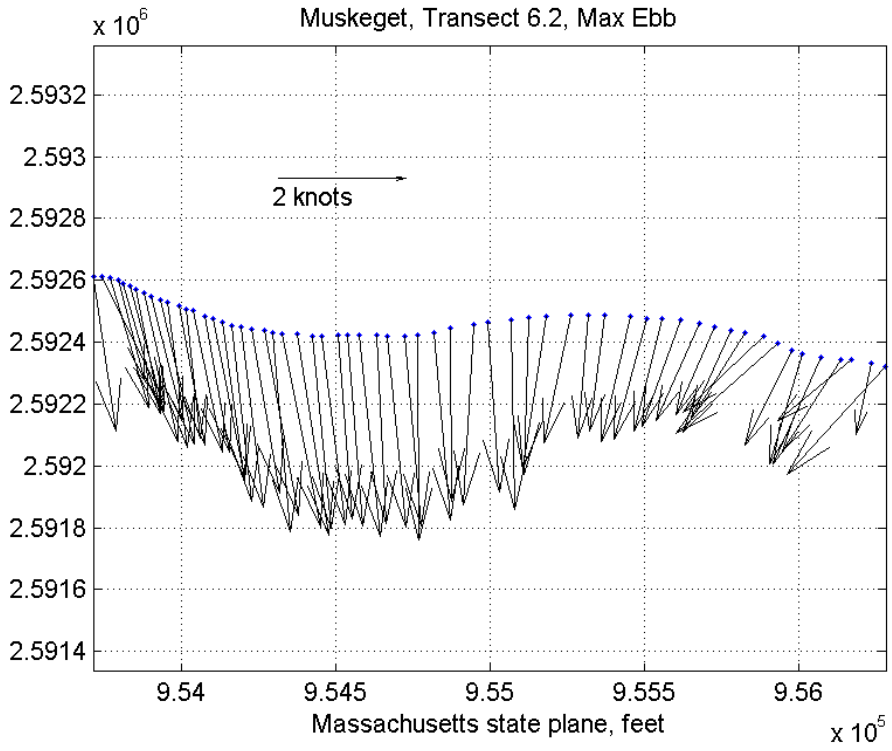
Muskeget, Transect 6.2, Max Ebb
x 10^6
2.5932
2.593
2.5928
2.5926
2.5924
2.5922
2.592
2.5918
2.5916
2.5914
2 knots
9.54
9.545
9.55
9.555
9.56
Massachusetts state plane, feet
x 10^5

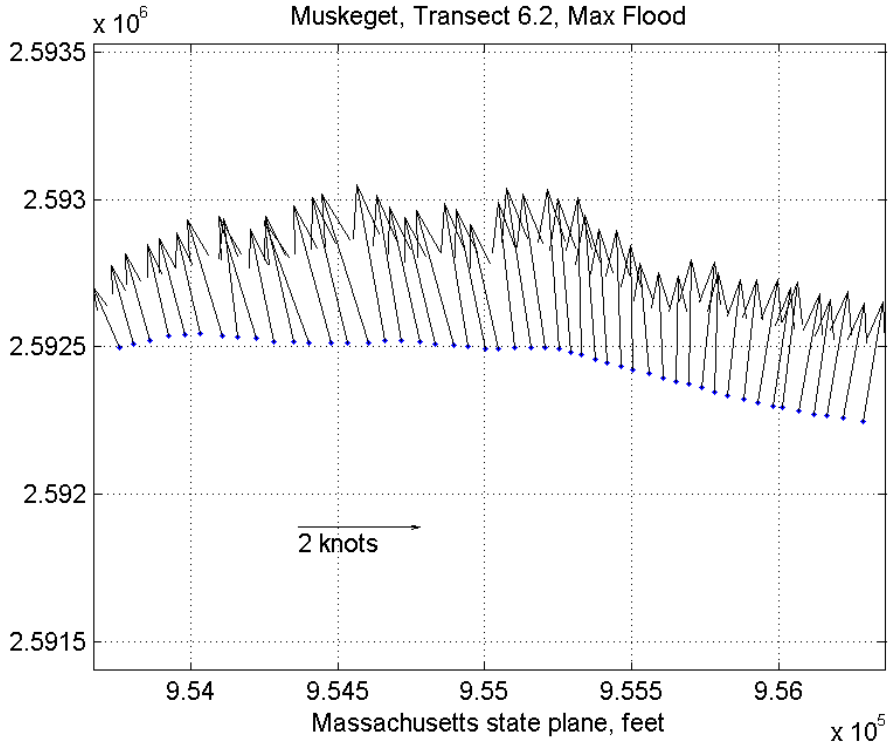
Muskeget, Transect 6.2, Max Flood
x 10^6
2.5935
2.593
2.5925
2.592
2.5915
2 knots
9.54
9.545
9.55
9.555
9.56
Massachusetts state plane, feet
x 10^5

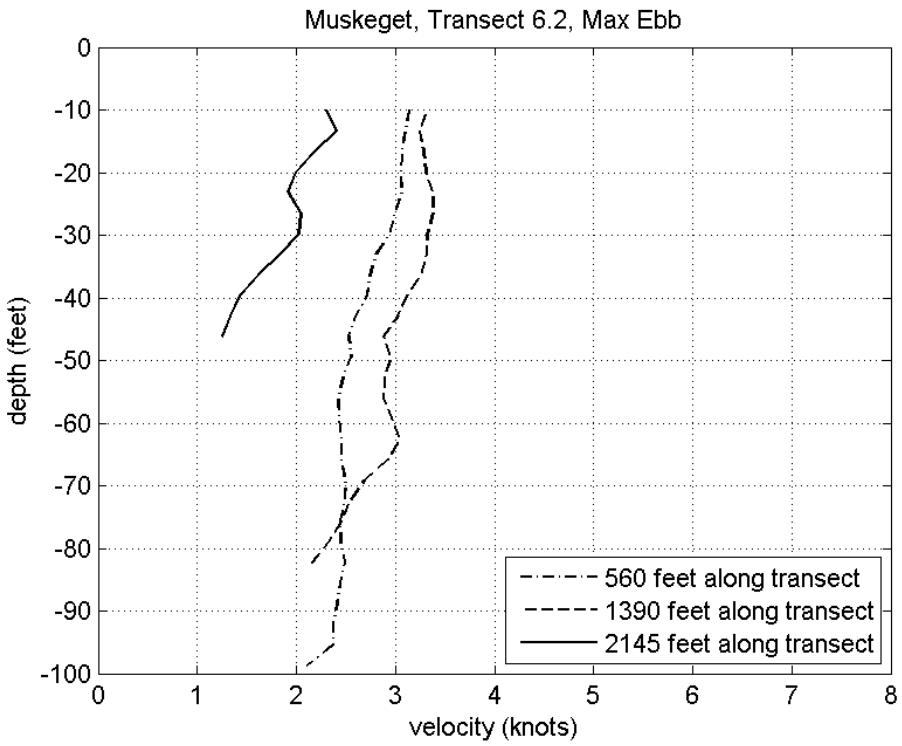
Muskeget, Transect 6.2, Max Ebb
depth (feet)
velocity (knots)
560 feet along transect
1390 feet along transect
2145 feet along transect

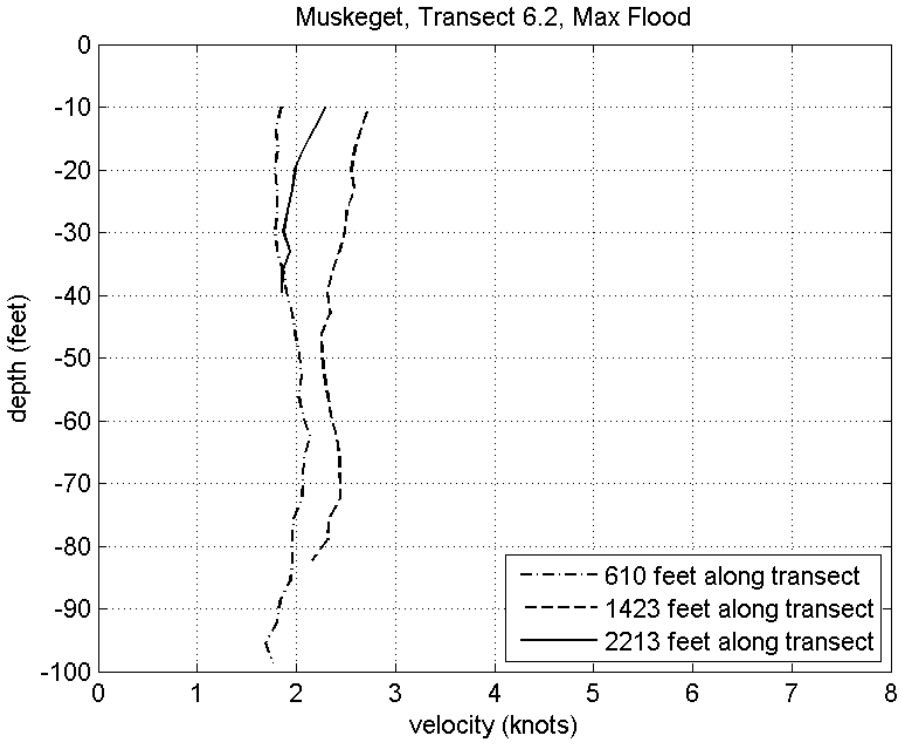
Muskeget, Transect 6.2, Max Flood
depth (feet)
velocity (knots)
610 feet along transect
1423 feet along transect
2213 feet along transect

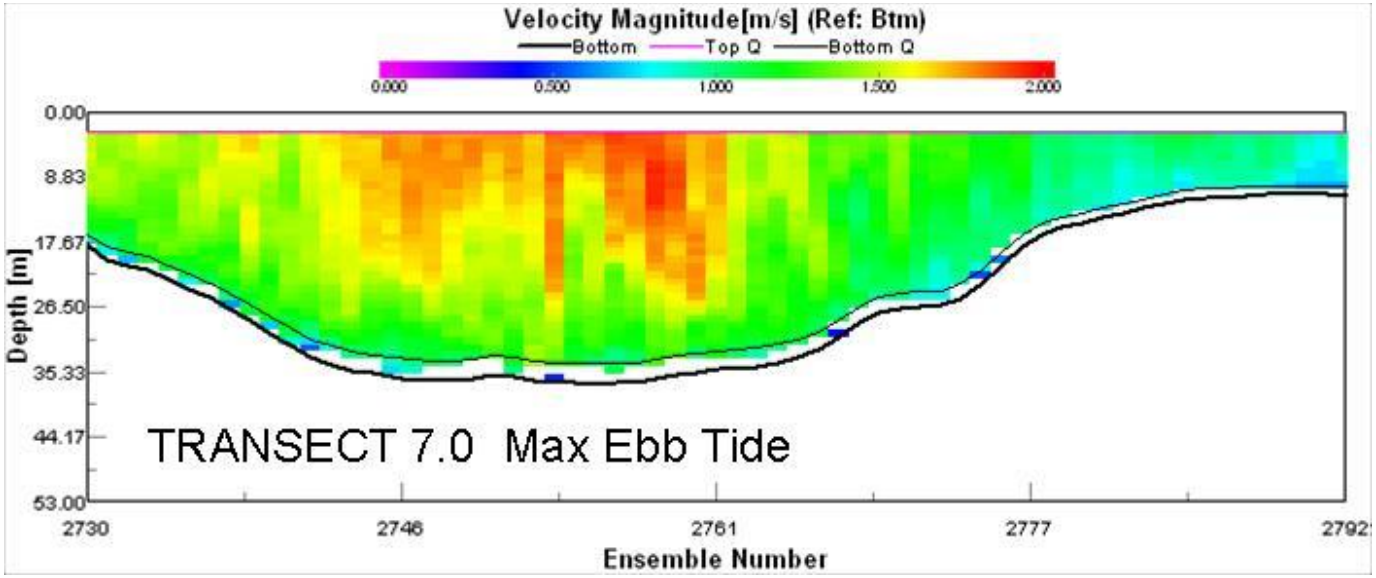
Velocity Magnitude[m/s] (Ref: Btm)
Bottom
Top Q
Bottom Q
0.000
0.500
1.000
1.500
2.000
0.00
8.83
17.67
26.50
35.33
44.17
53.00
Depth [m]
TRANSECT 7.0 Max Ebb Tide
2730
2746
2761
2777
Ensemble Number

Figure --

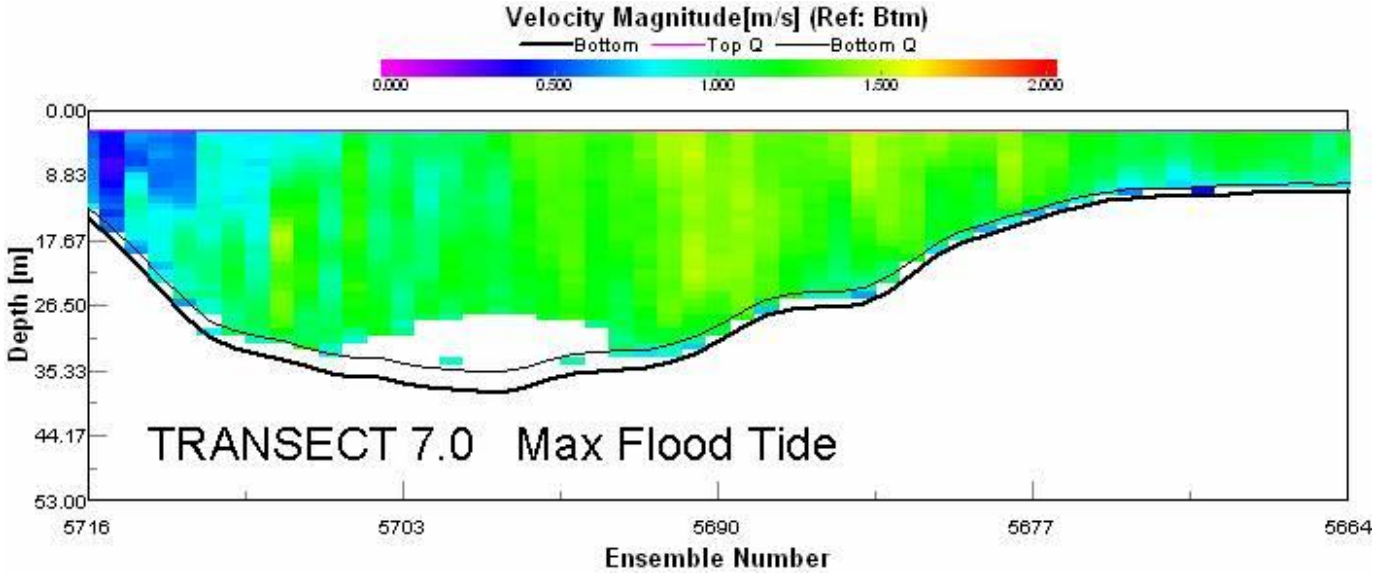
Velocity Magnitude[m/s] (Ref: Btm)
Bottom
Top Q
Bottom Q
0.000
0.500
1.000
1.500
2.000
0.00
8.83
17.67
26.50
35.33
44.17
53.00
Depth [m]
TRANSECT 7.0 Max Flood Tide
5716
5703
5690
5677
5664
Ensemble Number

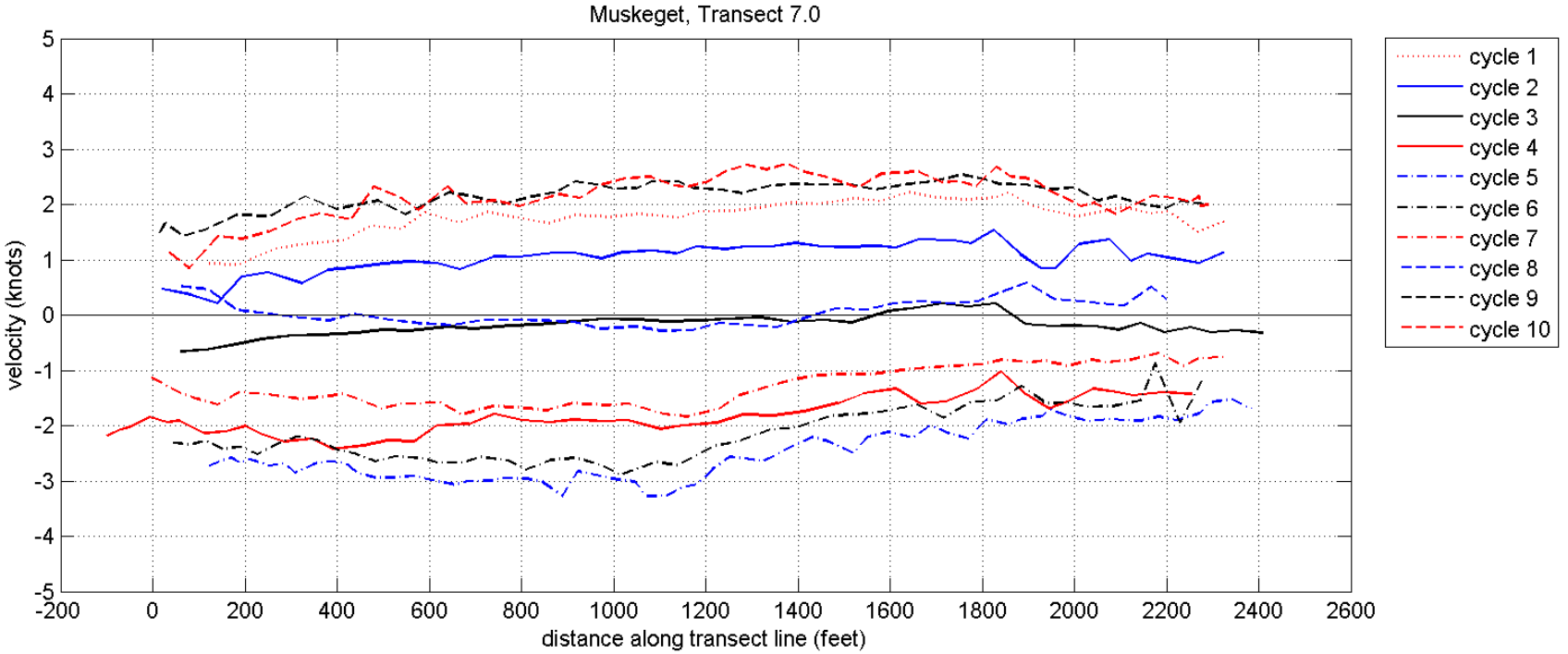
Muskeget, Transect 7.0
velocity (knots)
distance along transect line (feet)
cycle 1
cycle 2
cycle 3
cycle 4
cycle 5
cycle 6
cycle 7
cycle 8
cycle 9
cycle 10

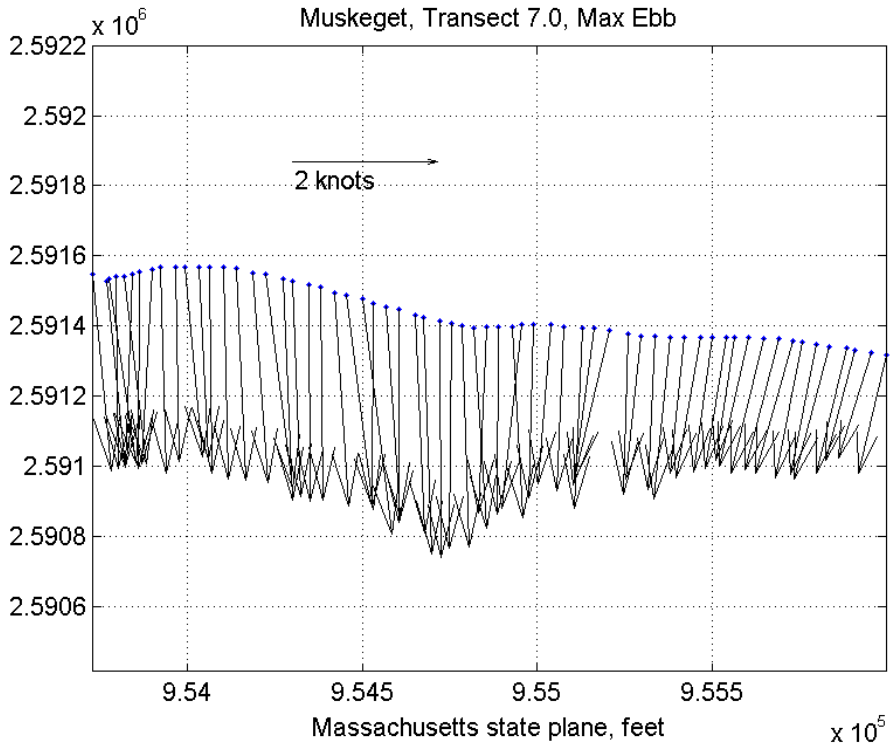
Muskeget, Transect 7.0, Max Ebb
x 10^6
2.5922
2.592
2.5918
2.5916
2.5914
2.5912
2.591
2.5908
2.5906
2 knots
9.54
9.545
9.55
9.555
Massachusetts state plane, feet
x 10^5

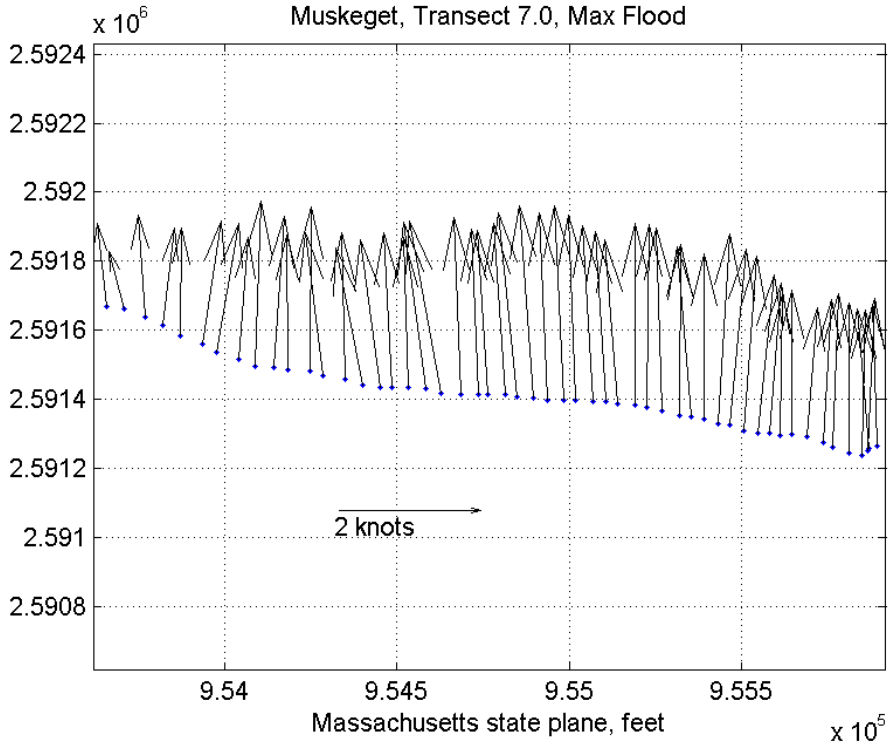
Muskeget, Transect 7.0, Max Flood
x 10^6
2.5924
2.5922
2.592
2.5918
2.5916
2.5914
2.5912
2.591
2.5908
2 knots
9.54
9.545
9.55
9.555
Massachusetts state plane, feet
x 10^5

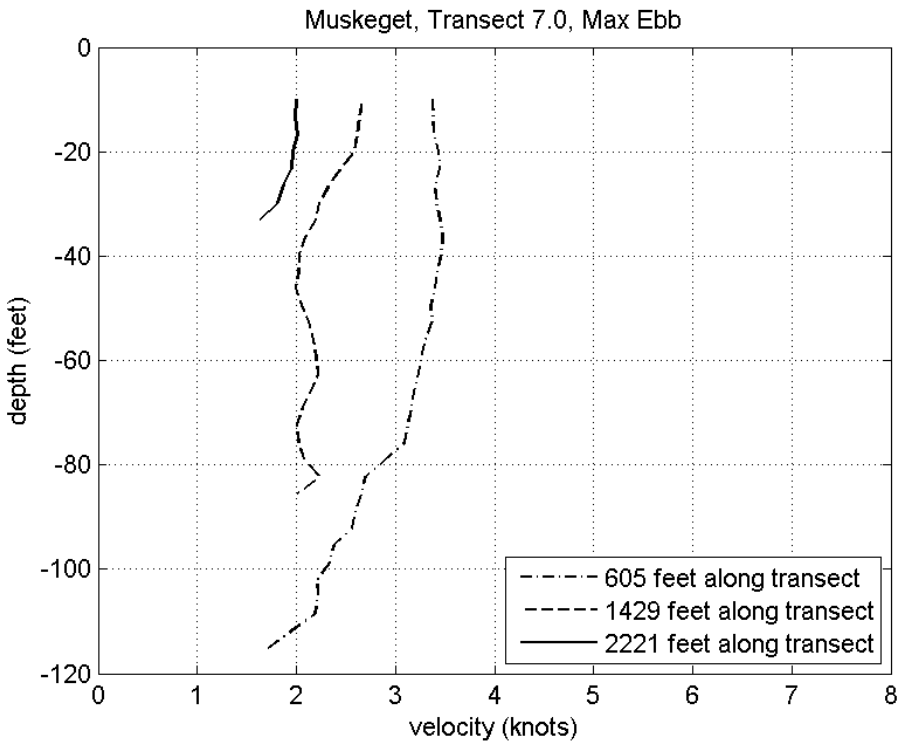
Muskeget, Transect 7.0, Max Ebb
depth (feet)
velocity (knots)
0
-20
-40
-60
-80
-100
-120
0
1
2
3
4
5
6
7
8
605 feet along transect
1429 feet along transect
2221 feet along transect

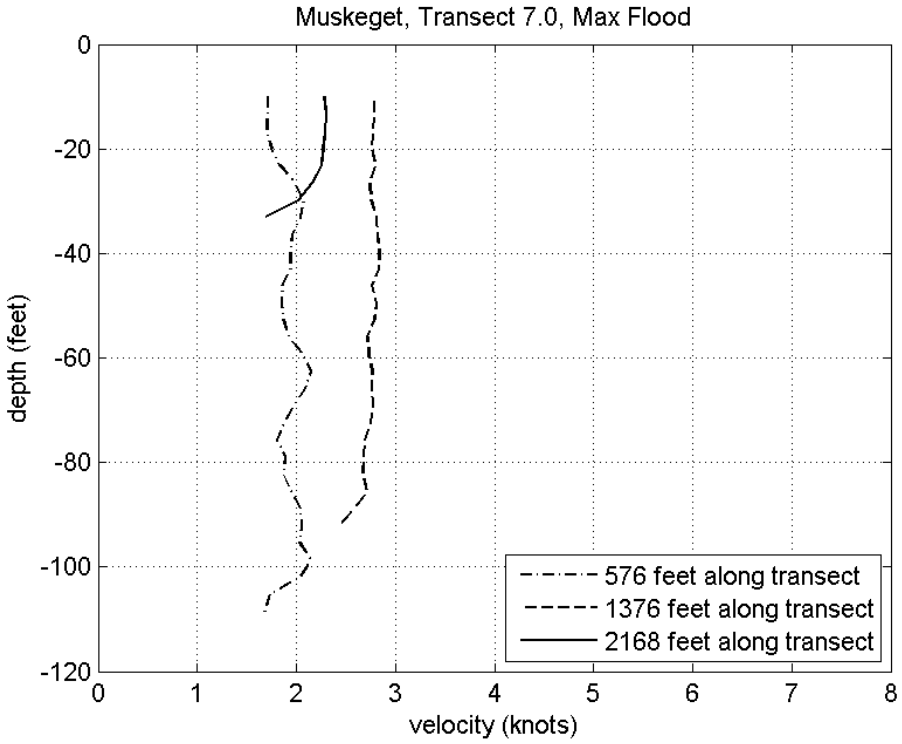
Muskeget, Transect 7.0, Max Flood
depth (feet)
velocity (knots)
0
-20
-40
-60
-80
-100
-120
0
1
2
3
4
5
6
7
8
576 feet along transect
1376 feet along transect
2168 feet along transect

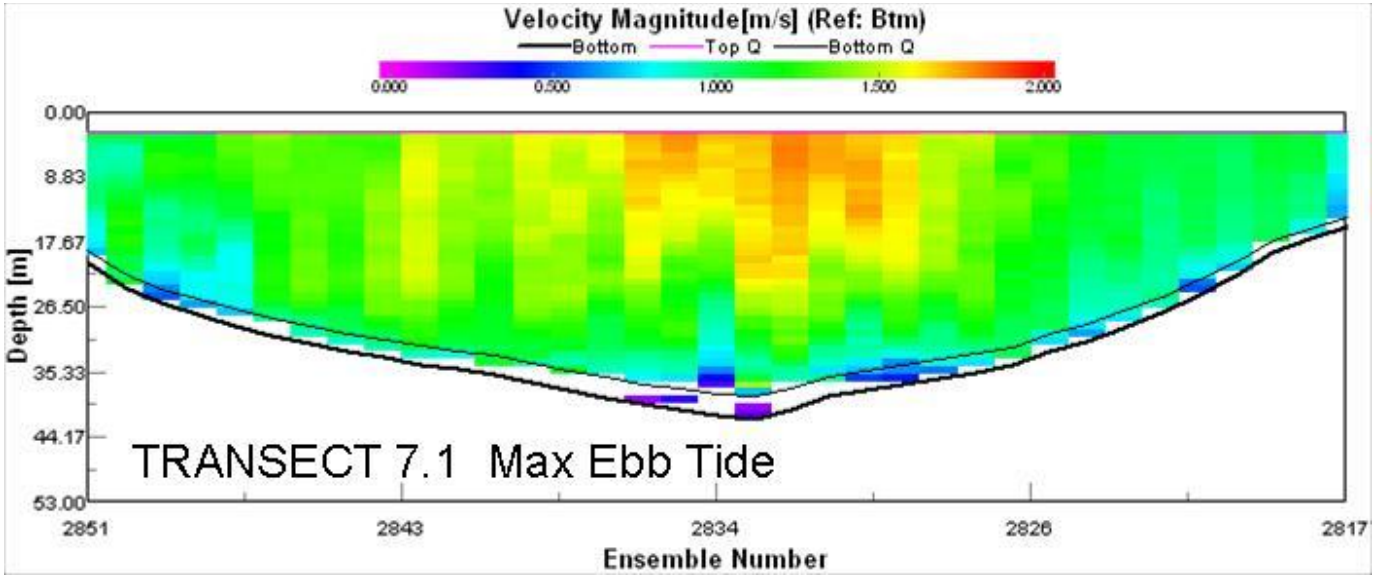
Velocity Magnitude[m/s] (Ref: Btm)
Bottom
Top Q
Bottom Q
0.000
0.500
1.000
1.500
2.000
0.00
8.83
17.67
26.50
35.33
44.17
53.00
Depth [m]
TRANSECT 7.1 Max Ebb Tide
2851
2843
2834
2826
2817
Ensemble Number

Figure --

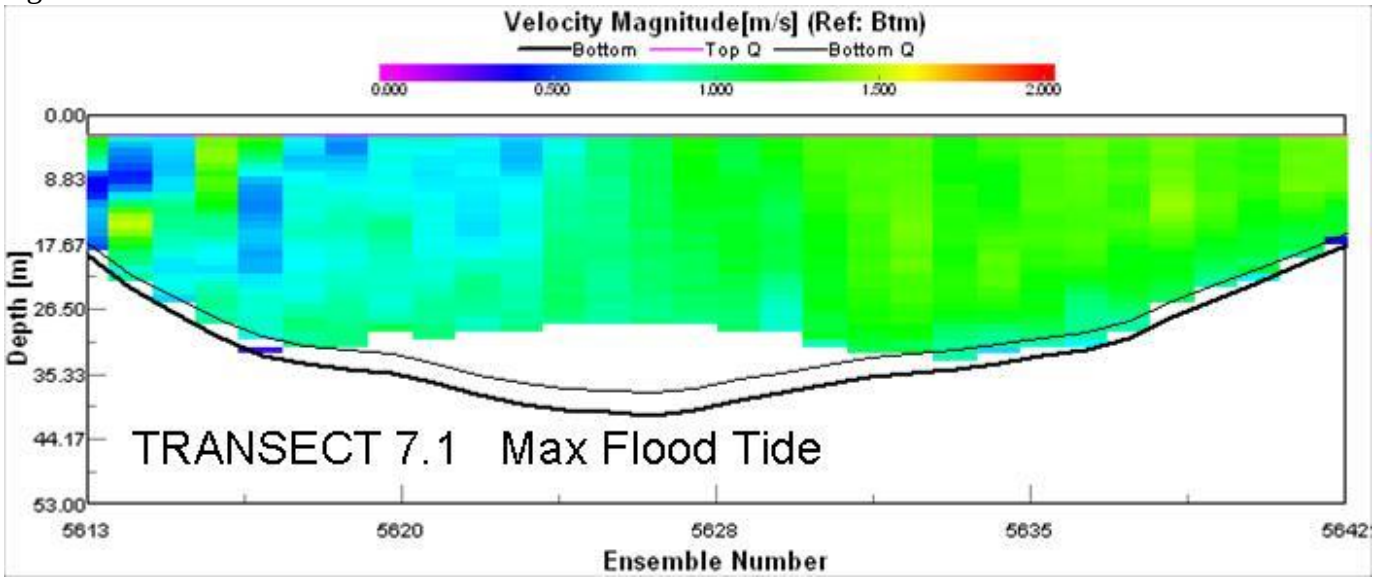
Velocity Magnitude[m/s] (Ref: Btm)
Bottom
Top Q
Bottom Q
0.000
0.500
1.000
1.500
2.000
0.00
8.83
17.67
26.50
35.33
44.17
53.00
Depth [m]
TRANSECT 7.1 Max Flood Tide
5613
5620
5628
5635
Ensemble Number

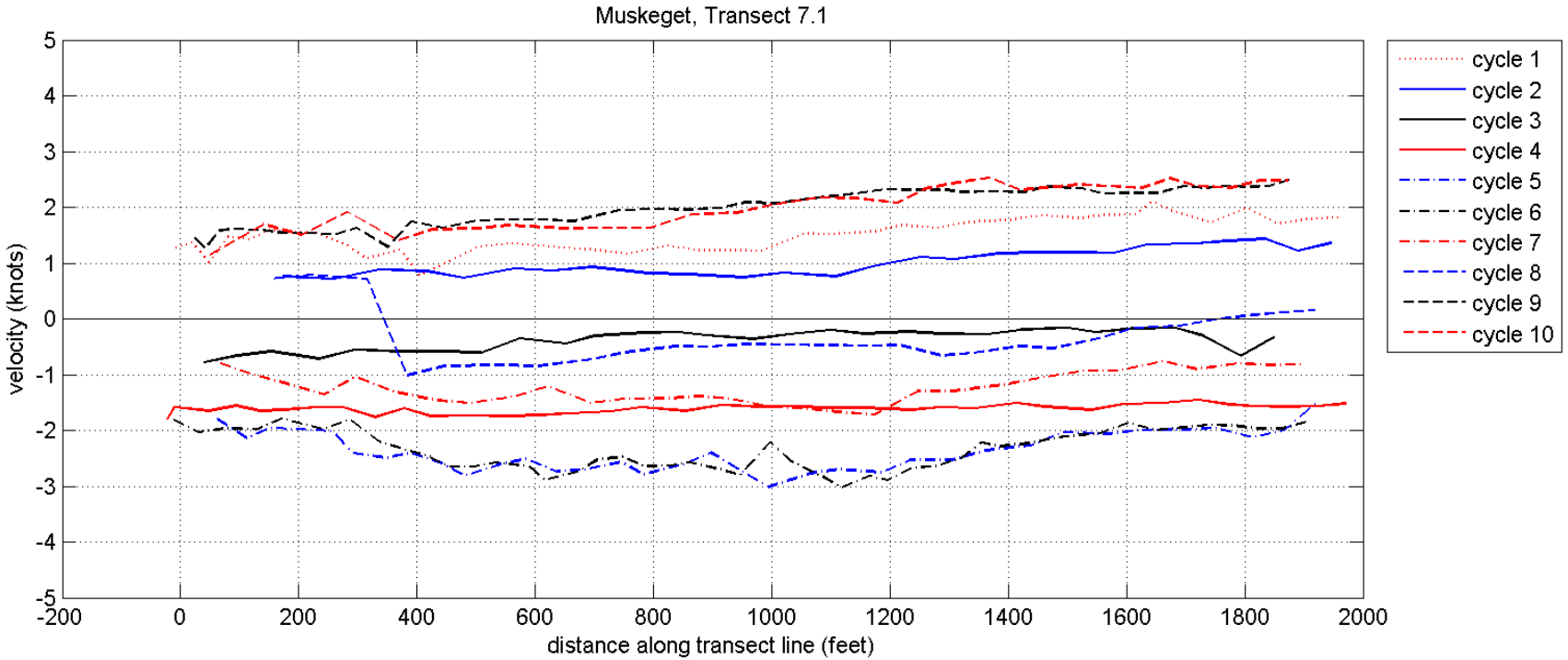
Muskeget, Transect 7.1
velocity (knots)
distance along transect line (feet)
cycle 1
cycle 2
cycle 3
cycle 4
cycle 5
cycle 6
cycle 7
cycle 8
cycle 9
cycle 10

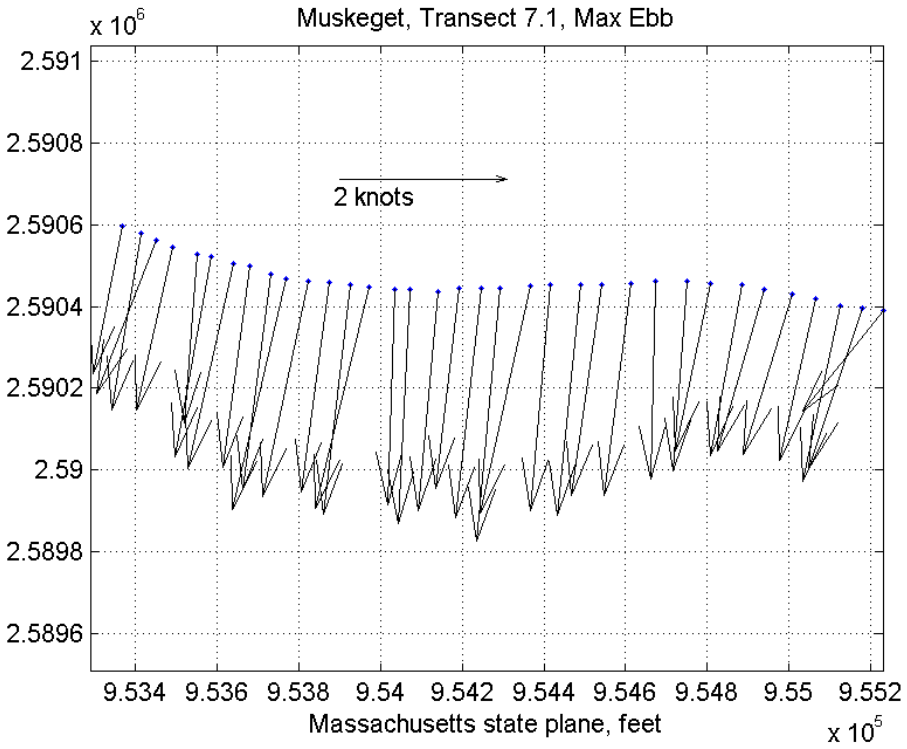
Muskeget, Transect 7.1, Max Ebb
x 10^6
2.591
2.5908
2.5906
2.5904
2.5902
2.59
2.5898
2.5896
2 knots
9.534 9.536 9.538 9.54 9.542 9.544 9.546 9.548 9.55 9.552
Massachusetts state plane, feet
x 10^5

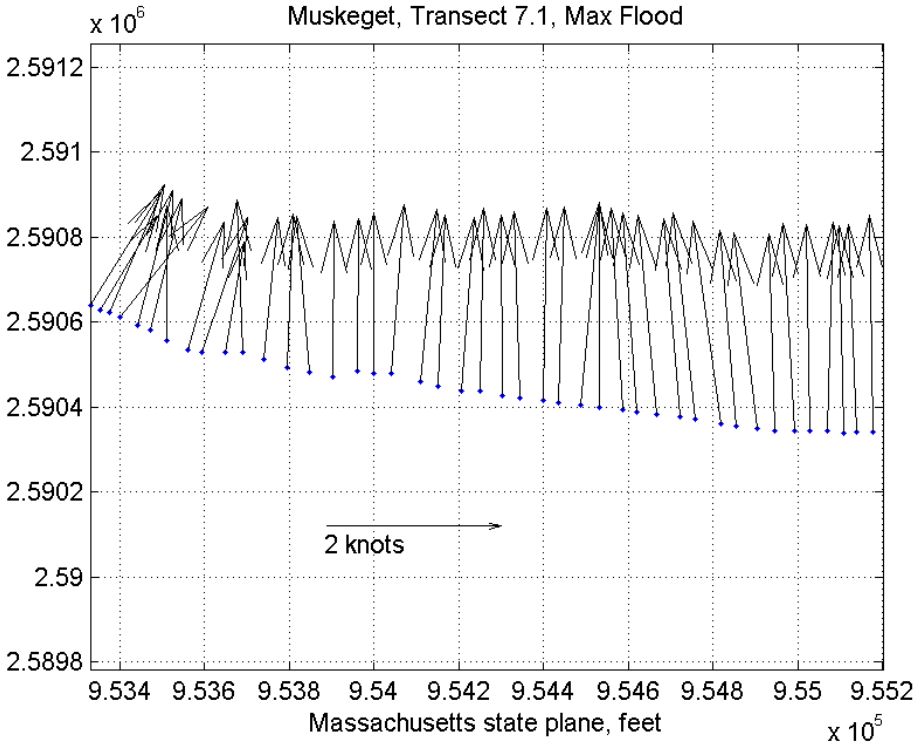
Muskeget, Transect 7.1, Max Flood
x 10^6
2.5912
2.591
2.5908
2.5906
2.5904
2.5902
2.59
2.5898
2 knots
9.534 9.536 9.538 9.54 9.542 9.544 9.546 9.548 9.55 9.552
Massachusetts state plane, feet
x 10^5

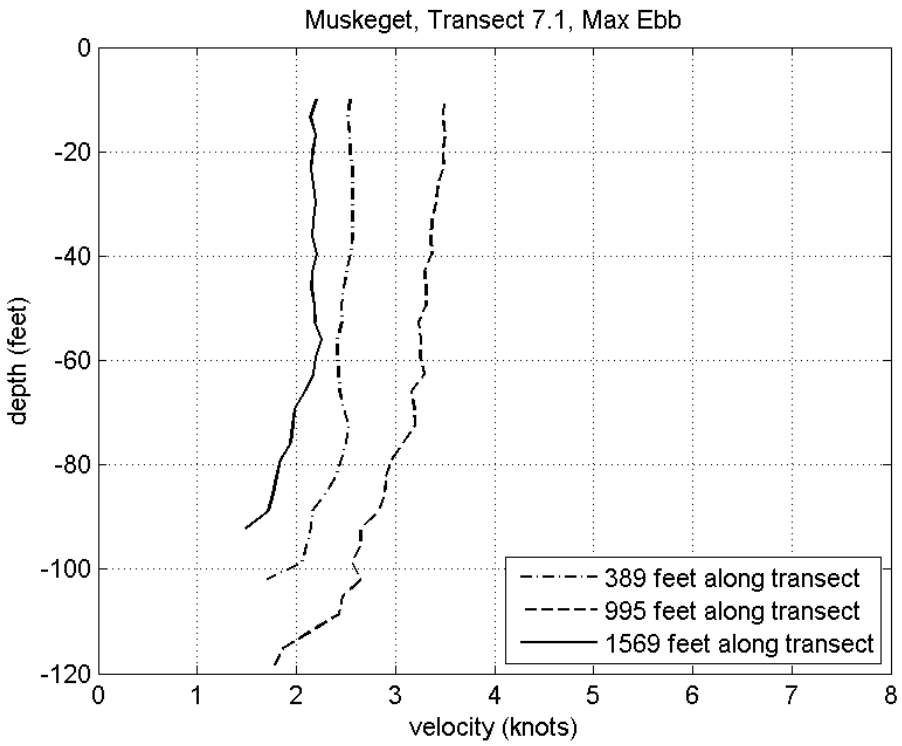
Muskeget, Transect 7.1, Max Ebb
depth (feet)
velocity (knots)
389 feet along transect
995 feet along transect
1569 feet along transect

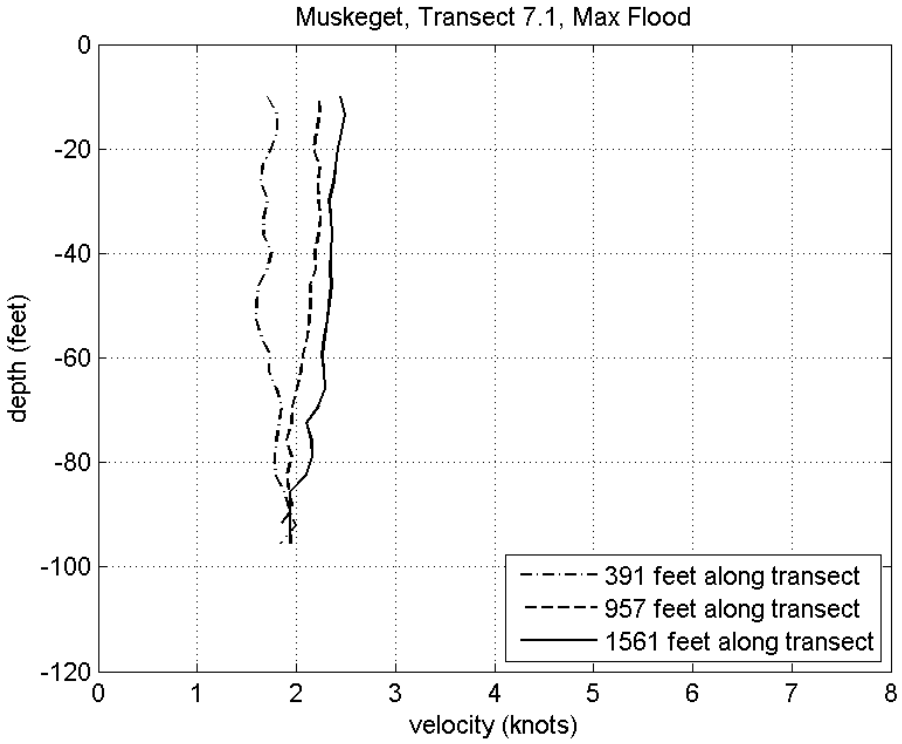
Muskeget, Transect 7.1, Max Flood
depth (feet)
velocity (knots)
391 feet along transect
957 feet along transect
1561 feet along transect

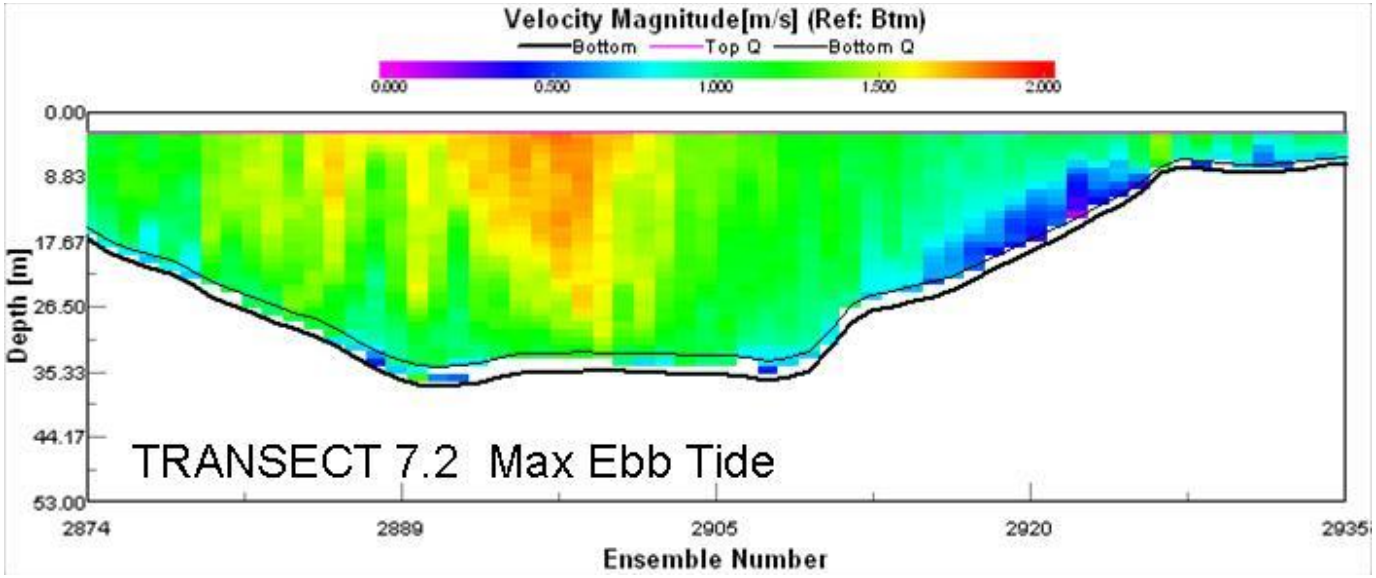
Velocity Magnitude[m/s] (Ref: Btm)
Bottom
Top Q
Bottom Q
0.000
0.500
1.000
1.500
2.000
0.00
8.83
17.67
26.50
35.33
44.17
53.00
Depth [m]
TRANSECT 7.2 Max Ebb Tide
2874
2889
2905
2920
Ensemble Number

Figure --

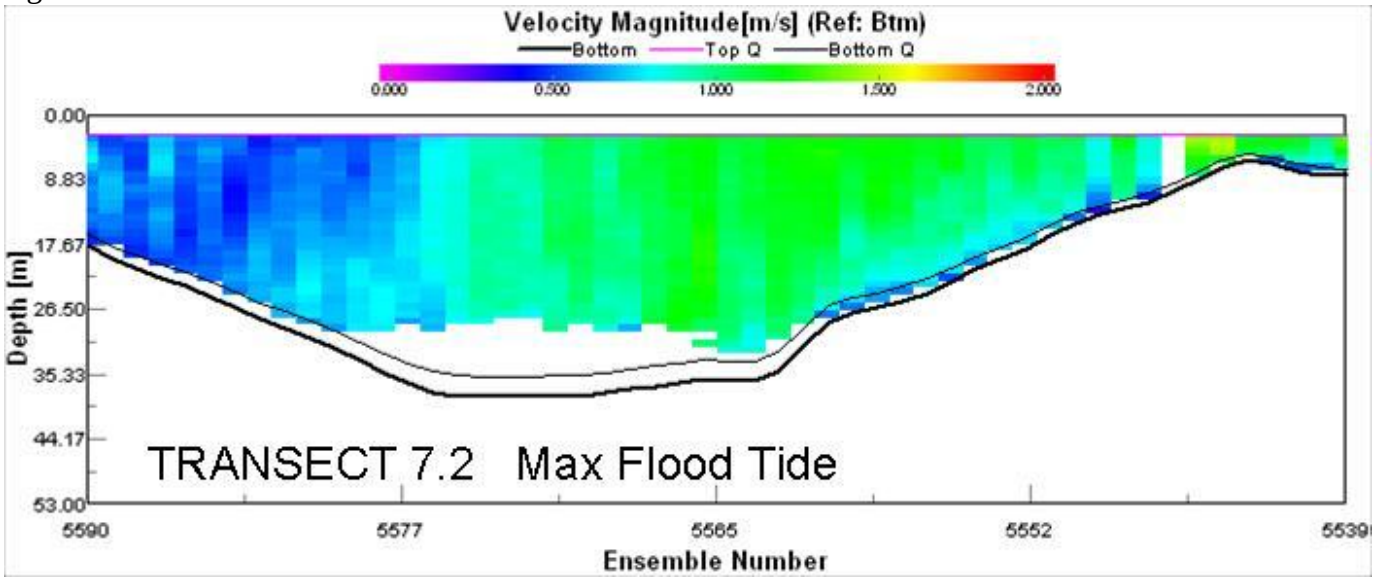
Velocity Magnitude[m/s] (Ref: Btm)
Bottom
Top Q
Bottom Q
0.000
0.500
1.000
1.500
2.000
0.00
8.83
17.67
26.50
35.33
44.17
53.00
Depth [m]
TRANSECT 7.2 Max Flood Tide
5590
5577
5565
5552
Ensemble Number

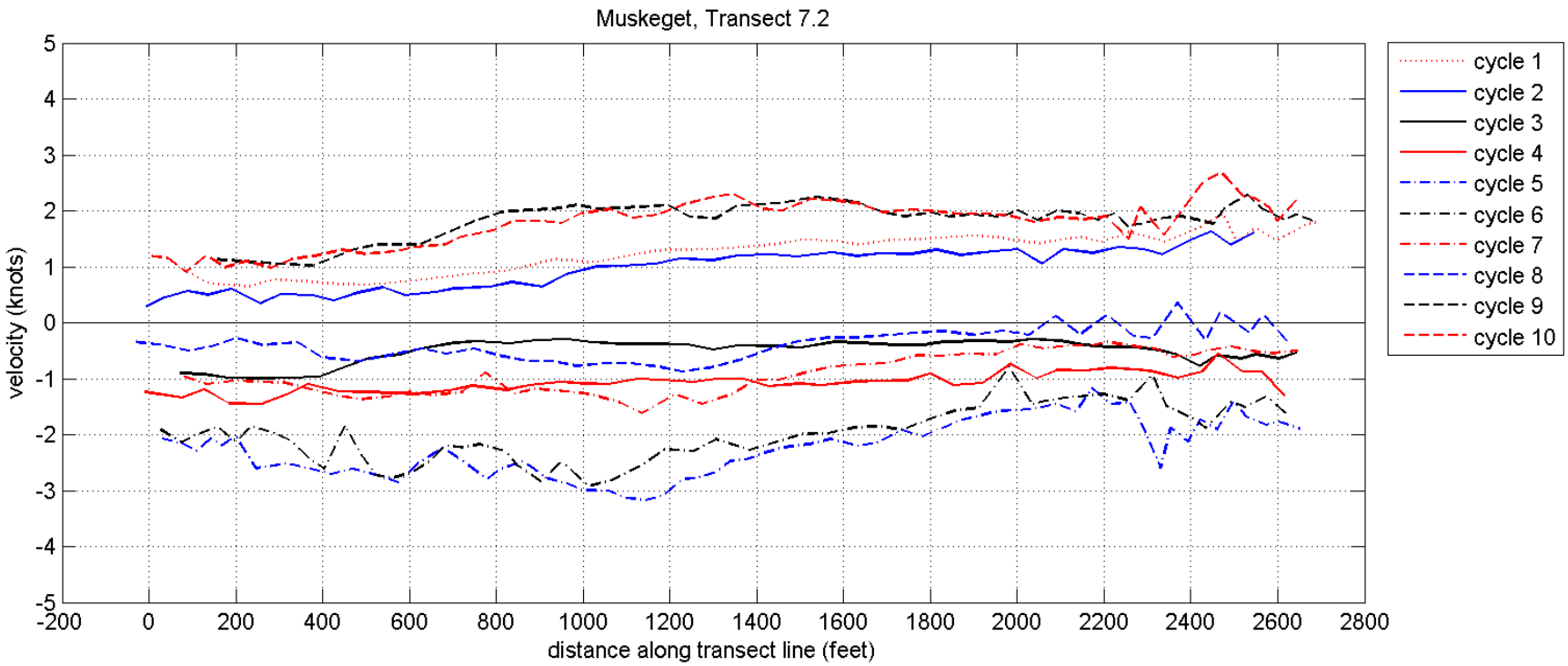
Muskeget, Transect 7.2
velocity (knots)
distance along transect line (feet)
cycle 1
cycle 2
cycle 3
cycle 4
cycle 5
cycle 6
cycle 7
cycle 8
cycle 9
cycle 10

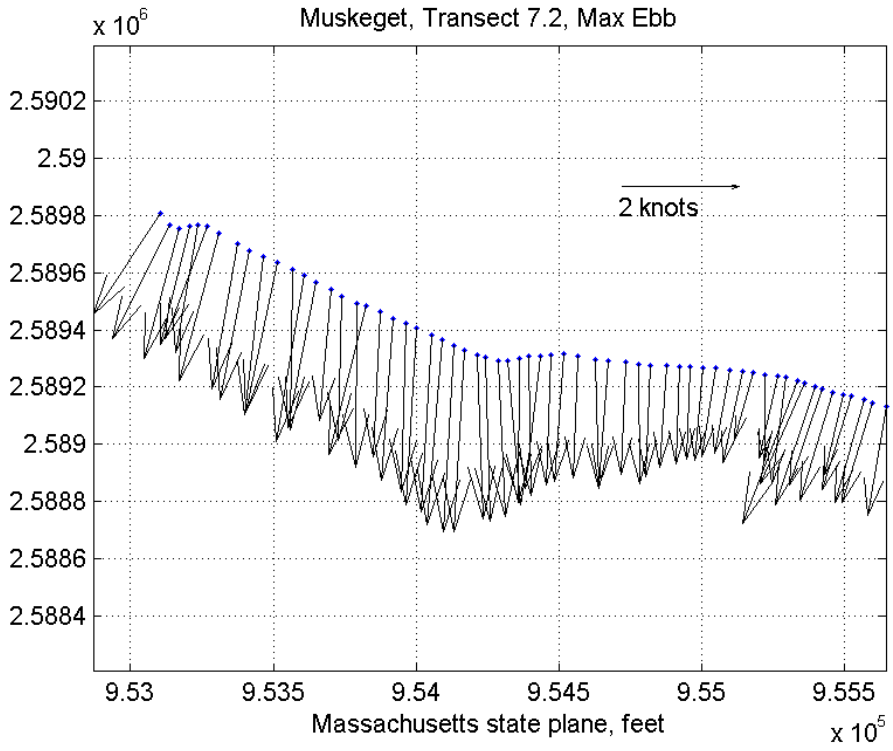
Muskeget, Transect 7.2, Max Ebb
x 10^6
2.5902
2.59
2.5898
2.5896
2.5894
2.5892
2.589
2.5888
2.5886
2.5884
2 knots
9.53
9.535
9.54
9.545
9.55
9.555
Massachusetts state plane, feet
x 10^5

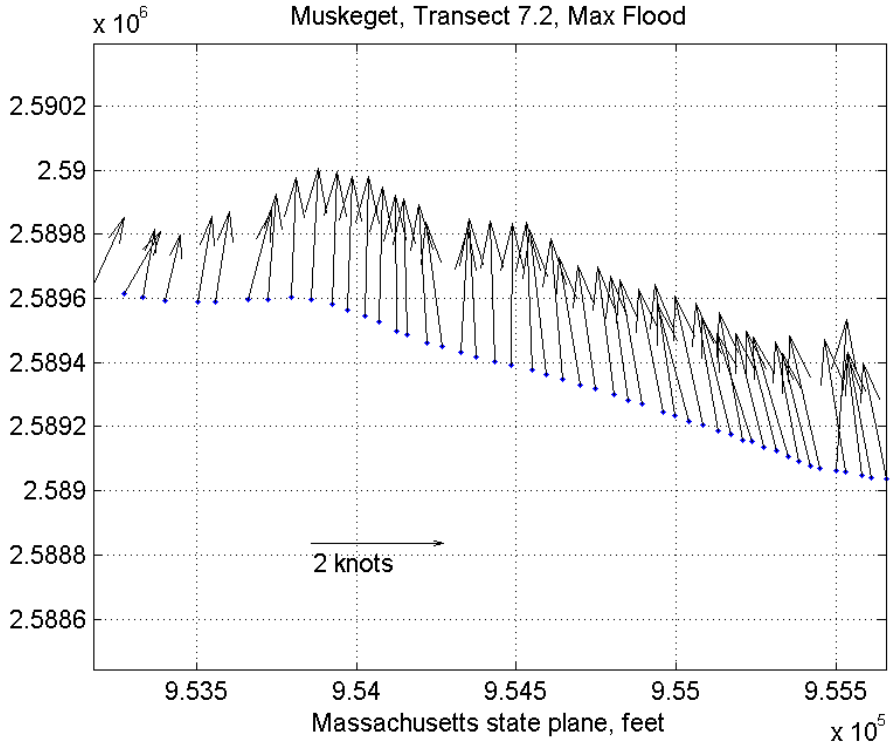
Muskeget, Transect 7.2, Max Flood
x 10^6
2.5902
2.59
2.5898
2.5896
2.5894
2.5892
2.589
2.5888
2.5886
2 knots
9.535
9.54
9.545
9.55
9.555
Massachusetts state plane, feet
x 10^5

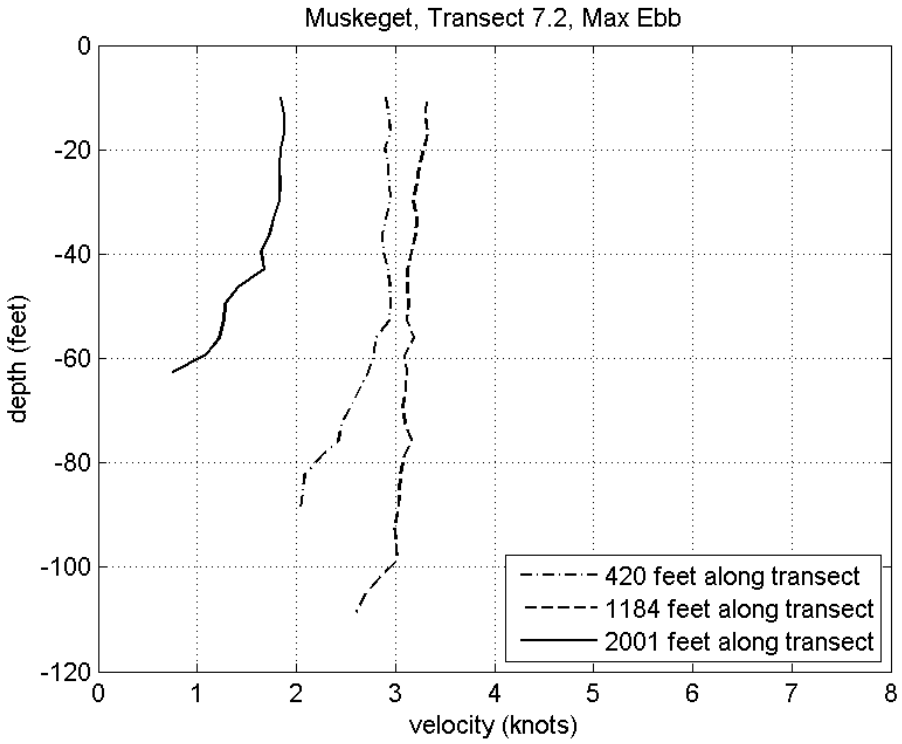
Muskeget, Transect 7.2, Max Ebb
depth (feet)
velocity (knots)
0
-20
-40
-60
-80
-100
-120
0
1
2
3
4
5
6
7
8
420 feet along transect
1184 feet along transect
2001 feet along transect

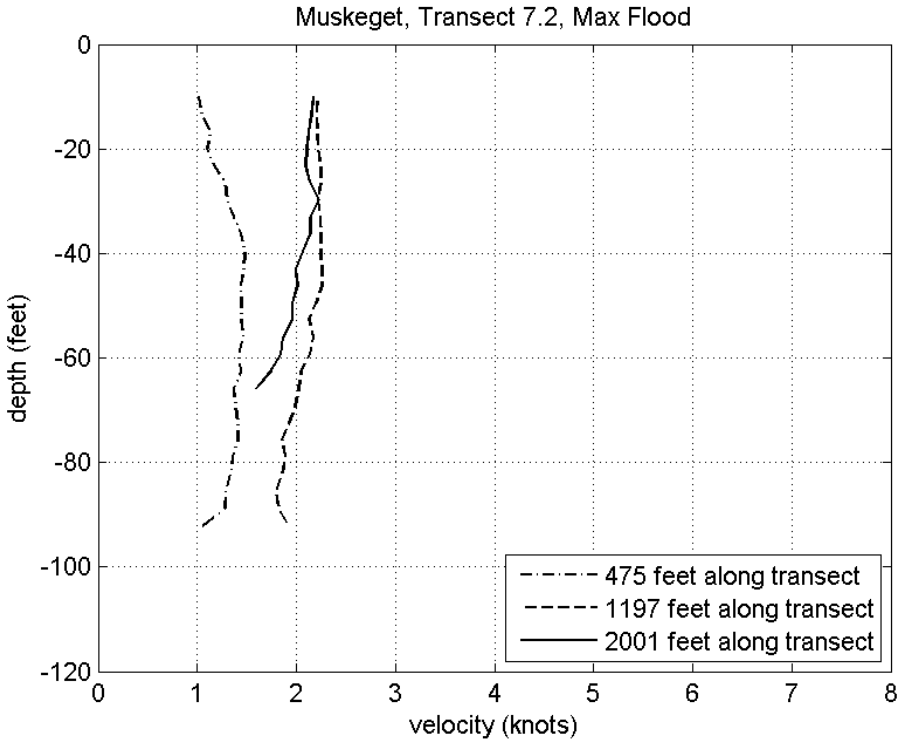
Muskeget, Transect 7.2, Max Flood
depth (feet)
velocity (knots)
0
-20
-40
-60
-80
-100
-120
0
1
2
3
4
5
6
7
8
475 feet along transect
1197 feet along transect
2001 feet along transect

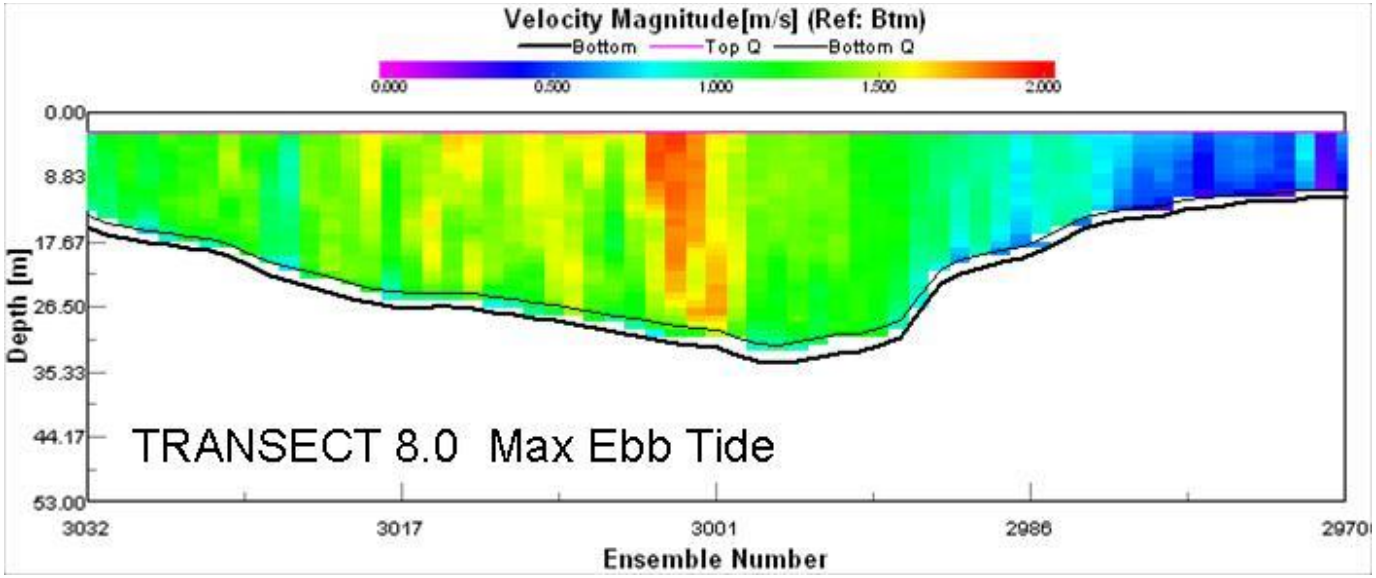
Velocity Magnitude[m/s] (Ref: Btm)
Bottom
Top Q
Bottom Q
0.000
0.500
1.000
1.500
2.000
0.00
8.83
17.67
26.50
35.33
44.17
53.00
Depth [m]
TRANSECT 8.0 Max Ebb Tide
3032
3017
3001
2986
Ensemble Number

Figure --

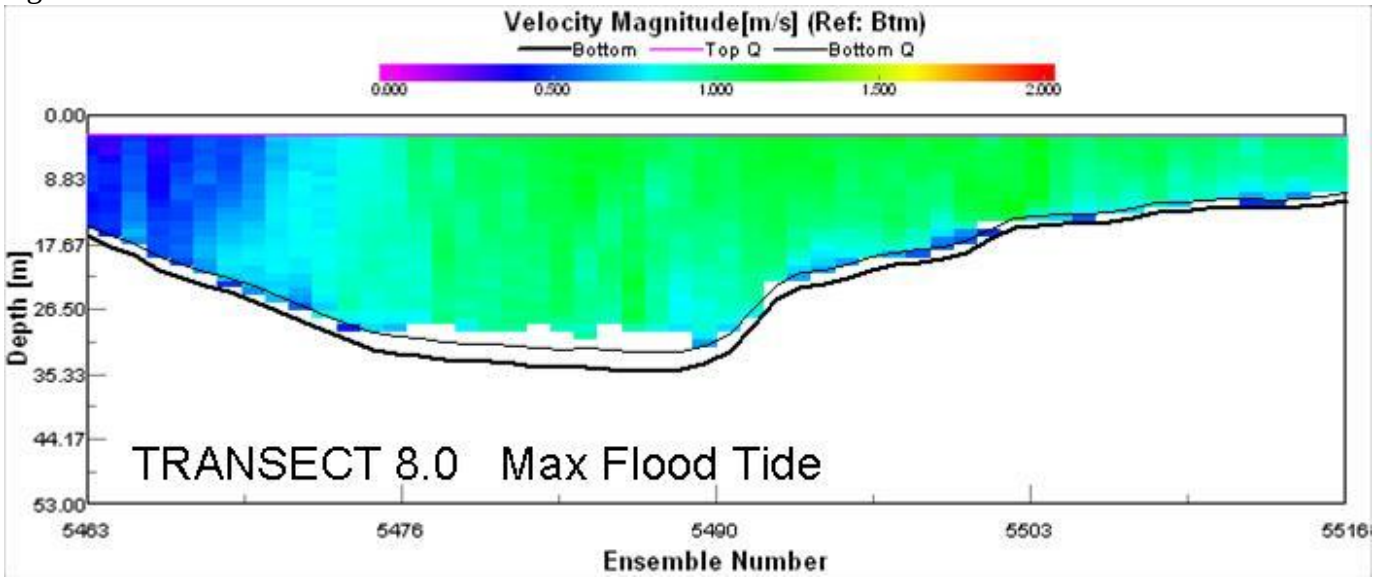
Velocity Magnitude[m/s] (Ref: Btm)
Bottom
Top Q
Bottom Q
0.000
0.500
1.000
1.500
2.000
0.00
8.83
17.67
26.50
35.33
44.17
53.00
Depth [m]
TRANSECT 8.0 Max Flood Tide
5463
5476
5490
5503
Ensemble Number

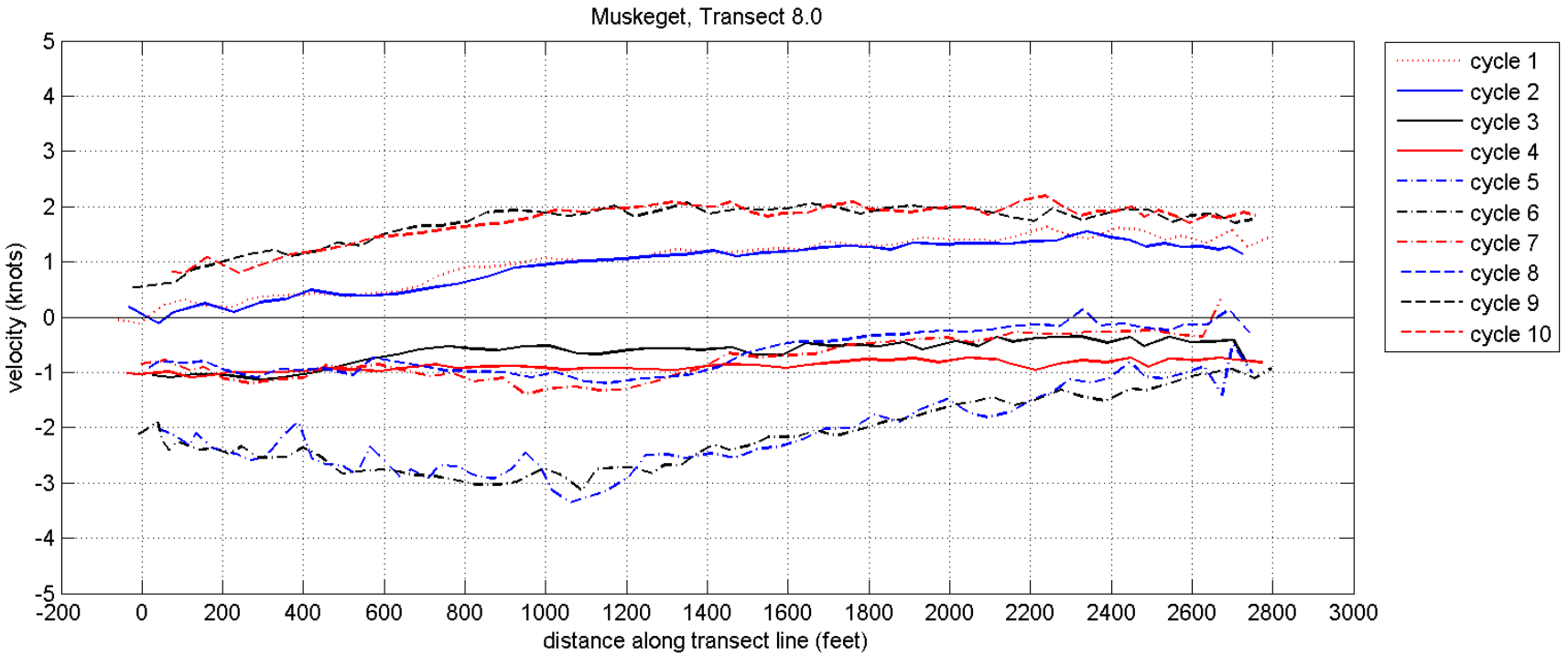
Muskeget, Transect 8.0
velocity (knots)
distance along transect line (feet)
cycle 1
cycle 2
cycle 3
cycle 4
cycle 5
cycle 6
cycle 7
cycle 8
cycle 9
cycle 10

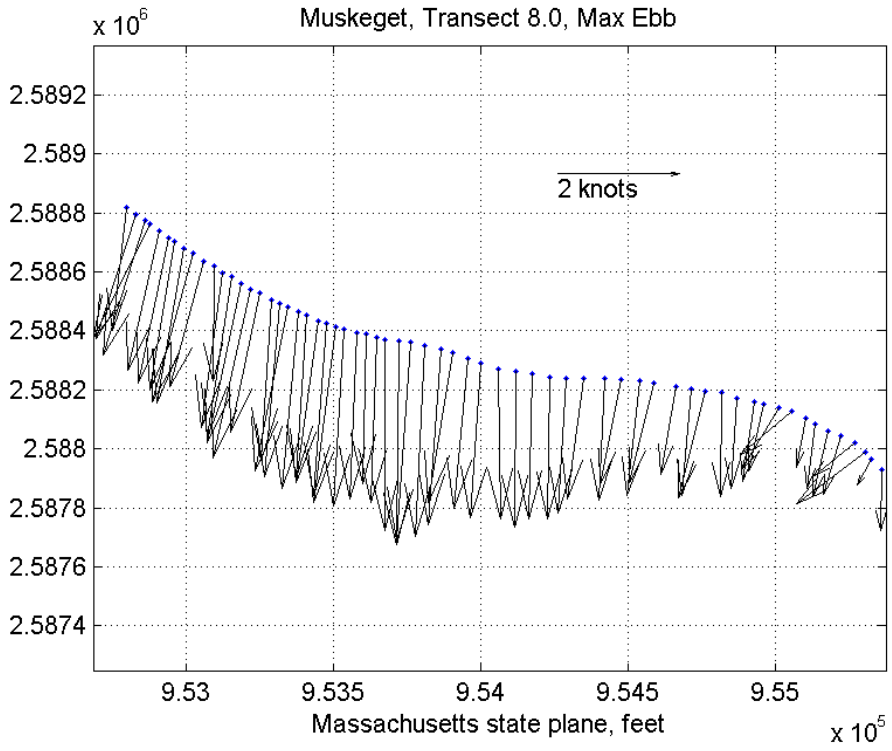
Muskeget, Transect 8.0, Max Ebb
x 10^6
2.5892
2.589
2.5888
2.5886
2.5884
2.5882
2.588
2.5878
2.5876
2.5874
2 knots
9.53
9.535
9.54
9.545
9.55
Massachusetts state plane, feet
x 10^5

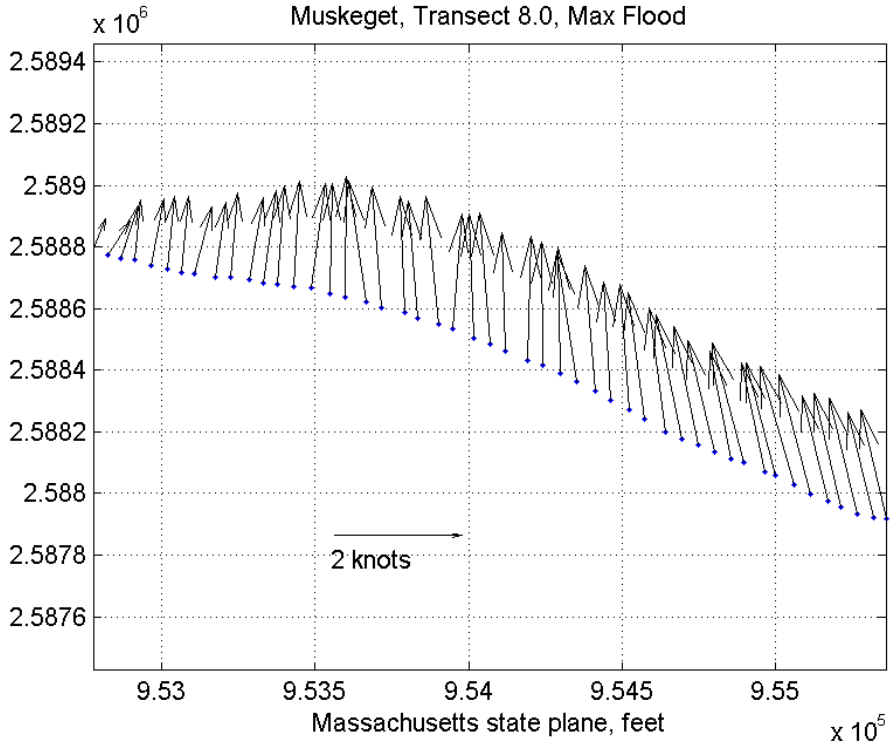
Muskeget, Transect 8.0, Max Flood
x 10^6
2.5894
2.5892
2.589
2.5888
2.5886
2.5884
2.5882
2.588
2.5878
2.5876
2 knots
9.53
9.535
9.54
9.545
9.55
Massachusetts state plane, feet
x 10^5

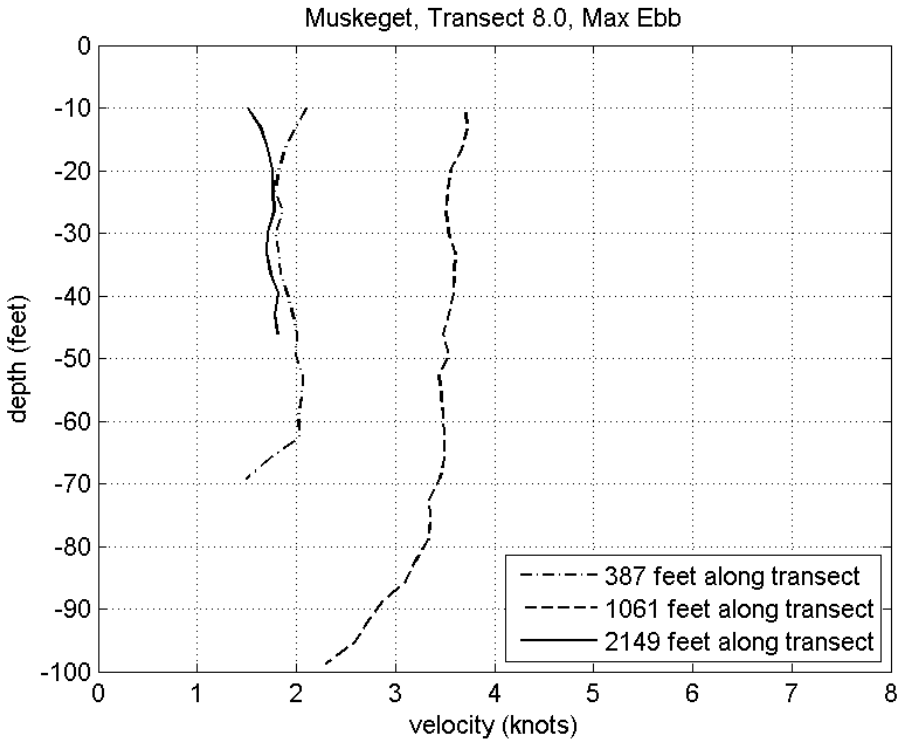
Muskeget, Transect 8.0, Max Ebb
depth (feet)
velocity (knots)
0
-10
-20
-30
-40
-50
-60
-70
-80
-90
-100
0
1
2
3
4
5
6
7
8
387 feet along transect
1061 feet along transect
2149 feet along transect

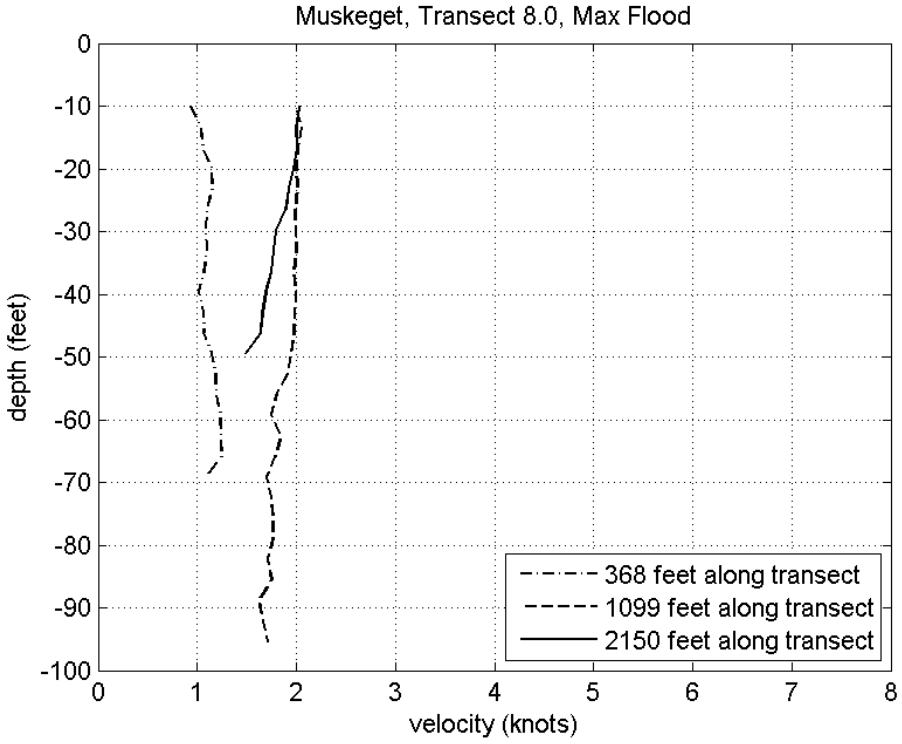
Muskeget, Transect 8.0, Max Flood
depth (feet)
velocity (knots)
0
-10
-20
-30
-40
-50
-60
-70
-80
-90
-100
0
1
2
3
4
5
6
7
8
368 feet along transect
1099 feet along transect
2150 feet along transect

Appendix 2
NOREIZ Grain Size Distribution

NOREIZ Station 1
41° 8.61' W 70° 18.149'
Sediment Grain Size Distribution

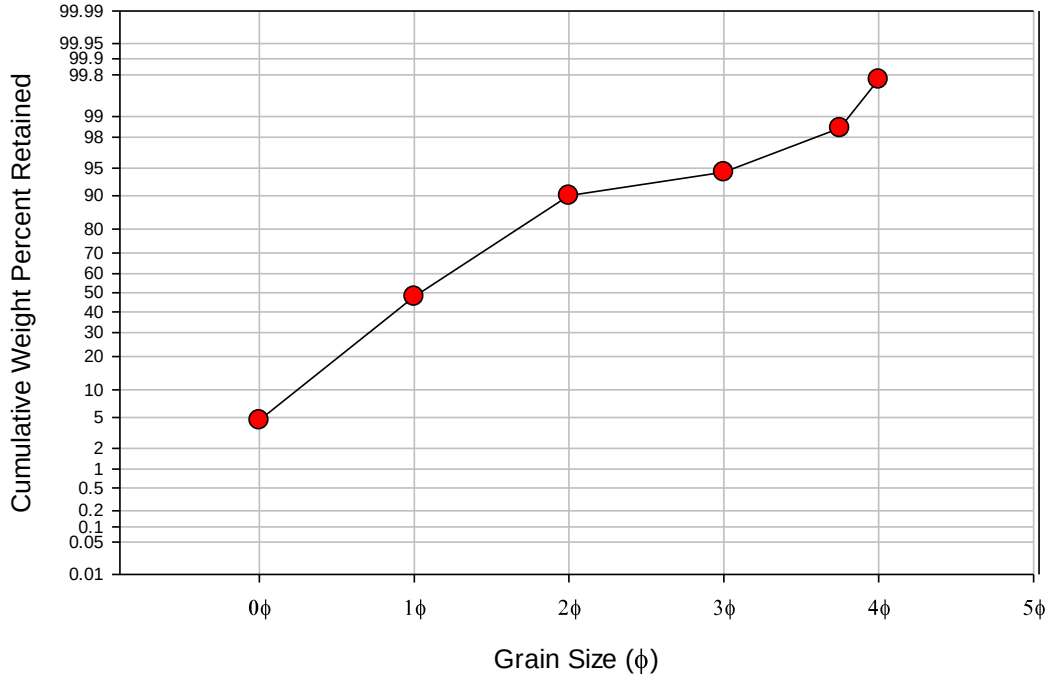

NOREIZ Station 2
N 41° 6.615' W 70° 18.133'
Sediment Grain Size Distribution

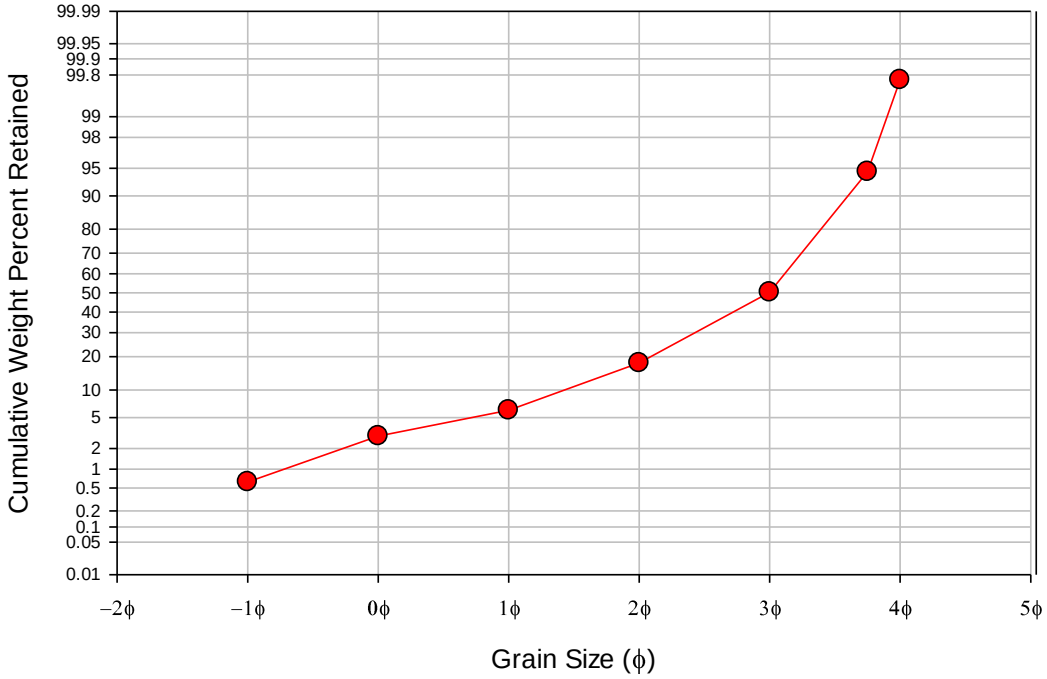

NOREIZ Station 3
N 41° 7.695' W 70° 16.558'
Sediment Grain Size Distribution

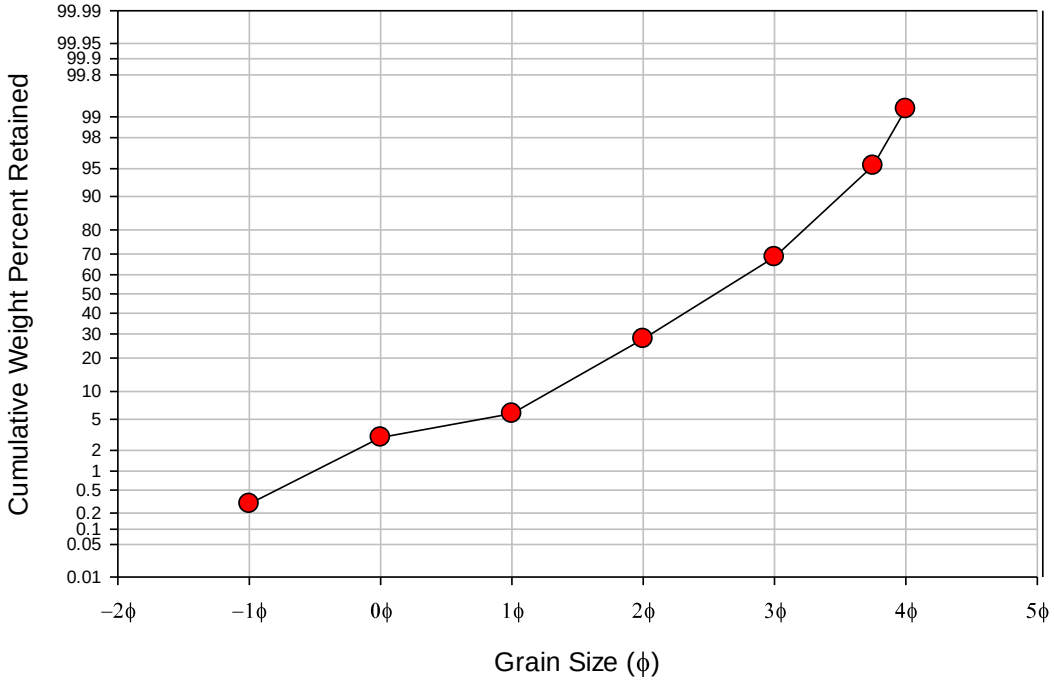

NOREIZ Station 4
N 41° 7.674' W 70° 13.578'
Sediment Grain Size Distribution

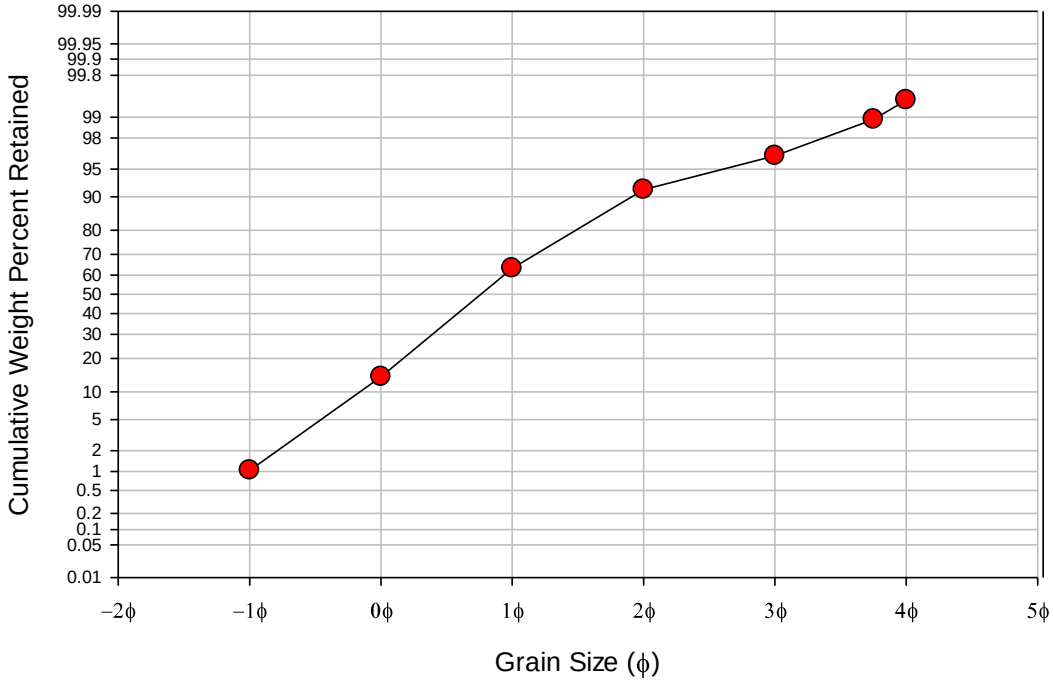

NOREIZ Station 5
N 41° 7.793' W 70° 10.745'
Sediment Grain Size Distribution

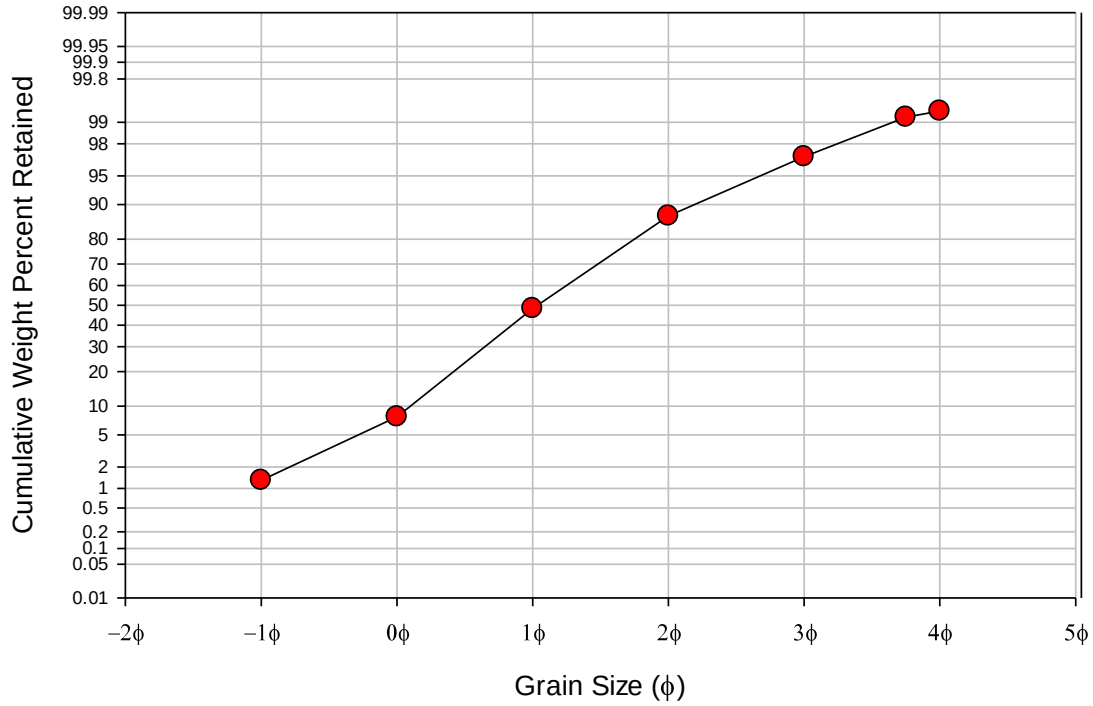

NOREIZ Station 6
N 41° 8.774 W 70° 15.172
Sediment Grain Size Distribution

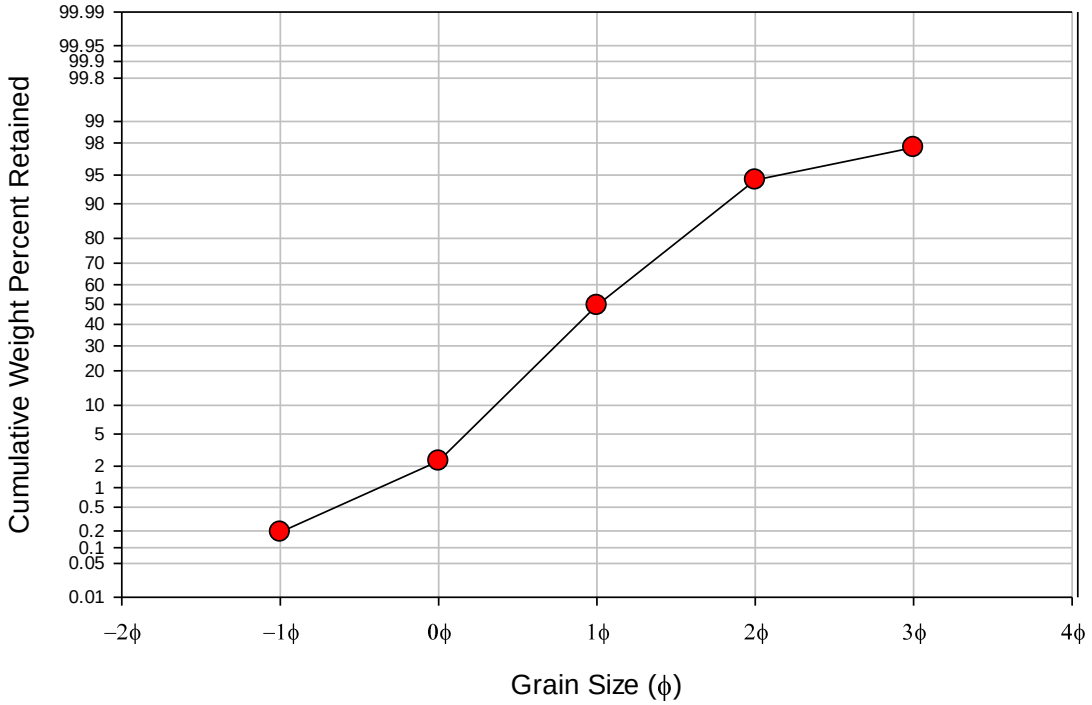

NOREIZ Station 7
N 41° 8.686' W 70° 11.547'
Sediment Grain Size Distribution

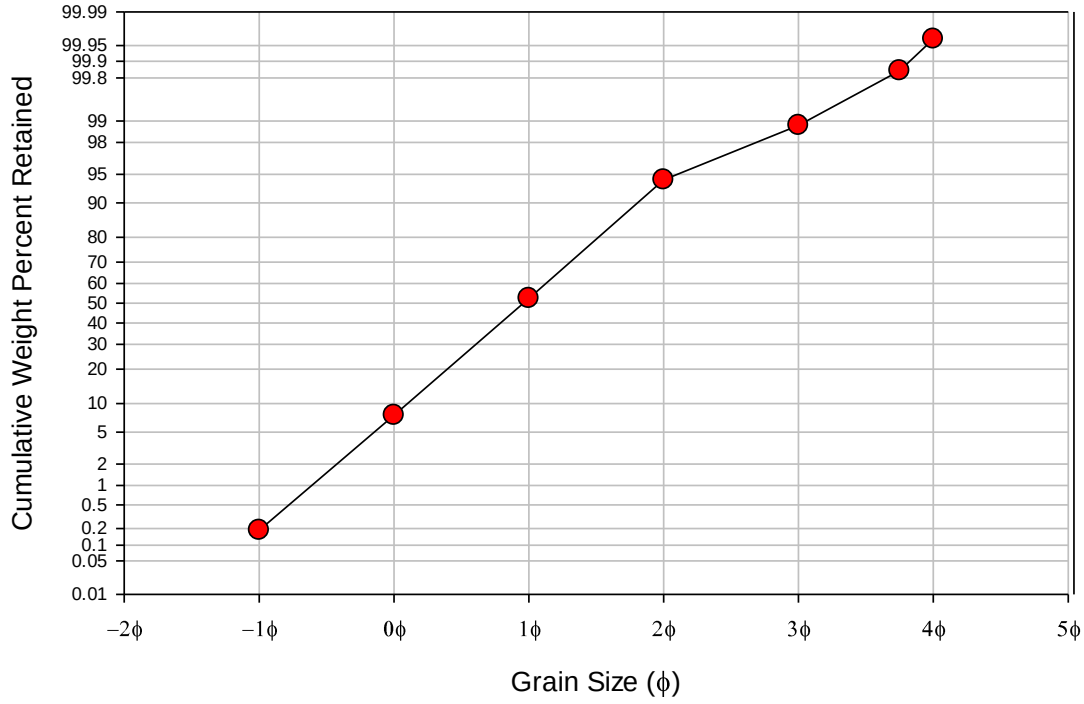

NOREIZ Station 8
N 41° 8.694' W 70° 8.997'
Sediment Grain Size Distribution

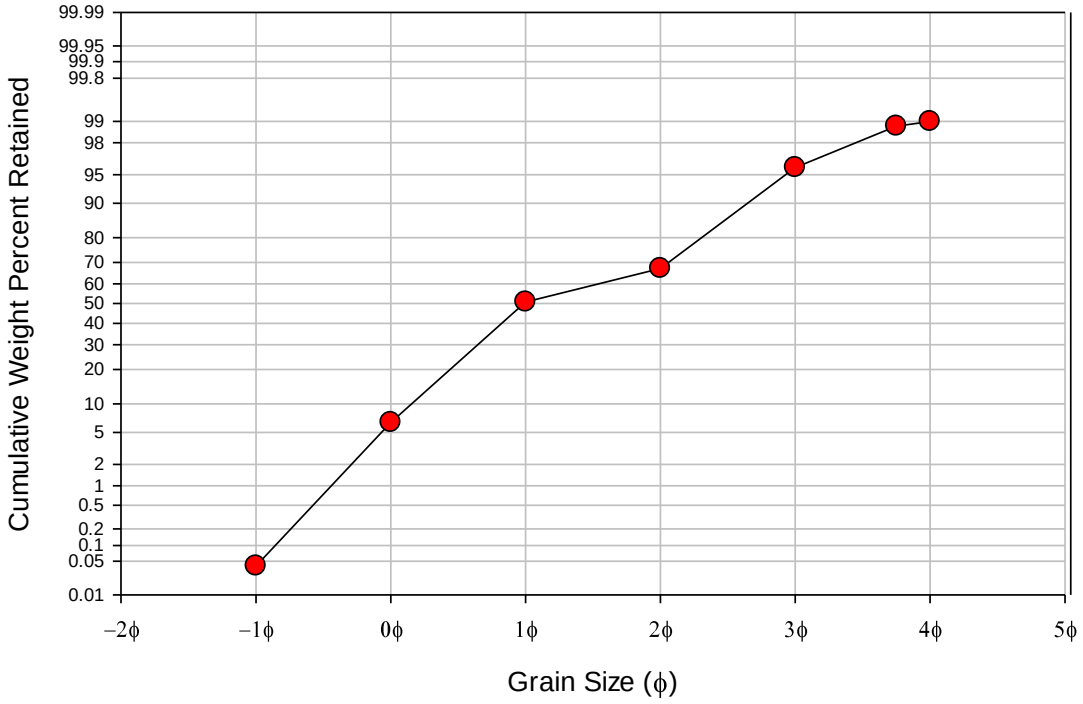

NOREIZ Station 9
N 41° 6.659' W 70° 8.866'
Sediment Grain Size Distribution

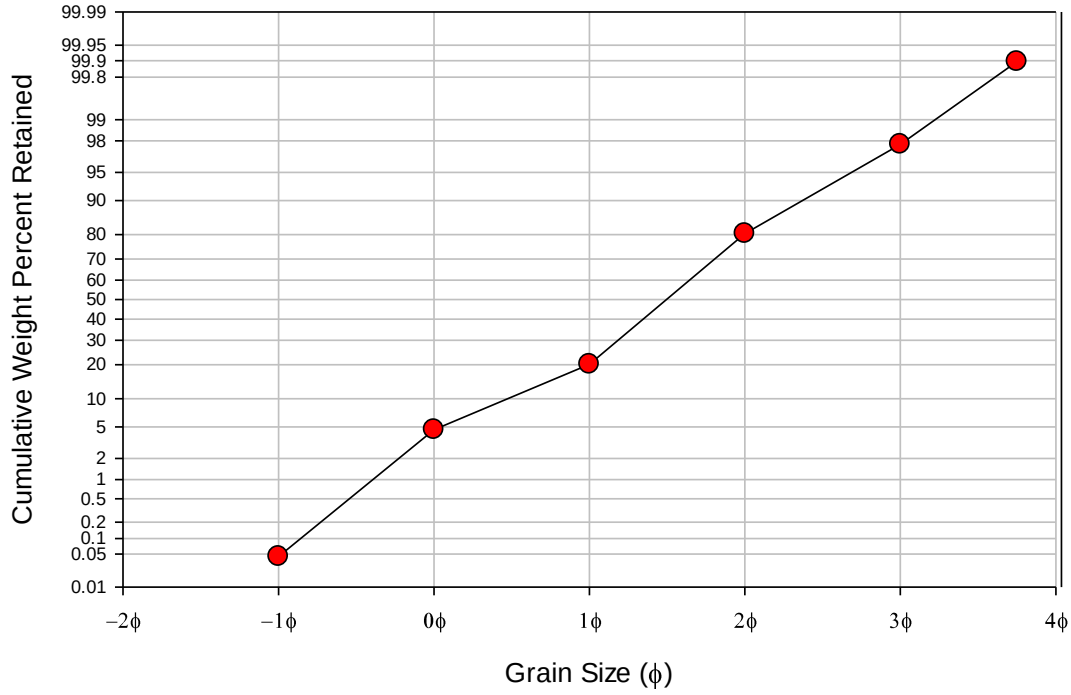

NOREIZ Station 10
N 41° 6.534' W 70° 12.295'
Sediment Grain Size Distribution

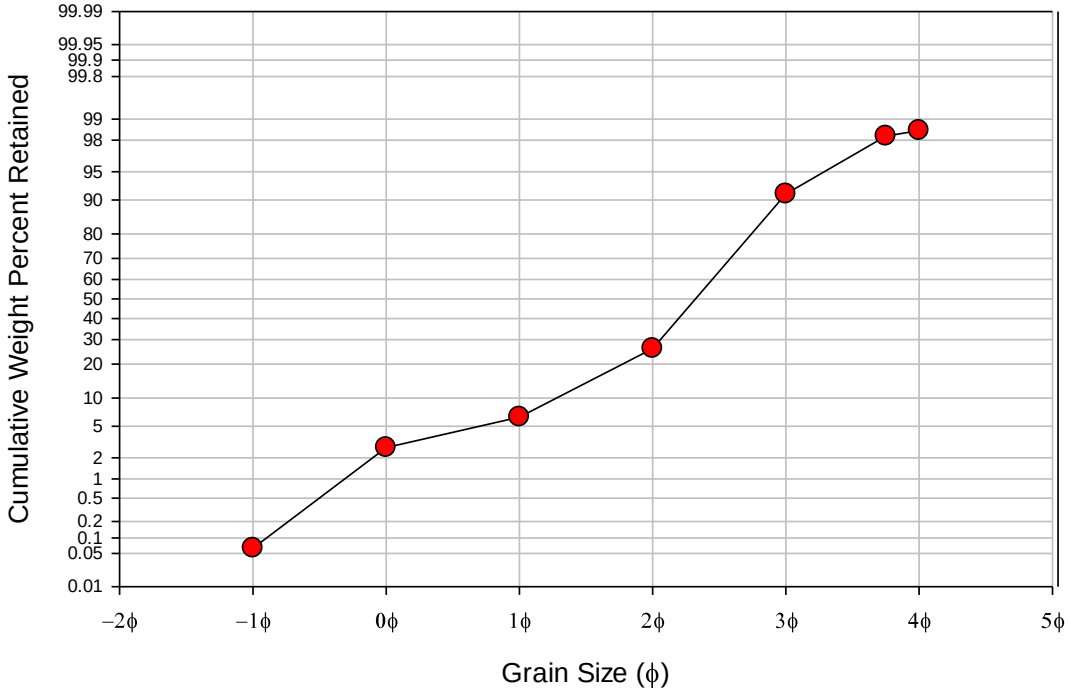

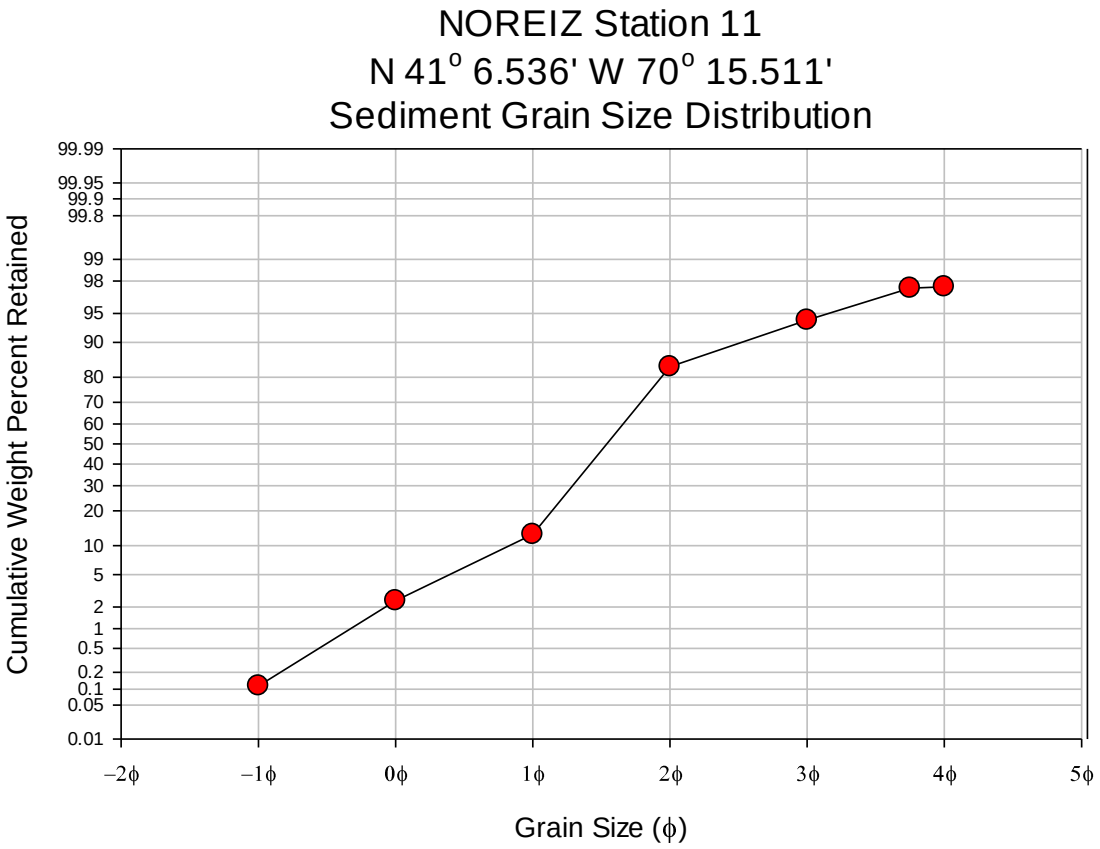
NOREIZ Station 11
N 41° 6.536' W 70° 15.511'
Sediment Grain Size Distribution
Cumulative Weight Percent Retained
99.99
99.95
99.9
99.8
99
98
95
90
80
70
60
50
40
30
20
10
5
2
1
0.5
0.2
0.1
0.05
0.01
−2ϕ
−1ϕ
0ϕ
1ϕ
2ϕ
3ϕ
4ϕ
5ϕ
Grain Size (ϕ)

Appendix 3`
Grain Size Analysis on Cable Transect

Pocha Cable Transect 100 m
N 41° 22.398' W 70° 26.791'
Sediment Grain Size Distribution

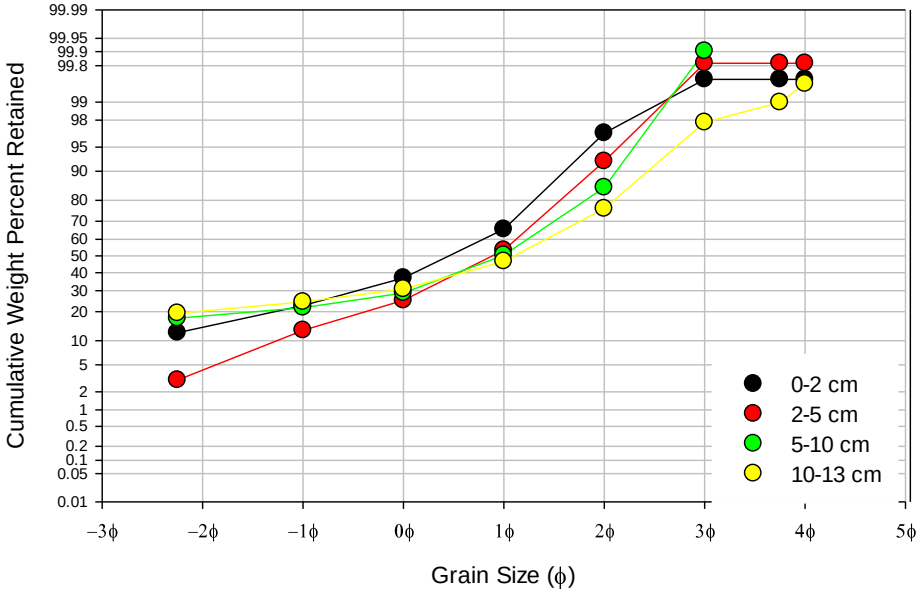

Pocha Cable Transect 150 m

Sediment Grain Size Distribution

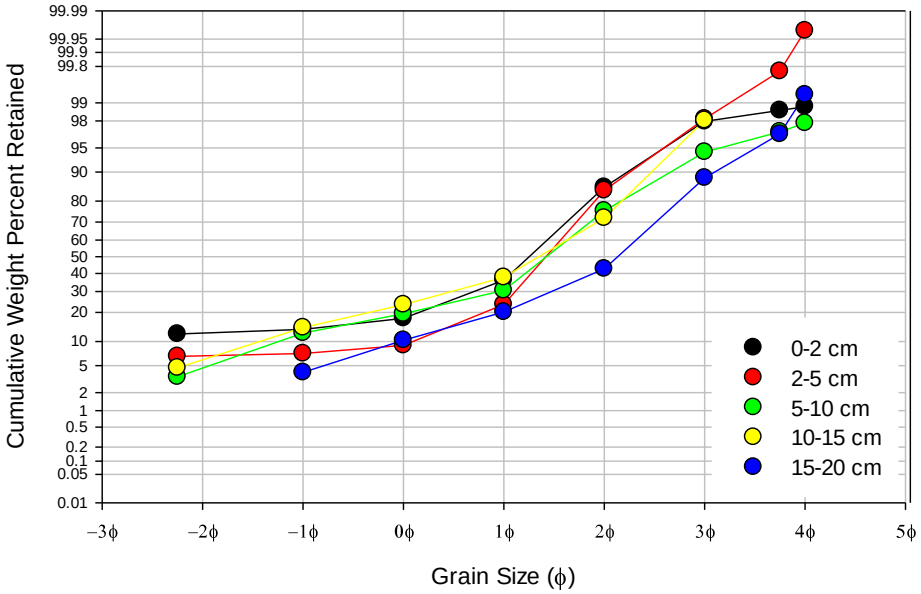

Pocha Cable Transect 200 m
N 41° 22.398' W 70° 26.721'
Sediment Grain Size Distribution

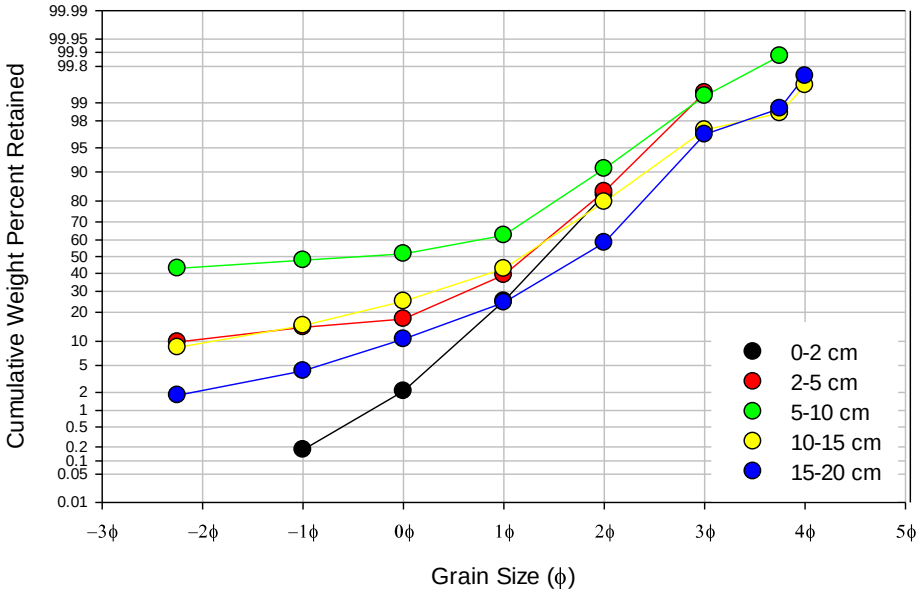

Pocha Cable Transect 250 m

Sediment Grain Size Distribution

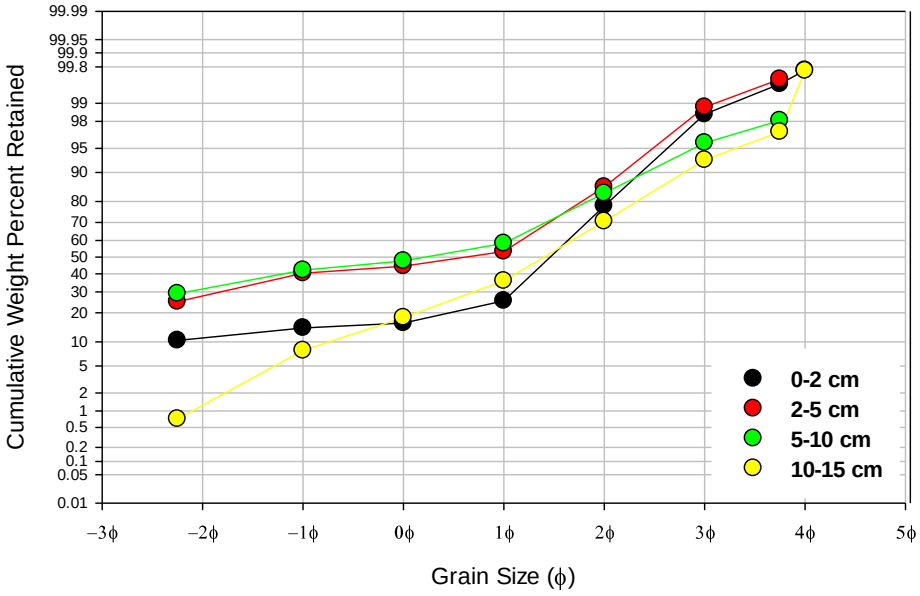

Pocha Cable Transect 300 m
N 41° 22.387' W 70° 26.647'
Sediment Grain Size Distribution

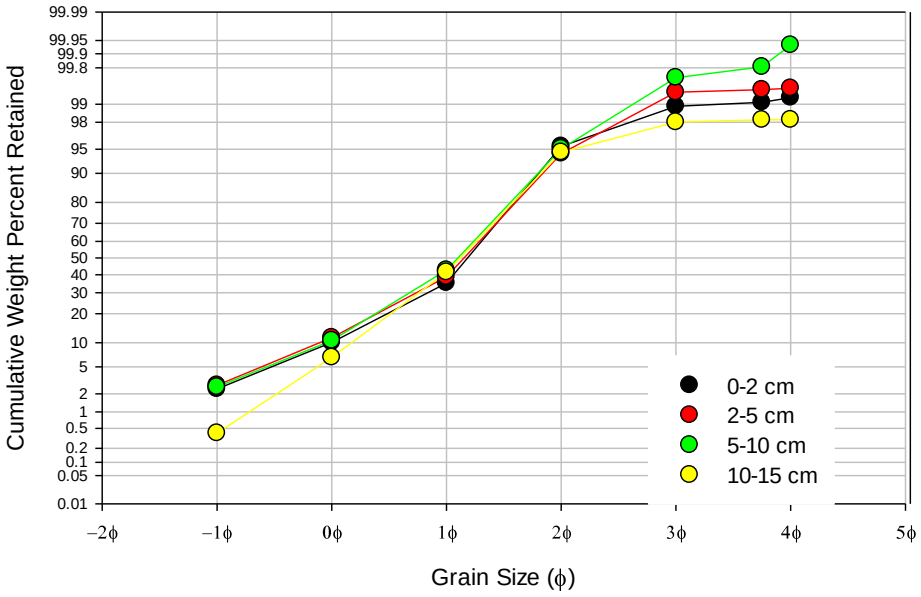

Pocha Cable Transect 350 m

Sediment Grain Size Distribution

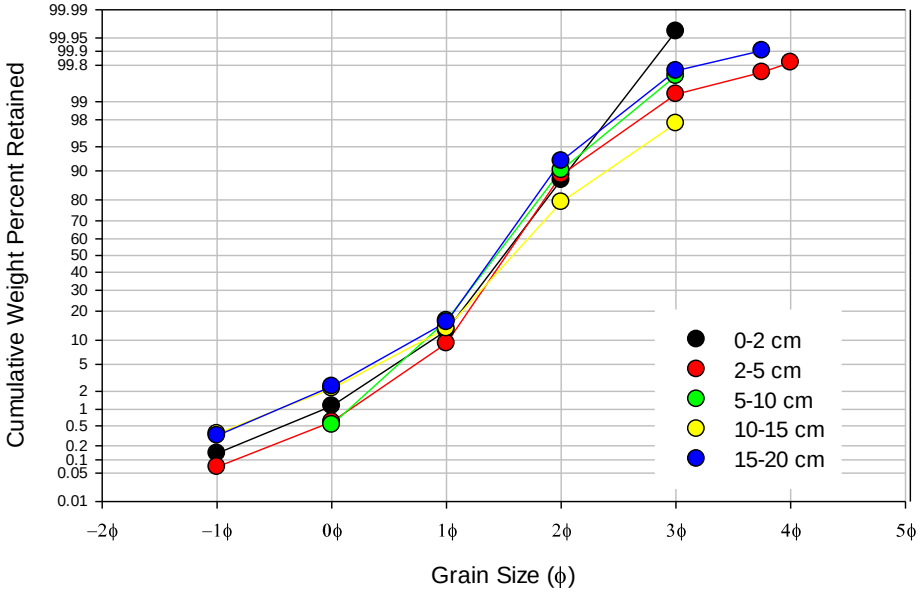

Pocha Cable Transect 400 m
N 41° 22.375' W 70° 26.597'
Sediment Grain Size Distribution

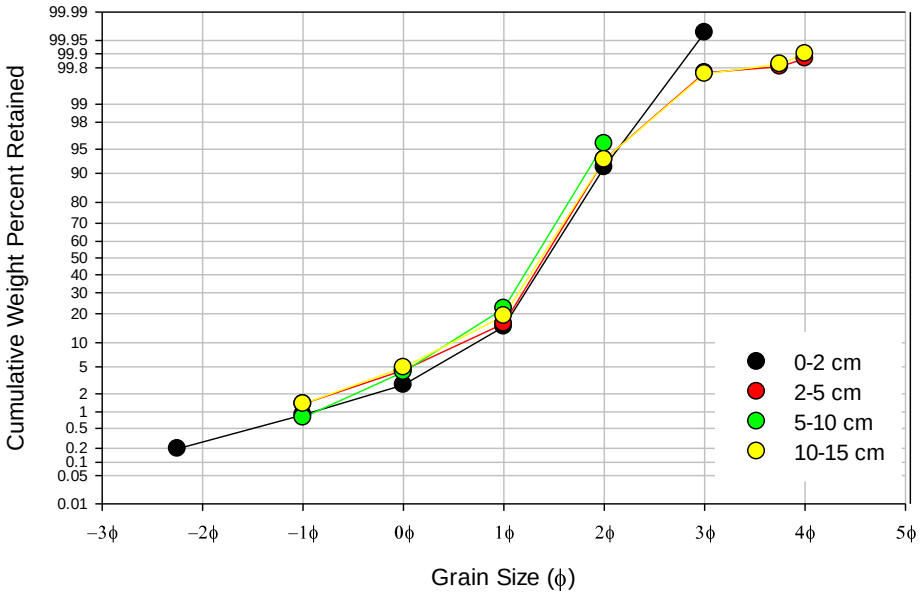

Pocha Cable Transect 450 m

Sediment Grain Size Distribution

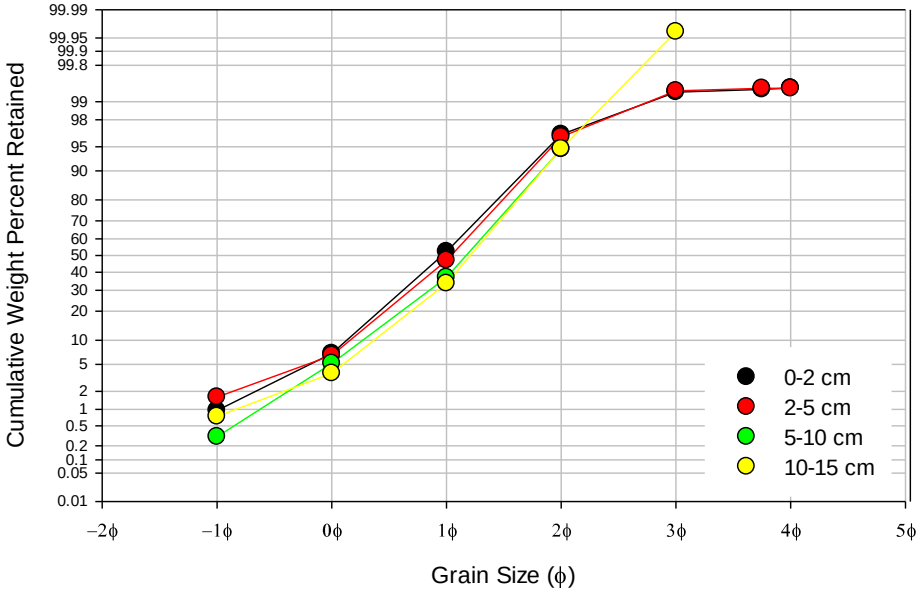

Pocha Cable Transect 500 m
N 41° 22.377' W 70° 26.511'
Sediment Grain Size Distribution

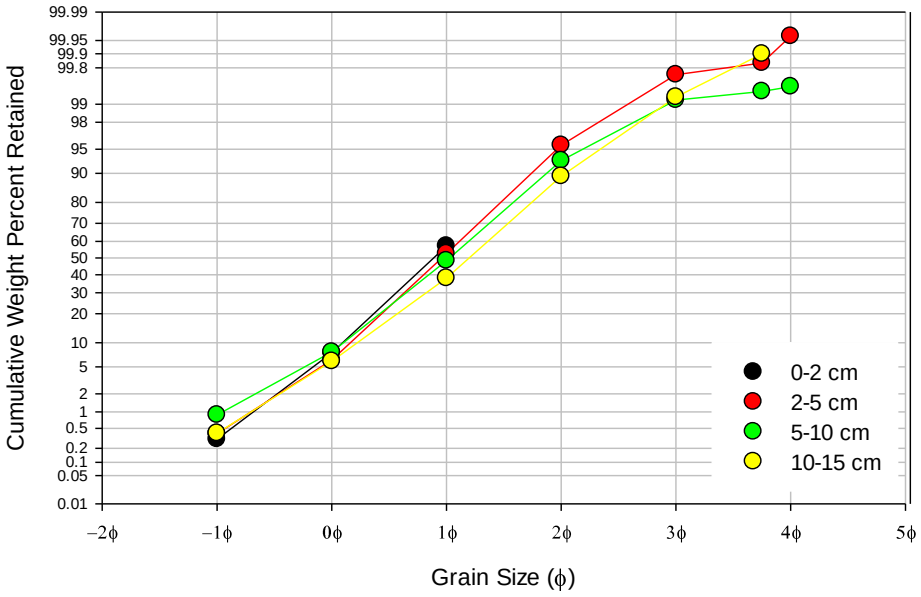

Pocha Cable Transect 550 m

Sediment Grain Size Distribution

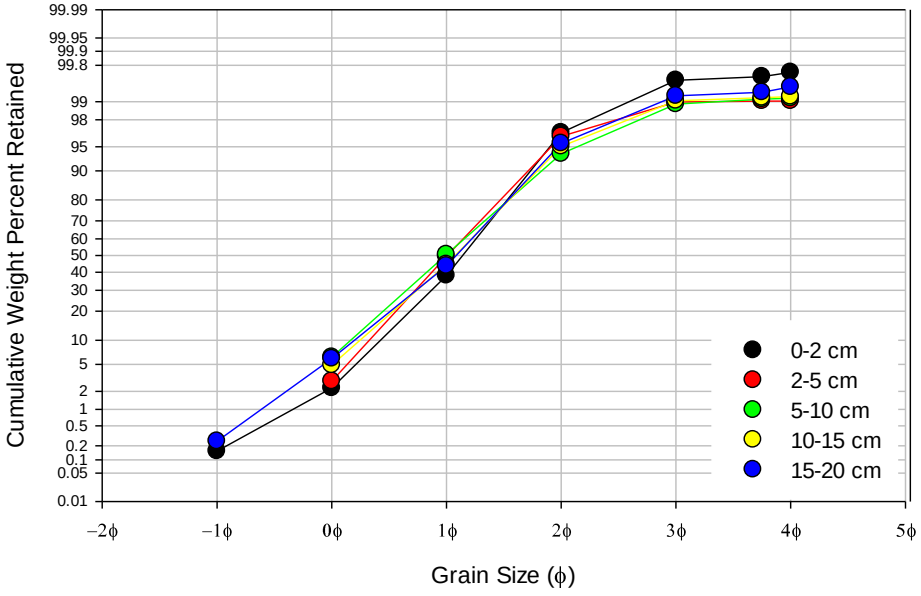

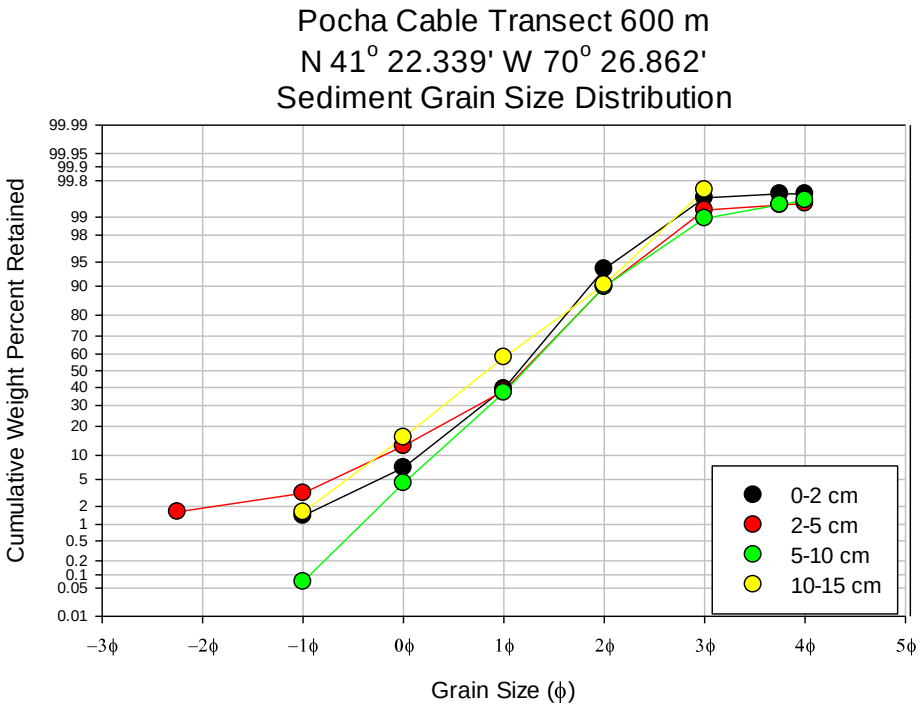
Pocha Cable Transect 600 m
N 41° 22.339' W 70° 26.862'
Sediment Grain Size Distribution
Cumulative Weight Percent Retained
99.99
99.95
99.9
99.8
99
98
95
90
80
70
60
50
40
30
20
10
5
2
1
0.5
0.2
0.1
0.05
0.01
−3ϕ
−2ϕ
−1ϕ
0ϕ
1ϕ
2ϕ
3ϕ
4ϕ
5ϕ
Grain Size (ϕ)
0-2 cm
2-5 cm
5-10 cm
10-15 cm

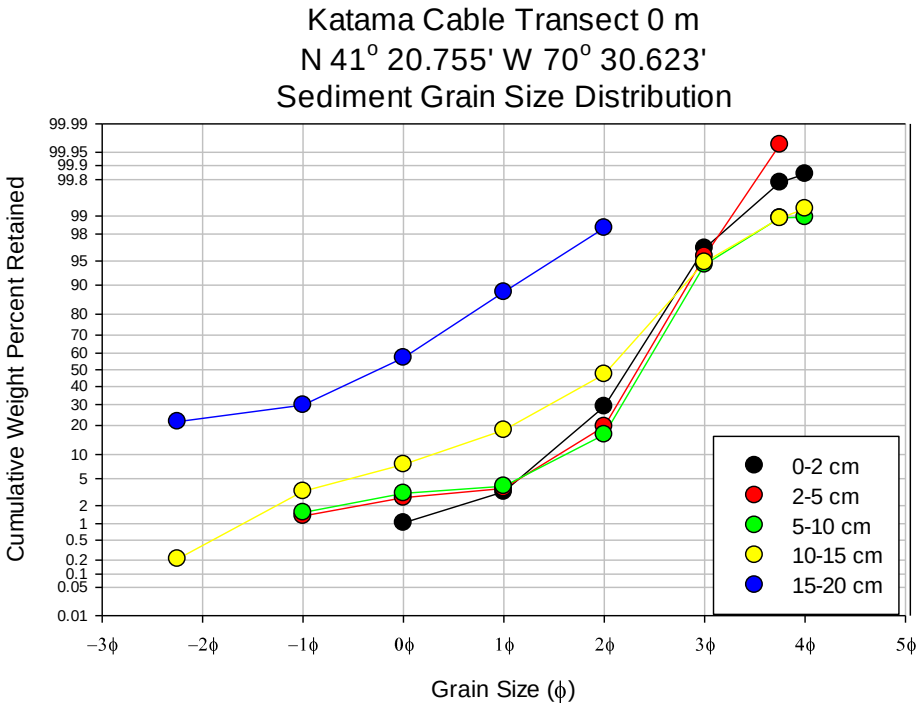
Katama Cable Transect 0 m
N 41° 20.755' W 70° 30.623'
Sediment Grain Size Distribution
Cumulative Weight Percent Retained
99.99
99.95
99.9
99.8
99
98
95
90
80
70
60
50
40
30
20
10
5
2
1
0.5
0.2
0.1
0.05
0.01
−3ϕ
−2ϕ
−1ϕ
0ϕ
1ϕ
2ϕ
3ϕ
4ϕ
5ϕ
Grain Size (ϕ)
0-2 cm
2-5 cm
5-10 cm
10-15 cm
15-20 cm

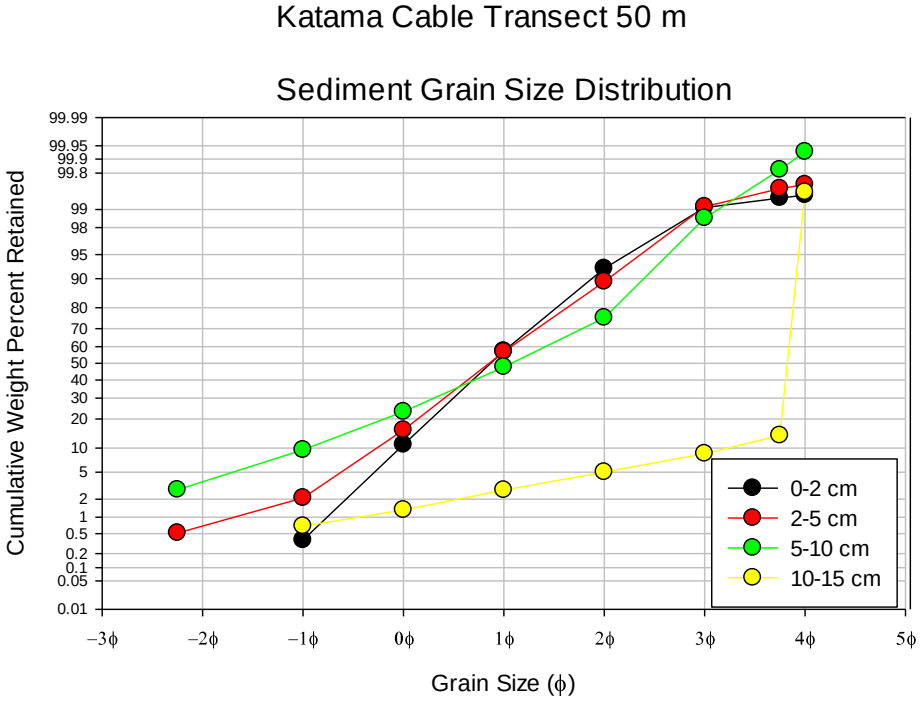
Katama Cable Transect 50 m
Sediment Grain Size Distribution
Cumulative Weight Percent Retained
99.99
99.95
99.9
99.8
99
98
95
90
80
70
60
50
40
30
20
10
5
2
1
0.5
0.2
0.1
0.05
0.01
−3ϕ
−2ϕ
−1ϕ
0ϕ
1ϕ
2ϕ
3ϕ
4ϕ
5ϕ
Grain Size (ϕ)
0-2 cm
2-5 cm
5-10 cm
10-15 cm

Katama Cable Transect 100 m
N 41° 20.705' W 70° 30.601'
Sediment Grain Size Distribution

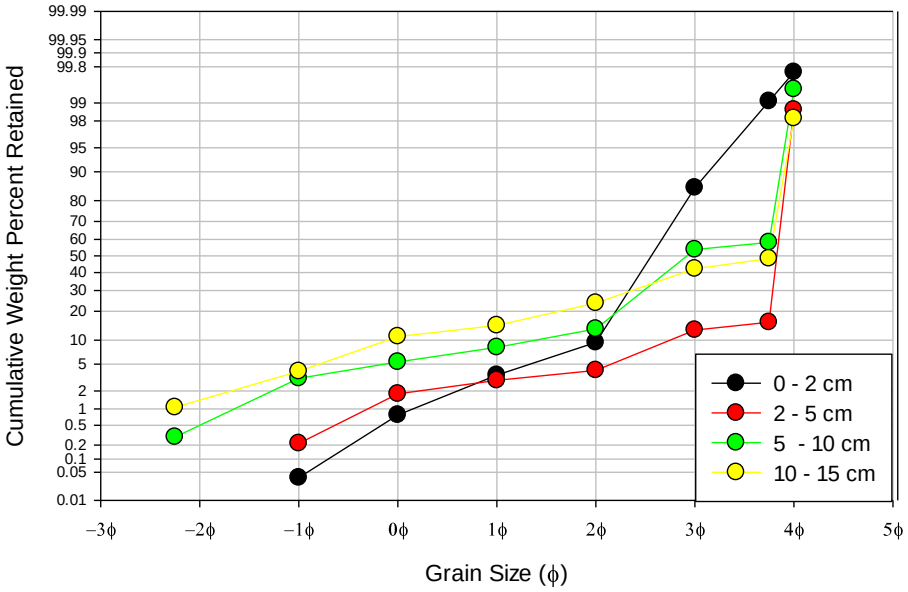

Katama Cable Transect 150 m

Sediment Grain Size Distribution

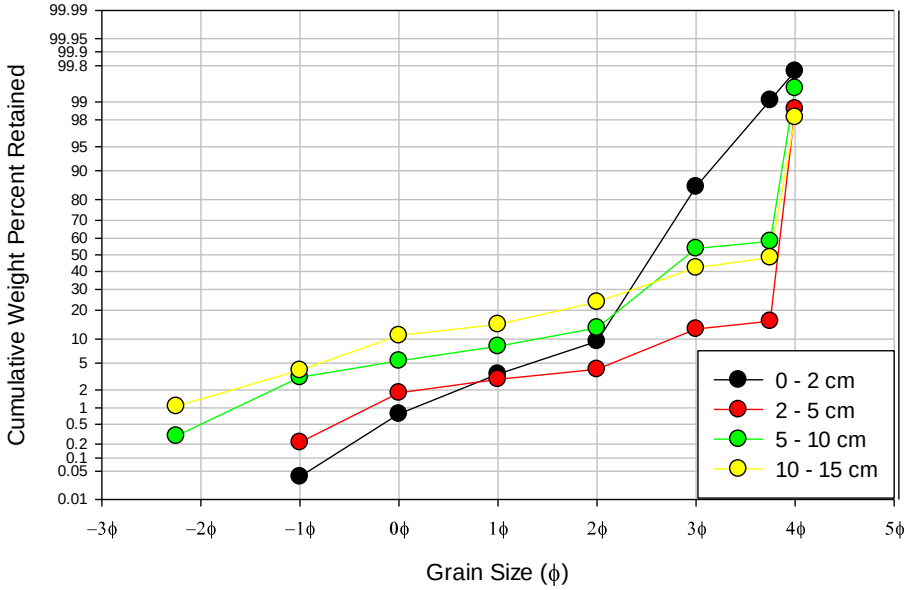

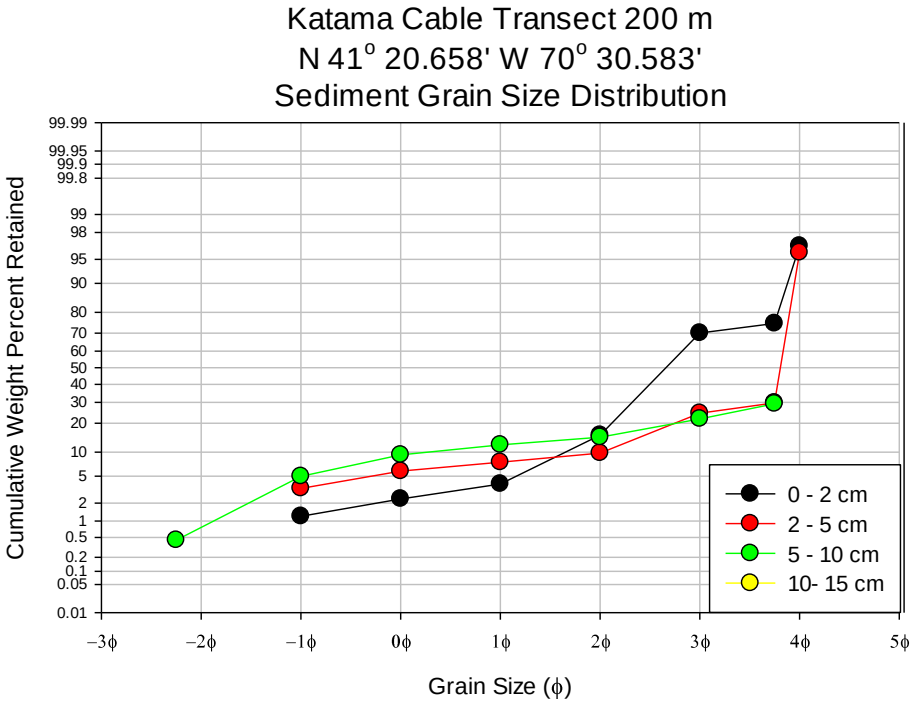
Katama Cable Transect 200 m
N 41° 20.658' W 70° 30.583'
Sediment Grain Size Distribution
Cumulative Weight Percent Retained
99.99
99.95
99.9
99.8
99
98
95
90
80
70
60
50
40
30
20
10
5
2
1
0.5
0.2
0.1
0.05
0.01
−3ϕ
−2ϕ
−1ϕ
0ϕ
1ϕ
2ϕ
3ϕ
4ϕ
5ϕ
Grain Size (ϕ)
0 - 2 cm
2 - 5 cm
5 - 10 cm
10- 15 cm

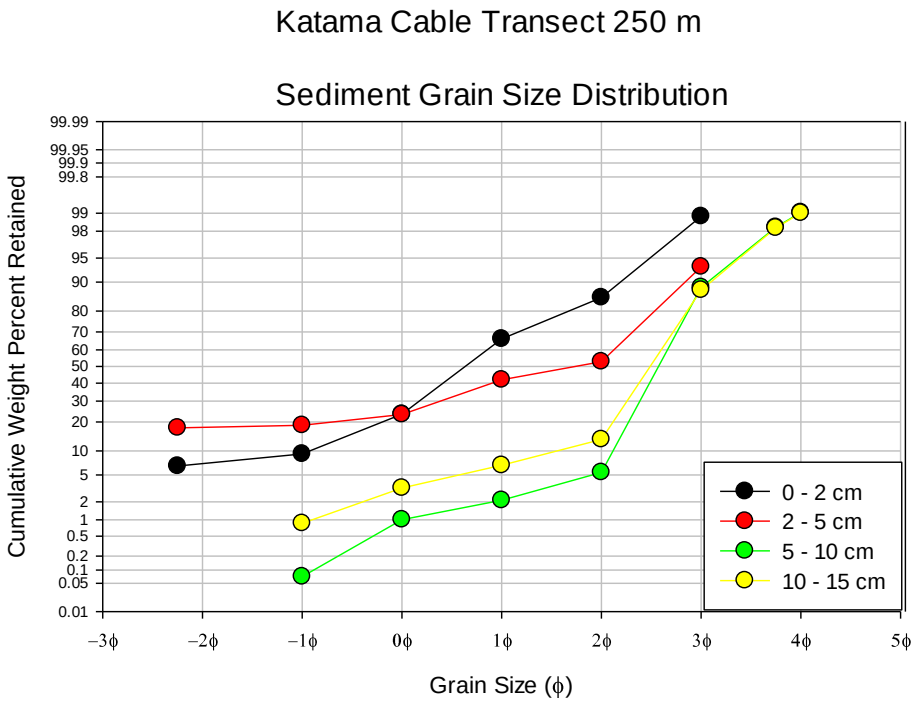
Katama Cable Transect 250 m
Sediment Grain Size Distribution
Cumulative Weight Percent Retained
99.99
99.95
99.9
99.8
99
98
95
90
80
70
60
50
40
30
20
10
5
2
1
0.5
0.2
0.1
0.05
0.01
−3ϕ
−2ϕ
−1ϕ
0ϕ
1ϕ
2ϕ
3ϕ
4ϕ
5ϕ
Grain Size (ϕ)
0 - 2 cm
2 - 5 cm
5 - 10 cm
10 - 15 cm

Katama Cable Transect 300 m
N 41° 20.606' W 70° 30.583'
Sediment Grain Size Distribution

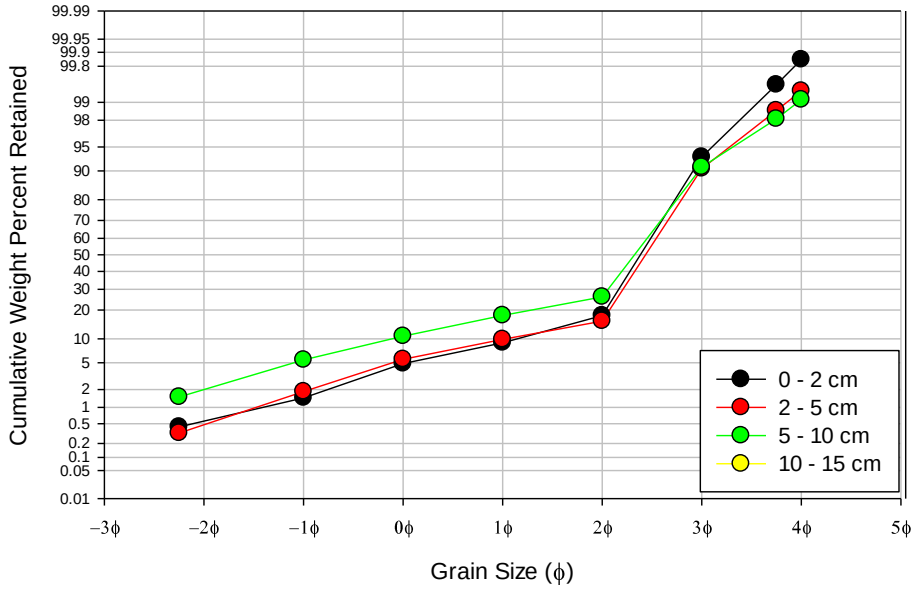

Katama Cable Transect 350 m

Sediment Grain Size Distribution

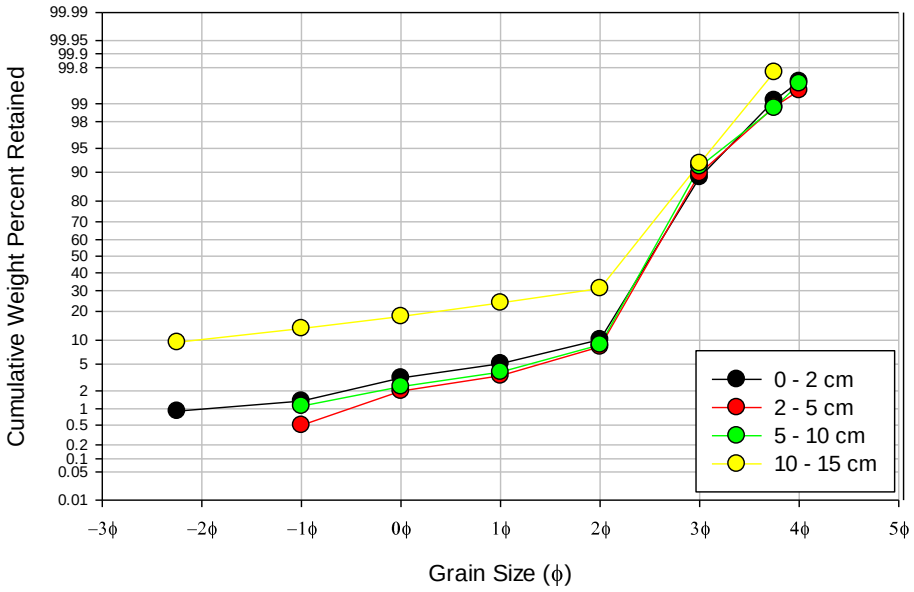

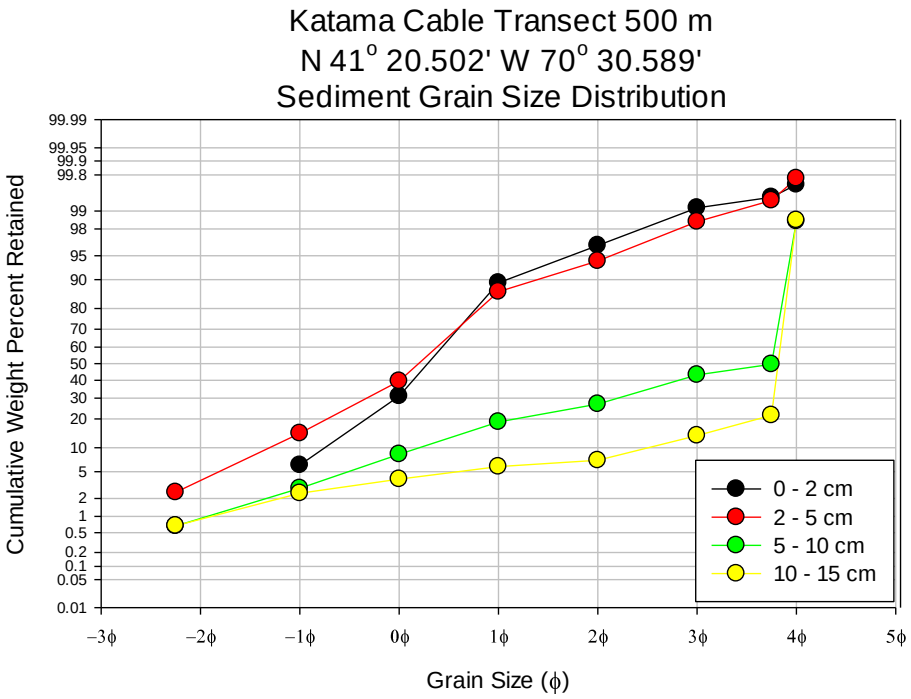
Katama Cable Transect 500 m
N 41° 20.502' W 70° 30.589'
Sediment Grain Size Distribution
Cumulative Weight Percent Retained
99.99
99.95
99.9
99.8
99
98
95
90
80
70
60
50
40
30
20
10
5
2
1
0.5
0.2
0.1
0.05
0.01
−3ϕ
−2ϕ
−1ϕ
0ϕ
1ϕ
2ϕ
3ϕ
4ϕ
5ϕ
Grain Size (ϕ)
0 - 2 cm
2 - 5 cm
5 - 10 cm
10 - 15 cm

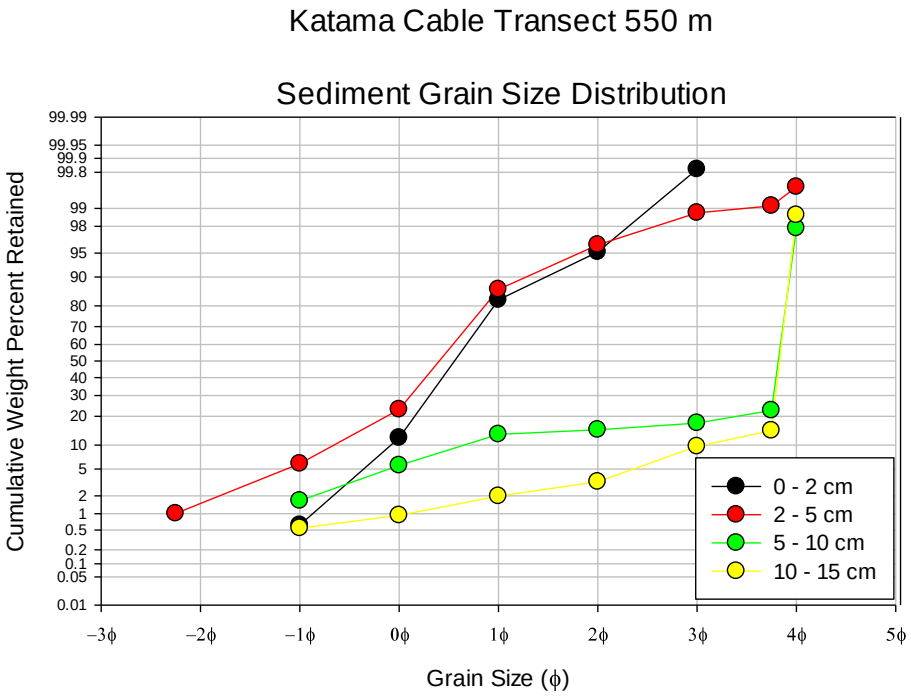
Katama Cable Transect 550 m
Sediment Grain Size Distribution
Cumulative Weight Percent Retained
99.99
99.95
99.9
99.8
99
98
95
90
80
70
60
50
40
30
20
10
5
2
1
0.5
0.2
0.1
0.05
0.01
−3ϕ
−2ϕ
−1ϕ
0ϕ
1ϕ
2ϕ
3ϕ
4ϕ
5ϕ
Grain Size (ϕ)
0 - 2 cm
2 - 5 cm
5 - 10 cm
10 - 15 cm

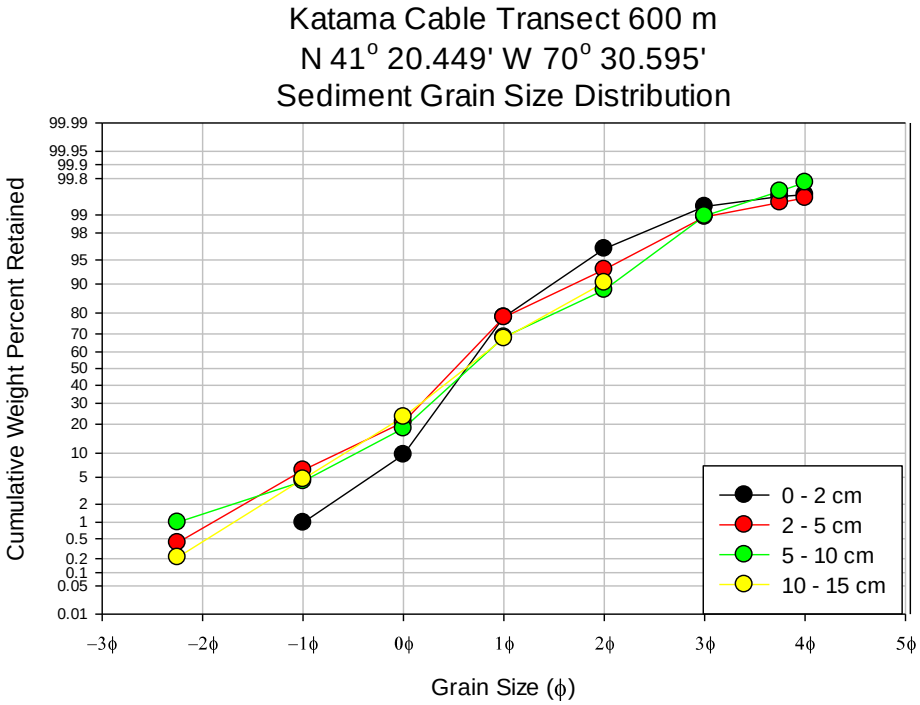
Katama Cable Transect 600 m
N 41° 20.449' W 70° 30.595'
Sediment Grain Size Distribution
Cumulative Weight Percent Retained
99.99
99.95
99.9
99.8
99
98
95
90
80
70
60
50
40
30
20
10
5
2
1
0.5
0.2
0.1
0.05
0.01
−3ϕ
−2ϕ
−1ϕ
0ϕ
1ϕ
2ϕ
3ϕ
4ϕ
5ϕ
Grain Size (ϕ)
0 - 2 cm
2 - 5 cm
5 - 10 cm
10 - 15 cm

MUSKEGET CHANNEL TIDAL ENERGY TEST FACILITY

Final Report

Principal Investigators:

M. Robinson Swift, Kenneth Baldwin, Martin Wosnik and Barbaros Celikkol

Graduate Student:

Tobias Dewhurst

Prepared for:

The New England Marine Renewable Energy Center
University of Massachusetts at Dartmouth

By:

The Center for Ocean Renewable Energy
University of New Hampshire
Durham, NH 03824

May 24, 2013

CONTENTS

ACKNOWLEDGMENTS

The authors would like to thank John Miller for his leadership and commitment to developing Muskeget Channel as a tidal energy test site.

The generous assistance and helpful discussions provided by Stephen Barrett are also gratefully acknowledged. His familiarity with studies, applications and planned developments pertaining to Muskeget was a source of critical information during this investigation.

This project was funded by MREC, University of Massachusetts at Dartmouth.

LIST OF FIGURES

LIST OF TABLES

EXECUTIVE SUMMARY

Conceptual designs were investigated for a tidal hydrokinetic device test facility at Muskeget Channel, MA. Muskeget Channel runs north-south between Martha's Vineyard and Nantucket Island. Peak tidal currents of approximately 2.5 m/s (5 knots) combined with depths on the order of 30 m (100 ft.) make the site ideal for testing large hydrokinetic systems.

Six platform concepts were investigated for devices of various sizes. A fixed, bottom gravity foundation would be below surface wave activity and marine traffic, thereby favoring long-term deployment, but there would be challenges in mounting and recovering turbines from the subsurface platform. A telescoping, bottom gravity foundation would allow surface mounting and retrieval of devices at the expense of mechanical complexity. A fixed, four-pile supported mid-water platform would have advantages and disadvantages similar to the gravity foundation. A two-pile surface-piercing structure that could raise and lower a device would be accessible and maintain a permanent surface presence. All permanent hard-structure systems were found to have considerable construction and installation costs and be subject to sedimentation or scour processes. A submerged buoyant platform held against the current by a flexible mooring system could also be arranged to surface for turbine attachment and retrieval. A floating platform would use a decked, twin-hulled configuration. The platform could be anchored in place during actual testing and brought in to a shore base between on-site test programs. A natural berth option was also considered. The instrumented natural berth concept would allow developers to evaluate complete systems incorporating the mounting structure and generator, as well as the tidal turbine itself. The current environment would be measured by bottom secured ADCPs, and the power output to a grid tie-in on Martha's Vineyard would be monitored.

Designs for each concept were developed for structural soundness, dynamic response, vibration, scour, corrosion, bio-fouling, electrical connection, monitoring, operating limits, ease of turbine installation and access, and cost. The floating platform and two-pile platform were found to be the most practical. A floating platform would require less installation work and would be easier to remove at the end of its service life, but would need to be towed to port for extreme weather. A two-pile, surface-piercing platform would constitute a more significant infrastructure investment.

CHAPTER 1

INTRODUCTION

Background and Previous Work

The need for tidal energy test facilities has increased significantly in the past decade. The desire to extract power from the tides while having minimal environmental impact has led many developers to pursue hydrokinetic turbines. These devices operate in high currents at low pressure head, much like wind turbines operate in air. Thus, they allow for energy generation without the need for dams or other high-impact infrastructure.

The majority of hydrokinetic technologies are still under development, and new concepts are continually emerging (Musial, 2008). These technologies must be tested as they are developed, but deploying devices in the ocean is expensive and extremely time consuming (Sterne et al., 2008). Therefore, accessible and cost-effective test sites are necessary for the industry to grow. However, very few facilities of this type exist.

The European Marine Energy Centre (EMEC) in Scotland's Orkney Islands is the only facility that has successfully demonstrated itself as a commercial test site for hydrokinetic devices. It has tested numerous devices at its eight tidal test berths—sections of seafloor at depths ranging from 12m (39 ft.) to 50m (164 ft.) with currents up to almost 4 m/s (8 knots) and grid connected power take-off equipment (European Marine Energy Centre Ltd., 2012). It has also begun testing devices at its scaled sites—locations with large anchoring systems provided in maximum currents of 2 m/s (4 knots) in depths of 21 m (69 ft.) to 25 m (82 ft.), which are not connected to the electrical grid. EMEC's approach to testing has been quite successful but is very expensive and is not conducive to technologies in the early stages of development. And, of course, the prospect of testing overseas raises a host of logistical challenges for developers in North America.

The Fundy Ocean Research Center for Energy (FORCE), located in the Bay of Fundy, Nova Scotia, employs a test model similar to that of EMEC. It is developing four grid-connected test beds in depths up to 45 m (148 ft.) with maximum velocities approaching 5 m/s (10 knots) and tested its first device during 2009 and 2010 (Fundy Ocean Research Center for Energy, 2012). Its goal is to provide the "ultimate test" for tidal developers who have already demonstrated their technology at milder sites and are ready to prove their devices in the harsh conditions of the Bay of Fundy.

In the United States, test options are extremely limited. One test site is under development by the Northwest Marine Renewable Energy Center in Snohomish County, WA (Univeristy of Washington, 2011). The proposed site would test devices in depths of 20 m (66 ft.) to 50 m (164 ft.), with currents reaching 2.5 m/s (5 knots) (Polagye, 2010). The University of Florida is also

developing a test location for hydrokinetic devices, although in the Gulf Stream rather than in tidal currents (Mueller et al., 2009). Neither of these sites was operational when this document was written.

The University of New Hampshire (UNH) Center for Ocean Renewable Energy (CORE) has successfully tested multiple hydrokinetic devices in a tidal estuary site, shown in Figure 1, which has currents that reach a maximum of 2.5 m/s (5 knots) in a depth of 8 m (24 ft.) at mean lower low water.

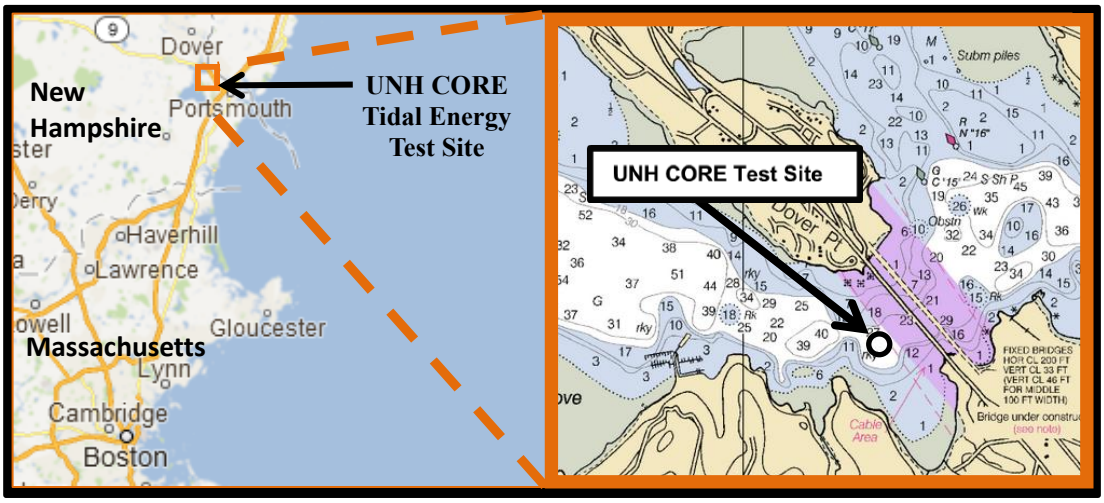

Figure 1. UNH CORE (GSB) Tidal Energy Test Site. Devices are tested at a natural constriction in a protected tidal estuary. Images from Google, NOAA, EarthNC.

To date, three turbines—one 1 m by 1.25 m (3 ft. by 4 ft.) cross-flow axis device, one 1 m by 2.5 m (3 ft. by 8 ft.) cross-flow axis device, and one 0.9 m (3 ft.) diameter in-stream axis device—have been deployed from a moored 10.7 m (35 ft.) floating platform, as described by Dutile et al. (2009), Wosnik et al., (2009) and Rowell (2013). A larger floating platform is under development which will be capable of testing turbines up to the sizes shown in Table 1. Larger turbines cannot be reasonably tested at this site because of the limited depth of the channel.

Table 1. Test capabilities of the UNH CORE Tidal Energy Test Platform Version 2. This platform is under development (Byrne, 2013).

Turbine type	Height		Width	
Ducted in-stream axis	4 m	(13 ft.)	4 m	(13 ft.)
Vertical cross-flow axis	3 m	(10 ft.)	2 m	(7 ft.)
Horizontal cross-flow axis	3 m	(10 ft.)	5 m	(16 ft.)

The need for an accessible test site for tidal energy technologies in the U.S. has led the North East Marine Renewable Energy Center (NE-MREC) to investigate the Muskeget Channel near Edgartown, MA, shown in Figure 2.

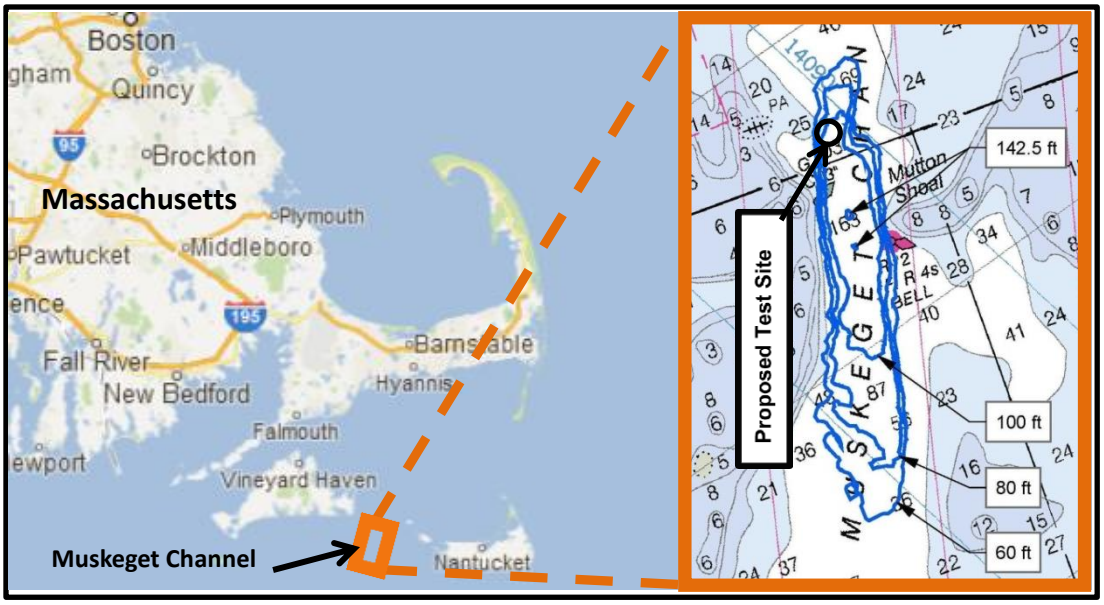

Figure 2. Muskeget Channel Tidal Energy Test Site. Inset: Contours of detailed bathymetry data taken by Howes et al. are overlaid on a nautical chart. The proposed test site lies in 100 ft. (30 m) of water. Images from Google, NOAA, EarthNC, Howes et al. (2009), Harris, Miller, Miller, and Hanson (2010).

The site is also being considered for a commercial tidal energy plant, which provides a unique opportunity for sharing the costs of permitting, site investigation, cabling, and monitoring. A preliminary permit was obtained from the Federal Energy Regulatory Commission (FERC) and a careful oceanographic, environmental, and logistical investigation of the site is ongoing (Barrett, 2010). Studies include Howes et al. (2009), Coastal Systems Program, University of Massachusetts-Dartmouth (2011), and Schlezinger (2012). It has been found that this site experiences maximum velocities of about 2.5 m/s (5 knots), with depths up to 43 m (143 ft.). Thus, this facility would complement the UNH CORE Tidal Energy Test Site by having more depth to accommodate larger full scale systems in an exposed ocean environment. In this sense, the UNH CORE site could serve as a "nursery site" for testing turbines of limited size in a sheltered environment, and the Muskeget Channel site could provide a full-scale test site as the next step in the scale-up process.

Objectives

The goal of this work was to develop a conceptual design for a test facility at Muskeget Channel for the testing of tidal hydrokinetic devices. The specific objectives for each design alternative considered were to:

- Identify design alternatives using different mounting structure approaches.
- Establish fundamental dimensions required for testing turbines of the desired sizes and identify suitable materials and equipment.
- Perform basic engineering calculations to demonstrate functionality.

- Estimate construction and installation costs.
- Compare alternatives and select the most suitable option(s).

Approach

Design criteria were formulated based on the expected needs of turbine developers. In this connection, a range of maximum size turbines to be tested was identified and the loading forces associated with each size were determined. Six design alternatives were generated and basic engineering calculations completed for each alternative. Designs include provision for mounting vertical and horizontal cross-flow axis turbines, as well as turbines with axes parallel to the flow. Costs for fabrication and installation of each concept for each maximum turbine size were estimated. Features of the natural berth concept were also documented. The positive and negative aspects of the concepts are discussed along with considerations regarding development of the site and long-term sustainability. A recommendation is made regarding the best approach for facility infrastructure.

Design Criteria

Site

The specific test site within the Muskeget Channel lies in SMAST Survey Transect 6 (shown on Figure 3), whose velocity cross-section is shown at its spring tide maximum in Figure 4 (Howes et al., 2009). It should be noted that the peak velocities occur near the surface.

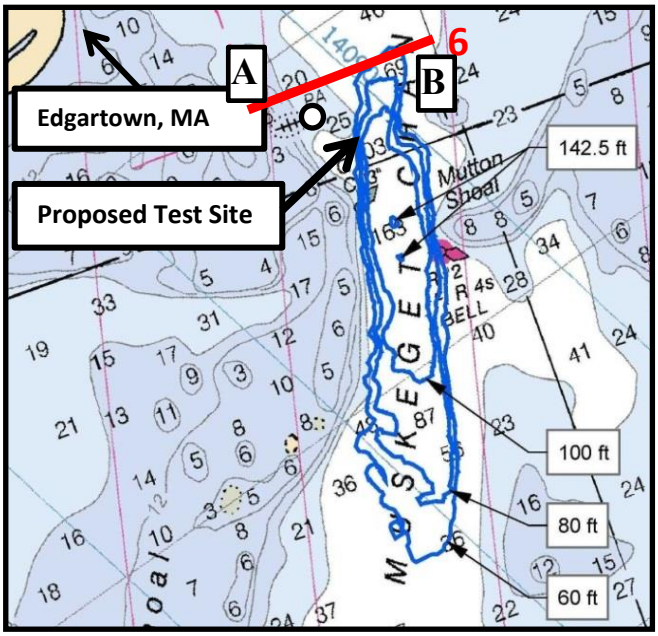

Figure 3. Bathymetry of Muskeget Channel. Contours of detailed bathymetry data taken by Howes et al. are overlaid on a nautical chart. The survey track of SMAST transect 6 is shown in red. The proposed test site lies in 100 ft. (30 m) of water. From Harris, Miller, Miller, and Hanson (2010).

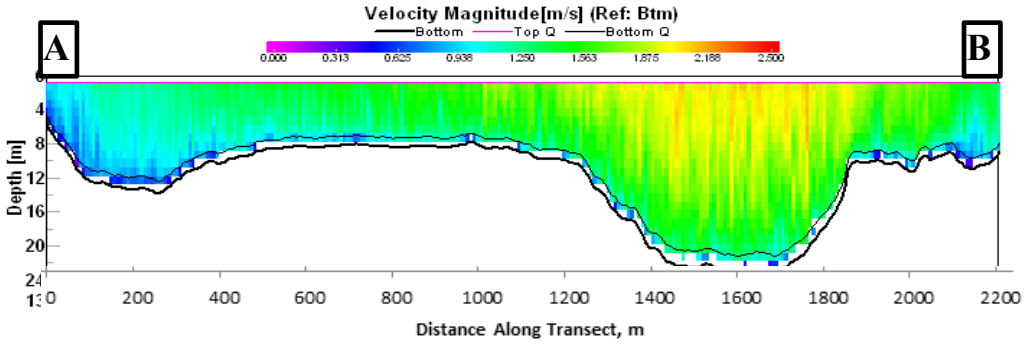

Figure 4. Example velocity profile along Transect 6 at the proposed Muskeget Channel test site at maximum flood tide (Howes et al., 2009). Maximum velocities occur near the surface.

This site has a similar maximum velocity environment as the UNH CORE site, but more than 3 times the depth, as compared in Table 2.

Table 2. Parameters of the proposed Muskeget test site compared with parameters of the existing UNH CORE site.

	Muskeget Channel				UNH CORE Site			
Water Depth	30	m	100	ft.	8	m	26	ft.
Max. Current	2.5	m/s	5	kts	2.5	m/s	5.0	kts
Min. Height from Seafloor	15	m	62	ft.	~			

Devices

The practical and financial feasibility of test platform concepts were investigated for testing of turbines with maximum diameters from 4.4 m (14 ft.) to 17.5 m (57 ft.). This would allow the Muskeget Channel platform to accommodate turbines up to about U.S. Department of Energy Technology Readiness Level (DOE TRL) 8 and the U.K. Department of Energy and Climate Change (DECC) Stage 4. (See Table 3 and Table 4.)

Table 3. U.S. Department of Energy Technology Readiness Levels (2009).

Relative Level of Technology Development	Technology Readiness Level	TRL Definition
System Operations	TRL 9	Actual system operated over the full range of expected conditions.
System Commissioning	TRL 8	Actual system completed and qualified through test and demonstration.
	TRL 7	Full-scale, similar (prototypical) system demonstrated in relevant environment
Technology Demonstration	TRL 6	Engineering/pilot-scale, similar (prototypical) system validation in relevant environment
Technology Development	TRL 5	Laboratory scale, similar system validation In relevant environment
	TRL 4	Component and/or system validation in laboratory environment
Research to Prove Feasibility	TRL 3	Analytical and experimental critical function and/or characteristic proof of concept
Basic Technology Research	TRL 2	Technology concept and/or application formulated
	TRL 1	Basic principles observed and reported

Table 4. U.K. Department of Energy and Climate Control Stages (2008).

Tidal-current Protocol	Protocol Stage
Production	
Commercial demonstrator tested at sea for an extended period.	5
(Scope of Protocol ends here)	
Full-scale prototype tested at sea	4
Subsystem testing at large scale	3
Subsystem testing at intermediate scale. Computational Fluid Dynamics. Finite Element Analysis. Dynamic analysis.	2
Tidal-current energy conversion concept formulated	1
(Scope of Protocol begins here)	

Four different turbine sizes were considered, and engineering analysis and costing were completed for the corresponding four sizes of each design alternative. The smallest maximum turbine size corresponded to the largest size that can be tested at the UNH CORE Tidal Energy Test Site. The other three had length scales 2, 3, and 4 times larger. This resulted in the largest maximum size having a diameter over half the Muskeget Channel depth, as detailed below.

The test platform needs to accommodate several types of turbine. Since the Muskeget site would complement the UNH CORE site, design criteria for the smallest maximum turbine size were chosen to correspond to the maximum size turbines that could be tested at the UNH CORE site. The weights and drag forces of these turbines are shown in Table 5.

Table 5. Turbine specifications for the smallest maximum turbine size considered. Drag forces shown are for the design flow speed of 2.5 m/s (5 knots).

	Area		Weight		C_d	Turbine Drag		Total Design Drag	
	m^2	ft^2	kg	lb		N	lbf	N	lbf
Ducted, In-stream axis	12.6	135.3	-	-	~	31,138	7,000	62,275	14,000
Vertical cross-flow axis	6.0	64.6	435	960	0.9	17,280	3,885	48,418	10,885
Horizontal cross-flow axis	15.0	161.5	2300	5100	0.9	43,200	9,712	74,338	16,712

The drag force on the cross-flow axis turbines was taken to be

$$D = \frac{1}{2}\rho C_d A V^2. \quad (1)$$

Here ρ is the density of seawater, A is the projected area of the turbine, V is the fluid velocity, and C_d is the turbine drag coefficient. Here, a value for cross-flow axis turbines was used, as acquired from tow-tank testing by Bachant (2010). Other device types might have much higher drag coefficients. In these cases, the maximum allowable turbine size would be smaller than shown in Table 6. Weights were estimated to be proportional to volume, scaled from an existing 45 kg (100 lb.) helical turbine and doubled to allow for the weight of support structure. Drag on the support structure was estimated from tow tank testing of a Froude-scaled model of the UNH CORE test site platform conducted by Byrne (2013). It was found that the drag on a structure capable of supporting any of the turbines in Table 5 was 31 kN (7,000 lbf.) at 2.5 m/s (5 knots). It was assumed that the size of this support structure would scale with the size of the turbine. Thus, since the drag force on the structure is proportional to its projected area, this force was taken to be proportional to the projected area of the largest turbine to be tested.

Of the turbines listed in Table 5, the horizontal axis helical turbine represents the greatest size, weight, and drag force. For convenience, an in-stream axis turbine with weight and drag characteristics equal to those of the horizontal axis turbine was chosen as the design device for each scale. The design criteria for each possible maximum turbine size are shown in Table 6,

along with a scale-up factor that is the ratio of each turbine size to the maximum size that could be tested at the UNH CORE site.

Table 6. Parameters of representative in-stream axis turbine for each possible maximum turbine size.

Diameter		Diameter/ Depth	Mass, kg	Weight, lb.	Drag		Scale-up factor from UNH CORE site
m	ft.				N	lbf	
4.4	14	1/7	2,300	5,100	74,000	17,000	1
8.7	29	1/3	14,200	31,000	297,000	67,000	2
13.1	43	2/5	43,000	94,800	669,000	150,000	3
17.5	57	3/5	96,000	211,700	1,189,000	267,000	4

Design Alternatives

Six platform concepts were investigated for testing hydrokinetic turbines of the specified parameters:

1. A gravity foundation fixed at mid-depth. A large concrete block supports a framework for attaching turbines at mid-depth.
2. A gravity foundation with telescoping piles. The extendable framework allows changing turbines at the surface, while the test position is at mid-depth.
3. A four-pile foundation fixed at mid-depth. A mid-depth platform on top of four piles serves as a permanent base for mounting turbines.
4. A two-pile, surface piercing pile foundation. A horizontal platform between two vertical piles can be moved vertically. Testing is normally done at mid-depth, while attaching and removing test turbines is done at the surface.
5. A submerged buoyant platform. The submerged platform will be held in place using a flexible mooring system. The platform may be brought to the surface for mounting and recovering test turbines.
6. A floating platform. The platform will consist of a catamaran-type hull-deck structure with a deck opening to lower and raise test turbines. The platform will be moored on station during testing and be towed to a shore base during storms and between test programs.

A Natural Berth option was considered in addition to these platform concepts. This option would supply the developer with a section of seafloor on which to install a turbine. All options would include instrumentation and power take-off.

CHAPTER 2

FIXED GRAVITY PLATFORM

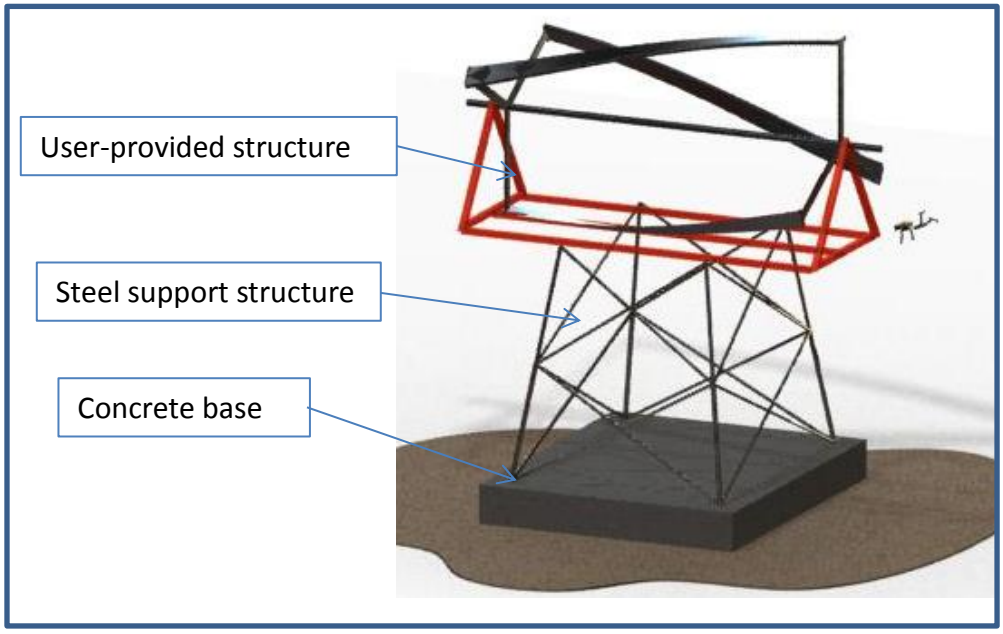

Figure 5. The Gravity Foundation platform concept shown mounting a 9 m by 15 m (29 ft by 49 ft) horizontal axis turbine. The permanent structure is shown in gray, while the user-provided mount-turbine structure is in orange. A 2 m (6.6 ft) diver is shown for scale.

A fixed-structure gravity foundation platform that would extend to mid-depth, illustrated in Figure 5, was considered for the following advantages:

- The platform would be below most surface traffic.
- The concept would be simple and robust.
- Material costs would likely be low.

Disadvantages include:

- The platform mounting structure must extend at least half the distance to the surface to place turbines in the high-velocity region.
- Maintenance and turbine installation/retrieval would likely be difficult and expensive.
- Scour would have to be considered.

The platform would include a box-shaped concrete base with sufficient weight and dimensions to resist tipping and sliding. This base would support a mounting structure designed as a truss sufficient to prevent yielding and buckling in its members. Figure 6 and Figure 7 show front and side views of this platform, respectively. Costs for constructing the structure onshore were determined from RS Means (2011) and quotes from steel producers and fabricators, and quotes for utilizing crane barges that could install the foundation were obtained.

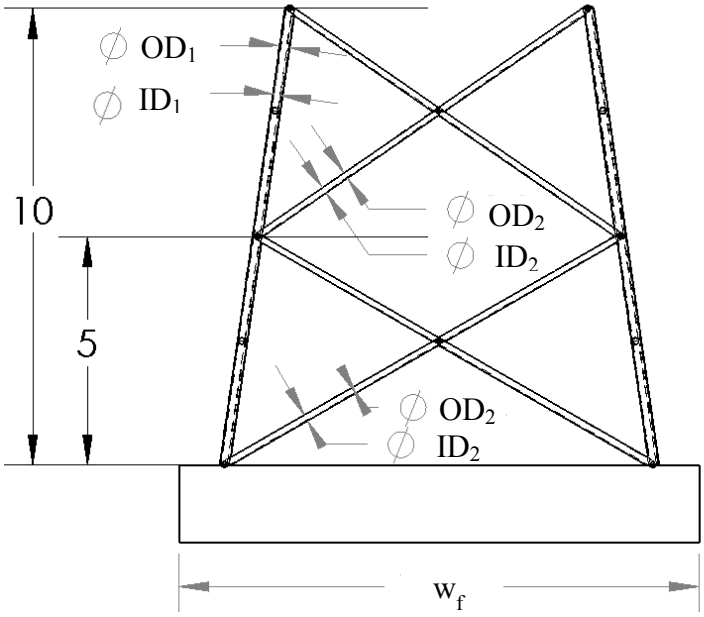

Figure 6. Front view of the Gravity Foundation platform. Fixed dimensions are given in meters. All other dimensions vary with maximum turbine size.

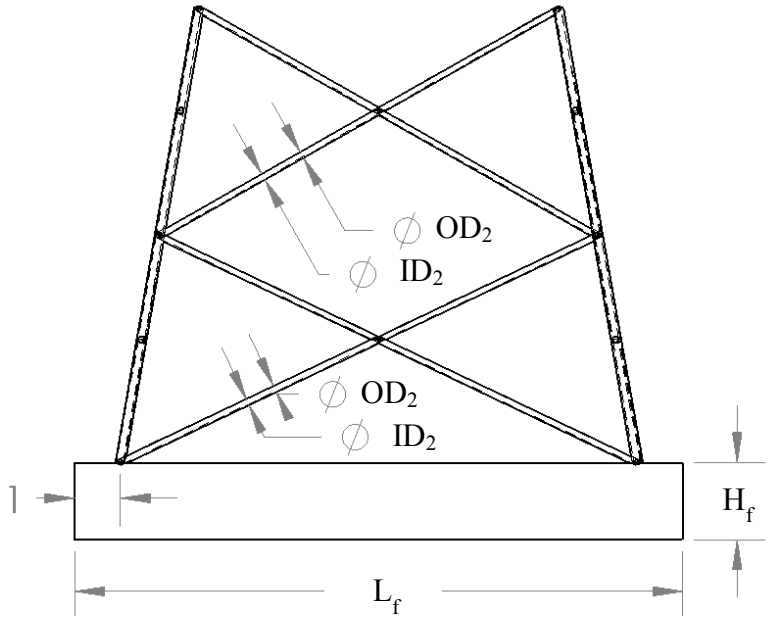

Figure 7. Side view of the Gravity Foundation platform. Fixed dimensions are given in meters. All other dimensions vary with maximum turbine size.

Specific Design Criteria

- The foundation must place the turbine hub 15 m (49 ft.) above the seafloor.
- The foundation must prohibit tipping or sliding. The foundation must have a minimum factor of safety of 3 (three) in the worst loading scenario.
- In the event of failure, the foundation must slide rather than tip. Specifically, the tipping factor of safety must exceed the sliding factor of safety by 25%.
- The foundation must resist cracking, e.g. during installation. That is, it must have a bending safety factor of 5 (not including reinforcing steel) under worst-case bending.
- Each member of the truss structure must have a safety factor of 3 (three) against material yielding and 4 (four) against buckling.
- The following assumptions were used in the analysis:
- A tipping condition is that in which the entire normal force acts at the rear lower corner of the level foundation.
- Friction can be sufficiently modeled by Coulomb's Law of Friction, in which the maximum friction force equals the normal force times a coefficient of friction between the two surfaces.
- The weight of the turbine is neglected for the tipping analysis. (This ensures that the foundation will be secure even if used to test a lightweight, high drag turbine.)
- A 2.5 m/s (5 knots) current is uniform over the entire depth.

Governing Equations

Foundation Design

A Free Body Diagram of the fixed gravity foundation platform is shown in Figure 8 and the variables therein are in Table 7.

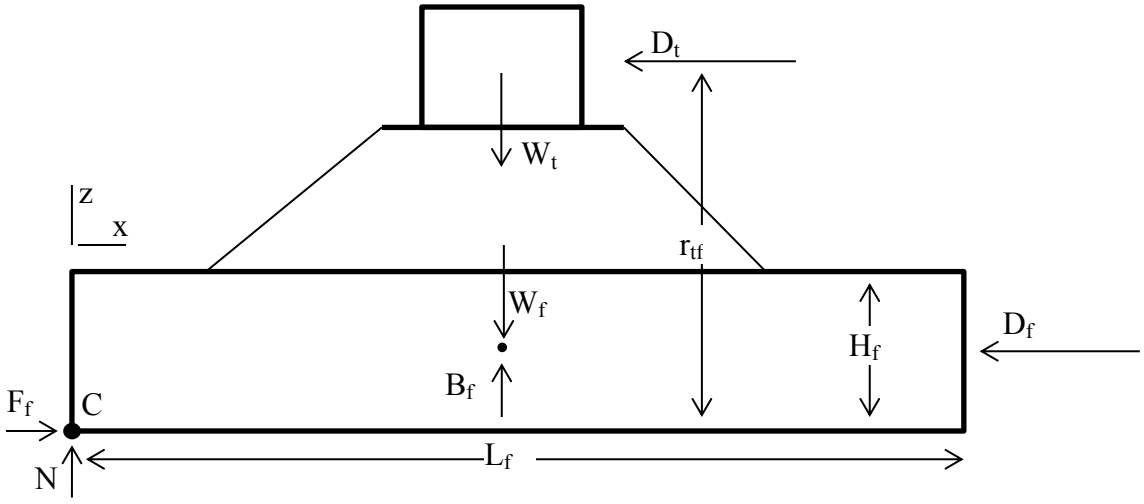

Figure 8. Free Body Diagram of Gravity Platform. The normal force N is located at the down-current edge of the platform base to model the onset of tipping. Drag force on the mounting structure was assumed negligible compared to turbine drag.

Table 7. Statics variables for Fixed Gravity Foundation.

W_f	Foundation Weight (Dry)
W_t	Turbine Weight
D_f	Foundation Drag
D_t	Turbine Drag
r_{tf}	Distance from bottom to Turbine Drag
B_f	Buoyant Force
H_f	Foundation Height
L_f	Foundation Length

To prevent sliding, the maximum friction force must equal or exceed the total drag. That is,

$$F_{f_{max}} \geq F_f = D_t + D_f. \tag{2}$$

Sliding was modeled using the Coulomb model of friction,

$$F_{f_{max}} = N\mu_s \tag{3}$$

where F_{fmax} is the maximum applicable friction force and μ_s is a static coefficient of friction for sand-gravel, given by AASHTO (Taly, 2010) as 0.55 for concrete on medium sand, gravel. Neglecting the weight of the turbine, the normal force, N, is the weight of the foundation minus the weight of displaced water, so that

$$N = W_f - B_b. \tag{4}$$

The weight of the foundation is

$$W_f = \rho_c g(L_f w_f H_f), \tag{5}$$

where ρ_c is the density of the concrete, and w_f is the width of the foundation. The buoyancy force is

$$B_f = \rho g(L_f w_f H_f). \tag{6}$$

Here drag on the foundation is given by

$$D_f = \frac{1}{2}\rho C_D U^2 A, \tag{7}$$

in which the coefficient of drag, C_D, is given by Hoerner (1965) as 1.05 for a block on a flat surface.

To prevent tipping, moments applied to the platform about point *c* must balance, so that

$$\sum M_c = 0, \tag{8}$$

so that

$$D_f \frac{H_f}{2} + D_t r_t \leq \left(W_f - B_f\right)\frac{L_f}{2}. \tag{9}$$

The equals sign pertains to the onset of tipping, shown in Figure 8; the "greater than" sign corresponds to the platform resting solidly on the sediment, with normal force *N* acting to the right of point *C*. As a result, there exist two factors of safety for the foundation: A tipping safety factor and a sliding safety factor, given by the maximum resisting moment over the design moment, and the maximum friction force over the drag force, respectively. Thus, the safety factors are

$$SF_{tip} = \frac{(W_f - B_f)\frac{L_f}{2}}{D_f\frac{H_f}{2} + D_t r_t} \tag{10}$$

and

$$SF_{slide} = \frac{(W_f - B_f)\mu_s}{D_t + D_f}. \tag{11}$$

Additionally, the low tensile strength of concrete necessitates a consideration of bending due to an uneven seafloor. A free-body diagram of the worst possible loading case is shown in Figure 9.

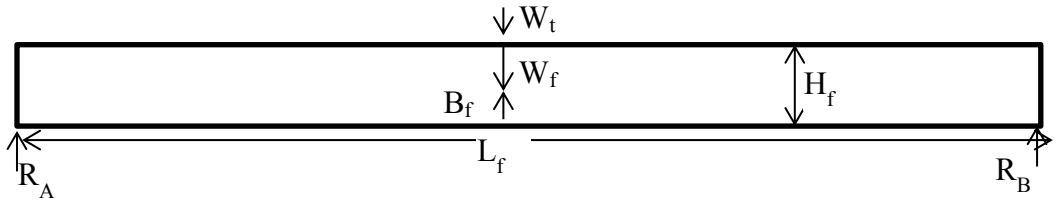

Figure 9. Free Body Diagram of Gravity Foundation modeled as a pinned-end beam, subject only to the larger vertical forces.

The maximum bending stress in the base was approximated by the formula

$$\sigma_{bend} = \frac{Mc}{I}. \tag{12}$$

Here M is the maximum bending moment, c is the distance from the neutral axis, and I is the area moment of inertia of the beam. Neglecting the ameliorating effects of steel rebar, the associated safety factor is concrete's Ultimate Tensile Strength divided by the maximum bending stress,

$$SF_{tensile} = \frac{\sigma_{UTS}}{\sigma_{bend}}. \tag{13}$$

Using the above analysis, the foundation dimensions were iterated for each turbine scale-up factor of interest to minimize weight under the constraints listed in Table 8, using a Generalized Reduction Gradient (GRG) nonlinear forward difference solver in the Microsoft Excel® Solver package.

Table 8. Gravity Foundation base constraints.

Platform will not slide:	$SF_{slide} \geq 3$
Platform will not crack in bending:	$SF_{tensile} \geq 5$
Platform will slide before tipping:	$SF_{tip} \geq 1.25 SF_{slide}$
Platform cannot be excessively narrow:	$w_f \geq 0.85 L_f$

The results of this analysis are shown in Table 9.

Table 9. Gravity Foundation base dimensions.

Turbine Diameter	4 m (14 ft)					9 m (29 ft)				
Foundation										
Foundation Height,	H_f	1.4	m	4.6	ft	2.1	m	6.8	ft	
Width of Foundation,	w_f	7.3	m	24.0	ft	8.8	m	29.0	ft	
Foundation Length,	L	8.6	m	28.3	ft	10.4	m	34.1	ft	
Foundation Mass,	m	213,053	kg	469,702	lbm	458,281	kg	1,010,337	lbm	

Legend:

Iterated values
Calculated values

Table 9. Gravity Foundation base dimensions (continued).

Turbine Diameter		13 m (43 ft)				17 m (57 ft)			
Foundation									
Foundation Height,	H_f	2.7	m	8.8	ft	3.6	m	11.8	ft
Width of Foundation,	w_f	9.9	m	32.3	ft	11.3	m	37.0	ft
Foundation Length,	L	11.6	m	38.0	ft	13.3	m	43.5	ft
Foundation Mass,	m	734,901	kg	1,620,180	lbm	1,285,038	kg	2,833,023	lbm

Legend:

Iterated values
Calculated values

Scour

Anti-scour structure must be designed with care. Rocker (1985) cites an example in which hinged concrete scour protection slabs were broken off of their main structure by deep water wave-induced scour in 30 m (100 ft.) of water. However, Gerwick points to successful installations of steel skirts around gravity foundations that reduce scour while increasing the foundation's ability to resist sliding. Another method, currently being implemented for offshore wind gravity foundations at the Thornton Bank Offshore Wind Farm off the Belgian coast uses layers of coarse sediment and gravel to minimize scour (Terra et Aqua). A steel scour skirt was designed using ¼" ASTM 252 Gr. 1 steel.

Support Structure

Statics

The mounting structure for the turbine was designed using Circular Hollow Section (CHS) truss members because of their high resistance to buckling and comparatively low drag coefficient, shown in Figure 10 and Figure 11 respectively.

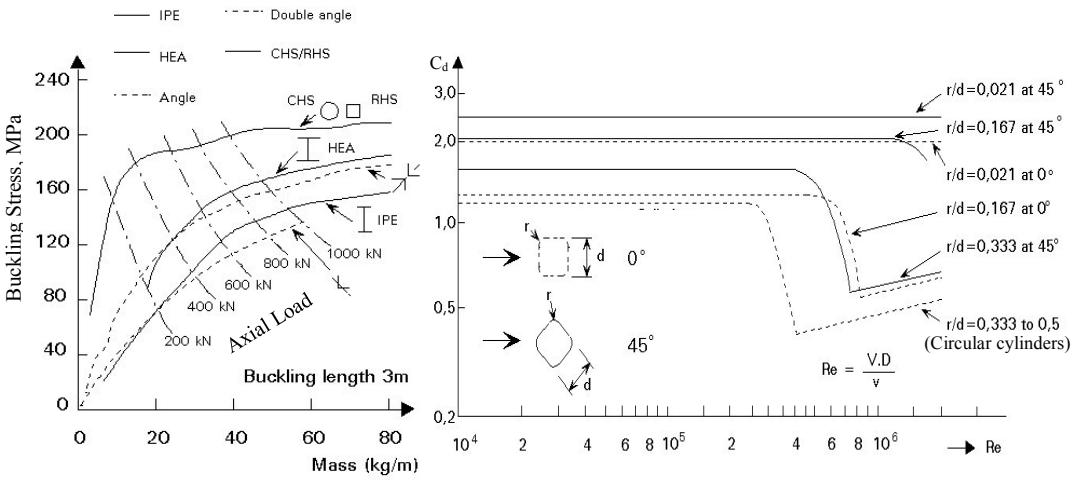

Figure 10. Comparison of the masses of hollow and open sections under compression in relation to the loading (European Steel Design Education Programme, 1994).

Figure 11. Approximate drag coefficient curves for single section (smooth surface) members with various corner radii, *r*, depending on the Reynolds number, *Re* (European Steel Design Education Programme, 1994).

A three-dimensional support structure was designed and analyzed with SolidWorks® finite element software. The analysis was first conducted using truss members (all joints pinned). Axial forces in each truss element were extracted and Euler's buckling analysis was conducted. In this analysis the axial load under which each element will buckle is given by

$$P_{crit} = \frac{\pi^2 EI}{L^2}, \tag{14}$$

where E is the elastic modulus, I is the area moment of inertia, and L is the effective length of the member. Under pinned end conditions—assumed for this analysis as a worst case—the effective length is the actual length of the member. Under fixed end condition (e.g. welding) the effective length is half the actual length. So using welded joints increases the critical load by a factor of four and thus quadruples the buckling safety factor, given by

$$SF_{buckling} = \frac{P_{crit}}{P}, \tag{15}$$

where P is the axial force in the member. This analysis was used to select section properties which resulted in the each member having $SF_{buckling} \geq 4$. Standard structural tubing sizes meeting those requirements were incorporated into the design, which was then reanalyzed using Solidworks® FEA software for both von Mises stress failure and for buckling using rigid connections (simulating a welded structure). For simplicity in construction, the entire mounting

structure was designed using only two sizes of mechanical tubing. Future detailed design would need to consider the distributed transverse drag load on each member. In each scenario the weight and drag forces of the turbine were applied to the truss structure along with vertical forces accounting for the moment arm between the top of the truss structure and the turbine's center of drag. The results for the final iteration truss design under loads corresponding to the 13 m (43 ft.) representative turbine are shown in Figure 12 and Figure 13. Note that the deflections illustrated in Figure 13 are greatly exaggerated; the maximum deflection is on the order of millimeters.

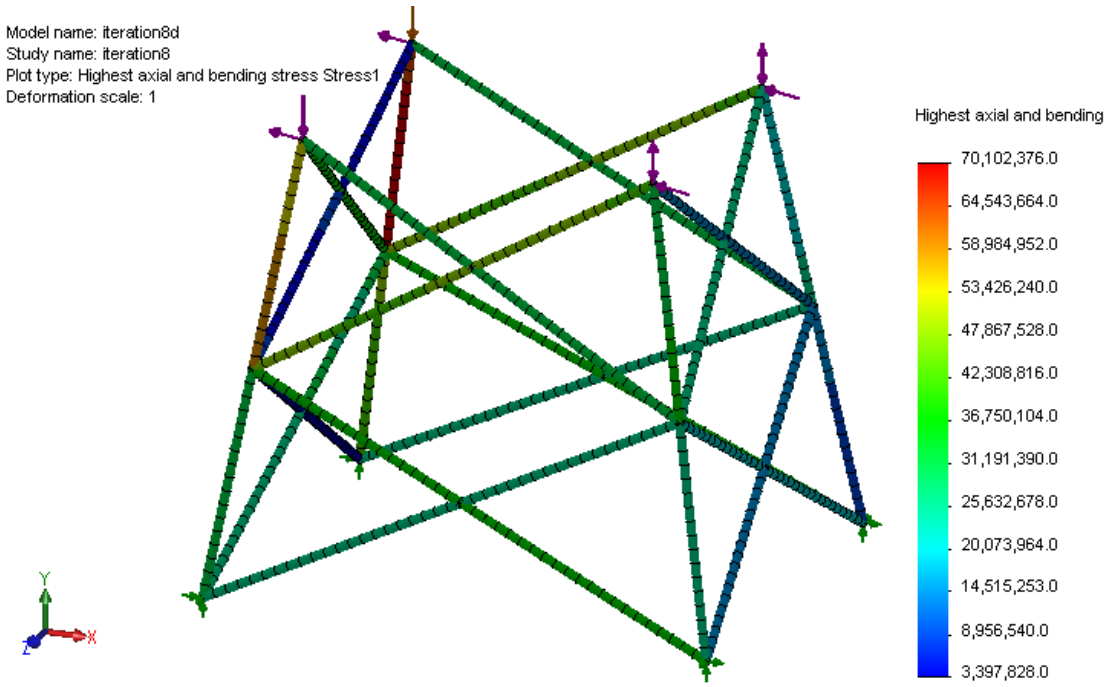

Figure 12. Finite element stress analysis of truss structure for Fixed Gravity Foundation Platform, capable of supporting a 13 m (43 ft.) turbine in a 2.5 m/s current. Maximum normal stress is shown in Pa. The yield stress for the chosen material (ASTM A333 Gr. 6) is 240 MPa.

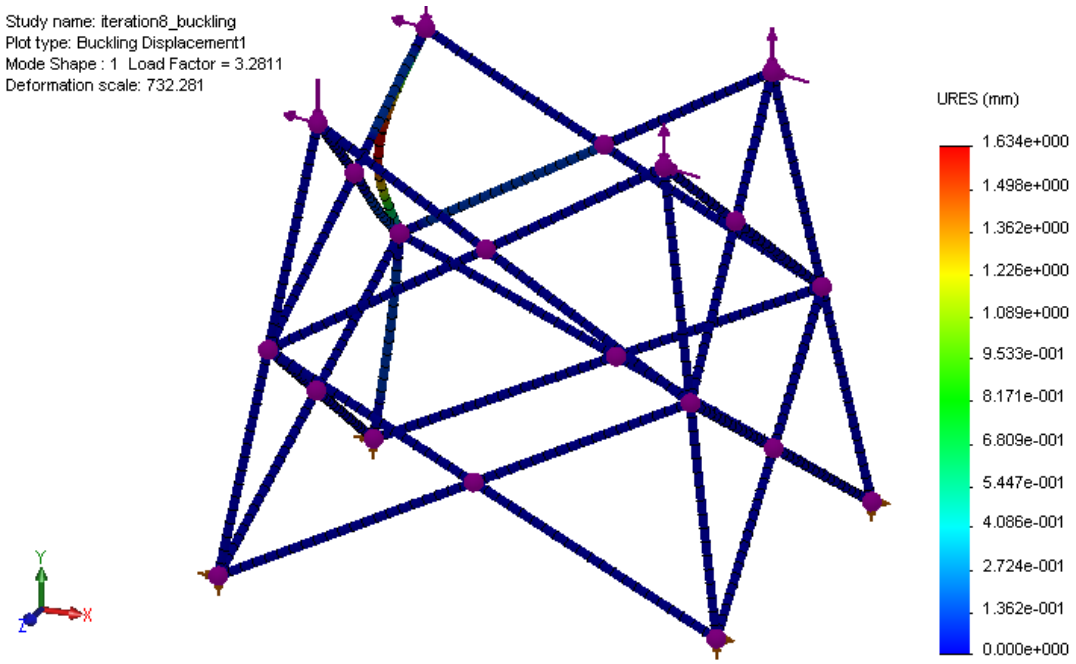

Figure 13. Finite element buckling analysis of truss structure for Fixed Gravity Foundation Platform, capable of supporting a 13 m (43 ft.) turbine in a 2.5 m/s current. Color graph shows the magnitude (RESultant) of the displacement vector U, U_{RES}. The load factor of 3.3 is the buckling safety factor.

The final mechanical tubing diameters for this scale are shown (in mm) in Figure 14.

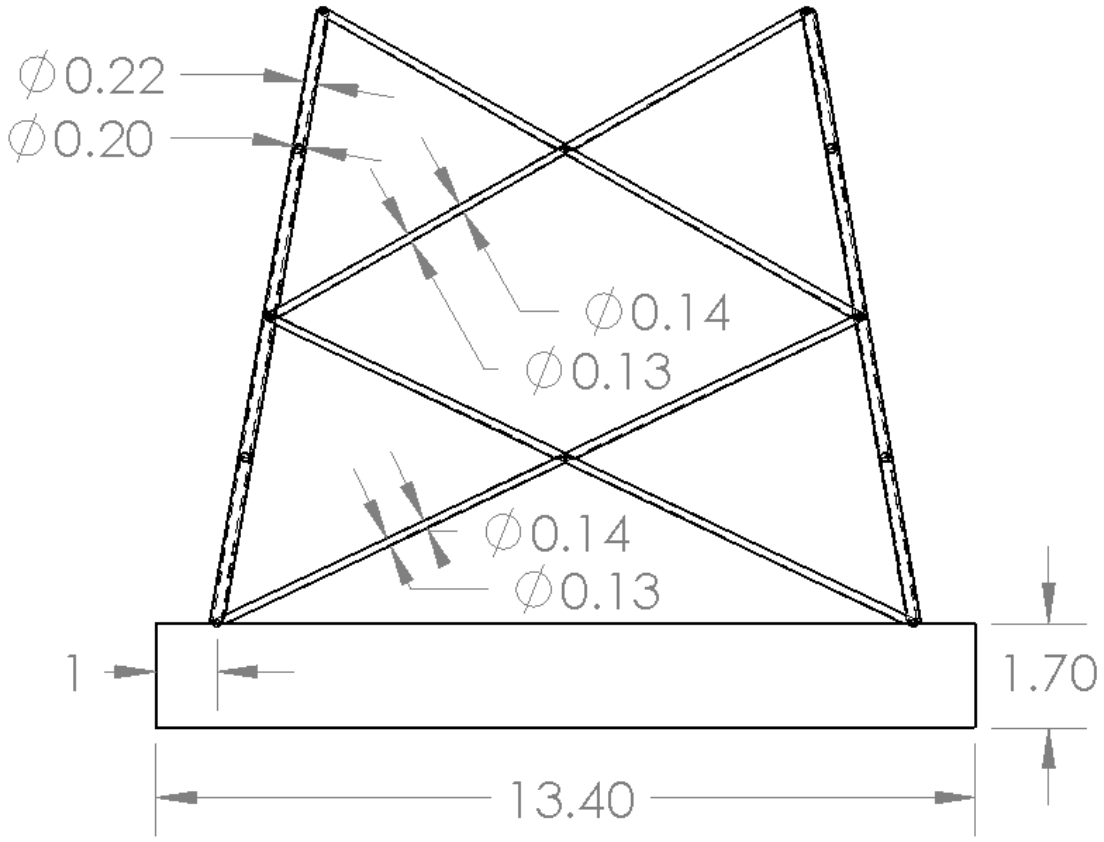

Figure 14. Mechanical tubing diameters capable of supporting a 13 m (43 ft.) turbine in a 2.5 m/s current. Members of equal outer radii also share inner radius dimensions. Dimensions are in meters. Base is 11.4 m (37 ft.) wide.

Once a mounting structure of sufficient dimensions was designed for a 13 m (43 ft.) turbine, the results were scaled to find approximate dimensions for platforms for different turbine sizes. The results are shown in Table 10.

Table 10. Gravity Foundation mounting structure dimensions.

Turbine Diameter		4 m (14 ft)				9 m (29 ft)			
Foundation									
Corner bracing, Outer Diameter	OD1	70	mm	2.8	in	150	mm	5.9	in
Corner bracing, Inner Diameter	ID1	60	mm	2.4	in	130	mm	5.1	in
Cross bracing, Outer Diameter	OD2	50	mm	2.0	in	90	mm	3.5	in
Cross bracing, Inner Diameter	ID2	40	mm	1.6	in	80	mm	3.1	in

Legend:

Iterated values

Table 10. Gravity Foundation parameters (continued).

Turbine Diameter		13 m (43 ft)				17 m (57 ft)			
Foundation									
Corner bracing, Outer Diameter	OD1	220	mm	8.7	in	290	mm	11.4	in
Corner bracing, Inner Diameter	ID1	200	mm	7.9	in	270	mm	10.6	in
Cross bracing, Outer Diameter	OD2	140	mm	5.5	in	190	mm	7.5	in
Cross bracing, Inner Diameter	ID2	130	mm	5.1	in	170	mm	6.7	in

Legend:

Iterated values

Dynamics—Vibration

Neglecting vibrational issues in marine structures can be catastrophic (Tomlinson, 2008, p. 413). Thus, after determining suitable dimensions for each member of the support structure to withstand its static loading, the vibrational response of each member was characterized using the method set forth by Tomlinson. According to standard beam theory the natural frequency of a beam is found to be

$$f_N = \frac{K\prime}{L^2}\sqrt{\frac{EI}{M}}. \tag{16}$$

where E is Young's Modulus, I is the area moment of inertia, M is mass/unit length of the beam (including the mass of the water contained in the beam and the mass of the displaced water), L is the length of the beam, and K' is a factor of 3.56 for the first mode of vibration in members with ends fixed against both translation and rotation. The Strouhal number can then be used to find the fluid velocity at which the frequency of vortex shedding will match the member's natural frequency. This critical velocity is given by

$$V_{crit} = K f_N \mathrm{d_o}, \tag{17}$$

where $\mathrm{d_o}$ is the outer diameter of the member and K is given in Table 11.

Table 11. Coefficients for modes of Vortex-Induced Vibration

1.2	Onset of in-line motion
2.0	Maximum in-line motion
3.5	Onset of cross-flow motion
5.5	Maximum cross-flow motion

According to Mittal and Kumar (1999), "in-line oscillations are significant only if the mass of the cylinder is not too large compared with the mass of the surrounding fluid it displaces." Since the mass of the cylinder is on the order of the mass of the surrounding fluid, it was assumed that only cross-flow motion is significant. The critical velocity (that which would cause the onset of

cross-flow motion) was determined for each member and the lowest was 3.8 m/s (7.4 knots)—far higher than the maximum velocities seen in the channel. Thus, the recommended designs will experience negligible vortex-induced vibration.

Because of its unique resistance to corrosion in seawater even after being welded, 316L stainless steel was originally investigated (Specialty Steel Industry of North America (SSINA), 2011). However, its cost was prohibitive. Several steels commonly found in marine applications were considered for this unique structure. Their properties are listed alongside alternatives in Table 12.

Table 12. Material Properties (ASTM International, 2010; 2011; 2009).

Material	Yield Strength		Ultimate Tensile Strength		Modulus of Elasticity	
	MPa	ksi	MPa	ksi	GPa	ksi
Stainless Steel 316L	**290**	**42**	**558**	**81**	**193**	**27,992**
Stainless Steel 410	410	59	483	70	210	30,458
ASTM A252 Grade 1	205	30	345	50	210	30,458
ASTM A252 Grade 2	240	35	414	60	210	30,458
ASTM A252 Grade 3	310	45	4550	66	210	30,458
ASTM A333 Grade 6	**240**	**35**	**415**	**60**	**200**	**29,008**
ASTM A514 Grade F	590	86	800	116	210	30,458

Table 12. Material Properties (continued).

Material	Shear Modulus of Elasticity		Poisson's Ratio	Endurance Limit		Density
	GPa	ksi		MPa	ksi	kg/m^3
Stainless Steel 316L	**77**	**11,168**	**0.5**	**279**	**40**	**7990**
Stainless Steel 410	80	11,603	0.5	242	35	7850
ASTM A252 Grade 1	80	11,603	0.5	173	25	7850
ASTM A252 Grade 2	80	11,603	0.5	207	30	7850
ASTM A252 Grade 3	80	11,603	0.5	228	33	7850
ASTM A333 Grade 6			**0.3**	**207**		
ASTM A514 Grade F				400		

It is important to note that high-strength steels do not necessarily offer weight savings in this application. Gerwick (2007) emphasizes that when buckling and vibration are key concerns, stiffness, rather than yield stress, governs failure. Also, the harsh Muskeget Channel environment mandates that any steel used must be specified for low-temperature service to prevent premature fatigue failure, especially in welded joints. Particularly, it must show high Charpy impact values at low temperatures. The American Petroleum Institute classifies steels in groups I—III by strength and classes C—A by toughness. Group I, Class A steel meets the above requirements, so quotes were sought for ASTM A333 Grade 6 tubing (American Petroleum Institute, 1993).

Corrosion

According to Corus (2005), steel in the continually immersed zone "acquires a protective blanket of corrosion products and marine growth" and exhibits an average mean corrosion rate of 0.035mm/year/side. Tomlinson (2008) echoes this in saying that in the continuously immersed zone, piles should use bare steel or cathodic protection. He quotes a study by Morley and Bruce (1983)of steel piles in the UK that reports an average loss of thickness of 0.05 mm/year in the immersion zone, with a 95% maximum probable rate of 0.14 mm/year. Furthermore, he points out that if the interior of a tubular member is sufficiently isolated from the external environment, the oxygen in the trapped seawater will quickly be "used up in the early corrosion process, leaving none to maintain the corrosion."

A sacrificial anode system is often an economical anti-corrosion measure. Such a system could be implemented simply by using commercially available zinc shaft collars around the truss members or by mounting zinc bars between members, as is sometimes practiced in offshore structures. While it would require occasional maintenance, the anodes would simply need to be replaced when they are observed to be depleted. As to concerns of biofouling, Blackwood et al. (2010) published their findings that "anodes remain effective even after being completely coated with biofouling."

If cathodic protection is used in conjunction with high-strength steels, Billingham et al. (2003) emphasizes that great care must be taken to mitigate hydrogen cracking. Gerwick (2007) adds that cathodic protection is prohibited in areas where the flow of water is restricted.

Costing

Materials and Construction

Material costs for the gravity foundation were based on shore forming and estimating the city-factored cost of concrete from RS Means (2011) with Overhead and Profit included, assuming that concrete would account for the entire weight of the structure (i.e. neglecting the possibility of using sediment as fill.) This included forming materials and anti-corrosion treatment. The components of the foundation are shown for each platform size in Table 13. The cost of the anti-scour skirt was determined from the per-pound estimate of ASTM A252 Gr. 3.

Table 13. Gravity base weight breakdown.

Turbine Diameter			**4 m (14 ft)**	**9 m (29 ft)**	**13 m (43 ft)**	**17 m (57 ft)**
Material	Type	Percent by Weight	Weight, tons			
Cement	Portland, type I,II	11%	26	56	89	156
Aggregate--coarse	Sand+stone, Crushed bank gravel, loaded at site	67%	157	338	543	949
Water		16%	38	81	130	227
Air		6%	14	30	49	85
Total		100%	235	505	810	1,417

The material cost of the mechanical tubing that constitutes the support structure was estimated from a quote from American Steel for ASTM A333 Gr. 6 mechanical tubing, also on a per-pound basis. Although it is recommended that the steel mounting structure be left bare as a cost-saving measure, the cost of corrosion protection was included in the estimate in case it is deemed necessary. This cost was based on a quote from L.B. Foster (2010) for marine-grade epoxy coating over the exterior surface area of the platform. Welding costs were estimated from a quote supplied to Jeff Byrne for his V2 design (2013). The material costs were subtracted from a quote that included deck beams and welded mechanical tubing and the remainder was assumed to be the welding cost, which was reduced to dollars per pound of tubing. (While this overestimates the fraction which is welding cost, it is worth noting that the quotes used to estimate the welding cost were for A36 steel, which may be easier to weld than ASTM A333 Gr. 6).

Installation

The installation cost was based on a crane barge of sufficient capacity to carry and install the foundation, in use for 7 (seven) days with 4 (four) days of mobilization/demobilization. Quotes were obtained from Manson Construction of Los Angeles (2010) and Weeks Marine of New Jersey (2012) for crane barges of various capacities. Alternative installation methods are under investigation. Gerwick (2007) describes detailed steps for constructing a gravity foundation "raft" consisting of a concrete honeycomb structure whose buoyancy is moderated by controlling the amounts of compressed air in each cell. The steel anti-scour skirt could also be utilized for buoyancy during installation. Such methods will bear further investigation in the more detailed phase of design. The estimated costs of a Fixed Gravity Foundation platform for the range of turbine sizes are shown in Table 14.

Table 14. Cost of Fixed Gravity Foundation Platform.

Turbine Diameter		**4 m**	**(14 ft)**	**9 m**	**(29 ft)**	**13 m**	**(43 ft)**	**17 m**	**(57 ft)**
Base	**Unit cost**	**Qty.**	**Cost**	**Qty.**	**Cost**	**Qty.**	**Cost**	**Qty.**	**Cost**
Cement	$0.12	51,667	$6,348	111,137	$13,656	178,220	$21,898	311,631	$38,291
Aggregate-coarse	$23.50	157	$3,698	338	$7,954	543	$12,755	949	$22,303
Anti-corrosion Treatment	$10.05	116	$1,167	250	$2,510	401	$4,025	700	$7,038
Forming	$10.95	1,162	$12,728	1,848	$20,237	2,467	$27,016	3,501	$38,335
Anti-scour Skirt	$1.87	16,820	$31,493	30,035	$56,236	43,139	$80,770	65,939	$123,459
Support Structure									
ASTM A333 Grade 6 Steel	$28-$140	2,667	$4,378	10,667	$17,511	24,000	$39,401	42,667	$70,045
Welding	$1.38	2,667	$3,671	10,667	$14,682	24,000	$33,035	42,667	$58,729
Anti-corrosion Coating	$4.02	111	$447	444	$1,789	1,000	$4,024	1,778	$7,154
Installation Vessel Mobilization/ Demobilization	$18,000-$24,000	4	$72,000	4	$96,000	4	$96,000	4	$96,000
Working	$41,000-$52,500	7	$287,000	7	$367,500	7	$367,500	7	$367,500
Total			**$422,929**		**$598,074**		**$686,425**		**$828,854**

O&P, shipping included throughout

Site work not included

CHAPTER 3

TELESCOPING GRAVITY PLATFORM

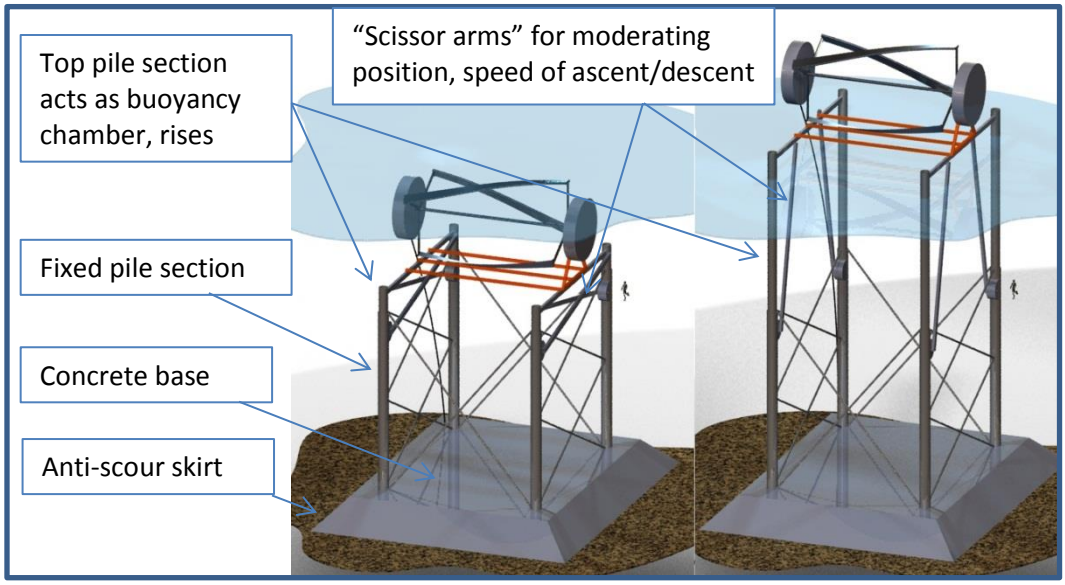

Figure 15. The Telescoping Gravity platform concept shown mounting a 9 m by 15 m (29 ft by 49 ft) horizontal axis turbine. The permanent structure is shown in gray, while the user-provided mount-turbine structure is in orange. A 2 m (6.6 ft) diver is shown for scale.

A telescoping pile gravity foundation platform, illustrated in Figure 15, was considered for the following advantages:

- The turbine mounting would reside below most surface traffic.
- The platform would be accessible from the surface for turbine installation, maintenance, and retrieval.

Disadvantages include:

- Scour would have to be considered.
- Moving underwater parts are vulnerable to biofouling, etc.

The Telescoping Gravity platform would comprise a concrete base, four telescoping piles rigidly connected by a truss structure, and a turbine mounting structure. The uppermost section of each telescoping pile would act as a buoyancy chamber. Devices would be deployed at mid-depth (with telescoping piles collapsed to minimum length, as shown in the left half of Figure 15) for the duration of testing. For installation, service, and retrieval, the turbine mounting platform would be raised above the surface (as shown in the right half of Figure 15). This would be accomplished by forcing air into each of the uppermost pile sections. Rate of ascent and final vertical position would be controlled by mechanical control arms, shown in Figure 15.

Dimensions of a gravity foundation were obtained by designing the base as a simple box-shaped concrete structure with sufficient weight and dimensions to resist tipping and sliding. The pile sections were designed to resist the axial loading, bending moment, and shearing forces. Costs were estimated for constructing the structure onshore, and quotes were obtained for crane barges that could install the platform.

Specific Design Criteria

- The foundation must prohibit tipping or sliding. A minimum factor of safety of 3 was specified for both failure modes.
- The foundation must resist cracking, e.g. during installation. That is, it must have a bending safety factor of 5 (not including reinforcing steel) under worst-case bending.
- Each pile section must have a safety factor of 2 against material yielding and 5 against shearing. (The high shearing safety factor is to prevent local buckling in the wall of the hollow cylinder.)
- Maximum horizontal deflection when platform is fully extended must be less than 0.3 m (1 ft.), neglecting the stiffening cross members.

The following assumptions were used in the analysis:

- A tipping condition is that in which the entire normal force acts at the rear lower corner of the level foundation.
- Friction can be sufficiently modeled by Coulomb's Law of Friction, in which the maximum friction force equals the normal force times a coefficient of friction between the two surfaces.
- The weight of the turbine is neglected for the tipping analysis. (This ensures that the foundation will be secure even if used to test a lightweight, high drag turbine.)
- A 2.5 m/s (5 knots) current is uniform over the entire depth.

Foundation Design

Governing Equations

A Free Body Diagram of the fixed gravity foundation platform is shown in Figure 16 and the variables used therein are given in Table 15.

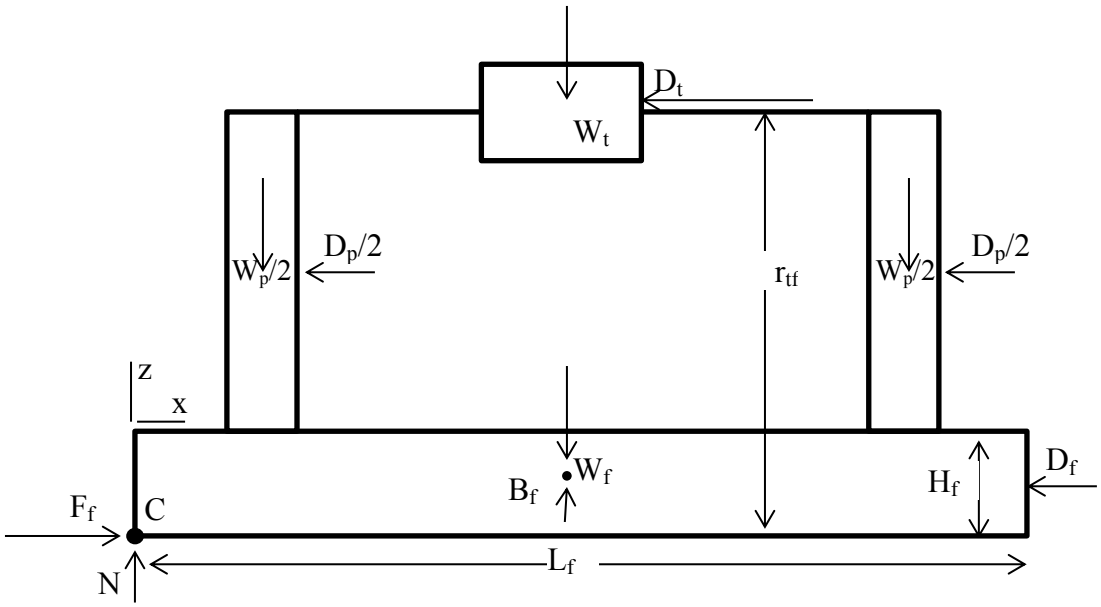

Figure 16. Free Body Diagram of gravity foundation for Telescoping Pile platform. The normal force N is located at the down-current edge of the platform base to model the onset of tipping. Drag force on the truss structure was assumed negligible compared to drag on the turbine, telescoping piles, and foundation.

Table 15. Statics variables for gravity foundation for Telescoping Pile platform

W_f	Foundation Weight (Dry)
W_t	Turbine Weight
D_f	Foundation Drag
D_t	Turbine Drag
r_{tf}	Distance from bottom to Turbine Drag
B_f	Buoyant Force
H_f	Foundation Height
L_f	Foundation Length
b_f	Foundation Breadth

To prevent sliding, the maximum friction force must equal or exceed the total drag. That is,

$$F_{f_{max}} \geq F_f = D_t + D_f + D_p. \tag{18}$$

Sliding was modeled using the Coulomb model of friction,

$$F_{f_{max}} = N\mu_s \tag{19}$$

where F_{fmax} is the maximum applicable friction force and μ_s is a static coefficient of friction for sand-gravel, given by AASHTO (Taly, 2010) as 0.55 for concrete on medium sand, gravel. The anti-sliding, anti-tipping effects of the anti-scour skirt were ignored in this analysis. Neglecting the weight of the turbine, the normal force, *N*, is the weight of the foundation minus the weight

of displaced water, so that

$$N = W_f + W_p - B_f - B_p, \tag{20}$$

where W_p is the total weight of the piles and B_p is the buoyant force on the piles.
The weight of the foundation is

$$W_f = \rho_c g(L_f w_f H_f), \tag{21}$$

where ρ_c is the density of the concrete, and w_f is the width of the foundation. The buoyancy force is

$$B_f = \rho g(L_f w_f H_f). \tag{22}$$

Here drag on the foundation is given by

$$D_f = \frac{1}{2}\rho C_D U^2 A, \tag{23}$$

in which the coefficient of drag, C_D, is given by Hoerner (1965) as 1.05 for a block on a flat surface.
To prevent tipping, moments applied to the platform about point *C* must balance, so that

$$\sum M_c = 0, \tag{24}$$

so that

$$D_f \frac{H_f}{2} + D_t r_t + D_p \frac{r_t}{2} \leq \left(W_f + W_p - B_f\right)\frac{L_f}{2}. \tag{25}$$

The equals sign pertains to the onset of tipping, shown in Figure 8; the "greater than" sign corresponds to the platform resting solidly on the sediment, with normal force *N* acting to the right of point *C*. As a result, there exist two factors of safety for the foundation: A tipping safety factor and a sliding safety factor, given by the maximum resisting moment over the design moment, and the maximum friction force over the drag force, respectively. Thus, the safety factors are

$$SF_{tip} = \frac{\left(W_f - B_f + W_p\right)\frac{L_f}{2}}{D_f\frac{H_f}{2} + D_t r_t + D_p\frac{r_t}{2}} \tag{26}$$

and

$$SF_{slide} = \frac{\left(W_f - B_f + W_p\right)\mu_s}{D_t + D_f + D_p}. \tag{27}$$

Additionally, the low tensile strength of concrete necessitates a consideration of bending due to an uneven seafloor. A free-body diagram of the worst loading case is shown in Figure 17.

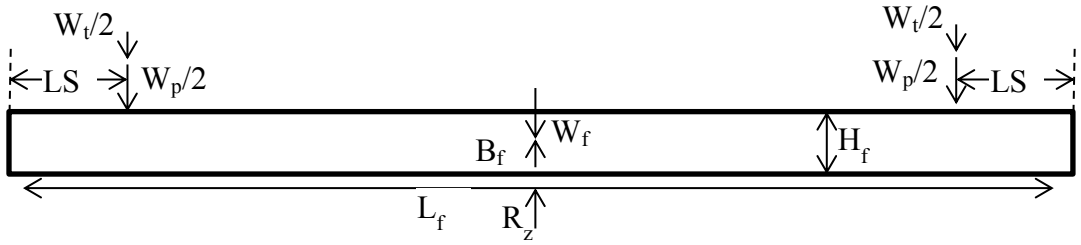

Figure 17. Free Body Diagram (in vertical) of Telescoping Gravity base supported at a single point subject only to the larger vertical forces.

The maximum bending stress in the base was approximated by the formula

$$\sigma_{bend} = \frac{Mc}{I} = \frac{\left(\frac{L_f}{2} - LS\right)\left(\frac{W_t}{2} + \frac{W_p}{2}\right)\left(\frac{H_f}{2}\right)}{\frac{1}{12} b_f H_f^3}. \quad (28)$$

Here M is the maximum bending moment, c is the distance from the neutral axis, and I is the area moment of inertia of the beam. Neglecting the ameliorating effects of steel rebar, the associated safety factor is concrete's Ultimate Tensile Strength divided by the maximum bending stress.

$$SF_{tensile} = \frac{\sigma_{UTS}}{\sigma_{bend}} \quad (29)$$

Using the above analysis, the foundation dimensions were iterated for each turbine scale-up factor of interest to minimize weight under the constraints listed in Table 16, using a Generalized Reduction Gradient (GRG) Nonlinear forward difference solver in the Microsoft Excel® Solver package.

Table 16. Gravity Foundation base constraints.

Platform will not slide:	$SF_{slide} \geq 3$
Platform will not crack in bending:	$SF_{tensile} \geq 5$
Platform will not tip:	$SF_{tip} \geq 3$
Platform cannot be excessively narrow:	$w_f \geq 0.85 L_f$

Scour

Anti-scour structure must be designed with care. Rocker (1985) cites an example in which hinged concrete scour protection slabs were broken off of their main structure by deep water wave-induced scour in 30 m (100 ft.) of water. However, Gerwick points to successful installations of steel skirts around gravity foundations that reduce scour while increasing the foundation's ability to resist sliding. Another method, currently being implemented for offshore wind gravity foundations at the Thornton Bank Offshore Wind Farm off the Belgian coast uses

layers of coarse sediment and gravel to minimize scour (Terra et Aqua). A steel scour skirt was designed using ¼" ASTM 252 Gr. 1 steel.

Support Structure

Statics

Each of the four telescoping members was modeled as a series of concentric beams, as shown in Figure 18. The variables used in the Free Body Diagrams are listed in Table 17.

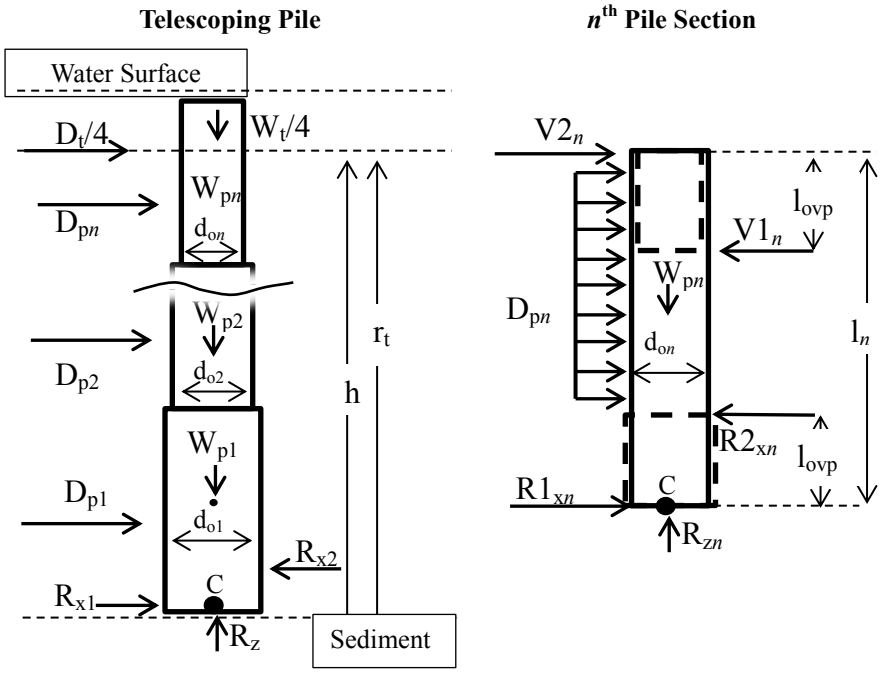

Figure 18. FBD of a telescoping member and of the n^{th} pile section. Distributed drag loads are shown as point loads in the left figure for visual clarity.

Table 17. Statics variables for pile section analysis.

W_{pn}	Weight (dry) of pile section
W_t	Turbine Weight
D_{pn}	Drag on pile section *n*
D_t	Turbine Drag
$V1_n$, $V2_n$	Horizontal force from pile section n+1
$R1_{xn}$, $R2_{xn}$	Horizontal reaction force from pile section n-1
R_z	Vertical reaction force on pile
R_z	Vertical reaction force on pile
r_{tf}	Distance from bottom to Turbine Drag
d_{on}	Pile diameter
l_{ovp}	Overlap between sections

This system was analyzed using singularity equations, in the method described by, for example, Beer et al. (2012). In this analysis the shear forces are integrated along the axis of the beam to find the bending moment distribution, which is integrated to find the slope of the beam along the axis, which is integrated to find the total deflection. The constants of integration arising in the process are determined by the boundary conditions. These boundary conditions are that the slope and deflection at the end of each pile section must match that in the adjacent section at the same vertical location. Additionally, the displacement and slope at the base of pile section n=1 (the bottommost section) are zero.

This analysis was implemented in MATLAB®. Due to geometric conditions and the given water depth, it was decided that each telescoping pile would consist of two pile sections. A pile wall thickness of 2 inches was specified and the outer diameter of the smallest pile section was iterated until the maximum bending and shear stresses in the pile sections were acceptable. (The inner diameter of each subsequent pile section was set to the outer diameter of the pile section above, with the same wall thickness.) Bending stress was calculated as

$$\sigma_B = \frac{Mc}{I_y} = \frac{M\left(\frac{d_{on}}{2}\right)}{I_y}. \tag{30}$$

Here M is the local bending moment, c is the distance from the neutral axis, and I_y is the area moment of inertia about the neutral axis. Shear stress was calculated as

$$\tau = \frac{VQ}{tI} = 2\frac{V}{A} \tag{31}$$

for a thin walled circular cylinder. Here V is the shear force; Q is the first moment of the cross-sectional area above the neutral axis; t is twice the wall thickness; I is the moment of inertia of the entire cross-section; and A is the area of the cross-section. Safety factors for bending and shear were defined respectively as

$$SF_B = \frac{\sigma_Y}{\sigma_{Bmax}}, \tag{32}$$

and

$$SF_V = \frac{\sigma_Y}{\tau_{max}}. \tag{33}$$

Pile section diameters were iterated until $SF_B \geq 2$ and $SF_V \geq 5$. For each design, maximum deflection was checked to ensure that it did not exceed the specified 0.3 m (1 ft.) Figure 19 shows the shear, and bending distributions, the slope, and the deflection along the telescoping

pile—for a turbine size of 13 m (43 ft.)—of a system in which each telescoping pile consists of two sections. The final design results are shown in Table 18.

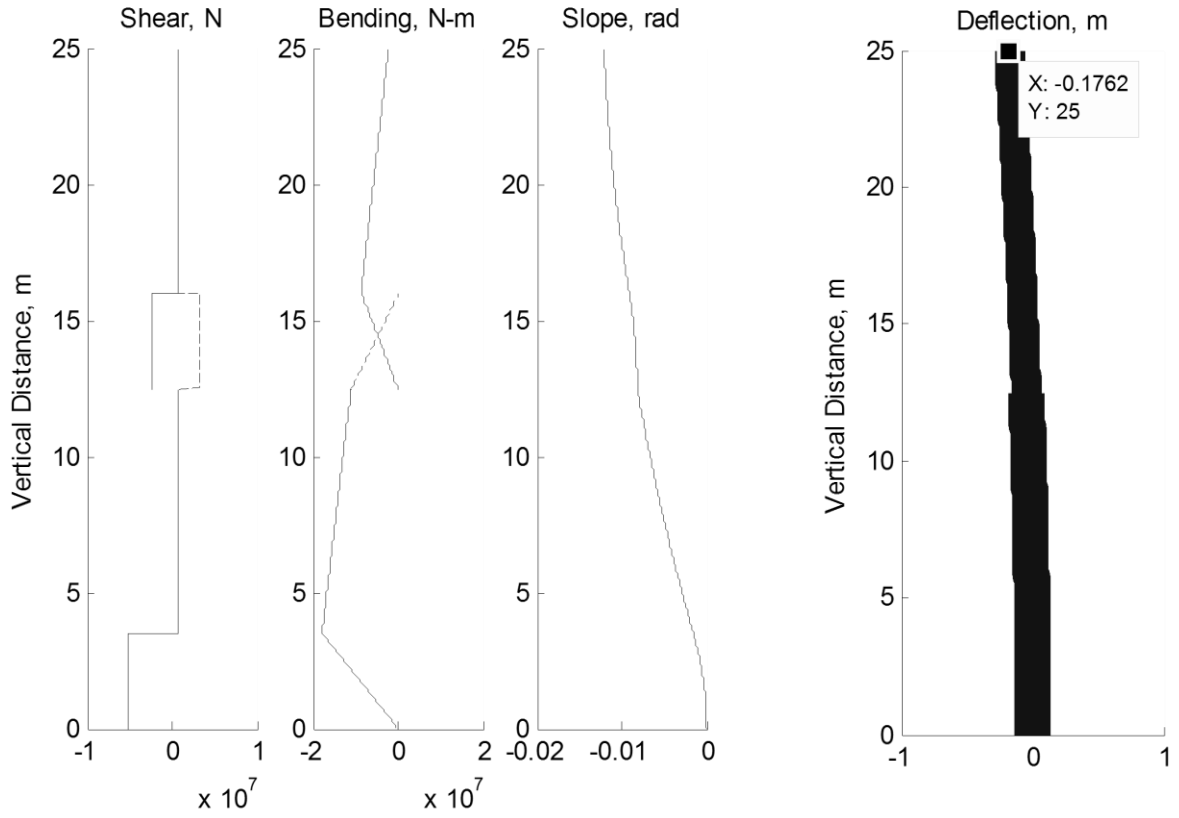

Figure 19. Shear force, bending moment, total slope and horizontal deflection along a telescoping pile with 2 sections. Values are calculated along each pile section. Dashed lines denote values associated with a lower pile in an overlap region. The lack of apparent slope in the shear-force diagram shows that the distributed drag on each pile section is small compared to the effect of turbine drag.

Table 18. Telescoping pile section diameters.

Turbine Diameter (representative in-stream axis)		Pile Diameter, m	
m	ft	Section 1 (lower)	Section 2 (upper)
4	14	0.60	0.50
9	29	1.15	1.05
13	43	1.70	1.60
17	57	2.20	2.10

Although the telescoping pile sections were designed to take the full load of the turbine, bracing members were added to the lower section to stiffen the structure. This is important because any curvature in the sections could increase friction significantly. The stiffening elements in the structure were designed using Circular Hollow Section (CHS) truss members because of their

high resistance to buckling and comparatively low drag coefficient, shown in Figure 20 and Figure 21 respectively.

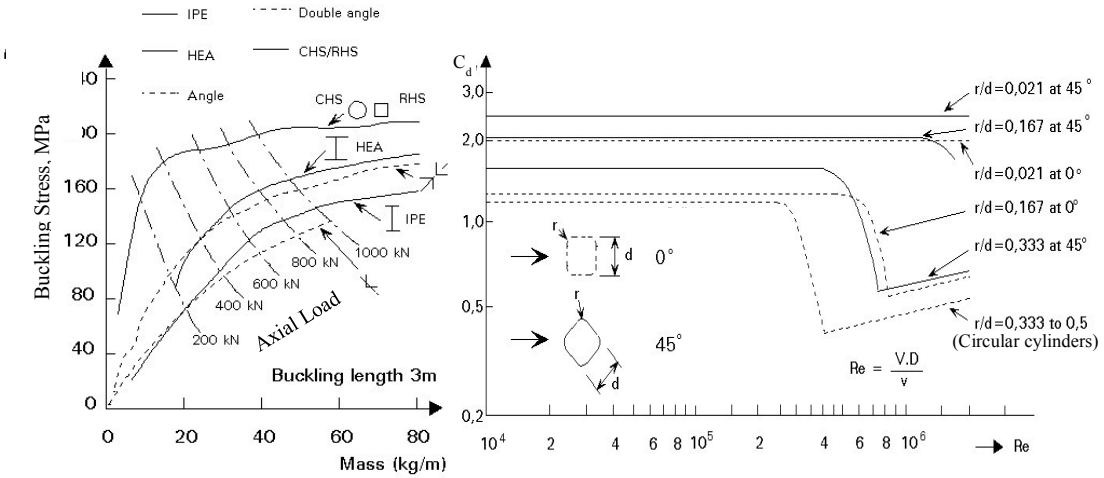

Figure 20. Comparison of the masses of hollow and open sections under compression in relation to the loading

(European Steel Design Education Programme, 1994)

Figure 21. Approximate drag coefficient curves for single section (smooth surface) members with various corner radii, *r*, depending on the Reynolds number, *Re* (European Steel Design Education Programme, 1994).

Dynamics—Vibration

Neglecting vibrational issues in marine structures can be catastrophic (Tomlinson, 2008, p. 413). According to standard beam theory the natural frequency of a beam is found to be

$$f_N = \frac{K'}{L^2}\sqrt{\frac{EI}{M}}, \tag{34}$$

where E is Young's Modulus, I is the area moment of inertia, M is mass/unit length of the beam (including the mass of the water contained in the beam and the mass of the displaced water), L is the length of the beam, and K' is a factor of 3.56 for the first mode of vibration in members with both ends fixed. The Strouhal number can then be used to find the fluid velocity at which the frequency of vortex shedding will match the member's natural frequency. This critical velocity is given by

$$V_{crit} = K f_N \mathrm{d_o}, \tag{35}$$

where $\mathrm{d_o}$ is the outer diameter of the member and K is given in Table 19.

Table 19. Coefficients for modes of Vortex-Induced Vibration(Tomlinson, 2008).

1.2	Onset of in-line motion
2.0	Maximum in-line motion
3.5	Onset of cross-flow motion
5.5	Maximum cross-flow motion

According to Mittal and Kumar (1999), "in-line oscillations are significant only if the mass of the cylinder is not too large compared with the mass of the surrounding fluid it displaces." Since the mass of the cylinder is on the order of the mass of the surrounding fluid, it was assumed that only cross-flow motion is significant. The above equations can be solved to find the required combined relative stiffness, CRS of any member of a given length subjected to a given fluid velocity, defined by

$$CRS = d_o\sqrt{EI/M} = \frac{V_{crit}L^2}{KK'}. \tag{36}$$

To prevent cross-flow vibration, the required combined relative stiffness of each structural member (based on its length) was computed and a cross-section with sufficient CRS (including a safety factor of two) was chosen.

Material

Because of its unique resistance to corrosion in seawater even after being welded, 316L stainless steel was originally investigated (Specialty Steel Industry of North America (SSINA), 2011). However, its cost was prohibitive. Several steels commonly found in marine applications were considered for this unique structure. Their properties are listed alongside alternatives in Table 20.

Table 20. Material Properties (ASTM International, 2010; 2011; 2009).

Material	Yield Strength		Ultimate Tensile Strength		Modulus of Elasticity	
	MPa	ksi	MPa	ksi	GPa	ksi
Stainless Steel 316L	**290**	**42**	**558**	**81**	**193**	**27,992**
Stainless Steel 410	410	59	483	70	210	30,458
ASTM A252 Grade 1	205	30	345	50	210	30,458
ASTM A252 Grade 2	240	35	414	60	210	30,458
ASTM A252 Grade 3	310	45	4550	66	210	30,458
ASTM A333 Grade 6	**240**	**35**	**415**	**60**	**200**	**29,008**
ASTM A514 Grade F	590	86	800	116	210	30,458

Table 20. Material Properties (continued).

Material	Shear Modulus of Elasticity		Poisson's Ratio	Endurance Limit		Density
	GPa	ksi		MPa	ksi	kg/m^3
Stainless Steel 316L	**77**	**11,168**	**0.5**	**279**	**40**	**7990**
Stainless Steel 410	80	11,603	0.5	242	35	7850
ASTM A252 Grade 1	80	11,603	0.5	173	25	7850
ASTM A252 Grade 2	80	11,603	0.5	207	30	7850
ASTM A252 Grade 3	80	11,603	0.5	228	33	7850
ASTM A333 Grade 6			**0.3**	**207**		
ASTM A514 Grade F				400		

It is important to note that high-strength steels do not necessarily offer weight savings in this application. Gerwick (2007) emphasizes that when buckling and vibration are key concerns, stiffness, rather than yield stress, governs failure. Also, the harsh Muskeget Channel environment mandates that any steel used must be specified for low-temperature service to prevent premature fatigue failure, especially in welded joints. Particularly, it must show high Charpy impact values at low temperatures. The American Petroleum Institute classifies steels in groups I—III by strength and classes C—A by toughness. For the reasons above, a Group I, Class A steel is desirable, so quotes were sought for ASTM A333 Grade 6 tubing (American Petroleum Institute, 1993).

Corrosion

According to Corus (2005), steel in the continually immersed zone "acquires a protective blanket of corrosion products and marine growth" and exhibits an average mean corrosion rate of 0.035mm/year/side. Tomlinson (2008) echoes this in saying that in the continuously immersed zone, piles should use bare steel or cathodic protection. He quotes a study by Morley and Bruce (1983)of steel piles in the UK that reports an average loss of thickness of 0.05 mm/year in the immersion zone, with a 95% maximum probable rate of 0.14 mm/year. Furthermore, he points out that if the interior of a tubular member is sufficiently isolated from the external environment, the oxygen in the trapped seawater will quickly be "used up in the early corrosion process, leaving none to maintain the corrosion."

A sacrificial anode system is often an economical anti-corrosion measure. Such a system could be implemented simply by using commercially available zinc shaft collars around the truss members or by mounting zinc bars between members, as is sometimes practiced in offshore structures. While it would require occasional maintenance, the anodes would simply need to be replaced when they are observed to be depleted. As to concerns of biofouling, Blackwood et al. (2010) published their findings that "anodes remain effective even after being completely coated with biofouling".

If cathodic protection is used in conjunction with high-strength steels, Billingham et al. (2003) emphasizes that great care must be taken to mitigate hydrogen cracking. Gerwick (2007) adds that cathodic protection is prohibited in areas where the flow of water is restricted.

Lifting

The telescoping piles will be raised by buoyant forces. Air will be pumped into the upper pile section (or released from a compressed air tank). The position and rate of ascent will be moderated by scissor arms (as shown in Figure 15).

As an alternative, water was also considered as the pumping fluid. A seawater pump could be mounted on either the foundation or the rising platform and used to pump pressurized seawater into the pile sections to effectively form a seawater hydraulic system. The U.S. Navy and other researchers have been investigating comparable systems in recent years (Krutz & Chua, 2004; Jokela & Kunsemiller, 1996), but the Muskeget Channel system would require much less pressure than most other systems because of the large cross-sectional areas of the piles. However, a seawater system would have to overcome major difficulties. For instance, the interface between pile sections would have to remain sealed while subjected to large lateral forces in a corrosive environment.

Costing

Materials/Construction

Material costs for the gravity foundation were based on shore forming and estimating the city-factored cost of concrete from RS Means (2011) with Overhead and Profit included, assuming that concrete would account for the entire weight of the base structure (i.e. neglecting the possibility of using sediment as fill.) This included forming materials and anti-corrosion treatment. The components of the foundation are shown for each platform size in Table 21. The cost of the anti-scour skirt was determined from the per-pound estimate of ASTM A252 Gr. 3.

Table 21. Gravity base weight breakdown.

Turbine Diameter			**4 m (14 ft)**	**9 m (29 ft)**	**13 m (43 ft)**	**17 m (57 ft)**
Material	Type	Percent by Weight			Weight, tons	
Cement	Portland, type I,II	11%	25	60	101	149
Aggregate--coarse	Sand+stone, crushed bank gravel, loaded at site	67%	155	364	617	905
Water		16%	37	87	147	216
Air		6%	14	33	55	81
Total		**100%**	**231**	**544**	**920**	**1,351**

The material cost of the piles was estimated from a quote from L.B. Foster for ASTM A252 Gr. 3 steel piles on a per-pound basis. Although it is recommended that the steel mounting structure be left bare as a cost-saving measure, the cost of corrosion protection was included in the estimate in case it is deemed necessary. This cost was based on a quote from L.B. Foster (2010) for marine-grade epoxy coating over the exterior surface area of the platform. The cost of the cross bracing and turbine mounting structure was scaled from an estimate by J.F. White (2011) of $50,000 for the corresponding elements of the pile foundations for a turbine size of 13 m (43 ft.). This cost was assumed to vary linearly with the turbine size.

The cost of the variable-buoyancy system was estimated by using the per-pound cost of ASTM A252 Gr. 3 as the cost of the integrated ballast tanks, the cost of ASTM A333 Gr. 6 for the necessary piping, and the per-pound welding cost as above. The price of twenty (20) stainless steel 2" ball valves with remote activation was obtained from Swagelok. The most expensive type was used in order to compensate for other valves, etc. not included in the cost analysis. (Corrosion in these components will need to be given careful consideration during the detailed design phase because stainless steel acts as the sacrificial anode to most structural steels.)

Installation

The installation cost was based on a crane barge of sufficient capacity to carry and install the foundation, in use for 7 (seven) days with 4 (four) days of mobilization/demobilization. Quotes were obtained from Manson Construction of California (2010) and Weeks Marine of New Jersey (2012) for crane barges of various capacities. The estimated costs of a Telescoping Pile platform for various turbine capacities are shown in Table 22.

Table 22. Cost of Telescoping Gravity Foundation Platform.

Turbine Diameter			**4 m**	**(14 ft)**	**9 m**	**(29 ft)**
	Unit cost	**Unit**	**Quantity**	**Cost**	**Quantity**	**Cost**
Base						
Cement	$0.12	lb	50,828	$6,245	119,585	$14,694
Aggregate-coarse	$23.50	ton	155	$3,638	364	$8,558
Anti-corrosion Treatment	$10.05	C.Y.	114	$1,148	269	$2,701
Forming	$10.95	SFCA	1,091	$11,943	1,827	$20,005
Anti-scour Skirt	$1.87	lb	31,465	$58,913	48,263	$90,364
Support Structure						
Piles	$1.87	lb	166,248	$311,270	348,537	$652,575
Anti-corrosion Coating	$4.02	ft^2	202	$812	423	$1,702
Platform	$1,852	EA	1	$1,852	1	$14,815
Variable Buoyancy						
Steel (Pressure Vessel, Bulkheading)	$1.87	lb	10,390	$19,454	21,784	$40,786
ASTM A333 Gr. 6 Piping	$1.64	lb	8312	$13,646	17427	$28,609
Welding			1	$1,852	1	$14,815
2" Ball Valves	$1,370	EA	20	$27,400	20	$27,400
Installation						
Mobilization/Demobilization	$24,000	days	4	$96,000	4	$96,000
Working	$52,500	days	7	$367,500	7	$367,500
Total				**$921,673**		**$1,380,524**

O&P, shipping included throughout

Site work not included

Table 22. Cost of Gravity Foundation Platform (continued).

Turbine Diameter			13 m	(43 ft)	17 m	(57 ft)
	Unit cost	Unit	Quantity	Cost	Quantity	Cost
Base						
Cement	$0.12	lb	202,484	$24,880	297,173	$36,514
Aggregate-coarse	$23.50	ton	617	$14,491	905	$21,268
Anti-corrosion Treatment	$10.05	C.Y.	455	$4,573	668	$6,712
Forming	$10.95	SFCA	2,551	$27,929	3,282	$35,936
Anti-scour Skirt	$1.87	lb	62,802	$117,585	76,082	$142,450
Support Structure						
Piles	$1.87	lb	530,827	$993,881	696,544	$1,304,158
Anti-corrosion Coating	$4.02	ft^2	644	$2,592	845	$3,401
Platform	$1,852	EA	1	$50,000	1	$118,519
Variable Buoyancy						
Steel (Pressure Vessel, Bulkheading)	$1.87	lb	33,177	$62,118	43,534	$81,510
ASTM A333 Gr. 6 Piping	$1.64	lb	26541	$43,573	34827	$57,175
Welding			1	$50,000	1	$118,519
2" Ball Valves	$1,370	EA	20	$27,400	20	$27,400
Installation						
Mobilization/Demobilization	$24,000	days	4	$96,000	4	$96,000
Working	$52,500	days	7	$367,500	7	$367,500
Total				**$1,882,521**		**$2,417,062**

O&P, shipping included throughout

Site work not included

It is important to note that the largest crane barge for which a quote was obtained is not sufficient for lifting the combined weight of the platform for turbine sizes 13 m (43 ft.) or 17 m (57 ft.) Alternative installation methods could include temporary buoyancy and towing to the site. Gerwick (2010) describes detailed steps for constructing a gravity foundation "raft" consisting of a concrete honeycomb structure whose buoyancy is moderated by controlling the amounts of compressed air in each cell. The telescoping piles or the steel anti-scour skirt could also be utilized for buoyancy during installation.

CHAPTER 4

FOUR-PILE FOUNDATION PLATFORM

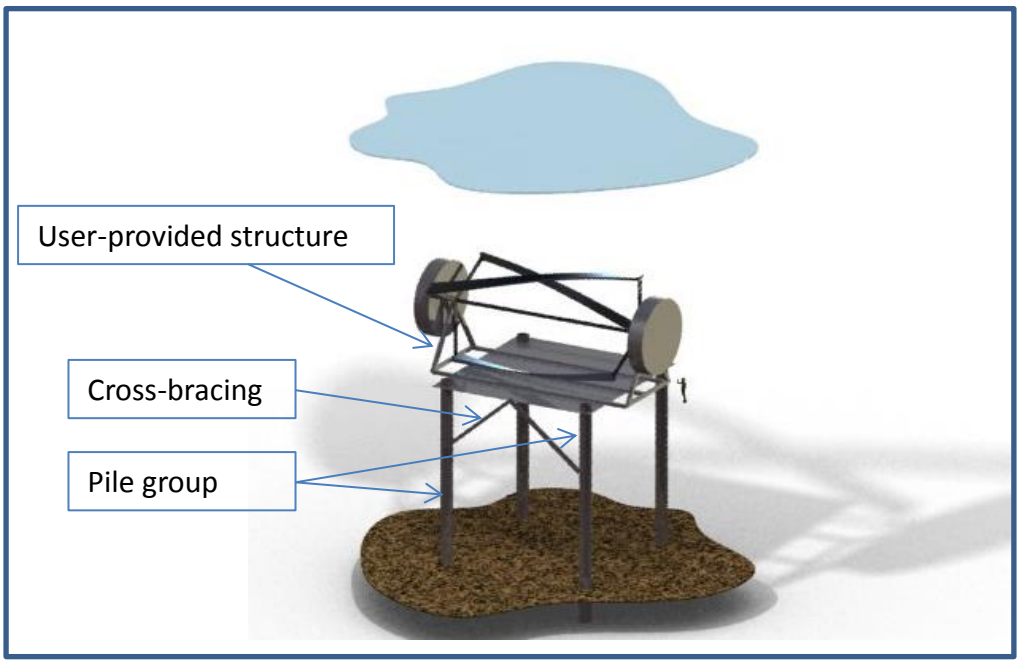

Figure 22. The 4-pile platform concept shown mounting a 9 m by 15 m (29 ft by 49 ft) horizontal axis turbine. A 2 m (6.6 ft) diver is shown for scale.

A subsurface, four-pile group with mounting structure at mid depth, illustrated in Figure 22, was considered for the following advantages:

- The platform would be below most surface traffic.
- A pile group offers greater resistance to lateral loading.
- A pile group would reduce the required depth of penetration into the seafloor.

Disadvantages include:

- Platform installation, maintenance, and turbine installation/retrieval would likely be expensive.
- Scour would need to be considered.

This platform concept would comprise four fixed piles connected by stiffening (cross-bracing) members. This platform would remain in a fixed position and developers would be responsible for installing their devices on the platform at mid-depth.

Specific Design Criteria

- The foundation must place the turbine hub 15 m (49 ft.) above the seafloor.
- Each pile must be able to act as an independent cantilevered beam. (This over-predicts the diameter of the piles required.)

- The structure must be able to sustain a 2.5 m/s (5 knots) current uniform over the entire depth. (This over-estimates the total drag.)
- Steel pipe piles must be used (based on offshore oil and other industry practice).
- 1" (0.025 m) wall thickness must be used (to accommodate in-situ welding, as per Tomlinson (2008)).
- Each pile must have a safety factor against yielding of at least two.
- The pile group must have a safety factor against uplift of at least five.
- The following assumptions were made for the analysis:

- The maximum bending moment exists at the seafloor (i.e. the top of the sediment layer).
- Due to the lack of information on the sediment composition below the seafloor, two possible cases were assumed:
  1. The depth of the sand-gravel mixture is sufficient to secure the piles.
  2. Bedrock exists just below the seafloor.

Governing Equations—Statics

Pile analysis began by designing a single pile as a beam cantilevered from the seafloor, of sufficient diameter to withstand the forces applied by the current and one quarter of those on the mounted turbine. A simple Free-Body Diagram is shown in Figure 23 and the associated variables are listed in Table 23.

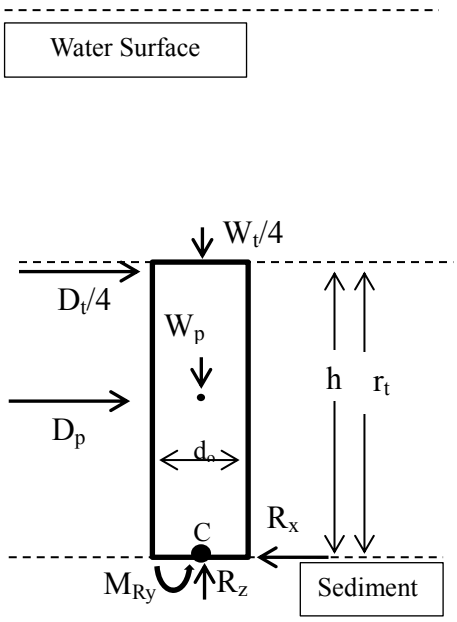

Figure 23. Free-Body Diagram of a single pile in the four-pile group.

Table 23. Pile Statics variables.

r_t	Turbine Hub from Seafloor
h	Length of Pile
W_p	Pile Weight
W_t	Turbine Weight
D_p	Pile Drag
D_t	Turbine Drag
R_z	Vertical Reaction Force
R_x	Horizontal Reaction Force
M_{Ry}	Reaction Moment
D_o	Pile Diameter

Horizontal equilibrium requires that

$$R_x = D_p + \frac{D_t}{4}. \tag{37}$$

And vertical equilibrium requires that

$$R_z = W_p + \frac{W_t}{4}. \tag{38}$$

Balancing moments about the base of the pile yields

$$M_{Ry} = D_p \frac{h}{2} + \frac{D_t}{4} r_t, \tag{39}$$

where

$$D_p = \frac{1}{2} \rho C_D A \, U_a^2, \tag{40}$$

in which

$$A = d_o h. \tag{41}$$

Using these forces and moments, the stresses at the base of the pile were calculated. Axial stress is given by

$$\sigma_A = -\frac{F_{Rz}}{A_c}, \tag{42}$$

where the cross-sectional area is

$$A_c = d_o \pi t, \tag{43}$$

where *t* is the thickness of the pile wall. Maximum bending stress, acting at the outer edge of the beam is

$$\sigma_B = \frac{M_y c}{I_y} = \frac{M_{Ry}\left(\frac{d_o}{2}\right)}{I_y}. \tag{44}$$

where the area moment of inertia of a pipe is

$$I_y = \frac{\pi d^3 t}{8}. \tag{45}$$

Maximum shear stress in a thin-walled hollow cylinder, acting at the neutral axis of the beam is given by

$$\tau_{max} = 2\frac{V}{A}. \tag{46}$$

where *V* is the shearing force.
Assuming a long pile, shear stress (being a minimum at the outer edge of the beam) is disregarded, so that the maximum normal stress in the pile is the sum of bending and stresses at

the downstream outer edge of the pile,

$$\sigma_{max} = \sigma_B + \sigma_A. \tag{47}$$

A factor of safety for the pile then, based on compressive failure of the pile material, is

$$SF = \frac{\sigma_{yield_{comp}}}{\sigma_{max}}. \tag{48}$$

Because of the interdependence between pile diameter and drag on the pile, the diameter was iterated until the safety factor equaled 2 for the chosen material. Results are combined with limits due to soil mechanics and are summarized in Table 27. The material chosen was ASTM A252 Grade 3 steel, which is a common material for marine piling. Its properties are listed in Table 24, alongside alternatives.

Table 24. Material properties (ASTM International, 2010; 2011; 2009).

Material	Yield Strength		Ultimate Tensile Strength		Modulus of Elasticity	
	MPa	ksi	MPa	ksi	GPa	ksi
Stainless Steel 316L	290	42	558	81	193	27,992
Stainless Steel 410	410	59	483	70	210	30,458
ASTM A252 Grade 1	205	30	345	50	210	30,458
ASTM A252 Grade 2	240	35	414	60	210	30,458
ASTM A252 Grade 3	**310**	**45**	**4550**	**66**	**210**	**30,458**

Table 24. Material properties (continued).

Material	Shear Modulus of Elasticity		Poisson's Ratio	Endurance Limit		Density
	GPa	ksi		MPa	ksi	kg/m^3
Stainless Steel 316L	77	11,168	0.5	279	40	7990
Stainless Steel 410	80	11,603	0.5	242	35	7850
ASTM A252 Grade 1	80	11,603	0.5	173	25	7850
ASTM A252 Grade 2	80	11,603	0.5	207	30	7850
ASTM A252 Grade 3	**80**	**11,603**	**0.5**	**228**	**33**	**7850**

Governing Equations—Soil Mechanics

A pile's bearing ability is broken down into its resistance to vertical and lateral loading. Both analyses are described below.

Vertical Capacity

For Case 2, in which bedrock exists just below the seafloor, it is assumed that the pile material will fail before the bedrock (Das, 2000) if the pile is embedded a depth of 3 diameters. For Case 1, in which there is a sufficient depth of sand-gravel to secure the pile, several methods are available for calculating a pile's vertical bearing capacity. Meyerhof's method (as described by Das) was used. This method calculates the point bearing capacity of the pile tip and the friction bearing capacity of the pile. Given the pile diameter and vertical reaction force found in the mechanics analysis, the pile depth into the sediment was iterated until the required safety factor was met. A safety factor of seven was imposed because of the high uncertainty involved with soil analysis. The soil parameters used in this analysis, along with intermediate values and the results of the Meyerhof calculations for sample pile dimensions are given in Table 25.

Table 25. Pile vertical capacity sample calculations, using Meyerhof's method.

Sediment Type		Sand			
Pile Diameter	Do	0.88	m	2.9	ft
Vertical Reaction Force		298,330		67,607	lbf
Pile Depth in Sediment	d	6.5	m	21	ft
Soil Density		Dense			
Point Bearing					
End Condition	end	open			
Point Area	Ap	0.07	m^2	0.77	ft^2
Unit Weight	gamma	17,000	N/m^3	108	lbf/ft^3
Soil Friction Angle	phi	0.61	rad	35	deg
Bearing Capacity Factor	N*q	143			
Effective Vertical Stress	q'	145,205	Pa	21	psi
Point Resistance	Q_p	1,477,318	N	332,114	lbf
Limiting Point Resistance	Ql	356,197	N	80,076	lbf
Skin Friction					
Effective Earth Pressure Coefficient	K	0.60			
Average Effective Overburden Pressure	sigmabar'0	155,250	Pa	23	psi
Soil-pile friction angle	delta'	35 deg			
Critical Depth	L'	13	m	44	ft
Embedment Ratio	L-D	7			
Ultimate Skin Resistance	Qs	897,248	N	201,709	lbf
Vertical Load Safety Factor:	SF_vert	4.2			

Legend:

Environmental parameters
Iterated values
Design inputs*
Calculated values

*Pile diameter and vertical reaction force are determined from the mechanics analysis.

Lateral Capacity

The ultimate lateral bearing capacity of a pile is significantly more complicated than the vertical capacity. As with the vertical capacity, a pile in bedrock is assumed to fail in material before the supporting rock gives way. But for Case 1, which entirely assumes a sand-gravel mix, Brom's method was used. This method is described for soils below the water table in the DOT Federal Highway Administration publication, *Design and Construction of Driven Pile Foundation* (1998). Given the pile diameter and lateral reaction force found in the mechanics analysis, the pile depth into the sediment was iterated until Brom's analysis showed that the pile was "long." This means that the pile material will yield before the soil. The inputs and results of each step of that analysis are shown in Table 26 for sample pile dimensions.

Table 26. Pile lateral capacity using Brom's method, sample calculation.

Brom's Method				From "Design and Construction of Driven Pile Foundations", VI p. 9-74	
Pile Diameter	Do	0.88	m		
Pile Depth in Sediment	d	6.5	m		
Soil Type		Cohesionless		Step #1	
Coefficient of Horizontal Subgrade Reaction	Kh	10857000	N/m^3	Step #2, for Dense, cohesionless soil below groundwater (From Terzaghi)	
Kh adjusted for loading, soil conditions	Kh_cyc	5428500	N/m^3	Step #3 For cyclic loading ("Cyclic loading (for earthquake loading) in cohesionless soil")	
Eccentricity of Applied Load	ec	15	m	Step #4	
Shape Factor	Cs	1.3		Step #4 For circular Piles	
Resisting Moment of Pile	My	6391111	N-m		
Length Factor	eta	0.374	/m	Step #5 for cohesionless piles	
Dimensionless Length Factor	etaD	2.4		Step #6	
Pile Length Type		Intermediate		Step #7a	
Rankine passive pressure coefficient for cohesionless soil	RKp	3.7		Step #8a	
Average Effective Unit Weight	gamma'	6955	N	Step #8b	Unit Weight of sand minus that of water
Cohesion	cu	0		Step #8c	Cohesionless
Long				Step #9d	
Dimensionless Factor	My/(b^4* gamma*Kp)	394.1			
Dimensionless Factor ec/b		16.8			
Dimensionless Load Factor	Qu/(Kp*b^3*gamma)	105		From Figure 9.30	
Short					
Dimensionless Factor, D/b		7.3		Step #9c	
Dimensionless Factor, ec/D		2.3			
Dimensionless Load Factor	Qu/(Kp*b^3*gamma)	75		From Figure 9.29	
Ultimate Lateral Load	Qu	1,364,266	N	Step #9	
Lateral Safety Factor	SF_lat	**7.9**			
Recommended Safety Factor	NY_SF	2.5		Step #10	
Max allowable load	Qm	545707			
Factor	y(EI)^3/5*Kh^(2/5)/(QaD)	0.2		Step #11	
Deflection at point of loading	y	0.001	m	From Figure 9.32	

Legend:

Environmental parameters
Iterated values
Design inputs*
Values calculated from formulae
Values determined from figures

*Pile diameter and the reaction bending moment are determined from the mechanics analysis.

Uplift

In addition to lateral and vertical bearing capacity, uplift must be considered to prevent pull-out in a pile group. A basic, worst-case view of this scenario—treating the pile group as rigid and neglecting the weight of a turbine and the reaction moment on each pile—is shown in Figure 24.

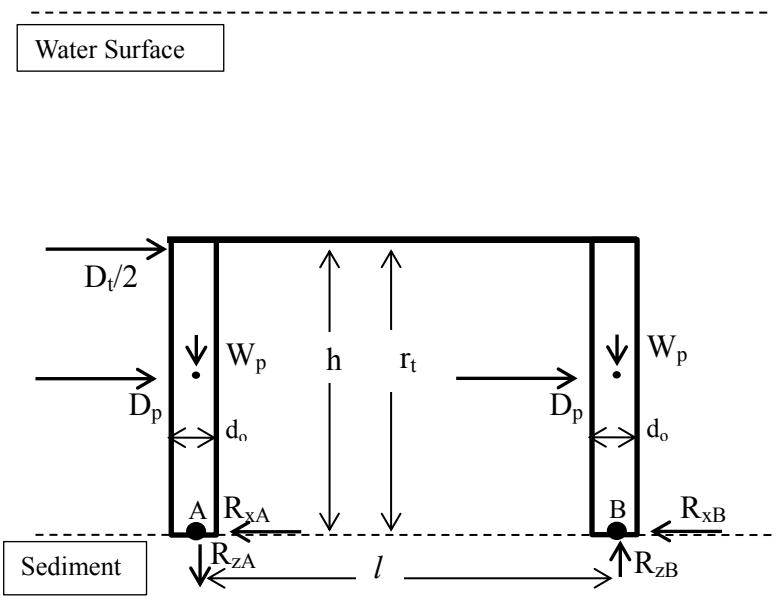

Figure 24. Free Body Diagram of pile group.

Summing the moments about point B shows that equilibrium is maintained if

$$R_{zA}l + W_p l = \frac{h}{2} 2D_p + h\frac{D_t}{2}. \tag{49}$$

So the Ultimate Skin Resistance (Q_s in Table 25) must exceed R_{zA} in this analysis to prevent pull-out. This requirement was quantified by defining an uplift safety factor,

$$SF_{uplift} = \frac{Q_s}{R_{zA}}, \tag{50}$$

which was found to be greater than five for each design.

Scour

Anti-scour structure must be designed with care. Rocker (1985) indicates that a steel skirt extending one diameter beyond each pile can adequately protect against scour and such features were included in the design of the pile foundation platform. Planned biofouling and scour experiments in the Muskeget Channel this summer will inform an investigation of the economics and effectiveness of various methods.

Results

The design processes above were integrated in the following procedure for each maximum turbine size specified:

- A pile wall thickness (1 inch for all designs) was selected (to accommodate in-situ welding).
- The diameter of each pile was iterated until the mechanics analysis showed that the required safety against yielding was met.
- The depth to which the pile would be driven into the soil was iterated until requirements for both vertical and lateral capacity were satisfied.
- Uplift was analyzed to ensure that the specified safety factor was satisfied.
- Vortex-Induced Vibration (VIV) was analyzed and it was found that the piles as designed would not experience significant vibration unless subjected to velocities at least twice those expected in the channel. Also, cross-bracing members were designed with sufficient Combined Relative Stiffness such that VIV would not occur unless subjected to the same velocities.

The results of the design of the four-pile platform are shown in Table 27.

Table 27. Four-pile platform parameters.

Turbine Diameter	4 m (14 ft)				9 m (29 ft)			
Pile Depth in Sediment	5	m	18	ft	8	m	26	ft
Turbine Distance from Bottom	15	m	49	ft	15	m	49	ft
Pile Height from Bottom	15	m	49	ft	15	m	49	ft
Pile								
Material	ASTM A252 Grade 3				ASTM A252 Grade 3			
Number of Piles	4				4			
Diameter of Pile	0.34	m	1.12	ft	0.64	m	2.12	ft
Thickness of Pile	0.0254	m	1.00	in	0.0254	m	1.00	in
Mass of Pile	4,366	kg	9,625	lbm	9,211	kg	20,306	lbm
Compression Safety Factor	**2.0**				**2.0**			
Max Stress/ Endurance Limit	**0.7**				**0.7**			
Pile Type in Soil	Long				Long			
Velocity for Transverse Vibration	1.4	m/s			4.1	m/s		

Legend:

Iterated values
Design inputs
Calculated values

Table 27. Four-pile platform parameters (continued).

Turbine Diameter	13 m (43 ft)				17 m (57 ft)			
Pile Depth in Sediment	10	m	32	ft	12	m	38	ft
Turbine Distance from Bottom	15	m	49	ft	15	m	49	ft
Pile Height from Bottom	15	m	49	ft	15	m	49	ft
Pile								
Material	ASTM A252 Grade 3				ASTM A252 Grade 3			
Number of Piles	4				4			
Diameter of Pile	0.95	m	3.12	ft	1.26	m	4.13	ft
Thickness of Pile	0.0254	m	1.00	in	0.0254	m	1.00	in
Mass of Pile	14,786	kg	32,598	lbm	21,018	kg	46,337	lbm
Compression Safety Factor	**2.0**				**2.0**			
Max Stress/ Endurance Limit	**0.7**				**0.7**			
Pile Type in Soil	Long				Long			
Velocity for Transverse Vibration	7.8	m/s			12.3	m/s		

Costing

Several Marine Contractors, including J.F. White, Pihl U.S., and Sea and Shore, were contacted for rough estimates of the cost for installation of two 56” (1.42 m) piles or four 24” (0.61 m) piles (corresponding to early designs for the 13 m (43 ft) turbine platform). J.F. White proposed the following installation procedure:

> A marine piling operation would be mobilized and consist of a 54' x 180' barge with a 200 TN lattice boom crane set on top. All construction materials, templates and equipment would also be placed on the barge. The barge would be mobilized from a main land marine facility and towed to the location of work. The sequence of work would be to construct templates, install piles and set platforms. In the event that bedrock is encountered above the proposed pile tip elevation, JFW would use a "down the hole hammer" to remove the bedrock and create a rock socket. Concrete and reinforcing steel would then be placed in the toe of the pile to provide the required embedment and stability of the pile system.

The contractor provided estimates for installing piles of the aforementioned size for both the case in which bedrock exists just beneath the seafloor and that in which there is sufficient sediment overburden to hold the piles, while strongly recommending that soil testing be conducted before installation. These estimates were scaled under the assumption that the entire installation cost was proportional to the volume of sediment removed by drilling or enclosed by the pile. The estimate carried $50,000 to construct the platform to which the turbine would mount. This was assumed to vary linearly with the size of the turbine. The results from this analysis are shown in Table 28.

Table 28. Cost of Fixed Four-pile Platform.

Turbine Diameter			**4 m**	**(14 ft)**	**9 m**	**(29 ft)**
	Unit Cost	Unit	Qty.	Cost	Qty.	Cost
Foundation						
Piles, Installed	$68,553	EA	4	$274,215	4	$956,860
Anti-corrosion Coating	$4.02	ft^2	740	$2,980	1562	$6,286
Anti-scour Mat	$1.87	lb	1854	$3,471	2271	$4,253
Support Structure						
Platform	$1,852-$118,519	EA	1	$1,852	1	$14,815
Total				**$282,518**		**$982,215**

O&P, shipping included throughout

Site work not included

Table 28. Cost of Fixed Four-pile Platform (continued).

Turbine Diameter			**13 m**	**(43 ft)**	**17 m**	**(57 ft)**
	Unit Cost	Unit	Qty.	Cost	Qty.	Cost
Foundation						
Piles, Installed	$68,553	EA	4	$1,991,978	4	$3,204,822
Anti-corrosion Coating	$4.02	ft^2	2508	$10,092	3565	$14,345
Anti-scour Mat	$1.87	lb	2693	$5,042	3119	$5,841
Support Structure						
Platform	$1,852-$118,519	EA	1	$50,000	1	$118,519
Total				**$2,057,112**		**$3,343,526**

O&P, shipping included throughout

Site work not included

CHAPTER 5

TWO-PILE FOUNDATION PLATFORM

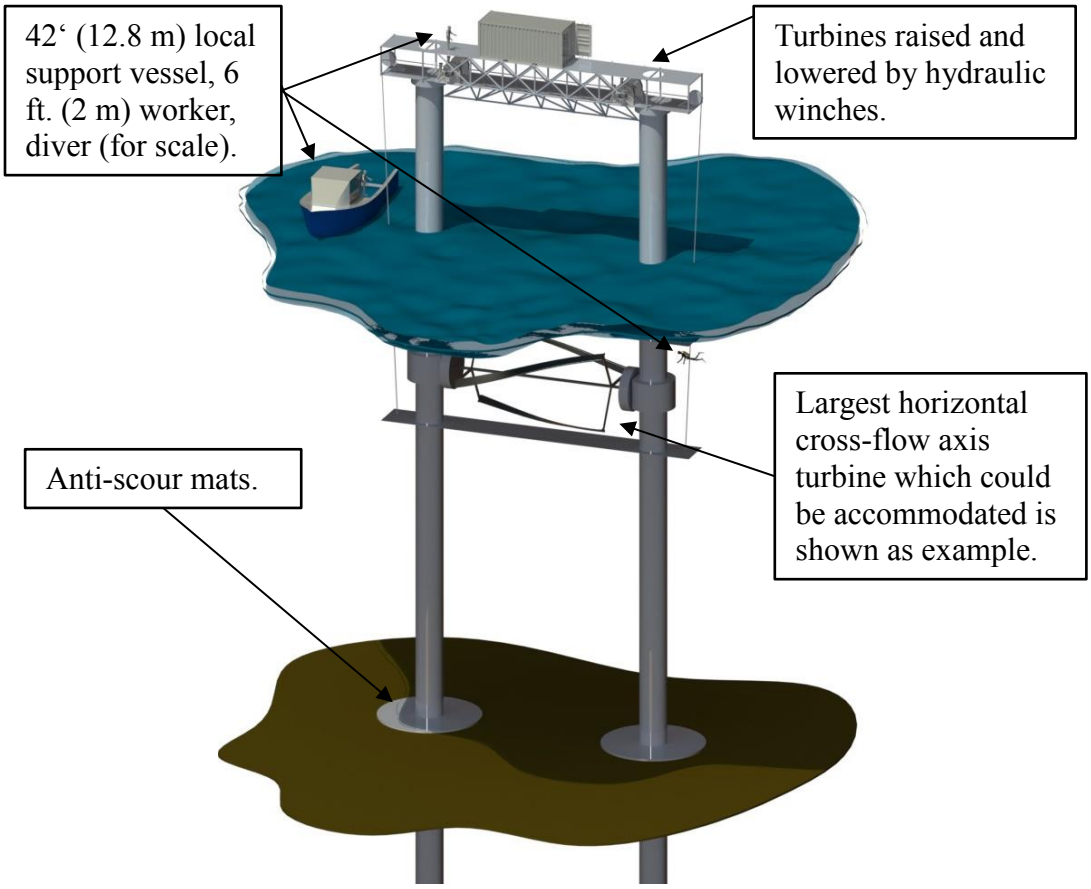

Figure 25. The 2-pile platform concept, shown mounting a 6 by10 m (20 by 33 ft.) cross-flow axis turbine.

A surface-piercing, self-raising, two-pile foundation, as shown in Figure 25, was considered for the following advantages:

- The platform would greatly reduce the cost and ease of turbine installation/retrieval and maintenance by bringing the device to the sea surface for service.
- A permanent, visible infrastructure presence could be useful for navigation and for public relations (Barrett, 2012).
- Disadvantages include the following:
- Marine traffic would need to avoid the surface presence.
- A surface presence could raise objections over alterations to the existing viewscape.
- The surface structure could become a target for vandalism.
- Scour would need to be considered.

This platform concept, shown in Figure 25, would include a mounting structure raised and lowered along two upright piles which provide the integrity of the overall structure. A working

platform would rigidly connect the two piles. A winch, wire-rope, and chain system (described later) would provide the lifting capability.

Specific Criteria

- The foundation must place the turbine hub 15 m (49 ft.) above the seafloor.
- In addition to current loading, the platform must survive a 15 m (49 ft.) storm wave.
- Each pile must be able to act as an independent cantilevered beam. (This over-predicts the diameter of the piles required.)
- The structure must be able to sustain a 2.5 m/s (5 knots) current uniform over the entire depth. (This over-estimates the total drag.)
- Steel pipe piles must be used (based on offshore oil and other industry practice).
- 2” (0.05 m) wall thickness must be used (in order to allow for in-situ welding).
- Each pile must have a safety factor against yielding of at least two.

The following assumptions were made for the analysis:

- The maximum bending moment exists at the seafloor.
- Due to the lack of information on the sediment composition below the seafloor, two possible cases were assumed:
  1. The depth of the sand-gravel mixture is sufficient to secure the piles.
  2. Bedrock exists just below the seafloor.

Governing Equations—Statics

Piles were analyzed as beams cantilevered from the seafloor, of sufficient diameter to withstand the forces applied by the current and the mounted turbine. A simple Free-Body Diagram is shown in Figure 26 and the associated nomenclature is given in Table 29

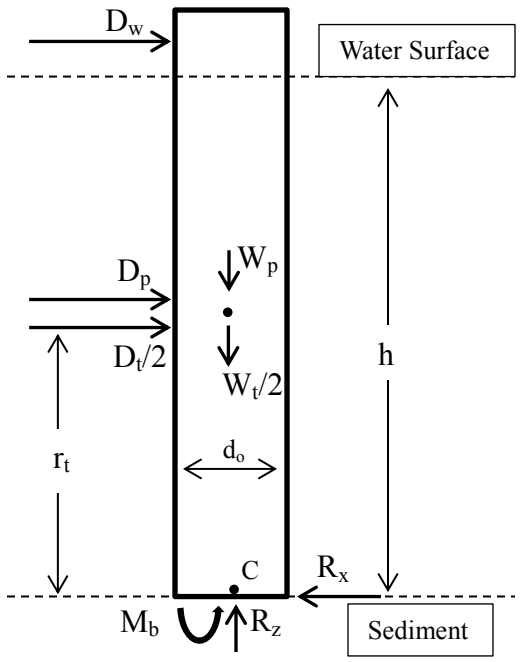

Figure 26. Free-Body Diagram of a single pile in a 2-pile group

Table 29. Pile Statics Variables

r_t	Turbine Hub from Seafloor
h	Length of Pile
W_p	Pile Weight
W_t	Turbine Weight
D_p	Pile Drag
D_t	Turbine Drag
D_w	Wind Drag on Pile
R_z	Vertical Reaction Force
R_x	Horizontal Reaction Force
M_b	Reaction Moment
d_o	Pile Diameter

Horizontal equilibrium requires that

$$R_x = D_p + D_W + \frac{D_t}{2}. \tag{51}$$

And vertical equilibrium requires that

$$R_z = W_p + \frac{W_t}{2}. \tag{52}$$

Balancing moments about the base of the pile yields

$$M_b = D_p \frac{h}{2} + D_W h + \frac{D_t}{2} r_t, \tag{53}$$

where

$$D_p = \frac{1}{2}\rho C_D A_S U^2, \tag{54}$$

and

$$D_W = \frac{1}{2}\rho_{air} C_D A_W U_W^2. \tag{55}$$

Here the submerged area is given by

$$A_S = h d_o, \tag{56}$$

and the area exposed to the wind is given by

$$A_E = h_2 d_o, \tag{57}$$

where h_2 is the height of the pile above the waterline. A value of C_D=0.7 was used to calculated both D_W and D_p. Furthermore, a design wind speed of 15 m/s (30 knots) was used to calculate the wind drag on the pile. Using these forces and moments, the stresses at the base of the pile were calculated. Axial stress is given by

$$\sigma_A = -\frac{R_z}{A_c}, \tag{58}$$

where the cross-sectional area is

$$A_c = d_o \pi t. \tag{59}$$

Here t is the thickness of the pile wall. Maximum bending stress, acting at the outer edge of the beam is

$$\sigma_B = \frac{M_y c}{I_y} = \frac{M_{Ry}\left(\frac{d_o}{2}\right)}{I_y}, \tag{60}$$

where the area moment of inertia of a pipe is

$$I_y = \frac{\pi d^3 t}{8}. \tag{61}$$

Maximum shear stress in a hollow cylinder, acting at the neutral axis of the beam is given by

$$\tau_{max} = 2\frac{V}{A}, \tag{62}$$

where V is the shearing force. Assuming a long pile, shear stress (being a minimum at the outer edge of the beam) is disregarded, so that the maximum normal stress in the pile is the sum of bending and stresses at the downstream outer edge of the pile,

$$\sigma_{max} = \sigma_B + \sigma_A. \tag{63}$$

A factor of safety for the pile then, based on compressive failure of the pile material, is

$$SF = \frac{\sigma_{yield_{comp}}}{\sigma_{max}}. \tag{64}$$

Because of the interdependence between pile diameter and drag on the pile, the diameter was iterated until the safety factor equaled 2 for the chosen material, ASTM A252 Grade 3 steel, which is a common material for marine piling. Results were combined with soil mechanics and wave loading analysis, and are given in Table 36. Steel properties are listed in Table 30, alongside alternatives.

Table 30. Material properties (ASTM International, 2010; 2011; 2009).

Material	Yield Strength		Ultimate Tensile Strength		Modulus of Elasticity	
	MPa	ksi	MPa	ksi	GPa	ksi
Stainless Steel 316L	290	42	558	81	193	27,992

Stainless Steel 410	410	59	483	70		210	30,458
ASTM A252 Grade 1	205	30	345	50		210	30,458
ASTM A252 Grade 2	240	35	414	60		210	30,458
ASTM A252 Grade 3	**310**	**45**	**455**	**66**		**210**	**30,458**

Table 30. Material properties (continued).

Material	Shear Modulus of Elasticity		Poisson's Ratio	Endurance Limit		Density
	GPa	ksi		MPa	ksi	kg/m^3
Stainless Steel 316L	77	11,168	0.5	279	40	7990
Stainless Steel 410	80	11,603	0.5	242	35	7850
ASTM A252 Grade 1	80	11,603	0.5	173	25	7850
ASTM A252 Grade 2	80	11,603	0.5	207	30	7850
ASTM A252 Grade 3	**80**	**11,603**	**0.5**	**228**	**33**	**7850**

In addition to static loading, low-cycle fatigue due to tidal cycles was also considered.

The endurance limit listed in Table 30 is the uncorrected limit, calculated as 50% of the ultimate tensile strength. To properly consider the effect of fatigue, the corrected endurance limit must be used, defined by the equation

$$S_e = C_{load} C_{size} C_{surf} C_{temp} C_{reliab} S_e', \tag{65}$$

whose terms are listed in Table 31 using the method for fully-reversed bending described by Norton (2006).

Table 31. Endurance limit correction factors.

S_e`	228 MPa	$0.5\sigma_{ut}$
C_{load}	1	For bending
C_{size}	0.6	For diameters>0.25 m
C_{surf}	0.41	For salt water corrosion
C_{temp}	1	For T<450^{o}C
$C_{reliability}$	0.81	For 99% reliability
S_e	46 MPa	

Using the corrected endurance limit, a S-N diagram (showing material strength, S, as a function of loading cycles, N) was created to show the effect of fatigue. An example (for the case of a platform capable of deploying a 9 m diameter turbine) is shown in Figure 27.

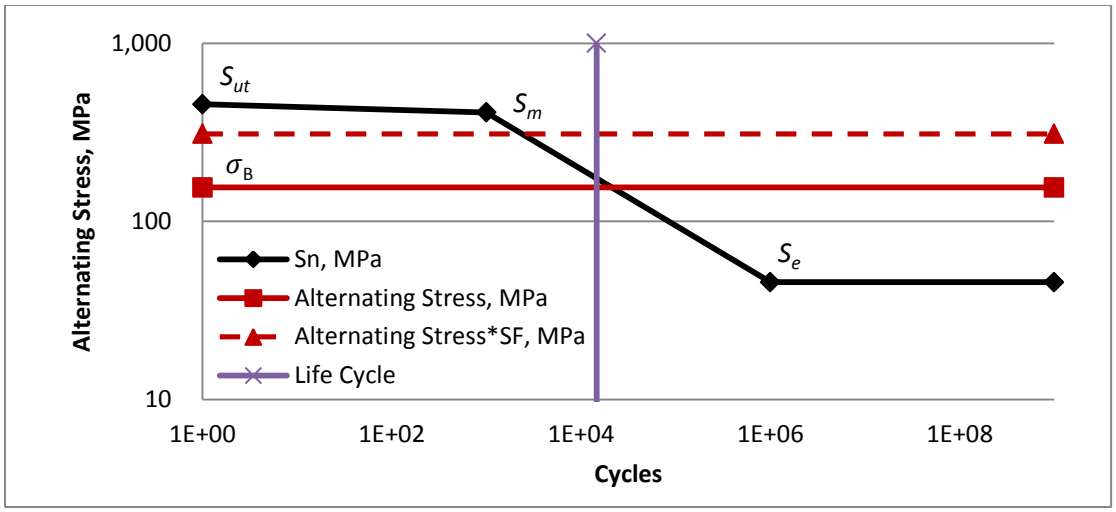

Figure 27. S-N diagram for steel pile in seawater under fully-reversed loading. 1.4X104 corresponds to a 20-year life cycle.

In this figure, S_m is the strength at 10^3 cycles, given as $S_m = 0.9S_{ut}$, where S_{ut} is the ultimate stress. The strength of the material is taken to decrease logarithmically from S_m to S_e between 10^3 and 10^6 cycles. A design life of 20 years corresponds to 14,600 tidal cycles over which the turbine and structure drag loading will be fully reversed. In the example shown, the calculated allowable stress at this point in the life cycle will be 326 MPa. Since the fully-reversed bending stress is 155 MPa, this results in a fatigue safety factor of about 2.2, which is higher than the safety factor of 2 required against yielding in the static analysis.

Governing Equations—Wave Loading

Since it would be permanently fixed to the seafloor, the Two-pile Foundation Platform must be capable of surviving a storm wave event. The design wave used was equal to the largest single wave observed at nearby Block Island, RI, during the 2012 Super-storm Sandy, with a height of 15 m and a period of 14 s (Seymour et al., 2012). The forces and moments that this wave would exert on the platform structure were determined as follows.

The problem of wave forces on a vertical cylinder is well known (see, for example, Techet (2004)). Morrison's Equation states that the total force in the direction of wave propagation, F_w is

$$F_w(t) = \rho C_m V \dot{U} + \frac{1}{2}\rho C_d A U|U|, \tag{66}$$

where ρ is the fluid density, C_m is the cylinder's mass coefficient, V is the volume, U is the fluid velocity, and C_d is the coefficient of drag. The mass coefficient for a cylinder in oscillating fluid flow is found from Table 32.

Table 32. Coefficients of mass and drag (Clauss et al., 1992).

	$Re<10^5$		$Re>10^5$	
KC	C_d	C_m	C_d	C_m
< 10	1.2	2.0	0.6	2.0
≥ 10	1.2	1.5	0.6	1.5

Here the Reynolds number is defined as

$$Re = \frac{d_o U_a}{\nu}, \tag{67}$$

where U_a is the amplitude of the wave velocity and ν is the dynamic viscosity of the fluid. In this application, Re was generally on the order of 10^7. Also, KC is the Keulegan-Carpenter number, given as

$$KC = \frac{U_a T}{d_o}, \tag{68}$$

where T is the wave period. KC was generally on the order of 20 or higher. Thus, a mass coefficient of 1.5 was used.

The fluid velocity, U, is given by

$$U = U_{wave} + U_{current}, \tag{69}$$

where $U_{current}$ is assumed constant and, from linear wave theory,

$$U_{wave} = \frac{H}{2}\sigma \frac{\cosh k(h+z)}{\sinh kh} \sin kx \sin \sigma t. \tag{70}$$

Here H is the wave height; σ is the wave radian frequency; k is the wave number; h is the water depth; z is the vertical coordinate with z=0 corresponding to the mean water level; and t is time.

The largest stress in each pile (modeled as a cantilevered beam) will be the bending stress at the base. Thus, the overturning moment from each of four contributions must be considered:

- Viscous loading on the pile.
- Viscous loading on the turbine.
- Inertial loading on the pile.
- Inertial loading on the turbine.

The maximum bending moment at the base of the pile due to the viscous drag on the pile, M_D, is found by integrating the product of the maximum drag force on the pile and the moment arm from the seafloor to the surface. That is,

$$M_{D_{max}} = \int_{-h}^{0} \frac{1}{2}\rho C_d d_o \left(\frac{H}{2}\sigma \frac{\cosh k(h+z)}{\sinh kh} + U_{current}\right)^2 (h+z)dz \tag{71}$$

$$= \frac{1}{16\left(-1+e^{2hk}\right)^2 k^2}\left(e^{2hk}\rho C_d d_o[H^2\sigma^2(1 + 2h^2k^2 - \cosh 2hk + 2hk\sinh 2hk) + 16u_{cur}(H\sigma[-hk + hk\cosh 2hk + 2\sinh hk - \sinh 2hk] + h^2k^2 u_{cur}\sinh^2 2hk)]\right).$$

The maximum bending moment at the base of the pile due to inertial wave forcing, M_I, is found by integrating the maximum inertial force on the pile from the seafloor to the mean water level (because the surface elevation is zero when horizontal fluid acceleration is at a maximum). Using linear wave theory and integrating the first term of Equation (66) gives

$$M_I = \int_{-h}^{0} \rho C_m V \left(\frac{H}{2}\sigma^2 \frac{\cosh k(h+z)}{\sinh kh}\right) z\, dz \tag{72}$$

$$= \rho C_m \frac{\pi}{4} d_o^2 \frac{H}{2}\sigma^2 \frac{kh\sinh(kh) - \cosh(kh)}{k^2\sinh(kh)}.$$

The maximum bending moment at the base of the pile due to viscous loading on the turbine is

$$M_{It} = r_t F_{It}. \tag{73}$$

The inertial force on the turbine, F_{It}, was assumed to be that of a flat disc multiplied by the solidity of the turbine, S, which is the actual projected area of the device divided by its outline area. (A value of $S = 0.3$ was used.) Thus,

$$F_{It} = M' \frac{dU}{dt} S. \tag{74}$$

This is assumed to be valid if the turbine under test is be braked. Since extreme wave events can generally be forecast days in advance, this should always be the case during such events. In the above equation, M', is given by Lamb (1932) as

$$M' = \frac{8}{3}\rho\pi a^3, \tag{75}$$

where a is the radius of the disc (or the radius of the in-stream axis turbine with the same area as the device mounted).

From Equation (70) it is evident that the maximum values of U_{wave} and $\dot{U_{wave}}$ occur 90 degrees out of phase. Therefore, maximum viscous and inertial loads cannot be simply summed to find the maximum total load. Rather, the maximum total bending moment takes the form

$$M = M_V \sin(\sigma t) + M_I \cos(\sigma t), \tag{76}$$

where t represents time and, again, M_V and M_I are magnitudes. Setting the time derivative of this

equation to zero shows that the maximum combined moment occurs at time $t = \sigma^{-1}\text{atan}(M_V / M_I)$. Using this value of *t* in Equation (76) and simplifying yields

$$M_{max} = \sqrt{M_V^2 + M_I^2}, \tag{77}$$

(This result can also be obtained by observing that *sine* and *cosine* are orthogonal functions). The bending stress induced by this total moment was calculated using the method described in the statics analysis. Pile dimensions were iterated until a safety factor of 2 was achieved.

Governing Equations—Soil Mechanics

A pile's bearing ability is broken down into its resistance to vertical and lateral loading. Both analyses are described below.

Vertical Capacity

For Case 2, in which bedrock exists just below the seafloor, it is assumed that the pile material will fail before the bedrock (Das, 2000) if the pile is embedded a depth of 3 diameters. For Case 1, in which there is a sufficient depth of sand-gravel to secure the pile, several methods are available for calculating a pile's vertical bearing capacity. Meyerhof's method (as described by Das) was used. This method calculates the point bearing capacity of the pile tip and the friction bearing capacity of the pile. Given the pile diameter and vertical reaction force found in the mechanics analysis, the pile depth into the sediment was iterated until the required safety factor was met. A safety factor of seven was imposed because of the high uncertainty involved with soil analysis. The soil parameters used in this analysis, along with the intermediate values and the results of the Meyerhof calculations for sample pile dimensions are given in Table 33.

Table 33. Two-Pile vertical capacity sample calculation using Meyerhof's method.

Soil				
Pile Diameter	1.72	m	5.64	ft
Vertical Reaction Load	1,356,003			
Sediment Type	Sand			
Pile Depth in Sediment	15	m	49	ft
Soil Density	Dense			
Point Bearing				
End Condition	open			
Point Area	0.14	m^2	1.55	ft^2
Unit Weight	17,000	N/m^3	108	lbf/ft^3
Soil Friction Angle	0.61	rad	35	deg
Bearing Capacity Factor	143			
"Atmospheric" Pressure	100,000	Pa	14.5	psi
Unit Point Resistance				
Effective Vertical Stress	239,091	Pa	35	psi
Point Resistance	4,934,803	N	1,109,388	lbf
Limiting Point Resistance	722,608	N	162,449	lbf
Skin Friction				
Effective Earth Pressure Coefficient	0.60			
Average Effective Overburden Pressure	270,000	Pa	39	psi
Soil-pile friction angle	0.61	rad	35	deg
Critical Depth	27	m	89	ft
Embedment Ratio	11			
Ultimate Skin Resistance	9,740,335	N	2,189,714	lbf
Vertical Load Safety Factor:	**7**			

Legend:

Environmental parameters
Iterated values
Design inputs*
Values calculated from formulae

*Pile diameter and vertical reaction force are determined from the mechanics analysis.

Lateral Capacity

The ultimate lateral bearing capacity of a pile is significantly more complicated than the vertical capacity. As with the vertical capacity, a pile in bedrock is assumed to fail in material before the supporting rock gives way. But for Case 1, which entirely assumes a sand-gravel mix, Brom's method, as described in the DOT Federal Highway Administration publication, *Design and Construction of Driven Pile Foundation* (1998) was used. Given the pile diameter and lateral reaction force found in the mechanics analysis, the pile depth into the sediment was iterated until Brom's analysis showed that the pile was "long." This means that the pile material will yield before the soil. The inputs and results of each step of that analysis are shown in Table 34 for sample pile dimensions.

Table 34. Two-Pile lateral capacity sample calculation using Brom's method.

Brom's Method			From "Design and Construction of Driven Pile Foundations", VI p. 9-74	
Pile Diameter	1.72	m		
Pile Depth in Sediment	15	m		
Soil Type	Cohesionless		Step #1	
Coefficient of Horizontal Subgrade Reaction	10,857,000	N/m^3	Step #2, for Dense, cohesionless soil below groundwater (From Terzaghi)	
Kh adjusted for loading, soil conditions	5,428,500	N/m^3	Step #3 For cyclic loading ("Cyclic loading (for earthquake loading) in cohesionless soil")	
Eccentricity of Applied Load	17	m	Step #4	
Shape Factor	1.3		Step #4 For circular Piles	
Resisting Moment of Pile	17,700,950	N-m		
Length Factor	0.287	/m	Step #5 for cohesionless piles	
Dimensionless Length Factor	4.3		Step #6	
Pile Length Type	**Long**		Step #7a	
The result at this stage is sufficient; Brom's analysis shows that the pile will fail before the soil.				
Rankine passive pressure coefficient for cohesionless soil	3.7		Step #8a	
Average Effective Unit Weight	6955	N	Step #8b	Unit Weight of sand minus that of water
Cohesion	0		Step #8c	Cohesionless
Long			Step #9d	
Dimensionless Factor	162.3			
Dimensionless Factor ec/b	12.2			
Dimensionless Load Factor	40		From Figure 9.30	
Ultimate Lateral Load	2,753,636	N	Step #9	
Lateral Safety Factor	7.5			
Recommended Safety Factor	2.5		Step #10	
Max allowable load	1,101,455			
Factor	2		Step #11	
Deflection at point of loading	0.072	m	From Figure 9.32	

Legend:

Environmental parameters
Iterated values
Design inputs*
Values calculated from formulae
Values determined from figures

*Pile diameter and the reaction bending moment are determined from the mechanics analysis.

Dynamics—Vibration

Neglecting vibrational issues in marine structures can be catastrophic (Tomlinson, 2008, p. 413). After a suitable pile wall thickness and diameter were selected, vortex-induced vibration was investigated.

According to standard beam theory the natural frequency of a beam is found to be

$$f_N = \frac{K'}{L^2}\sqrt{\frac{EI}{M}}, \tag{78}$$

where E is Young's Modulus, I is the area moment of inertia, M is mass/unit length of the beam (including the mass of the water contained in the beam and the mass of the displaced water), L is the length of the beam, and K' is a factor of 3.56 for the first mode of vibration in members with both ends fixed. The Strouhal number can then be used to find the fluid velocity at which the frequency of vortex shedding will match the member's natural frequency. This critical velocity is given by

$$V_{crit} = K f_N d_o, \tag{79}$$

where d_o is the outer diameter of the member and K is given in Table 35.

Table 35. Coefficients for modes of Vortex-Induced Vibration(Tomlinson, 2008).

1.2	Onset of in-line motion
2.0	Maximum in-line motion
3.5	Onset of cross-flow motion
5.5	Maximum cross-flow motion

According to Mittal and Kumar (1999), "in-line oscillations are significant only if the mass of the cylinder is not too large compared with the mass of the surrounding fluid it displaces." Since the mass of the cylinder is on the order of the mass of the surrounding fluid, it was assumed that only cross-flow motion is significant. So a value of K=3.5 was chosen. Equation (79) was evaluated for each design and the minimum velocity required for the onset of vortex-induced vibration was found in all cases to exceed twice that seen in Muskeget Channel.

Scour

Anti-scour structure must be designed with care. Rocker (1985) indicates that a steel skirt extending one diameter beyond each pile can adequately protect against scour. Such structures, made of 1 inch steel, were incorporated into the design and are shown in Figure 25.

Lifting

Two main concepts were considered for raising/lowering the platform: A rack-and-pinion system and a hydraulic winch system. Each must be capable of lifting the weight of the turbine plus the friction force between the turbine mounting structure and the piles. The coefficient of friction was taken to be 0.5 for wet steel on steel (a worst-case approximation). Thus, the friction force was half the drag force on the turbine at max current.

Significant mechanical advantage can be achieved in the winch system by using block and tackle configurations. However, this should be avoided in the splash zone and underwater because of the harsh environmental factors (including biofouling, corrosion, and ice blockage). Thus, the platform was designed to house this system in the protection of the above-surface platform. This would reduce the total cost of the required marine grade winches from $300,000 to $90,000 (as per Lantech). A resulting design is shown in Figure 28.

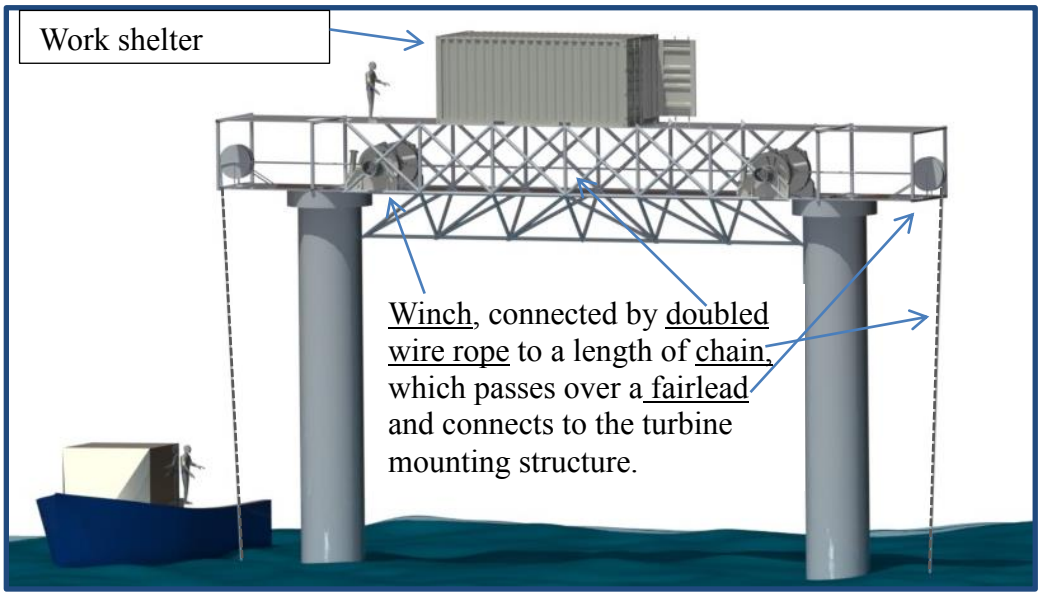

Figure 28. Close-up of work-platform and lifting structure. 42 ft. support vessel and workers are shown for scale. Each winch is connected to opposite side wire rope/chain. Design shown is for mounting a 6 by10 m (20 by 33 ft.) cross-flow axis turbine. Larger systems would use a rack-and-pinion lifting system.

In this design, each winch coils a wire rope, which is connected to a length of chain, which is attached to the turbine mounting structure. This allows the winch to coil only the wire rope, while only the chain is submerged or exposed in the splash zone. Issues of wire rope set were addressed by including clevises below the fairleads, which would be capable of bearing the full tension in the chains when the mounting platform is not being raised or lowered. It should be noted that a hydraulic drive system would need to be incorporated to power the winches.

A rack-and-pinion system would provide a robust operating system with excellent positional control during the raising/lowering process and during operation. However, such systems are

costly. LeTourneau Technologies quoted a system at $406,000 (including the electric induction drive system) using the smallest unit they offer (which could handle all turbines of the scales investigated). Thus, this concept would only be applied to platforms capable of deploying in-stream axis turbines of 13 m (43 ft.) diameter or greater.

Results

The design processes describe above were integrated in the following procedure for each maximum turbine size specified:

- A pile wall thickness (2 inches for all designs) was selected.
- The diameter of each pile was iterated until the mechanics analysis showed that the required safety against yielding was met.
- The depth to which the pile would be driven into the soil was iterated until requirements for both vertical and lateral capacity were satisfied.
- Vortex-Induced Vibration (VIV) was analyzed and it was found that the piles as designed would not experience significant vibration unless subjected to velocities at least twice those expected in the channel.

Table 36. Two-pile Surface-Piercing Platform parameters.

Turbine Diameter	**4 m**		**(14 ft)**		**9 m**		**(29 ft)**	
Turbine Distance from Bottom	25	m	82	ft	25	m	82	ft
Pile								
Material	ASTM A252 Grade 3				ASTM A252 Grade 3			
Number of Piles	2				2			
Diameter of Pile	1.04	m	3.42	ft	1.89	m	6.20	ft
Thickness of Pile	0.0508	m	2.00	in	0.0508	m	2.00	in
Pile Depth in Sediment	12	m	39	ft	17	m	56	ft
Pile Height Above Surface	10.5	m	34	ft	15.0	m	49	ft
Total Length of Pile	47.4	m	156	ft	57.1	m	187	ft
Width of structure	9	m	28	ft	13	m	43	ft
Mass of Pile	61,926	Kg	136,524	lbm	135,246	Kg	298,166	lbm
Compression SF	2.0		-		2.0		-	
Max Stress/ Endurance Limit	0.7		-		0.7		-	
Lifting								
Number of Winches	2				2			
Maximum Winch Line Pull Required	26,594	N	5,979	lbf	138,414	N	31,117	lbf
Winch Selected	M18				LWS 570			
Pile Type in Soil	Long				Long			
Velocity for Transverse Vibration	4.1	m/s			11.1	m/s		
Legend:								
Iterated values								
Design inputs								
Calculated values								

Table 36. Two-pile Surface-Piercing Platform parameters (continued).

Turbine Diameter	13 m		(43 ft)		17 m		(57 ft)	
Turbine Distance from Bottom	25	m	82	ft	25	m	82	ft
Pile								
Material	ASTM A252 Grade 3				ASTM A252 Grade 3			
Number of Piles	2				2			
Diameter of Pile	2.77	m	9.10	ft	3.69	m	12.11	ft
Thickness of Pile	0.0508	m	2.00	in	0.0508	m	2.00	in
Pile Depth in Sediment	21	m	71	ft	26	m	84	ft
Pile Height Above Surface	19.5	m	64	ft	24.0	m	79	ft
Total Length of Pile	66.0	m	217	ft	74.5	m	244	ft
Width of structure	18	m	57	ft	22	m	72	ft
Mass of Pile	229,387	Kg	505,711	lbm	344,645	Kg	759,813	lbm
Compression SF	**2.0**		-		**2.0**		-	
Max Stress/ Endurance Limit	**0.7**		-		**0.7**		-	
Lifting								
Number of Winches	2				2			
Maximum Winch Line Pull Required	383,517	N	86,218	lbf	809,960	N	182,086	lbf
Winch Selected	LWD3500				LWD3500			
Pile Type in Soil	Long		0.01		Long			
Velocity for Transverse Vibration	20.7	m/s			32.6	m/s		

Legend:

Iterated values
Design inputs
Calculated values

Costing

Several Marine Contractors, including J.F. White, Pihl U.S., and Sea and Shore, were contacted for rough estimates of the cost for installation of two 56” (1.42 m) piles or four 24” (0.61 m) piles. J.F. White (2011) proposed the following installation procedure:

> A marine piling operation would be mobilized and consist of a 54' x 180' barge with a 200 TN lattice boom crane set on top. All construction materials, templates and equipment would also be placed on the barge. The barge would be mobilized from a main land marine facility and towed to the location of work. The sequence of work would be to construct templates, install piles and set platforms. In the event that bedrock is encountered above the proposed pile tip elevation, JFW would use a "down the hole hammer" to remove the bedrock and create a rock socket. Concrete and reinforcing steel would then be placed in the toe of the pile to provide the required embedment and stability of the pile system.

The contractor provided estimates for installing piles of the aforementioned size for both the case in which bedrock exists just beneath the seafloor and that in which there is sufficient sediment overburden to hold the piles, while strongly recommending that soil testing be conducted before installation. These estimates were scaled under the assumption that the entire installation cost was proportional to the volume of sediment removed by drilling or enclosed by the pile. The estimate carried $50,000 to construct the platform to which the turbine would mount. This was assumed to vary linearly with the size of the turbine.

For the turbine lifting mechanism, quotes were obtained from TWG Lantech (2011) for winches of various sizes. Also, a rack-and-pinion system which could handle the required loads for any of the turbine sizes investigated was quoted by Letourneau Technologies (2011).

The results of this cost analysis are shown in Table 37.

Table 37. Cost of Two-pile Surface-piercing Platform.

Turbine Diameter			**4 m**	**(14 ft)**	**9 m**	**(29 ft)**
	$/	Unit	Quantity	Cost	Quantity	Cost
Foundation						
Piles, Installed	$68,553	EA	2	$618,006	2	$1,793,351
Anti-corrosion Coating	$4.02	ft^2	5251	$21,133	11469	$46,154
Anti-scour Matt	$1.87	lb	2820	$5,279	3993	$7,476
Support Structure						
Platform	$1,852	EA	1	$1,852	1	$14,815
Hydraulic Winch	$23,000	EA	2	$46,000	2	$90,000
Total				**$692,270**		**$1,951,795**

O&P, shipping included throughout

Site work not included

Table 37. Cost of Two-pile Surface-piercing Platform (continued).

Turbine Diameter		**13 m**	**(43 ft)**	**17 m**	**(57 ft)**
	Quantity	Cost	Quantity	Cost	Quantity
Foundation					
Piles, Installed	2	$3,614,986	2	$5,865,824	2
Anti-corrosion Coating	19452	$78,280	29225	$117,613	19452
Anti-scour Matt	5212	$9,759	6479	$12,131	5212
Support Structure					
Platform	1	$50,000	1	$118,519	1
Skidder Gear Unit RH	2	$279,475	2	$279,475	2
Rack Skidder	140	$126,598	140	$126,598	140
Total		**$4,159,097**			**$6,520,160**

O&P, shipping included throughout

Site work not included

CHAPTER 6

SUBMERGED BUOYANT PLATFORM

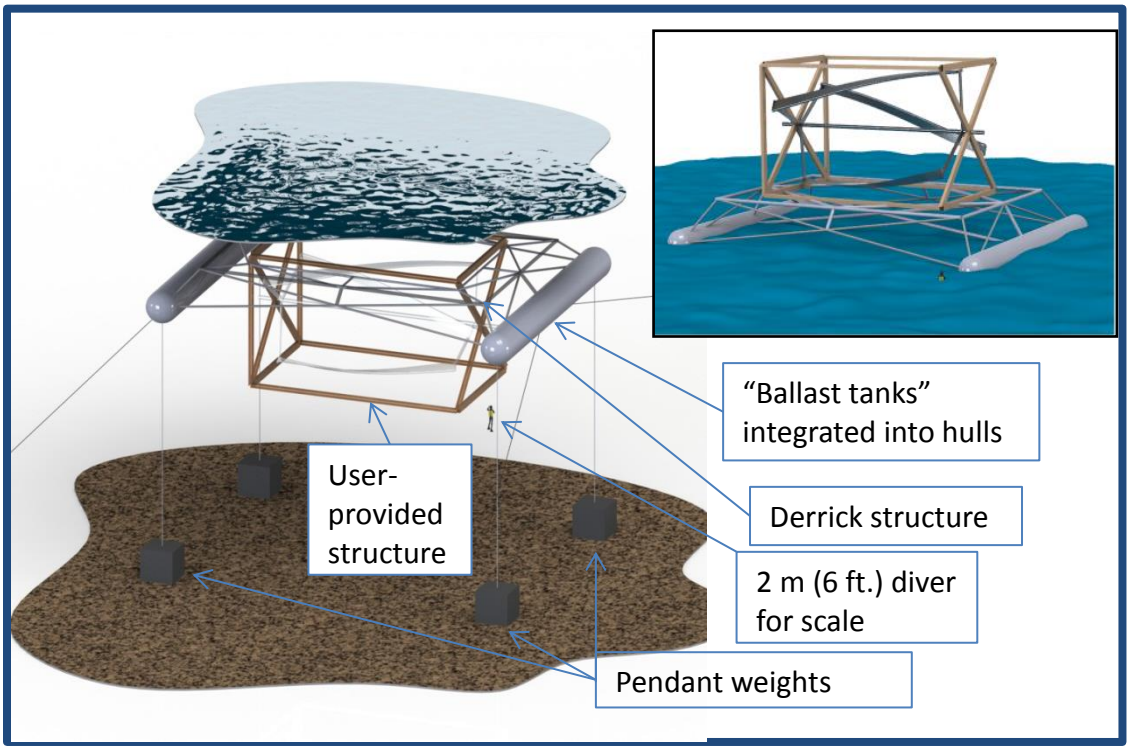

Figure 29. Submerged Buoyant platform concept, shown mounting a 9 m by 15 m (29 ft by 49 ft) horizontal axis turbine. The main figure illustrates the system deployed under water; the inset shows it surfaced with the turbine/mount raised. The derrick structure is shown in gray, while the user-provided mount-turbine structure is in orange. A 2 m (6.6 ft) diver is shown for scale.

A Submerged Buoyant platform, illustrated in Figure 29, was considered for the following advantages:

- The platform could be raised to the surface and even towed to a shore facility for ease of turbine installation and repairs, and also platform maintenance.
- The platform would operate below surface activity.

Disadvantages include:

- Multiple moving systems may be required.
- Mooring array may require large seafloor footprint.

The Submerged Buoyant platform would comprise two cylindrical hulls rigidly connected by a truss structure, a derrick for raising and lowering the turbine, and a mooring system. This platform would be towed to and from the site with the device in the "up" position (as shown in the inset of Figure 29). Once on site, the platform would be connected to the mooring system,

including a pendant weight. The turbine would then be lowered to the "down" position. The platform would then be submerged by allowing compartments in the bulkheaded pontoons to fill with seawater, until the pendant weight rested on the seafloor. This would keep the platform at the desired depth for the duration of testing. Once testing was completed, the process would be reversed: The platform would be raised to the surface by expelling the seawater from the pontoons using compressed air; the turbine would be raised to the "up" position; the mooring would be disconnected; and the platform would be towed back to shore.

Specific Design Criterion

- The platform must be stable at the surface, while submerged, and at all points in between. This means that when the pontoons are on the surface the platform must not tip more that 1^{o} when subjected to any foreseeable load (e.g. strong wind), and while submerged the hydrostatic restoring moment must exceed the overturning moment when tipped any small angle.

Cost estimates for a Submerged Buoyant platform were obtained by designing a steel structure of suitable size, strength, and stability and estimating total expenses. Costs include those for material and labor to construct the platform, variable buoyancy system, the turbine lift system, the mooring line handling system, and the mooring system, including installation.

Governing Equations-Hydrostatics

The submerged-buoyant platform was analyzed for pitch, roll, and vertical stability under both submerged and surface conditions.

Submerged

The free-body diagram of the platform deploying a turbine at mid depth is shown in Figure 30 and variables therein are identified in Table 38.

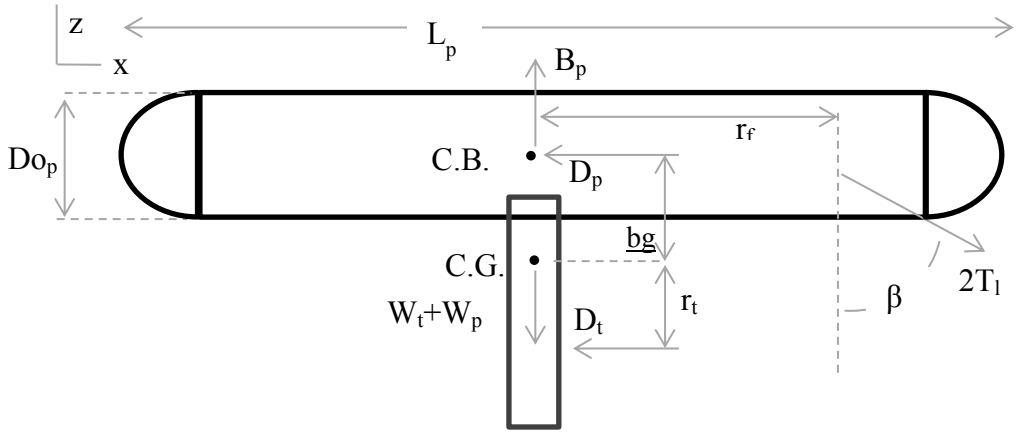

Figure 30. FBD of Submerged Buoyant platform. Current is from right to left.

Table 38. Submerged Buoyant platform hydrostatics variables.

r_t	Distance from C.G to Turbine Drag	R_f	Distance from CG to Mooring Attachments
θ	Bow-down Angle	β	Mooring Line Angle from Vertical
W_p	Platform Weight	T_l	Tension in a Single Mooring Line (two used)
W_t	Turbine Weight	Do_p	Pontoon Diameter
D_p	Platform Drag	DR_p	Platform Draft
D_{Wt}	Drag from Wind Loading	L_b	Platform Length (At waterline)
D_t	Turbine Drag	M_B	Righting Moment
B_p	Buoyant Force		

Note: The tension in pendant lines is assumed to be negligible.

When submerged, the platform must satisfy horizontal, vertical, and rotational equilibrium. In the horizontal direction,

$$2T_l \sin\beta - D_p - D_t = 0; \tag{80}$$

vertically,

$$-2T_l \cos\beta - W_p - W_t + B_p = 0; \tag{81}$$

in rotation,

$$-\mathrm{r_f} 2T_l \cos\beta - r_t D_t + \underline{bg} D_p = 0. \tag{82}$$

Stability for a completely submerged rigid body is achieved when, for any reasonable tipping angle, the righting moment (due to the distance between the center of gravity and the center of buoyancy) exceeds the tipping moment (due to the new angle of attack of the body). This criterion requires,

$$(W_t + W_p)\overline{bg}\theta > C_M A q L_b q A, \tag{83}$$

where q is the free-stream dynamic pressure, $1/2\rho U^2$ with U being the free-stream velocity of the fluid. Furthermore, A is the area of the base of the body, and C_M is the pitching moment coefficient, which is a function of θ. Table 39 gives values of C_M for a long cylindrical body with a nose cone at a Reynolds number, *Re*, comparable to that of the flow over the submerged platform. In this case, the *Re* is defined by

$$Re = \frac{LU}{\nu}, \tag{84}$$

where L is the length of the body and v is the dynamic viscosity of the fluid.

Table 39. Pitching moment coefficients (Penland & Fetterman, D. E., 1956).

Platform Reynolds Number	5.90E+07	
Experiment Reynolds Number	1.50E+06	
Angle of Attack		C_M
Degrees	Radians	
-4	-0.070	-0.052
0	0.000	0.012
5	0.087	0.055
10	0.175	0.085
15	0.262	0.108

Surfaced

In addition to remaining stable while submerged, the platform must safely function as a surface vessel while being towed to and from the site. To this end, the hydrostatics in both the vertical direction and the pitch direction were analyzed. The forces present in these analyses are shown in Figure 31.

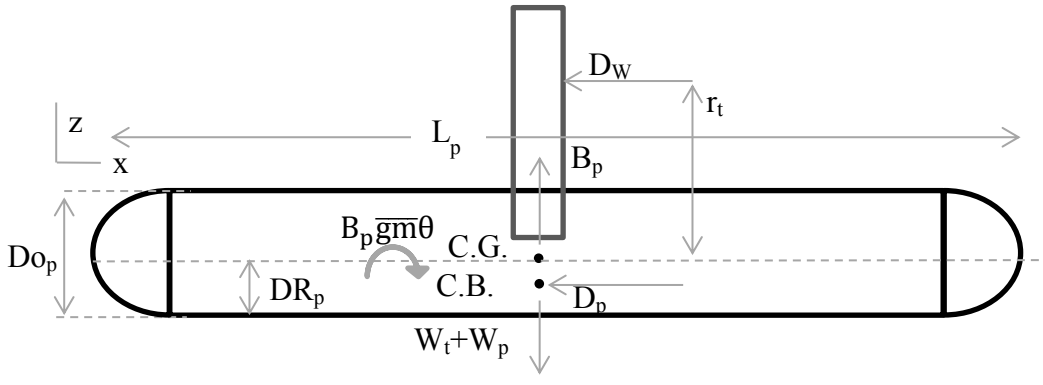

Figure 31. FBD of Submerged-Buoyant Platform at Surface

On the surface, the platform must satisfy vertical equilibrium and not pitch or roll more than the maximum allowed angle. Vertical equilibrium mandates

$$V_s \rho g - W_t - W_p = 0. \tag{85}$$

Here V_s is the submerged volume in the pontoons, found by specifying a draught of 0.4 times the pontoon diameter, so that any tipping increases the platform's area moment of inertia at the waterplane. Pitch stability is found by summing moments about the center of gravity, such that

$$D_t r_t + B_p \overline{gm} \theta = 0, \tag{86}$$

where θ is specified to be less than 0.017 rad (1^o). The stabilizing effect of the mooring is not taken into account because the platform must be stable while being towed to and from the site, independent of the mooring system. (Roll stability is calculated the same way, but the area moment of inertia, and thus the metacentric height, $\overline{gm}$, is always greater in that direction for this platform.) Here the wind drag, D_W was estimated as

$$D_W = 2(\tfrac{1}{2} \rho_a A_t C_D U_a^2), \tag{87}$$

where ρ_a is the density of air, A_t is the projected area of the turbine, C_D is the coefficient of drag of the turbine (1.4) and U is the design wind speed, 15 m/s (29 knots). The drag force on the turbine was doubled to account for surrounding structure.

Variable Buoyancy

The submerged floating platform would operate on the principle of variable buoyancy. This method of suspending buoyant structures at fixed depths has been demonstrated extensively in the aquaculture industry (Celikkol et al., 2006).

Variable buoyancy systems can be highly unstable if the air-ballast water chambers include large free surfaces. In this case, a small perturbation will cause a large in the location of both the center of gravity and the center of buoyancy. To prevent this, each pontoon was divided into several chambers by bulkheads, shown in Figure 32.

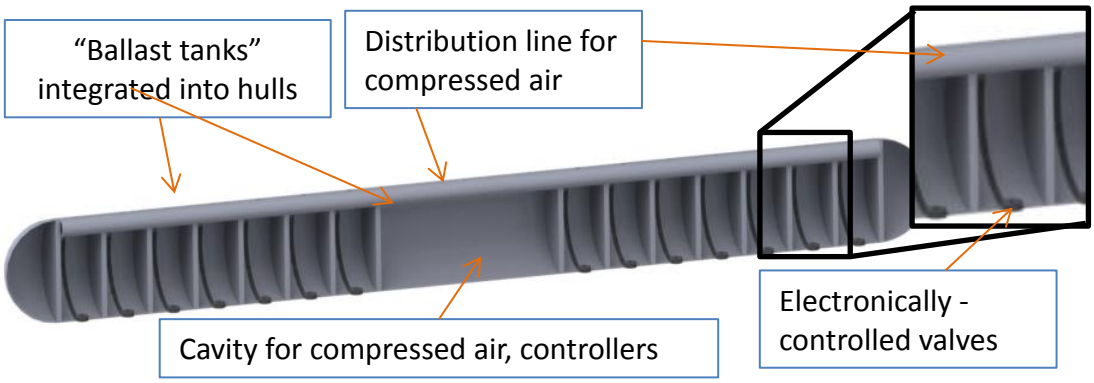

Figure 32. Cut-away view of a Submerged Buoyant platform pontoon. Bulkheads increase stability (and structural rigidity). A central space is included for compressed air storage and controls.

When the platform is being lowered, chambers will be filled sequentially. This process of ballasting will start with each of the four corner chambers and then move to the next furthest chamber from the center of gravity until the total buoyancy is sufficiently reduced. Beginning with the outermost chambers ensures that the platform's mass moment of inertia is always at a maximum, making it less susceptible to impulsive perturbations.

A critical criterion in the design of a variable buoyancy system is that pressure of the stored air must be much greater than the ambient pressure of the seawater to expel the fluid from the ballast tanks. At any given depth h, the absolute air pressure required is given by

$$P_A = \rho g h + 1\ atmosphere. \tag{88}$$

For this application P_A is approximately 250 kPa (36 psi). Thus, commercially available air-storage systems capable of storage pressure, P_S=30 MPa (4300 psi) are more than sufficient.

The volume of water that must be expelled from the integrated ballast tanks each time the platform is raised is

$$V_W = V_{p1} - V_{p2}. \tag{89}$$

Here V_{p1} is the total volume of the pontoons (that required for surface stability), and V_{p2} is the volume required by hydrostatics in the submerged case. Incorporating the ideal gas law with negligible temperature change, the required volume for storing the compressed air is

$$V_S = \frac{P_{atm}}{P_A} V_W. \tag{90}$$

Mooring System

Variable buoyancy systems can be very difficult to control in the open ocean. To eliminate the need for an exact force balance, a pendant system was incorporated into the

Submerged Buoyant platform design. This system, illustrated in Figure 29, would hold the platform at the desired depth. This would be accomplished by leaving reserve buoyancy in the platform ballast tanks. Thus, the actual volume of air in the pontoons would always exceed the calculated volume required for vertical equilibrium, V_{p2}. To ensure effectiveness of the system, the required vertical force that the pendant system exerted on the platform was calculated as twice the vertical component of the mooring force.

In addition to the pendant system, the platform would be held in place with four mooring lines, each extending to an embedment anchor. During each tidal cycle the aft pair of lines would be slack. Thus, the platform would not pivot to match the tidal cycle. However, the moorings would be laid out such that the platform would align with the dominant current direction on both the ebb and flood tides, which are approximately 20 degrees off of a perfect 180 degree alignment (Howes et al., 2009). Anchors were chosen which provided a pull-out safety factor, SF_{pull}, greater than 5, where

$$SF_{pull} = \frac{T_l \cos\beta}{T_{hold}}. \tag{91}$$

Here T_{hold} is the rated holding power of the anchor in sand/gravel, T_l is the tension in a single mooring line, and β is the angle between the mooring line and the horizontal, assumed fixed. (Note that a proper mooring system in which a length of heavy chain connects the mooring line to the anchor, would effectively make cosβ=1.)

Solving

Since both the submerged and surfaced conditions depend on the weight and dimensions of the platform, they cannot be solved independently. Thus, the surface and submerged equations were simultaneously solved numerically under the stability conditions. Equation (84) was then solved for the necessary distance between the center of buoyancy and center of gravity, $\overline{bg}$, for each angle in the above table and the maximum was used. This value was generally found to be on the order of ½ the pontoon diameter. Thus the platform can be constructed to be stable independent of the aid of a bridle system, but it will require careful distribution of the platform's mass. The results of this design work are shown for each turbine size in Table 40.

Table 40. Submerged Buoyant Platform parameters.

Turbine Diameter	**4 m**		**(14 ft)**		**9 m**		**(29 ft)**	
Platform Structure								
Required Pontoon Diameter, Surfaced	1.89	m	6.2	ft	2.57	m	8.4	ft
Required Pontoon Diameter, Submerged	1.00	m	3.3	ft	1.35	m	4.4	ft
Pontoon Length	6.7	m	21.9	ft	13.3	m	43.7	ft
Beam (between centers of pontoons)	8.7	m	28.4	ft	17.3	m	56.9	ft
Deck Length (Width)	4.0	m	13.1	ft	8.0	m	26.2	ft
Pontoon Volume, Submerged	11	m^3	371	ft^3	38	m^3	1,352	ft^3
Platform Wall Thickness	0.0064	m	1/4	in	0.0064	m	1/4	in
Mass of Pontoons	3,942	kg	8,691	lbm	10,731	kg	23,658	lbm
Mass of Truss Members	2,628	kg	5,794	lbm	7,154	kg	15,772	lbm
Mass of additional items	1,314	kg	2,897	lbm	3,577	kg	7,886	lbm
Total (estimated) Mass of Structure	7,885	kg	17,383	lbm	21,462	kg	47,316	lbm
Submerged Mooring								
Scope	1/7				1/7			
Surface Stability								
Draft	0.76	m	2.5	ft	1.03	m	3.4	ft
Chord of Pontoon at Waterline	1.85	m	6.1	ft	2.52	m	8.3	ft
Submerged Volume (Total)	14	m^3	492	ft^3	52	m^3	1,824	ft^3
Rolling Angle	0.002	rad	0.1	deg	0.001	rad	0.1	deg
Pitching Angle	0.010	rad	0.6	deg	0.006	rad	0.3	deg
Pendant Weight								
Pendant Safety Factor	2				2			
Pendent Mass	4,367	kg	9,628	lbm	16,284	kg	35,900	lbm
Size of one whole cubic Pendent	1.22	m	4.0	ft	1.89	m	6.2	ft
Submerged Stability								
Required Distance from CG to CB	0.743	m			1.106	m		
Ballast								
Required Storage Volume	0.0528	m^3	53	L	0.1922	m^3	192	L
Lifting								
Number of Winches	2				2			
Maximum Winch Line Pull Required	53,188	N	11,957	lbf	276,828	N	62,233	lbf
Winch Selected	M18				LWD3500			
Mooring Equipment								
Desired Working Safety Factor	2				2			
Chain Length	80	m	87.5	ft	80	m	175.0	ft
Line Length	393	m	1290.5	ft	393	m	1203.0	ft
Stingray	1000	kg	1,102	lbm	1000	kg	1,102	lbm
Legend:								

Legend

Iterated Values
Design Variables
Calculated Values

Table 40. Submerged Buoyant Platform parameters (continued).

Turbine Diameter	**13 m**		**(43 ft)**		**17 m**		**(57 ft)**	
Platform Structure								
Required Pontoon Diameter, Surfaced	3.23	m	10.6	ft	3.89	m	12.7	ft
Required Pontoon Diameter, Submerged	1.72	m	5.6	ft	2.09	m	6.9	ft
Pontoon Length,	20.0	m	65.6	ft	26.7	m	87.5	ft
Beam (between centers of pontoons)	26.0	m	85.3	ft	34.7	m	113.7	ft
Deck Length (Width)	12.0	m	39.4	ft	16.0	m	52.5	ft
Pontoon Volume, Submerged	93	m^3	3,272	ft^3	183	m^3	6,469	ft^3
Platform Wall Thickness	0.0064	m	1/4	in	0.0064	m	1/4	in
Mass of Pontoons	20,246	kg	44,635	lbm	32,453	kg	71,547	lbm
Mass of Truss Members	13,497	kg	29,756	lbm	21,635	kg	47,698	lbm
Mass of additional items	6,749	kg	14,878	lbm	10,818	kg	23,849	lbm
Total (estimated) Mass of Structure	40,492	kg	89,269	lbm	64,906	kg	143,093	lbm
Submerged Mooring								
Scope	1/7				1/7			
Surface Stability								
Draft	1.29	m	4.2	ft	1.55	m	5.1	ft
Chord of Pontoon at Waterline	3.17	m	10.4	ft	3.81	m	12.5	ft
Submerged Volume (Total)	123	m^3	4,329	ft^3	236	m^3	8,342	ft^3
Rolling Angle	0.001	rad	0.1	deg	0.001	rad	0.0	deg
Pitching Angle	0.004	rad	0.2	deg	0.003	rad	0.2	deg
Pendant Weight								
Pendant Safety Factor	2				2			
Pendent Mass	35,956	kg	79,269	lbm	63,384	kg	139,737	lbm
Size of one whole cubic Pendent	2.47	m	8.1	ft	2.98	m	9.8	ft
Submerged Stability								
Required Distance from CG to CB	1.290	m			1.394	m		
Ballast								
Required Storage Volume	0.4654	m^3	465	L	0.9201	m^3	920	L
Lifting								
Number of Winches	2				2			
Maximum Winch Line Pull Required	767,034	N	172,436	lbf	1,619,921	N	364,173	lbf
Winch Selected	LWD3500				LWD3500			
Mooring Equipment								
Desired Working Safety Factor	2				2			
Chain Length	80	m	262.5	ft	80	m	350.0	ft
Line Length	393	m	1115.5	ft	393	m	1028.0	ft
Stingray	1000	kg	1,102	lbm	1000	kg	1,102	lbm

Legend

Iterated Values

Design Variables

Calculated Values

Costing

The material cost of the pontoons was estimated from a quote from L.B. Foster (2010) for ASTM A252 Gr. 3 steel piles on a per-pound basis. The material cost of the mechanical tubing that constitutes the platform structure was estimated from a quote from American Steel for ASTM A333 Gr. 6 mechanical tubing, also on a per-pound basis. Corrosion protection costs were based on a quote from L.B. Foster for marine-grade epoxy coating over the exterior surface area of the platform. Welding costs were estimated from a quote supplied to Jeff Byrne for his V2 design (2010). The material costs were subtracted from a quote that included deck beams and welded mechanical tubing and the remainder was assumed to be the welding cost, which was reduced to dollars per pound of tubing. (While this is clearly an over-estimate of the fraction which is welding cost, it is also worth noting that the quotes used to estimate the welding cost were for A36 steel, which may be easier to weld than ASTM A333 Gr. 6). The cost of final assembly was also taken to be a function of structure weight and was estimated from a quote for the V2 platform. The cost of forming a concrete pendent weight was determined from R.S. Means (2011) and the cost of the required lines was obtained as for the mooring lines, described below.

The cost of the variable-buoyancy system was estimated by using the per-pound cost of ASTM A252 Gr. 3 as the cost of the integrated ballast tanks, the cost of ASTM A333 Gr. 6 for the necessary piping, and the per-pound welding cost as above. The price of twenty (20) stainless steel 2 in. ball valves with remote activation was obtained from Swagelok (2011). The most expensive type was used in order to compensate for other valves, etc. not included in the cost analysis. (Corrosion in these components will need to be given careful consideration during the detailed design phase because stainless steel acts as the sacrificial anode to most structural steels.)

For the turbine lifting mechanism, quotes were obtained from TWG Lantech (2011) for winches of various sizes. Quotes for the mooring equipment were obtained from Jeyco (2011) and Puget Sound Rope (2011). The cost of installing the mooring grid was estimated as the cost of a 100 ft. working vessel hired for seven (7) days. The results of this cost analysis are shown in Table 41.

Table 41. Cost of Submerged Buoyant Platform.

Turbine Diameter			**4 m (14 ft)**		**9 m (29 ft)**	
	Unit Price		**Qty.**	**Cost**	**Qty.**	**Cost**
Pontoons						
Steel Piles	$1.87	lb	8,691	$16,273	23,658	$44,295
Anti-Corrosion Coating	$4.02	ft^2	1,857	$7,474	4,920	$19,798
Tubing						
ASTM A333 Gr. 6 Mechanical Tubing	$1.64	lb	5,794	$9,512	15,772	$25,893
Anti-Corrosion Coating*	$4.02	ft^2	5,058	$20,355	5,058	$20,355
Welding	$1.38	lb	5,794	$7,976	15,772	$21,709
Assembly						
Assembly	$0.57	lb	14,486	$8,230	39,430	$22,403
Pendent Weight						
Concrete Weight	$96	ea.	4	$385	4	$1,231
28 mm Plasma 12 Strand	$14.63	ft	197	$2,880	197	$2,880
Mooring						
1000 kg Stingray Anchor	$3,537	ea.	4	$14,148	4	$14,148
36mm Studlink Chain	$3,000	shot	4	$12,000	4	$12,000
28 mm Plasma 12 Strand	$14.63	ft	1,378	$20,160	1,378	$20,160
Variable Buoyancy						
Steel (Pressure Vessel, Bulkheading)	$1.87	lb	543	$1,017	1,479	$2,768
ASTM A333 Gr. 6 Piping	$1.64	lb	290	$476	789	$1,295
Welding			1	$7,976	1	$21,709
2" Ball Valves	$1,370	ea.	20	$27,400	20	$27,400
Lifting						
M18Winch	$23,000-$175,000	ea.	2	$46,000	2	$350,000
Total				**$202,262**		**$608,045**

Table 41. Cost of Submerged Buoyant Platform (continued).

Turbine Diameter			**13 m (43 ft)**		**17 m (57 ft)**	
	Unit Price		**Qty.**	**Cost**	**Qty.**	**Cost**
Pontoons						
Steel Piles	$1.87	lb	44,635	$83,570	71,547	$133,958
Anti-Corrosion Coating	$4.02	ft^2	9,197	$37,011	14,674	$59,053
Tubing						
ASTM A333 Gr. 6 Mechanical Tubing	$1.64	lb	29,756	$48,851	47,698	$78,305
Anti-Corrosion Coating*	$4.02	ft^2	5,058	$20,355	5,058	$20,355
Welding	$1.38	lb	29,756	$40,958	47,698	$65,654
Assembly						
Assembly	$0.57	lb	74,391	$42,268	119,244	$67,752
Pendent Weight						
Concrete Weight	$96	ea.	4	$2,526	4	$4,261
28 mm Plasma 12 Strand	$14.63	ft	197	$2,880	197	$2,880
Mooring						
1000 kg Stingray Anchor	$3,537	ea.	4	$14,148	4	$14,148
36mm Studlink Chain	$3,000	shot	4	$12,000	4	$12,000
28 mm Plasma 12 Strand	$14.63	ft	1,378	$20,160	1,378	$20,160
Variable Buoyancy						
Steel (Pressure Vessel, Bulkheading)	$1.87	lb	2,790	$5,223	4,472	$8,372
ASTM A333 Gr. 6 Piping	$1.64	lb	1,488	$2,443	2,385	$3,915
Welding			1	$40,958	1	$65,654
2" Ball Valves	$1,370	ea.	20	$27,400	20	$27,400
Lifting						
M18Winch	$23,000-$175,000	ea.	2	$350,000	3	$525,000
Total				**$750,751**		**$1,108,868**

CHAPTER 7

FLOATING PLATFORM

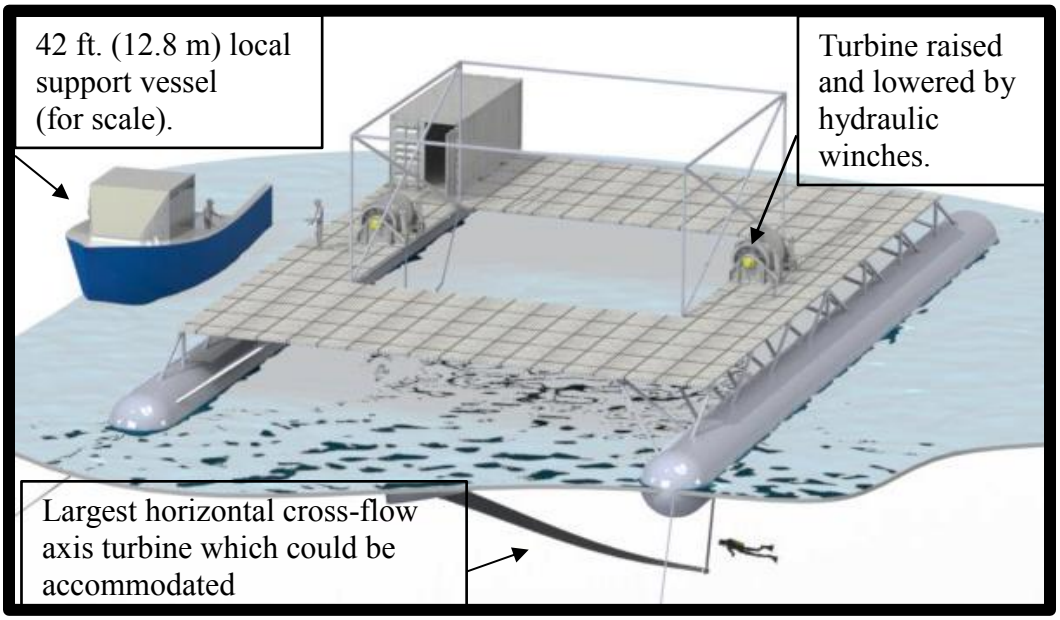

Figure 33. Floating platform concept, shown mounting a 9 m by 15 m (29 ft. by 49 ft.) horizontal axis turbine. The turbine is raised and lowered along a derrick structure by hydraulic winches.

A floating platform, illustrated in Figure 33, was considered for the following advantages:

- The platform could be towed to harbor for repair, maintenance, and turbine operations, and also in the threat of extreme storms, etc.
- Turbines would be tested in the high-velocity region near the surface.

Disadvantages include the following:

- The rough seas in the Muskeget Channel are adverse to a moored surface platform.
- Marine traffic would need to avoid the surface presence.
- A surface presence could raise objections over alterations to the existing viewscape.
- The surface structure could become a target for vandalism.

Specific Design Criteria

- The Muskeget platform must not tip more than 1^{o} under steady-state design loading, to maintain adequate freeboard at the up-current end.
- The platform must not allow more than one water-deck contact event per hour when operating in waves.
- Accelerations must remain below normal thresholds for crew operations.

Initial cost estimates for a floating platform were obtained by scaling up existing plans for the UNH CORE Tidal Energy Site platform (Byrne, 2013). Scaling and costing were conducted

under the following assumptions:

- Critical forces are buoyancy, weight, and drag. Drag is in an asymptotic range due to high Reynolds number. Thus, Froude scaling is applicable.
- Cost is proportional to the weight of material, and that is proportional to the volume of the body.

Platform Hydrostatics

Governing Equations

The forces and dimensions relative to the hydrostatic analysis governing the surface platform are shown in Figure 34, and the associated variables are explained in Table 42.

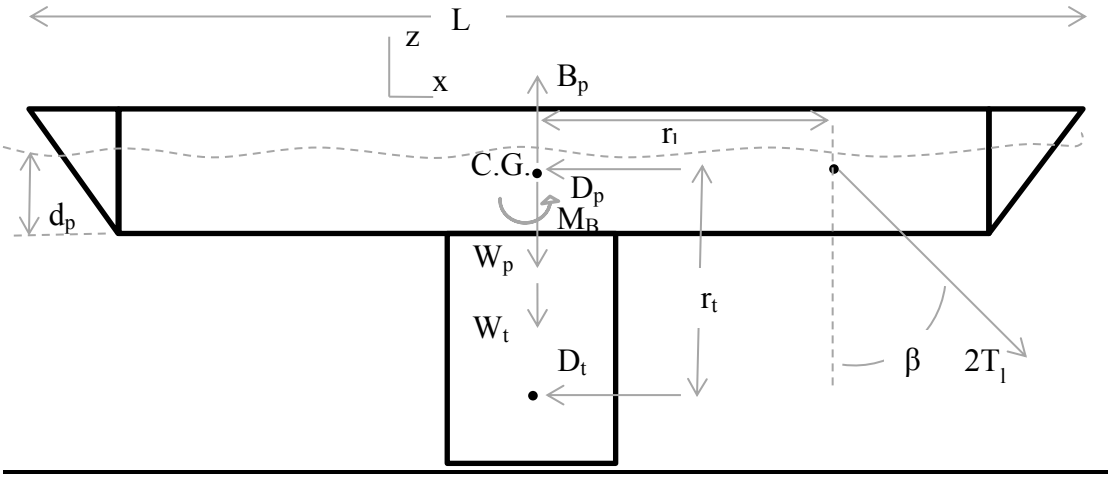

Figure 34. Floating platform Free Body Diagram. Current is from right to left. Two mooring lines are used, each attached to the outside of the platform.

Table 42. Floating Platform hydrostatics variables.

r_t	Turbine Hub from Surface	r_l	Distance from CG to Mooring Attachments
θ	Bow-down Angle	β	Mooring Line Angle from Vertical
W_p	Platform Weight	T_l	Tension in a Single Mooring Line
W_t	Turbine Weight	Bp	Buoyant Force
D_p	Platform Drag	d_p	Platform Draft
D_t	Turbine Drag	L	Platform Length (At waterline)
r_t	Distance from CG to Turbine Drag	M_B	Righting Moment

Satisfying Newton's second law in the horizontal direction relates the mooring line tension to platform drag, turbine drag, and mooring angle, so that

$$2T_l \sin\beta = D_p + D_t. \tag{92}$$

Vertical equilibrium yields the buoyant force in terms of platform and turbine weight, mooring line angle, and mooring line tension,

$$B_p = W_p + W_t + 2T_l \cos\beta. \tag{93}$$

Moment equilibrium about the center of gravity requires the righting moment to balance the turbine drag and mooring line moments, so that

$$-D_t r_t - 2T_l \cos(\beta) r_l + B_p \overline{gm}\theta = 0 \tag{94}$$

where $FB\overline{gm}\theta$ is the righting moment when tipped a small angle, θ. Furthermore, from submerged volume considerations, the metacentric height, $\overline{gm}$, is given by

$$\overline{gm} \approx \frac{I}{V} = \frac{\frac{(2w_h)L^3}{12}}{d_p(2w_h)L} = \frac{L^2}{12d_p} \tag{95}$$

where w_h is the width of each platform hull.

Design Process

The drag force and weight of the turbine and support structure were taken from Table 6. The platform dimensions were taken to be proportional to those of the UNH CORE Tidal Energy Test Site 64 ft. (19.5 m) platform. Thus, since drag is proportional to projected area,

$$D_p = D_{p0}\left(\frac{L}{L_0}\right)^2 \tag{96}$$

where L_0=64 ft. (19.5 m) and D_{p0} is the drag on the 64 ft. platform at the design current speed of 2.5 m/s (5 knots), as determined from tow tank testing of a Froude scaled model by Byrne (2013). Similarly, the weight of the platform was taken to be

$$W_p = W_{p0}\left(\frac{L}{L_0}\right)^3 \tag{97}$$

where W_{p0} is the weight of the 64 ft. platform, equal to 88,000 lbf (390 kN).

A mooring line length-to-water-depth ratio (scope) of 7:1 was used, which is standard for use with embedment anchors. The mooring line was assumed to be straight in all cases, so the 7:1

scope results in a mooring angle of β=82 degrees (1.4 radians).

For each maximum turbine size to be tested, a maximum allowable draft for the platform hulls was chosen to be proportional to that of the 64 ft. UNH CORE Tidal Energy Test Site platform, so that

$$d_p = d_{p0}\left(\frac{L}{L_0}\right) \tag{98}$$

where d_{p0} is the draft of the 64 ft. platform, equal to 1.4 ft. (0.4 m).

The distance between the platform's center of gravity and the mooring line attachment points, r_l, was taken to be proportional to the size of the maximum turbine size to be tested. These values are shown in Table 43.

For each maximum turbine size, the equations above were solved iteratively—using a Generalized Reduction Gradient (GRG) nonlinear forward difference solver in the Microsoft Excel® Solver package—to find the platform length, L, that resulted in a tipping angle of 1 degree (0.17 radians) at the design current speed of 2.5 m/s (5 knots). The design inputs and results of this analysis are shown in Table 43 for each maximum turbine size investigated.

Table 43. Floating Platform Parameters.

		Changes with turbine size							
		Calculated value							
	Symbol	Design Input							
Turbine Size		4 m (14 ft)				9m (29 ft)			
Platform Weight	W_p	236,541	N	53,176	lbf	1,047,525	N	235,493	lbf
Distance from CG to Turbine Drag	r_t	3	m	8	ft	5	m	16	ft
Distance from CG to Mooring Attachments	r_l	5.1	m	17	ft	8.3	m	27	ft
Mooring Scope		1/7				1/7			
Tension in Single Mooring Line	T_l	42,372	N	9,526	lbf	163,210	N	36,691	lbf
Platform Draft	d_p	0.364	m	1.2	ft	0.597	m	2.0	ft
Tipping Angle	θ	0.017	rad	1.0	deg	0.017	rad	1.0	deg
Platform Length (at waterline)	L	15.3	m	50.1	ft	25.1	m	82.3	ft
Total Platform Width		8.8	m	29	ft	14.4	m	47	ft

Table 43. Floating Platform Parameters (continued).

Changes with turbine size
Calculated value
Design Input

Turbine Size	Symbol	13 m (43 ft)				17 m (57 ft)			
Platform Weight	W_p	2,478,888	N	557,276	lbf	4,535,647	N	1,019,654	lbf
Distance from CG to Turbine Drag	r_t	8	m	25	ft	10	m	33	ft
Distance from CG to Mooring Attachments	r_l	11.1	m	36	ft	13.6	m	45	ft
Mooring Scope		1/7				1/7			
Tension in Single Mooring Line	T_l	361,061	N	81,170	lbf	635,383	N	142,840	lbf
Platform Draft	d_p	0.796	m	2.6	ft	0.973	m	3.2	ft
Tipping Angle	θ	0.017	rad	1.0	deg	0.017	rad	1.0	deg
Platform Length (at waterline)	L	33.4	m	109.7	ft	40.9	m	134.2	ft
Total Platform Width		19.2	m	63	ft	23.5	m	77	ft

Mooring System

The platform would be held in place by four mooring lines. Each would connect to an embedment anchor via a length of heavy chain. During each tidal cycle the aft pair of lines would be slack. Thus, the platform would not pivot to match the tidal cycle. However, the moorings would be laid out such that the platform would align with the dominant current direction on both the ebb and flood tides, which are approximately 20 degrees off of a perfect 180 degree alignment (Howes et al., 2009).

Once the mooring line tension was determined for each platform size, a mooring line was chosen that would have a safety factor greater than two for even the largest platform investigated. Plasma 12 strand rope was chosen for its low stretch, low creep, ease of handling, easy splicing, neutral buoyancy in water, and the fact that it does not torque when loaded. Once a suitable mooring line was chosen, studlink chain with a similar breaking strength was selected. The properties of the selected rope and chain are shown in Table 44.

Table 44. Rope and chain specifications.

Material	Nominal Diameter		Breaking Strength	
Rope	mm	in	N	lbf
Plasma 12 Strand, 28 mm	28	1.1	653,900	296,600
Chain				
36mm U3 Stud Link Chain	36	1.42	731,826	332,000

Stingray embedment anchors were chosen for their high ratio of holding power to weight. A safety factor of 5 was required (partially because the holding power of the anchor is specified for sand, and the seafloor in the Muskeget Channel is sand-gravel). As with the mooring line, one anchor size was chosen which would be sufficient for each maximum turbine size to be tested. The properties of Stingray anchors of several sizes are shown in Table 45.

Table 45. Stingray anchor specifications. The selected anchor is shown in bold.

Weight		Holding Power in Sand	
kg	tonne	N	lbf
250	30.9	303,000	668,000
375	42.6	418,300	922,200
500	**53.6**	**525,800**	**1,159,200**
750	74.0	725,800	1,600,100
1000	93.0	912,300	2,011,300

Platform Dynamics

The initial design criteria for the Floating Platform concept, addressing static stability, were expanded to include the platform's dynamic behavior in the Muskeget Channel environment. The objective was to design a floating platform with minimal operational downtime due to the sea state. A mathematical model was developed by Dewhurst (2013) and Dewhurst et al. (2013) to predict the platform response to waves in addition to current. After model validation in field experiments, this computer simulation was used to calculate the seakeeping behavior of platform designs in seas characteristic of Muskeget Channel as inferred from historical wave data. Operating limits, based on crew functionality and wave-deck contact criteria, were determined.

The two-dimensional mathematical model enabled prediction of forces and motions associated with a moored, floating platform mounting a tidal turbine in current and waves. The model was used to calculate heave, pitch, and surge response to collinear waves and current. Waves considered were single frequency or random seas with a specified spectrum. The mooring consisted of a fixed anchor, heavy chain (forming a catenary), a lightweight elastic line, and a mooring ball tethered to the platform. The equations of motion and mooring equations were solved using a marching solution approach implemented using MATLAB.

In the field validation study, the model was applied to the UNH CORE 35 foot (10.7 m) twin-hulled platform used to deploy a 0.9 m shrouded, in-line horizontal axis turbine. Added mass and damping coefficients were obtained empirically using a 1/9 scale physical model in wave tank experiments. Full scale tests were used to specify drag coefficients for the turbine and platform. The computer model was then used to calculate full scale mooring loads, turbine forces and

platform motion in preparation for a full scale test of the UNH CORE tidal turbine in Muskeget Channel. During the field experiments, wave, current and platform motion were recorded. The field measurements were used to compute Response Amplitude Operators (RAOs), essentially normalized amplitudes or frequency responses, for heave, pitch and surge. The measured RAOs were compared with those calculated using the model. The very good agreement indicated that the model could serve as a reliable design tool for larger test platforms.

Model Application

The mathematical model was used to simulate the response of a Muskeget test facility platform that was larger than, but proportional to, the UNH CORE 35 ft. platform. Thus, the free-release tests on the scale model of the UNH platform could simply be scaled using a new Froude scale factor. The initial length of the platform design was found using hydrostatics, as the minimum length that allowed less than 1 degree tipping at 2.5 m/s current with no waves while deploying a 9 m (29 ft.) turbine (as described in "Floating Platform: Governing Equations-Hydrostatics"). The platform's operability range was then analyzed using the mathematical model with long-term wave data as described below. Tow design criteria were applied to determine operating limits—loss of crew functionality and wave contact with the platform ends. This was repeated until a design was found that could operate for more than 90% of the days in an average year.

Operating Limits

Wave data was obtained from the Martha's Vineyard Coastal Observatory (MVCO), roughly six miles west of the southern opening of Muskeget Channel, one mile off of the coast of Martha's Vineyard in 12 m (39 ft.) water. There are differences between the MVCO site and the Muskeget site (depth, currents, wind patterns, etc.) but this was the most relevant data available at the time of analysis. The observatory calculates wave height spectra for twenty-minute segments by using ADCP instrumentation to measure the fluid velocity and direction near the surface (specifically, at 85% of the distance to the mean free surface, with the full distance calculated from a pressure sensor in the ADCP). That value is then extrapolated to the surface using linear wave theory (Wood's Hole, 2012). These data are plotted in Figure 35 and Figure 36 for a typical winter and summer month, respectively.

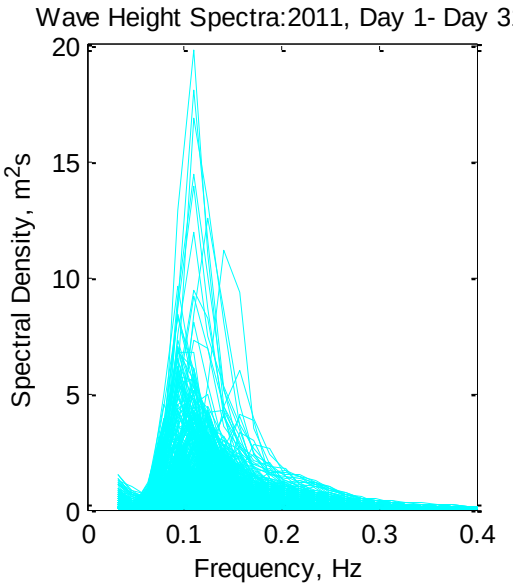

Figure 35. Wave height spectra at MVCO, January 2011

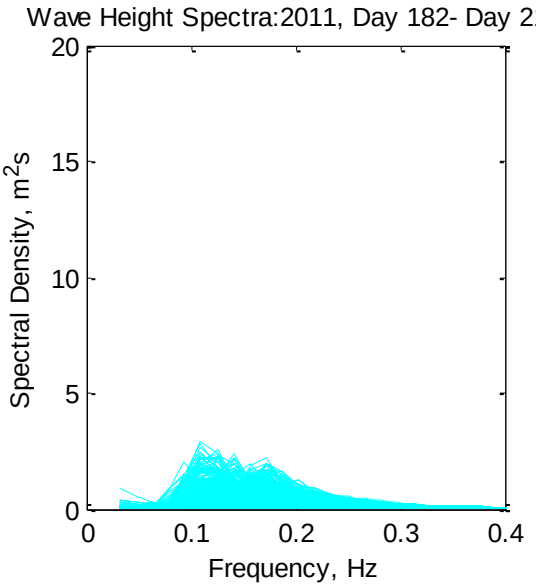

Figure 36. Wave height spectra at MVCO, July 2011

UNH's 35-foot (10.67 m) tidal energy test platform was used to test a hydrokinetic turbine in Muskeget Channel on July 15, 16 and 19, 2012 (Dewhurst et al., 2012). During the testing, significant wave height measurements were generally within 10% of those at the MVCO site. Thus, it was concluded that the historical data from MVCO was sufficiently representative of the wave climate in Muskeget Channel.

The percentage of time during which the platform could operate was found as follows. The historical wave height spectrum data (Figure 37-A) from the Martha's Vineyard Coastal Observatory was converted to wave heave acceleration spectra using the relationship,

$$S_a = \sigma_o^4 S_\zeta \tag{99}$$

where S_a is the wave acceleration spectra (Figure 37-C), σ_o is the wave frequency in rad/s (Figure 37-B) and S_ζ is the wave height spectrum. This results from the relationship of vertical acceleration, $\ddot{\zeta}$, to elevation at the surface, ζ, for a linear wave,

$$\ddot{\zeta} = -\sigma^2 \zeta \tag{100}$$

The heave Response Amplitude Operator (RAO) for the platform was found using a range of single frequency waves in the mathematical model. Vertical displacement RAOs were found at both the bow and stern of the vessel, and it was found that the RAO at the stern (Figure 37-D) was consistently higher than that at the bow. This is due to the phase relationship between heave

and pitch. The wave acceleration spectrum was then multiplied by the square of the stern RAO to find the stern acceleration spectrum, S_ap (Figure 37-E). This spectrum was numerically integrated over the frequency range to find the variance of the platform acceleration. Finally, the Root-Mean-Squared (RMS) acceleration was found as the square-root of the variance.

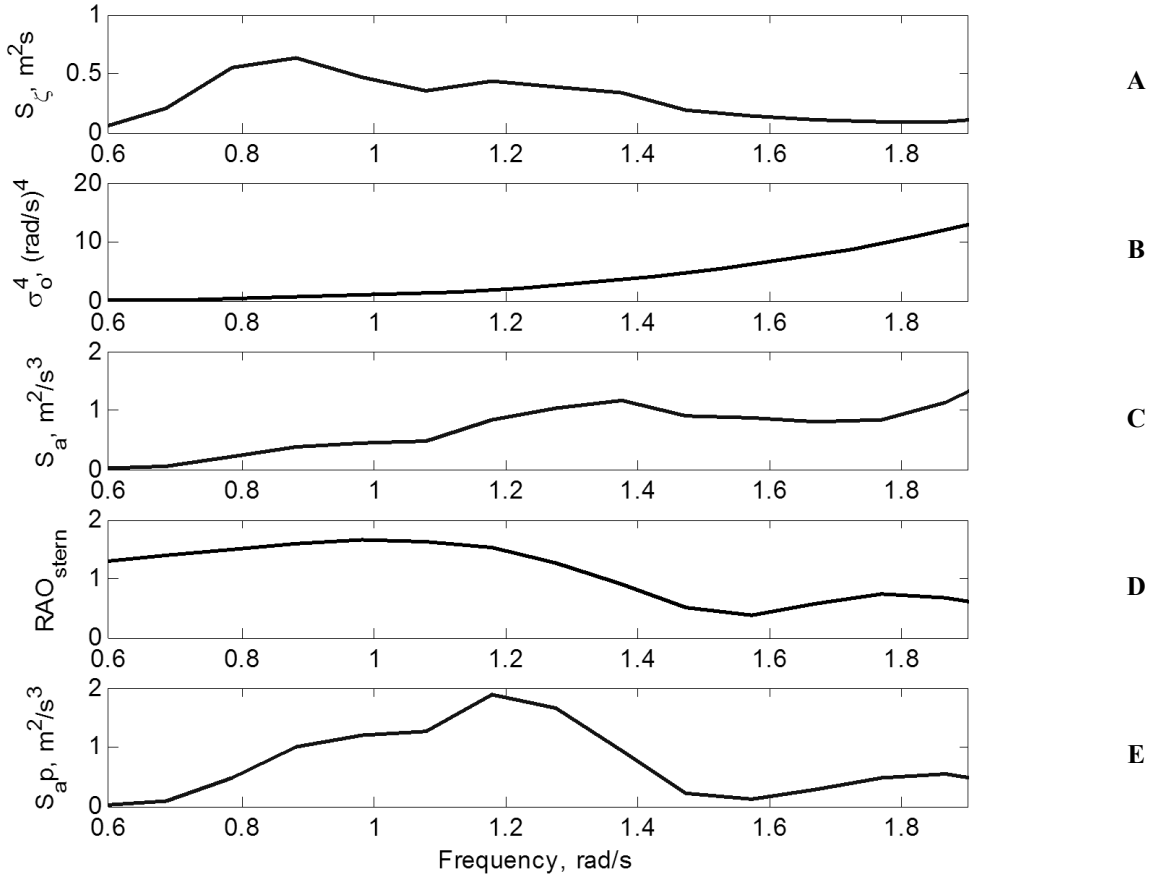

Figure 37. Example of the development of the platform acceleration response spectrum beginning with an arbitrarily-selected wave height spectrum. This spectrum was used to compute RMS accelerations (averaged over 20 minute segments) throughout a typical year.

Thus, the maximum RMS acceleration experienced on the platform for any wave height spectrum was found as

$$a_{RMS} = \sqrt{\int RAO_{stern}^2 \sigma_o^4 S_h df}, \tag{101}$$

where f is the wave frequency. This value was calculated for each wave spectrum acquired from the MVCO (20-minute samples) for the year 2011 and compared to a maximum operable RMS acceleration. This limit was taken to be 0.2 g (1.96 m/s^2), which the International Standards Organization (1997) says is "not tolerable for longer periods" and "quickly causes fatigue" and allows only "light manual work by people adapted to ship motions." The RMS accelerations that

would have been experienced on the platform throughout 2011, in reference to this maximum acceleration limit, are shown in Figure 38. It was found that the accelerations experienced exceeded the limit of 0.2 g for about 1.5% of a typical year.

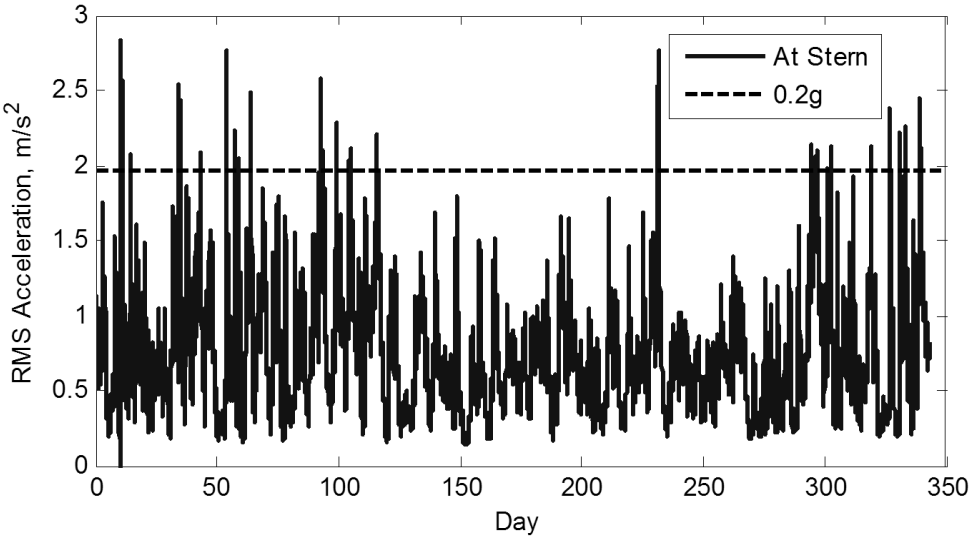

Figure 38. RMS accelerations predicted, using 2011 wave data from the MVCO.

In addition to the crew's ability to work on the platform, wave contact and water-on-deck events were also considered. In the mathematical model, a platform design meeting the maximum acceleration criteria was subjected to a range of single frequency waves. The difference between the surface elevation at the bow and the vertical position of the bow was compared to the freeboard of the platform at equilibrium, specified as one tenth the length of the platform. The height of the single-frequency wave in which the freeboard was regularly exceeded was taken to be the maximum significant wave height in which the platform could operate. This maximum significant wave weight was 3.4 m (10.4 ft.).

After the maximum single-frequency wave height was found, a similar approach was used with irregular waves. In the mathematical model the design was subjected to a Bretschneider wave spectrum. The significant wave height (and period) of this spectrum was increased until the frequency of wave contact/water-on-deck events exceeded once per hour. This resulted in a maximum allowable significant wave height of 2.6 m. It was noted in the course of this analysis that the non-linearity in the system's pitch response makes it particularly vulnerable to storm events. Since this method yielded a lower significant wave height than the single frequency approach, the more conservative value of 2.6 m was used to compute operational limits.

The significant wave height data for the past five years (obtained in 20-minute averages) was examined to calculate the percent time in which wave heights were below the 2.6 m limit. Table 46 shows the percentage of days in each month during which the significant wave height

exceeded 2.6 m. These results show that the platform could operate for 90% of the days during a typical year.

Table 46. Percentage of days in which the 25.1 m platform would be inoperable.

	Jan	Feb	Mar	Apr	May	Jun	Jul	Aug	Sep	Oct	Nov	Dec	Avg.
2007	16%	11%	32%	10%	6%	7%	3%	0%	0%	3%	7%	10%	**9%**
2008	19%	32%	19%	27%	0%	0%	0%	0%	3%	13%	17%	35%	**13%**
2009	10%	36%	23%	13%	3%	0%	3%	10%	7%	0%	7%	26%	**12%**
2010	10%	7%	13%	0%	3%	0%	0%	0%	7%	10%	13%	10%	**6%**
2011	3%	18%	6%	23%	0%	0%	0%	6%	3%	0%	0%	19%	**7%**
Avg.	**12%**	**21%**	**19%**	**15%**	**2%**	**1%**	**1%**	**3%**	**4%**	**5%**	**9%**	**20%**	**9%**
SD.	0.06	0.11	0.09	0.10	0.02	0.03	0.01	0.04	0.03	0.05	0.06	0.10	0.10

It should be noted that non-operating conditions are due to periods of high waves that could reasonably be attributed to major storm events. These could presumably be forecast in advance, allowing the platform to be towed into a safe port.

Final Design

The final iteration of the floating platform was longer than the initial design, which was based only on hydrostatics. Also, unlike the initial design, cylindrical pontoons are employed. The specifications of a platform capable of deploying a 9 m (29 ft.) turbine for 90% of the days in an average year are shown in Table 47.

Table 47. Floating platform specifications for deploying a 9 m (29 ft.) turbine.

Pontoon Diameter	2.12	m	6.9	ft
Pontoon Length	29.7	m	97.3	ft
Beam (between centers of pontoons)	17.3	m	56.9	ft
Freeboard (at equilibrium)	2.3	m	7.1	ft
Total (estimated) Mass of Structure	39,344	kg	86,738	lbm
Draft	0.66	m	2.2	ft
Chain Diameter	76	mm	3	in
Total Chain Length	90	m	295	ft
Total Line Length	715	m	2346	ft

Legend:

Iterated values
Design inputs
Calculated values

Costing

The material and fabrication costs for the floating platform were estimated by prorating quotes obtained for the UNH CORE V2 platform (Byrne, 2013). Quotes for hulls fabricated from A36 steel and coated with marine-grade epoxy were scaled by the cube of the length ratio (the length of the Muskeget platform divided by the length of the V2 platform). The same was done for the deck (grade 50 steel), derrick, and cage structures and a quote for assembling the platform. For the lifting mechanism, quotes were obtained from TWG Lantech (2011) for winches of various sizes. Quotes for the mooring equipment were obtained from Jeyco, of Austalia (2011) and Puget Sound Rope, CT (2011). The cost of installing the mooring grid was estimated as the cost of a 100 ft. working vessel hired for seven (7) days. The results of this cost analysis are shown in Table 48.

Table 48. Cost of Floating Platform.

Turbine Diameter			**4 m**	**(14 ft)**	**9 m**	**(29 ft)**
Costing	Unit cost		Quantity	Cost	Quantity	Cost
Structure						
Hulls	$64,000	64’	55 ft	$38,674	97 ft	$217,679
Beams, Derrick	$37,000	64'	55 ft	$22,358	97 ft	$125,846
Assembly	$50,000	64'	55 ft	$30,214	97 ft	$170,062
Mooring						
500 Kg Stingray Anchors	$1,458	ea.	4	$5,832	4	$5,832
28 mm Plasma Rope	$15	/ft.	2756	$40,320	2756	$33,600
Lifting						
M18Winch	$23,000	ea.	2	$46,000	2	$350,000
Installation						
Nobska	$5,000	/day	7	$35,000	7	$35,000
Total				**$218,398**		**$938,018**

Table 48. Cost of Floating Platform (continued).

Turbine Diameter			**13 m**	**(43 ft)**	**17 m**	**(57 ft)**
Costing	Unit cost		Quantity	Cost	Quantity	Cost
Structure						
Hulls	$64,000	64’	119 ft	$405,292	146 ft	$741,567
Beams, Derrick	$37,000	64'	119 ft	$234,309	146 ft	$428,718
Assembly	$50,000	64'	119 ft	$316,634	146 ft	$579,349
Mooring						
500 Kg Stingray Anchors	$1,458	ea.	4	$5,832	4	$5,832
28 mm Plasma Rope	$15	/ft.	2756	$40,320	2756	$40,320
Lifting						
M18Winch	$23,000	ea.	2	$350,000	3	$525,000
Installation						
Nobska	$5,000	/day	7	$35,000	7	$35,000
Total				**$1,387,387**		**$2,355,786**

CHAPTER 8

NATURAL BERTH

A Natural Berth would comprise only an unmodified section of seafloor with monitoring equipment and electrical power connection provided and the necessary permits in place for testing hydrokinetic devices. Thus, developers would be responsible for device installation and could test integrated systems that include a turbine, a generator, and a foundation system. This would allow developers to test concepts at the highest Technology Readiness Level defined by the Department of Energy (2009) before commercial deployment.

A Natural Berth option was considered for the following advantages:

- The complete system would be tested.
- The developer would have maximum freedom
- The berth could accommodate systems up to TRL 9 (DECC stage 5) which allows for commercial demonstration.

Disadvantages include:

- The developer is faced with substantial installation, maintenance, and removal costs.
- The type of foundation is undefined, potentially raising permitting obstacles.
- The berth would not be conducive to devices in the early stages of development.

The Natural Berth option would provide a permitted, instrumented (including electrical power connection and measurement and flow measurement) section of seafloor whose baseline has been thoroughly investigated. Developers would be responsible for installing their devices, including any necessary foundation or mooring system, and would remove devices after testing is completed. Thus, developers would be able to see how well their foundation concepts are suited to the high sediment transport environment on the Muskeget seafloor. The European Marine Energy Centre (EMEC) reports that it has successfully employed this model for several years (2011).

The Natural Berth option could exist in place of or in parallel with a platform option, alternatives for which are shown in the following section. A schematic is shown in Figure 39. Note that this figure indicates hardwired ADCP connections and also incorporates the Edgartown Tidal Power Pilot Project.

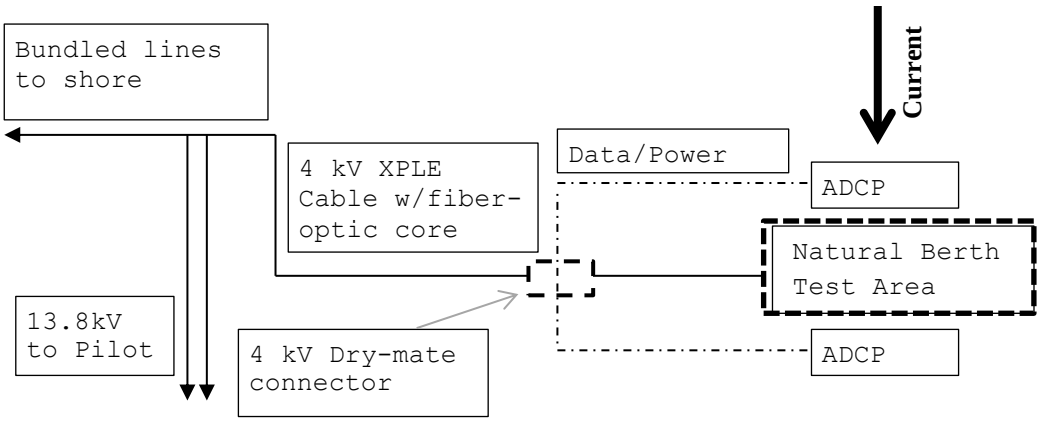

Figure 39. Schematic of Natural Berth layout.

CHAPTER 9

ELECTRICAL POWER CONNECTION AND INSTRUMENTATION

The test site will include, at a minimum, means of accepting the electrical power generated by the test device and instrumentation to measure the generated power and the flow conditions.

Electrical Power Connection

The site will be equipped with a submersible three-phase electrical power connection to transmission lines running to shore. This type of connection, shown in Figure 40, has been implemented at the European Marine Energy Center. This will connect the device to either the grid or local users via armored 3-phase XLPE undersea cabling, shown in Figure 41. If the device is connected to the grid it will be via a 4 kV line to an on-land substation along one of the routes shown in Figure 42, whose distances are given in Table 49. Determining the cost of installing these cables was outside of the scope of this thesis. However, it was noted that similar cable-laying projects on the northeastern coast of the U.S. have cost about $1 million/mile of cable.

Figure 40. Subsea electrical power connection (EMEC).

Figure 41. Typical XLPE 3-phase undersea cable with fiber-optic core (EMEC).

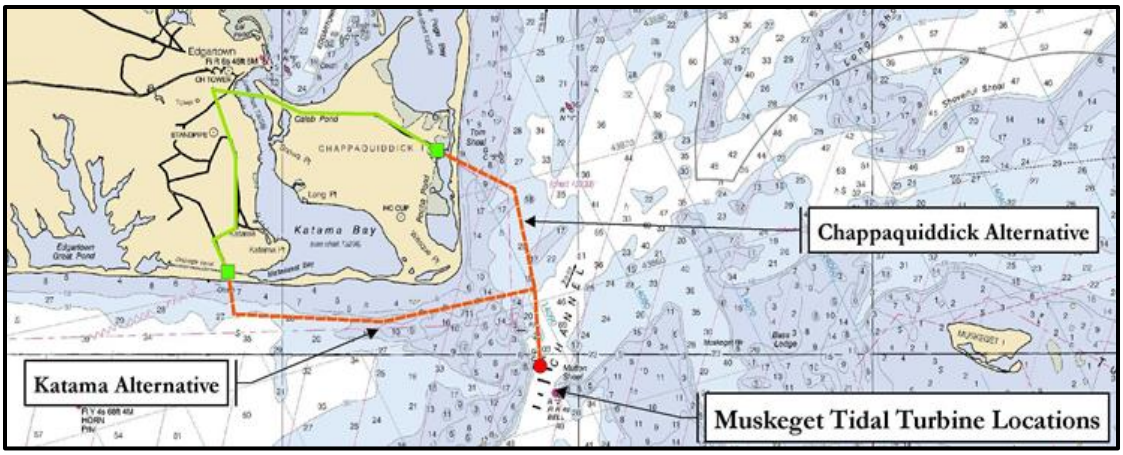

Figure 42. Potential cable routes.From Harris, Miller, Miller, and Hanson (2010).

Table 49. Grid connection distances.

Option 1: Via Chappaquiddick	5.6	km	3.5	miles
Option 2: Via Katama	8	km	5.0	miles

Instrumentation

Instrumentation will be in accordance with the guidelines set forth in *Assessment of Performance of Tidal Energy Conversion Systems*, which were developed in consultation with The European Marine Energy Centre Ltd and with other interested parties in the UK tidal energy community.

The guidelines for power measurement found therein can be satisfied by including a "3- or 2-phase power measurement device, such as a transducer…[which] shall conform to [accuracy] Class 0.5, or better, as defined in IEC 60044-1" (International Electrotechnical Commission, 2002) as close to the device as practicable. The data from this device could be transmitted to shore via the fiber-optic core of the power cable, if such a cable is laid and the necessary connector is installed.

The requirements for flow measurement can be satisfied by placing vertical-looking ADCPs up- and downstream of the test area. The specifications for the ADCPs can be easily met by, for example, the RDI Workhorse Sentinel V at 600 kHz (Teledyne RD Instruments, 2012). These would be mounted in bottom-mounted trawl-resistant housings and equipped with acoustic release mechanisms or, for a floating platform, on the platform itself. Three options exist for acquiring ADCP data from bottom-mounted systems:

- Hardwiring to the power/data cable for transmission to shore
- Equipping with acoustic modems
- Manually retrieving self-recorded data

Hardwiring is attractive for its real-time transmission, reliability, and its ability to supply power to the ADCP, allowing indefinite deployment. However, it involves expensive equipment, and its longevity is a concern. A hardwire connection on an ADCP installed at the European Marine Energy Centre failed in one year (Devine, 2011). The designer of that system cautions against such a transmission system and questions the need for real-time ADCP data (Wood, 2011).

Acoustic modems can also provide real-time data if coupled with a gateway buoy. However, these can be plagued with reliability issues (Codiga et al., 2004), making them undesirable for this application.

Relying on the self-recording mechanism requires divers to manually retrieve data from the ADCPs. However, this method is extremely reliable and requires the least capital cost. Additionally, the cost of retrieving data manually may not greatly exceed the maintenance cost of other data-acquisition options, as divers may periodically be required to visit the devices regardless of the method used.

The baseline capital costs for flow measurement are shown in Table 50. It is important to note that data retrieval, power measurement, and connection costs are not included.

Table 50. Flow measurement equipment costs.

ADCPs	$/unit	Quantity	Cost
RDI Workhorse Sentinel	$30,000	2	$60,000
Trawl-resistant Bottom Mounts	$20,000	2	$40,000
Acoustic Release	$7,000	2	$14,000
Total			**$114,000**

CHAPTER 10

COST SUMMARY AND COMPARISON

Six design alternatives were identified, and basic engineering calculations were performed for each. Costs for each were estimated primarily from manufacturer and contractor quotes and estimates. The results are compared in

Figure 43 for each scale investigated. These estimates do not include instrumentation or cabling cost. Note that the natural berth is not included because its structural cost is zero.

.

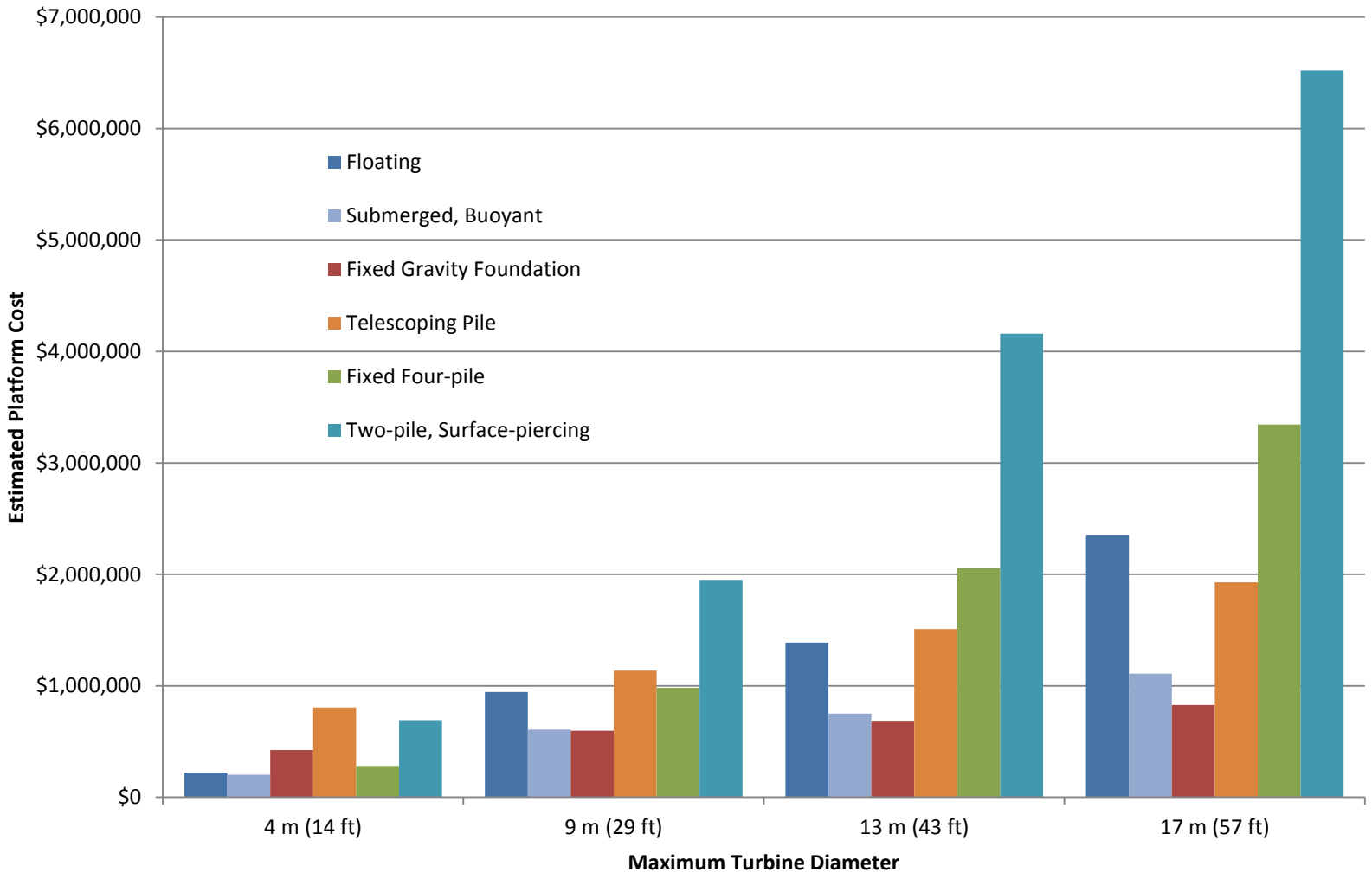

Figure 43. Estimated Platform Cost Comparison.

CHAPTER 11

CONCLUSION

Recommendation

Six design alternatives for a test platform were considered for technical and economic feasibility, in addition to a natural berth test bed concept. Neither the four-pile platform nor the fixed gravity foundation platform provided convenient access for developers. The submerged buoyant platform and the telescoping gravity foundation platform both provided access for developers but would require extensive proof-of-concept work and further development before being implemented. Since developer-friendliness and reliability were crucial factors in comparing design alternatives, all four of these concepts were rated lower after the preliminary engineering calculations and costing were completed.

Both the floating platform and the two-pile, surface piercing platform were analyzed in detail. This analysis focused on platforms capable of testing a maximum turbine diameter of 9 m (29 ft.) because the core of the maximum tidal current extends vertically over this range in the upper portion of the water column.

The floating platform would incur lower construction and installation costs (approximately $1 million) than the two-pile platform. It could be easily removed from the site when necessary, which could be very useful as the test site and testing procedures are being developed. As for a floating platform's performance in Muskeget's wave environment, it was found that a floating platform could typically operate for more than 90% of the year.

The two-pile, surface piercing platform would require more capital for construction and installation (approximately $2 million). However, testing from a fixed platform can be very beneficial to the developer and a permanent presence in the Muskeget Channel could be advantageous.

Furthermore, a natural berth would be necessary for developers wishing to evaluate complete systems (including mounting structure). Thus, it is recommended that natural berth be incorporated in addition to a testing platform.

The floating platform, the two-pile platform, and the natural berth were presented to the U.S. Coast Guard Waterways Management Division for comment. It was indicated that either option could be implemented in the Muskeget Channel (E.G. LeBlanc, *personal communication*). It was noted that the two-pile platform could even be used as an aid to navigation.

Given the lower cost of the floating platform and the present experience with such platforms, it is recommended that the Muskeget Channel tidal energy facility implement a floating platform as the near-term testing solution. Then, as the tidal energy industry grows, demand for the facility

increases, experience with the testing site is gained, and funding becomes available, a two-pile, surface piercing platform could be implemented.

Future Work

It is important to note that cost estimates for both the floating platform and the two-pile platform are based on certain assumptions (which are detailed in this document). Although this analysis was conducted carefully, exact quotes for a completed design should be sought before making final decisions. For the floating platform, this will require detailed structural design of platform. For the two-pile platform, this will require more detailed structural analysis of the "bridge" section connecting the two piles, sub-bottom profiling and, possibly, exploratory boring to ensure that installation quotes will be accurate.

REFERENCES

American Petroleum Institute, 1993. *Recommended Practice for Planning, Designing and Constructing Fixed Offshore Platforms -- Working Stress Design.* Washington.

ASTM International, 2009. *Standard Specification for High-Yield-Strength, Quenched and Tempered Alloy Steel Plate, Suitable for Welding.* West Conshohocken.

ASTM International, 2010. *Standard Specification for Welded and Seamless Steel Pipe Piles.* West Conshohocken.

ASTM International, 2011. *Standard Specification for Seamless and Welded Steel Pipe for Low-Temperature Service.* West Conshohocken.

Bachant, P., 2010. *Development of Hydrokinetic Test Bed and Turbine Performance Evaluation.* Boston. p. 26.

Barrett, S., 2010. *Muskeget Channel Tidal Energy Project.* Boston, New England Marine Renewable Energy Conference.

Barrett, S., 2012. *TECHNICAL MEMORANDUM: Muskeget Channel Tidal Energy Test Facility, Draft Progress Report - Comments.* Burlington, MA

Beer, F. P., Johnston, E. R. J., DeWolf, J. T. & Mazurek, D. F., 2012. *Mechanics of Materials.* 6 ed. New York: McGraw-Hill.

Billingham, J., Sharp, J. V., Spurrier, D. J. & Kilgallon, D. P. J., 2003. *Review of the performance of high strength steels used offshore,* Cranfield: School of Industrial and Manufacturing Science .

Blackwood, D., Lim, C. & Teo, L., 2010. Influence of fouling on the efficiency of sacrificial anodes in providing cathodic protection in Southeast Asian tropical seawater. 26(7).

Byrne, J., 2013. Design of a Test Platform for Hydrokinetic Turbines in a Tidal Estuary. MS Thesis, University of New Hampshire. *In preparation.*

Celikkol, B. et al., 2006. *Engineering Overview of the University of New Hampshire's Open Ocean Aquaculture Project,* Boston: IEEE.

Clauss, G., Lehmann, E. & Ostergaard, C., 1992. Offshore Structures Conceptual Design and Hydromechanics. *Springer-Verlag,* Volume I.

Coastal Systems Program, University of Massachusetts at Dartmouth. 2011. *Siting Optimization Surveys for Edgartown FERC Permit Area.* [Online]

Available at:
http://www.smast.umassd.edu/news_frontpage/2011/muskeget_turbine_test_summary.php.
[Accessed 7 December 2012].

Codiga, D. L., Rice, J. A. & Baxley, P. A., 2004. Networked Acoustic Modems for Real-Time Data Delivery from Distributed Subsurface Instruments in the Coastal Ocean: Initial System Development and Performance. Volume 21.

Corus Construction and Industrial, 2005. *A corrosion protection guide -- For steel bearing piles in temperate climates,* Scunthorpe: Orchard Corporate Ltd..

Das, B., 2000. *Fundamentals of Geotechnical Engineering.* Brooks/Cole: Pacific Grove.

Devine, P., 2011. *ADCPs in Renewable Energy.* Cambridge, 3rd Annual New England Marine Renewable Energy Center Technical Conference .

Dewhurst, T., Rowell, M., DeCew, J. Baldwin, K., Swift, M. R., & Wosnik, M. 2012. *Turbulent inflow and wake of a marine hydrokinetic turbine, including effects of wave motion.* San Diego, 65th Annual Meeting of the APS Division of Fluid Dynamics, Volume 57, Number 17.

Dewhurst, T., 2013. *Muskeget Channel Tidal Energy Test Facility.* MS Thesis, University of New Hampshire. Durham, NH.

Dewhurst, T., Swift, M. R., Wosnik, M., Baldwin, K., DeCew, J., & Rowell, M., 2013. *Dynamics of a Floating Platform Mounting a Hydrokinetic Turbine.* Marine Technology Society Journal, *Submitted for publication.*

Dutile, K., Pelletier, M.; Browne, J., Buruchian, K., Dreyer, D., Ducharme, T. 2009. *Tidal Power Generation: Infrastructure,* Durham: University of New Hampshire.

European Marine Energy Centre Ltd., 2012. *EMEC: About Us.* [Online]
Available at: http://www.emec.org.uk/about-us/
[Accessed 7 December 2012].

European Marine Energy Centre, Ltd.; Department for Business Enterprise and Regulatory Reform, 2009. *Assessment of Performance of Tidal Energy Conversion Systems,* Wakefield: The Charlesworth Group .

European Marine Energy Centre, 2011. *Charting Achievement ,* Stromness: European Marine Energy Centre, Ltd..

European Steel Design Education Programme, 1994. *Tubular Structures, 13.1: Application of Hollow Sections in Steel Structures,.* [Online]
Available at: http://www.fgg.uni-lj.si/kmk/esdep/master/wg13/l0100.htm

[Accessed 25 February 2011].

Fundy Ocean Research Center for Energy, 2012. *FORCE.* [Online]
Available at: http://fundyforce.ca/ [Accessed 7 December 2012].

Gerwick, B. C. J., 2007. *Construction of Marine and Offshore Structures.* Boca Raton: CRC Press.

Hoerner, S. F., 1965. *Fluid-dynamic drag: practical information on aerodynamic drag and hydrodynamic resistance.*

Howes, B., Schlezinger, D, Bartlett, M., & Benson, J. 2009. *Marine Renewable Energy Survey of Muskeget Channel,* New Bedford:

International Electrotechnical Commission, 2002. *Instrument transformers – Part 1: Current transformers,* Geneva: IHS.

International Standards Organization, 1997. *Mechanical Vibration and Shock Evaluation of Human Exposure to Whole Body Vibration—Part 1.*

Jokela, G. & Kunsemiller, J., 1996. *Phase II Demonstration: Seawater Hydrualic Transfer Pump,* Port Hueneme: Naval Facilities Engineering Service Center.

Krutz, G. W. & Chua, P. S. K., 2004. *Water Hydraulics--Theory and Applications 2004.* Louisville, Workshop on Water Hydraulics, AETC '04.

Kumar, S. & Mittal, V., 1999. Finite Element Study of Vortex-Induced Cross-Flow and In-Line Oscillations of a Circular Cylinder ot Low Reynolds Numbers. Issue 31.

Lamb, H., 1932. *Hydrodynamics.* 6 ed. Cambridge: Cambridge University Press.

Morley, J. & Bruce, D., 1983. *Survey of Steel Piling Performance in Marine Environments,* Luxembourg: European Coal and Steel Community.

Mueller, M., Jeffre, H., Wallace, R. & Von Jouanne, A., 2009. Centers for Marine Renewable Energy in Europe and North America. *Marine Renewable Energy | Technology Development and Deployment,* 22(2), pp. 42-52.

Musial, W., 2008. *Status of Wave and Tidal Power Technologies for the United States,* Golden: National Renewable Energy Laboratory.

Norton, R. L., 2006. *Machine Design.* Upper Sadle River: Pearson Prentice Hall.

O Rourke, F., Boyle, F. & Reynolds, A., 2010. Tidal energy update 2009. *Applied Energy,* 87(2), pp. 398-409.

Penland, J. A. & Fetterman, D. E., 1956. *The Effects at a Mach Number of 6.86 of Drag Brakes on the Lift, Drag, and Pitching Moment of an Ogive Cylinder,* Washington: National Advisory Committee for Aeronautics.

Polagye, B., 2010. *National Tidal Energy Platform: Concept Proposal.*

R.S. Means, 2011. *Site work & landscape cost data.*

Rocker, K. J., 1985. *Handbook for Marine Geotechnical Engineering.* Palm City: Pile Buck.

Rowell, M., 2013. *Experimental Evaluation of a Mixer-Ejector Hydrokinetic Turbine at Two Open-Water Test Sites.*MS Thesis, University of New Hampshire.

Schlezinger, D., 2012. *In situ testing of tidal turbines in Muskeget Channel.* Boston, Energy Ocean 2012.

Seymour, R. J., Olfe, C. B. & Thomas, J. O., 2012. *CDIP wave observations in Superstorm Sandy.* San Diego: Scripps Institution of Oceanography.

Smith, W., 1967. Computation of Pitch and Heaving Motions for Arbitrary Ship Forms. *International Shipbuilding Progress,* 14(155).

Specialty Steel Industry of North America (SSINA), 2011. *Frequently Asked Questions.* [Online]
Available at: http://www.ssina.com/faq/index.html
[Accessed 30 May 2011].

Sterne, J., Jensen, T. C. & Keil, J. R.-C. R., 2008. *Ocean Renewable Energy: A Shared Vision and Call for Action.*

Taly, N., 2010. *Design of Reinforced Masonry Structures.*McGraw Hill Professional.

Techet, A., 2004. *Design Principles for Ocean Vehicles.* [Online]
Available at: http://ocw.mit.edu/courses/mechanical-engineering/2-22-design-principles-for-ocean-vehicles-13-42-spring-2005/readings/r13_morrison.pdf
[Accessed 15 November 2012].

Teledyne RD Instruments, 2012. *Workhorse Sentinel.* [Online]
Available at: http://www.rdinstruments.com/datasheets/wh_sentinel.pdf
[Accessed 5 January 2012].

Terra et Aqua, *Gravity Base Foundations for the Thornton Bank Offshore Wind Farm.* [Online]
Available at: http://www.terra-et-aqua.com/dmdocuments/terra115_3.pdf
[Accessed 27 June 2011].

Tomlinson, M. J., 2008. *Pile Design and Construction Practice.* New York: Taylor and Francis.

U.K. Department of Energy and Climate Change, 2008. *Tidal-current Energy Device Development and Evaluation Protocol,* London.

U.S. Department of Energy, 2009. *Technology Readiness Assessment Guide,* Washington.

U.S. Department of Energy, 2012. *DOE Reports Show Major Potential for Wave and Tidal Energy Production Near U.S. Coasts.* [Online]
Available at: http://apps1.eere.energy.gov/news/progress_alerts.cfm/pa_id=664
[Accessed 4 December 2012].

U.S. DOT Federal Highway Administration, 1998. *Design and Construction of Driven Pile Foundations--Workshop Manual.* Washington D.C.: Office of Technology Application.

U.S. Energy Information Administration, 2012. *Annual Energy Outlook 2012,* Washington.

Univeristy of Washington, 2011. *Northwest National Marine Renewable Energy Center.* [Online]
Available at: http://depts.washington.edu/nnmrec/about.html
[Accessed 7 December 2012].

Wood, J. 2011. *Personal Correspondance.*

Wood's Hole, 2012. *Martha's Vineyard Coastal Observatory.* [Online]
Available at: http://mvcodata.whoi.edu/cgi-bin/mvco/mvco.cgi
[Accessed 19 September 2012].

Wosnik, M., Swift, M. R., Baldwin, K. C. Despins, R., & Celikkol, B. 2010. *Infrastructure Development towards a Calibrated Tidal Energy Test Site at the University of New Hampshire*. Proceedings of First European Congress of the Int'l Association of Hydraulic Research (IAHR), Edinburgh, Scotland, May 4-6, 2010.

Final Report

Wave Observations and Modeling in the NOREIZ

Dr. E. Terray
Department of Applied Ocean Physics and Engineering
Woods Hole Oceanographic Institution

Overview: This project supplemented the acquisition of a Datawell MK-III Directional Waverider (DWR) by the New England Marine Renewable Energy Center (MREC) at the University of Massachusetts Dartmouth. Because high-quality, stand-alone measurements of waves is not a readily-available capability, it was understood that in addition to using the DWR in connection with this project, insofar as possible we would coordinate with other MREC activities in order to support them with wave measurements. We include a brief description of those supporting activities below.

The original motivation for this project was to develop an operational capability to use the DWR, in terms of its mooring, telemetry, and data recovery, and to use the buoy measurements to validate a wave prediction model for MREC's proposed National Offshore Renewable Energy Innovation Zone (NOREIZ). This region, which was proposed as a testbed for wind and hydrokinetic power generation technology, is shown in Figure 1. The Commonwealth of Massachusetts and the Department of the Interior have announced Requests for Interest (RFIs) to lease blocks for wind power development in an area that abuts the western boundary of the NOREIZ region. For hydrokinetics, the main area of interest is the Muskeget Channel, which is located just to the east of Martha's Vineyard and lies at the northern edge of the NOREIZ. There is a strong tidal flow in this channel and MREC investigators were involved in a study commissioned by Edgartown to investigate the feasibility of installing tidal turbines there to provide supplemental power to the town. For the development and operation of both wind and tidal power generation facilities, knowledge of the wave climate is important mostly in relation to construction and maintenance since the waves are the primary limiting factor for operations at sea. Consequently, the availability of reliable forecasts of the likely sea state (in terms of the heights, periods and directions of the most energetic waves) is an important capability.

These quantities are measured very well by the DWR system. A more detailed, spectral, description of the waves is required for the efficient operation of wave power generation devices. But since this is not a good region for wave power generation, we have not considered that application as a strong motivating factor.

At the start of this project, there was general consensus in the wave community that the SWAN spectral wave model (developed at the Delft University of Technology) was the leading model for predicting wave evolution in intermediate- and shallow-depth water. Although we started implementing that model, personnel changes prevented us from completing the work. However, over the life of the project, the performance of the NOAA wave model Wavewatch-III in intermediate and shallow water has improved

considerably to the point where it is equivalent to SWAN in terms of our needs. We discuss this more fully below, but a major advantage of Wavewatch-III is that as an operational model run by NOAA, its predictions are available on-line.

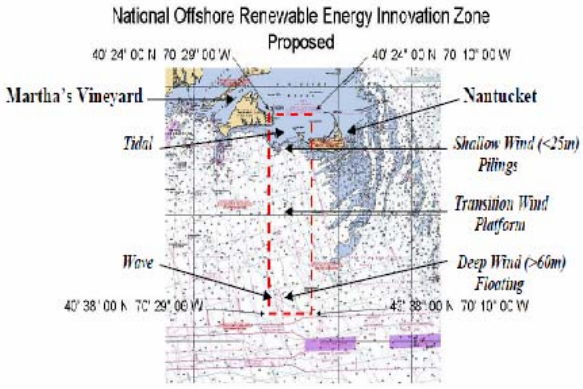

Figure 1 The proposed MREC NOREIZ region

Wave Buoy: The Datawell Mk-III Directional Waverider (DWR) is widely regarded as the premier moored wave height-direction measurement system available today. For example, the Coastal Data Information Program (CDIP) operated by the Scripps Institution of Oceanography uses DWRs extensively. A picture of the buoy in its transportation cradle is shown in Figure 2. The DWR used in this study is the 70 cm model. The hull is a sphere weighing ~ 225 lbs (with batteries sufficient for roughly 1 year of autonomous operation). Consequently a mid-size coastal vessel is required for deployment and recovery. The spherical shape of the hull minimizes pitching and rolling motions, and the mooring is highly compliant so that the buoy acts like a particle-follower at the surface. A schematic of the mooring arrangement for shallow- and intermediate-depth water is shown in Figure 3. The buoy is equipped with a GPS receiver and an Argos transmitter. In addition to the buoy position provided by service Argos, summary data are also relayed that include the buoy's GPS position, mean wave parameters and battery voltage. Additional telemetry options are available including GSM cellular, Orbcomm and Iridium, and HF (high-frequency) radio.

The DWR senses waves using a triplet of accelerometers mounted on a mechanically-stabilized platform which measure the three-dimensional acceleration of the buoy in a leveled coordinate system (*i.e.* transverse to the local gravitational acceleration). The azimuthal orientation of the buoy is determined using a three-axis magnetometer, and the measured buoy acceleration referenced to a fixed earth frame. The six auto- and cross-spectra that can be formed from the three accelerations in a fixed frame are used to estimate the wave height spectrum and the first two ($n = 1, 2$) complex Fourier coefficients of the frequency-direction spectrum $S(f, \vartheta)$, defined here as

$$c_n(f) = a_n - ib_n = \int_{-\pi}^{+\pi} d\vartheta \exp(-in\vartheta) S(f, \vartheta) \qquad (1.1)$$

Figure 2. A 70 cm DWR in its transportation cradle

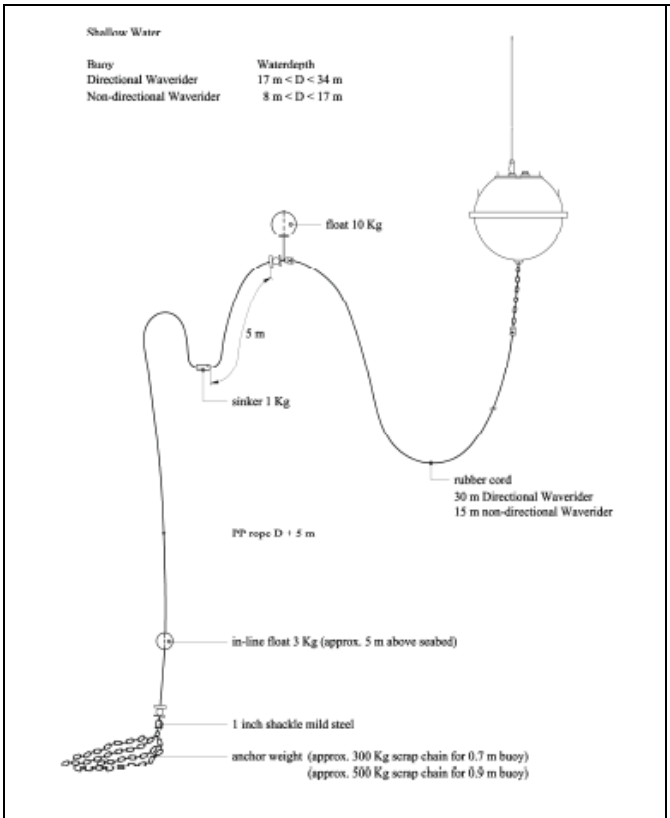

Figure 3a. Mooring configuration for shallow water depths

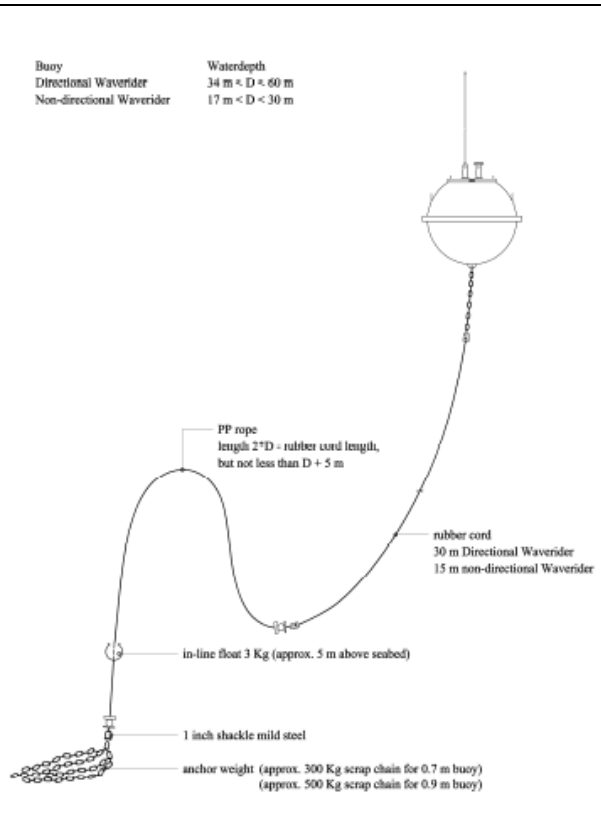

Figure 3b. Intermediate water depth mooring configuration

These coefficients have a physical interpretation: $a_0(f)$ is the non-directional spectrum of wave height, $\overline{\vartheta(f)} = \arctan 2(b_1, a_1)$ is the mean wave direction (in the sense of a vector average over the propagation directions, and $\delta\vartheta(f) = \sqrt{2(1-m_1)}$ is a measure of the directional spread (where $m_1 = (a_1^2 + b_1^2)^{1/2} / a_0$).

The wave heights and periods based on the estimated height spectrum $a_0(f)$ are fairly robust to uncertainties introduced by the buoy dynamics and the influence of the mooring. The directional information is less robust, but the mean direction is a crude estimator, and a higher degree of uncertainty is acceptable. For example, if a sea is bimodal with equal energy propagating in each direction, then $\overline{\vartheta}$ will point along the bisector of the angle between the two peaks. There are even more caveats concerning the estimator for the directional spread, and although alternate estimators are available, all rest on various assumptions concerning the shape of the directional distribution. Consequently, the information returned by any wave buoy has to be interpreted carefully within the context of the intended application.

Wave Measurements: We carried out two deployments of roughly 3 months duration each, in both shallow (12 m) and intermediate (~ 40 m) water depths. These deployments gave us operational experience with the two mooring configurations shown in Figure 3, above. The shallow water deployment was adjacent to the 12 m underwater node at the Martha's Vineyard Coastal Observatory (MVCO), which a facility of the Woods Hole Oceanographic Institution (Figure 4). The site is roughly 2 km south of the eastern end of Martha's Vineyard. The second deployment was farther south by roughly 20 km in approximately 40 meters of water.

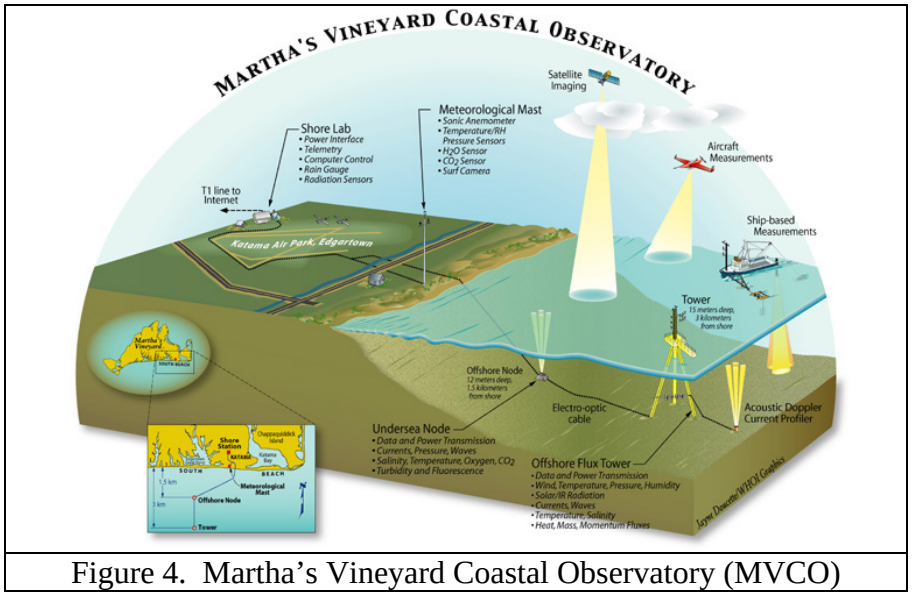

Figure 4. Martha's Vineyard Coastal Observatory (MVCO)

Because we expect that the DWR-III will be used extensively in the future in this general area, we felt that reliable telemetry between these locations and the Woods Hole Oceanographic Institution (WHOI) would be desirable. The buoy currently is equipped with an HF telemetry system transmitting at a frequency of close to 30 MHz. The 12 m site is only 10 km or so distant from the Oceanographic, but is blocked by the island of Martha's Vineyard. The more distant site (at 40 m depth) has a clearer line of sight but is over 40 km away. For both of these deployments, we were unable to receive the buoy HF telemetry at WHOI using the receive antenna provided by the manufacturer of the buoy. Consequently, we purchased a high-gain, 3-element Yagi antenna from an Amateur Radio supplier. The antenna is large (the longest element is 18 feet), but it is light (< 10 lbs) and so is relatively easy to handle. It gives 8 dB forward gain and has a front to back rejection ratio of greater than 20 dB. This is especially important when looking seaward since most of the interference will come from the land (*i.e*. behind). With the new antenna mounted on the roof of the NIST/LOSOS building at the WHOI Quissett Campus, the received signal strength was very high and we were able to acquire the buoy telemetry with essentially no transmission errors.

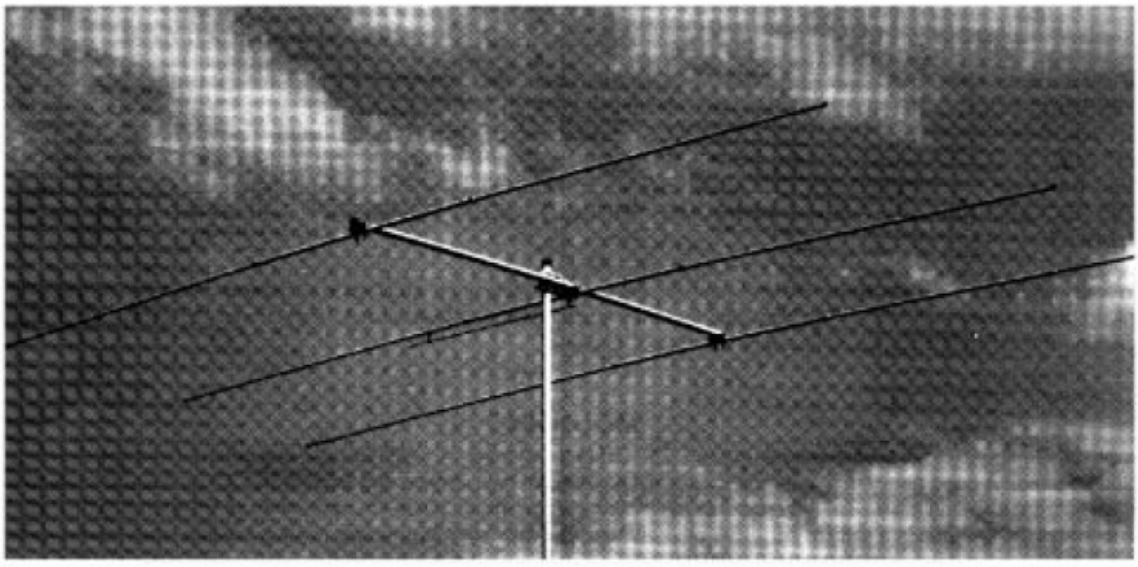

Figure 5. Cushcraft TEN-3 30 MHz Yagi

Deployment 1: This deployment was next to the MVCO 12 m underwater node. The node is equipped with an upward-facing 1200 kHz Acoustic Doppler Current Profiler (ADCP – Figure 6) which is used to estimate low order wave statistics (heights, periods and direction). The use of ADCPs to measure waves now a relatively well-known technique (see Terray *et al*., 1995, 1997; Strong *et al*., 2000; Work *et al*., 2005). This method was used, for example, by Cape Wind to acquire environmental data to support their application to construct a wind farm on Horseshoe Shoals in Nantucket Sound.

However, it requires that the ADCP be stably mounted – usually on the bottom; a requirement that severely limits the useful range of water depths (although we note that once turbines are in place, an ADCP could be attached to a pylon at some elevation above the bottom, and therefore that this measurement technique is likely to be useful for continued wave monitoring once the wind farm has been built). Despite the growing acceptance of the use of ADCPs to measure waves, we are aware of only one comparison study against a co-located directional buoy (Work *et al*., 2008). Those authors used an AXYS Technologies ''Triaxis'' buoy, and to our knowledge there has never been a careful intercomparison between an ADCP and a nearby Datawell DWR-III. However, the issue of using ADCPs to measure waves clearly is a relevant one for the future development of offshore wind power.

Figure 6. 1200 kHz, 4-beam ADCP of the kind deployed at the MVCO 12 m node

This initial deployment had several goals:

1) to test the buoy in the field and gain experience with it,

2) to gather a comparison data set between the MVCO ADCP and the DWR-III, and

3) to support a graduate student thesis (Haven, 2012) that investigated whether surface waves could be measured by an autonomous underwater vehicle (AUV) that was itself being moved around by the waves.

We address the results for each of these goals in turn.

1) As discussed above, this deployment was a success in terms of the mechanics of preparing the buoy, and deploying and recovering it. It was also a success in that the data yield was 100%. The only problem was that we were not able to reliably receive the HF buoy telemetry at WHOI using the vendor-provided receive antenna (which is omni-directional). This problem was corrected in our next deployment.

2) As mentioned above, we acquired a high quality data set from the buoy. The MVCO ADCP data is analyzed for wave height and direction, and is available on the web at (http://www.whoi.edu/page.do?pid=71756). The wave results posted

there have been obtained using a variant of the triplet processing method that is applied to the buoy sensor data. Comparison of the significant wave height and the mean propagation direction of the dominant waves (*i.e*. those at the peak of the spectrum) as measured by the buoy and MVCO ADCP are shown in Figures 7 & 8. The comparison of the significant wave heights (Figure 7) is quite reasonable, and both instruments track periods of rapid change in wave energy. Similarly, the comparison of the mean direction of the energetic waves (Figure 8) is reasonable, although there is a small (~ 10 degree) offset between the ADCP and directional buoy results. This is likely due to an error in calibration of either or both of their compasses. We note in passing that the errors in both compasses can, in principle, be determined using S. Haven's REMUS data since that vehicle carried a high-grade inertial navigation system that determines north non-magnetically by sensing the earth's rotation.

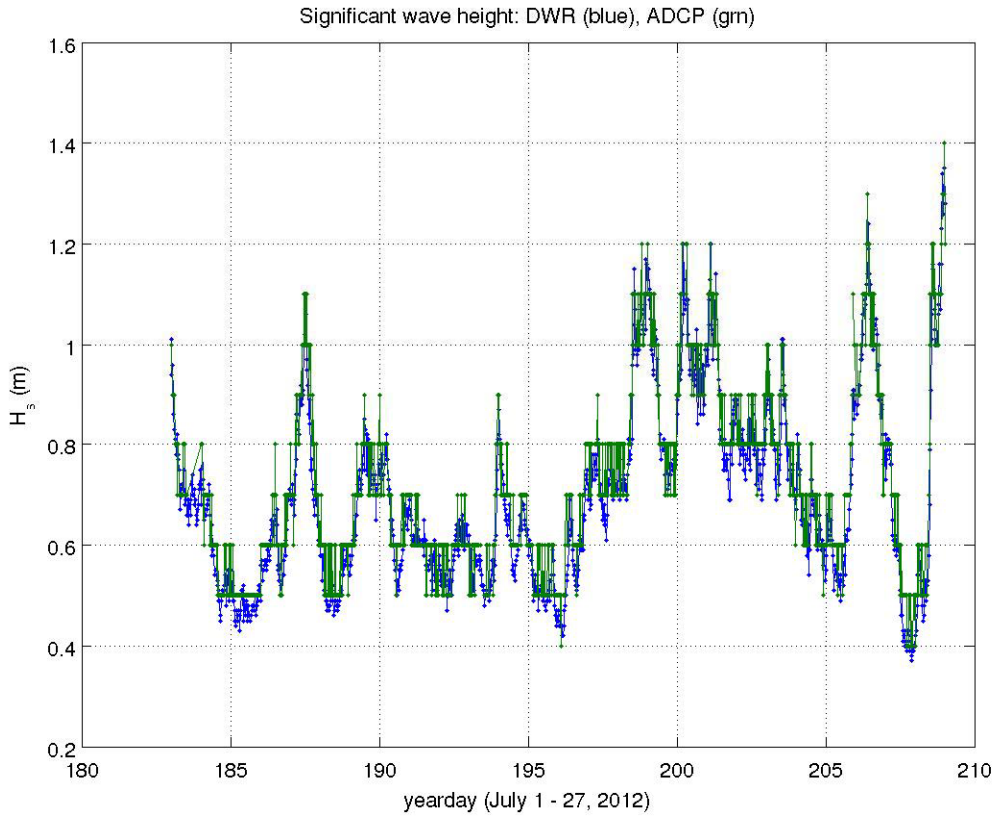

Figure 7. Significant wave height (m) obtained from the DWR-III (blue) and the MVCO ADCP (green).

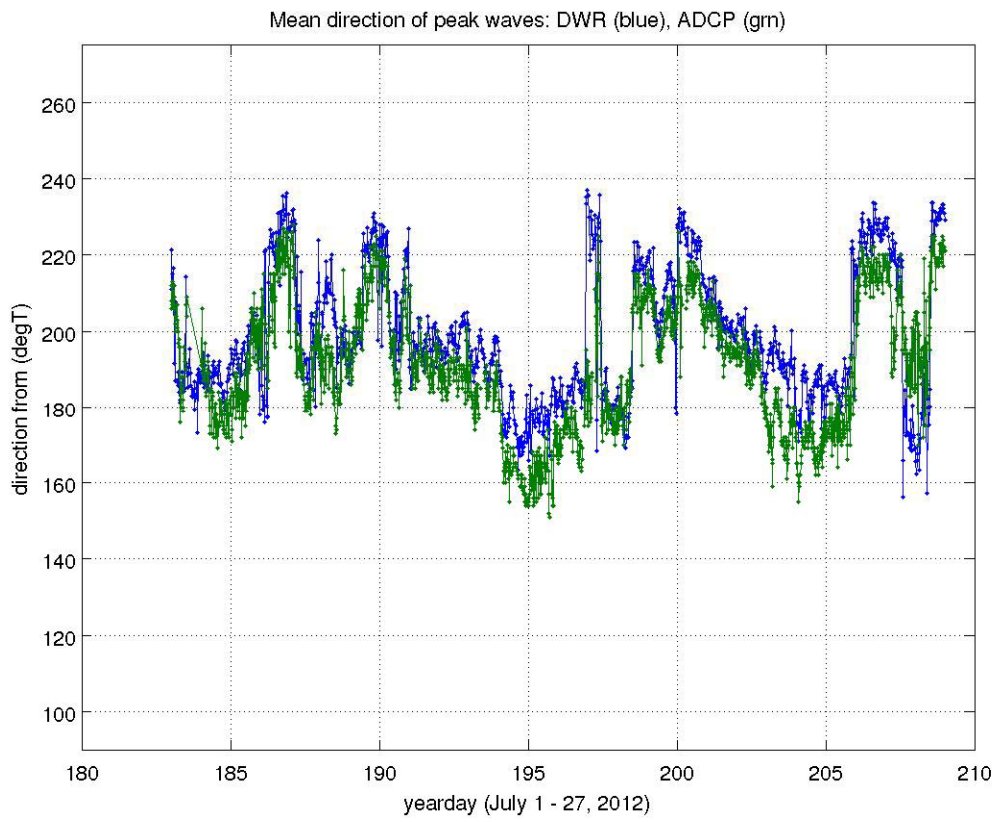

Figure 8. Mean direction (degT from) for waves around the peak of the height spectrum obtained from the DWR-III (blue) and the MVCO ADCP (green).

3) The central problem in measuring waves from an AUV is that the vehicle (because it is approximately neutrally-buoyant) moves in response to the waves, and hence the wave velocities it measures are biased to some degree. The same problem affects ADCPs moored close to the surface on a subsurface float. Haven used a REMUS AUV (Figure 9) provided by the Oceanographic Systems Laboratory in the Department of Applied Ocean Physics and Engineering at WHOI. In addition to upward- and downward-looking ADCPs (which are now almost universal on all small commercial AUVs), the REMUS also carried a Kearfott Inertial Navigation System (INS). This system returns the vehicle's three-dimensional velocity with great precision, but its high cost (~ $75K) precludes it from being used in lower cost AUVs. However, Haven also equipped the vehicle with a low cost (< $1.8 K) MEMS-based "Attitude-Heading Reference Sensor" (AHRS – see Figure 10). Although the low cost AHRS is not navigation quality, Haven's work (Haven 2012) showed that it is adequate to measure the wave-induced velocity of the vehicle and remove the bias. This result opens the way for wave measurements in deep water using moored ADCPs – a capability that will be useful to developers of offshore renewable energy as they move into greater depths. We note for reference that wave height and direction have been

measured successfully from a subsurface ADCP moored in deep water (over 1400 m), but the method required two ADCPs, one looking up to measure the wave velocities, and the other looking down to measure the instrument motion with respect to water below the wave-affected layer – see Wood *et al*. (2005). Haven's result will permit the downward-pointing ADCP to be replaced by an inexpensive inertial sensor, and should lead to the use of moored ADCPs to measure waves in shelf-depth waters.

Figure 9. WHOI OSL REMUS. The green module is an upward/downward-facing 1200 kHz ADCP. The orange "fin" is a GPs antenna used for navigation.

Figure 10. Inexpensive MEMS Attitude-Heading Reference Sensor

Deployment 2: This deployment was delayed several times in order to coordinate with other on-going MREC activities. Resolute Marine Energy Inc. (RME) had planned with MREC assistance to deploy their Wave Energy Conversion (WEC) device in summer 2012 a little offshore of Madaket Beach on Nantucket. The wave buoy was to be deployed farther off shore to provide real-time measurements of the on-coming waves (via telemetry to a station on the beach). Unfortunately, RME had technical difficulties with their device and the demonstration was cancelled. The second delay involved coordinating with a project funded by the Massachusetts Clean Energy Center (MassCEC) to deploy an HF radar ("SeaSonde") at Madaket to complement two other SeaSondes deployed along the southern coast of Martha's Vineyard. Delays were encountered in deploying the Nantucket radar, but the radar array became fully operational earlier this year, and we deployed the DWR-III in June.

We had several goals in this deployment:

1) to gain additional experience mooring (deploying/recovering) the DWR-III in deeper water, and to see if HF telemetry could be used reliably to distances of over 30 km,

2) to support HF radar measurements in a region covering the "area of interest" by both Massachusetts and the Department if the Interior for leasing to offshore wind power developers (see Figure 11), and

3) to collect a high quality data set that can be used to test wave models to predict the wave climate in the lease region.

We address each of these below:

1) As discussed earlier in this section, we were successful in using a new HF antenna having substantially greater directivity to extend the useful range of the HF telemetry from the buoy. This will greatly facilitate future buoy deployments in this general region.

2) The goal of the HF radar work is to improve the ability of direction-finding (DF) HF radars to obtain information about the waves in the footprint of the radar. It is known that the backscattered power measured by a phased-array (PA) HF radar can be inverted to estimate the frequency-direction spectrum of the waves. However, such radars must employ relatively large arrays of antennas. For example, a 30 MHz radar has a 10 m wavelength. So a 16 element linear array with a half-wavelength spacing would be 75 m long. A longer-range radar operating at, say, 15 MHz would need an array over 150 m in extent. For this reason, people have preferred HF radars that make use of compact antennas (such as crossed dipoles) which require much less space to deploy. Such radars measure currents using direction-finding algorithms, but the wave signal is averaged over an annular region in azimuth and range, and cannot be obtained

directly by inversion. Consequently, to test new ideas of how to extract wave information it is critical to have high quality wave measurements within the radar footprint. We recently recovered the buoy and were successful in obtaining a 3 month record of wave height and direction, contemporaneous with the radar, that can be used for this purpose.

3) Our third goal was to obtain a relatively long record of wave observations in intermediate water depth, both to compare with wave models, and to see if the in-situ data could be used to initialize a simple wave model that would permit us to propagate waves kinematically over relatively short distances past he buoy. Although the potential DOI offshore lease area extends to much deeper water, our feeling is that 30-40 m is likely to be an upper limit for developers for the foreseeable future because the cost of the turbine support structures rises rapidly with increasing water depth. Consequently the buoy was just seaward of the regions that are likely to receive serious consideration by developers.

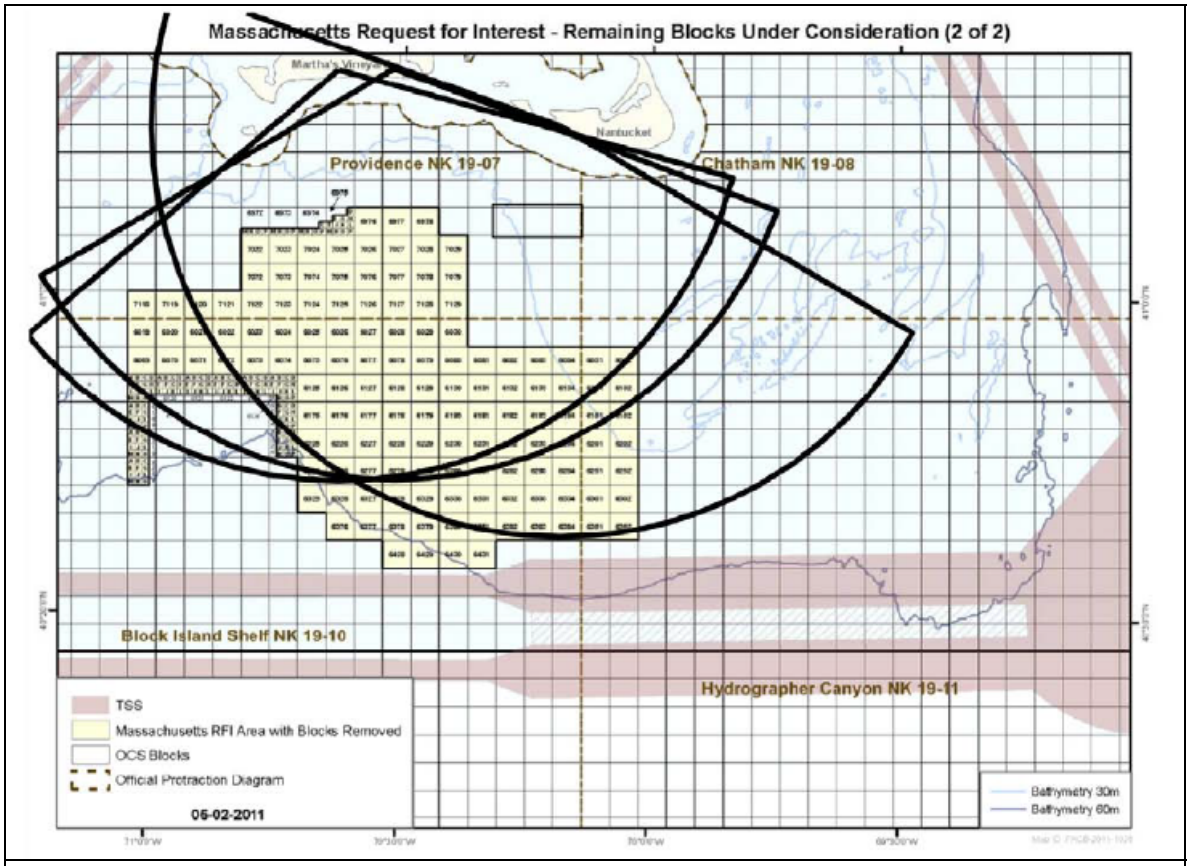

Figure 11. Massachusetts RFI area for offshore wind power development and the footprint of the WHOI SeaSonde radar array.

Wave Modeling: As we discussed in the overview section, due to limitations on staff availability, and the delays in acquiring the necessary field data, we were not able to complete the modeling work as originally envisioned. However, as also discussed there, because of developments in the modeling community, our original plan to develop the capability at MREC to run a wave model in real time most likely is no longer required.

Our current view is that most developer needs for wave prediction on the New England shelf (and elsewhere in the U.S.) can be satisfied by WaveWatch-III, which currently is an operational model supported by NOAA (see http://polar.ncep.noaa.gov/waves). Consequently, the only "support" that would be required by MREC might be to write scripts to download and display the data automatically.

This expectation can be tested against our recent "Deployment 2" data set to see how well the model performs since that deployment was in the general area designated for offshore wind power development. Unfortunately that data were not available at the time of writing this report.

Instead, we have compared the WaveWatch-III output to the DWR and ADCP wave measurements at MVCO which are in 12 m water depth. The Wavewatch-III results for the significant wave height and peak direction are shown in Figures 12 & 13.

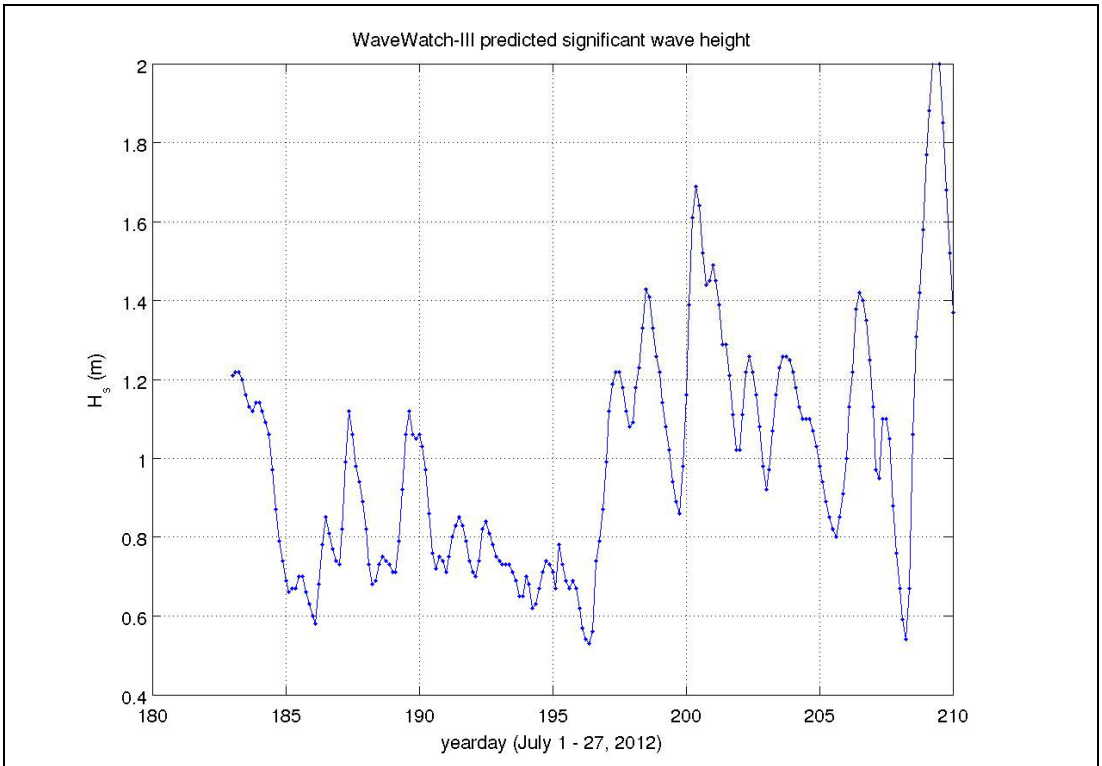

Figure 12. Wavewatch-III operational model output for the significant wave height during the month of July, 2012 at the MVCO site.

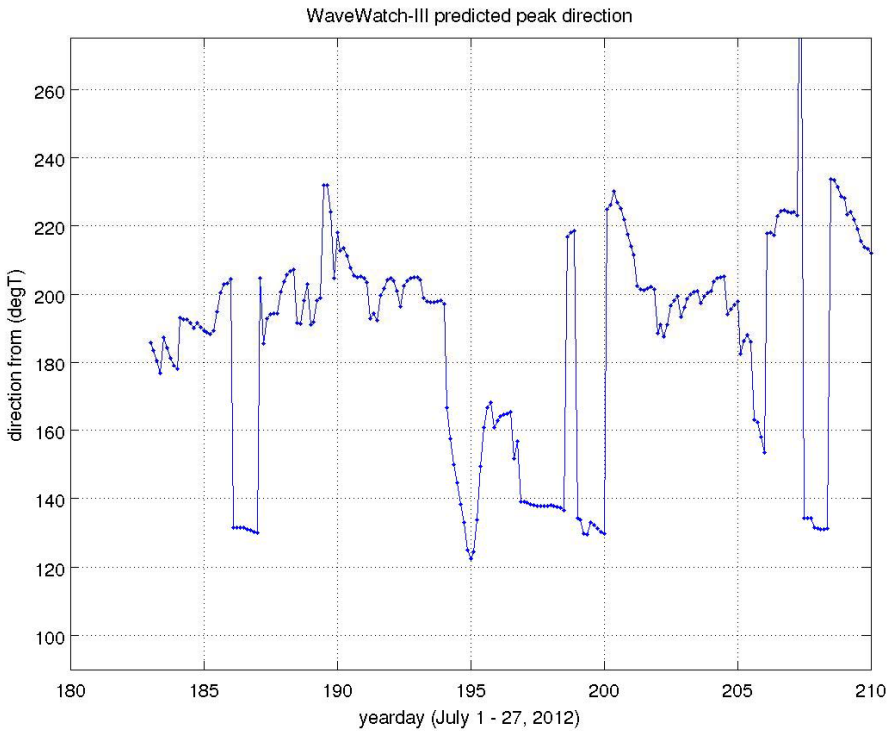

Figure 12. Wavewatch-III operational model output for the mean direction of waves at the spectral peak during the month of July, 2012 at the MVCO site.

Comparison of Figures 12–13 with 7–8 show that the comparison is qualitatively reasonable in that changes in the heights and directions of the dominant waves more or less track temporally. However, WaveWatch-III consistently over-predicts the significant wave height, while under-predicting many of the directional changes. Recall, however, that we are comparing model output and measurements at a relatively shallow near-shore site. The magnitude of bottom friction is one of the most uncertain "source terms" in wave modeling, and so it is entirely possible that the discrepancies are due to the gentle bottom slope in this region, which forces the waves to interact with the bottom over a long distance. Carrying out a similar comparison with our more recent buoy data where the water depth was around 40 m is an important task.

A second approach that bears investigation is to use our "Deployment 2" data to initialize a kinematic model to propagate the waves over relatively short distances. Since a wind farm is fairly localized on the scale of dynamical changes in the wave field, it should be possible to place a wave buoy close to the site and to predict the nearby wave field based mostly (or entirely) on the propagation effects on the wave spectrum of spatial variations in the water depth, bottom slope and current field (we note, incidentally, that the HF radar array recently deployed on Nantucket and Martha's Vineyard provides real-time maps of the spatial structure of the current field – so the collaboration with them is a two-way affair). Dynamical effects of processes such as wind input (at least to the longer waves), and a variety of nonlinear wave dynamical processes, such as wave-wave interaction, and wave breaking, will be increasingly important over larger distances, but perhaps can be

accounted for as relatively small perturbations at sufficiently short ranges. A recent paper by Donelan *et al*. (2012) proposes computationally efficient parameterizations of these "source terms" and is likely to provide a good starting point if they need to be taken into account.

We are currently collaborating on these issues with Dr. S. Daylander, who is a wave modeler on the staff at the U.S. Geological Survey, St. Petersburg Coastal and Marine Science Center.

Acknowledement: We want to acknowledge the encouragement and assistance of Mr. John Miller who was the MREC manager during this project. He resolved contract issues, and facilitated the collaborations with other MREC projects that, we believe, have improved the relevance of this work for environmental characterization and monitoring of waves in connection with offshore renewable energy development.

References:

Donelan, M.A., M. Curcic, S.S. Chen and A.K. Magnuson (2012). Modeling waves and wind stress. *J. Geophys. Res*., **117**, C00J23, doi:10.1029/2011JC007787, 26 pp.

Haven, S. (2012). Measuring surface ocean wave height and directional spectra using an Acoustic Doppler Current Profiler from an Autonomous Underwater Vehicle. M.S. Thesis, MIT/WHOI Joint Program in Oceanography / Applied Ocean Science and Engineering, 119 pp.

Strong, B., B. Brumley, E.A. Terray and Gregory W. Stone (2000). The performance of ADCP–derived directional wave spectra, and comparison with other independent measurements. *Proc. Oceans 2000*, 1195–1203.

Terray, E.A., B.H. Brumley and B. Strong (1999). Measuring waves and currents with an upward-looking ADCP. *Proc. IEEE 6th Working Conf. on Current Measurement*, IEEE Press, 66-72.

Terray, E.A., R.L. Gordon and B.H. Brumley (1997). Measuring wave height and direction using upward-looking ADCPs. *Proc. Oceans'97*, 287–290.

Wood, Jon D., Eugene Terray, Brandon Strong and Baldeo Singh (2005). Measurement of deepwater ocean waves from a subsurface mooring. *Proc. IEEE Oceans'05 Europe*, ISBN: 0-7803-9104-7, June 20–23, 2005, Brest, France.

Work, P.A. (2008). Nearshore directional wave measurements by surface-following buoy and acoustic Doppler current profiler. *Ocean Engr*., **35**, 727 – 737.

Final Report

Development of a Low–Cost Lidar for Wind Profiling in the Marine Atmospheric Boundary Layer

Dr. Eugene A. Terray and Frederick Sonnichsen

Department of Applied Ocean Physics and Engineering
Woods Hole Oceanographic Institution

Overview: The goal of this project was to improve the performance of vertically-profiling wind Lidars using a pulse-compression technique borrowed from HF radar, and to demonstrate the feasibility of the approach by constructing a single beam profiling Lidar. We carried out the design study for a demonstration Lidar (in terms of the required optical and electrical engineering) before we realized that the basic idea was flawed. Although we believe we now have a different way to achieve our original goal, unfortunately we did not work it out until close to the end of the project period, and so were unable to acquire the necessary optical components (which differed from those required by our original proposal) required to demonstrate the approach.

This report is structured as follows: First, to motivate the rest of the discussion, we will review the technical underpinnings of the approach universally adopted (with small variations) by the vendors of the currently commercially-available Lidar vertical wind profilers. This will be followed by a recap of our original proposal and a discussion of what we believe is wrong with it. We conclude with an analysis of the expected performance of a new method (at least when applied to Lidar) to reduce the velocity error. This method is widely used to improve the performance of Doppler sonar for measuring water velocity, and we find it somewhat ironic that a method borrowed from radar was not appropriate in the optical domain, despite the equality of the propagation speeds, whereas a technique from acoustics likely will work.

Review of Current Technology: All but one of the Lidar vertical wind profilers we are aware of, and all of the scanning profilers, are based on pulsed transmissions. The one outlier is the Qinetic ZephIR which is a continuous wave device that achieves range resolution by means of a mechanically-stepped variable focal length lens. Unlike pulsed devices, where the along-beam spatial resolution is independent of distance, the range resolution of he ZephIR is proportional to the square of the range (or height). We will not consider it further here, and will confine our review and analysis of the performance Lidar wind profilers to pulsed devices. Our review will be brief – more detailed discussion can be found in the articles by Freilich (1997, 2001, 2013), and references therein.

Relation Between Velocity and Doppler Shift: It is important to note that monostatic backscatter Lidars measure the Doppler shift caused by the component of wind velocity projected along the beam. The Doppler frequency shift is given by

$$f_d = 2\mathbf{k} \cdot \mathbf{u} \tag{1.1}$$

where **u** is the mean vector velocity (in some weighted sense) of the scatterers within the range cell, and **k** is a vector in the direction of light propagation whose magnitude is $2\pi / \lambda$ (note that the factor of 2 that appears this formula reflects the fact that the light has to travel out and back – or twice as far as the distance to the range cell).

Range Resolution: Pulsed Lidar wind profilers typically measure velocity at a number of range cells, or "bins" along a at least 3 beams, inclined with respect to the vertical by an angle β. Some Lidars have independent beams arranged at fixed azimuthal increments, but most move a single beam to different azimuths, stopping long enough to acquire a "good" velocity measurement. The location and along-beam width of a range bin is determined by timing. So, for example, if a pulse of duration T is transmitted at time 0, then the signal from scattering at a distance *R* along the beam arrives at a time $t = 2R / c$, and the along-beam range resolution is $\Delta R = cT / 2$.

Maximum Velocity Range: If the received signal was quadrature demodulated, then the maximum measurable velocity would be directly related to the speed of the digitizer used. However, the commercial wind profiling Lidars intead mix the signal to an intermediate frequency using an Acoustic Optical Modulator (AOM). A typical AOM frequency might be ~ 68 MHz which corresponds (in the near-IR) to a velocity of around 50 m/s. Hence this would be the maximum negative velocity that could be measured unambiguously.

Doppler Frequency / Velocity Resolution: Commercial pulsed Lidar wind profilers transmit a uniform, monochromatic (*i.e*. single frequency) pulse of some duration *T*. The pulse scatters back and is shifted by the Doppler frequency. Then the lowest Doppler frequency that can be detected (*i.e*. the frequency resolution) is $\delta f = 1 / T$. This translates to a velocity resolution of

$$\delta u = \lambda / 2T = c\lambda / 4\Delta R \tag{1.2}$$

If the backscattered signal remained perfectly correlated for times much longer than this, then the frequency/velocity resolutions above would also determine the uncertainty in the estimates. But because the pulse scatters from a random assemblage of particles within the range cell, the received signal has an intrinsic finite correlation time, τ, and consequently the velocity error given in (1.2) doesn't get arbitrarily small as we increase the pulse length indefinitely.

Signal Correlation Time: For all coherent systems that sense the Doppler shift of volumetric backscatter (i..e lidar, radar, sonar) the signal correlation time is determined essentially by three processes. One of these is simply the resident time of scatterers within the scattering volume. In the case of a Lidar, because the speed of light is so much

larger than the wind speed, the residence time effect is by far the smallest of the three sources of decorrelation, and consequently we can focus on the other two – decorrelation due to beam spreading and turbulence. The first of these is due to the fact that the laser beam eventually spreads in a plane transverse to the direction of propagation (in other words the wavefronts are not planar but are slightly curved. Hence particles within the scattering volume are illuminated by wavenumbers that are spread slightly across the centerline propagation direction, and consequently particles passing at right angles through the beam create a small fluctuation in the phase of the received signal (so long as the beam spreads symmetrically this is a zero-mean fluctuation and does not bias the measured velocity). The second source of signal decorrelation is due to the small-scale turbulent motions within the scattering volume that change the relative positions of the particles during the passage of the pulse. This second contribution will depend on the size of the range bin and the level of small-scale turbulence. Hence the mix of these two effects can change over the profiling range.

Note also that all of these estimates are lower bounds because we have assumed an infinite optical signal-to-noise ratio (SNR), and the errors are larger when the SNR is finite. It's useful to put in some numbers: commercial wind profilers typically use near-infrared light, which has a wavelength in the vicinity of 1500 nm = 1.5×10^{-4} cm (they do this because this wavelength is "eye safe" – so that's one less worry – and because the lasers and other parts are widely used in optical telecommunications equipment, and so are relatively inexpensive). Suppose that the along-beam range resolution is 10 m (note that this would correspond to a vertical resolution of 8.7 m for a beam slanted at 30 degrees), then the single pulse velocity uncertainty will be of order 10 m/s. To get this uncertainty down to something of order 1 cm/s would then require that we average 10^6 pulses. Let's imagine that the light only travels about 300 m or so before being scattered or absorbed. Then the round-trip travel time is 2 μs, and therefore it takes a minimum of 2 s of "dwell time" to transmit enough pulses to beat the random error down to 1 cm/s. If a single beam is being rotated through 4 (or more) azimuthal positions, then a complete "scan" can take upwards of 10 s.

This is acceptable if all you want to do is to measure the mean velocity (which is all that the commercial vendors claim). But if you could cut the averaging time down significantly, then you might be able to measure turbulence directly – such a capability would be very useful in understanding, for example, loads on turbine blades.

Original Proposal: The analysis above was the motivation for our original interest to reduce the velocity error. We proposed to borrow a technique from HF Doppler radar where, because of peak power limitations, they typically transmit a pulse train of relatively long linear frequency chirps. The range is then related to the frequency shift between the received and transmitted signals, and range resolution is determined by the bandwidth of the chirp. The Doppler frequency, and hence the velocity of the scatterers at each range, is determined by the phase shift between successive demodulated pulses (Gurgel, *et al*., 1999). So the technique can be described as a combination of classical pulse compression to achieve a high range resolution (*i.e*. much shorter than the duration of the chirp), with a conventional pulse-pair Doppler estimator (Zrnic, 1979). In the

pulse-pair technique (which also is widely used in Doppler weather radar), the time between successive pulses has to be long enough that the return from the previous pulse has died away before the next one is sent. If the time between pulses is *T*, then this limits the maximum range to $R_{\max} = cT/2$. The Doppler is estimated from the phase change between successive pulses, so the maximum Doppler frequency that can be unambiguously determined (*i.e*. without aliasing) is $f_{\max} = 1/2T$ (this is just the Nyquist criterion). The corresponding maximum velocity is then $V_{\max} = \lambda f_{\max}/2 = \lambda/4T$. Hence the product

$$R_{\max} V_{\max} = \lambda c/8 \tag{1.3}$$

depends only on the wavelength and propagation speed of the signal. This relation is known as the "range–velocity ambiguity", and is a fundamental limitation of pulse-coherent systems.

In the case of HF radar, although *c* is the speed of light, the wavelength is typically a few 10s of meters, so that the right-hand side of (1.3) is on the order of 10^8. Hence, even for a maximum range of 100 km, $V_{\max}$ can be as large as 10^3. In the case of light, however, the right-hand side is of order 50. Hence for a maximum range of 200 m, the maximum unambiguous velocity would be 0.25 m/s, which is several orders of magnitude smaller than what is required. So it is the difference in wavelength that dooms this approach.

It is possible to dispense with the pulse-pair approach and attempt to jointly estimate range and Doppler directly from the chirped pulse. However, the chirp mixes range and Doppler (Rihaczek, 1996). This might be something that could be worked around if the scattering was from a single "hard target" in "clutter", but is likely to fail in the distributed scattering environment we envision here where everything is "clutter".

An Alternate Approach: Our principal goal is to reduce the velocity error, rather than to significantly improve the range resolution (since we only need ranges of a few hundred meters, we likely are not peak power limited - note, this is unlike HF radar where power is a limiting factor since we want to maximize the range). For example, a range resolution of 10 m would be considered "high resolution" in measuring winds around a wind turbine. In this case, we can still transmit "long" pulses (*i.e*. keep a 10 m range resolution), but broaden the pulse bandwidth by modulating it with a pseudo-random code. The code is repeated at least once, and the Doppler shift estimated over a lag equal to the length of 1 cycle of the code. The pulse then provides roughly *N* estimates of the Doppler shift, where *N* is proportional to the time-bandwidth product of the code – or equivalently the number of "chips" in 1 cycle of the code (Brumley *et al*., 1991; Pinkel and Smith, 1992; Wanis *et al*., 2010).

We denote the length of the code by *T*, so that the code repeated once has length *2T*. Then the range resolution is *cT*. Estimating the Doppler shift using a lag of *T*, then the maximum frequency that can be detected unambiguously is *1/2T*, which gives a corresponding maximum unambiguous velocity of $\lambda/4T$. If we require this to be, say, 30

m/s, then T ~ 12.5 ns, and the range resolution would then be cT ~ 3.75 m. Since we only require ~ 10 m range resolution, the code can be repeated 6 times. Optical modulators are available for telecommunications applications at near-IR wavelengths that have 20 GHz bandwidths – which would give 250 "chips" in a 12.5 ns pulse, or 750 chips for a repeated pulse having a net range resolution of ~ 11 m.

The standard deviation of the random velocity error is (Brumley *et al*., 1991; Pinkel and Smith, 1992)

$$\sigma_U = \frac{U_a}{\pi\rho}\frac{1}{\sqrt{2N}} \tag{1.4}$$

where U_a ~ 30 m/s is the ambiguity velocity, N ~ 750 is the total number of code elements in the overall pulse, and ρ is the magnitude of the code auto-correlation coefficient at lag T. ρ can be estimated from data, or modeled as

$$\rho = (1 - N_p^{-1})\exp(-B^2T^2/2)/(1 + SNR^{-1}) \tag{1.5}$$

Where N_p is the number of code repeats (in our case this is 6), and $1/B$ is the intrinsic correlation time of the backscattered signal. We'll assume $BT < 1$ and $SNR >> 1$, so that ρ ~ 0.83. With these estimates, $\sigma_u \sim U_a/100 \sim 0.3$ m/s.

We compare this to the error for an uncoded (*i.e*. monochromatic) pulse with a range resolution of ~ 10 m, which can be written as

$$\sigma_u^{uncoded} > \lambda/4\pi T = \lambda c/8\pi\Delta R \sim 1.8 \text{ m/s} \tag{1.6}$$

So the coding can improve the error by a factor of around 6.

A system using this approach would require some additional features beyond what is normally done. Most importantly, we would have to quadrature–demodulate the signal to baseband, rather than just shift it to an intermediate frequency, as is now done. 90° optical hybrid mixers are available (again courtesy of the telecommunications industry, where they are used for BPSK and QPSK modulation – which is exactly what we are doing here), and one could then dispense with the AOM modulator. Since this procedure effectively produces a complex signal, rather than a real signal shifted in frequency, the spectrum of the signal + noise is now 2-sided, rather than being cut off at 0 Hz, which can reduce the possibility of biasing by system filters. So in general we would expect that such a system would be a little more robust. But both the optical and signal processing would be more complex and somewhat more costly – so that the issue of whether it is worth the extra complexity to improve the velocity error by a factor or around 6 depends on the specific application.

References:

Brumley, B.H., R.G. Cabrera, K.L. Deines and E.A. Terray (1991). Performance of a broad-band acoustic Doppler current profiler. *J. Oceanic Engr*. **16**, 402–407.

Frehlich, Rod (2013). Scanning Doppler Lidar for input into short-term wind powr forecasts. *J. Atmos. & Oceanic Technol*., **30**, 230–244.

Frehlich, Rod (2001). Estimation of velocity error for Doppler Lidar measurements. *J. Atmos. & Oceanic Technol*., **18**, 1628–1638.

Frehlich, Rod (1997). Effects of wind turbulence on coherent Doppler Lidar performance. *J. Atmos. & Oceanic Technol*., **14**, 54–74.

Gurgel, K.-W., G. Antonischki, H.-H. Essen, and T. Schlick (1999). Wellen Radar (WERA): A new ground-wave HF radar for ocean remote sensing. *Coastal Engr*., **37**, 291–234.

Pinkel, R. and J. Smith (1992). Repeat-sequence coding for improved precision of Doppler sonar and Sodar. *J. Atmos. & Oceanic Technol*., **9**, 149–163.

Rihaczek, A. (1996). *Principles of High-Resolution Radar*. Artech house Inc., 489 pp.

Wanis, P., B. Brumley, J. Gast and D. Symonds (2010). Sources of measurement variance in broadband Acoustic Doppler Current Profilers. *Oceans2010*, 1–5, 10.1109/oceans.2010.5664327.

Zrnic, D. (1979). Estimation of spectral moments for weather echoes. *IEEE Trans. On Geosci. Elect*., GE-**17**, 113–128.

Wind Resource Assessment for the National Offshore Renewable Energy Innovation Zone

Prepared for
Marine Renewable Energy Center
1213 Purchase Street
New Bedford, Massachusetts 02740
by
Frederick Letson
James F. Manwell
October 20, 2011

Wind Resource Assessment for the National Offshore Renewable Energy Innovation Zone

Prepared for

Marine Renewable Energy Center
1213 Purchase Street
New Bedford, Massachusetts 02740

by

Frederick Letson
James F. Manwell

October 20, 2011

Wind **E**nergy **C**enter
University of Massachusetts, Amherst
160 Governors Drive, Amherst, MA 01003
http://www.umass.edu/windenergy • (413) 545-4359 • rerl@ecs.umass.edu

TABLE OF CONTENTS

TABLE OF FIGURES

ACKNOWLEDGEMENTS

Advice and technical support surrounding the analysis of MERRA data was provided by William Henson of ISO New England, and of the Wind Energy Center at the University of Massachusetts, Amherst.

EXECUTIVE SUMMARY

A wind resource assessment for the National Offshore Renewable Energy Innovation Zone (NOREIZ) was performed by the Wind Energy Center (WEC) at The University of Massachusetts, Amherst. This resource assessment was based primarily on re-analysis data from the Modern Era Retrospective-Analysis for Research and Applications (MERRA) project by the NASA Goddard Earth Sciences center.

Based on nine years of re-analysis data, the long-term mean wind speed representative of the NOREIZ area was calculated to be 8.33 m/s (18.6 mph*). The 50-year maximum expected hourly average wind speed was calculated to be 30.3 m/s (67.8 mph*).

Prevailing winds in the NOREIZ area are from westerly directions: generally Northwest in the winter and Southwest in the summer.

Additional information about interpreting the data presented in this report can be found in the Fact Sheet, "Interpreting Your Wind Resource Data," produced by the WEC and the Massachusetts Technology Collaborative (MTC). This document is found through the WEC
website: http://www.umass.edu/windenergy/publications/published/communityWindFactSheets/R ERL_Fact_Sheet_6_Wind_resource_interpretation.pdf

* 1 m/s = 2.237 mph.

SECTION 1 – Introduction

The Wind Energy Center (WEC) at UMass Amherst undertook a study to characterize the wind climate in the National Offshore Renewable Energy Innovation Zone (NOREIZ). This study is unusual in that the NOREIZ is a large area that extends a significant distance offshore. Measured data adequate to predict wind turbine loading and performance are not available in this area. Numerical modeling data from the MERRA project were used to characterize the wind resource for the NOREIZ, and to describe how that resource varies with season and location.

SECTION 2-Data Sets

In order to characterize the wind climate throughout the NOREIZ, two sources of long-term wind data were used. The primary data used in this characterization were from MERRA reanalysis data, described in the following section. Eight MERRA data locations close to the NOREIZ were used. These locations, along with the identifier used for each in this report, are show in red in Figure 1. Data from BUZM3, a NOAA monitoring station, were used in addition to the MERRA data primarily for validation. BUZM3 is shown in Figure 1 in yellow. The area of the NOREIZ is delineated by green dots at its corners.

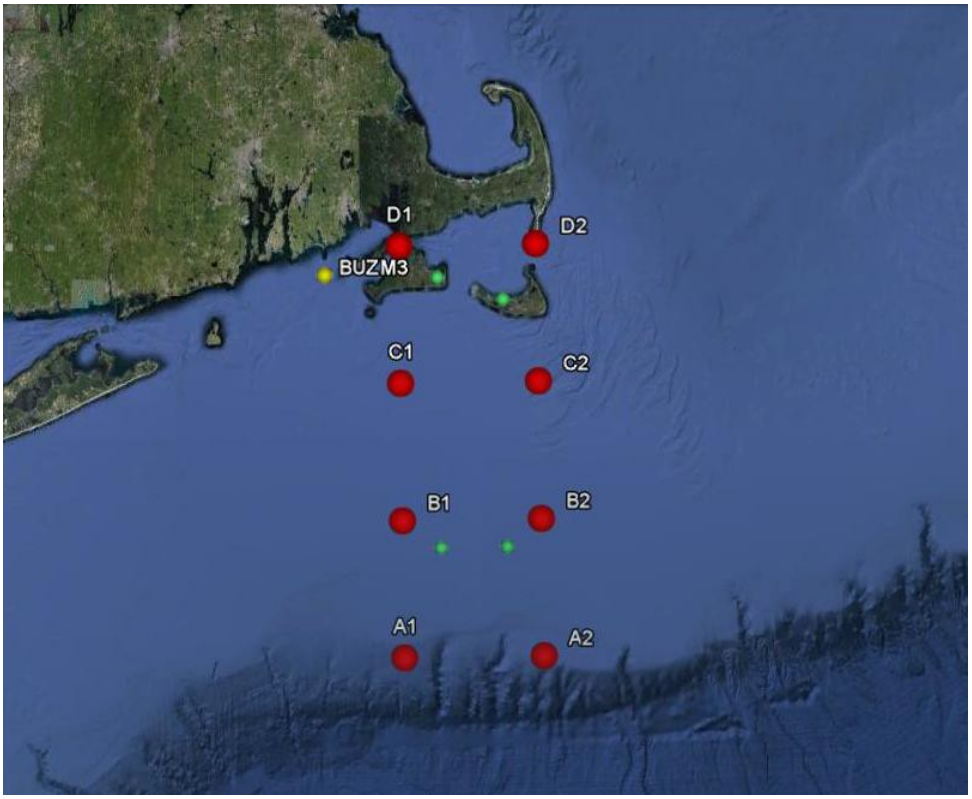

Figure 1 – Wind Data Locations

MERRA Data

The Modern Era Retrospective-Analysis for Research and Applications (MERRA) is a project by NASA Goddard Earth Sciences to provide a continuous, long-term data record of atmospheric and climatological data. MERRA data is based on a numerical model which is informed by data from satellite observation.
MERRA data are available at grid points every 1/2 degree latitude and every 2/3 of a degree longitude. The eight MERRA data points closest to the NOREIZ were used in

characterizing the NOREIZ wind climate. Point C1, shown in Figure 1, above, is the closest MERRA grid point to the center of the NOREIZ. This point is taken to be representative of the area and data from here are used to characterize wind conditions. Data from the other MERRA points are used to describe the way in which the mean wind speed varies throughout the NOREIZ. MERRA wind speed and direction data used in this report represent 50 meters above mean sea level. Nine years of data were used, from 2001 to 2009, inclusive. These data are reported hourly.

Station BUZM3

BUZM3 is a C-Man station operated by the National Oceanic and Atmospheric Administration (NOAA) in Buzzards Bay. This station is an offshore platform with a variety of atmospheric sensors. Of relevance to this study are wind speed and direction data, measured at 24.8 meters above sea level. BUZM3 is located at 41°23'48" N 71°2'0" W. The layout of station BUZM3 is show in Figure 1. [2] Nine years of wind data (2001 to 2009) from BUZM3 were used for comparison to the MERRA data. Data from the station are reported as 10 minute averages. These data were converted to hourly averages for comparison to the MERRA data.

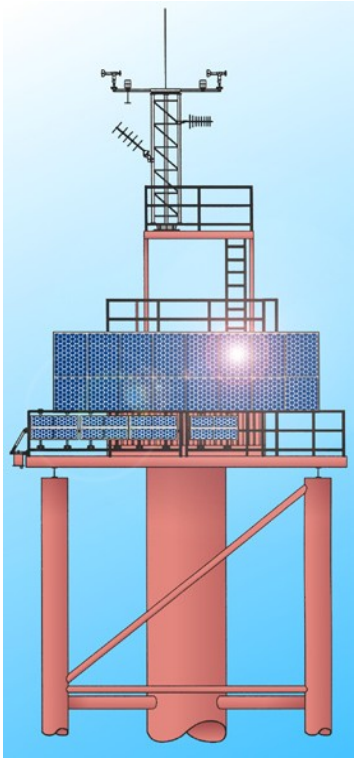

Figure 2 – BUZM3 [2]

SECTION 3- Data Summary and Analysis

Below is a summary of the MERRA wind speeds and wind directions representing each month of the year. Table 1 includes the mean wind speeds, the maximum hourly wind speed and the prevailing wind. These values represent the entire nine year period of the MERRA data. The data summarized here are from MERRA point C1, closest to the center of the NOREIZ.

Table 1. Wind Speed and Direction Data Summary for 50 Meters Above Sea Level

Month	Mean Wind Speed [m/s]	Max Wind Speed [m/s]	Prevailing Wind Direction [Deg]
Jan	9.78	28.33	NW
Feb	9.62	24.54	NW
Mar	9.21	24.51	NW
Apr	8.58	26.89	WSW
May	7.76	20.70	WSW
Jun	7.04	19.89	WSW
Jul	6.75	16.68	SW
Aug	6.34	15.41	SW
Sep	7.00	20.00	SW
Oct	8.71	25.52	WSW
Nov	9.14	26.87	WSW
Dec	10.13	25.49	WNW
Total	**8.33**	**28.33**	**WSW**

Spatial Variation in Wind Speeds

This section describes the way in which mean wind speed varies with height and with distance from shore. The tools described below could be used to calculate the mean wind speed for an arbitrary location in the NOREIZ at a height near 50 meters above sea level.

The standard method in the wind industry for describing the change in wind speed with height is the power law shear model, described here. The data summarized in Table 1 are representative of winds 50 meters above sea level in the NOREIZ. One may use the

following formula to estimate the average wind speed, $U(z)$, at height z, when the average wind speed, $U(z_r)$, at height z_r is known:

$$U(z) = U(z_r)\left(\frac{z}{z_r}\right)^{\alpha}$$

For open-water offshore sites, such as the NOREIZ, it is common to assume a power law shear exponent, α, of 0.1. The change in wind speed with height is a very complicated relationship related to atmospheric conditions, wind speed, wind direction, time of day and time of year. This formula and the shear exponent $\alpha = 0.1$should only be used to modify the long-term mean wind speed.

In order to characterize the way mean wind speed varies throughout the area of the NOREIZ, the relationship between mean wind speed and distance from shore was investigated. Table 2 summarizes the data and statistics used in this investigation. Points D1 and D2 were excluded from the analysis, since they are north of Martha's Vineyard and Nantucket, and not representative of the open ocean.

Table 2. Summary of position and mean wind speed for MERRA grid points

Grid point	mean wind Speed [m/s]	latitiude [Deg N]	longitude [Deg W]	distance from shore (km)
A1	8.58	70.66	40.00	138.76
A2	8.58	70.00	40.00	135.30
B1	8.56	70.66	40.50	81.69
B2	8.56	70.00	40.50	80.77
C1	8.33	70.66	41.00	29.56
C2	8.50	70.00	41.00	25.70
D1	6.92	70.66	41.50	-
D2	8.13	70.00	41.50	-

In order to interpolate between the MERRA grid points to calculate a mean wind speed for an arbitrary location within the NOREIZ, two polynomial fits to the data in Table 2 were constructed: one linear and one quadratic. These fits are shown in Figure 3.

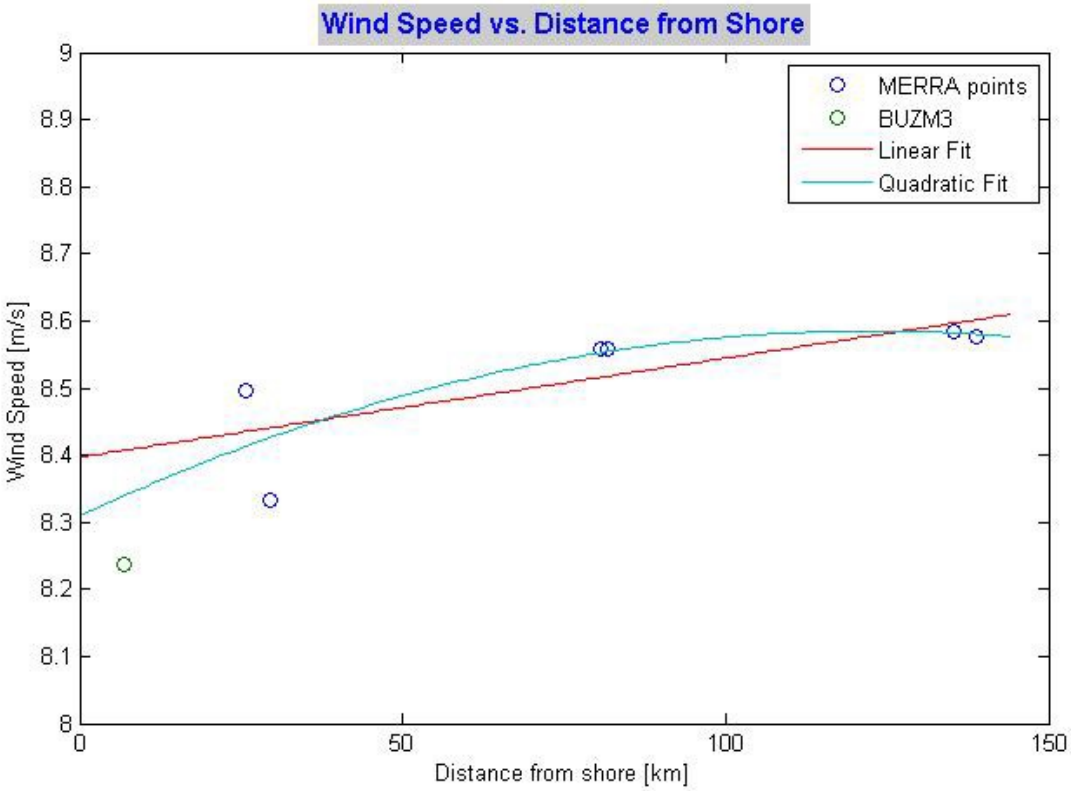

Figure 3 – Wind Speed as a Function of Distance from Shore

The fits shown above can be used to calculate mean wind speed as a function of location within the NOREIZ. The linear and quadratic fits are described by the following 2 equations, respectively:

$$\bar{U}(s) = 0.001474s + 8.397$$

$$\bar{U}(s) = -1.83\times10^{-5}\,s^2 + 0.004488s + 8.309$$

Where $\bar{U}$ is the long-term mean wind speed in m/s and s is the distance from shore in km.

Also shown in Figure 3 are the distance from shore and mean wind speed for Station BUZM3. This mean wind speed has been adjusted using the shear model described above to represent a height of 50 meters above sea level. It can be seen that this data point falls near the quadratic fit of the MERRA data supporting the idea that the numerical model used in MERRA represents measured wind speed data reasonably well. The correlation coefficient of wind speeds from MERRA point C1 and Station BUZM3 is 0.85. This is a reasonable correlation for two measured wind data sets this distance apart. These two facts support the use of MERRA data to characterize wind climate in this area, though having measured, on-site data would be superior.

Extreme Wind Speeds

Extreme wind speeds for the NOREIZ were calculated by fitting a distribution to the wind speed data and examining the cumulative distribution function (CDF) to identify wind speeds with various recurrence periods. The Generalized Extreme Value Distribution (GEV) was used. The GEV distribution, or family of distributions, is a superset of the Gumbell-type, Weibull-type and Fréchet-type distributions [3]. Being a three-parameter distribution it has more degrees of freedom to fit a measured distribution than the Gumbell or Weibull distributions often used in this application. It provides a better fit to the MERRA data at the NOREIZ site than the Gumbell or Weibull.

The pdf for the GEV distribution is given below:

$$f(x;\mu,\sigma,\xi) = \frac{1}{\sigma}\left[1+\xi\left(\frac{x-\mu}{\sigma}\right)\right]^{-1/\xi-1} \exp\left\{-\left[1+\xi\left(\frac{x-\mu}{\sigma}\right)\right]^{-1/\xi}\right\}$$

The parameter giving the best fit to the MERRA point C1 were calculated and are given below:

ξ = -0.1146456
σ = 3.505618
μ = 6.658787

The GEV probability distribution function (pdf) based on these parameters is compared with the distribution of wind speed data in Figure 4.

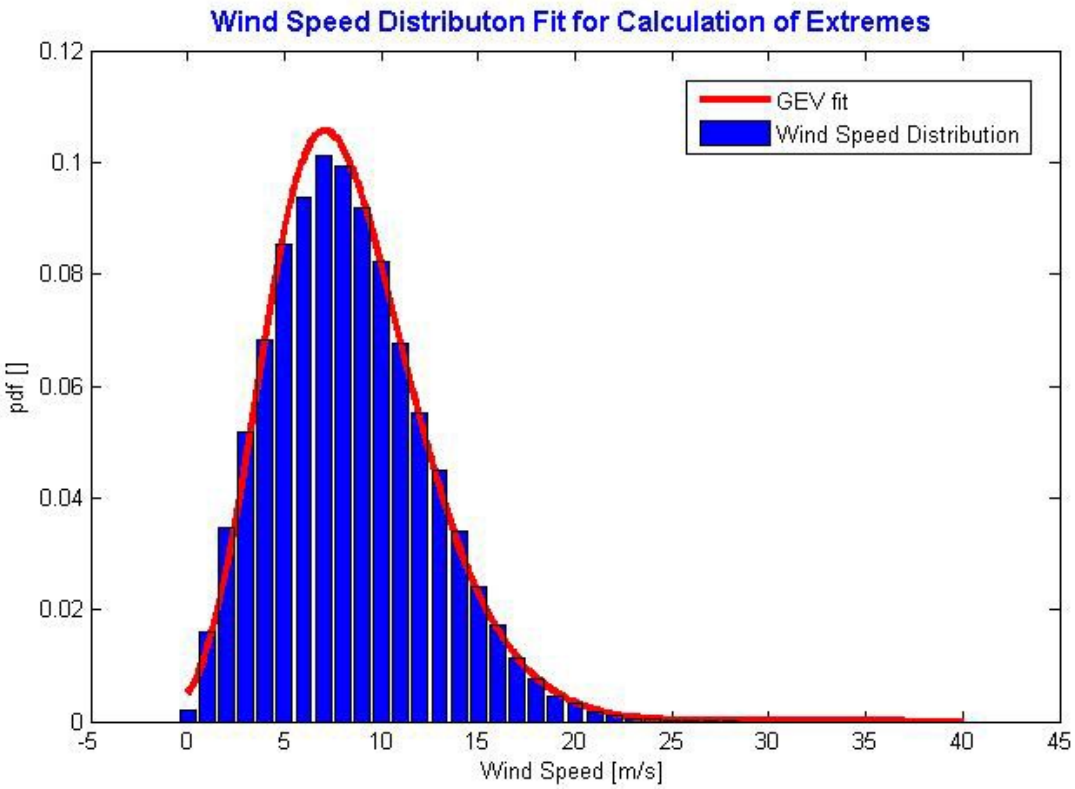

Figure 4 – Wind Speed Distribution and GEV fit

These parameters were used to calculate the GEV CDF, which was in turn used to calculated the expected extreme hourly wind speed with a recurrence period of N years, U_N, for N=1,10,and 50 years.

$$U_1 = 26.44 m/s$$
$$U_{10} = 28.95 m/s$$
$$U_{50} = 30.34 m/s$$

These extreme wind speeds may underestimate the actual extremes observed at the NOREIZ site over a long period of time due to non-local extreme weather effects such as hurricanes and tropical storms.

SECTION 4 - Graphs

This report contains several types of wind data graphs. Each graph represents nine years of data at 50 meters above sea level at MERRA point C1. The following graphs are included:

- Time Series – 10-minute average wind speeds are plotted against time.
  - Seasonal variation of wind speeds can be seen.
- Wind Speed Distribution – A histogram plot giving the percentage of time that the wind is at a given wind speed.
  - It can be seen in this figure that wind speeds are most often between 5 and 10 m/s.
- Monthly Average – A plot of the monthly average wind speed over a 12-month period. This graph shows the trends in the wind speed over the year.
  - The windiest months are October through March.
- Diurnal – A plot of the average wind speed for each hour of the day.
  - It should be noted that timestamps in these data are in GMT.
- Wind Rose – A plot, by compass direction showing the percentage of time that the wind comes from a given direction and the average wind speed in that direction.
  - Prevailing winds are from the southwest.
  - Mean wind speeds vary somewhat by direction.

Data for the wind speed histograms, monthly and diurnal average plots, and wind roses are included in Appendix A.

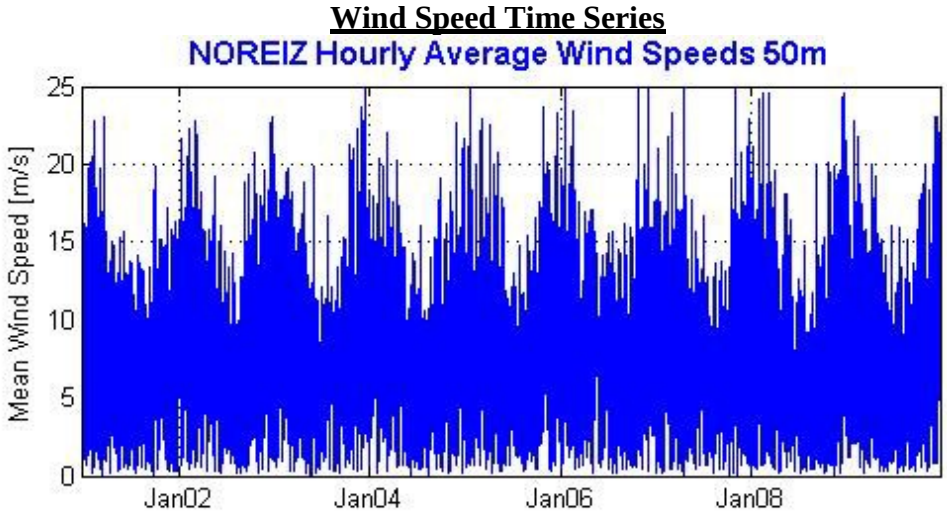

Figure 5 – Wind Speed Time Series

Wind Speed Distributions

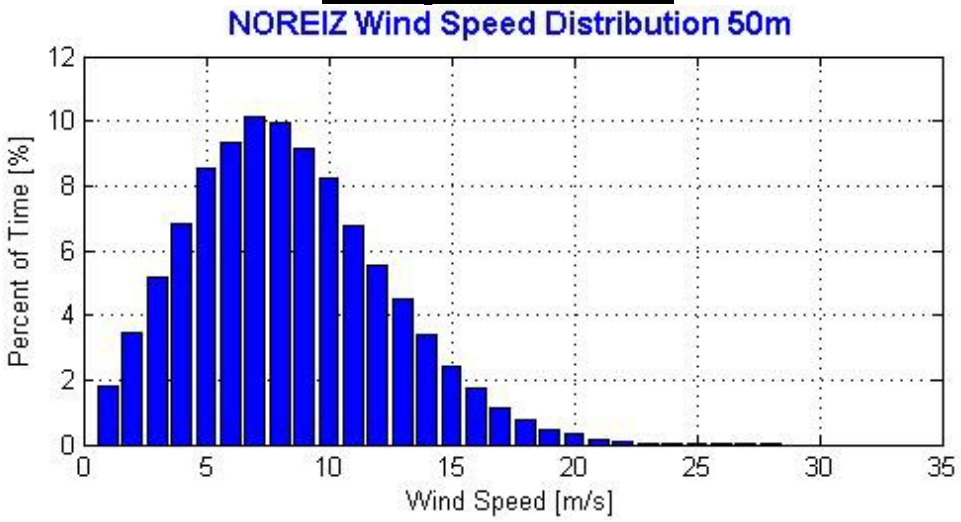

Figure 6 – Wind Speed Distribution

Monthly Average Wind Speeds

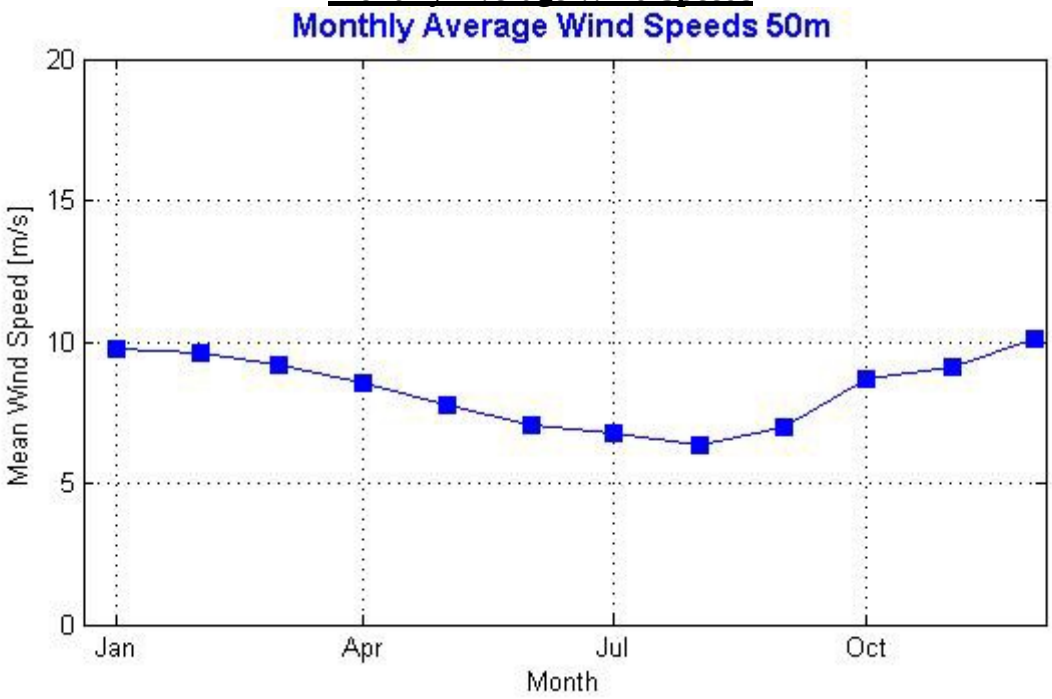

Figure 7 – Monthly Average Wind Speed

Diurnal Average Wind Speeds

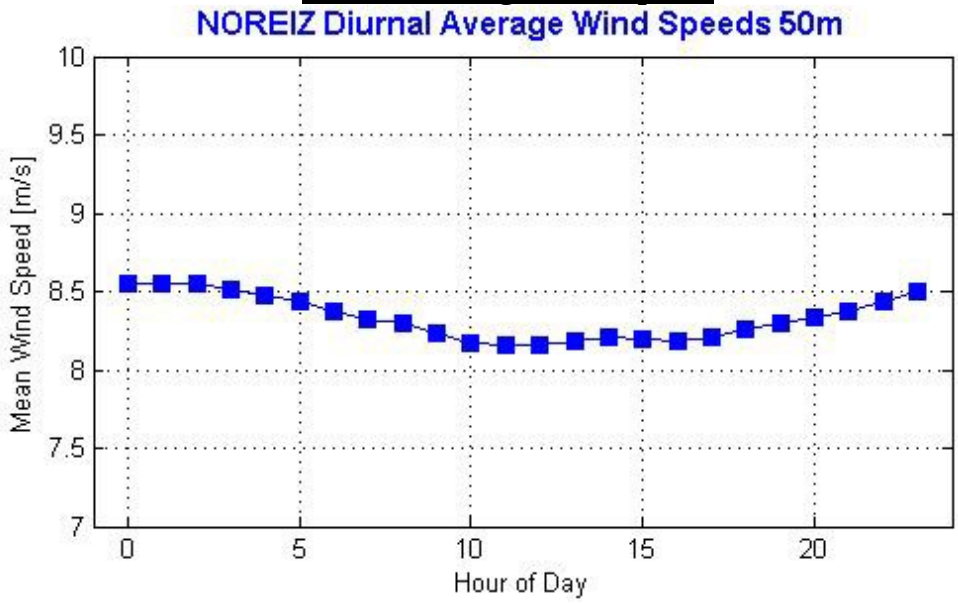

Figure 8 – Diurnal Average Wind Speeds

Wind Rose

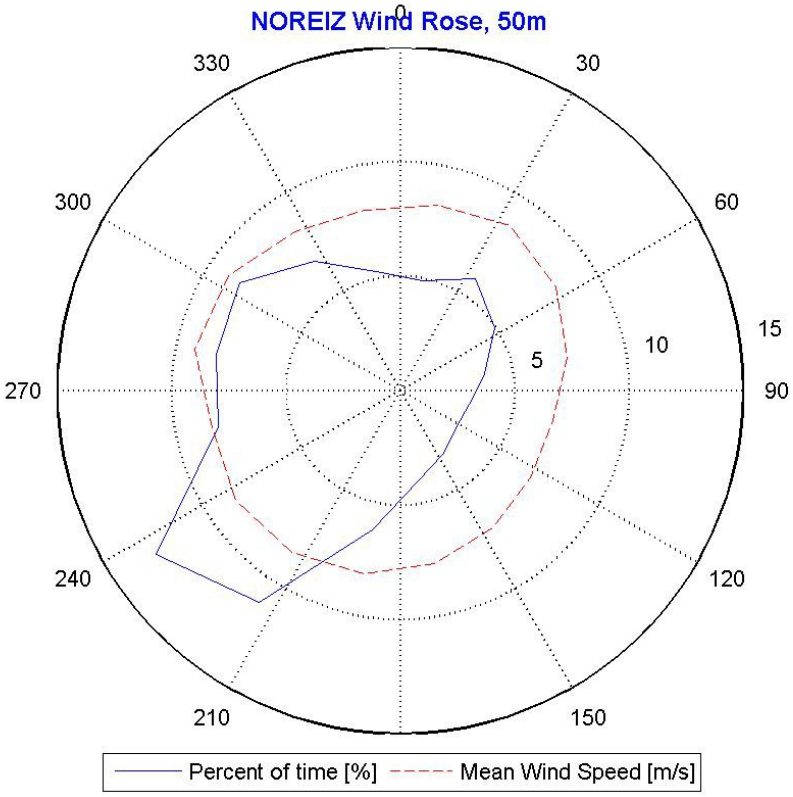

Figure 9 – Wind Roses

SECTION 5- Recommendations for Future Work

The WEC recommends collecting on-site wind data for the NOREIZ. Measured data, either from conventional anemometry or remote sensing would increase confidence in the wind climate characterization described in this report. Ideally, wind data would be collected with anemometry on an offshore tower and a LIDAR would be used as well to better assess the wind speeds at greater heights. In addition, wave data should be taken simultaneously so that joint probability of occurrences of wind and waves could be ascertained. Simultaneous wind and wave date would also facilitate better understanding of the variation of wind speed with height under various climatic conditions.

References

[1] Global Modelling and Assimilation Office Website
http://gmao.gsfc.nasa.gov/research/merra/

[2] National Data Buoy Center Website
http://www.ndbc.noaa.gov/station_page.php?station=buzm3

[3]Kotz, S. and S. Nadarajah, Extreme Value Distributions: Theory and Applications, Imperial College Press 2000

APPENDIX A- Plot Data

Wind Speed Distribution Data

Mean Wind Speed [m/s]	Frequency [%]
1	1.7949
2	3.4568
3	5.1744
4	6.8274
5	8.5323
6	9.3588
7	10.1143
8	9.9267
9	9.1738
10	8.2294
11	6.7564
12	5.5332
13	4.4874
14	3.4099
15	2.4085
16	1.7303
17	1.1218
18	0.7732
19	0.4563
20	0.3194
21	0.1623
22	0.1116
23	0.0608
24	0.0418
25	0.0177
26	0.0076
27	0.0089
28	0.0038
29	0
30	0

Monthly Average Wind Speed Data

Month	Mean Wind Speed at 50 meters [m/s]
Jan	9.7756
Feb	9.6215
Mar	9.2076
Apr	8.5777
May	7.7568
Jun	7.0368
Jul	6.7507
Aug	6.3446
Sep	6.9968
Oct	8.7083
Nov	9.1435
Dec	10.1279

Diurnal Average Wind Speed Data

Hour of Day	Mean Wind Speed [m/s]
0	8.55
1	8.56
2	8.54
3	8.52
4	8.48
5	8.43
6	8.37
7	8.33
8	8.29
9	8.23
10	8.18
11	8.15
12	8.16
13	8.18
14	8.20
15	8.19
16	8.19
17	8.21
18	8.26
19	8.30
20	8.34
21	8.38
22	8.43
23	8.50

Wind Rose Data

Bin Center [deg]	Percent Time [%]	Mean Wind Speed [m/s]
11.25	4.8727	8.246
33.75	5.8932	8.6685
56.25	4.9716	8.1821
78.75	3.7395	7.4274
101.25	3.0676	6.807
123.75	2.9016	6.8542
146.25	3.3427	7.2398
168.75	4.0107	7.7351
191.25	6.2164	8.1753
213.75	11.1563	8.5268
236.25	12.8575	8.6723
258.75	8.1318	8.3923
281.25	8.2218	9.1616
303.75	8.4791	9.051
326.25	6.8135	8.3552
348.75	5.324	8.0364

F-2

A REVIEW AND COMPARISON OF THE ENVIRONMENTAL IMPACTS OF CONSTRUCTION OF OFFSHORE WIND FARMS: NEARSHORE BOTTOM MOUNTED VS FARSHORE FLOATING

Prepared for
Marine Renewable Energy Center
1213 Purchase Street
New Bedford, Massachusetts 02740
by

Micah Brewer
Jon McGowan
James F. Manwell

December 30, 2011

A REVIEW AND COMPARISON OF THE ENVIRONMENTAL IMPACTS OF CONSTRUCTION OF OFFSHORE WIND FARMS: NEARSHORE BOTTOM MOUNTED VS FARSHORE FLOATING

Final Project Report

NOREIZ SUBCONTRACT- UMASS DARTMOUTH
UNIVESITY OF MASSACHUSETTS AMHERST

By

Micah Brewer, Jon McGowan, and James Manwell

Wind Energy Center
Department of Mechanical and Industrial Engineering
University of Massachusetts Amherst

December 30, 2011

ABSTRACT

Similar to onshore wind systems, the environmental effects of offshore wind farms are expected to play an important part of the development of future large-scale wind energy systems. This report presents a detailed review of the status of, and recent developments in, research on the environmental impacts of fixed and floating offshore wind turbine systems. A significant amount of information that has been reviewed has come from European sources where a large number of offshore installations have been installed, but some work on this subject has been carried out recently in the United States. By synthesizing available information on the environmental impacts of benthic organisms, fish, marine mammals, avian species and bats, an extensive review of the effects of fixed and floating offshore wind turbines is presented. The environmental impacts between floating and fixed systems are anticipated to be highly variable due to multiple parameters that need to be taken into account when identifying environmental impacts, however general patterns are identified. Additionally, these impacts varied throughout the lifecycle of the offshore wind system. The focus was narrowed down to analyze the environmental impacts through the scope of barrier and habitat impacts in addition to the rate of mortality for avian species and bats. In addition a noise propagation model was used to determine the extent of effects due to the installation of fixed and floating support structures using piling installation methods. Finally, a summary of progress in all the major environmental impact areas is given along with recommendations for future research on this important subject.

TABLE OF CONTENTS

LIST OF TABLES

LIST OF FIGURES

CHAPTER 1

INTRODUCTION

1.1 Introduction and Background

There is a consensus among leading researchers and scientists that the climate is changing largely due to human activities. One of the largest concerns of these anthropogenic factors are the rising levels of carbon dioxide from the combustion of carbon based fuels. This impact on the global atmosphere adversely impacts society and species on a global level (U.S. Fish and Wildlife Service, 2010). Partially out of concern for these impacts and rising energy costs, a number of renewable energy systems have been deployed. Out of these systems, wind energy has had the largest number of developments and has become one of the fastest growing sectors in the energy industry (Arnett et al., 2008; Musial & Ram, 2010).

The majority of wind energy development have been on land. This is partially due to concerns for issues ranging from aesthetics to noise. As ideal sites on land become developed, especially in Europe, there has been a shift in the focus of development to the offshore environment (Arnett et al., 2008; Henderson & Witcher, 2010). However, as the development of offshore wind farms (OWF's) increase, concern has grown about the possible environmental impact; many of which are still unknown (Vella, 2002). These impacts will have a large degree of variability, due to the changing bathymetry and geophysical differences. This will influence the type of support structure and other

system components used in offshore wind turbines (OWTs) (Geo-Marine Inc., 2010; Henderson & Witcher, 2010; Musial & Ram, 2010; Wilson & Elliott, 2009).

1.2 Goals and Objectives

A primary focus of this report is a review of the available literature on the environmental impacts of offshore wind turbines, both fixed and floating. A majority of the environmental studies have been out of Europe, but there have been important environmental impact assessments performed in the United States: most notably Cape Wind (Minerals Management Service, 2009). The complexity that arises from the number of likely design concepts for both fixed and floating wind turbine support structures limits the scope of the analysis to just seven types of systems (see Figure 1.1):

1. **Fixed Foundations:** Monopile, Gravity Base, Suction Bucket, Jacket Support Structure
2. **Floating Support Structures:** Barge, Spar Buoy, Tension Leg Platform

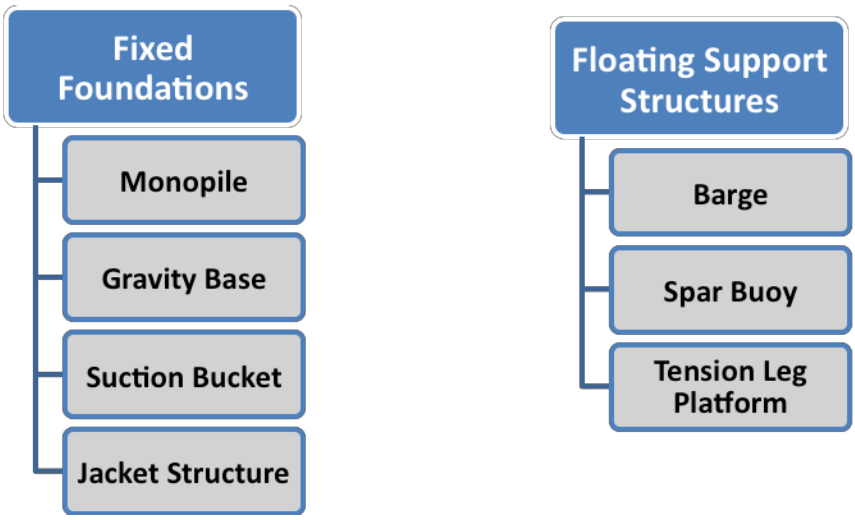

Figure 1.1: Support Structures

A comprehensive evaluation in this report will be limited by the assortment of ecosystems and ocean areas that have either current, operational OWFs or are in regions in which developments are likely. Five groups of species are evaluated: benthic organisms, fish, marine mammals, avian species and bats. In this review the environmental impacts that are notable to specific support structures are specifically indicated. Otherwise it can be assumed that the effects will occur across the various support structure types.

Likewise, a noise propagation study is performed for the installation via piling of fixed monopile foundations and floating support structures using pile anchors. The noise propagation is quantified with empirical models that have been validated through existing studies.

CHAPTER 2

OFFSHORE WIND ENERGY SUPPORT STUCTURES

A major difference between land and offshore wind turbine systems is the additional cost and complexity of civil works involved in their construction, specifically the additional costs in regard to the support structures. Of the OWFs that have so far been deployed, the support structure that has primarily been used has been the monopile (Butterfield, Musial, & Jonkman, 2005; Musial & Butterfield, 2006). From information gathered from the online source www.4coffshore.com, which is shown in Table 2.1 (Limited, 2011), monopiles account for approximately 80% of the existing support structure installations as a function of the total offshore energy capacity.

	OFFSHORE SUPPORT STRUCTURES 2010		
	FIXED FOUNDATIONS	**FLOATING SUPPORT STRUCTURES**	**MW**
MONOPILES	X		2834
GRAVITY BASE FOUNDATIONS	X		620
SUCTION BUCKETS	X		11
JACKET STRUCTURES	X		72
BARGES		X	0
SPAR BUOYS		X	2.3
TENSION LEG PLATFORMS		X	0
TOTAL			3539.3

Table 2.1: Capacity as a Function of the Type of Support Structure Used

The support structure design will be a function of a variety of parameters from economic constraints to environmental and operational conditions. The environmental data that is

used in the design will consist of varying conditions including: water depth, wave depth, sea currents, wave heights, wind speeds, marine growth and the characteristics of the soil (Musial & Butterfield, 2006; Twidell & Gaudiosi, 2010). The energy potential for developments will vary geographically with the changing wind resource shown by the results of an analysis performed for the United States by the Minerals Management Service (2006) shown in Table 2.2.

	5 to 20 Nautical Miles			20 to 50 Nautical Miles		
Region	< 30 m deep	=> 30 m deep	% Exclusion	< 30 m	=> 30 m	% Exclusion
New England	9,900	41,600	67	2,700	166,300	33
Mid-Atlantic States	46,500	8,500	67	35,500	170,000	33
California	2,650	57,250	67	0	238,300	33
Pacific Northwest	725	34,075	67	0	93,700	33
Total	59,775	141,425	67	38,200	668,300	33

Table 2.2: Offshore Resource Estimates (Minerals Management Service, 2006)

There are numerous support structure variations that can be derived from core concepts, however only seven support structure designs are analyzed.

2.1 Fixed Support Structure Types

Although there have been numerous conceptual designs, the fixed support structures that are discussed in further detail below are the monopile, gravity base foundation, suction bucket and the jacket support structure. The first three are displayed in Figure 2.1 (Musial & Ram, 2010). Of the designs that are evaluated, only one of the concepts has not yet moved beyond the prototype stage: the suction bucket (Breton & Moe, 2009; Houlsby & Byrne, 2000).

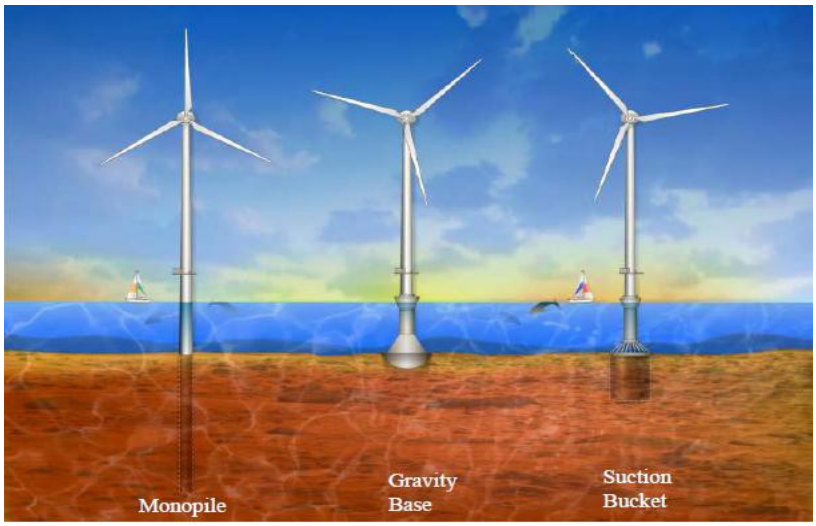

Figure 2.1: Fixed offshore support structure types (Musial & Ram, 2010)

Depending on the foundation design and the seabed conditions, there may be a need for scour protection. This could consist of a protective rock mattress of large rocks on top of smaller rocks, or synthetic fronds (Wilson & Elliott, 2009). This helps in maintaining the stability by mitigating the erosion around the foundation base (Houlsby & Byrne, 2000; Wilhelmsson & Malm, 2008; Wilson & Elliott, 2009). This additional substrate complexity has been shown to increase the opportunities for ecological development and increase the overall biodiversity and biomass. Although scour protection is an important component in the offshore system, support structures are the focus of the analysis below with little discussion of scour protective measures (Geo-Marine Inc., 2010; Wilson & Elliott, 2009).

2.1.1 Monopile

The primary type of foundation that has been used in commercial developments has been the steel monopile. Their relatively low cost is associated with the simplicity and minimal

design of the structure resulting in low fabrication costs, but the installation is expensive due to the need for heavy installation equipment (Breton & Moe, 2009; Houlsby & Byrne, 2000). The limitations due to the structural integrity of the support structure and the installation tools have so far confined monopiles up to depths of approximately 20 meters, typically in types of seabed consisting of less rocky soil (Breton & Moe, 2009; Musial & Butterfield, 2006; de Vries & Krolis, 2007).

The method of installation will be determined by the soil conditions, which function as a support by way of friction and bearing forces and influence the pile and cross sectional dimensions along with the installation depth (Geo-Marine Inc., 2010; Twidell & Gaudiosi, 2010). The installation requires a substantial amount of equipment such as specialized jack-up barges in order to take part in drilling operations, grouting or driving (Houlsby & Byrne, 2000). Often, after the installation is complete, scour protection is employed in order to minimize the erosion around the base and maintain the structural stability of the pile. (Oud & Nedam, 2002; Twidell & Gaudiosi, 2010).

Decommissioning is thought to roughly mirror the installation. This involves extracting a portion of the pile out of the seabed either through explosives, jet water cutting or other types of decommissioning tools, although available methods may change by the time of decommissioning. Experience from the oil and gas industry has shown that the remaining embedded portion is typically left behind. Due to regulations, this extraction depth in the U.S. is five meters below the seabed (Geo-Marine Inc., 2010). Proposed

decommissioning methods have ranged from the use of hydraulic vibratory extractors to explosives (Geo-Marine Inc., 2010; Houlsby & Byrne, 2000).

2.1.2 Gravity Base Foundation

The gravity base foundation requires minimal design and overcomes the stiffness limitations of the monopile. It functions by relying on its dead weight which acts as an anchor resisting the overturning loads inherent in the offshore environment (Houlsby & Byrne, 2000). Designs usually consist of a heavy weight in the form of caissons made of either concrete or steel (Twidell & Gaudiosi, 2010). Errosion around the wind turbine is typically minimized with scour protection (Twidell & Gaudiosi, 2010). According to Mark Seidell of RePower, typical diameters of the foundation base have been around 20 to 30 meters with the scour protection substantially larger up to 50 meters in diameter. The average weight of the existing installations has been approximately 3000 tons.

Conditions in which this support structures are best suited are in soil conditions unsuitable for monopiles. More explicitly this is terrain including ledges or rocky seabed conditions (Twidell & Gaudiosi, 2010). However, before the installation there must be significant preparation of the seabed at each unit location (Geo-Marine Inc., 2010). This preparation includes soil analysis and seabed leveling in order to minimize the potential of the foundation from settling unevenly (Musial & Butterfield, 2006).

This type of support structure could be a more cost effective support structure than the monopile, depending on the site conditions (Musial & Butterfield, 2006). The longevity

of the foundation could significantly reduce the lifecycle cost with the operating lifespan of some gravity base foundations extending roughly fifty years due to the corrosion resistance of concrete material (Brook-Hart, 2009). Further reductions in cost could arise from future methods of transportation, installation and decommissioning involving the use of submersible launch barges (Brook-Hart et al., 2009). However, current developments have used vessels ranging from heavy lift ships to jackup vessels during the installation of gravity structures (Wang & Bai, 2010). The systems have been constrained to shallow water primarily due to the increase in material needed at increased depths which has rapidly increased the costs (Breton & Moe, 2009; Houlsby & Byrne, 2000).

Recent experiences have raised questions in regards to the viability of these support structures for larger wind farms, with some of larger developments using gravity base foundations indicating that they are ill-suited primarily due to logistics. Although this could be a transient phenomenon as technology is further developed and further research is performed (Twidell & Gaudiosi, 2010).

2.1.3 Suction Bucket

While still under development, the suction bucket is a promising technology that could be used in the offshore wind industry. This could further reduce system prices for OWTs in shallow offshore areas (Musial & Butterfield, 2006). The suction bucket maintains the OWT systems stability with a pressure differential across the caisson surface (Houlsby & Byrne, 2000).

A variety of possible support structure configurations have been proposed with this technology. This has included hybrids of the suction bucket technology with other support structures designs including the monopile, tripod and the jacket support structure.

Installations are anticipated to entail lowering the system to the ocean floor where the rim of the bucket would cut into the seabed. There a pressure differential is formed by pumping water out of the buckets cavity (Musial & Butterfield, 2006). The tripod or jacket configuration would have a bucket on the end of each leg and could have separate controls, providing an easier process leveling the system during the installation (Houlsby & Byrne, 2000). Decommissioning would involve pumping surrounding water into the cavity of the bucket leading to an over pressurization in the cavity and force the bucket from the seabed. Both installation and decommissioning are anticipated to be much more cost effective than the current installations of other types of support structures (Houlsby & Byrne, 2000).

Tests performed in the North Sea at the Sleipner T and Draupner E sites using 15 and 12 meter diameter buckets have indicated that the suction bucket would be able to work under typical shallow offshore conditions by supporting the applied loads under various operating conditions (Houlsby & Byrne, 2000). However, there are still several uncertainties in how the system will function under various seabed conditions. Recent research has demonstrated that the installation in layered material is not well understood, although some experiments indicate that installing a bucket into a layer of sand over clay

should be possible. Conversely research has hinted that installing bucket in clay, layered over sand may be problematic in terms of reliability (Byrne & Houlsby, 2006).

2.1.4 Jacket Support Structure

Due to the cost constraints and structural limitations of other fixed support structures, the three and four legged jacket foundations are the only viable fixed alternatives at increased water depths (Twidell & Gaudiosi, 2010). Similar to structures used in oil platforms, jacket support structures are typically light in weight and consist of either three or four columns that are slightly inclined to the vertical. Many of the design elements that are used in the oil and gas industry can be integrated into the jacket support structures used for OWTs and it is anticipated that this technology will have a good potential to mature into established solution for OWTs. Although, this type of support structure is still at an early stage (Seidel, 2007).

Currently, these support structures can be used in depths down to 50 meters and could be a solution for offshore wind farms beginning at approximately 20 meters. The structural limitations due to static and dynamic instability are expected to constrain these designs to depths less than 80 meters, although other engineers have found that these could be viable solutions up to 100 meters and greater (Twidell & Gaudiosi, 2010). To increase the stiffness of the structure and minimize the risk of structural instability, horizontal cylindrical connections are installed at varying heights. The necessary scour protection and seabed preparation could be minimal depending on the type of foundation used in the jacket (Twidell & Gaudiosi, 2010).

The design of jacket support structure for OWTs is in principle similar to the design procedures for other fixed offshore installations. Currently two types of designs are possible for OWTs, either with piles or suction buckets but so far only steel piles have been used (Seidel, 2007). The dimensions of the support structure will vary but are primarily dependant on the ground conditions and acceptable pile loads. For larger footprints the structural support that is needed will decrease and the necessary cross sectional area of the pile will likewise decrease. According to Mark Seidell of RePower, in water depths of 30 to 40 meters for a 5 MW wind turbine, typical dimensions are 6 to 12 meters in width at the jacket top while at the seabed the structure ranges between 16 to 25 meters. Typical member sizes for the legs are 850 millimeters in diameter with a thickness of around 40mm, with local strengthening for the welded joints. For the bracings typical sizes are 580 millimeters in diameter with a thickness of approximately 20 millimeters with local strengthening in the joints.

Installation of the jacket support structures typically involve pile driving steel piles through the jacket sleeves to the design depth after having been transported to the site by either barge or crane barge. Decommissioning of a jacket using piles would be similar to an individual monopile in which the piles would be cut at or below the seabed (Twidell & Gaudiosi, 2010).

2.2 Floating Support Structure Types

The potential opportunity in siting larger wind turbines further offshore has increased as various floating support structure designs have continued to be researched and tested. As

the technology matures and the opportunities for the development of OWFs in shallow waters decrease, the economics along with the prospect of the development of floating OWFs will become more favorable (Nedwell & Howell, 2004). Likewise, the higher costs of the installation of fixed support structures at greater depths along with the increase in wind speeds at further distances from the coast will further enhance the viability of floating OWTs (Henderson & Witcher, 2010).

The reliability of floating support structures has already been demonstrated in the oil and gas industry with mooring systems used in depths over 1000m (Tracy, 2007). However, the cost effectiveness of floating OWTs has yet to be adequately proven (Butterfield, Musial, & Jonkman, 2005; Musial & Butterfield, 2006). Furthermore, because floating OWTs are partially decoupled from the seabed, the turbine loads and tower - top motions will be higher than conventional fixed-bottom OWTs due to system wide interactions (Musial & Ram, 2010). These additional engineering considerations are addressed during the design process of the support structure, in order to insure the static stability and an appropriate dynamic response of the OWT system. More specifically, this is to maintain the position of the turbines rotor while staying within the range required for the power cable under loading. These loads on the system include the environmental forces from waves, wind and sea current as well as the as the thrust, torque and yawing of the wind turbine system (Henderson & Witcher, 2010). These considerations lead to a careful selection in the type of mooring system as well as the buoyancy or ballast needs of the structure, which will largely depend on the site conditions (Twidell & Gaudiosi, 2010; Tracy, 2007).

The mooring systems come in different variations but they have primarily consisted of either slack mooring lines, tensioned lines or a hybrid of the two (Butterfield, Musial, & Jonkman, 2005; Tracy, 2007) The composition of these mooring lines could be similar to those used in the oil and gas industry, ranging from tubular segments, locked-coil ropes or chains (Casale et al., 2010). Each type of mooring system will function in different ways. Tension mooring uses vertical lines under tension in order to provide restoring forces in pitch and roll. While slack catenary mooring is primarily used for station keeping of the floating support structure, providing little restoring forces in surge, pitch and roll due to the low tension of the mooring line. Taut catenary mooring lines, a hybrid of slack and tensioned lines, incorporate stiffer lines than catenary lines but less than tensioned lines. Subsequently, taut catenary mooring produce only moderate restoring forces in all of the system degrees of freedom. Configurations of the mooring lines in floating OWTs other than those previously mentioned, have high levels of instability deemed to be unacceptable (Tracy, 2007).

The stability of the support structure may vary depending on the type of system considered, within an acceptable degree of oscillation as shown in Figure 2.2. Some system designs are buoyancy stabilized using a large area of the water plane, like barges or ships, allowing for slack or taut catenary mooring for place holding. Others are stabilized with an increased ballast or mass at the bottom of the floating structure with a large draft in the design. This maintains the stability of the system against overturning moments and allows for the use of slack catenary moorings for station keeping. Finally,

support structures could be stabilized with the tensioned lined mooring system. These would be fixed to the sea floor and would incorporate a buoyancy force much greater than the weight of the OWT system (Casale et al., 2010).

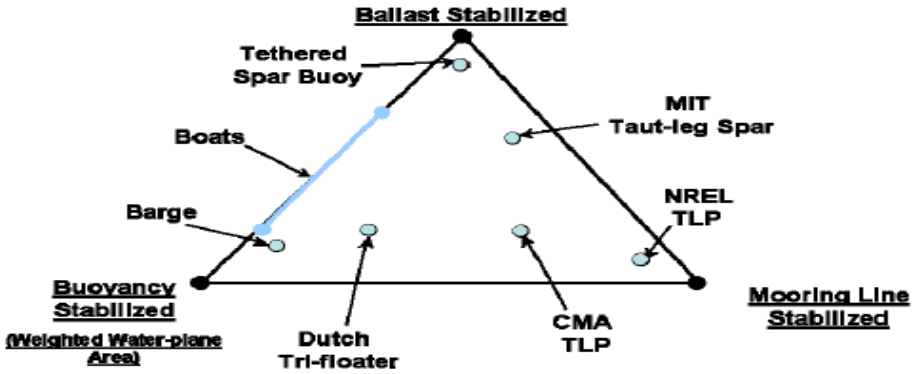

Figure 2.2: Floating Platform Static Stability Triangle (Butterfield, Musial, & Jonkman, 2005)

Four types of anchoring concepts that have been proposed are listed below:

1. Embedded anchoring
2. Pile anchoring
3. Suction caisson anchoring
4. Gravity anchoring

Of the proposed anchoring concepts, only the embedded anchoring system have not been previously discussed in the fixed support structure portion of this paper. The embedded anchor is similar to a ship anchor, providing strong vertical reactionary forces (Henderson & Witcher, 2010).

Although floating support structures have not yet been commercially developed, a variety of prototypes from design concepts like those shown in Figure 2.3, are undergoing testing (Butterfield, Musial, & Jonkman, 2005).

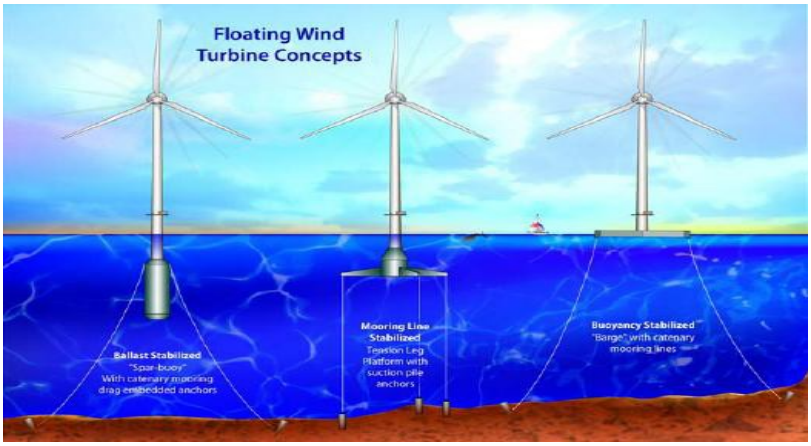

Figure 2.3: Floating Offshore Support Structure Types (Butterfield, Musial, & Jonkman, 2005)

As the cost constraints on floating support structures are overcome, partially through technical innovation, the potential of offshore wind energy could be further realized.

2.2.1 Barge

The barge is a relatively simple design much like that of barge ships or disk buoys. The stability of the OWT system is maintained by distributing the loads on the barge whose area spans across a wide water plane. The barge is typically ballasted to achieve a shallow yet reasonable draft, in order to minimize the repeated slamming of the structure by the waves (Jonkman, 2007). In order to maintain the system stability of the NREL 5 MW baseline turbine, a study concluded that the minimum diameter of the barge is 40

meters. However, this area will scale based on the system size (Twidell & Gaudiosi, 2010).

The wide area of the barge and the subsequent buoyancy force provides a significant resistance to the overturning moments. In order to insure station keeping either slack or taut catenary mooring lines are generally used both of which would counter the mean turbine and wave drift loads (Jonkman, 2007). On the other hand, instability could be significant due to the high center of mass of the barge turbine system and susceptible to wave induced motion due to the large platform area (Butterfield, Musial, & Jonkman, 2005; Twidell & Gaudiosi, 2010).

A test in the North Sea involving a full scale barge prototype supporting a wind turbine was conducted at water depth of approximately 150 m. The system suffered from excessive pitching motions during extreme wave conditions (Breton & Moe, 2009). Because of the significant reactions to dynamic forces, these systems would be ideal in areas relatively protected from extreme environmental conditions.

2.2.2 Tension Leg Platform

The tension leg platform (TLP) is assumed to provide the most stable platform of the proposed designs and, unlike the spar buoy which requires greater depths, can be used in water as shallow as 50 meters (Henderson, Witcher, & Morgan, 2009; Henderson & Witcher, 2010). In order to stabilize the highly buoyant structure, the mooring lines would be winched down in order to lower the support structure to a point below the water

line. The operational stability of the OWT is maintained from the highly tensioned mooring lines and the buoyancy of the structure (Butterfield, Musial, & Jonkman, 2005).

The support structure will vary in size based on various conditions. Research performed by Tracy (2007) resulted in the minimum design dimensions of a TLP supporting a NREL 5 MW baseline turbine. The platform itself would have a platform of 21 meters in diameter with a draft of 30.17 meters. Although these dimension depend a great deal on environmental conditions that Tracy assumed.

A study conducted in Italy by the ERSE indicated that at present, TLPs could be the most viable concept of the proposed floating support structures. These systems have little dynamic movement from external factors and therefore experience very small tilting movements (Casale et al., 2010). More explicitly, these systems have a high level of stability and mitigate the vertical, roll and pitch responses from environmental and operational forces (Twidell & Gaudiosi, 2010). The potential disadvantage of this system is the heavy reliance on the mooring lines for stability. Depending on the number of redundant tensioned mooring lines, the TLP supporting the OWT system could topple in the case of failure of one or more of the tensioned lines (Henderson & Witcher, 2010).

2.2.3 Spar Buoy

The slender spar buoy is stabilized with a large ballast at the bottom of the support structure and consists of a small cross sectional area relative to the large draft of the design (Tracy, 2007). Often these support structures are compared to monopiles, having a

simple design which subsequently means an ease in their fabrication during manufacturing. Preliminary estimates have indicated that the cost of the construction and fabrication of spar buoys should be lower than jacket support structures and TLPs which could increase the attractiveness of using the systems in the development of future OWFs (Twidell & Gaudiosi, 2010). The technological viability of these systems for their adaption to OWTs has recently been demonstrated by Statoil with the installation of a full scale grid-connected prototype off the coast of Norway (Henderson & Witcher, 2010).

The minimum depth and the buoyancy needs along with the mooring lines and anchoring system will depend on the system size and environmental conditions. However, initial design concepts incorporate three slack mooring lines anchored with drag embedded anchors (Casale et al., 2010; Henderson, Witcher, & Morgan, 2009). The movement due to the dynamic response from external loads could be damped due to the mass at the base of the spar along with the added mass of the surrounding ocean water (Casale et al., 2010; Musial, Butterfield, & Boone, 2003). Even with these and other stabilizing components, spar buoys could move excessively in response to the varying environmental and operational forces acting on the system (Twidell & Gaudiosi, 2010).

Research performed by Tracy (2007) resulted in the minimum design dimensions of a Spar Buoy supporting a NREL 5 MW baseline turbine. The support structure would have a radius of 4 meters at its largest cross section with a draft of 50 meters. Although these dimensions heavily depend on the environmental conditions that Tracy assumed.

Because the OWT system will be under additional dynamic loads, further research is necessary in order to insure the stability of these systems in the offshore wind industry (Butterfield, Musial, & Jonkman, 2005). The continued transfer of the technology from the offshore oil and gas industry along with the current tests that are being performed off the coast of Norway is expected to continue to increase the commercial viability of these spar buoy systems.

CHAPTER 3

ENVIRONMENTAL IMPACTS

The implementation of OWFs is a relatively new intrusion in the offshore environment. The rapidly growing industry is competing against more traditional industries for limited space. Not only are there a variety of potential environmental impacts with the introduction of OWFs but if poor siting occurs, adverse environmental impacts could result (Burkhard et al., 2009).

To a certain degree, the environmental impacts from the development of OWTs will depend on the type of support structure that is used. The types of systems will vary based on the environmental conditions in which they are installed with Table 3.1 indicating the varying conditions under which each of the systems are anticipated to operate in.

	Depth Range (m)	Sea state	Suitable seabed conditions	Unsuitable seabed conditions	Example Locations
Monopile	3 < d < 25	Design Dependant	Boulder, stiff clay	Weak/rocky soil	-
Gravity base foundation	3 < d < 25	Design Dependant	Insesitive to seabed parameters	Weak soil	-
Suction bucket	10 < d < 20	Calm	Stiff clay	Weak/rocky soil	-
Jacket structure	8 < d < 100	Design dependent - Ice free flow	Insesitive to seabed parameters	Insesitive to seabed parameters	-
Barge	50 < d < 300	Calm seas, protected cove areas	Insesitive to seabed parameters	Insesitive to seabed parameters	-
Tension leg platform	50 < d < 300	Varying	Insesitive to seabed parameters	Insesitive to seabed parameters	United Kingdom, Ireland, Norway, Sweden, Finland,Denmark & Korea
Spar buoy	150 < d < 500	Design Dependant	Insesitive to seabed parameters	Insesitive to seabed parameters	Korea

Table 3.1: Anticipated environmental conditions of offshore support structures

Studies have suggested that it is during the installation period that some of the greatest environmental impacts occur in the offshore wind industry, although depending on the method of decommissioning, this portion of the wind turbine lifecycle could have the largest impact (Geo-Marine Inc., 2010; Tong, 1998). In order to better determine the effects, a better understanding of the species affected is essential. Therefore in order to better determine the effects, five different groups of species were studied to improve on the understanding of their behavior in the offshore environment.

3.1 Affected Species

The ocean covers approximately two thirds of the earth. The wide range of conditions and species that inhabit this area, increases the difficulty in anticipating the type of habitat and species that will be affected with the development of OWFs. Some of the factors determining the makeup of the marine habitats that could be affected are the locations, bathymetry and environmental conditions, however, this is still largely not well understood. Because of this complexity, the focus of this study was narrowed to five general groups of species, shown in Figure 3.1.

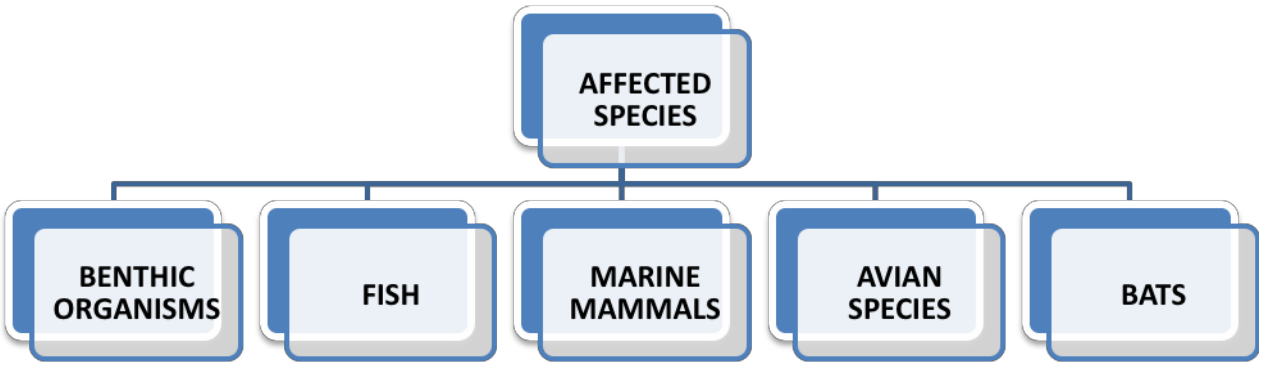

Figure 3.1: Affected Species

3.1.1 Benthic Organisms

In many regards, the harbingers of change in an ecosystem are species inhabiting the benthos. In this zone, at the bottom of the sea floor, lie groups of organisms and species rich in biodiversity which have a special function in the marine food web, namely as a food source for other groups (Glover & Smith, 2003; Morkel et al., 2007). Benthos organisms will vary based on local conditions including; the type of substrata, salt content, light conditions, temperature and bathymetry (Koller, Koppel, & Peters, 2006).

Many of the existing offshore wind farms have been developed in sandy sea shoal areas in shallow waters, which are important habitats for a variety of organisms. At first glance these areas look relatively barren, however, it is estimated that under every square meter of seafloor, hundreds of species can be found along with tens of thousands of organisms (Morkel et al., 2007).

The benthic communities in coral reefs on the other hand are both more dense and diverse than sand sea shoals and surrounding soft bottom areas and are one of the most important ecosystems in the offshore environment. However, anthropogenic activities, and in particular bottom trawling, have either partially or totally destroyed large numbers of coral reefs in shallow water, eliminating much of the natural hard substrate habitats. The majority of existing coral reefs now reside in water depths greater than 200 meters on the edge of the continental shelf, as shown in Figure 3.2 (Roberts & Hirshfield, 2004). These depths are in the range of proposed floating offshore wind developments.

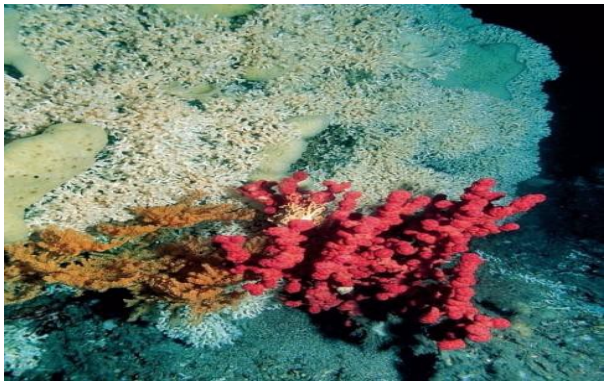

Figure 3.2 : Deep Sea Coral Reefs (Roberts & Hirshfield, 2004)

The low flux of organic energy from the decreased currents and sun synthesis typically limits the biomass to 0.001-1% of shallow water corals (Morkel et al., 2007; Glover & Smith, 2003; Rowe & Kennicutt, 2001). Although observations from one study indicated that down to approximately 2600 m the fish biomass remains relatively constant, while there is a negative density gradient in fish (Rowe & Kennicutt, 2001). A hypothesis that has gained traction is that this is partially due to carbon seeps from the continental shelf which provide more feeding opportunities. These seeps emerge from fractures in the rock

formations beneath the sea floor that contain oil and gas deposits. Even with these unknowns and limitations, deepwater coral still has been observed with three times as much biomass and a much higher biodiversity than surrounding soft bottom areas. Attention must be given to the siting of offshore installations in order to prevent further damage (Roberts & Hirshfield, 2004).

3.1.2 Fish

The spatial distribution of fish species is still not well understood, nevertheless there is a variety of research that has indicated that the number of fish species decrease at further depths and distances from the shore. One study, shown in Figure 3.3, concluded that at depths of approximately 160 meters, fish densities effectively dropped to zero (Rowe & Kennicutt, 2001; Stanley & Wilson, 2000). However, more recent studies show that the biomass stays relatively constant at increased depths while the fish densities decline at depths approaching 2600 meters. This indicates that the biomass increases over the continental slope, increasing with depth (Rowe & Kennicutt, 2001).

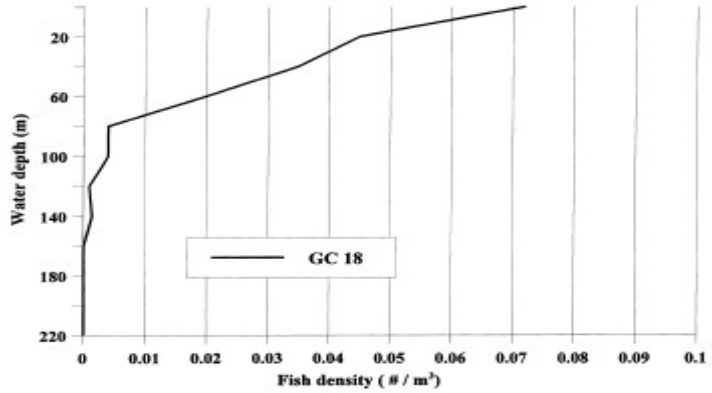

Figure 3.3 : Fish Density as a Function of Depth (Stanley & Wilson, 2000)

Physiological studies have indicated that the vast majority of fish possess highly developed hearing sensory systems, in which, the sensory hair cells play an important role (Thomsen et al., 2006). These sensory systems not only detect the current and vibrations but function by detecting predators and prey, utilized for intraspecific communication and for orientation and navigation (Wahlberb & Westerberg, 2005).

There are also large variations that exist in the anatomical, behavioral and physiological characteristics of a variety of fish species, including the ear and its associated structures. This suggests that marine species will have hearing thresholds at different levels (Nedwel et al., 2004). This is illustrated in Figure A.5 in appendix A, which shows the hearing threshold of a variety of fish species as a function of the frequency of the noise emissions.

In some fish species, the Earth's geomagnetic fields also play an important role in their orientation and navigation (Ohman, Sigray, & Westerberg, 2007). Other studies, however, have shown that fish use landmarks as a pseudo mental map for orientation (Chung, 2008). Nevertheless, various groups of species like elasmobranches, such as catfish and sharks, are known to rely on the Earth's magnetic field and are partially comprised of magnetic material. These consist of organs that detect low levels of electric current, while other types of species like the electric eel actually produce an electrical current. The level of sensitivity to disruptions in the magnetic field has been indicated by the behavioral reactions in a variety of different groups of fish (Ohman, Sigray, & Westerberg, 2007).

3.1.2 Marine Mammals

As with fish, hearing sensory systems are an integral part of a large number of marine mammal sensory systems. These sensory systems function as mechanisms to assist in orientation, prey and predator detection as well as intraspecific communication to navigation (Morkel, 2007; Wartzok & Ketten, 1999). The range of frequencies in which marine mammals can detect sound varies. For larger marine mammals, the hearing threshold corresponds to lower frequencies, while smaller-sized species have enhanced hearing capabilities in the upper frequency range (Geo-Marine Inc., 2010). In Figure A.6, in appendix A, a graphical representation of hearing thresholds based on results found from audiograms and brain stem responses for a variety of marine mammal species is shown.

The differences in the hearing capcity of marine mammals has been shown to occur due to the variations in the structure and number of components in the hearing physiology (Wartzok & Ketten, 1999). However, the existing data on the hearing in marine species is insufficient to conclusively determine the hearing thresholds, both in terms of frequency and sound pressure level, as well as the quality of data on the onset of hearing loss.

Vision, on the other hand, is a function of depth, at increased distance below the surface lighting becomes more limited. Between the species, the range of visual acuity varies in quality which increases the prominence of hearing in order to function in deeper water (Wartzok & Ketten, 1999). This provides an important function while foraging, with

some marine mammals, such as Harbor Porpoises and Grey Seals, have been found to feed on both fish and benthic organisms in the benthos (Geo-Marine Inc., 2010).

The spatial and seasonal distributions of the behavior of marine mammals offshore is still not well understood. Studies trying to address these issues have found that in many cases the number of a given species changes in time and space. In Germany off the German Bight, studies found that Grey Seals spent up to 70% of their time foraging out to 40 km offshore. Another study off the coast of New Jersey tracked marine mammals over the course of two years with average densities shown in Figure 3.4 (Geo-Marine Inc., 2010; Morkel et al., 2007).

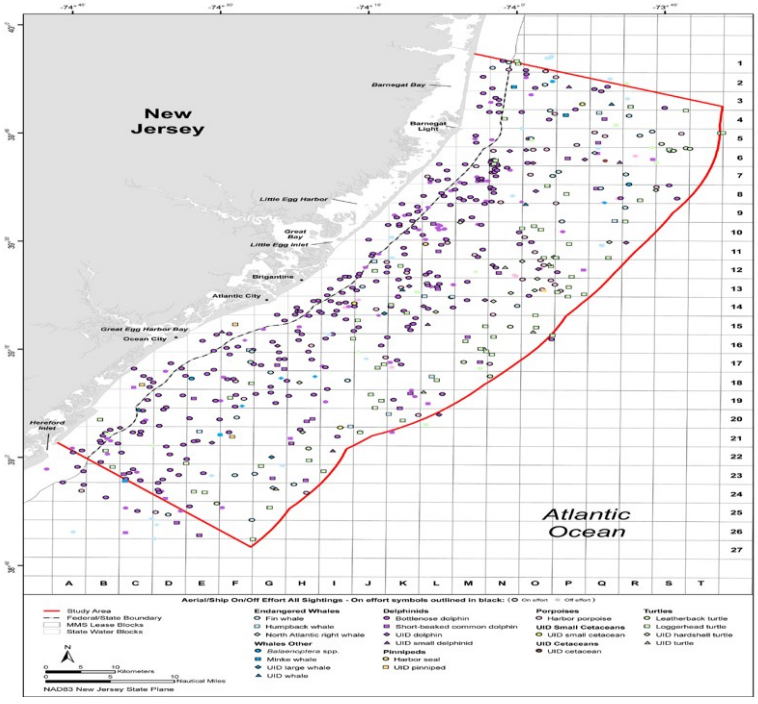

Figure 3.4: Spatial Distribution of a Variety of Marine Mammals (Geo-Marine Inc., 2010)

3.1.4 Avian Species

Birds tend to cycle through different phases from the breeding period, the migration to their wintering area and the reverse migration. The onset of migration, observed over the North Sea, has primarily occurred at night during a small number of migratory waves (Morkel et al., 2007). Conditions which determine the onset for migration, range from weather conditions to their mode of navigation (Geo-Marine Inc., 2010).

To prepare for annual long distance migrations, many avian species increase their fuel stores by substantially increasing their body fat prior to the migration. In some cases the body mass of some species may more than double due to the energy intensive nature (Klaassen, 1996). This is particularly true as birds cross long distances such as oceans without feeding (Allison, Jedrey, & Perkins, 2008).

The range of migration is dependent on the quantity of the feeding sites en route and the species type (Battley et al., 2000; Klaassen, 1996). Some migratory species have been found to fly in the range of 2,500 to 4,000 km and non-stop flights of 10,200 kilometers have been recorded for the Bar-tailed Godwit (Shaffer, et al., 2006).

Heights in which migratory birds fly, are generally at higher altitudes than foraging or breeding seabirds. A study performed for the Cape Wind Energy project indicated that migratory avian species flew at heights extending up to 6000 feet above ground (Minerals Management Service, 2009; University of Maine, 2011). Although this will be specific to the species type (Schwartz, 2004).

Likewise, foraging behavior will be species specific. Consequently within foraging areas feeding behavior will vary depending on the species type (Cherel et al., 2002). Behaviors have included the pursuit of underwater prey by using their wings or feet for propulsion to diving in after their prey (Jenkin, 1957). The extent of the foraging grounds will change as well. While in the breeding season, seabirds will typically remain near the breeding areas, other birds will generally display spatial fluctuations in their foraging behavior due to the uneven distribution of food (Morkel et al., 2007).

Regardless of the type of behavior that is exhibited or the time of the season, multiple studies have concluded that avian species tend to decrease in density at greater distances from the coast (Geo-Marine Inc., 2010).

3.1.5 Bats

Researchers have identified approximately 1,100 different types of bat species worldwide. In general there is only little knowledge of their behavior in the offshore environment (Zuccaa et al., 2010). On land, some species have been observed migrating hundreds of kilometers. Offshore, however, much less is known, although there have been sighting of flocks of bats landing on ships up to 130 kilometers from the coast (Cryan & Brown, 2007; University of Maine, 2011).

Studies performed off the coast of Sweden have observed that the weather conditions conducive for bat activity primarily occur during clear nights when wind speeds are lower than 10 m/s (Ahlen et al., 2007). The weather conditions correlate with the largest

concentration in bat fatalities and bat activity onshore, which typically occur during wind speeds of approximately 4 m/s (Ahlen, Baagoe, & Bach, 2009; Arnett et al., 2008). However, migration or foraging are limited during bad weather conditions with limited bat activity (Ahlen et al., 2007). This has been hypothesized to occur due to conditions such as rainy weather, which interferes with their echolocation sensory systems (Ahlen et al.,2007). This echolocation is a physiological tool used for a variety of functions, most notably to forage and navigate, giving them a mental map of their surroundings (Cryan & Brown, 2007). There is some question whether echolocation is used during migration. Some studies have indicated that during migration over land bats turn off their echolocation sensory system, while other researchers have detected its use (Geo-Marine Inc., 2010).

Even though there is some research on bat species offshore, much is still unclear. This ranges from the distance from the coast at which bats are found to the foraging and migratory behavior offshore. This will require more research in the future (Ahlen et al., 2007).

3.2 Effects

There have been studies that have indicated that the development of OWFs will cause a variety of environmental impacts (Musial & Ram, 2010). The greatest impacts on marine species have been observed during the construction phase and are anticipated to be mirrored during decommissioning. On the other hand, all stages of the OWT lifecycle are anticipated to affect varying groups of species. Studies performed on the environmental

impacts at offshore wind farms have begun to expand on this knowledge and understanding (Koller, Koppel, & Peters, 2006; Maar et al., 2009).

3.2.1 Barrier Effects

This type of effect either occurs when a species does not pass through a wind project or when greater amounts of energy are used to avoid a wind farm. Some of the largest effects that have been observed, both on land and in the offshore environment, have been the barrier effects created by wind turbine systems (U.S. Fish and Wildlife Service, 2010). The types of barrier effects (see Figure 3.5) depend on the system or method in which they arise; the sources that are analyzed in this paper are listed below:

1. Noise Emissions
2. Transmission Lines
3. Physical Obstruction

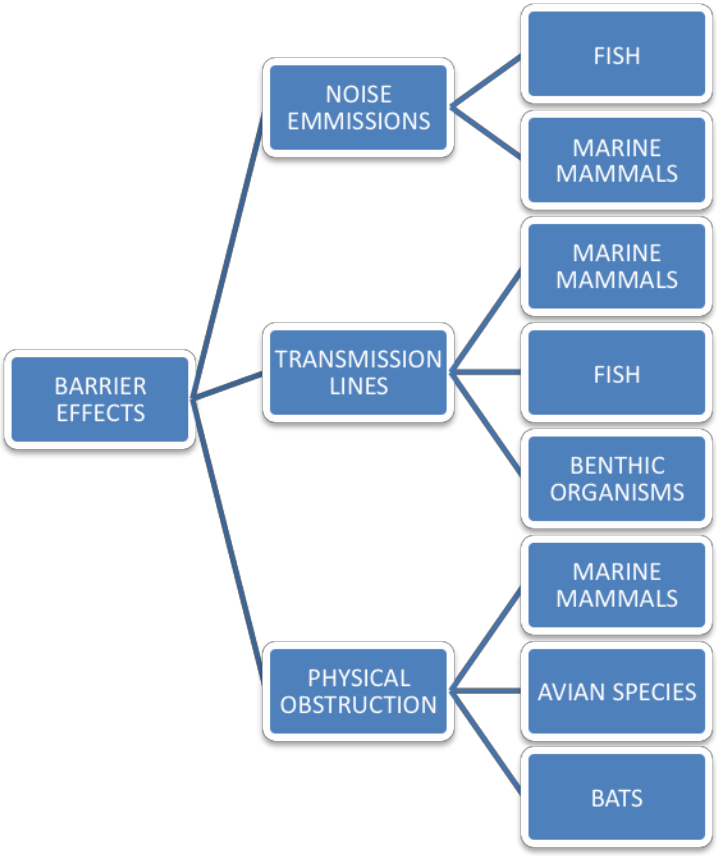

Figure 3.5 : Types of Barrier Effects Analyzed

A) Noise Emissions

Noise emissions have a significant impact on a variety of marine species, affecting their hearing sensory systems and possibly causing behavioral changes. These effects, which range from avoidance to attraction, have been observed in a number of marine species (Nedwell & Howell, 2004; Thompson et al., 2010).

Studies have indicated that marine species will be adversely affected during the installation and decommissioning of support structures due to noise emissions and will generally display avoidance behaviors (Geo-Marine Inc., 2010; Morkel et al. 2007). Installation methods generally take large amounts of energy in order to complete, with

some energy dissipation leading to noise emissions (Nedwell & Howell, 2004). The level of emissions will deviate based on the installation method, although existing studies have indicated that the largest impacts will occur during pile driving operations. Studies on pile driving have found that the noise level is proportional to the pile diameter (See Figure A.7). The piling installations could lead to significant barrier effects or auditory injury, ranging from permanent to temporary threshold shifts (Bailey et al., 2010). The extent of the impact will depend on the sound propagation which will partially depend on the bathyometry and geographical and background noise conditions (Bailey et al., 2010).

Other types of support structures such as gravity base foundations, will have much lower noise emissions than those emitted during the installation of pile support structures. Although the duration of noise exposure could be longer due to the extensive site preparation required in gravity base foundations (Nedwell & Howell, 2004). Likewise, the installation of suction caissons and the anchoring for floating platforms are unlikely to permanently affect the hearing of marine species and are expected to have lower levels of noise emissions than emissions originating from pile driving (Twidell & Gaudiosi, 2010).

The response will vary based on the species hearing physiology, but at present, there is only a small number of species for which this is known. The majority of existing studies on the noise impacts in the marine environment have been on commercially important fish species and marine mammals. A numerical model that is used (shown in Figure A.11 and Figure A.12) indicates that in like conditions, the number of species affected will be

roughly proportional to the pile size, with greater numbers affected with larger pile sizes. In some cases these existing studies could be used to compare effects in other species from the extrapolation of known data. Although the results could be prone to substantial error due to species specific behavior and unique environmental conditions that make up each area (Wahlberb & Westerberg, 2005).

Empirical models are routinely used to predict the level of the impact and gives rough approximations of the noise emissions in water referenced at 1 μPa, over large distances. This is based on the sound pressure level (SPL), a metric that is used to determine the noise propagation and site specific parameters such as geometric spreading and absorption losses. The model, however, breaks down within a certain distance from the sound source. This distance is generally considered within 100 meters. In order to determine the noise emissions at this point, a logarithmic linear interpolation to the source is typically used to provide a rough approximation of the actual noise level (Thomsen et al., 2006; Wahlberb & Westerberg, 2005). A underwater noise propagation simulation was run derived from equations 2-9 in Appendix A, and modeled into the code as shown in Appendix B.

Near the sound source during pile driving, it is anticipated that the high levels of noise originating from the installation could lead to permanent injury or death of marine species in the underwater environment. Depending on the magnitude of the installation, the noise level could be greater than 130 decibels above the hearing threshold of a number of species, which is generally considered the onset of physical damage from

noise. Sound levels of 90 decibels above the hearing threshold is the point in which almost all marine species have been observed to display avoidance behaviors (Parvin, Nedwell, & Harland, 2007). The proportion of marine species that would react to the sound pressure levels would fall as the distance from the sound source increases as seen in Figures A.11 and A.12. The effects of permanent or temporary injury would adversely affect their likelihood of survival by hindering their ability to detect both predators and prey (Koller, Koppel, & Peters, 2006).

As can be seen in Figure 3.6, as the range of the sound propagation increases, the range and effectively the volume of the sea that is affected likewise increases, which would increase the number of individuals affected. It is likely that at high enough SPLs, individual species would exhibit a sustained avoidance reaction, but for lower sound levels it is hypothesized that an initial reaction would be followed by an eventual habituation. Although this is yet to be seen and more research must be performed.

It should also be noted that the effects for the deployment and installation of anchoring for floating support structures using piling anchoring, is anticipated to have a smaller impact than fixed systems due to the smaller piles used shown in Appendix A in Figure A.11 and Figure A.12. However, more pilings will be needed with each system which could have adverse impacts due to the greater length in time that would be needed for the overall installation. As floating wind farms begin to develop, more conclusive studies will be needed to determine the extent of the environmental impact on the marine environment.

A-1) Fish

In comparison to avian species and marine mammals, much less research has been conducted on the effects of OWFs on fish. What is known is that the hearing physiology of fish is generally different than in marine mammals (Thomsen et al., 2006). From present research and understanding, it is anticipated that solely during the period of installation and decommissioning that noise emissions would cause artificial barriers, preventing fish from reaching breeding, spawning or foraging sites and disrupting intraspecies communication, which could occur over relatively large spatial scales. During operations however, no physical damage has been observed (Geo-Marine Inc., 2010; Wahlberb & Westerberg, 2005).

A-2) Marine Mammals

The behavior of marine mammals has been found to be variable with the detection of noise. Behavioral variations have ranged from the investigation of noise emissions to the display of avoidance behaviors (Morkel et al., 2007; Thomsen et al., 2006). Observations made at the Horns Rev wind farm during the installation showed that harbor porpoises reacted by avoiding the installation sites from distances up to 14 km from the development (Morkel et al., 2007). Likewise, measurements taken during installations off the coast of Scotland of a 5 MW wind turbines supported by a 4 legged steel jacket, indicated that noise propagated up to 70 km from the sound source, distances in which harbor porpoises displaying avoidance behaviors. As indicated by Figure 3.6, this was above the hearing threshold of a variety of marine mammals, measured at two fixed

frequencies; 1kHz and 10 kHz (Bailey et al., 2010). Because the hearing threshold is a function of frequency, the effects will vary based on the frequency of the emitted noise.

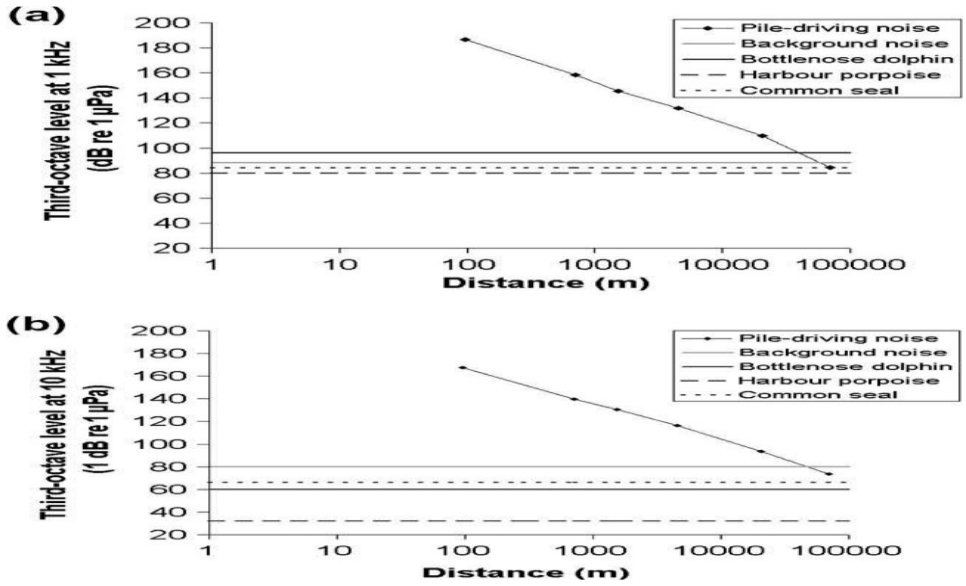

Figure 3.6: Noise Propagation from the Installation of Two, Four Legged Jacket Support Structures (Bailey et al., 2010)

Furthermore, a study out of Denmark, which used telemetry data, found that during pile driving activities of piles measuring 4.6 meters in diameter in water depths of 18 meters, avoidance behaviors in harbor seals occurred up to at least 40 km from the installation site (Lindeboom et al., 2011).

However, the density levels of a variety of marine mammals were similar between pre and post construction activities. This was based on data collected from echolocation detection tools, leading to initial assessments that the barriers that have been observed during installation are only temporary. Over time, marine mammals seem to habituate to

this new environment leading to negligible impacts during normal operating conditions (Morkel et al., 2007).

The reactions of whales are largely unknown due to the few studies regarding their auditory sensitivity. It is possible that blue, grey and minke whales will respond to the low-frequency sound originating from vibrations and during normal operations that wind farms are likely to produce. However, the response will largely be species specific, depending on migratory routes and foraging areas of whales and the location of the offshore developments (Vella, 2002).

B) Transmission Lines

Transmission lines act as a conduit in the offshore wind industry, transferring electricity between OWT's and mainland facilities. The primary type of power transmission that is currently used in the offshore wind industry is alternating current (AC). However, as development continues to expand out to further distances from shore, direct current (DC) transmission is anticipated to be used more frequently (Ohman, Sigray, & Westerberg, 2007). There is some concern that these transmission lines could adversely impact the local marine environment (Geo-Marine Inc., 2010).

One of the concerns regarding the potential environmental impacts of transmission lines is the electric dissipation from the transmission lines and the subsequent localized heating of the seafloor. This could adversely impact thermophillic species unable to habituate to these new environmental conditions and cause artificial barriers and draw in invasive

species attracted to these new conditions (Koller, Koppel, & Peters, 2006). Furthermore, heat dissipation could lead to physio-chemical conditions in the sediment, possibly increasing bacteria activity in the near spatial area (Geo-Marine Inc., 2010). However, in both cases it is anticipated that this will only have minor effects because the affected area would be limited to areas near the transmission lines.

Meanwhile, it is the generation of electromagnetic fields (EMFs) and magnetic fields (MFs) that are believed to have the largest impacts. Some species have been shown to have remarkable sensitivity to electric fields in seawater (Geo-Marine Inc., 2010). The EMF intensity will vary based on a variety of factors from the current used, conductor core geometry, insulation type, nature of the seabed and the depth of buried transmission lines (Wilson et al., 2010).

Some studies have taken measurements at existing OWF's that used monopolar cabling and found that the MF strength is an order of magnitude greater than that of the natural geomagnetic field. This has raised concerns about what impacts this will have on electro sensitive species (Koller, Koppel, & Peters, 2006; Kramer et al., 2010). Observations of a variety of marine species in the vicinity of existing transmission lines have displayed avoidance behaviors at varying distances from the cables. Furthermore, research has indicated that noticeable behavioral responses were observed due to EMFs up to several hundred meters from a transmission line even when buried under several meters of seafloor (Geo-Marine Inc., 2010). However, with advances that have been made in transmission technology, the EMFS can now be reduced, if one is generated at all, with

specific cabling configurations capable of reducing EMFs with alternating or direct current cables (Geo-Marine Inc., 2010).

There has also been a certain degree of variability in the avoidance reactions among different species (Gill & Taylor, 2001). In some studies there has been no discernable effects at the current level of strength used in the offshore wind industry (Koller, Koppel, & Peters, 2006). Additionally, a recent two year study concluded that EMFs from cables do not seem to have a major impact upon fish and other mobile organisms attracted to the hard bottom substrates for foraging, shelter or protection (Lindeboom et al., 2011).

Finally, unlike the research that has been conducted on the behavioral and avoidance mechanisms of marine species, no research has yet been made on the effects that EMFs will have on cellular activity regarding abnormal growths, as well as the potential impacts of heavy metals from materials in the transmission lines leaching into the surrounding substrate (Geo-Marine Inc., 2010; Kramer et al., 2010).

C) Physical Obstruction

Operational barriers for the purposes of this paper are the physical obstruction and the associated avoidance response that is generated solely due to the presence of OWTs. The effects of floating OWFs are largely unknown, although they are anticipated to affect larger marine species such as marine mammals. On the other hand, extensive research on the avoidance response in avian species and migratory birds has been seen on land and at some OWFs. Unlike avian species, the OWF barriers affecting bats in the marine environment are still largely unknown but the research that has been performed on land

has indicated that instead of displaying avoidance behaviors to wind turbines, bats are attracted to them. An overview of the known impacts and a more extensive overview of the anticipated impacts of these three groups of species is presented below.

C-1) Marine Mammals

Little is known of the potential environmental impacts from floating wind turbine systems. Over time, there is a possibility that marine mammals could habituate to floating OWFs. But the possibility also exists that permanent avoidance could occur. Environmental impacts arising from other industries with components similar to proposed designs, could be mirrored in the wind industry. In this regard, two plausible concerns are collision and entanglement.

Floating support structures with slack mooring lines could have dynamic motion excited by external forces which could lead to marine species colliding with offshore wind systems. This would primarily be a concern for larger marine species because of the small surface area of the mooring lines, attaching the support structure to the anchors, in relation to the size of the total system, possibly making detection more difficult (Pacific Energy Ventures, 2O11).

In the fishing industry there has been documentation of fatalities and injuries due to entanglement in a variety of fishing gear, most notably from fishing nets. This has raised concerns of the possibility that the effects could transfer to the floating support structures used in offshore wind. Slack mooring lines in floating systems are expected to be the

primary threat for entanglement. Other concerns include the debris such as derelict fishing gear that could becomes tangled upon the mooring lines (Global Energy Partners, 2004; Melnyk & Andersen, 2009). Furthermore, because floating support structures are expected to act as fish aggregate devices, the probability for the entanglement of marine species will increase due to the greater foraging opportunities (Pacific Energy Ventures, 2O11; Polagye et al., 2010). For example a foraging baleen whale could become entangled due to the mooring line catching in its mouth. This would effectively cause entanglement because of its inability to swim backward (Pacific Energy Ventures, 2O11). This risk could increase with a corresponding increase in the number of wind turbines.

C-2) Avian Species

There have been numerous environmental studies of avian species regarding the impacts due to the development of wind energy, although many uncertainties remain. However, initial assessments indicate that some of the largest threats generally posed are impacts from barrier effects and collision (Drewitt & Langston, 2006).

Barrier effects arise, in avian species, from the circumnavigation and the avoidance of the wind farm areas (see Figure 3.7, Masden et al., 2009). Studies performed off the coast of Denmark found that over 75% of all bird species displayed avoidance behaviors at approximately 1.5-2 kilometers before reaching a wind farm. Inside the wind farm, observations have shown additional avoidance behavior, including dramatic changes in flight patterns in order to maximize the distance between wind turbines (Schwartz, 2004).

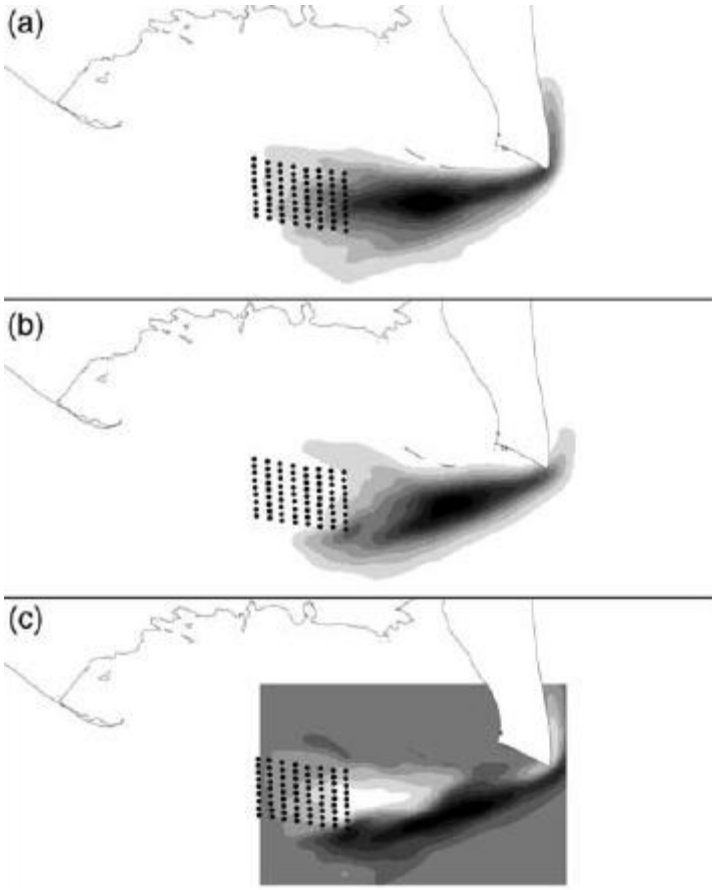

Figure 3.7 : Pre (a) and Post (b) Construction Flight of Common Eiders at Nysted Wind Farm & the Difference (c) in Space use between Pre and Post Construction. Darker Colors Indicate Greater Use (Masden et al., 2009).

Other studies have indicated that the avoidance for some species has more to do with the presence of the structures themselves rather than from the operations. At Tuno Knob, a Danish wind farm, studies were conducted both during operation and downtime. Observations in both cases indicated that the avoidance displayed by Common Eiders was highly correlated solely to the presence of wind systems (Geo-Marine Inc., 2010). Though, the effects due to the wind turbine barriers will vary between and among species, with some groups of birds reacting strongly and will display avoidance behaviors when detecting wind farms, while other findings out of Denmark have found that some

species such as divers, guillemots and razorbills do not show a marked avoidance (Lindeboom et al., 2011).

In either case, one of the impacts due to barrier effects on birds will be an increase in the expenditure of energy, which could cause a larger number of deaths. This arises from secondary effects due to the skewing of the migration patterns leading to possible exhaustion from extended flight paths. In order to approximate the magnitude of the barrier effect, an analysis is typically conducted to determine the extent that the flight paths must be increased in order to avoid the wind farms. This approximates the energetic cost of the increased flight distances and the likelihood of survival (Norman, Buisson, & Askew, 2007).

Indirectly, reproduction rates could decrease due to the shortened mating season from the longer migratory distances and the additional foraging that would be needed to compensate for the increased energy expenditure (Allison, Jedrey, & Perkins, 2008). Recent studies have concluded that existing offshore wind developments have had little impact, but as more offshore wind farms are installed the cumulative impact could become substantial (Masden et al., 2009).

C-3) Bats

There have been relatively few studies that have been conducted to analyze the impacts that wind turbine barriers will have on bats, and this is especially true in the offshore environment (Ahlen et al., 2007). The information that is available indicates that in some

cases bats, unlike birds, are attracted to wind turbines. Furthermore, studies that have been performed on land have found that on average the bat fatalities at a given site are much higher than those for avian species (Schwartz, 2004; Rodrigues et al., 2008). The literature that has been reviewed indicates that barrier effects will be negligible; in fact the opposite seems likely in which bats are drawn to offshore wind turbines due to increased foraging opportunities.

3.2.2 Habitat Disruption

Environmental impacts may vary among species throughout the lifecycle of OWTs, ranging from the turbidity of the water during the installation to the introduction of artificial substrate and changes in foraging areas (Hoffmann et al., 2000). Of these possible sources of disruption the focus was narrowed down to three possible types, as shown in Figure 3.8.

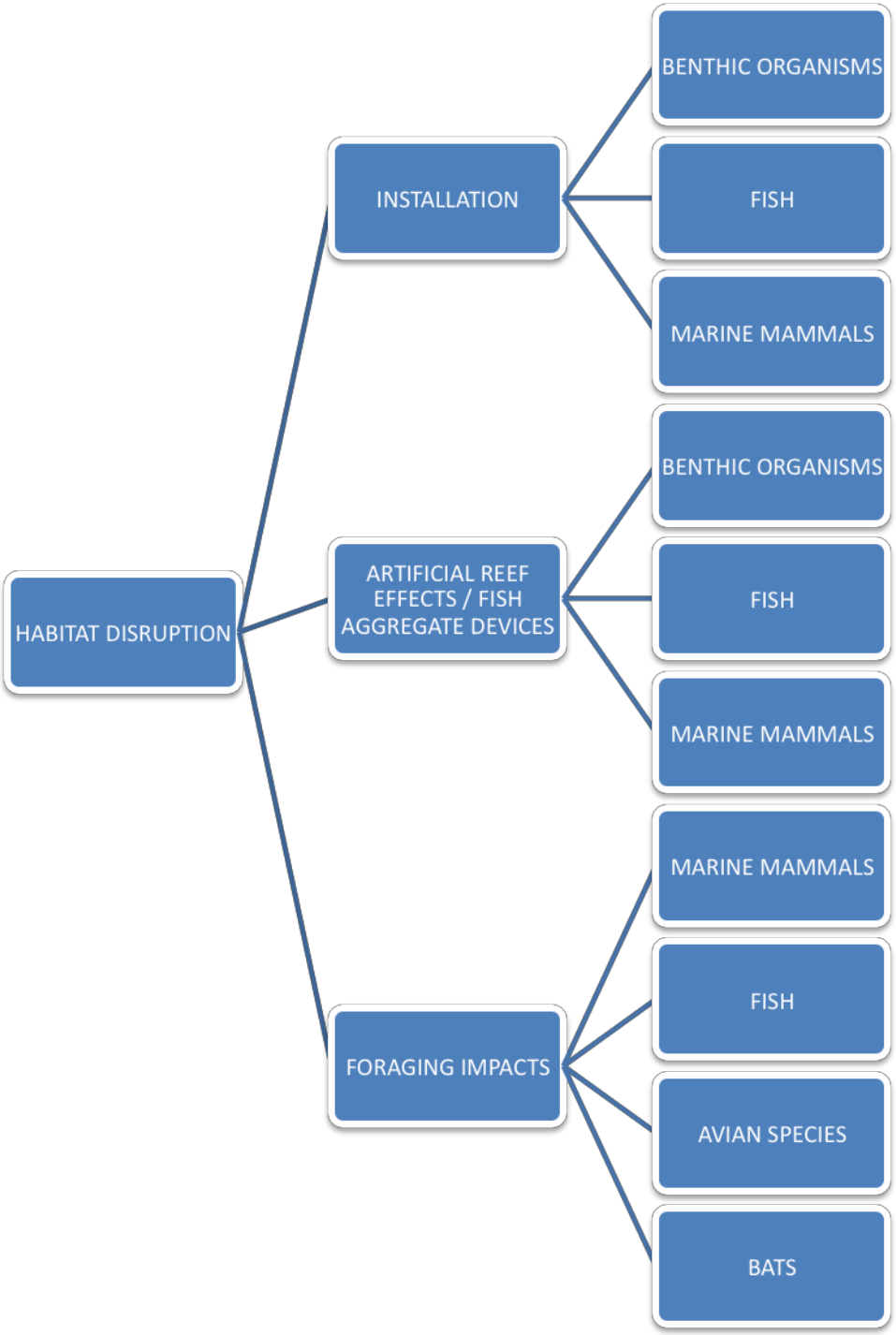

Figure 3.8: Analyzed Habitat Effects

A) Installation

During seafloor preparation, construction and cable installation, the seafloor will see intrusive activities which could result in the death of immobile species or those with extremely limited mobility. This could arise from either being crushed by the system being installed or from asphyxiation due to sedimentary plumes and the subsequent rapid resettlement (Polagye et al., 2010). The scale of the disturbance will depend on the type of the support structure that is used and the installation method. This is not only an issue associated with support structures, both fixed and floating, but is also a concern during the installation of transmission lines (see Figure 3.9) (Geo-Marine Inc., 2010; Lissner et al., 1991).

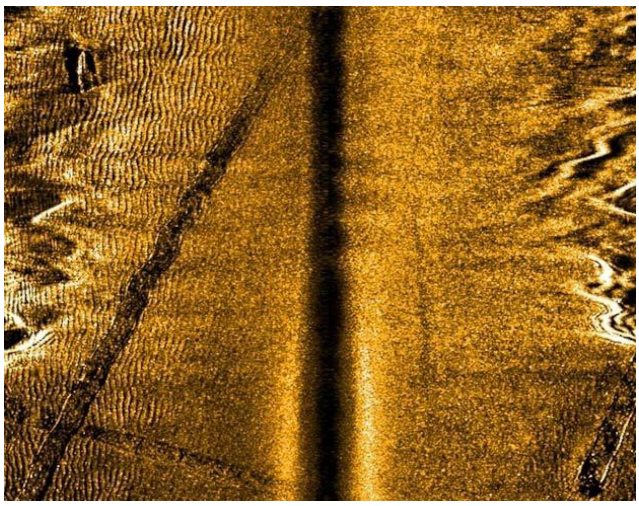

Figure 3.9: Transmission Line Installation (Geo-Marine Inc., 2010)

The adverse impacts that result during the installation of both fixed and floating support structures are expected to be similar, although the magnitude of disturbance will depend on the anchor, mooring line or support structure that is used. One example would be the pile compared to the gravity base foundation. The latter would have larger effects on the

seabed due to its wider surface area at its base and the extensive site preparation required (Geo-Marine Inc., 2010; Koller, Koppel, & Peters, 2006).

Likewise, the installation of the transmission lines will disturb the sea bed. The installation methods range from mechanical plows to directional drilling which can lead to crushing or the asphyxiation of sessile species (Tong, 1998). However, the impacts are localized to areas in the vicinity of the installation (Bailey et al., 2010).

In any case, portions of the habitat are thought to recover relatively quickly from the damage. For example, the FINO 2 research platform in the Baltic Sea saw signs of recovery immediately following the structures installation (Geo-Marine Inc., 2010; Koller, Koppel, & Peters, 2006). Furthermore, at Nysted Wind Farm, eel grass recovered completely within two years after the installation of the transmission lines, although other species were found to still be recovering. Deep water corals could be effected with the installation of floating supporting structures. Because little is known of the distribution of deep water corals, if they are inadvertently effected, recovery time could be on the order of centuries due to their slow growth (Jaap, 2000; Roberts & Hirshfield, 2004).

In general, benthic communities have adapted to sediment disturbances and over time have become relatively tolerant of these disturbances, leading to relative insensitivity to smothering. It is anticipated that feeding and respiration would return to normal soon after the installation and it is likely that, in general, benthic communities would make a rapid recovery (Geo-Marine Inc., 2010).

B) Artificial Reef – Fish Aggregate Devices

The development of OWFs could cause changes in the habitat in the vicinity of the installation, depending on the nature of the device and the preconstruction habitat. Benthic plants and animals could be affected by the changing environmental conditions (Polagye et al., 2010). These species living in the benthos are an important food source for many marine species and humans, often acting as a driver of offshore ecosystems. The magnitude of the impact is dependent on the local environment. Factors include the type of substrate available, influencing the colonization and species present in an area, along with the change in the local ocean current (Koller, Koppel, & Peters, 2006). This could change the localized conditions in the ecosystem, attracting foreign species (Langhamer, Wilhelmsson, & Engstrom, 2009).

After the effects of the installation of the OWF, the development could act as a artificial reef or a turn into a fish aggregate device (FAD) depending on the system type (Geo-Marine Inc., 2010). This could result in changes in the concentrations of prey and alterations to the existing ecosystem (Polagye et al., 2010). The foundation or anchoring used will replace the natural substratum that is lost during construction, which means that in areas with soft seabed, the species composition would be affected (Koller, Koppel, & Peters, 2006). This would increase the hard substrate surface area available for algae, fish and other benthos species. In sandy seabed locations, this could change the entire benthos composition, having a localized impact on the food chain and attracting invasive species. A study that was carried out on installed monopiles by Wilhelmsson & Malm (2008), indicated that the biodensity of some species increased, while other species such as algae

tended to decrease. Some of the results are shown in Figure 3.10. An additional impact from the foundation is the change in hydrodynamic patterns, impacting food supply flux which could lead to additional biomass accumulation on the foundation (Lissner et al., 1991). Another possible driver that could increase the biomass is the addition of scour protection. The increase in the porosity of the structure and the complexity of the substrata would effectively increase the surface area available. This could increase the settlement capacity and draw in a more diverse and complex taxa which has been shown to increase the health of an ecosystem (Wilson et al., 2009).

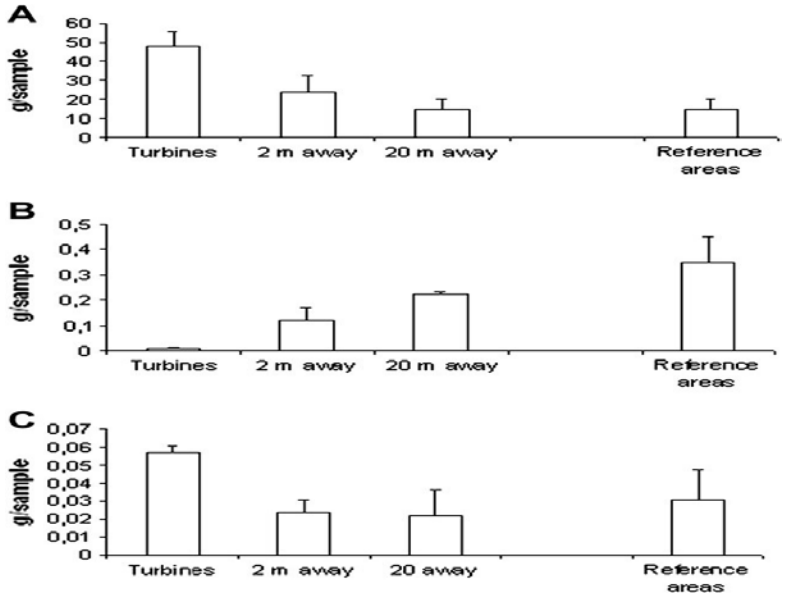

Figure 3.10: Fouling Assemblages on Offshore Wind Turbines (Wilhelmsson & Malm 2008)

Floating support structures could impact the offshore environment in much of the same way that other industries have experienced. Some of the effects could originate from the anchoring systems, which could incorporate various types of mooring lines (tensioned, slack or hybrids systems) (Twidell & Gaudiosi, 2010). Of these mooring lines, as

indicated by Lissner, et al. (1991) , slack lines are anticipated to continuously shift with the current and could keep the sediment layer in a constant flux. This could continuously affect the makeup of the benthos in the vicinity of the anchoring system and decrease the probability of a successful recolonization of the affected area.

Furthermore, experience from other industries has demonstrated that floating support structures will function as FADs (Geo-Marine Inc., 2010). The attraction of both juvenile and adult fish species to FADS typically leads to an increase in the abundance of species, thereby attracting larger predators to the area (Langhamer, Wilhelmsson, & Engstrom, 2009; Wilson et al., 2007). If marine mammals, such as seals or sea lions, are attracted to the wind development due to the increased foraging opportunities, they could use support structures, when possible such as with barges, as artificial haul out areas. This may increase their abundance, artificially increasing the carrying capacity of the ecosystem (Global Energy Partners, 2004).

Likewise, seabird abundance with some species has positively correlated with foraging opportunities. Some seabird studies that have been performed in offshore wind farms have indicated that when boulder scour protection is used in wind farms, there is an increase in the total number of birds. This is likely due to the increased feeding opportunities from the increased prey and greater biodiversity (Drewitt & Langston, 2006).

Overall, various types of support structures from fixed to floating have been consistently shown to have greater biomass densities and diversity than sandy soft bed regions, which are where the majority of proposed and current OWFs have been developed (Langhamer, Wilhelmsson, & Engstrom, 2009).

C) Foraging Impact

Artificial reef effects and foraging impacts are intertwined, both having tangible impacts on marine and avian species. Decoupled from these effects are the impacts on the foraging behavior of bats.

C-1) Marine Mammals

A majority of the European studies that have been performed have shown that marine mammals display an initial avoidance reaction during the wind farm construction phase. Population levels typically return to pre-construction levels, however, some studies have concluded that the population levels of some types of marine mammals decrease after the construction phase, and remain lower than levels observed before construction (Morkel et al., 2007; Vella, 2002). One study at the Nysted Wind Farm, demonstrated that porpoises which left the area after construction did not return during the operational phase while other Danish studies indicated no detectable differences in the presence of harbor porpoises between the inside and outside of analyzed wind farms. On the other hand, at the Egmond aan Zee Offshore Windfarm, more porpoises were detected in the wind farm than in comparison to two reference locations that were studied. The available data on the behavior of marine mammals cannot easily be extrapolated to other locations and site

specific analysis must be performed in order to better understand the potential impacts (Lindeboom et al., 2011).

There will be variability in the level of noise emissions during construction. Potential effects could include avoidance behaviors as well as a permanent or temporary loss in habitat depending on the ability of species to adapt to the increased levels of noise (Bailey et al., 2010; Madsen et al., 2006). During operation, studies performed at a number of European offshore wind farms on porpoises and seals indicated that the noise emissions would be slightly higher than ambient background noise. This would have no adverse impact or cause any behavioral reactions unless the marine mammals are in the immediate vicinity of the foundation (Tougaarda & Damsgaard H., 2009).

Overall, an increase in the overall number of marine mammals in a offshore wind development is expected, mainly due to the increase in biomass or the increased foraging opportunities that are available near the support structure (Vella, 2002). Furthermore, the exclusion of fisheries and reduced vessel traffic in the area of the wind farm will offer a semblance of a sanctuary shielded from anthropogenic activity (Lindeboom et al., 2011).

C-2) Fish Species

Feeding opportunities for fish has been shown to increase in OWFs as well. Shortly after the installation of the FINO1 Operation Research Platform, the surface was colonized by an epifauna consisting of a high biomass of few species. Likewise in developed wind farms, the absence of fisheries has been highly correlated to higher fish biodiversity in comparison to surrounding areas and to larger fish aggregations (Lindeboom et al., 2011).

Predators and scavengers profit from the additional food sources provided by biomaterial falling from the platform. This biomaterial, such as feces, could spread over large areas contributing to dense aggregations of pelagic fish which has been observed around the FINO1 platform (Geo-Marine Inc., 2010).

C-3) Avian Species

The offshore impacts on avian species have been studied extensively, primarily in Europe, but an extensive assessment of the potential environmental impacts at the proposed Cape Wind project in the northeastern United States was performed concerning habitat loss and disturbances. The magnitude of the various types of environmental impacts is highly site and species specific (Drewitt & Langston, 2006).

Habitat losses arise from the construction and installation of wind turbine systems, disrupting foraging areas and migratory birds. The displacement effects can be inferred from the sensitivity of species to disturbance and their associated avoidance. This behavior could occur throughout all stages of the life cycle of the wind farm, from siting to decommissioning (Drewitt & Langston, 2006). As a consequence, sensitive species would be displaced from large offshore areas. Factors associated with the magnitude of the disturbance include the seasonal diurnal patterns, and the location of the wind farm with respect to important habitats and the availability of alternative foraging areas.

As the number of wind farms and the size of wind turbines increase along the coast, the cumulative impact increases and the greater potential for the loss of habitat (Geo-Marine

Inc., 2010). The wind farm layout would be another driver in the avian species displacement, possibly fragmenting resting and feeding areas (Koller, Koppel, & Peters, 2006). The response could include an avoidance to the vicinity of the wind farm development area even if the habitat and food availability remain unchanged post construction. If the birds are reluctant to approach to turbines within half the distance between them, the whole area of a wind farm could be lost as a potential feeding area (Lindeboom, et al., 2011).

In Denmark, comparisons between the pre and post-construction abundance and distribution of water birds in and around two offshore farms demonstrate that water birds generally display avoidance behaviors for up to three years, following the construction. However, some species habituated to these new offshore conditions which led to an increased presence of species in the offshore development. Studies have also indicated that they feed in and around the analyzed wind farm where they were observed using monopiles and meteorological masts for platforms while foraging offshore (Lindeboom et al., 2011).

The behavior however will be highly species specific. Gulls for the most part seem largely indifferent to wind farms, taking advantage of the increased foraging opportunities. On the other hand migrating land birds sometimes showed strong avoidance behaviors. Flocks of passerines, the majority of the migrating birds in the area, showed both deflection around the entire wind farm and individual turbines when paths crossed through wind farms. However based on the layout and system used, birds that

tend to avoid wind farms will oftentimes enter the wind farms with higher spacing between turbines and occasionally when wind turbines are stationary (Lindeboom et al., 2011).

Many of the current developments and proposed locations are in sandy bottom areas or shoals. These are important habitats for a variety of seabirds and these installations could cause significant disruptions (Snyder & Kaiser, 2009). The extent of these impacts can be readily determined from engineering plans in tandem with known foraging and migratory paths (Allison, Jedrey, & Perkins, 2008). This information, combined with the results of the changes to the marine habitat, can be used to determine the extent of the transformation of the food sources. This may be of importance for foraging birds and can be used to approximate the impact of the wind farm installations on avian habitats (Fox et al., 2006). Some studies have indicated that over time there seems to be a decrease in the presence of avian species due to behavioral responses associated with the wind turbine installations (Drewitt & Langston, 2006). The overall effect on the modified habitat has been insignificant due to the relatively small footprint of the wind farm with respect to the total foraging area, yet future developments could lead to significant environmental impacts (Musial & Ram et al., 2010).

C-4) Bats

Because bats have a low reproduction rate and a long life span, it is expected that the effects of wind energy systems will be significant (Ahlen et al., 2007). With sightings of flocks of bats landing on ships up to 130 km from coastal areas, it is possible that impacts

could occur in the range of both fixed and floating support structures (Cryan & Brown, 2007; University of Maine, 2011).

In contrast to the possible barrier effects, it is foraging that is anticipated to cause the most adverse impacts. Some studies have hypothesized that insect concentrations and crustaceans at OWTs could attract foraging bats (Ahlen, Baagoe, & Bach, 2009; Geo-Marine Inc., 2010). A study performed off the coast of Sweden found that bats used behaviors rarely seen on land, sometimes seen landing on artificial structures at sea (Ahlen, Baagoe, & Bach, 2009).

Bats, known to feed on concentrations of insects at lights onshore, could have similar behavior offshore (Ahlen, Baagoe, & Bach, 2009). Other studies at land-based wind farms indicated that instead of avoiding wind turbines, bats actively investigated both fixed and moving blades (Schwartz, 2004). The high fatality rate at land-based sites has also been hypothesized to occur because of the mating behavior of some types of species. This, instead of foraging, was reaffirmed in at least one study due to the statistically significant presence of fatalities in mature migratory tree bat species such as the Hoary bat (Cryan & Brown, 2007). Their mating behavior involves seeking out the highest structure in an area during the late summer to early fall through attract mating partners (Arnett et al., 2008). However it is unlikely that the mating behavior hypothesis would transfer over to the offshore environment.

One effect that would be specific to jacket support structures is due to the lattice formation. This would give bats additional opportunities in which they could perch. This could lead to an increased risk of barotraumas or increase the risk of collision.

3.2.3 Observed Fatalities

Avian species and bats are noted to be at a higher risk of death due to wind development than other species, primarily due to the effects of collision and barotrauma (Arnett et al., 2008; Cryan & Brown, 2007; Fox et al., 2006). Because of the difficulty in gathering numerical evidence offshore, arising from unaccounted carcasses falling into the ocean, the prediction of the number of avian fatalities have increasingly come from numerical models along with visual observations. Environmental studies have integrated technologies to minimize error such as infrared video monitoring to thermal imaging cameras (Morkel et al., 2007). In any case, while both groups of species have been shown to have high risks of mortality, studies have indicated that there is a substantial difference in their cause.

Furthermore in both groups of species, environmental factors that have been shown to increase this risk include; weather conditions in which there is reduced visibility, strong headwinds or in conditions in which there is poor lift (Cryan & Brown, 2007; Geo-Marine Inc., 2010; de Lucas et al., 2008). Under adverse weather conditions, studies have indicated that avian species not already in flight tend to avoid flying and foraging. Likewise, observations of water birds have found fewer migratory species during these aversive conditions minimizing their potential for collision. However, while already in

flight birds sometimes have been observed to reduce their altitude in order to fly at lower elevations (Koller, Koppel, & Peters, 2006). A change in this flight altitude has been shown to sometimes increase the potential for collision in migratory species (Geo-Marine Inc., 2010).

A) Avian Species

Based on a variety of studies of migratory behavior in birds, the findings have indicated that they tend to fly at heights in which they are at risk of collision (Geo-Marine Inc., 2010). Furthermore, the altitudes in which they are likely to migrate are elevations in which the tailwinds can best be utilized in order to minimize their energy expenditure. In the marine environment, tailwinds occur at lower altitudes which could put them on a course with OWFs.

Studies have also indicated that avoidance to wind farms occurs at greater distances for diurnal rather than nocturnal species. This indicates that nocturnal birds are at higher collision risk (Morkel et al., 2007). Other concerns, regarding nocturnal species are that under poor visibility nocturnal migrants have been found to be attracted to the illuminated safety lights on wind turbines (Geo-Marine Inc., 2010).

There have been indications of strong avoidance reactions to OWFs. However, as wind turbines are further spaced it is assumed that there will be greater concentrations of avian species flying in-between the wind turbines (Koller, Koppel, & Peters, 2006; Morkel et al., 2007). There has also been documentation of habituation with some types of seabirds.

If other species are displaced from their foraging grounds they could intrude on other seabirds. This could lead to overcrowding and increase the risk of collision (Geo-Marine Inc., 2010).

It is hard to quantify the mortality rate at these offshore sites due to the absence of suitable numerical data, although some studies have estimated that this ranges from 0.01-1.2 birds per turbine per year (Drewitt & Langston, 2006). Although this is relatively low, this could be unacceptable for long lived species with low reproductive rates (Minerals Management Service, 2009).

B) Bats

There is far less that is known of the mortality risk of bats due to OWTs. Some studies on migratory tree bats have indicated that there are large concentrations of fatalities during the late summer and early fall which correlates with their mating and migratory seasons (Geo-Marine Inc., 2010). Due to statistically significant differences in the carcasses of juveniles and adults, one of the many hypotheses on the large number of fatalities is that there could be a link to their mating behavior, but this is unlikely to transfer over to OWFs (Cryan & Brown, 2007). The few offshore studies that have been conducted have indicated that bats tend to feed on insects and crustaceans, either during migration or while foraging and because of the greater foraging opportunities at OWTs there could be an increased fatality risk (Arnett et al., 2008; Ahlen, Baagoe, & Bach, 2009).

The studies that have been performed on land have indicated that the overall number of bat fatalities at onshore wind farms has been much greater in comparison to avian

species. For bats as shown in Table 3.1, fatalities have ranged from 0.1 – 75 fatalities/turbine/year (Arnett et al., 2008). The mortality rate of avian species on the other hand have ranged between 0.01 - 20+ fatalities/turbine/year (Thelander, 2006). This larger number of mortalities could hold true in the offshore environment (Schwartz, 2004). However, due to the limited research and the variety of unknowns it is still largely unclear on what impacts OWFs will have.

Study area location[a]	Estimated mean fatality/ turbine	Estimated mean fatality/MW	Estimated mean fatality/2,000-m^2 rotor-swept area
Canada			
CRAB	0.5	0.8	0.6
MLAB	0.5	0.7	0.5
SVAB	18.5	10.6	7.4
Eastern USA			
BMTN1[b]	20.8	31.5	24.0
BMTN2[b]	35.2	53.3	40.6
BMTN2[c]	69.6	38.7	27.7
MRNY1[d]	24.5	14.9	9.4
MYPA[d]	23.0	15.3	11.3
MTWV1	48.0	32.0	23.6
MTWV2[d]	38.0	25.3	18.7
Rocky Mountains, USA			
FRWY	1.3	2.0	1.9
Pacific Northwest, USA			
HWCA	3.4	1.9	1.4
KLOR	1.2	0.8	0.6
SLOR	1.1	1.7	1.3
VAOR	0.7	1.1	0.8
NCWA	3.2	2.5	2.1
Midwestern USA			
BRMN1[e]	0.1	0.2	0.2
BRMN2[f]	2.0	2.7	2.4
BRMN3[g]	2.1	2.7	2.3
LIWI	4.3	6.5	5.0
TOIA	7.8	8.7	7.4
South-central USA			
WOOK[h]	1.2	0.8	0.7

Table 3. 2: Aggregate of Bat Fatalities across North America (Arnett et al., 2008)

CHAPTER 4

CONCLUSIONS

4.1 Summary and Conclusions

Lessons learned from the oil and gas industry as well as the continued research being performed at OWFs will continue to clarify the environmental impacts of the offshore wind industry. Based on current studies, there will be a significant number of direct benefits with the development of OWFs, ranging from the creation of artificial reefs to the sanctuaries established from industrial fishing in the offshore developments. There will also be other benefits including no carbon emissions during power production. Although it is the adverse impacts that are given the most focus because it is essential to understand the negative effects in order to mitigate and when possible prevent their impacts. There will be overlap between the impacts between fixed and floating support structures with specific impacts on the type of support structure that is utilized (see Table 4.1 & Table 4.2).

Fixed Support Structure Conclusions						
	Environmental	***Benthic***	***Fish***	***Marine***	***Avian***	***Bats***
Impacts	**Effects**	**Species**		**Mammals**	**Species**	
Electromagnetic Fields/Warming of the Seafloor	Dependent on species, could cause confusion with orientation, navigation, and behavior	***Undesirable but tolerable depending on the species***	***Undesirable but tolerable depending on the species***	***Undesirable but tolerable depending on the species***	***Negligible***	***Negligible***
Noise Emissions	Impacts depend on species hearing threshold, frequency and strength of noise emissions . Primary Impacts are assumed to occur during piling.	***Negligible***	***Serious concern depending on stage of wind turbine lifecycle.***	***Serious concern depending on stage of wind turbine lifecycle.***	***Undesirable but of limited concern***	***Undesirable but of limited concern***
Physical Obstruction	Below the surface, effects correspond to artificial reef impacts . Above surface, wind turbine could cause significant physical obstruction i.e. cumulative wind farms. Potential risk of collision, death.	***Negligible***	***Negligible***	***Negligible***	***Serious Concern depending on the magnitude of the installation***	***Rise for concern but tolerable depending on a variety of conditions.***
Installation	Localized effects, dredging, piling, noise emissions and temporary sediment resuspension and redeposition. Adverse noise emissions dependent on support structure used.	***Undesirable but tolerable depending on scale and duration.***	***Undesirable but of limited concern***	***Undesirable but of limited concern***	***Undesirable but tolerable depending on scale and duration.***	***Undesirable but tolerable depending on scale and duration.***
Artificial reefs	Could lead to a significant increase in bioconcentrations. If surrounding seabed is different natural ecosystem is adversely impacted.	***Significant positive gain***	***Significant positive gain***	***Significant positive gain***	***Negligible***	***Negligible***
Foraging	Increased foraging opportunity. Artificial reefs enrich ecosystem with higher marine specie concentrations. For flying species, increased potential for fatalities.	***Significant positive gain***	***Significant positive gain***	***Significant positive gain***	***Serious Concern depending on the magnitude of the installation***	***Rise for concern but tolerable depending on a variety of conditions.***
	Table Key	***Adverse Impact***	***Positive Impact***	***Concern***	***Some Concern***	***Neutral***

Table 4.1: Conclusions on the Environmental Impacts of Fixed Support Structures

Floating Support Structure Conclusions						
	Environmental	***Benthic***	***Fish***	***Marine***	***Avian***	***Bats***
Impacts	**Effects**	**Species**		**Mammals**	**Species**	
Electromagnetic Fields/Warming of the Seafloor	Dependent on species, could cause confusion with orientation, navigation, and behavior	***Undesirable but tolerable depending on the species***	***Undesirable but tolerable depending on the species***	***Undesirable but tolerable depending on the species***	***Negligible***	***Negligible***
Noise Emissions	Impacts depend on species hearing threshold, frequency and strength of noise emissions. Primary impacts are assumed to occur during piling, however installation will have less adverse impacts	***Negligible***	***Undesirable but limited concern due to smaller size of installations***	***Undesirable but limited concern due to smaller size of installations***	***Negligible, decreased probability of species effected***	***Negligible, decreased probability of species effected***
Physical Obstruction	Below surface effects correspond to artificial reef impacts . Above surface, wind turbine could cause physical obstruction-death although less risk at increased distances from the coast.	***Negligible***	***Negligible***	***The impact gives rise to some concern due to potential entanglement in floating support structure systems***	***Undesirable but of limited concern. Distance from the coast will lead to decreased avian densities.***	***Undesirable but of limited concern. Distance from the coast will lead to decreased bat densities.***
Installation	Localized effects, dredging, piling, noise emissions and temporary sediment resuspension and redeposition. Adverse noise emissions dependent on support structure used.	***Undesirable but tolerable depending on scale and duration.***	***Undesirable but of limited concern***	***Undesirable but of limited concern***	***Negligible***	***Negligible***
Artificial reefs	Could lead to a significant increase in bioconcentrations. If surrounding seabed is different, natural ecosystem is adversely impacted. Biomass and biodiversity of coral reefs decrease with increased distance.	***Significant positive gain***	***Significant positive gain***	***Significant positive gain***	***Negligible***	***Negligible***
Foraging	Increased foraging opportunity. Artificial reefs enrich ecosystem with higher marine species concentrations. For flying species, increased potential for fatalities. Although decreased densities.	***Significant positive gain***	***Significant positive gain***	***Significant positive gain***	***Concern depending on the magnitude of the installation***	***Rise for concern but tolerable depending on a variety of conditions.***
	Table Key	***Adverse Impact***	***Positive Impact***	***Concern***	***Some Concern***	***Neutral***

Table 4.2: Conclusions on the Environmental Impacts of Floating Support Structures

The transmission of electricity has been found to be a source of potential adverse impacts which include the electric dissipation and the creation of EMFs or MFs. Preliminary findings have found minimal changes to the behavior in electro-sensitive species or signs of disorientation. With advances in transmission technology the potential impact can be further mitigated or prevented.

It has been the emissions of noise during the installation that has been the greatest cause for concern reflected in the number of studies that have been performed. Although the installation method will also determine the level of emissions, the method that has had the greatest impact to date has been from piling installations. The adverse impact from the noise level of the emissions can be mitigated by varying measures ranging from bubble curtains for monopiles to slow start up times during impact piling operations. Although it has been during the installation that has caused the greatest concern, the noise emissions over the lifecycle of the wind turbine could affect species ranging from marine mammals to fish.

In order to quantify the impacts from noise emissions, semi-empirical noise propagation models are often used. These simplified models give nontrivial results and are much less computationally expensive than other existing modeling schemes. One semi-empirical model that is more complex than other single variable semi-empirical models which rely solely on distance is a model developed by Thiele (2002). His model takes into account frequency and distance along with other site parameters.

Physical barriers could inadvertently occur with the development of offshore wind turbines. For floating systems, as they become commercially viable, entanglement or collision could occur for birds or underwater marine species. The increase in the number of developments will correspond to an increase in the possibility of species being negatively affected. In the presence of fixed wind turbines, both on land and offshore, a majority of the avian species that have been observed have shown avoidance behaviors, although certain types of seabirds seem to have habituated to some offshore developments. As more wind farms are built, barrier effects could be problematic and severely impact birds from the increased energy use due to longer flight times and a potential for the higher loss in habitat. Yet, until there are more commercial wind farm installations, the full effects of the cumulative commercial developments can only be anticipated.

During the installation phase of the OWTs, sessile species inhabiting the benthos are susceptible to being crushed or asphyxiated. The primary determinant in the extent of the effect is the size of the installation. Suffocation could occur from the sedimentary plumes arising during installation and the rapid resettlement. At the end of the lifecycle of the wind turbine, during the decommissioning ,the artificial habitat that was created by the OWTs could be destroyed.

The installation phase primarily results in transient impacts. After the installation, observations have shown that the effects mirror what has been seen in other anthropogenic offshore structures. This effect is a rapid recolonization of the affected

area. The types of species attracted to these installations could be invasive and could lead to a change in local ecosystem. This would range from the changes in the composition of benthos organisms up the food chain to larger species.

The installation of OWFs could also lead to the fragmentation of areas used for foraging and resting by seabirds and migratory avian species. The implications from studies have so far shown that this is of minimal concern, however, as developments continue and the effects accumulate, significant effects could occur from the large areas of habitat that are lost.

A review of existing studies on the offshore environmental impacts on bats has yielded inconclusive findings on the effects. The few available studies that have been performed have indicated that it is while foraging offshore in which adverse effects will be seen, from the effects of barotrauma to inadvertent collisions. Still, more studies are needed to better understand what could occur.

Based on the available information on the number of fatalities caused by wind developments onshore a focus was directed on the potential morality risk of avian and bat species offshore. The inherent difficulties in collecting data offshore has led to few studies accurately tallying the number of deaths but models have been created to estimate the mortality risk. It is hypothesized that as wind farm developments move further offshore, the number of fatalities will decrease due to the decreased density of both bat and avian species that has been observed.

Finally, the knowledge of where the impacts will occur will dictate the type of preventative measures that should be taken. As a result, preventative actions to mitigate adverse impacts could be formulated and incorporated into the design of offshore wind developments. However, further research must be performed in order to gain a better understanding of the environmental effects due to offshore wind energy.

CHAPTER 5

FUTURE RESEARCH NEEDS

5.1 Areas of Future Research

There are many areas in which gaps in available data and understanding signify the need for further research. This ranges from the spatial and temporal distributions of species to the effects of decommissioning.

In order to speed up the transfer of information and understanding, there is a need for a standardized guideline for the research regarding specific environmental effects. Arnett et al. (2008) stated that this would improve the comparability of studies and credibility of the efforts. Studies so far have varied in both space and time. More explicitly, these studies have occurred during different times of year for varying lengths of time, using different methods of observation and relying on various bias correction factors for models. This increases the difficulty in analyzing and grasping the full effects that OWFs will have.

The effects from the generation of electromagnetic or magnetic fields are still not fully understood. Questions arise, not only of the possibility of behavioral changes among a variety of species, but also about the potential impact on migratory species. Studies have been conducted on a short term basis, but have largely yielded inconclusive results. A more clear understanding is needed and should include long term studies on the impacts.

There are many things that remain unknown regarding the spatial and temporal patterns along with the offshore behavior of marine species. With an increased understanding, better methods could be used to anticipate and mitigate the effects of OWTs. For instance, little is known about the distribution of deepwater corals even though they make up the vast majority of known corals, with some species only located in a single location, while others have been found to be distributed worldwide. Without the knowledge of the makeup of the offshore ecosystem, damage could unknowingly occur from the offshore development. It remains unclear of the long term effects of OWFs and their spatial impacts on species and the changes to the system dynamics of ecosystems. The insertion of thousands of wind turbine foundations could cause a deterioration in the marine ecosystem or the generation of new, artificial reef-like systems. Furthermore, it has not been possible to accurately estimate the extent in which benthic colonization will progress which will be a big factor in the changing diversity in the ecosystem. Other areas that should be further researched are the conditions under which groups of species migrate and forage and the extent of the foraging behavior and migratory routes.

Particular focus should be given on the noise propagation of wind energy systems and the further development of numerical models in order to better anticipate the risks and impacts associated with offshore wind development. Although such assessments are now made regularly, the actual underwater noise levels produced are rarely measured. Furthermore, little is known about the accuracy of different sound propagation models, particularly at longer ranges from source and in shallow coastal waters. Further research is needed in order to determine the hearing thresholds of marine species. The number of

species that could be affected is vast and a database of the behavioral reactions of exposed marine species and the hearing thresholds would help to more accurately determine the extent of the impacts from the development of OWFs . Currently, the development of models that assess the effects on marine species are hindered by these unknowns. As the effects become better understood, models of these effects could be coupled in numerical sound propagation methods to better understand the implications of the development of OWFs.

Installation techniques could likewise be further modified with the further development of methods dealing with noise mitigation. Monopiles, which are used in the majority of existing wind farms, could incorporate noise mitigating strategies in order to reduce the potential adverse effects seen from installation through piling. However, the extent of behavioral disruption from pile driving remains uncertain. Given the scale of future offshore developments, there is an urgent need to develop engineering solutions to reduce the noise propagation emitted from pile-driving at deep water sites. Alternative construction techniques that generate less intensive noise could be developed as well. With the planned installation of several gigawatts in the offshore environment, installation could occur over several years which could permanently effect marine species due to the large level of noise emissions anticipated in the absence of mitigating strategies.

Another area in which there is little understanding is of the long term effects over the lifecycle of a wind farm or the development of multiple wind farms. The cumulative

effect of a number of developments could result in a different set or scale of effects. There have been assumptions that impacts could include permanent barrier effects for marine mammals and fish with respect to the cumulative noise levels from sources in operation and also an increased risk of entanglement and avoidance behaviors in marine species. This can be addressed by engineering the minimum separation needed in floating OWF design configurations that minimize or prevent entanglement.

Adverse impacts to avian species could multiply with the development of multiple wind farms, but this all needs to be further examined in order to more accurately forecast the potential impacts. There have been some models that have been created that replicate the avoidance behaviors of avian species to wind turbines. The avoidance behavior will not only be species specific but will also vary amongst the species. These models could be integrated with power production models and be used in order to optimize the placement of offshore wind turbines in order to decrease the potential impact to avian species while maximizing power production. This would lead to a decrease in the potential of environmental impacts from barrier effects and a decreased conflict with the habitat of birds.

Finally, the environmental impacts due to decommissioning must be studied as offshore wind farms begin to go offline. Although, there have been suggestions that decommissioning would be similar to the processes that take place in the oil and gas industry, industry specific impacts must be analyzed.

APPENDIX A

NOISE

Noise has been shown to influence the growth and reproduction of a variety of marine species (Tech Environmental, 2006). In order to provide an objective and quantitative assessment of the degree of the environmental impacts due to the development of OWFs, models must be used that function to further quantify the full extent of their effects. Models have ranged in use, from the analysis of barrier effects to habitat alterations seen in the marine environment. One phenomenon that has received much attention is noise propagation and its effect on the marine environment during installation. This portion of the report focuses on the effects due to the future installation of floating support structures with piled anchoring and fixed piled support structures.

A.1 Noise Overview

Sound derives from pressure disturbances, which can be described as sound pressure levels (SPLs). At a microscopic level, this arises from the molecular oscillations in a medium, oriented in the direction of the propagating wave (Nedwell & Howell , 2004). The speed and range in which sound propagates in the ocean is much higher than what is observed in air, with speeds of approximately 1500 m/s versus 343 m/s respectively. The relations governing speed are displayed in equation 1 (Nedwell et al., 2007).

$$c = \sqrt{\frac{\gamma\beta}{\rho_o}} \qquad (1)$$

c = speed of propagation of an acoustic wave

γ = specific heat ratio

β = isothermal bulk modulus

ρ_o = ambient medium density

More specifically the rate at which sound waves propagate through a medium is dependent on the elasticity and density of the medium with typical parameters shown in Table A1for sea water and air.

	c	β	ϒ	
	m/s	*MPa*		*kg/m^3*
****Sea Water**	1509.3	2310	1.0106	1024.75
Air	342.68	0.101	1.401	1.205
	**Salinity of water 35 g/Kg At Standard Temperature and atmospheric pressure			

Table A.1: Parameters for Air and Sea Water

The multiple paths in which noise could propagate arise due to the reflections between the surface and the seabed and also the medium in which it spreads. For the analysis of OWF noise emissions, the mediums can consist of either the seabed, air or what is primarily used in analysis, the ocean (Nedwell & Howell, 2004). In geographic conditions such as in channels, sound could propagate over much further distances. This would limit the noise attenuation from the geometric losses that would arise from it spreading; conversely, in areas where water is shallower, sound attenuation could occur at a much more rapid rate (Nedwell & Howell, 2004). Overall, the bathymetry in an area and the corresponding water depth may affect the level of noise and its propagation. This

results in different sound levels depending on the position in relation to the sound source (Bailey et al. 2010).

Close to a sound source, complex waves form which leads to a significant increase in the difficulty in predicting the SPLs. This is due to the distortion of the sound, partially from refraction and absorption and also from the rapid variations in the acoustic pressure field, often over comparatively short distances, typically defined as the near field. To predict the level of the sound source, as shown in Figure A.1, linear logarithmic approximations are typically used (Nedwell & Howell, 2004). This is done by extrapolating from the far field in near steady state conditions where measurements have been made to the more unpredictable near field, measured at one meter from the sound source with a reference pressure of 1μPa in the underwater environment (Bailey et al., 2010).

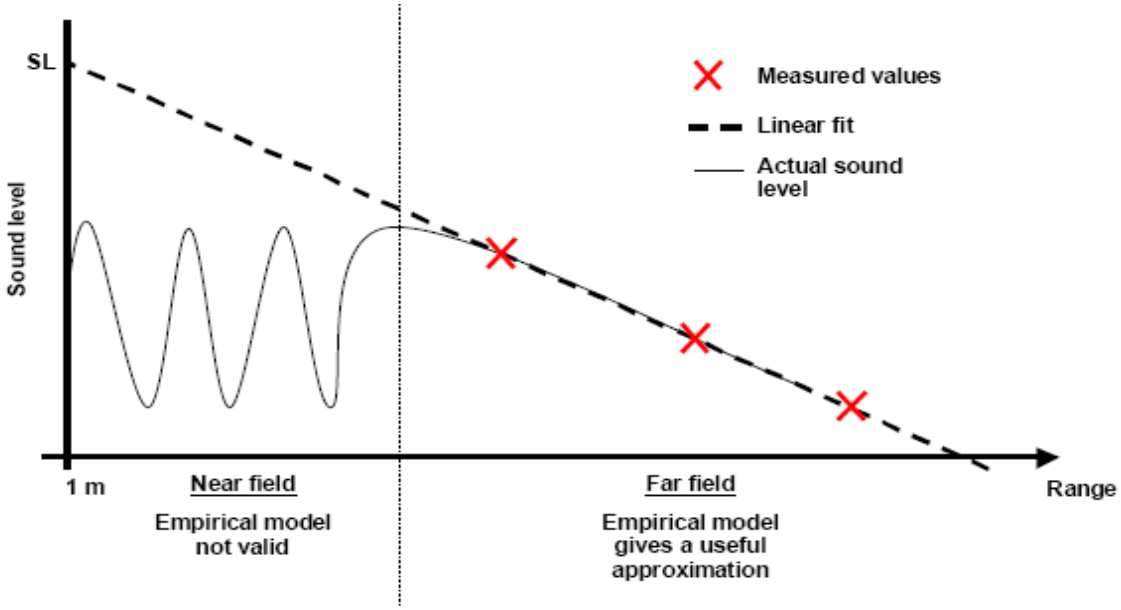

Figure A.1: Source Level Transmission Loss Model (Bailey et al., 2010)

Due to the difficulty in analyzing sound levels in the near field, roughly within 100 meters of the sound source depending on the magnitude of the installation, models are typically used only in the far field to insure any degree of certainty.

A.2 Wind Energy Noise Overview

The noise emitted from wind turbines will occur throughout the wind turbines' lifecycle ranging through installation, operation and decommissioning. During the operation phase, the wind turbines' noise emissions arise from both mechanical equipment and the aerodynamic noise generated from the turbine blades (Carlos, 2007). It has been shown in studies that it is primarily during the installation and decommissioning stage and not during normal operations that marine species are adversely impacted. From industry experience, it has been the noise emissions generated during piling which has caused the majority of adverse impacts, however it is anticipated that decommissioning could have larger effects if explosives are used (Nedwell & Howell, 2004).

During the piling phase, only a very small amount of the impact energy is radiated directly into the water, but the energy that is emitted creates high levels of hydrodynamic sound. There is a potential that the energy can be transferred into the ground or through the air and emitted back into the water, although the noise emissions from the sound source overwhelmingly propagate directly from the pile into the water column, as shown in Figure A.2 (Morkel et al., 2007).

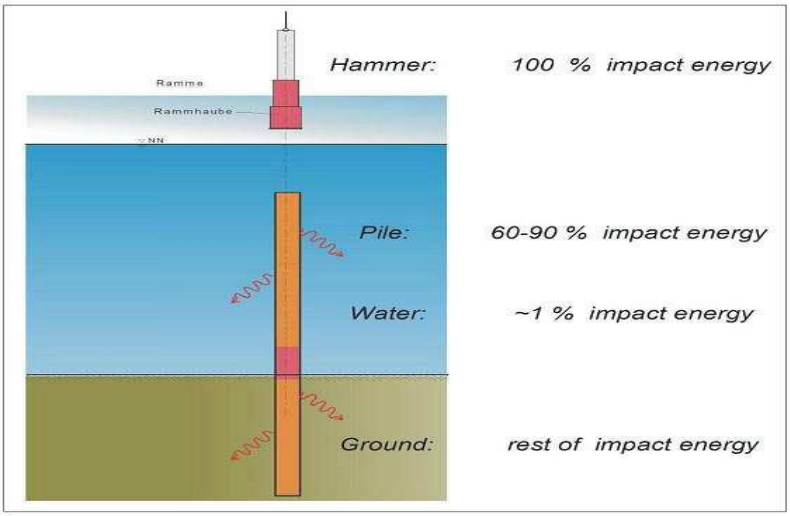

Figure A.2: Noise Emissions during Piling (Morkel et al., 2007)

During this piling phase, the SPL levels, show by Figure A.3, are characterized by multiple rapid oscillations over time (Morkel et al., 2007). The acoustic pressure varies above and below the ambient pressure. Even though some effects of underwater sound, such as physical injury, average or peak SPL's could be inadequate measures because a sound, having a given pressure level and duration, may have the same effect as one of half the duration and twice the level (Nedwell & Howell, 2004). This is primarily dependent on the type of assumptions that are made of the effected marine species. But, because many marine species will avoid and escape the noise emissions, the effects due to the impulse from piling are expected to be lower than the pressure gradients created during installation (Nedwell, Lovell, & Turnpenny, 2003).

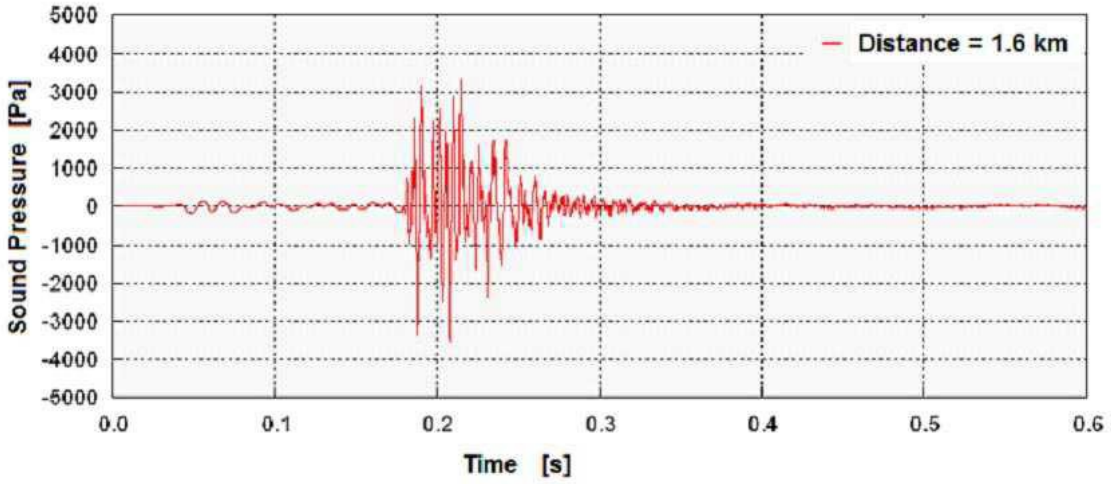

Figure A.3: SPL Over Piling Impact Time (Nedwell, Lovell, & Turnpenny, 2003)

Relationships that help to determine the noise levels at the source during pile driving are the length and the diameter of the pile, although, factors such as seabed type, impact force and water depth will affect the sound level (Thomsen et al., 2006). Although of these factors, a sensitivity analysis performed in one study indicated that the primary factor in determining the SPL is the diameter of the pile (Nedwell et al., 2007).

A.3 Wind Energy Noise Propagation as a Function of Frequency

One factor that limits the extent that noise will propagate is the frequency of the noise emissions (Morkel et al., 2007). Depending on the species that are in the vicinity of the source, the frequencies that are emitted could either be infrasonic or ultrasonic, outside of the range of hearing. For most fish, sound is perceived up to frequencies of 1 kHz (however this is not represented in the audiograms that were collected, see Figure A.5), at which levels above are considered ultrasonic, conversely many marine mammals cannot perceive sound below 1 kHz where it is perceived as infrasonic (Bailey et al., 2010).

For frequencies less than 1 kHz, the absorption is less than 0.1 dB/km, however at higher frequencies absorption substantially increases causing significant losses (Morkel et al., 2007). The majority of pile-driving signals that have been measured have primarily contained low frequencies up to 3000 Hz with the highest energy content at frequencies between approximately 170 and 1100 Hz (Mueller-Blenkle et al., 2010).

Studies have varied in their results, with one study that was performed during the installation of two jacketed structures with 1.8 meter piles in the Scotish Firth, indicated that close to the sound source, the noise was highly broadband, with peak sound energy occurring between 100 Hz to 2 kHz, along with substantial energy up to 10 kHz. The elevated attenuation of the high frequency content limited the majority of sound to frequencies less than 5 kHz at distances of 4 km's away from the sound source. The power spectral density of the piling of a five MW support structure is shown in Figure A.4 (Bailey et al., 2010).

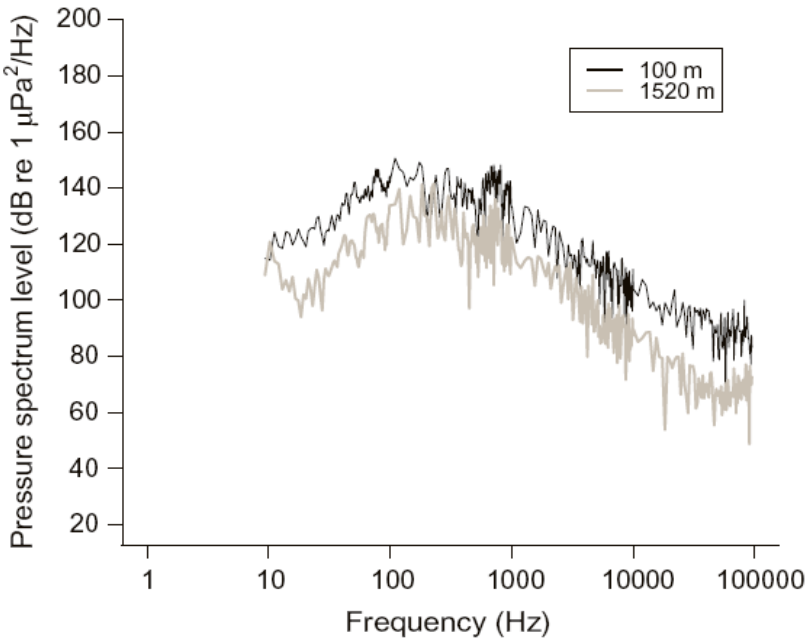

Figure A.4: Power Spectral Density of Three Seconds of Pile Driving Noise of a Jacket Pile (Bailey et al., 2010)

A.4 Hearing Thresholds

A metric created to approximate the effects of noise, the hearing threshold scale, is based on the onset of hearing for different species. This is based on empirical evidence from data collected from audiograms and brain stem response tests which are used to determine the extent of the impact caused by a given SPL (Thompson et al., 2010). This metric enables better estimates of the behavioral effects of sound disturbance (Nedwell, Lovell & Turnpenny, 2003).

Background noise must also be taken into account in order to determine the onset of hearing. In a noisy environment, marine species would most likely have a lower sensitivity to sound, effectively increasing the level of noise that would be deemed the hearing threshold. Conversely, for species living in a quiet environment, the sensitivity to

sound would be higher and the hearing threshold lower (Nedwell & Howell, 2004). Various tests have shown, by using this scale, that the vast majority of species indicate avoidance reactions at SPLs at 90 dBs (90 dB_{HT}) above the hearing threshold (Nedwell et al., 2007). Other studies have indicated that the zone of injury is believed to occur at sound pressure levels of approximately 130 dB_{HT} (Nedwell, Lovell, & Turnpenny, 2003).

The hearing threshold is also dependent on the frequency of the noise. This range of hearing will depend on the species and can extend over a broad range of frequencies for hearing generalists, to a limited frequency range for species known as hearing specialists (Nedwell & Howell, 2004).

The scale used to quantify the effects of noise on a marine species will be determined in part, by the quality of the information that is available concerning auditory detection. The audiogram is the fundamental measure of hearing, which presents the threshold of hearing of the subject as a function of frequency. The available information is inherently unreliable due to the small number of audiograms that are available for marine species, although as more audiograms are taken and different methods such as brainstem response analysis become used in greater volume, the reliability of future data will continue to improve (Nedwell & Howell, 2004).

For this analysis, the hearing thresholds of a variety of marine species were collected from public domains. A continuum in the data was established by using a fourth order

non linear least square regression. The data was split into two parts; the fish hearing thresholds in Figure A.5 and the marine mammal hearing thresholds in Figure A.6.

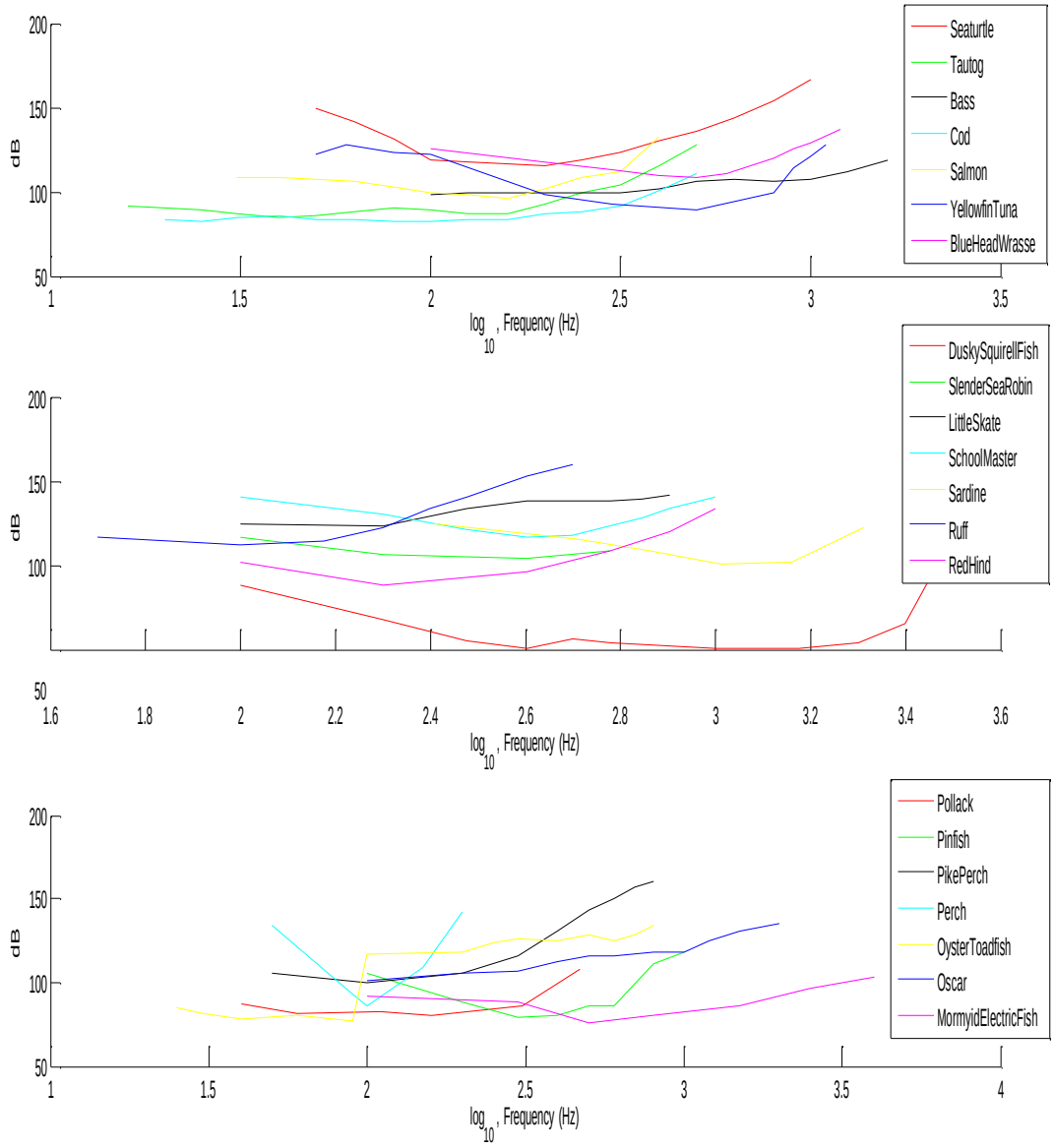

Figure A.5: Fish Hearing Thresholds

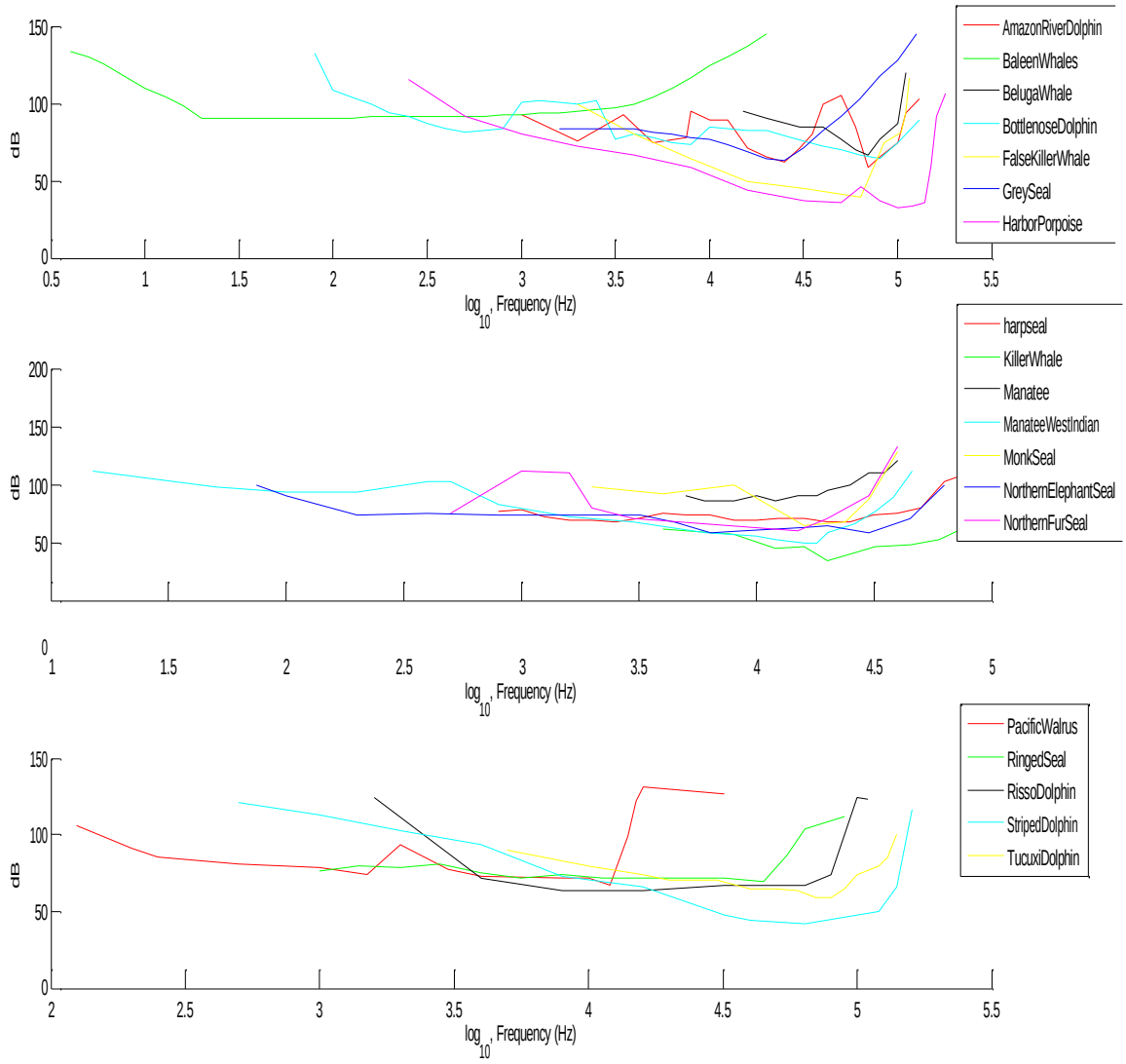

Figure A.6: Marine Mammal Hearing Thresholds

This sampling was for the hearing thresholds of 67 different types of marine species. Although, there are some issues in reliability with the dB_{HT} scale, it is still used in order to better quantify the likelihood of behavioral effects and damage to the hearing physiology for a wide range of species.

A.5 Model Formulation

In order to quantify environmental effects due to noise emissions from the installation of support structures via piling, it is necessary to estimate the sound level as a function of the range from the source. In general, this is too complicated to precisely model due to many factors including the water temperature, pressure and salinity, as well as the sediment characteristics and reflections from both the bathymetry and sea surface; however simplified models have been developed (Schecklman et al., 2011).

One way to model sound propagation or the strength of the SPL, is by using the Source Level (SL) – Transmission Loss (TL) model, which has been validated by a variety of studies. Using this technique, the apparent sound SL is approximated and the TL, or the rate at which the sound decays during its propagation, is formulated as shown in equation two (Nedwell & Howell, 2004):

$$SPL = SL - TL \text{ [dB]} \qquad \textbf{(2)}$$

SPL = Sound Pressure Level
SL = Sound Source Level
TL = Transmission Loss

The source level is generally quantified as a measure at one meter from the source and referenced at 1 μPa, while the transmission loss is generally broken apart by geometric spreading and absorption losses (equation 3).

$$TL = Nlog(R) + aR \text{ [dB]} \qquad \textbf{(3)}$$

N = geometric loss factor
a = absorption loss coefficient
R = range from the source

Assumptions on transmission loss are central to the calculation of the zone of audibility. In deeper water areas the geometric loss factor is the overriding factor regarding the losses, while the absorption loss coefficient is generally negligible. The absorption coefficient has a larger influence in shallow water (Bailey et al., 2010). The geometric loss factor is generally modeled as a spherical spreading factor (N) of 20 in deeper water areas or as a cylindrical spreading factor (N) of 10 in shallow waters. If the noise source is close to the ground the sound will propagate in a hemispherical pattern in a similar fashion as a pressure front from an explosion. However, true cylindrical spreading is rarely realized under natural conditions and is generally a mix between cylindrical and spherical spreading with the spreading factor typically taken as 15 (Tougaarda & Damsgaard, 2009).

A.5.1 Model Abstract

A linear equation modeling the source level was formulated by using the least square regression method from available data of piling installations shown in Table A.2. Although a source level model formulated from the Talisman Environmental Impact Assessment Report was validated in a number of Northern European offshore sites and used in the impact assessment on marine species shown in Figure A.10 through Figure A.12. The majority of noise propagation studies use a transmission loss model, shown in Equation 3, which takes into account the distance from the sound source. Although a model developed by Thiele in 2002, incorporated various noise emission frequencies along with the distance from the sound source and was modelled for various pile diameters (Bailey, 2010).

A) Source Level

In general, there is no reliable way of predicting the noise level of pile emissions at its source. To account for this, it is typical to measure the SL indirectly from far field locations (Nedwell & Howell, 2004). However, a linear model was developed for this study with a linear least square regression analysis. The method minimizes the errors based on available empirical evidence in order to analyze future events.

$$\widehat{SL} = b_0 + b_1 D \quad \textbf{(4)}$$

$\widehat{SL}$ = predicted Source Level value of dependent variable
D= Diameter of pile
b_0= constant
b_1 = regression coefficient

where is determined by the following:

$$b_1 = \frac{\sum[(x_i - \bar{x})(y_i - \bar{y})]}{\sum(x_i - \bar{x})^2} \quad \textbf{(5)}$$

x_i = ith value of independent dataset X
y_i = ith value of dependent dataset Y
$\bar{x}$ = mean of independent dataset X
$\bar{y}$ = mean of independent dataset Y

For this study, data was collected from eleven different sources in varying geological and ambient conditions as shown below in Table A.2:

Diameter (m)	0.5	0.7	0.9	1.5	1.8	4	4	4.2	4.3	4.7	4.7
Source Level (dB)	189	211	201	228	250	262	249	257	243	252	249

Table A.2: Diameter versus Source Level

The analysis resulted in the following relationship between the sound source level and the pile diameter.

$$SL = 12.0687 * D + 201.204 \quad \textbf{(6)}$$

This resulted in significant differences with what was formulated in the Talisman Environmental Impact Assessment which was discussed by Nedwell et al (2005) as shown in Figure A.7:

$$SL = 24.3 * D + 179 \quad \textbf{(7)}$$

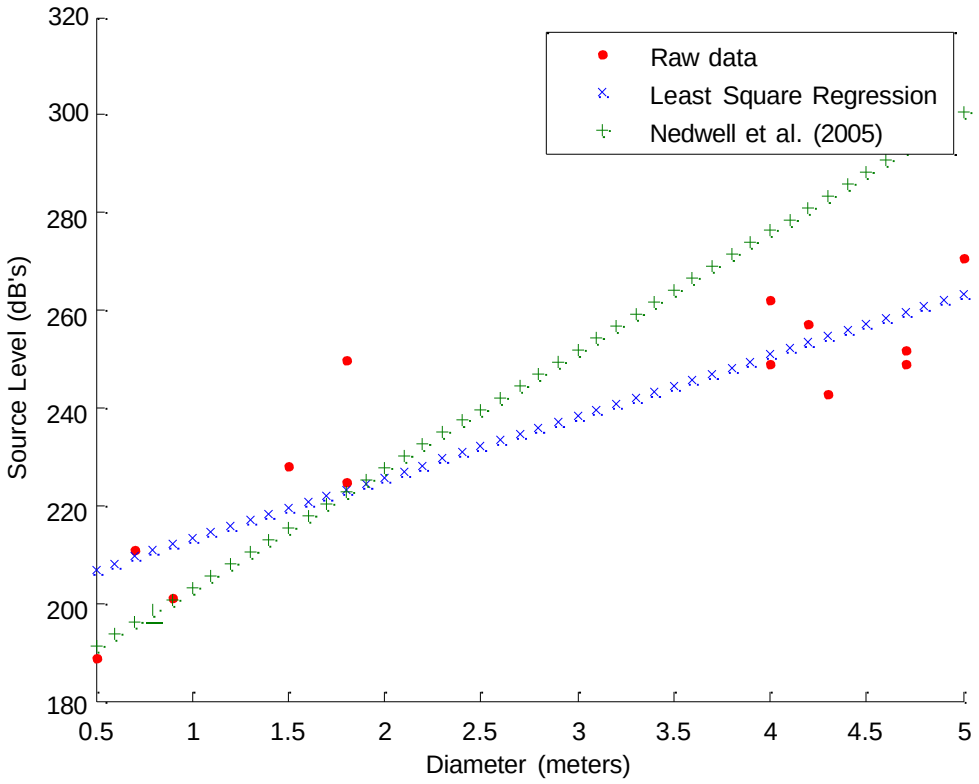

Figure A.7: Source Level as a Function of Diameter

Factors that may have contributed to these relatively high source levels with smaller diameter piles arise from high transmission losses or from the substrate composition from the sampled locations. This could be a mixture of hard rock and sediment which could result in higher source levels than in areas of soft sediment. Finally, varying ambient

conditions could have skewed results leading to higher source levels. However, the empirical formulation that was developed in the Talisman Environmental Impact Assessment has been validated in a variety of studies for piling operations in areas composed of soft sediment. Because this relationship has been validated and due to the dearth of data available to further analyze the relationships between pile size and noise emissions, all further analysis of the effects due to piling on marine species uses Equation 7.

B) Transmission Loss

The transmission loss in this report was modeled with two different empirical formulations. The first model was discussed in the model formulation section which is shown in Equation 3. The second model is a formulation developed by Thiele in 2002 which is applicable for coastal water depths up to 100 m in areas with sandy seabed conditions and wind-speeds less that 10.3 m/s, in the range of wind speeds that are conducive for installation (Bailey et al., 2010). An added benefit of using this model is that the frequency of the noise emissions is taken into account in calculating the transmission loss.

$$TL = (16.07 + 0.185FL)\left(\log\left(\frac{r}{1\ m}\right) + 3\right) + (0.174 + 0.045FL + 0.005FL^2)r \quad \textbf{(8)}$$

$$FL = 10\log\left(\frac{f}{1kHz}\right) \quad \textbf{(9)}$$

r = distance from the sound source (m)
f = frequency (kHz)

This model has been tested under a variety of conditions and locations and validated in both the North and Baltic Sea environments.

A.5.2 Model Results

The SPL was calculated by using Equation 8 which considered different pile sizes at varying frequencies. The range of the frequency emissions was taken to be between 100 to 1500 Hz which correlates with the frequencies that correspond to the highest energy content from findings by Bailey et al (2008). The frequency of the noise emissions partially determined the level of attenuation of the SPL. The results from Figure A.8 along with other published findings indicate that higher frequencies lead to higher attenuation with the upper limit of the frequencies analyzed, regardless of the pile diameter used, having a much more rapid decrease in the SPL.

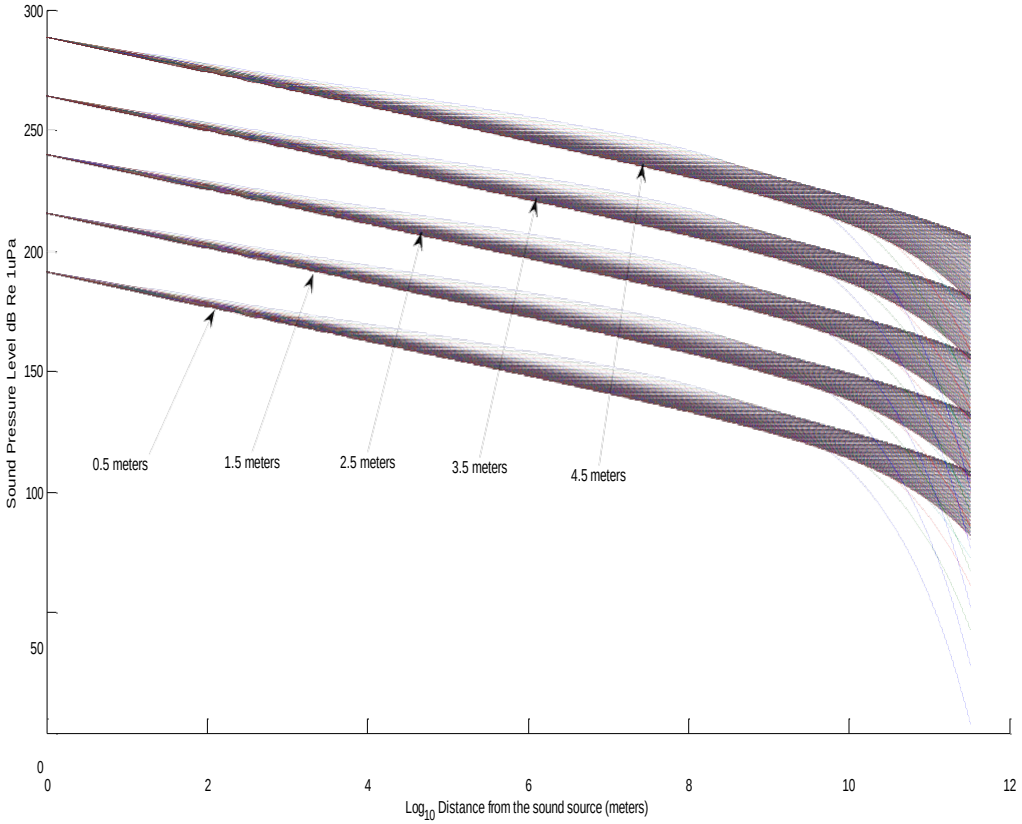

Figure A.8: Sound Pressure Level Using the Talisman Equation

Using Equation 3 for the transmission loss, the sound pressure level was initially modeled at a constant frequency of 3000 Hz, a geometric spreading factor (N) of 15 and an absorption coefficient (α) of 0.0004 with the results graphically represented in Figure A.9. These empirical constants were used in the Bailey et al. (2008) analysis of jacket structure installations in deeper waters. The numerical value representing the geometric spreading factor is a mix between spherical and cylindrical spreading.

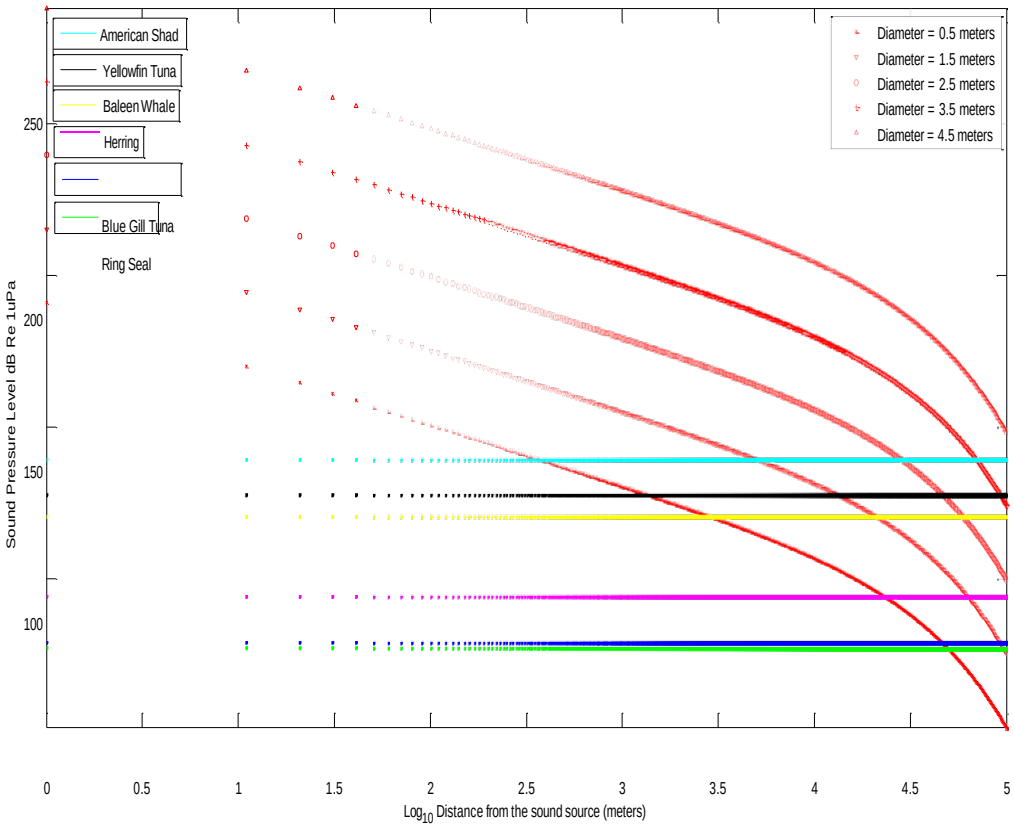

Figure A.9: Sound Pressure Level from Piling emanating at 3000 Hz

Because there is no available data on the impacts due to noise emissions during the installation of floating support structures, an analysis was attempted with the SL-TL model, by accounting for a variety of possible support structure sizes and by assuming specific water conditions, with the results shown in Figure A.10.

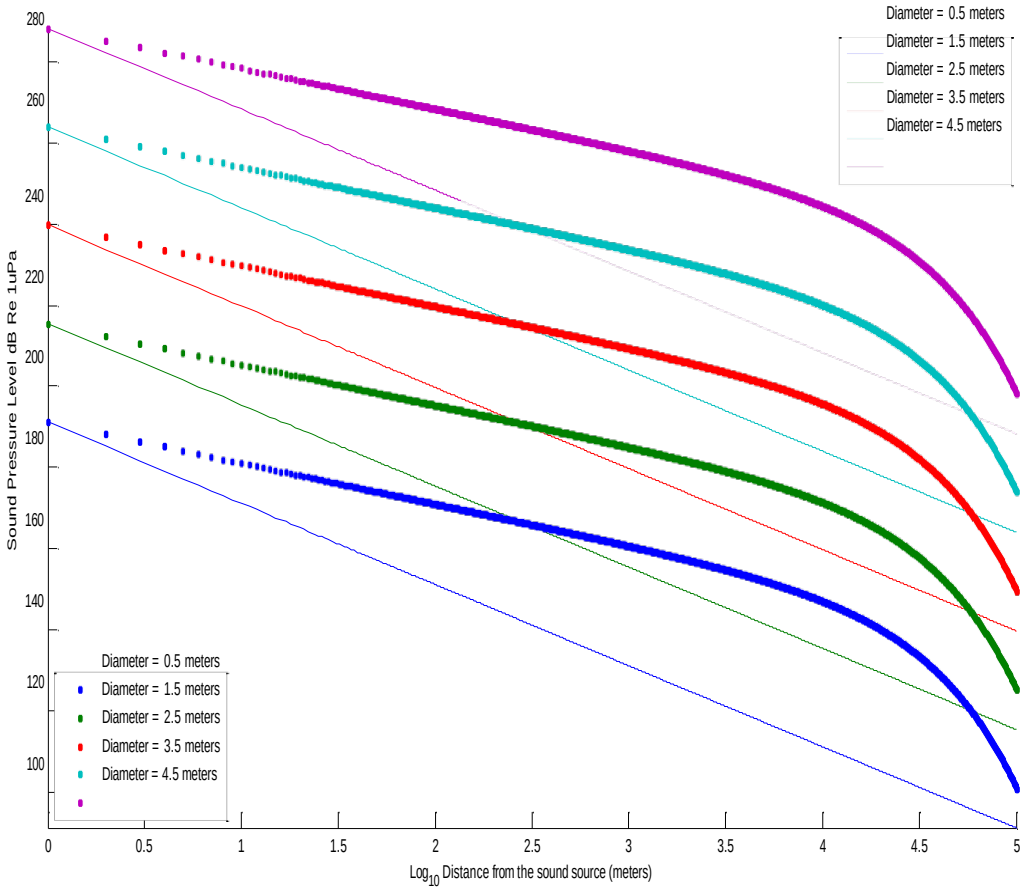

Figure A.10: (-) Floating vs. (...) Fixed Sound Propagation Levels

The noise transmission model was based on a soft seabed environment. In deep water conditions where floating support structures are likely, a geometric spreading term (N), equal to 20 acting in a purely spherical manner and an absorption coefficient (α) equal to 0 was used. The fixed installation meanwhile was assumed to emit sound in a purely cylindrical fashion with a N equal to 10 and the α equal to 0.004 dB/m. As indicated by Figure A11 and Figure A12, the fixed piling would have larger impacts over further distances than the floating support structures which would have higher attenuation and a

quicker resettlement of noise over further distances, with the noise emissions analyzed at a frequency of 1500 Hz..

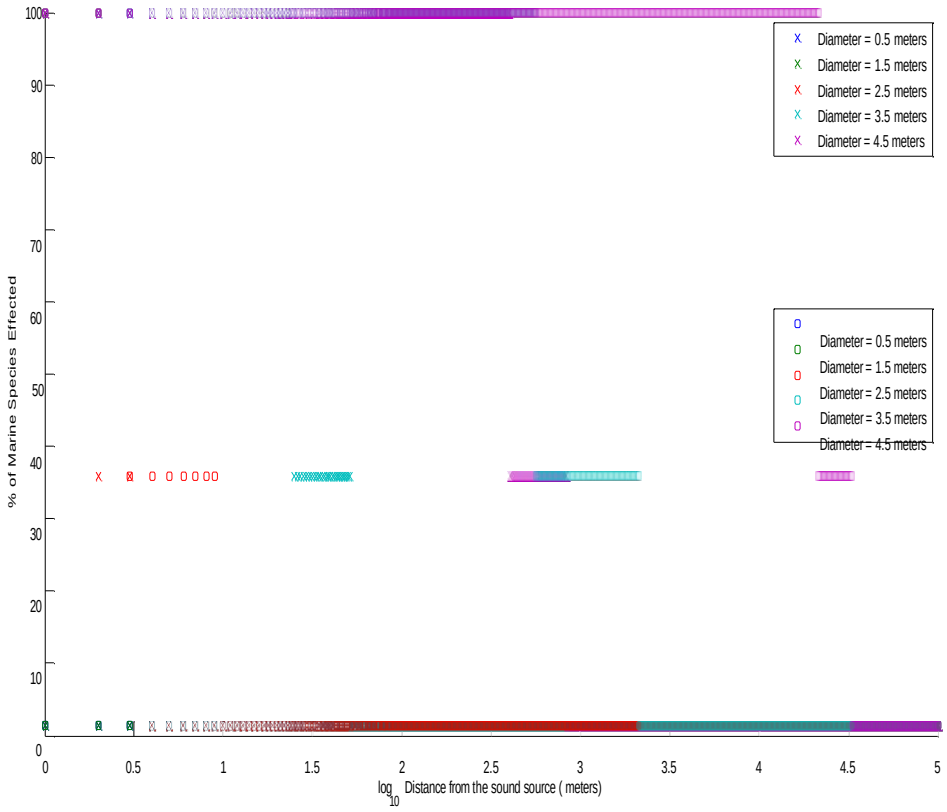

Figure A.11: Floating (x) versus Fixed (o), % of Marine Species Effected due to 90 dBht

Based on the hearing threshold scale and the assumed 90dBht avoidance reactions and 130dBht relation to physiological damage, all of the marine species analyzed indicated a sensitivity to the piling of 4.5 meter piles.

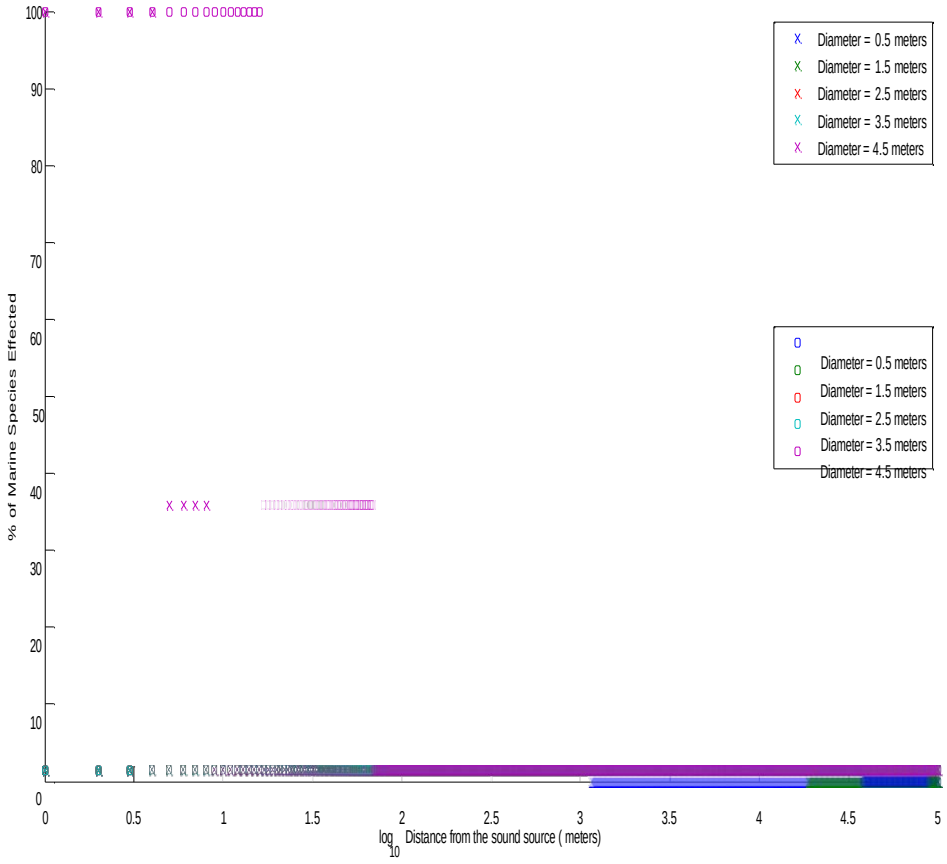

Figure A.12: Floating (x) versus Fixed (o), % of Marine Species Effected due to 130 dBht

Based on the results obtained from the model that was simulated in Matlab, the percentage of species effected is much higher for larger piles regardless of either of the conditions that were tested: fixed or floating. The noise propagation also extended out at higher SPLs in conditions in which fixed pile support structures are used.

APPENDIX B
SOFTWARE CODES IMPLEMENTED

B.1 Analysis of Sound Pressure Loss as a function of range and frequency

```
%% Analysis using Thiele 2002 report
%
clc, close all, clear all
global RawData r freq
RawData=load('Aggregate.txt');
%Allocation of Memory Defining Vectors
freq=0.01:0.01:1.5;
r=1:100000;
FL=f(freq);
D=0.5:1:4.5;

% Determining SPLs at various frequencies and distances
 for i = 1:length(D)                          % Changing Diameters of pile between 0.5 to 4.5
      for cnt= 1:length(freq);
         TRL(:,cnt)=TL(r,FL(cnt));
         SL = 24.3*D(i) + 179;                      % Determining Source Level Noise eqn: from "Thiele
(2002) "
         SPL(:,cnt,i)=SL-TRL(:,cnt)-0.036*freq(cnt).^1.5;    % Sound Pressure Level (Length x Frequency x
Diameter)
      end
 end

frequency=freq * 10^3; % Frequency to compare to marine species frequencies
x=1:length(frequency);
y=1:length(RawData(1,:)-1); % Length of extent of marine mammals
P_S=1:length(D);
M_freq=zeros(max(r),max(x),max(P_S)); %Allocation of storage Points
M_mammals=zeros(max(r),max(y),max(P_S));
Time_1st_Loop = zeros(length(x),1);
tic
for i = 1:length(frequency)
   tic
   for j= 2 : length(RawData(:,1));
      if frequency(i) >= RawData(j-1,1) && frequency(i) <= RawData(j,1) % Frequency Filter
         for k = 2 : length(RawData(1,:));
            for M = 1:length(D)
               tic
               for Distance = 1:length(r)
                  if    SPL(Distance,i,M) > (RawData(j,k)+130) %&& RawData(j,M+1)>0 SPL Filter
                     M_freq(Distance,i,M) = 1; % i frequency Range, Index, j = Species Frequency Hearing
                     M_mammals(Distance,k-1,M) = 1; % k Length of Raw Data
                  end
               end
               secondinnermostloop = toc;
            end
         end
      end
   end
   Time_1st_Loop(i) = toc;
```

```
   i
end
timefor1stentireloop=toc;
tic
r=r';

 for j= 1:length(D)
    for i = 1:length(M_freq)
       FRQNCY(i,j)=sum(M_freq(i,:,j));
       MME(i,j)=sum(M_mammals(i,:,j));
   end
 end

Time_2nd_Loop = toc;

clc, close all, clear all
RawData=load('Aggregate.txt');
global D  TL
D=0.5:1:4.5; %Pile Diameter
r=1:100000; %Distance from the source
N=20;       %Transmission Loss Term
alpha = 0;
SL = 24.3*D + 179;
TL=N*log10(r)+alpha*r;
for i=1:length(D)
SPL(:,i)=SL(i)-TL;
end

n=find(RawData(:,1)==1500);
for M = 1:length(D);
  for Length = 1:length(r)
      cnt=0;
       for k = 2 : length(RawData(1,:)); % Species
          if    SPL(Length,M) > (RawData(n,k)+130) %&& RawData(j,M+1)>0
          MME(Length,M) = 1+cnt; % i frequency Range, Index, j = Species Frequency Hearing
          TMME(Length,k,M) = 1+cnt; % k Length of Raw Data
                    cnt=1+cnt;

                else
                   break
                end
               end

        end
end
```

B2. Analysis of Sound Pressure Loss as a function of range

```
%% Fixed Platform Systems

N=10;       %Transmission Loss Term
alpha = 0.0004;
TL=N*log10(r)+alpha*r;
for i=1:length(D)
SPL1(:,i)=SL(i)-TL;
end

for M = 1:length(D);
  for Length = 1:length(r)
     cnt=0;
      for k = 2 : length(RawData(1,:)); % Species
        if    SPL1(Length,M) > (RawData(n,k)+130) %&& RawData(j,M+1)>0
        MME1(Length,M) = 1+cnt; % i frequency Range, Index,
j = Species Frequency Hearing
        TMME1(Length,k,M) = 1+cnt; % k Length of Raw Data

                        cnt=1+cnt;
              else

                 break
               end
             end
          end

end
```

B.3 Analysis of Source Level

```
clc, clear all, close all
D  = [ 0.5 0.7 0.9 1.5 1.8 1.8  4    4  4.2 4.3 4.7 4.7  5];
SL = [ 189 211 201 228 225 250  262 249 257 243 252 249 270.7 ];
p_first=polyfit(D,SL,1)

hold on
Diameter=0.5:0.1:5;
SourceLevel=p_first(1)*Diameter+p_first(2);
SL_B=24.3*Diameter+179;
plot(D,SL,'r.',Diameter,SourceLevel,Diameter,SL_B)
xlabel('Diameter (meters)')
ylabel('Source Level (dB"s)')
% title('Source Level as a function of Diameter')
legend('Raw data','Least Square Regression','Nedwell et al.')
```

BIBLIOGRAPHY

Minerals Management Service. (2009). *CAPE WIND ENERGY PROJECT Final Environmental Statement.* U.S. Department of the Interior, Minerals Management Service. Herndon: OCS.

Ahlen, I., Baagoe, H. J., & Bach, L. (2009). Behavior of Scandinavian Bats During Migration and Foraging at Sea. *Journal of Mammology , 90* (6), 1318-1323.

Ahlen, I., Bach, L., Baagoe, H. J., & Pettersson, J. (2007). *Bats and offshore wind turbines studied in southern Scandinavia.* Swedish Environmental Protection Agency. Stokholm, Sweden: Vindval.

Allison, T. D., Jedrey, E., & Perkins, S. (2008). Avian Issues for Offshore Wind Development. *Marine Technology Society Journal , 42* (2), 28-36.

Arnett, E. B., Brown, K. W., Erickson, W. P., Fiedler, J. K., Hamilton, B. L., Henry, T. H., et al. (2008). Patterns of Bat Fatalities at Wind Energy Facilities in North America. *The Journal of Wildlife Management , 72*, 61-78.

Bailey, H., Senior, B., Simmons, D., Rusin, J., Picken, G., & Thompson, P. M. (2010). Assessing underwater noise levels during pile-driving at an offshore windfarm and its potential effects on marine mamals. *Marine Pollution Bulletin , 60*, 888-897.

Battley, P. F., Piersma, T., Dietz, M. W., Tang, S., Dekinga, A., & Hulsman, K. (2000). Empirical evidence for differential organ reductions during trans-oceanic bird flight. *The Royal Society , 267*, 191-195.

Breton, S., & Moe, G. (2009). Status, plans and technologies for offshore wind turbines in Europe and North America. *Renewable Energy , 34*, 646-654.

Brook-Hart, W. (2009). Concrete foundations for offshore wind turbines. *Concrete* , 21-22.

Brook-Hart, W., Jackson, P., Meyts, M., & Sayer, P. (2009, June 23). *Competitive concrete foundations for offshore wind turbines.* Retrieved May 10, 2010, from Giffords: http://www.gifford.uk.com/fileadmin/uploads/Documents/Research_and_Opiniom/Competitive_Concrete_Foundations_for_Offshore_Wind_Turbines.pdf

Burkhard, B., Burkhard, B., Opitz, S., Lenhart, H., Ahrendt, K., Garthe, S., et al. (2009). Ecosystem based modeling and indication of ecological integrity in the German North Sea—Case study offshore wind parks. *Ecological Indicators* .

Butterfield, S., Musial, W., & Jonkman, J. (2005). *Engineering Challenges for Floating Offshore Wind Turbines.* National Renewable Energy Laboratory. Golden: National Renewable Energy Laboratory.

Byrne, B., & Houlsby, G. (2006). *Assessing Novel Foundation Options for Offshore Wind Turbines.* London: World Maritime Technology Conference.

Carlos, R. (2007). Very shallow water noise impact of offshore wind farms. Parameters to considered. *15th International Congresss on Sound and Vibration* (pp. 1074-1081). Daejeon, Korea: Environmental Acoustics, Instituto de Acustica-CSIC.

Cherel, Y., Bocher, P., De Broyer, C., & Hobson, K. A. (2002). Food and feeding ecology of the sympatric thin billed Pachyptila belcheri and Antarctic P. desolata prions at Iles Kerguelen, Southern Indian Ocean. *MARINE ECOLOGY PROGRESS SERIES , 228*, 263-281.

Chung, S. (2008). Appropriate maze methodology to study learning in fish. *Journal of Undergraduate Life Sciences , 2* (1), 52-55.

Cryan, P. M., & Brown, A. C. (2007). Migration of bats past a remote island offers clues toward the problem of bat fatalities at wind turbines. *Biological Conservation , 139*, 1-11.

de Lucas, M., Janss, G. F., Whitfield, D. P., & Ferrer, M. (2008). Collision fatality of raptors in wind farms does not depend on raptor abundance. *Journal of Applied Ecology , 45* (6), 1695-1703.

de Vries, W., & Krolis, V. (2007). *Effects of deep water on monopile structures for offshore wind turbines.* Delft University of Technology, Civil Engineering and Geosciences. Delft, DK: Delft University of Technology.

Drewitt, A. L., & Langston, R. H. (2006). Assessing the impacts of wind farms on birds. *Ibis , 148*, 29-42.

Fox, A., Desholm, M., Kahlert, J., Kjaer, C. T., & Petersen, I. K. (2006). Information needs to support environmental impact assessment of the effects of European marine offshore wind farms on birds. *Ibis , 148*, 129-144.

Geo-Marine Inc. (2010). *Ocean/Wind Power Ecological Baseline Studies.* New Jersey Department of Environmental Protection, Office of Science. New Jersey Department of Environmental Protection Office of Science.

Gill, A. B., & Taylor, H. (2001). *The potential effects of electromagnetic fields generated by cabling between offshore wind turbines upon Elasmobranch Fishes.* University of Liverpool, Applied Ecology Research Group. Liverpool, UK: Countryside Council for Wales.

Global Energy Partners, L. (2004). *Offshore Wave Power in the US: Environmental Issues.* Electric Research Power Institute. Electric Research Power Institute.

Glover, A. G., & Smith, C. R. (2003). The deep-sea floor ecosystem: current status and prospects of anthropogenic change by the year 2025. *Environmental Conservation , 30* (3), 219-241.

Henderson, A. R., & Witcher, D. (2010). Floating Offshore Wind Energy - A review of the Current Status and an Assessment of the Prospects. *Wind Engineering , 34* (1), 1-16.

Henderson, A. R., Witcher, D., & Morgan, C. A. (2009). *Floating Support Structures Enabling New Markets for Offshore Wind Energy.* Garrad Hassan & Partners. Bristol, UK: Garrad Hassan & Partners.

Hoffmann, E., Astrup, J., Larsen, F., Munch-Petersen, S., & Stottrup, J. (2000). *Effects of marine wind farms on the distribution of fish, shellfish and marine mammals in the Horns Rev area.* Danish Institute for Fisheries Research, Department of Marine Fisheries. Charlottenlund: Danish Institute for Fisheries Research.

Houlsby, G. T., & Byrne, B. W. (2000). Suction Caisson Foundations for Offshore Wind Turbines and Anemometer Masts. *Wind Engineering , 24* (4), 249-255.

Jaap, W. C. (2000). Coral reef restoration. *Ecological Engineering , 15*, 345-364.

Jenkin, P. M. (1957). The Filter-Feeding and Food of Flamingoes (Phoenicopteri). *Royal Society Publishing , 240* (674), 401-493.

Klaassen, M. (1996). Metabolic Constraints on Long-Distance Migration in Birds. *The Journal of Experimental Biology , 199*, 57-64.

Koller, J., Koppel, J., & Peters, W. (2006). *Offshore Wind Energy Research on Environmental Impacts* (1st Edition ed.). (J. Koller, J. Koppel, & W. Peters, Eds.) Berlin, Germany: Springer.

Kramer, S., Preavisic, M., Nelson, P., & Woo, S. (2010). *Deployment Effects of Marine Renewable Energy Technologies Framework for Identifying Key Environmental Concerns in Marine Renewable Energy Projects.* U.S. Department of Energy. RE Vision Consulting, LLC.

Langhamer, O., Wilhelmsson, D., & Engstrom, J. (2009). Artificial reef effect and fouling impacts on offshore wave power foundations and buoys - a pilot study. *Estuarine, Coastal and Shelf Science , 82*, 426-432.

Limited, 4. O. (2011). *Global Offshore Wind Portal: Offshore Wind Farms*. Retrieved May 31, 2011, from 4C Offshore: http://www.4coffshore.com/wind farms/

Lindeboom, H. J., Kouwenhoven, H., Bergman, M. J., Bouma, S., Brasseur, S., Daan, R., et al. (2011). Short-term ecological effects of an offshore wind farm in the Dutch coastal zone; a compilation. *Environmental Research Letters , 6*, 1-13.

Lissner, A. L., Taghon, G. L., Diener, D. R., Schroeter, S. C., & Dixon, J. D. (1991). Recolonization of Deep-Water Hard-Substrate Communities: Potential Impacts From Oil and Gas Development. *Ecological Applications , 1* (3), 258-267.

Maar, M., Bolding, K., Petersen, J. K., Hansen, J. L., & Timmermann, K. (2009). Local effects of blue mussels around turbine foundations in an ecosystem model of Nysted off-shore wind farm. Denmark. *Journal Of Sea Research , 62*, 159-174.

Madsen, P., Wahlberg, M., Tougaard, J., Lucke, K., & Tyack, P. (2006). Wind turbine underwater noise and marine mammals: implications of current knowledge and data needs. *MARINE ECOLOGY PROGRESS SERIES , 309*, 279-295.

Masden, E. A., Haydon, D. T., Fox, A. D., Furness, R. W., Bullman, R., & Desholm, M. (2009). Barriers to movement: impacts of wind farms on migrating birds. *International Council for the Exploration of the Sea , 66*, 746-753.

Melnyk, M., & Andersen, R. (2009). *Offshore Power: Building Renewable Energy Projects in U.S. Waters* (1st Edition ed.). (S. Hill, Ed.) Waltham Abbey, Essex, U.S.: PennWell Corp.

Morkel, L., Toland, A., Wende, W., & Koppel, J. (2007). 2nd Scientific Conference on the Use of Offshore Wind Energy by the Federal Ministry for the Environment. *Proc. of 2nd Scientific Conference on the Use of Offshore Wind Energy by the Federal Ministry for the Environment* (pp. 1-181). Berlin, DE: Federal Ministry for the Environment.

Mueller-Blenkle, C., McGregor, P., Gill, A., Andersson, M., Metcalfe, J., Bendall, V., et al. (2010). *Effects of pile-driving noise on the behaviour of marine fish.* COWRIE. Cefas.

Musial, W., & Butterfield, S. (2006). *Energy From Offshore Wind.* National Renewable Energy Laboratory. Golden, CO: National Renewable Energy Laboratory.

Musial, W., & Ram, B. (2010). *Large-Scale Offshore Wind Power in the United States assessment of opportunities and barriers.* National Renewable Energy Laboratory. Oak Ridge: U.S. Department of Energy.

Musial, W., Butterfield, S., & Boone, A. (2003). *Feasibility of Floating Platform Systems for Wind Turbines.* Department of Energy, National Renewable Energy Laboratory. Golden, CO: National Renewable Energy Laboratory.

Nedwel, J. R., Edwards, B., Turnpenny, A., & Gordon, J. (2004). *Fish and Marine Mammal Audiograms: A summary of available information.* Fawley Aquatic Research Laoratories Ltd. Fawley Aquatic Research Laboratories Ltd.

Nedwell, J., & Howell, D. (2004). *A review of offshore windfarm related underwater noise.* Collaborative Offshore Wind Research Into the Evironment. Bishops Waltham: COWRIE.

Nedwell, J., Lovell, J., & Turnpenny, A. (2003). *Experimental validation of a species-specific behavioral impact metric for underwater noise*. Retrieved October 10, 2010, from www.subacoustech.com

Nedwell, J., Parvin, S., Edwards, B., Workman, R., Brooker, A., & Kynoch, J. (2007). *Measurement and interpretation of underwater noise during construction and operation of offshore wind farms in UK waters.* COWRIE Ltd.

Nedwell, J., Turnpenny, J. L., Parvin, S., Workman, R., Spinks, J., & Howell, D. (2007). *A validation of the dBht as a measure of the behavioural and auditory effects of underwater noise.* U.K. Department of Business, Enterprise and Regulatory Reform. Subachoustech Ltd.

Norman, T., Buisson, R., & Askew, N. (2007). Proc. of COWRIE workshop on the cumulative impact of offshore wind farms on birds. *COWRIE workshop on the cumulative impact of offshore wind farms on birds* (pp. 1-71). St Ives, U.K.: RPS.

Ohman, M. C., Sigray, P., & Westerberg, H. (2007). Offshore windmills and the effects of electromagnetic fields on fish. *Ambio , 36* (8), 630-633.

Oud, J. C., & Nedam, B. (2002). *Foundation Design Monopile Comparison extra steel consumption versus scour protection 3.6 & 6.0 MW wind turbines.* Retrieved March 19, 2010, from Energy Research Center of the Netherlands: www.ecn.nl/fileadmin/ecn/units/wind/docs/dowec/10067_001.pdf

Pacific Energy Ventures, L. (2O11, May 8). *Planning & Assessment Frameworkds-Entanglement-Entrapment.* Retrieved May 8, 2011, from Advance H20 Power: http://www.advancedh2opower.com/framework/Site%20Pages/Entanglement-Entrapment_DRAFT.PDF

Parvin, S. J., Nedwell, J. R., & Harland, E. (2007). *Lethal and physical injury of marine mammals, and requirements for Passive Acoustic Monitoring.* The Department of Trade and Industry. London, U.K.: Subacoustech.

Polagye, B., Coping, A., Kirkendall, K., Boehlert, G., Walker, S., Wainstein, M., et al. (2010). Environmental Effects of Tidanl Energy Development. In B. Polagye, A. Coping, K. Kirkendall, G. Boehlert, S. Walker, M. Wainstein, et al. (Ed.), *A Scientific Workshop* (pp. 29-40). Seattle: University of Washington.

Roberts, S., & Hirshfield, M. (2004). Deep-sea corals: out of sight, but no longer out of mind. *Frontiers in Ecology and the Environment , 2* (3), 123-130.

Rodrigues, L., Bach, L., Dubourg-Savage, M., Goodwin, J., & Harbusch, C. (2008). *Guidelines for consideration of bats in wind farm projects.* Bonn, DE: UNEP/EUROBATS.

Rowe, G. T., & Kennicutt II, M. C. (2001). *Deepwater Program: Northern Gulf of Mexico Continental Slope Habitats and Benthic Ecology.* U.S. Department of the Interior , Minerals Management Serevice. U.S. Department of the Interior Minerals Management Serevice Gulf of Mexico OCS Region.

Checklman, S., Houser, D., Cross, M., Hernandez, D., & Siderius, M. (2011). Comparison of methods used for computing the impact of sound on the marine environment. *Marine Environmental Research , 71*, 342-350.

Schwartz, S. S. (2004). Proc.of the Wind Energy and Birds/Bats Workshop: Understanding and Resolving Bird and Bat Impacts. *Wind Energy and Birds/Bats Workshop: Understanding and Resolving Bird and Bat Impacts* (pp. 1-132). Washington, DC.: RESOLVE Inc.

Shaffer, S. A., Tremblay, Y., Weimerskirch, H., Scott, D., Thompson, D. R., Sagar, P. M., et al. (2006). Migratory shearwaters integrate oceanic resources across the Pacific Ocean in an endless summer. *PNAS , 103* (34), 12799–12802.

Snyder, B., & Kaiser, M. J. (2009). Ecological and economic cost-benefit analysis of offshore wind energy. *Renewable Energy , 34*, 1567-1578.

Stanley, D. R., & Wilson, C. A. (2000). Variation in the density and species composition of fishes associated with three petroleum platforms using dual beam hydroacoustics. *Fisheries Research , 47*, 161-172.

Tech Environmental, I. (2006). *Cape Wind Energy Project Nantucket Sound.* Waltham: Cape Wind.

Thelander, C. G. (2006, June 27). *U.S. Fish & Wildlife: Wind Energy Development.* Retrieved May 31, 2011, from U.S. Fish & Wildlife: http://www.fws.gov/midwest/greatlakes/windpowerpresentations/Thelander.pdf

Thompson, P. M., Lusseau, D., Barton, T., Simmons, D., Rusin, J., & Bailey, H. (2010). Assessing the responce of coastal cetaceans to the construction of offshore wind turbines. *Marine Pollution Bulletin , 60*, 1200-1208.

Thomsen, F., Lüdemann, K., Kafemann, R., & Piper, W. (2006). *Effects of offshore wind farm noise on marine mammals and fish.* Collaborative Offshore Wind Research into the Environment. 2006: COWRIE Ltd.

Tong, K. (1998). Technical and economic aspects of a floating offshore wind farm. *74-76*, 399-410.

Tougaarda, J. T., & Damsgaard H., O. D. (2009). Underwater noise from three types of offshore wind turbines:Estimation of impact zones for harbor porpoises and harbor seals. *Acoustical Society of America , 125* (6), 3766-3773.

Twidell, J., & Gaudiosi, G. (2010). *Offshore Wind Power* (1st Edition ed.). (J. Twidell, & G. Gaudiosi, Eds.) Brentwood, Essex, UK: Multi-Science Publishing Co. Ltd.

U.S. Wildlife Service. (2010). *The U.S. Fish and Wildlife Service Draft Land-Based Wind Energy Guidelines Recomendations on measures to avoid, minimize, and compensate for effects to fish, wildlife, and their habitats.* The U.S. Fish and Wildlife Service. The U.S. Fish and Wildlife Service.

University of Maine. (2011). *Draft environmental assessment for University of Maine's deepawater offshore floating wind turbine testing and demonstration project.* U.S. Department of Energy Office of Energy Efficiency and Renewable Energy Golden Field Office.

Vella, G. (2002). *The Environmental Implications of Offshore Wind Generation.* Retrieved May 31, 2011, from The Environmental Implications of Offshore Wind Generation: http://offshorewind.net/Other_Pages/Links%20Library/The%20Environmental%20Implications%20of%20Offshore%20Wind%20Generation.pdf

Wahlberb, M., & Westerberg, H. (2005). Hearing in Fish and their reations to sound from offshore wind farms. *Marine Ecology Progress Series , 288*, 295-309.

Wang, W., & Bai, Y. (2010). Investigation on Installation of Offshore Wind Turbines. *Journal of Marine Science Applications , 9*, 175-180.

Wartzok, D., & Ketten, D. R. (1999). Marine Mammal Sensory Systems. *Biology of Marine Mammals* , 117-175.

Wilhelmsson, D., & Malm, T. (2008). Fouling assemblages of offshore wind power plants and adjacent substrata. *Estuarine, Coastal and Shelf Science , 79*, 459-466.

Wilhelmsson, D., Torleif, M., & Ohman, M. C. (2006). The influence of offshore windpower on demersal fish. *Journal of Marine Science , 63*, 775-784.

Wilson, B., Batty, R. S., Daunt, F., & Carter, C. (2007). *Collision risks between marine renewable energy devices and mammals, fish and diving birds.* Scottish Executive. Oban: Scottish Association for Marine Science.

Wilson, J. C., & Elliott, M. E. (2009). The Habitat-creation Potential of Offshore Wind Farms. *Wind Energy , 12*, 203-212.

Wilson, J. C., Elliott, M., Cutts, N., Mander, L., Mendao, V., Perez-Dominguez, R., et al. (2010). Coastal and Offshore Wind Energy Generation: Is it Environmentally Benign? *energies , 3*, 1383-1422.

Zuccaa, P., Palladini, A., Baciadonnac, L., & Scaravelli, D. (2010). Handedness in the echolocating Schreiber's Long-Fingered Bat (Miniopterus schreibersii). *Behavioural Processes , 84*, 693–695.

Final Report

Development of a Low–Cost Lidar for Wind Profiling in the Marine Atmospheric Boundary Layer

Dr. Eugene A. Terray and Frederick Sonnichsen

Department of Applied Ocean Physics and Engineering
Woods Hole Oceanographic Institution

Overview: The goal of this project was to improve the performance of vertically-profiling wind Lidars using a pulse-compression technique borrowed from HF radar, and to demonstrate the feasibility of the approach by constructing a single beam profiling Lidar. We carried out the design study for a demonstration Lidar (in terms of the required optical and electrical engineering) before we realized that the basic idea was flawed. Although we believe we now have a different way to achieve our original goal, unfortunately we did not work it out until close to the end of the project period, and so were unable to acquire the necessary optical components (which differed from those required by our original proposal) required to demonstrate the approach.

This report is structured as follows: First, to motivate the rest of the discussion, we will review the technical underpinnings of the approach universally adopted (with small variations) by the vendors of the currently commercially-available Lidar vertical wind profilers. This will be followed by a recap of our original proposal and a discussion of what we believe is wrong with it. We conclude with an analysis of the expected performance of a new method (at least when applied to Lidar) to reduce the velocity error. This method is widely used to improve the performance of Doppler sonar for measuring water velocity, and we find it somewhat ironic that a method borrowed from radar was not appropriate in the optical domain, despite the equality of the propagation speeds, whereas a technique from acoustics likely will work.

Review of Current Technology: All but one of the Lidar vertical wind profilers we are aware of, and all of the scanning profilers, are based on pulsed transmissions. The one outlier is the Qinetic ZephIR which is a continuous wave device that achieves range resolution by means of a mechanically-stepped variable focal length lens. Unlike pulsed devices, where the along-beam spatial resolution is independent of distance, the range resolution of he ZephIR is proportional to the square of the range (or height). We will not consider it further here, and will confine our review and analysis of the performance Lidar wind profilers to pulsed devices. Our review will be brief – more detailed discussion can be found in the articles by Freilich (1997, 2001, 2013), and references therein.

Relation Between Velocity and Doppler Shift: It is important to note that monostatic backscatter Lidars measure the Doppler shift caused by the component of wind velocity projected along the beam. The Doppler frequency shift is given by

$$f_d = 2\mathbf{k} \cdot \mathbf{u} \tag{1.1}$$

where **u** is the mean vector velocity (in some weighted sense) of the scatterers within the range cell, and **k** is a vector in the direction of light propagation whose magnitude is $2\pi / \lambda$ (note that the factor of 2 that appears this formula reflects the fact that the light has to travel out and back – or twice as far as the distance to the range cell).

Range Resolution: Pulsed Lidar wind profilers typically measure velocity at a number of range cells, or "bins" along a at least 3 beams, inclined with respect to the vertical by an angle β. Some Lidars have independent beams arranged at fixed azimuthal increments, but most move a single beam to different azimuths, stopping long enough to acquire a "good" velocity measurement. The location and along-beam width of a range bin is determined by timing. So, for example, if a pulse of duration T is transmitted at time 0, then the signal from scattering at a distance *R* along the beam arrives at a time $t = 2R / c$, and the along-beam range resolution is $\Delta R = cT / 2$.

Maximum Velocity Range: If the received signal was quadrature demodulated, then the maximum measurable velocity would be directly related to the speed of the digitizer used. However, the commercial wind profiling Lidars intead mix the signal to an intermediate frequency using an Acoustic Optical Modulator (AOM). A typical AOM frequency might be ~ 68 MHz which corresponds (in the near-IR) to a velocity of around 50 m/s. Hence this would be the maximum negative velocity that could be measured unambiguously.

Doppler Frequency / Velocity Resolution: Commercial pulsed Lidar wind profilers transmit a uniform, monochromatic (*i.e*. single frequency) pulse of some duration *T*. The pulse scatters back and is shifted by the Doppler frequency. Then the lowest Doppler frequency that can be detected (*i.e*. the frequency resolution) is $\delta f = 1 / T$. This translates to a velocity resolution of

$$\delta u = \lambda / 2T = c\lambda / 4\Delta R \tag{1.2}$$

If the backscattered signal remained perfectly correlated for times much longer than this, then the frequency/velocity resolutions above would also determine the uncertainty in the estimates. But because the pulse scatters from a random assemblage of particles within the range cell, the received signal has an intrinsic finite correlation time, τ, and consequently the velocity error given in (1.2) doesn't get arbitrarily small as we increase the pulse length indefinitely.

Signal Correlation Time: For all coherent systems that sense the Doppler shift of volumetric backscatter (i..e lidar, radar, sonar) the signal correlation time is determined essentially by three processes. One of these is simply the resident time of scatterers within the scattering volume. In the case of a Lidar, because the speed of light is so much

larger than the wind speed, the residence time effect is by far the smallest of the three sources of decorrelation, and consequently we can focus on the other two – decorrelation due to beam spreading and turbulence. The first of these is due to the fact that the laser beam eventually spreads in a plane transverse to the direction of propagation (in other words the wavefronts are not planar but are slightly curved. Hence particles within the scattering volume are illuminated by wavenumbers that are spread slightly across the centerline propagation direction, and consequently particles passing at right angles through the beam create a small fluctuation in the phase of the received signal (so long as the beam spreads symmetrically this is a zero-mean fluctuation and does not bias the measured velocity). The second source of signal decorrelation is due to the small-scale turbulent motions within the scattering volume that change the relative positions of the particles during the passage of the pulse. This second contribution will depend on the size of the range bin and the level of small-scale turbulence. Hence the mix of these two effects can change over the profiling range.

Note also that all of these estimates are lower bounds because we have assumed an infinite optical signal-to-noise ratio (SNR), and the errors are larger when the SNR is finite. It's useful to put in some numbers: commercial wind profilers typically use near-infrared light, which has a wavelength in the vicinity of 1500 nm = 1.5×10^{-4} cm (they do this because this wavelength is "eye safe" – so that's one less worry – and because the lasers and other parts are widely used in optical telecommunications equipment, and so are relatively inexpensive). Suppose that the along-beam range resolution is 10 m (note that this would correspond to a vertical resolution of 8.7 m for a beam slanted at 30 degrees), then the single pulse velocity uncertainty will be of order 10 m/s. To get this uncertainty down to something of order 1 cm/s would then require that we average 10^6 pulses. Let's imagine that the light only travels about 300 m or so before being scattered or absorbed. Then the round-trip travel time is 2 μs, and therefore it takes a minimum of 2 s of "dwell time" to transmit enough pulses to beat the random error down to 1 cm/s. If a single beam is being rotated through 4 (or more) azimuthal positions, then a complete "scan" can take upwards of 10 s.

This is acceptable if all you want to do is to measure the mean velocity (which is all that the commercial vendors claim). But if you could cut the averaging time down significantly, then you might be able to measure turbulence directly – such a capability would be very useful in understanding, for example, loads on turbine blades.

Original Proposal: The analysis above was the motivation for our original interest to reduce the velocity error. We proposed to borrow a technique from HF Doppler radar where, because of peak power limitations, they typically transmit a pulse train of relatively long linear frequency chirps. The range is then related to the frequency shift between the received and transmitted signals, and range resolution is determined by the bandwidth of the chirp. The Doppler frequency, and hence the velocity of the scatterers at each range, is determined by the phase shift between successive demodulated pulses (Gurgel, *et al*., 1999). So the technique can be described as a combination of classical pulse compression to achieve a high range resolution (*i.e*. much shorter than the duration of the chirp), with a conventional pulse-pair Doppler estimator (Zrnic, 1979). In the

pulse-pair technique (which also is widely used in Doppler weather radar), the time between successive pulses has to be long enough that the return from the previous pulse has died away before the next one is sent. If the time between pulses is *T*, then this limits the maximum range to $R_{\max} = cT/2$. The Doppler is estimated from the phase change between successive pulses, so the maximum Doppler frequency that can be unambiguously determined (*i.e*. without aliasing) is $f_{\max} = 1/2T$ (this is just the Nyquist criterion). The corresponding maximum velocity is then $V_{\max} = \lambda f_{\max}/2 = \lambda/4T$. Hence the product

$$R_{\max} V_{\max} = \lambda c/8 \tag{1.3}$$

depends only on the wavelength and propagation speed of the signal. This relation is known as the "range–velocity ambiguity", and is a fundamental limitation of pulse-coherent systems.

In the case of HF radar, although *c* is the speed of light, the wavelength is typically a few 10s of meters, so that the right-hand side of (1.3) is on the order of 10^8. Hence, even for a maximum range of 100 km, $V_{\max}$ can be as large as 10^3. In the case of light, however, the right-hand side is of order 50. Hence for a maximum range of 200 m, the maximum unambiguous velocity would be 0.25 m/s, which is several orders of magnitude smaller than what is required. So it is the difference in wavelength that dooms this approach.

It is possible to dispense with the pulse-pair approach and attempt to jointly estimate range and Doppler directly from the chirped pulse. However, the chirp mixes range and Doppler (Rihaczek, 1996). This might be something that could be worked around if the scattering was from a single "hard target" in "clutter", but is likely to fail in the distributed scattering environment we envision here where everything is "clutter".

An Alternate Approach: Our principal goal is to reduce the velocity error, rather than to significantly improve the range resolution (since we only need ranges of a few hundred meters, we likely are not peak power limited - note, this is unlike HF radar where power is a limiting factor since we want to maximize the range). For example, a range resolution of 10 m would be considered "high resolution" in measuring winds around a wind turbine. In this case, we can still transmit "long" pulses (*i.e*. keep a 10 m range resolution), but broaden the pulse bandwidth by modulating it with a pseudo-random code. The code is repeated at least once, and the Doppler shift estimated over a lag equal to the length of 1 cycle of the code. The pulse then provides roughly *N* estimates of the Doppler shift, where *N* is proportional to the time-bandwidth product of the code – or equivalently the number of "chips" in 1 cycle of the code (Brumley *et al*., 1991; Pinkel and Smith, 1992; Wanis *et al*., 2010).

We denote the length of the code by *T*, so that the code repeated once has length *2T*. Then the range resolution is *cT*. Estimating the Doppler shift using a lag of *T*, then the maximum frequency that can be detected unambiguously is *1/2T*, which gives a corresponding maximum unambiguous velocity of $\lambda/4T$. If we require this to be, say, 30

m/s, then T ~ 12.5 ns, and the range resolution would then be cT ~ 3.75 m. Since we only require ~ 10 m range resolution, the code can be repeated 6 times. Optical modulators are available for telecommunications applications at near-IR wavelengths that have 20 GHz bandwidths – which would give 250 "chips" in a 12.5 ns pulse, or 750 chips for a repeated pulse having a net range resolution of ~ 11 m.

The standard deviation of the random velocity error is (Brumley *et al*., 1991; Pinkel and Smith, 1992)

$$\sigma_U = \frac{U_a}{\pi\rho}\frac{1}{\sqrt{2N}} \tag{1.4}$$

where U_a ~ 30 m/s is the ambiguity velocity, N ~ 750 is the total number of code elements in the overall pulse, and ρ is the magnitude of the code auto-correlation coefficient at lag T. ρ can be estimated from data, or modeled as

$$\rho = (1 - N_p^{-1})\exp(-B^2T^2/2)/(1 + SNR^{-1}) \tag{1.5}$$

Where N_p is the number of code repeats (in our case this is 6), and $1/B$ is the intrinsic correlation time of the backscattered signal. We'll assume $BT < 1$ and $SNR >> 1$, so that ρ ~ 0.83. With these estimates, $\sigma_u \sim U_a/100 \sim 0.3$ m/s.

We compare this to the error for an uncoded (*i.e*. monochromatic) pulse with a range resolution of ~ 10 m, which can be written as

$$\sigma_u^{uncoded} > \lambda/4\pi T = \lambda c/8\pi\Delta R \sim 1.8 \text{ m/s} \tag{1.6}$$

So the coding can improve the error by a factor of around 6.

A system using this approach would require some additional features beyond what is normally done. Most importantly, we would have to quadrature–demodulate the signal to baseband, rather than just shift it to an intermediate frequency, as is now done. 90° optical hybrid mixers are available (again courtesy of the telecommunications industry, where they are used for BPSK and QPSK modulation – which is exactly what we are doing here), and one could then dispense with the AOM modulator. Since this procedure effectively produces a complex signal, rather than a real signal shifted in frequency, the spectrum of the signal + noise is now 2-sided, rather than being cut off at 0 Hz, which can reduce the possibility of biasing by system filters. So in general we would expect that such a system would be a little more robust. But both the optical and signal processing would be more complex and somewhat more costly – so that the issue of whether it is worth the extra complexity to improve the velocity error by a factor or around 6 depends on the specific application.

References:

Brumley, B.H., R.G. Cabrera, K.L. Deines and E.A. Terray (1991). Performance of a broad-band acoustic Doppler current profiler. *J. Oceanic Engr*. **16**, 402–407.

Frehlich, Rod (2013). Scanning Doppler Lidar for input into short-term wind powr forecasts. *J. Atmos. & Oceanic Technol*., **30**, 230–244.

Frehlich, Rod (2001). Estimation of velocity error for Doppler Lidar measurements. *J. Atmos. & Oceanic Technol*., **18**, 1628–1638.

Frehlich, Rod (1997). Effects of wind turbulence on coherent Doppler Lidar performance. *J. Atmos. & Oceanic Technol*., **14**, 54–74.

Gurgel, K.-W., G. Antonischki, H.-H. Essen, and T. Schlick (1999). Wellen Radar (WERA): A new ground-wave HF radar for ocean remote sensing. *Coastal Engr*., **37**, 291–234.

Pinkel, R. and J. Smith (1992). Repeat-sequence coding for improved precision of Doppler sonar and Sodar. *J. Atmos. & Oceanic Technol*., **9**, 149–163.

Rihaczek, A. (1996). *Principles of High-Resolution Radar*. Artech house Inc., 489 pp.

Wanis, P., B. Brumley, J. Gast and D. Symonds (2010). Sources of measurement variance in broadband Acoustic Doppler Current Profilers. *Oceans2010*, 1–5, 10.1109/oceans.2010.5664327.

Zrnic, D. (1979). Estimation of spectral moments for weather echoes. *IEEE Trans. On Geosci. Elect*., GE-**17**, 113–128.

Final Report:

UNH/CORE MHK Sites' Resource Assessment Preliminary Results

Submitted by:

Center for Ocean Renewable Energy

Chase Ocean Engineering Laboratory

University of New Hampshire

Durham, NH 03824

Submitted to:

John Miller

Marine Renewable Energy Center

University of Massachusetts at Dartmouth

New Bedford, MA

Introduction

To support emerging technologies in the ocean renewable energy field, the University of New Hampshire (UNH) established two *in-situ* test sites located in the coastal waters of New Hampshire. The proposal for this project stated "As the University of New Hampshire gains experience in evaluating ocean renewable energy devices in field experiments, accurately characterizing the UNH in-situ testing sites has become critical." A marine hydrokinetic (MHK) turbine test site was founded in the Great Bay Estuary (adjacent to the General Sullivan Bridge) to allow test testing of up to ½ scale commercial devices. The wave testing site is 10 km southeast of Portsmouth, NH. This is the former Open Ocean Aquaculture site which was established in 1996. Before new technologies and/or energy devices are deployed at the sites, it was important to fully understand the tidal currents and wave climatology at the respective sites

To support this effort UNH commenced a measurement agenda to more completely define tidal current velocities at the General Sullivan Bridge (GSB) site. The tidal energy site at the General Sullivan Bridge site needed an examination of the tidal currents as a function of depth, across the channel as a function of position and time. These measurement and analysis of the tidal currents provide a more detailed perspective on the structure of the tidal currents in space and how this varies with time. This required performing ADCP transects across the site. For the wave test site, it was important to have an understanding of the significant wave heights and dominate periods broken down by month to optimize best deployment windows. Therefore, wave data was obtained, organized and presented in a format ideal for wave device fabricators. This document is the final report for the UNH Center of Ocean Renewable Energy (CORE) MHK Site resource assessment project.

This report is the final report for the MREC project focused on defining the hydrokinetic resource assessment at the General Sullivan Bridge tidal energy site and presenting the wave data at the offshore wave energy site. The remainder of this report presents an overview of the data acquired and used in the plots provided. The detailed data are not included in this report to keep things tidy. All the data are available and undergoing more careful scrutiny for a refereed publication. Summary plots and typical plots are presented for each site

General Sullivan Bridge ADCP Transects

The University of New Hampshire has established a Tidal Energy Test site located adjacent to the General Sullivan Bridge in Great Bay Estuary, NH (see figure 1). The tidal current velocities at the site can approach 6 knots, thus provide an ideal testing ground for research applications. It is important to note that the test site does not span the entire channel. The section of the channel adjacent to span 6 of the General

Sullivan Bridge is best suited for the test site. The water depth is maximum, and the tidal currents are swift. The tidal velocities of the GBS have been surveyed multiple times over the past years to support the founding of this test site. However, the data collected was only at one point in the tidal cycle. In addition, the navigation of the larger vessels used at the time was difficult due to the high water velocities and nearby bridge caissons, limiting the amount of useful data. To obtain a more robust and complete data set, an ADCP was mounted on the CBASS jet-ski [1], providing high maneuverability and enabling multiple transects across the site. The General Sullivan Bridge site was surveyed for tidal currents on 27 & 28 October 2011 using an RDI Workhorse ADCP mounted on the CBASS jet-ski. The jet-ski instrumentation included other devices for surveying the shallow marine environment. The GPS system was the device which was important in this study.

The majority of the GSB/ADCP transect data presented in this report is from a two day, high density ADCP survey utilizing the CBASS jet-ski, the ADCP deployment vessel of opportunity. The ADCP was an RDI Workhorse operating at 1200 kHz. The data acquired were stored on board and the transect direction was determined with a differential GPS system which was fed into the same data acquisition system to keep all the data on the same clock. The GSB site was surveyed with the jet-ski just to the south of the bridge as shown on Figure 1which provides an overhead picture of the site and the location of the 'basic transect'. The survey occurred on Oct. 27, 2011 in the afternoon on the falling tide and on Oct 28 in the morning on the rising tide. These were the so-called "King Tides". The data were acquired over the two days for approximately six hours each day covering the tidal event from slack water up to the end of the event.

Attached are time averaged transects summarizing the tidal flow. Two are time series of the near surface velocity (average of top 4 bins) as measured from the prospective of the moving CBASS. The windows over which mean current profiles across the river are calculated are indicated on the plots. The 17 other figures are approximately 0.6 hour averages of the flows. The current velocity magnitude is shown in the upper plot on each figure, and current direction is shown in the lower panels (relative to North). The 180° +/- current directions are upriver (flood currents). The 0° +/- deg current directions are downriver (ebb currents). The effects of the bridge piers on the flood currents are observed as sharp delineations across-river. The maximum instantaneous near surface along river flows were +/- 6 knots during this survey. The maximum mean flows were +/- 5 knots. These data were acquired with the CBASS jet-ski moving at 5-6 knots.

The GSB site was surveyed with an ADCP on a number of occasions using vessels of opportunity. These transects were reported in previous reports and are included here at the end of this report for completeness.

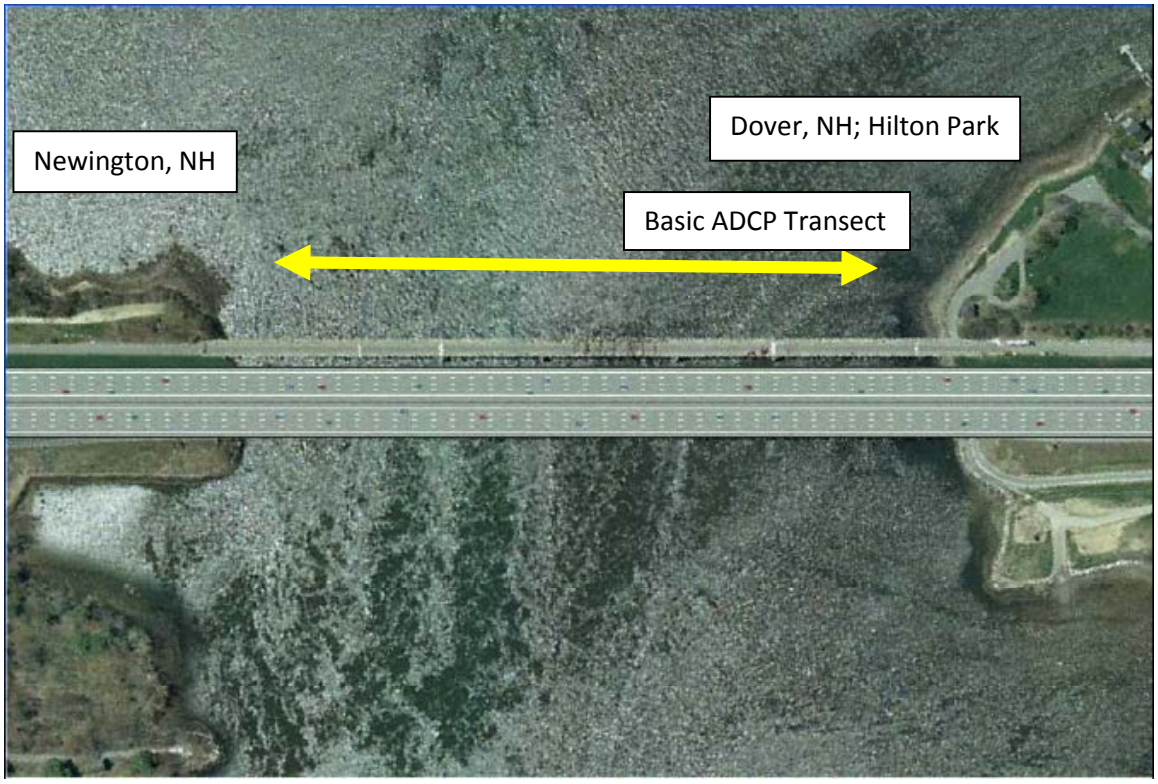

Figure 1. This figure shows an overhead view of existing General Sullivan Bridge and Little Bay Bridge with the 'new' Little Bay Bridge shown in between the two. The ADCP transects were acquired along the general transect shown in yellow on the picture. The same transect was traversed for both the ebb and flood tides.

The plots presented below are oriented with the left side being the Dover, NH, Hilton Park side of the estuary and the right side being the Newington, NH side. These are opposite of the view presented in Figure 1. The ADCP transects cover the entire cross-section which changes with tidal elevation changes. The transect section which is of interest is approximately from 250 m to 350 m, towards the Newington side where the depth is maximum. This is one span over from the navigation channel.

Note: Figures 2 -17 have the following attributes in common:

- The left side is the Dover side of the transect
- The right side is the Newington side of the transect
- The section from 250 – 350 m is essentially the test site
- These are 0.6 hour averages plotted

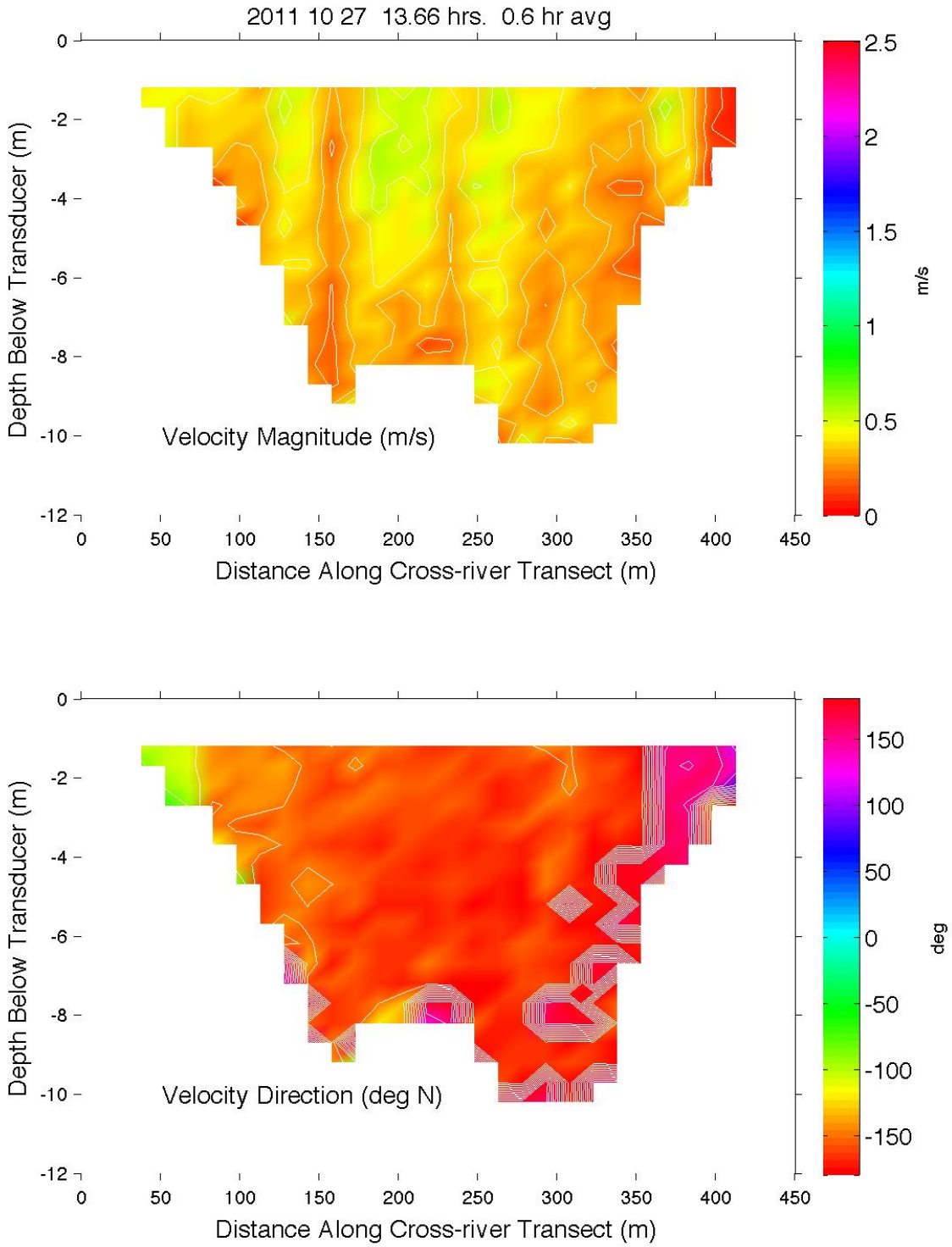
2011 10 27 13.66 hrs. 0.6 hr avg
Depth Below Transducer (m)
Velocity Magnitude (m/s)
Distance Along Cross-river Transect (m)
m/s
Depth Below Transducer (m)
Velocity Direction (deg N)
Distance Along Cross-river Transect (m)
deg

Figure 2

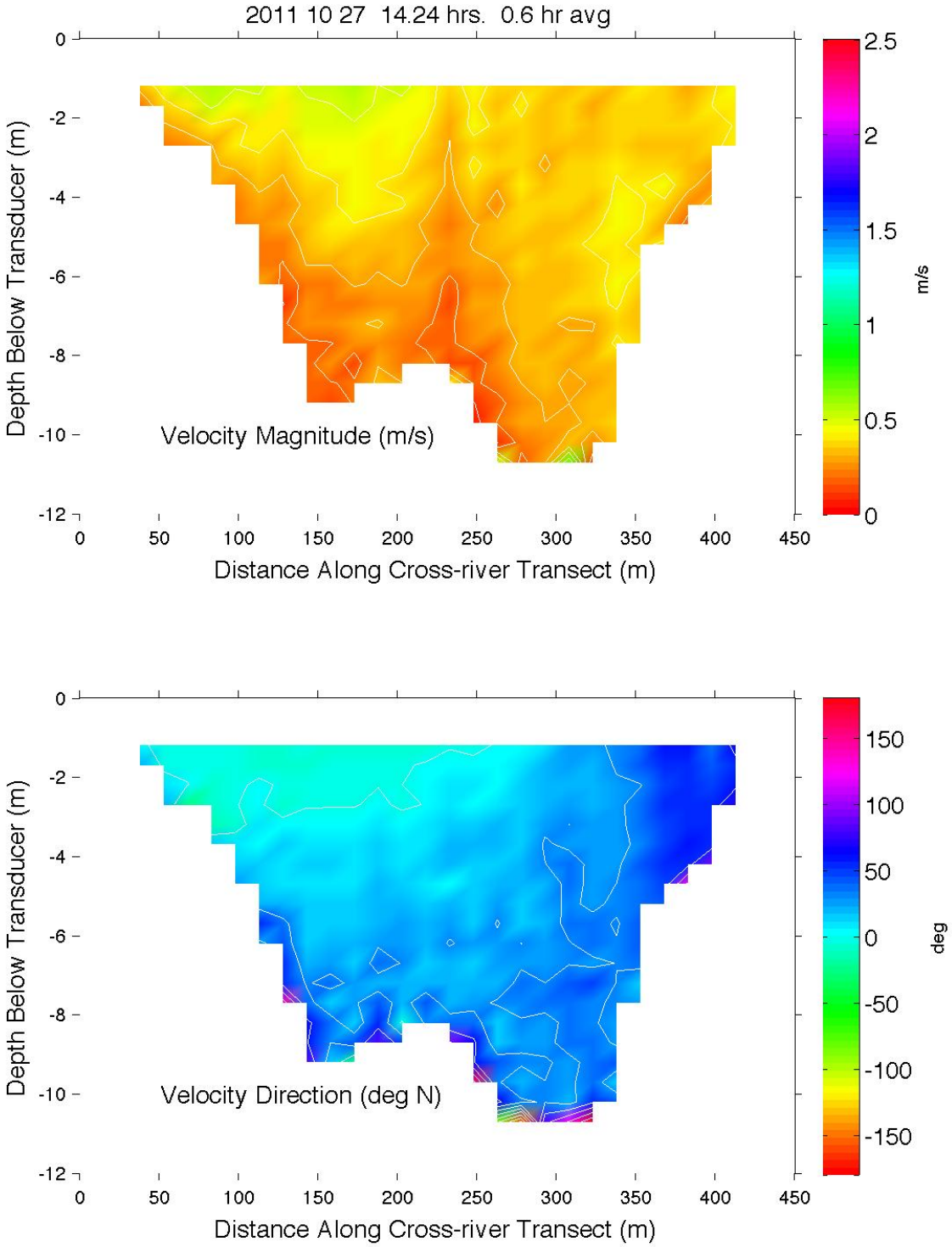
2011 10 27 14.24 hrs. 0.6 hr avg
Depth Below Transducer (m)
Velocity Magnitude (m/s)
Distance Along Cross-river Transect (m)
m/s
Depth Below Transducer (m)
Velocity Direction (deg N)
Distance Along Cross-river Transect (m)
deg

Figure 3

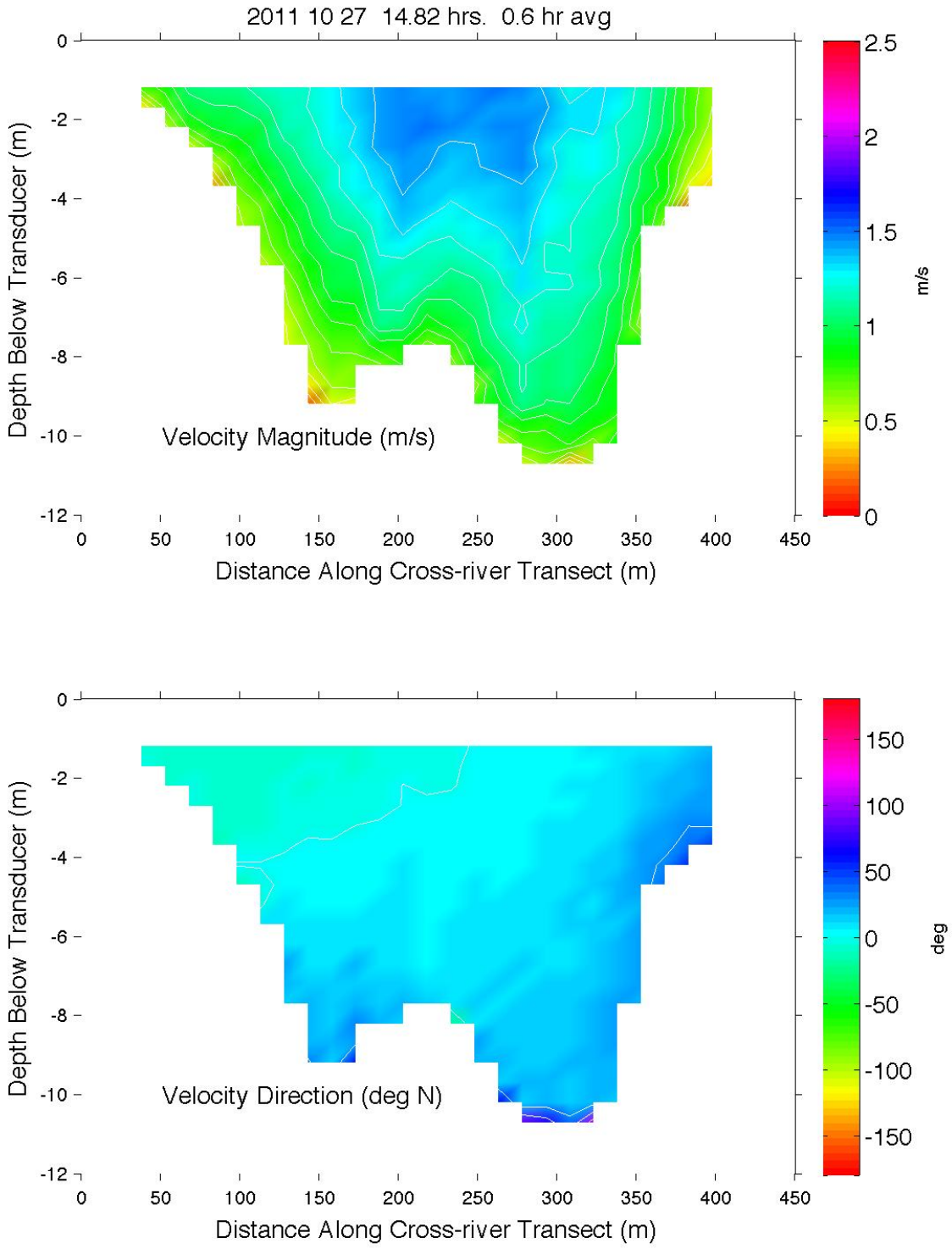
2011 10 27 14.82 hrs. 0.6 hr avg
Depth Below Transducer (m)
Velocity Magnitude (m/s)
Distance Along Cross-river Transect (m)
m/s
Depth Below Transducer (m)
Velocity Direction (deg N)
Distance Along Cross-river Transect (m)
deg

Figure 4

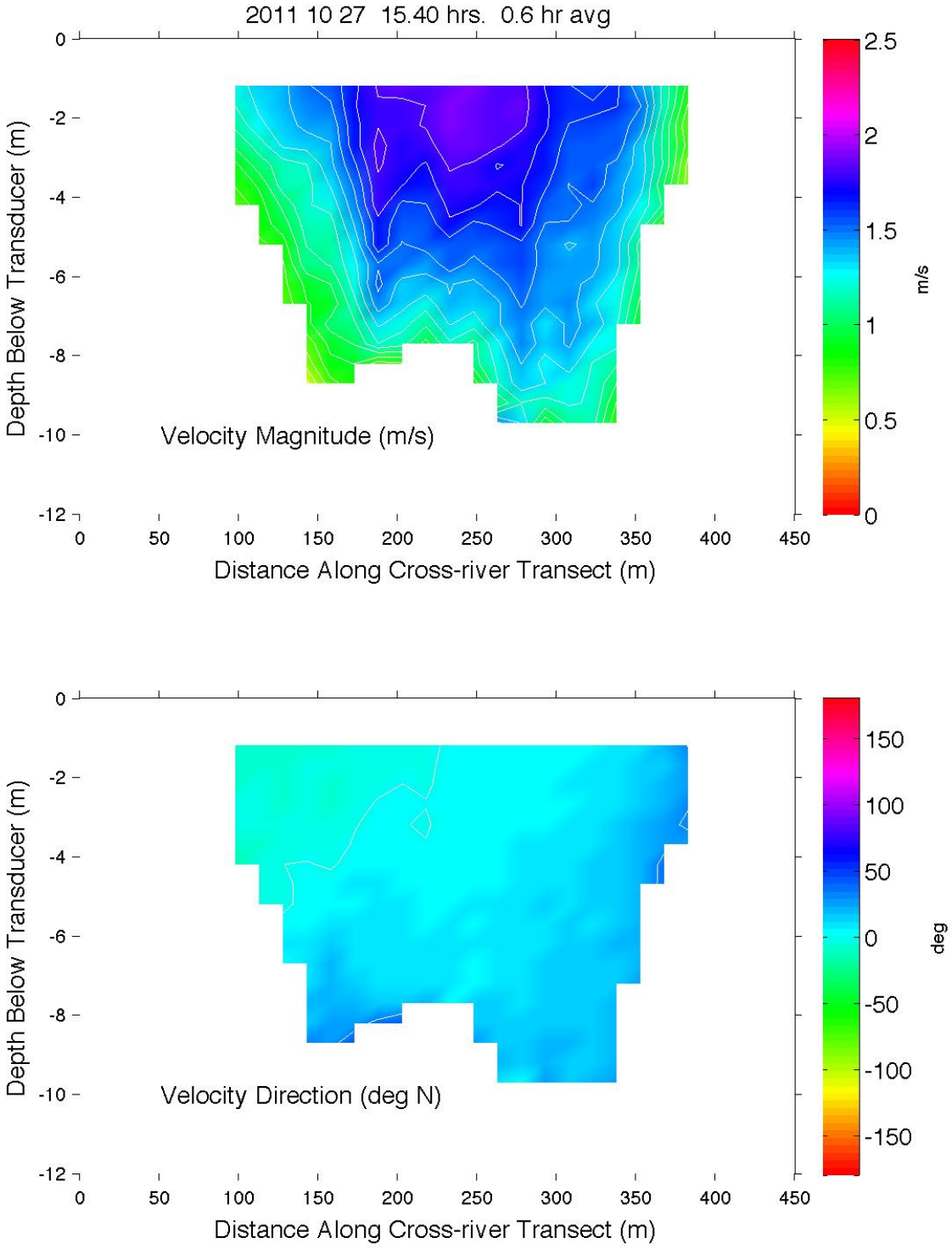
2011 10 27 15.40 hrs. 0.6 hr avg
Depth Below Transducer (m)
Velocity Magnitude (m/s)
Distance Along Cross-river Transect (m)
m/s
Depth Below Transducer (m)
Velocity Direction (deg N)
Distance Along Cross-river Transect (m)
deg

Figure 5

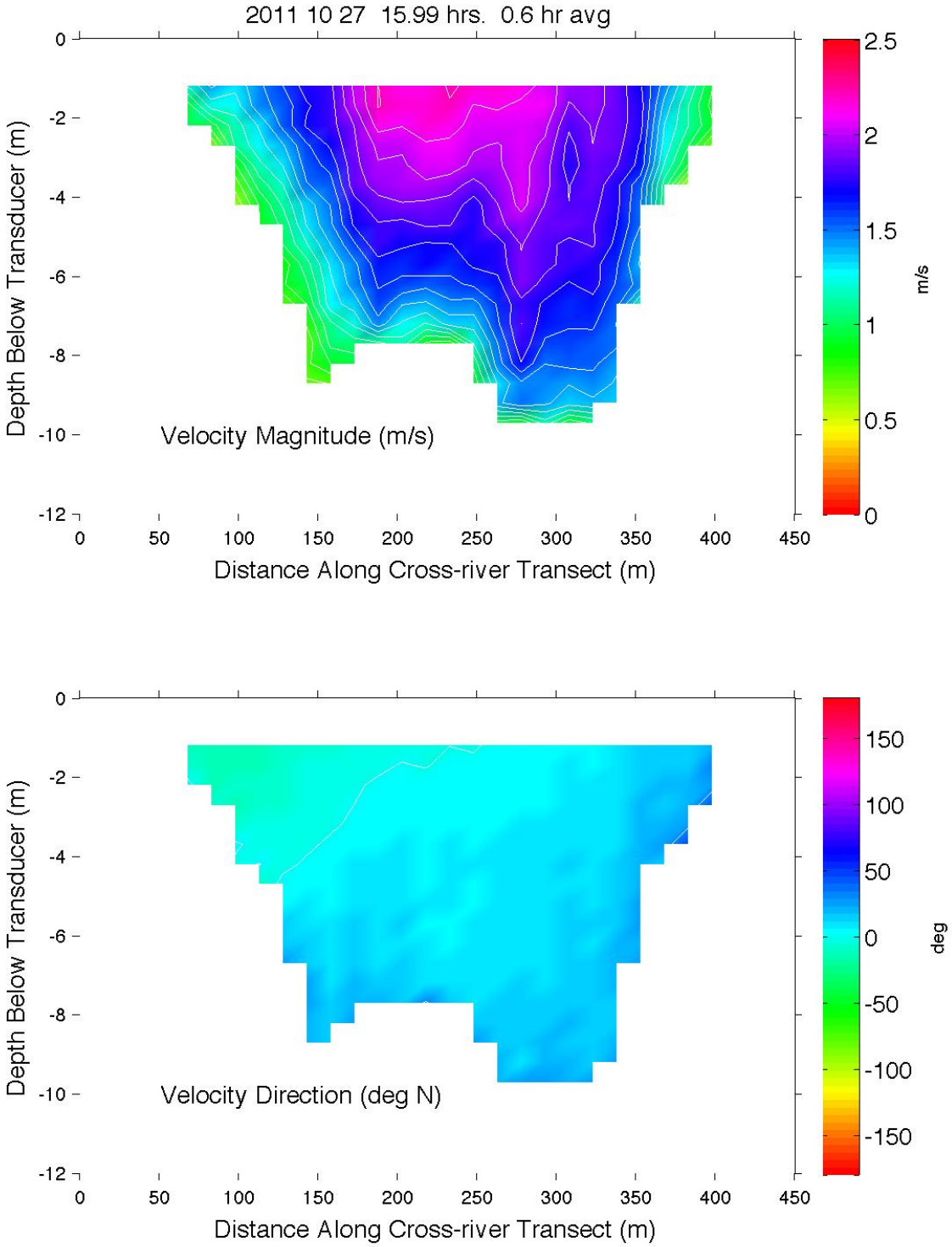
2011 10 27 15.99 hrs. 0.6 hr avg
Depth Below Transducer (m)
Velocity Magnitude (m/s)
Distance Along Cross-river Transect (m)
m/s
Depth Below Transducer (m)
Velocity Direction (deg N)
Distance Along Cross-river Transect (m)
deg

Figure 6

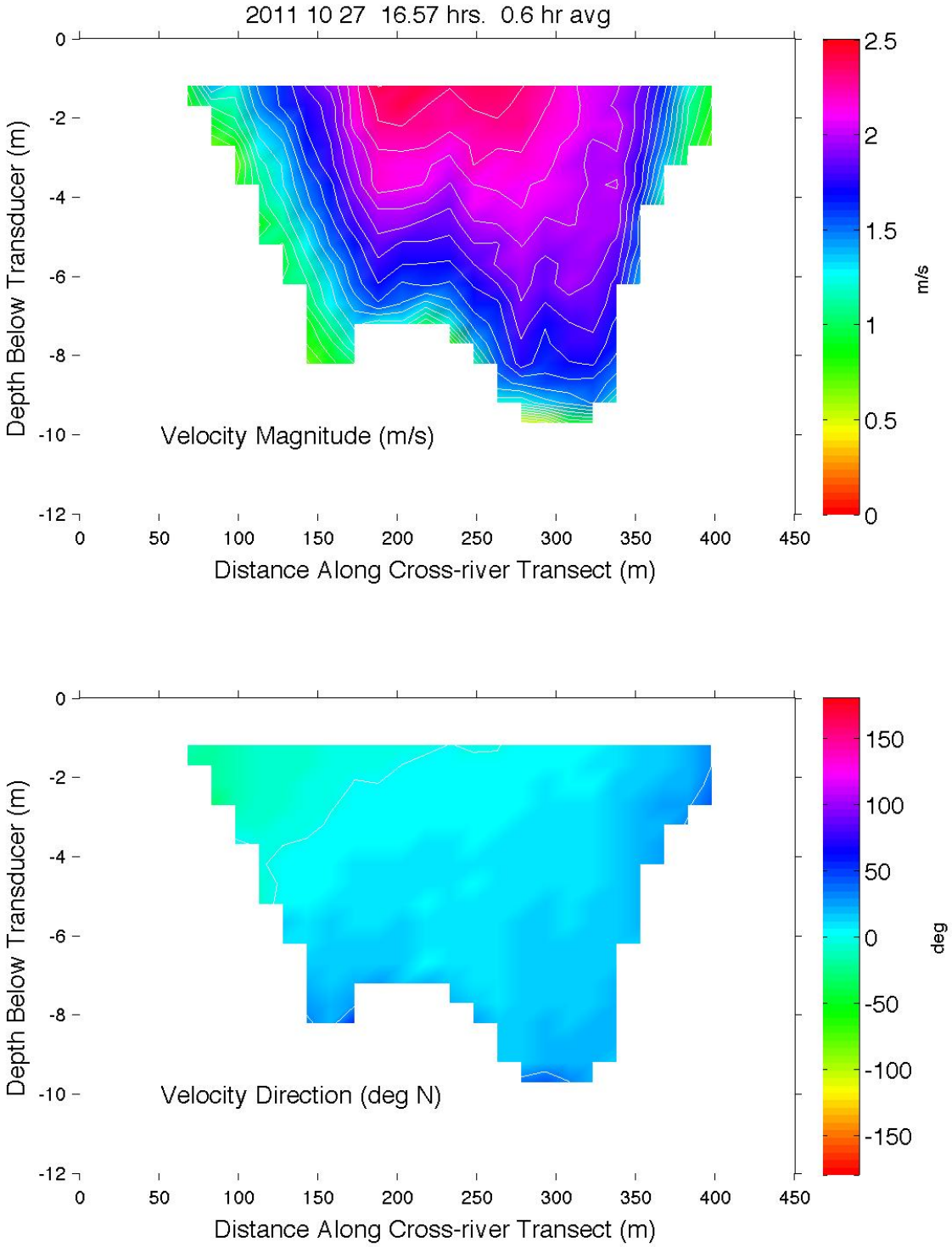
2011 10 27 16.57 hrs. 0.6 hr avg
Depth Below Transducer (m)
Velocity Magnitude (m/s)
Distance Along Cross-river Transect (m)
m/s
Depth Below Transducer (m)
Velocity Direction (deg N)
Distance Along Cross-river Transect (m)
deg

Figure 7

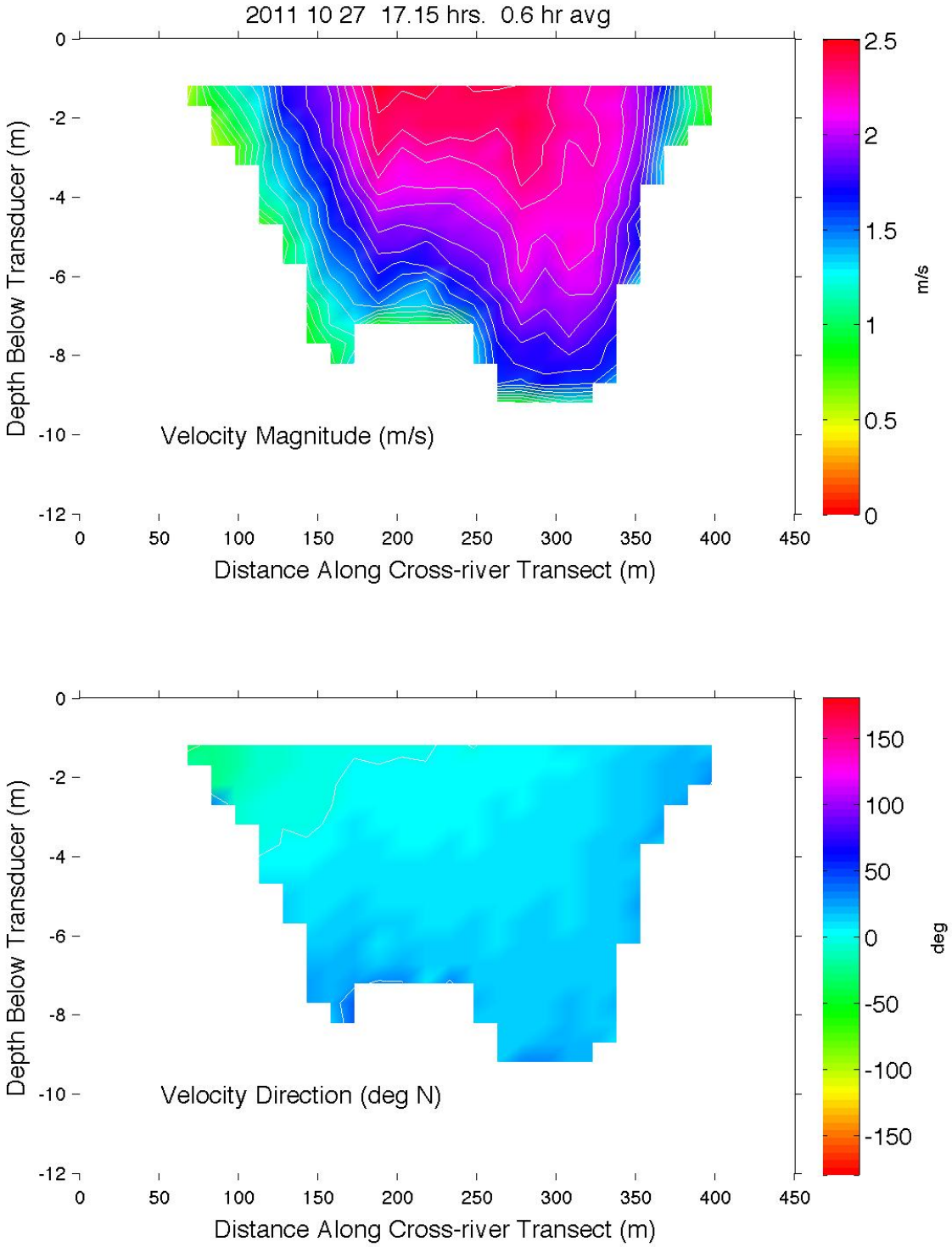
2011 10 27 17.15 hrs. 0.6 hr avg
Depth Below Transducer (m)
Velocity Magnitude (m/s)
Distance Along Cross-river Transect (m)
m/s
Depth Below Transducer (m)
Velocity Direction (deg N)
Distance Along Cross-river Transect (m)
deg

Figure 8

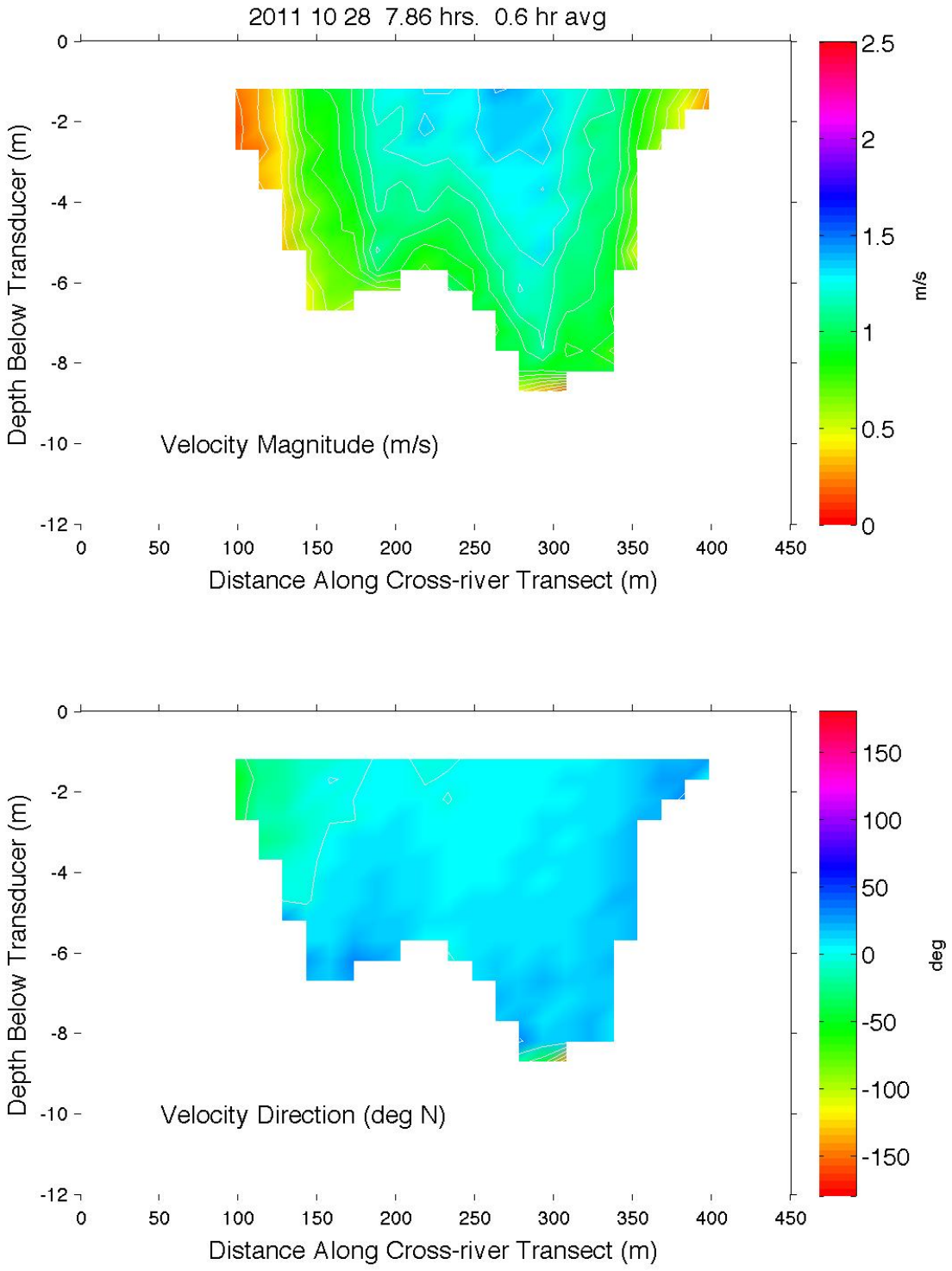
2011 10 28 7.86 hrs. 0.6 hr avg
Depth Below Transducer (m)
Velocity Magnitude (m/s)
m/s
Distance Along Cross-river Transect (m)
Depth Below Transducer (m)
Velocity Direction (deg N)
deg
Distance Along Cross-river Transect (m)

Figure 9

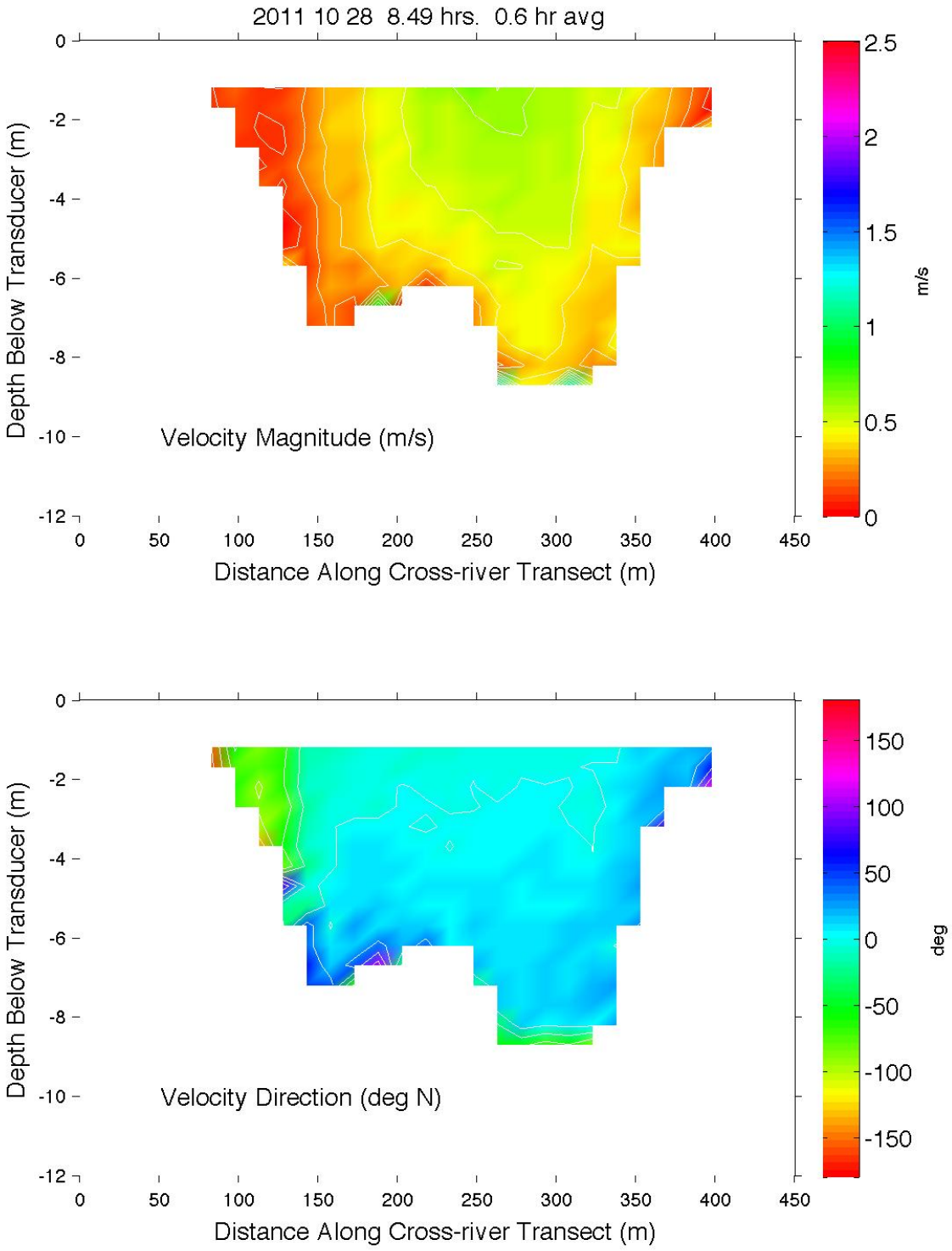
2011 10 28 8.49 hrs. 0.6 hr avg
Depth Below Transducer (m)
Velocity Magnitude (m/s)
Distance Along Cross-river Transect (m)
m/s
Depth Below Transducer (m)
Velocity Direction (deg N)
Distance Along Cross-river Transect (m)
deg

Figure 10

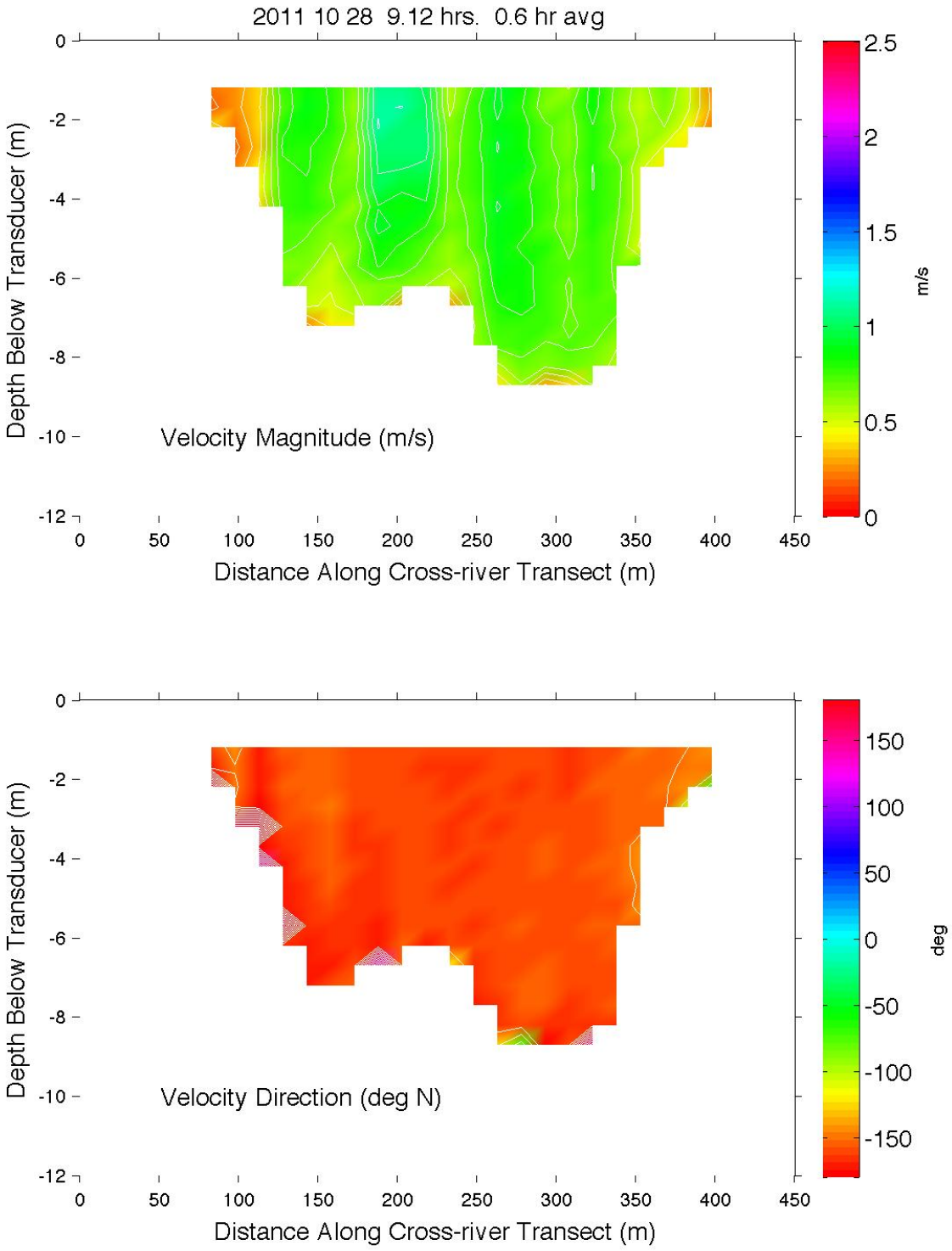
2011 10 28 9.12 hrs. 0.6 hr avg
Depth Below Transducer (m)
Velocity Magnitude (m/s)
Distance Along Cross-river Transect (m)
m/s
Depth Below Transducer (m)
Velocity Direction (deg N)
Distance Along Cross-river Transect (m)
deg

Figure 11

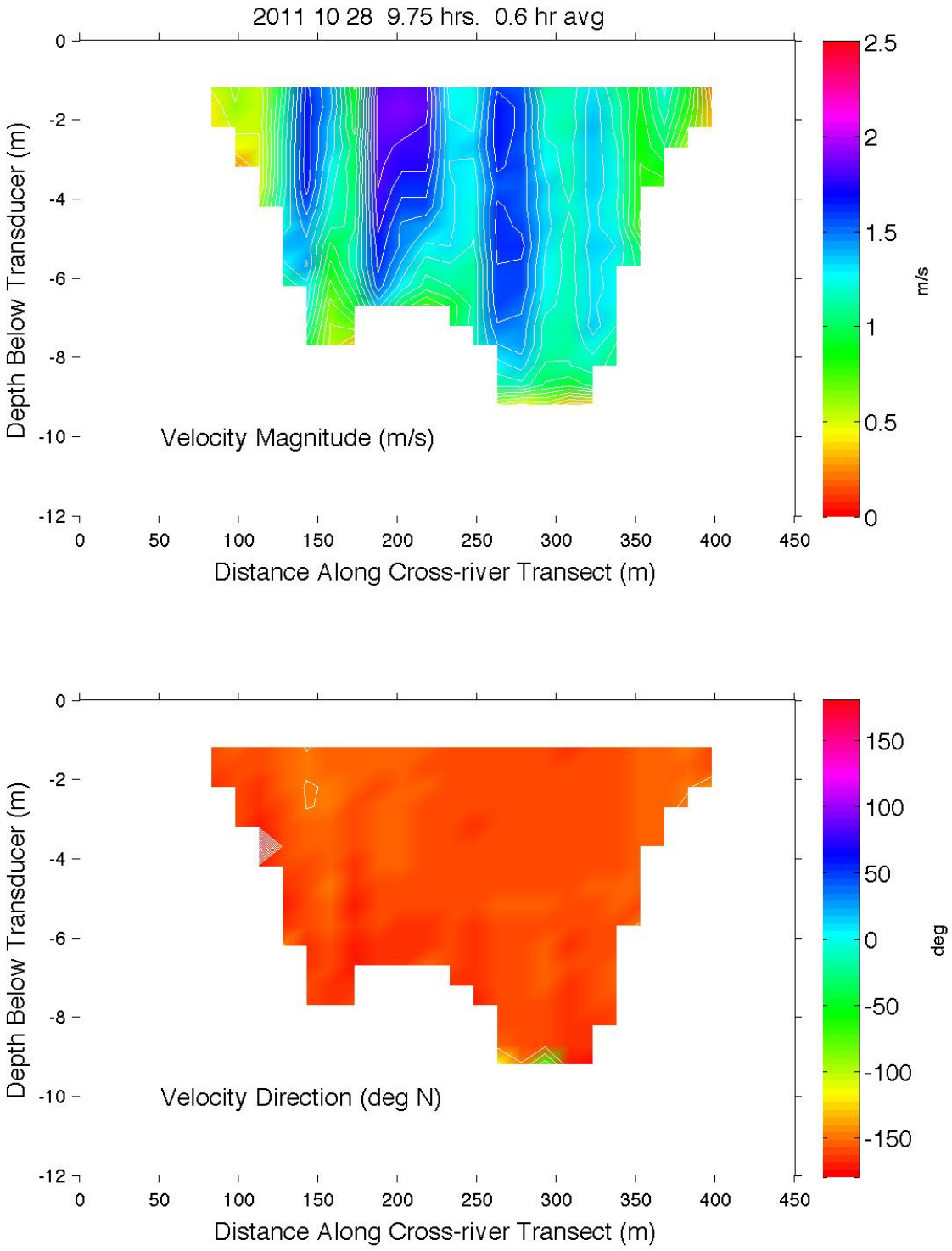
2011 10 28 9.75 hrs. 0.6 hr avg
Depth Below Transducer (m)
Velocity Magnitude (m/s)
Distance Along Cross-river Transect (m)
m/s
Depth Below Transducer (m)
Velocity Direction (deg N)
Distance Along Cross-river Transect (m)
deg

Figure 12

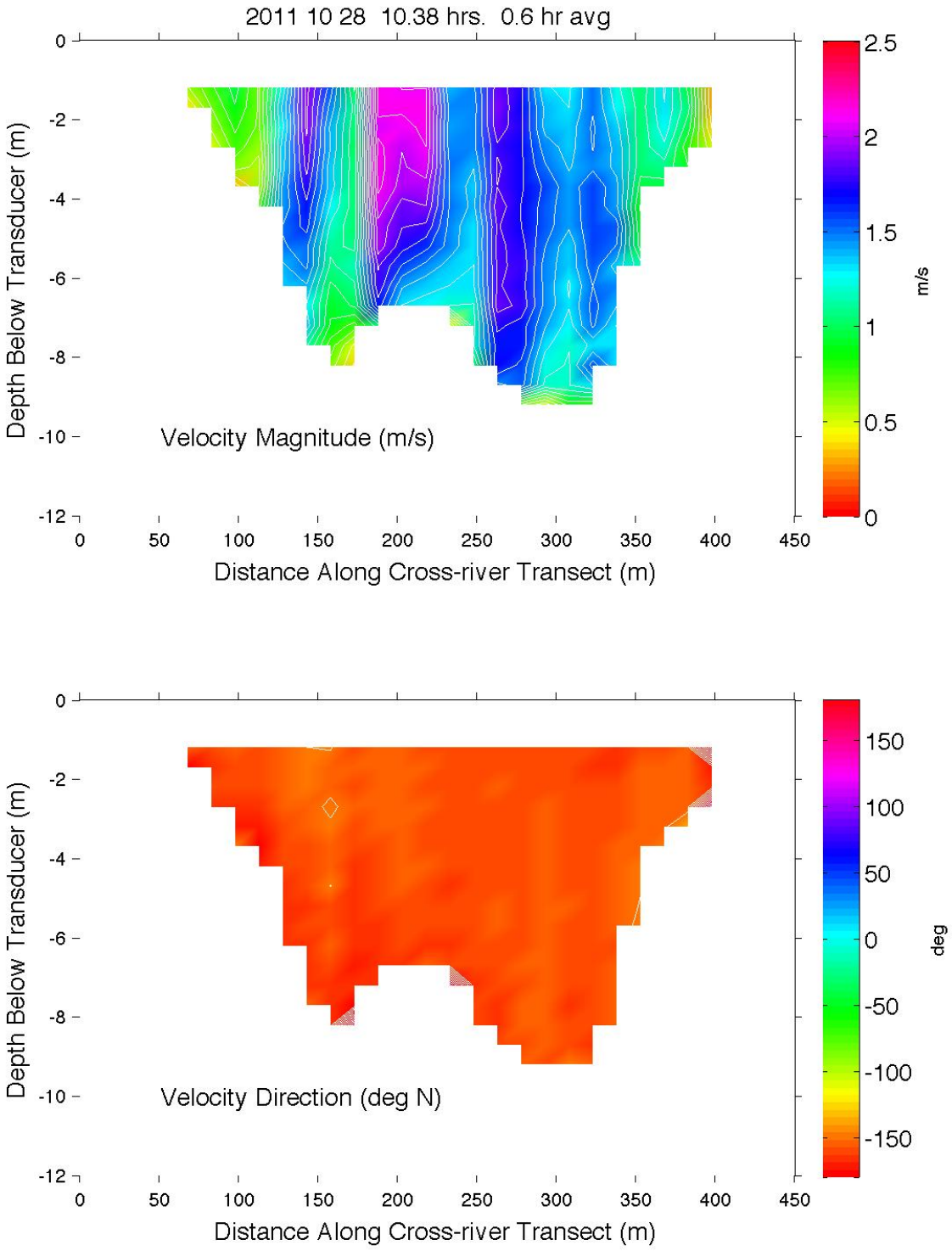
2011 10 28 10.38 hrs. 0.6 hr avg
Depth Below Transducer (m)
Velocity Magnitude (m/s)
Distance Along Cross-river Transect (m)
m/s
Depth Below Transducer (m)
Velocity Direction (deg N)
Distance Along Cross-river Transect (m)
deg

Figure 13

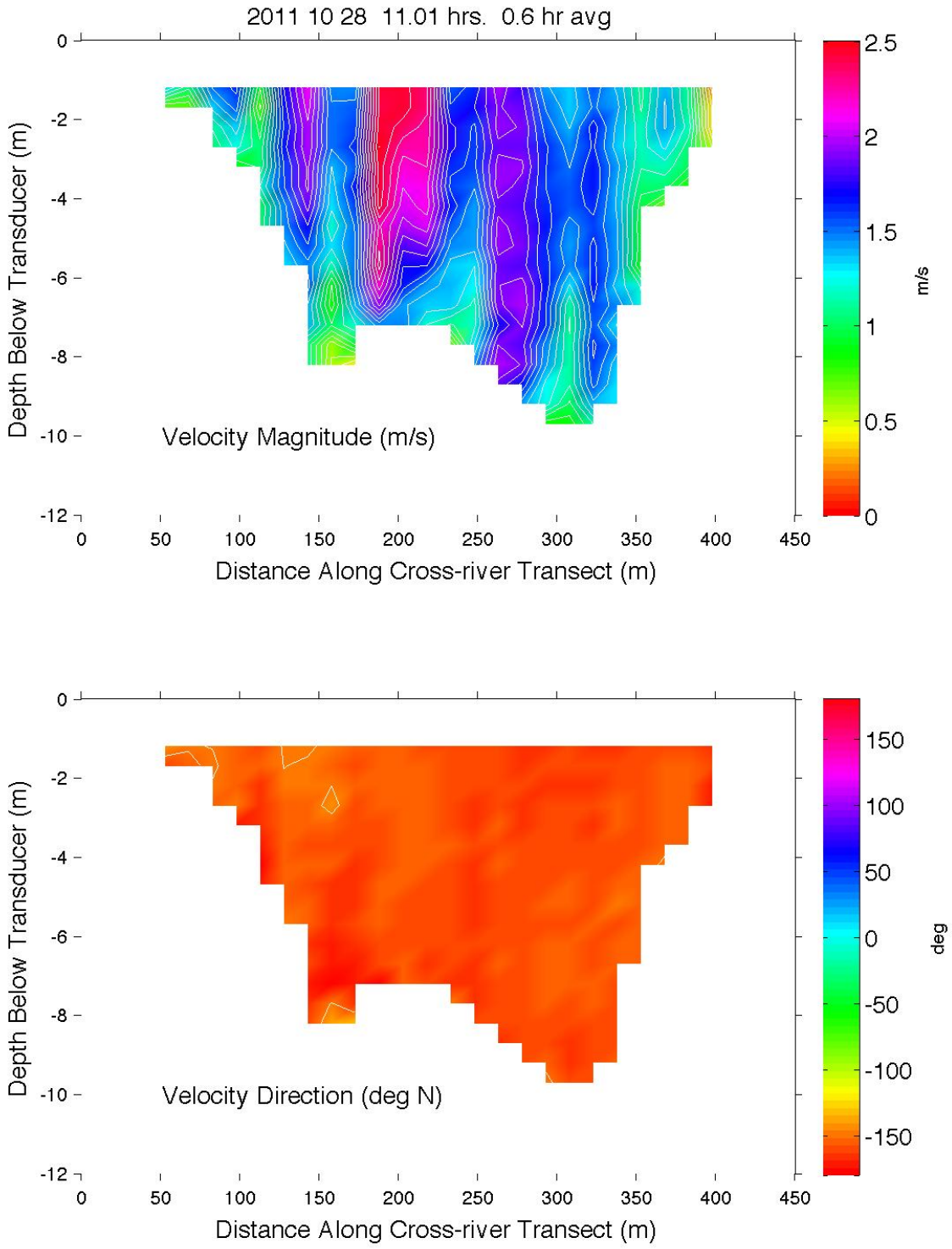
2011 10 28 11.01 hrs. 0.6 hr avg
Depth Below Transducer (m)
Velocity Magnitude (m/s)
Distance Along Cross-river Transect (m)
m/s
Depth Below Transducer (m)
Velocity Direction (deg N)
Distance Along Cross-river Transect (m)
deg

Figure 14

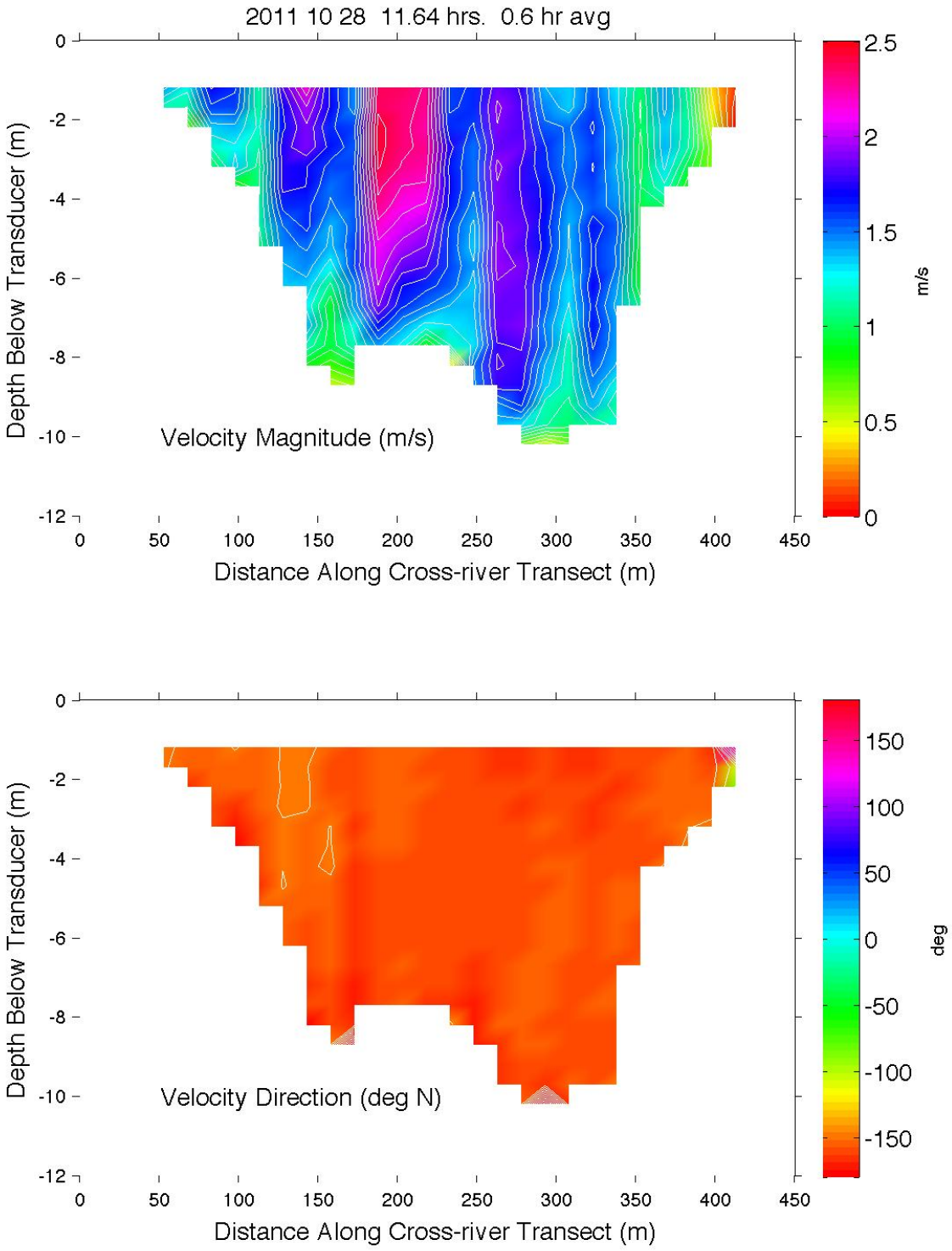
2011 10 28 11.64 hrs. 0.6 hr avg
Depth Below Transducer (m)
Velocity Magnitude (m/s)
Distance Along Cross-river Transect (m)
m/s
Depth Below Transducer (m)
Velocity Direction (deg N)
Distance Along Cross-river Transect (m)
deg

Figure 15

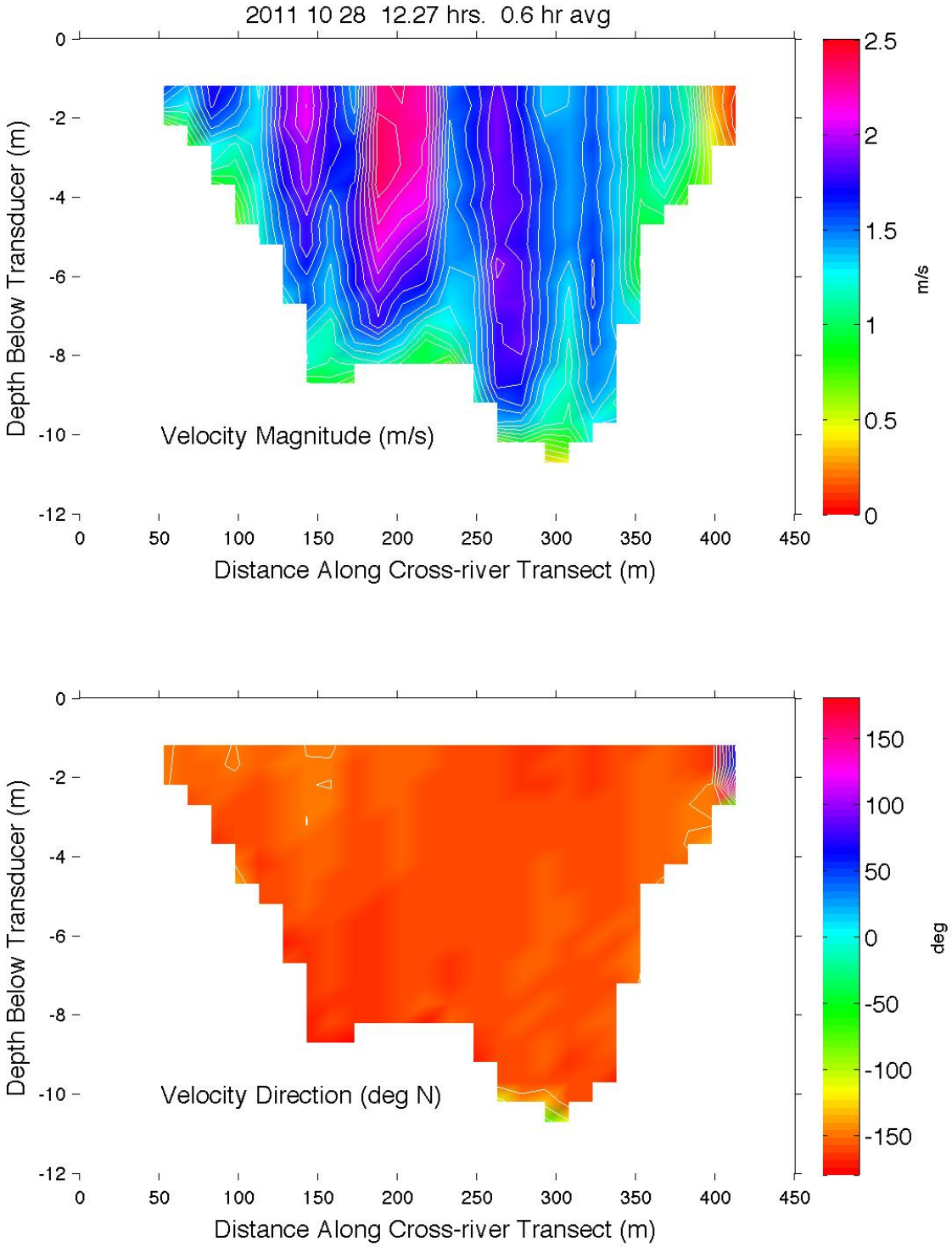
2011 10 28 12.27 hrs. 0.6 hr avg
Depth Below Transducer (m)
Velocity Magnitude (m/s)
m/s
Distance Along Cross-river Transect (m)
Depth Below Transducer (m)
Velocity Direction (deg N)
deg
Distance Along Cross-river Transect (m)

Figure 16

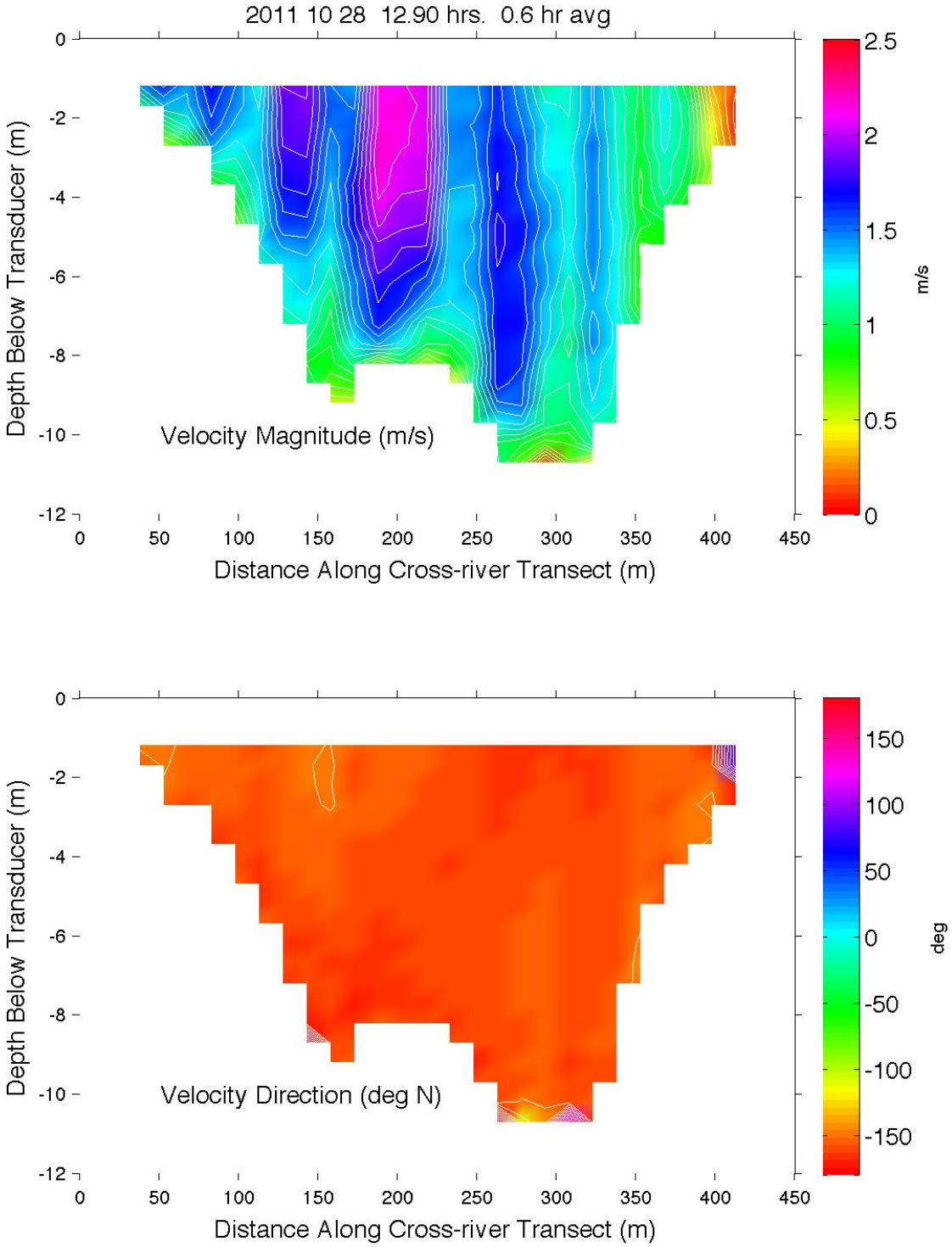
2011 10 28 12.90 hrs. 0.6 hr avg
Depth Below Transducer (m)
Velocity Magnitude (m/s)
Distance Along Cross-river Transect (m)
m/s
Depth Below Transducer (m)
Velocity Direction (deg N)
Distance Along Cross-river Transect (m)
deg

Figure 16

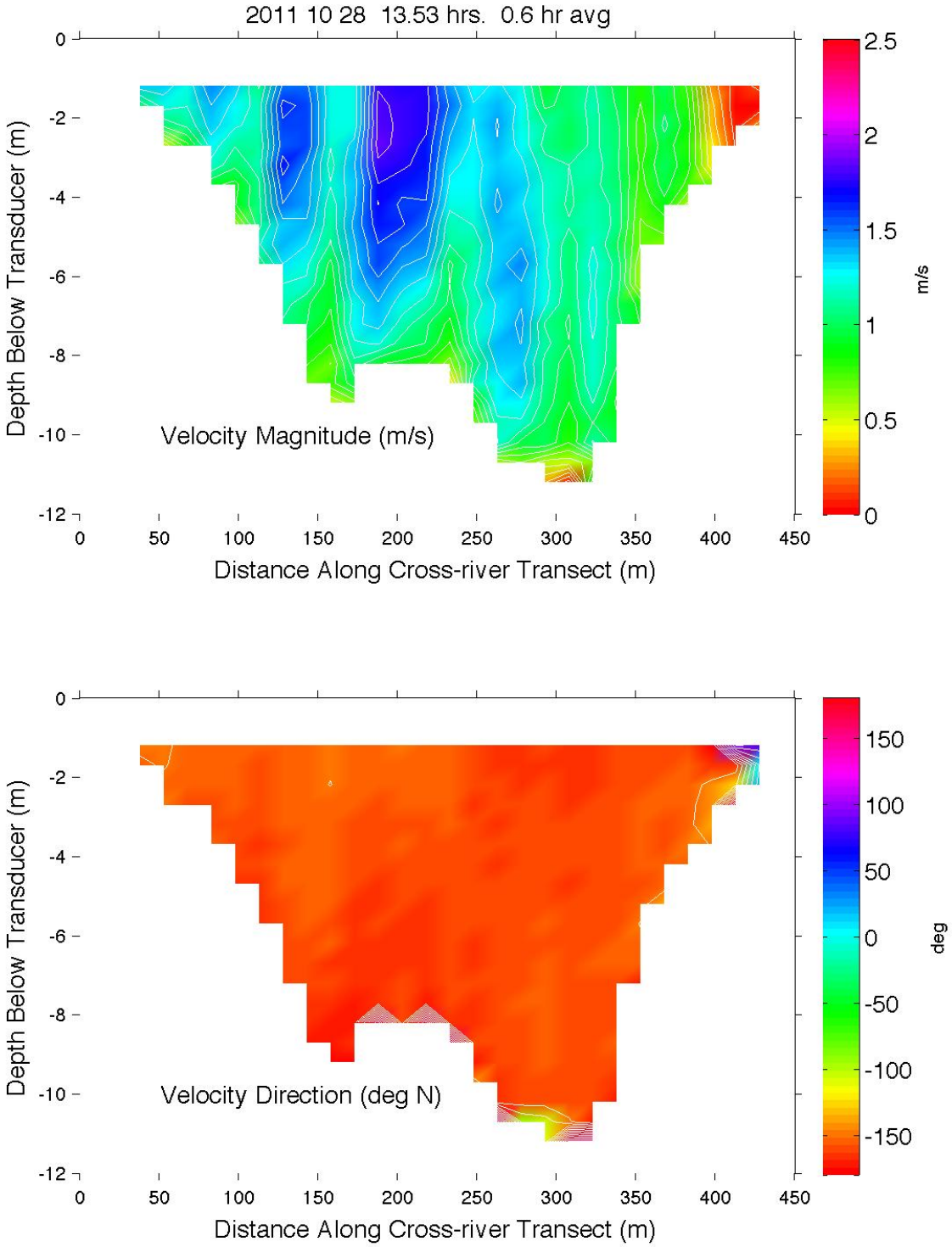
2011 10 28 13.53 hrs. 0.6 hr avg
Depth Below Transducer (m)
Velocity Magnitude (m/s)
Distance Along Cross-river Transect (m)
m/s
Depth Below Transducer (m)
Velocity Direction (deg N)
Distance Along Cross-river Transect (m)
deg

Figure 17

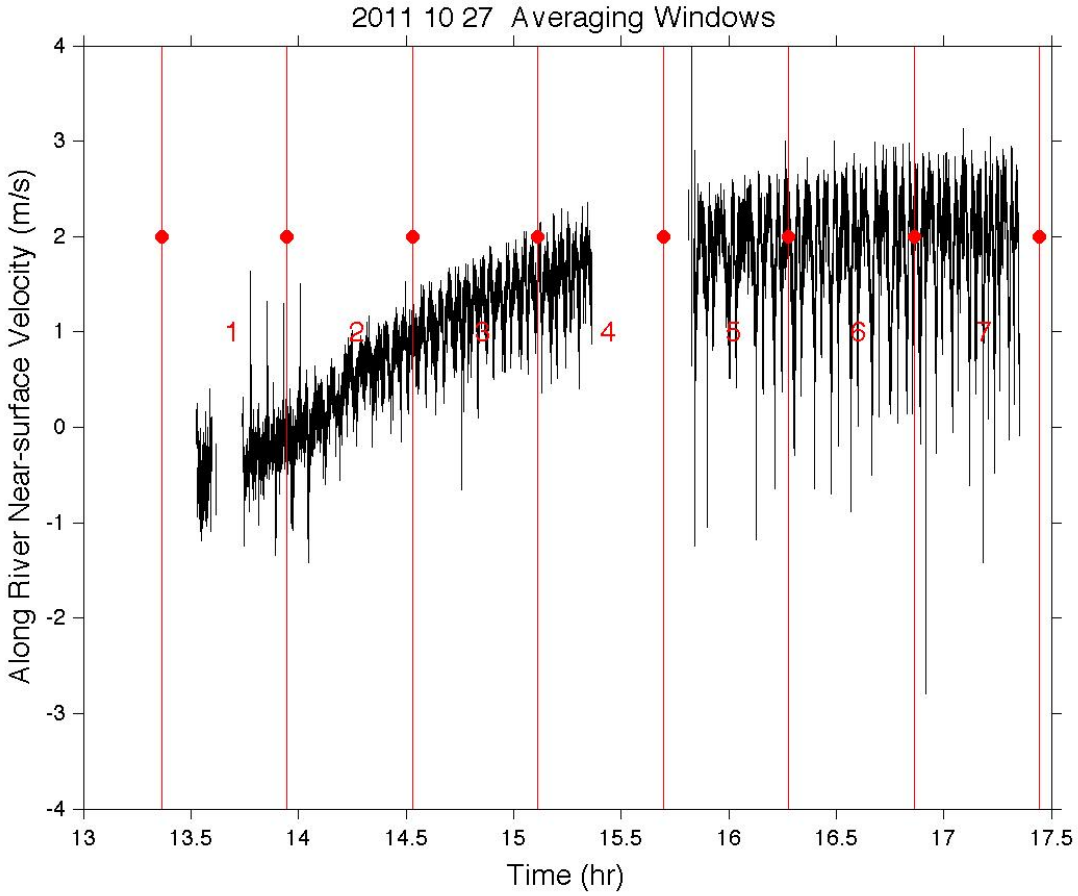

Figure 18. This plot shows the near surface velocity vs time from slack water, 0 m/s at approximately 1350, to full flow at $2^{+/-}$ m/s at 1700^{+}. Note there is 1m/s (2 knots) approximately 1 hour after slack tide.

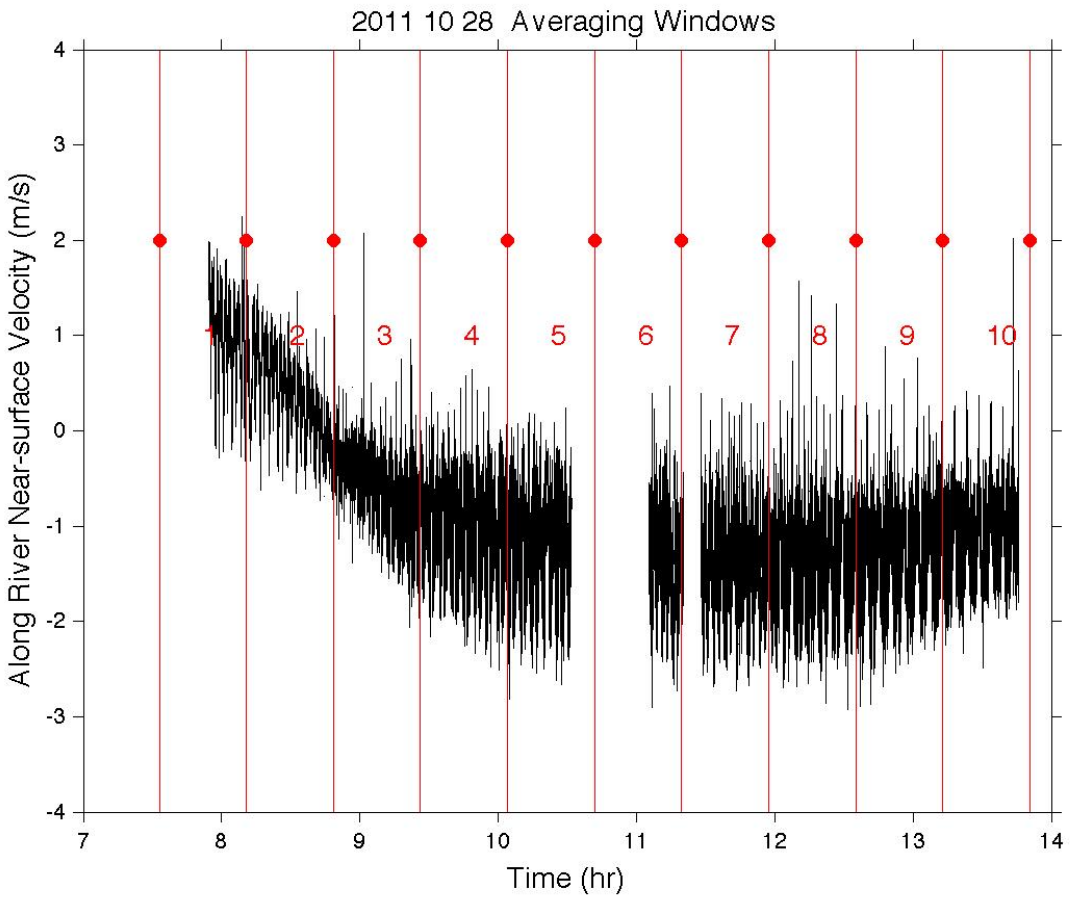

Figure 19. This plot shows the near surface velocity vs time from a high water time through slack water, 0 m/s, at approximately 900, to full flow at $2^{+/-}$ m/s at 1000^{+}. Note there is 1m/s (2 knots)less than 1 hour after slack tide.

Offshore Wave Site

In 1999, the University of New Hampshire (UNH) established an open ocean aquaculture site in 52 meters of water approximately 10 km from the New Hampshire coast in the Gulf of Maine (see Figure 20). For 10 years the site was utilized to test the engineering and biological feasibility of offshore aquaculture including the deployment of fish cages, moorings, surface buoys, etc. during this time, UNH deployed an environmental monitoring buoy to measure the waves at the site. In 2010, the aquaculture gear was removed due of shifting national funding priorities.

UNH developed a suite of expertise in the analysis, deployment and testing of floating marine structures. To support the interest of wave energy device developers looking for a test site, UNH focused on permitting the site for wave energy applications. The first task was to effectively organize all the wave data obtained over the years. Although UNH had a wave buoy present for 60-70% of the time (buoy was removed for maintenance, for example), the data stream was not continuous. In addition, UNH personnel wanted the data in a format that was similar to that employed by the National Data Buoy Center, so wave data could be easily compared across the country and other test sites.

Data were obtained from the NDBC #44005 [2]. This buoy was found to have similar wave characteristics as the UNH site, as documented by Fredriksson (2001) [3]. The wave data presentation was done using locally written MatLab code to perform the requisite spectral analysis and present the significant wave height and period and statistical values on a daily basis. The maximum, mean and standard deviation of the significant wave height and dominate period for each hour of data were obtained. These data were then grouped into days, and plotted for each month. This presentation provides the interested developer with an easily understandable perspective about what to expect at the site during specific periods of time during the year.

The results for calendar year 2009 are displayed here. Any ‘missing’ days are due to data not being available from the source. The primary reason for these holes is a buoy malfunction followed by the time period necessary to re-establish the sensor functionality. These data will eventually be available on a UNH/CORE server/website for developer and other users.

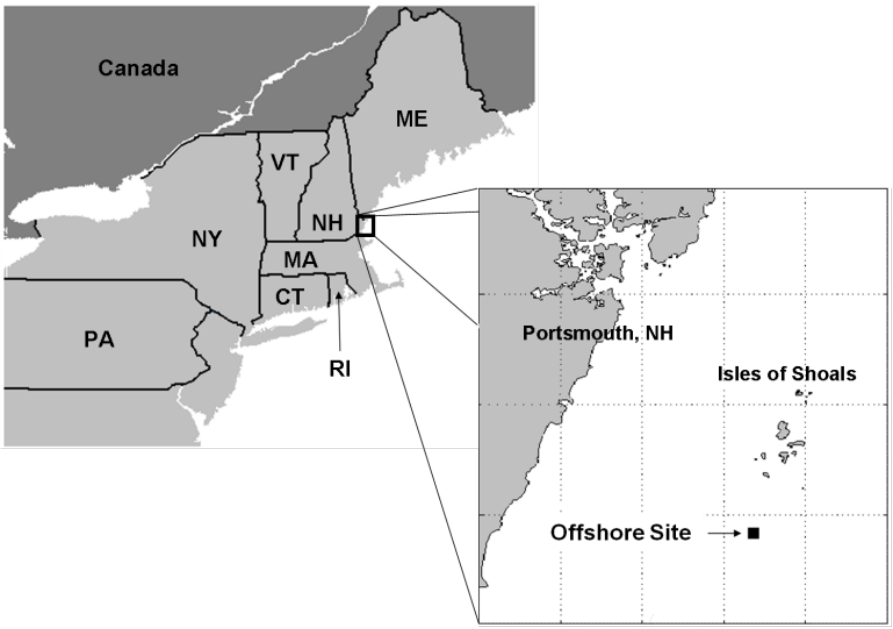

Figure 20. UNH offshore site is located 10 km from Portsmouth NH and is 52 m deep.

The following plots, Figures 21 - 32 are the monthly presentations of the wave data. The *mean* is the average value of the significant wave height, $H_{1/3}$, based on 24 , $H_{1/3}$ determinations per day. The *range* shows the upper and lower limits of $H_{1/3}$ for each day. The *standard deviation* is based on the 24 daily determinations of , $H_{1/3}$.

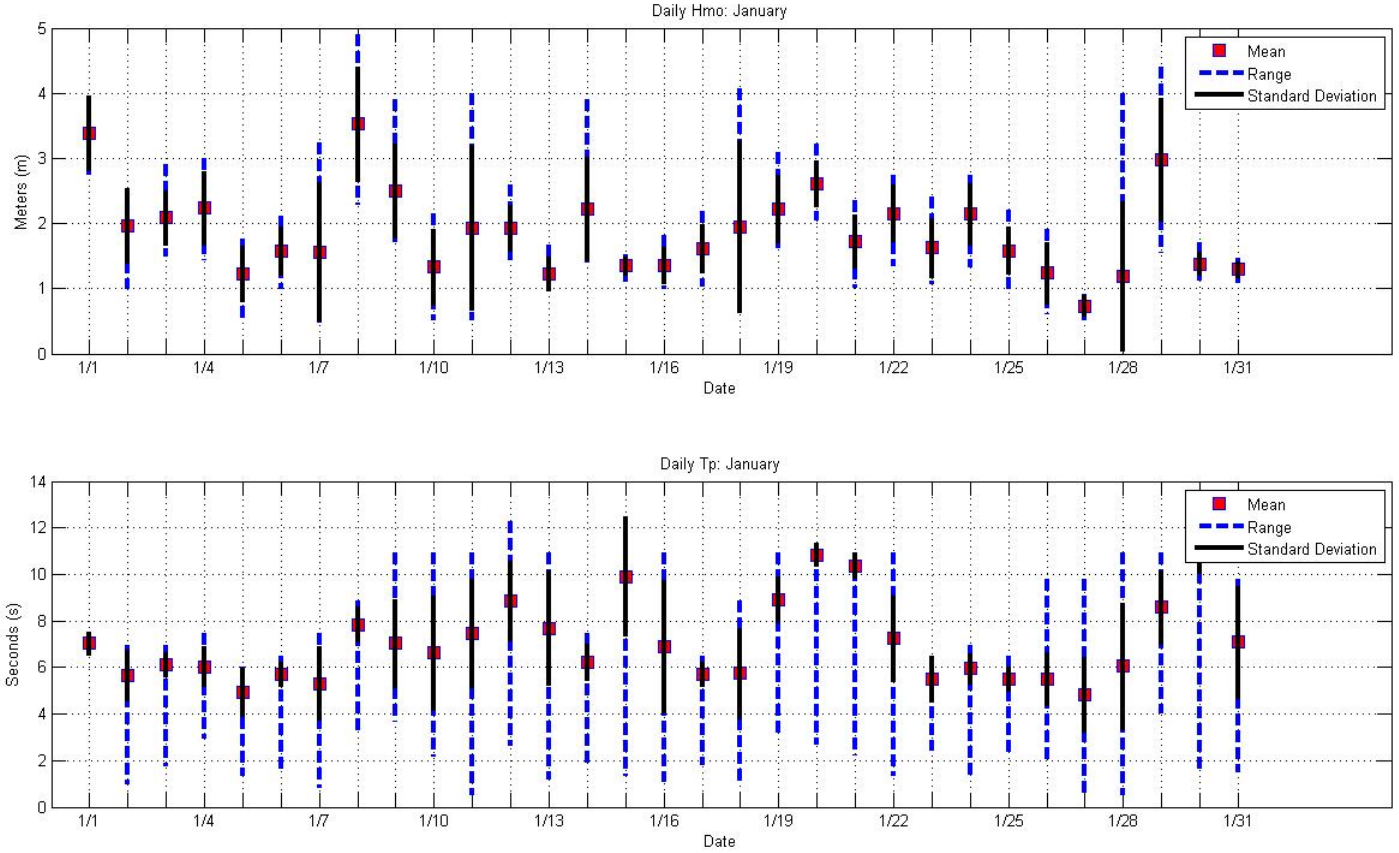

January 2009

Figure 21

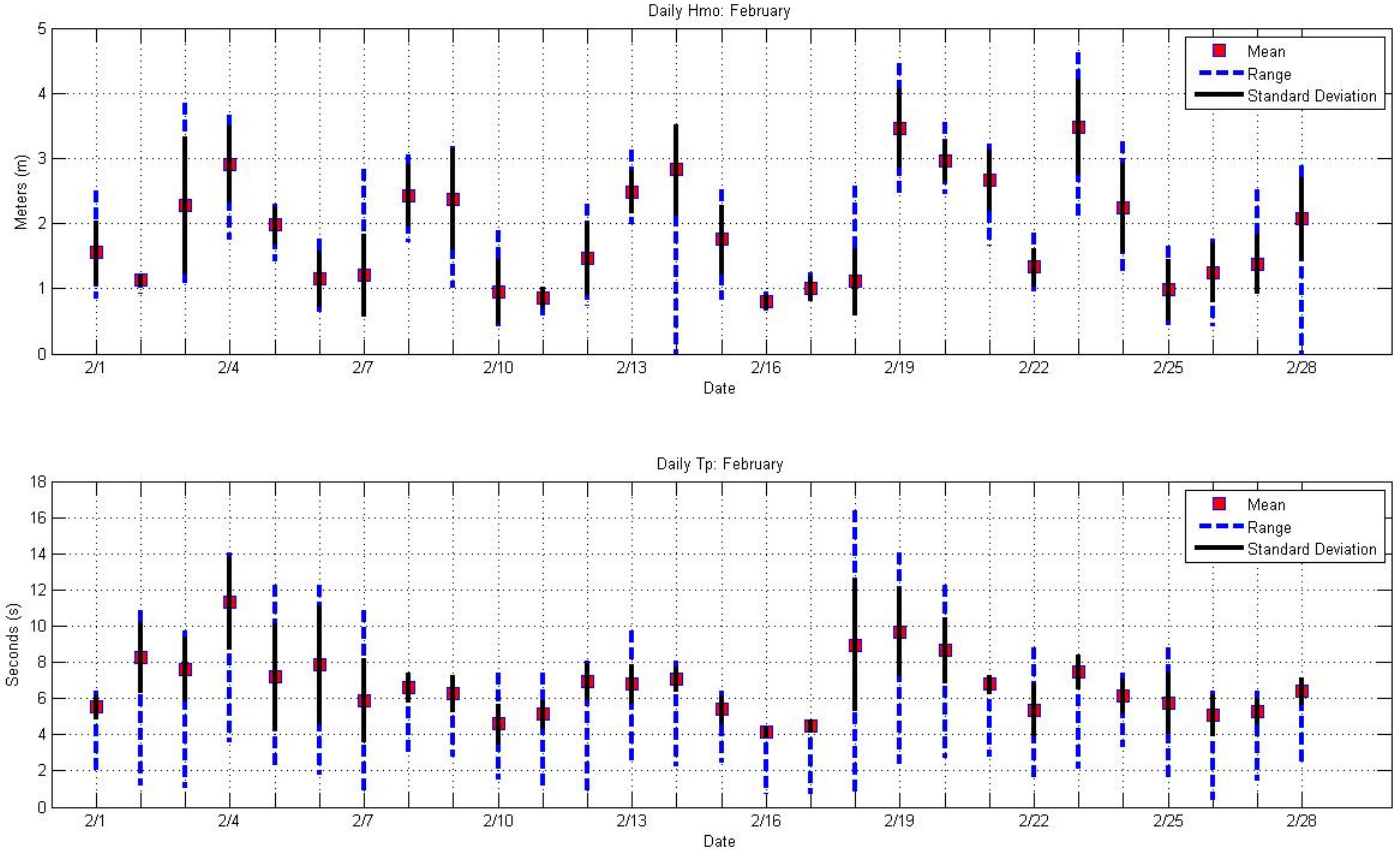

February 2009

Figure 22

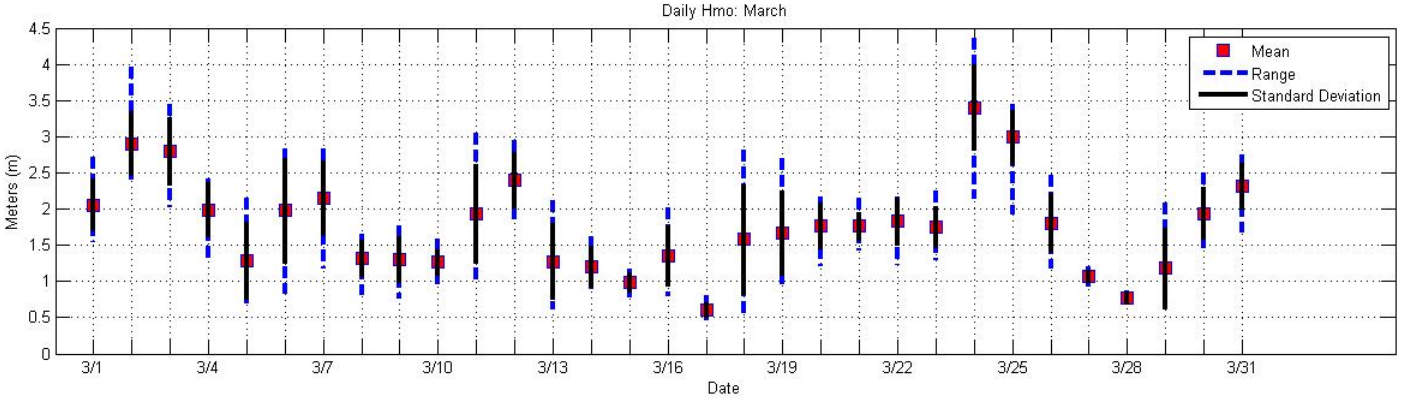

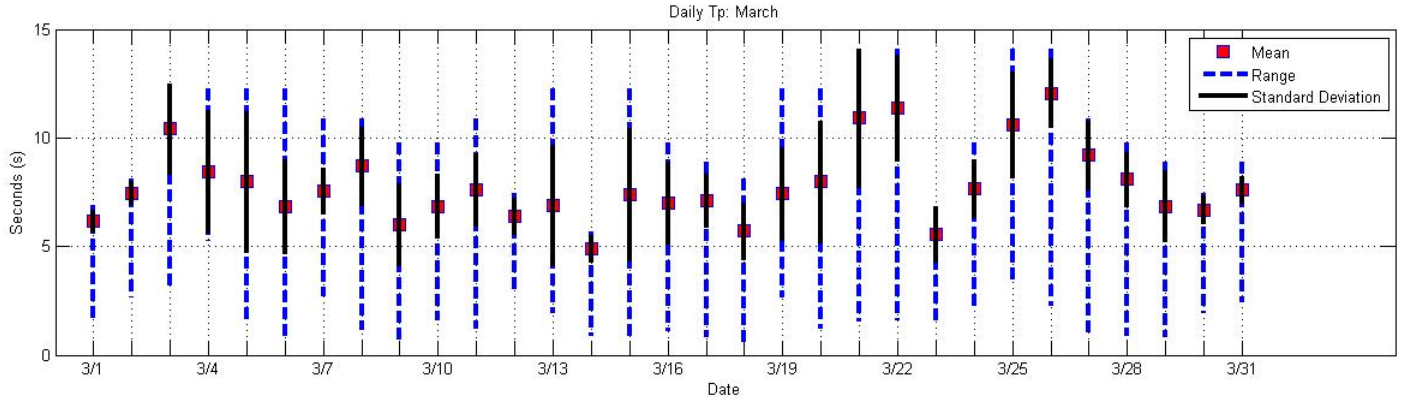

March 2009

Figure 23

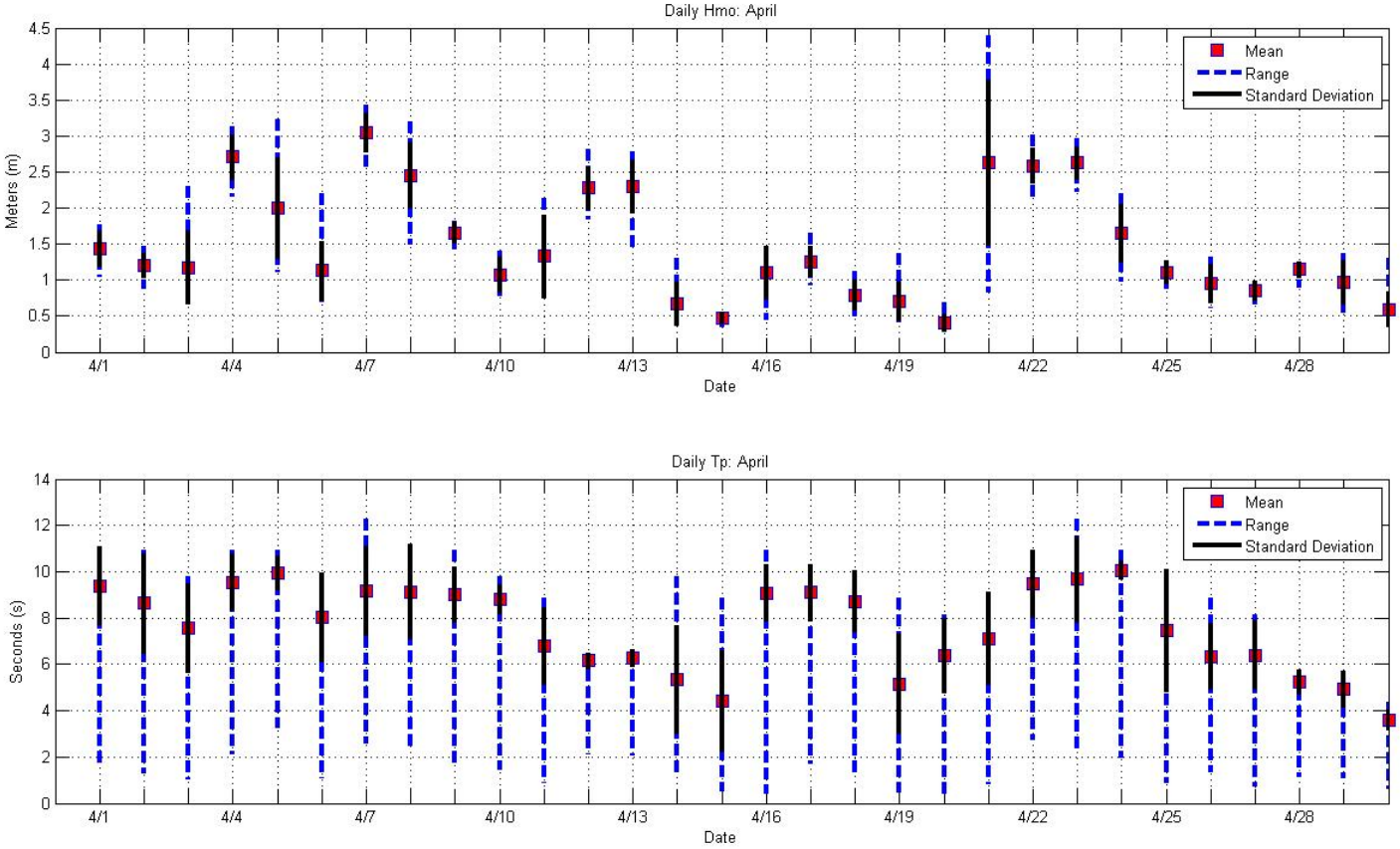

April 2009

Figure 24

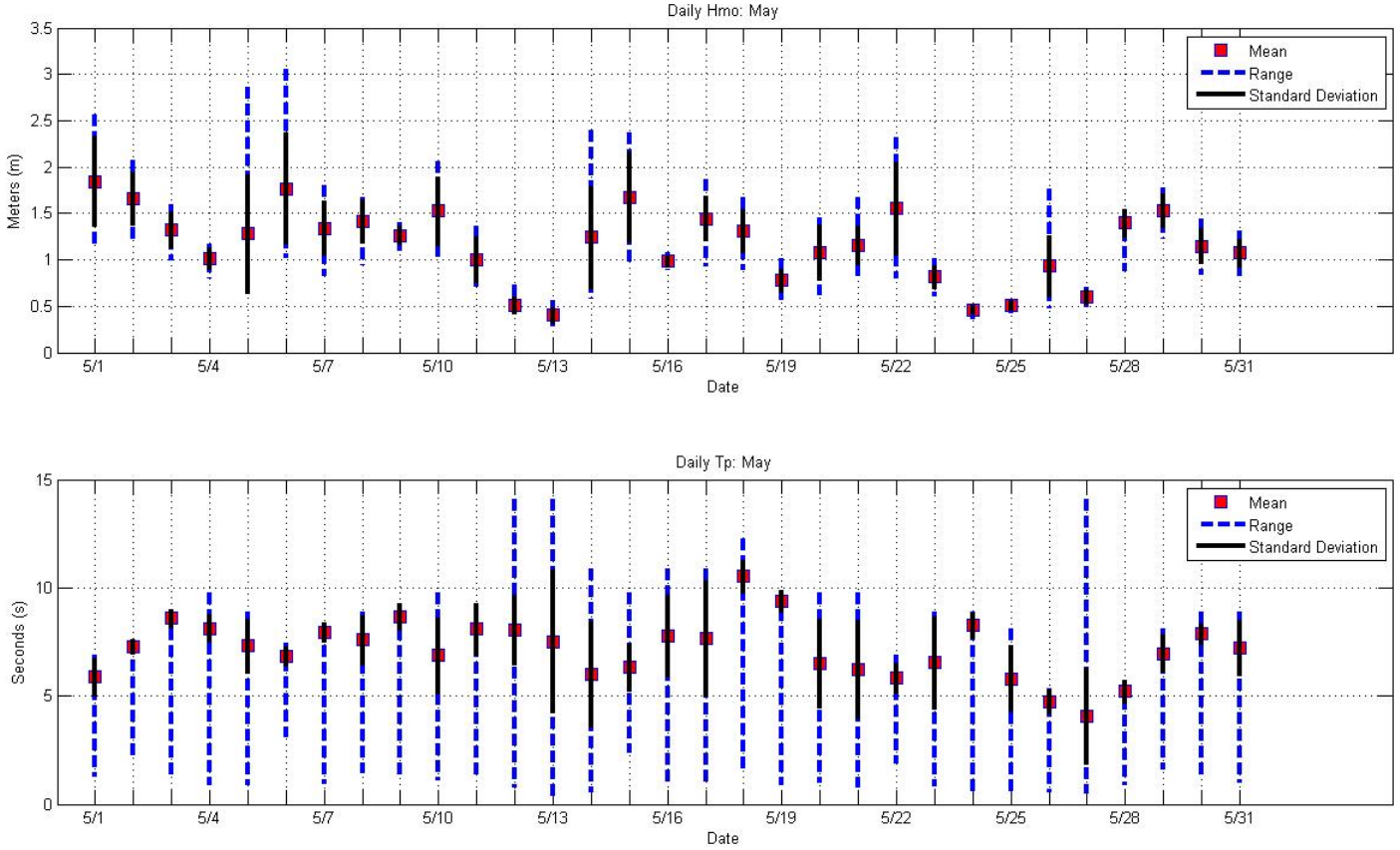

May 2009

Figure 25

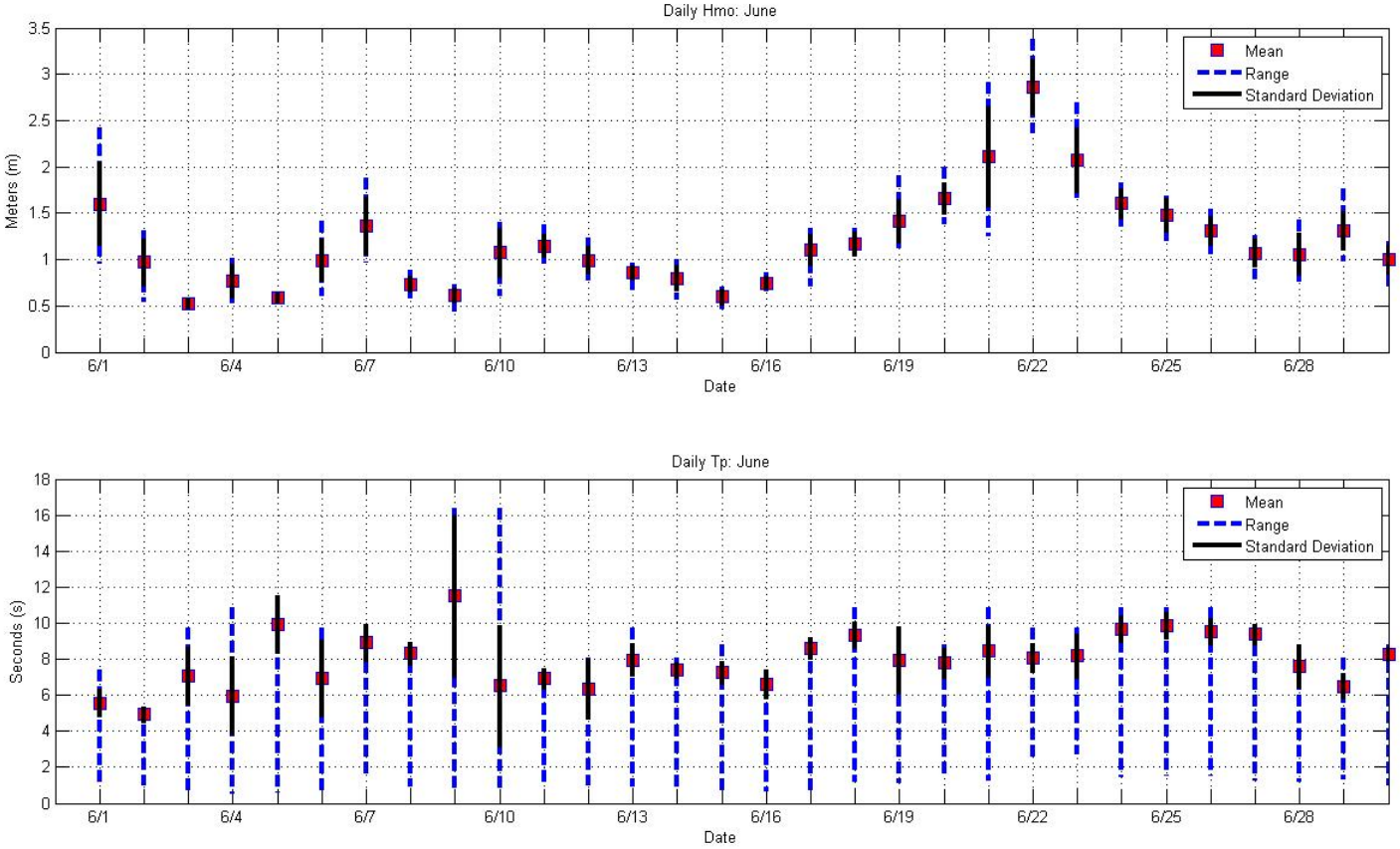

June 2009

Figure 26

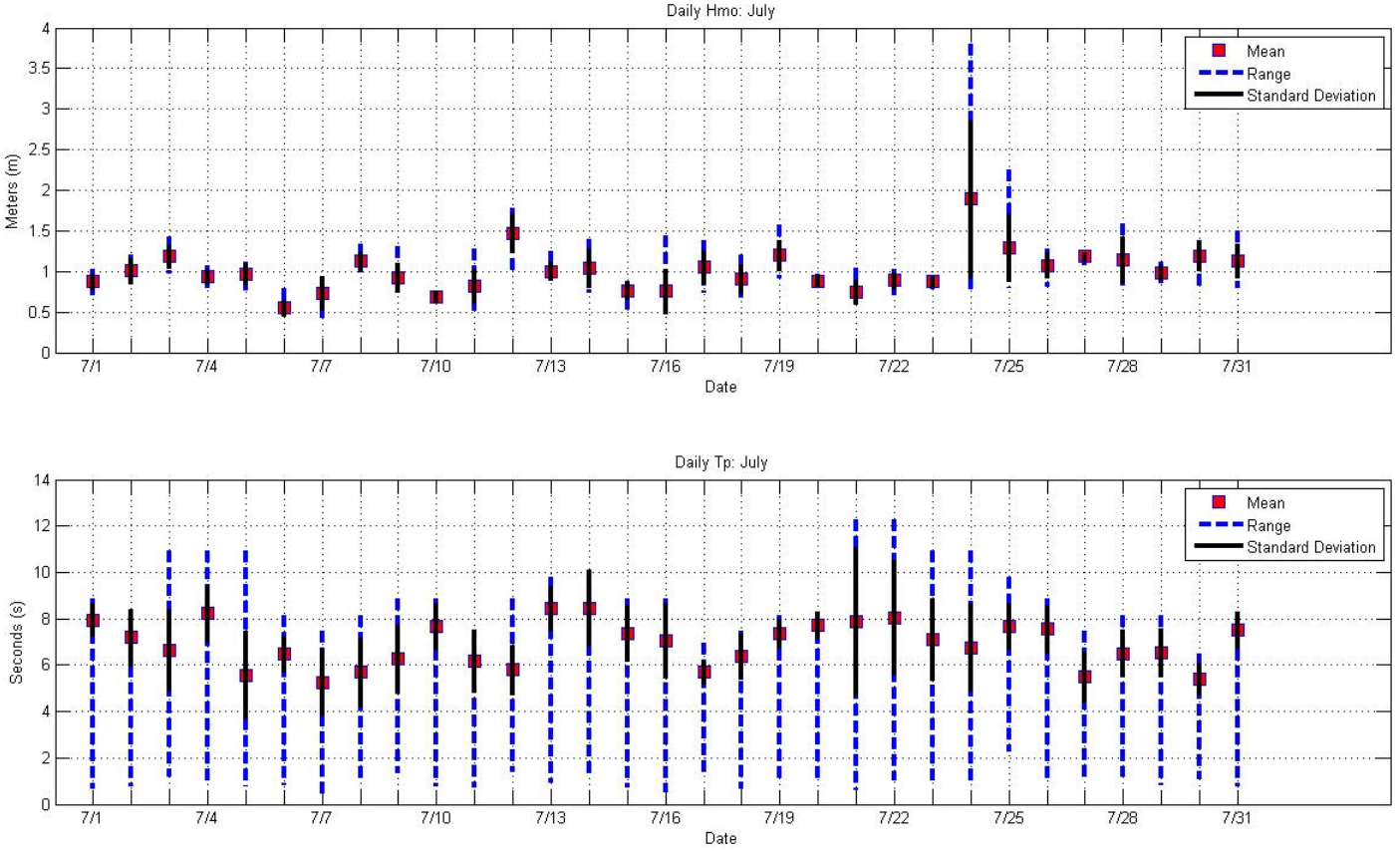
Daily Hmo: July
Meters (m)
Date
Mean
Range
Standard Deviation
0
0.5
1
1.5
2
2.5
3
3.5
4
7/1
7/4
7/7
7/10
7/13
7/16
7/19
7/22
7/25
7/28
7/31
Daily Tp: July
Seconds (s)
Date
Mean
Range
Standard Deviation
0
2
4
6
8
10
12
14
7/1
7/4
7/7
7/10
7/13
7/16
7/19
7/22
7/25
7/28
7/31

July 2009

Figure 27

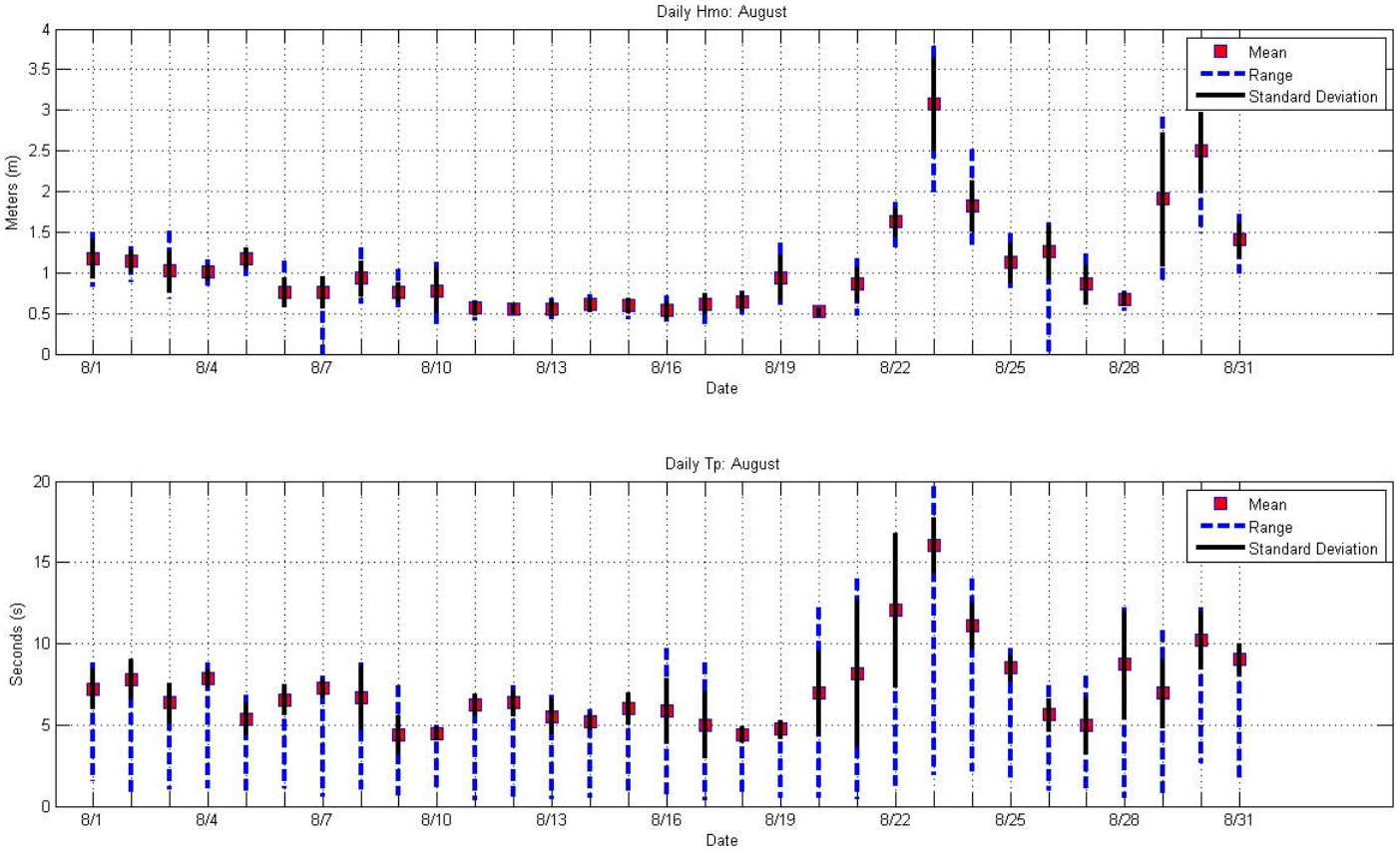

August 2009

Figure 28

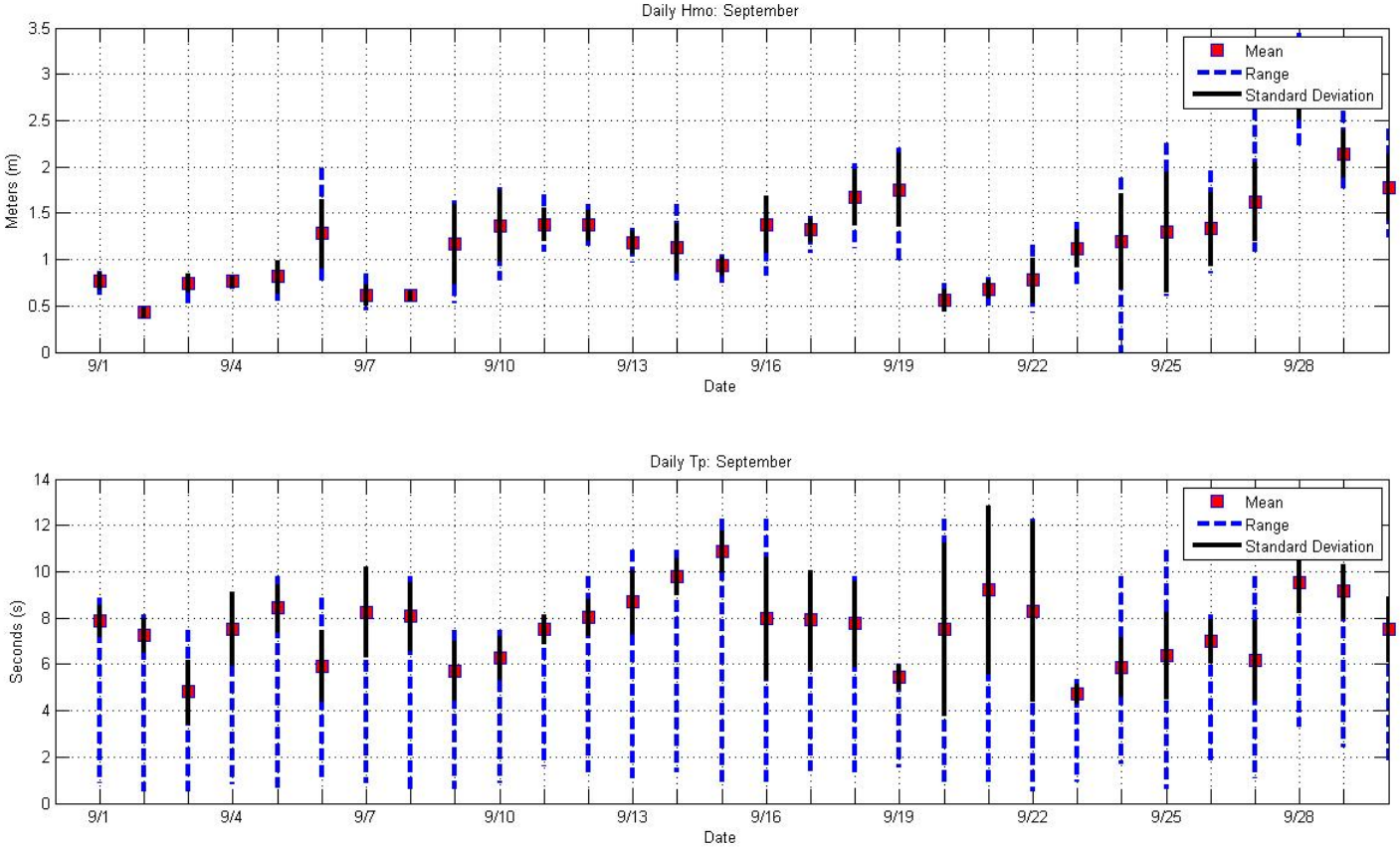

September 2009

Figure 29

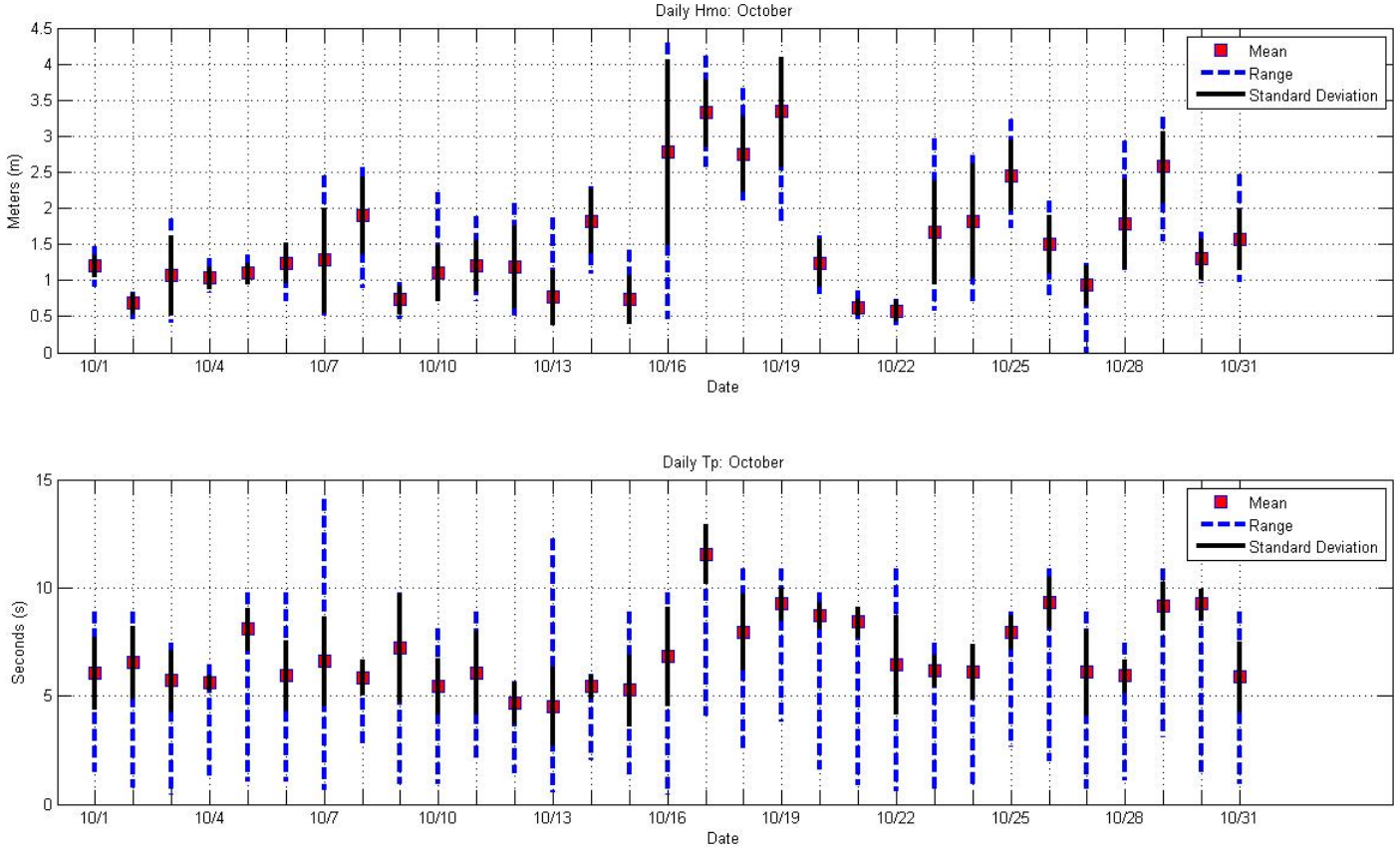

October 2009

Figure 30

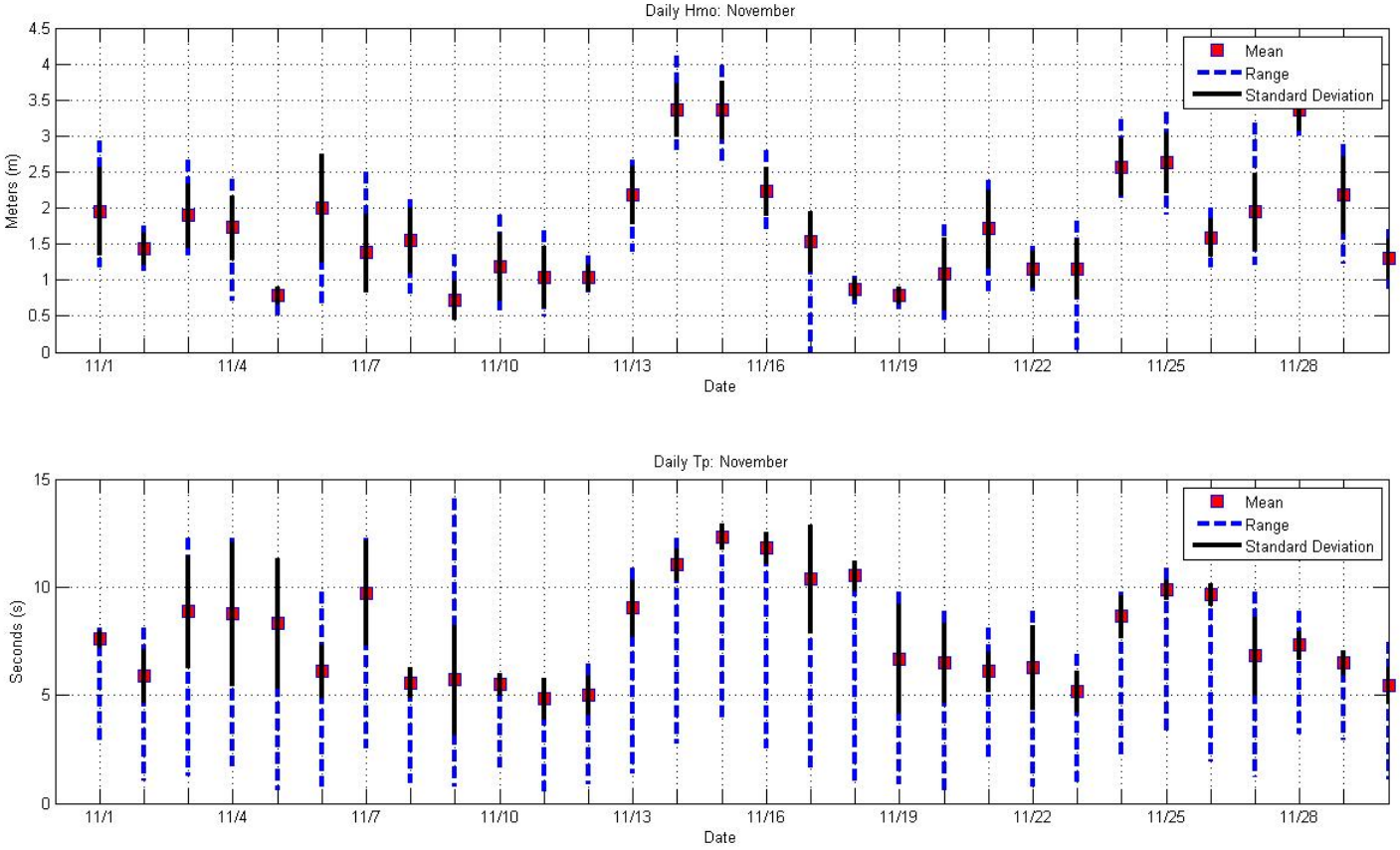

November 2009

Figure 31

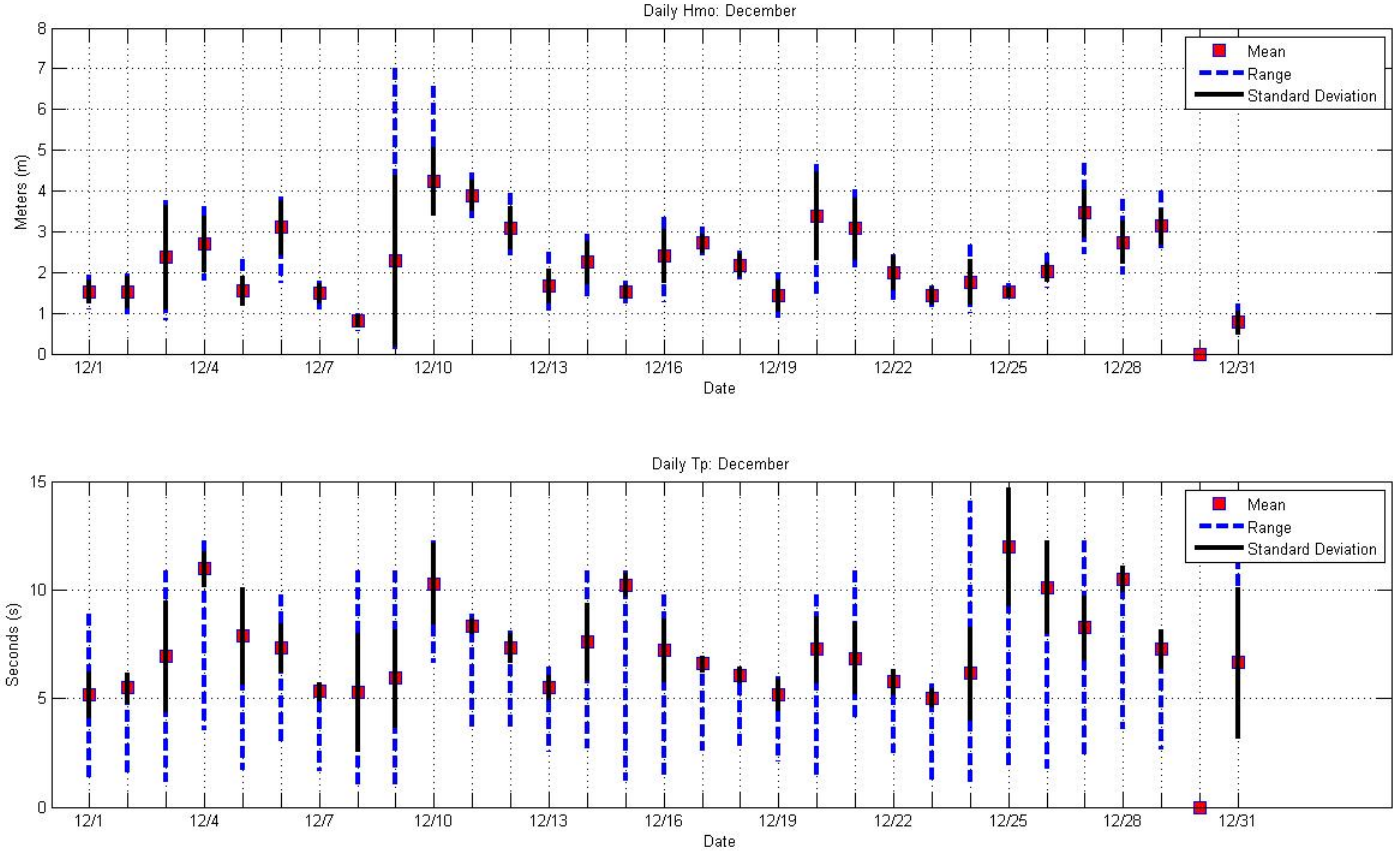

December 2009

Figure 32

The following figures are from an earlier report. The ADCP transects were acquired using the R/V Gulf Challenger. The ADCP transects cover the portion of the cross section where the tidal energy test platform will be moored. The broad red arrow in each of the plots indicates the area of specific interest for tidal energy testing. The stage of the tide, ebb or flood, is indicated on the pictures showing the location of the ADCP transects relative to the GSB. During these measurements the current speed was greater than 2.0 m/sec, which is effectively 4 knots, at the section indicated by the red arrow. The darker blue areas on either side of the arrows are the bridge piers. Because the measurements were all made downstream from the bridge the flow behind the piers is slower. Downstream is contingent on the tidal stage as indicated.

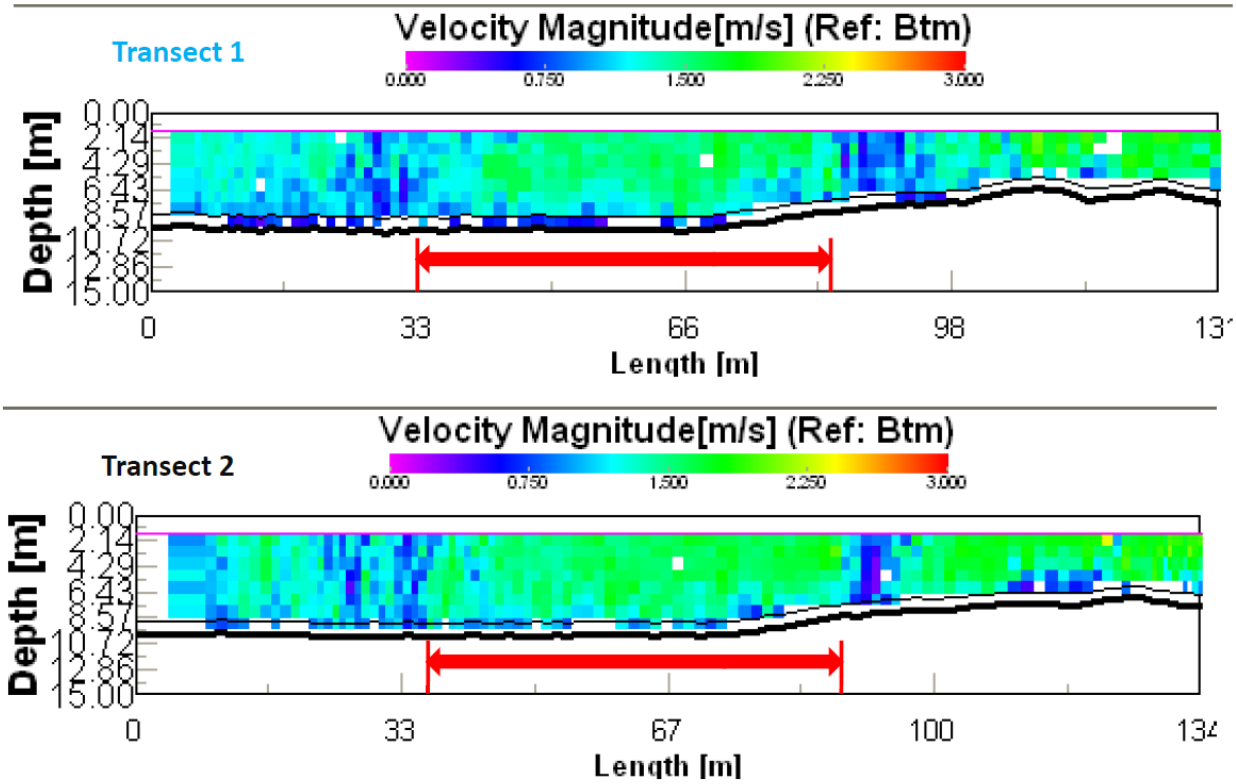

Figure 33. Incoming, flood, tide ADCP current profiles at the GSB site are show at two different times on the same flood event 14 October 2010. The broad red arrow indicates the location of interest.

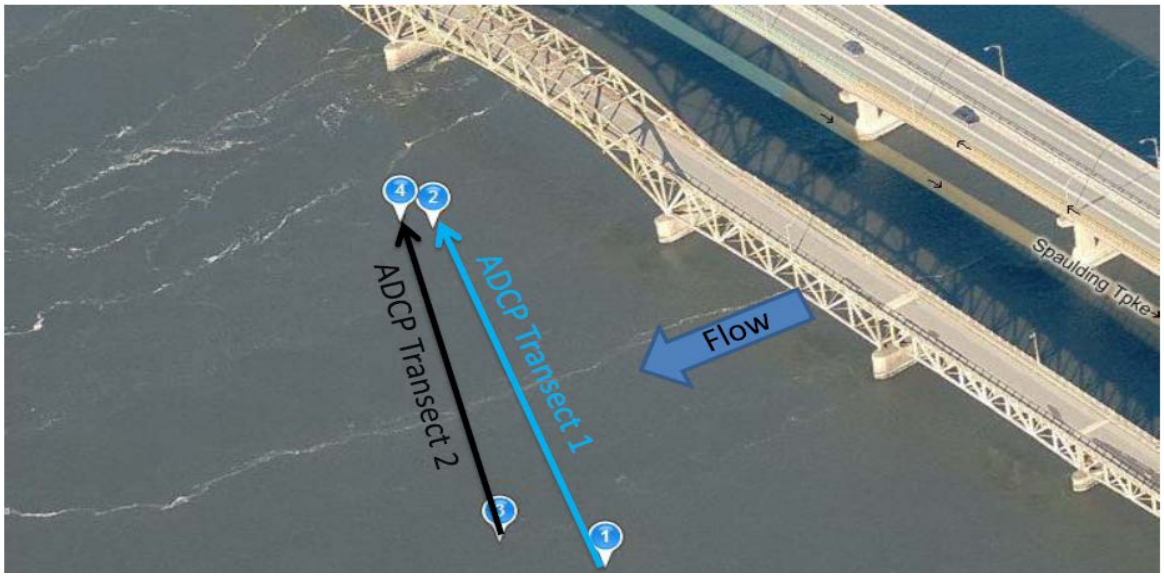

Figure 34. The ADCP transect locations superimposed on an aerial photograph of the GSB site.

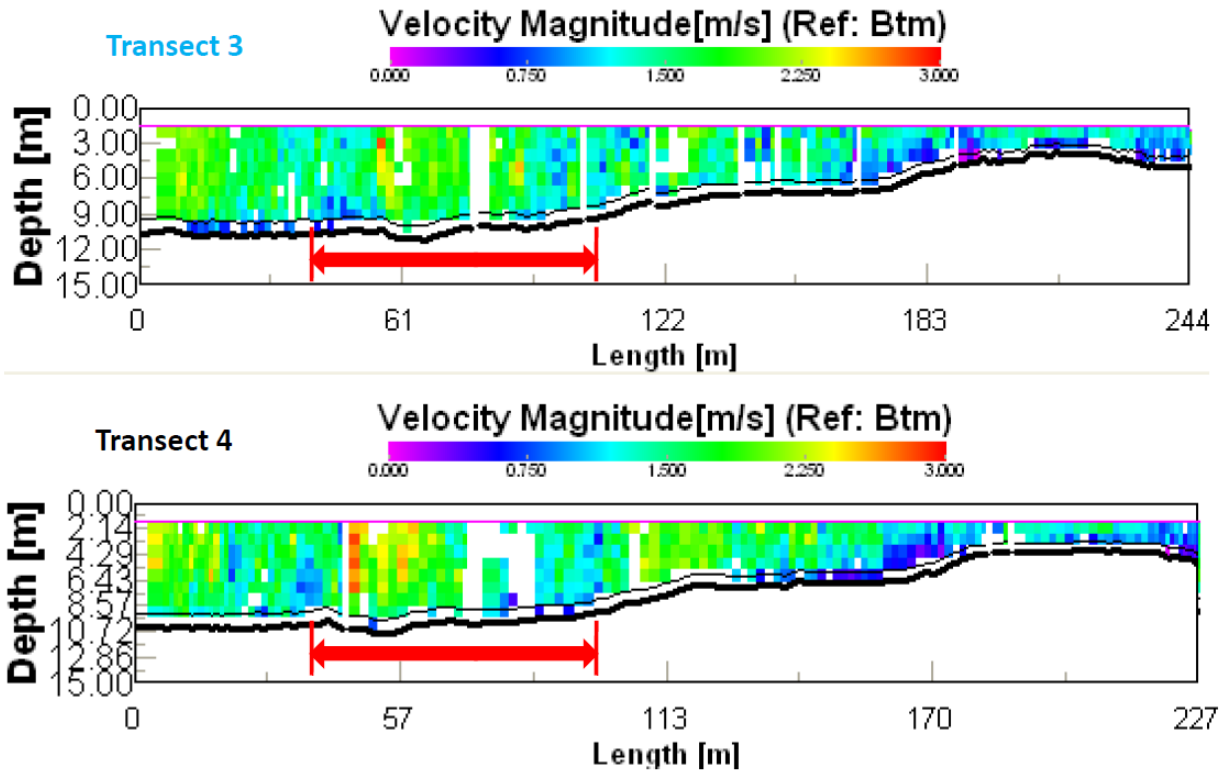

Figure 35. Ebb tide ADCP current profiles at the GSB site for two different times on the same ebb tide event 21 October 2010. The broad red arrow on the length axis indicates the location at span six (6).

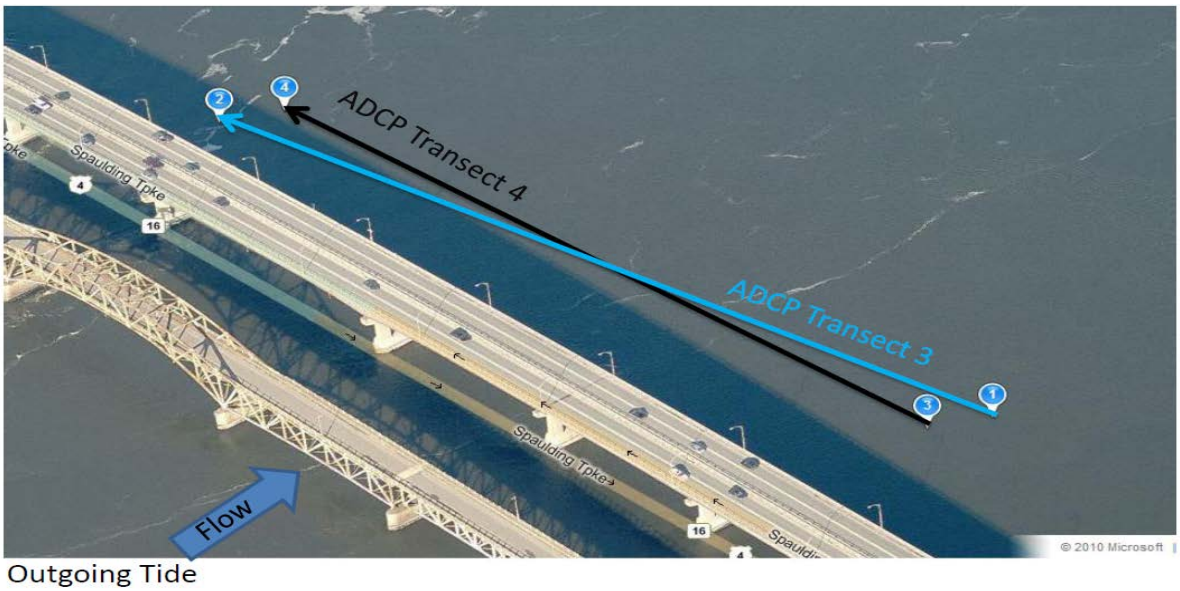

Outgoing Tide

Figure 36. The ADCP transect location are superimposed on an aerial photograph of the GSB site. Note the ebb tide direction is indicated by the Flow arrow.

References

[1]. Lippmann, T. C., and G. M. Smith, Shallow surveying in hazardous waters, *U. S. Hydro '09.*, http://www.ushydro2009.com, 1-11, 2009.

[2]. National Data Buoy Center, NDBC #44005, http://www.ndbc.noaa.gov/

[3]. Fredriksson, D.W, (2001). *Open Ocean Fish Cage and Mooring System Dynamics*. Ph.D. Dissertation submitted to the University of New Hampshire in partial fulfillment of the Engineering Systems Design Program. Durham, NH.

Final report

Development of an Integrated Design Tool for Wave Energy Conversion Devices used to Power Coastal Surveillance Systems

Principal Investigator: A. Grilli, Res. Asst. Prof.

Prepared by Annette Grilli and Taylor Asher
for
New England Marine Renewable Energy Consortium

April 13, 2011

Department of Ocean Engineering
University of Rhode Island

1. BACKGROUND AND RESEARCH CONTEXT

Since 2006, as part of projects funded by ONR (SBIRs and STTRs) and the State of Rhode Island (STAC Alliance), the University of Rhode Island (URI) and Electro Standards Laboratories Inc. (ESL) have teamed up to work on the design, numerical simulation, and scale model and field testing, of small buoy systems for multi-directional wave energy harvesting (free-floating or slackly moored). The targeted application for these systems is not large energy production for single units (except perhaps in a buoy farm configuration), but instead the development of simple, easily deployable, and storm resilient systems, to provide a renewable wave power source of (order of 1 kW) for distributed marine surveillance and instrumentation systems (e.g., autonomous target recognition instruments, persistence and ubiquitous sensor systems, tracking and identification of maritime vessels, and miniature underwater sensor networks). The targeted full scale sea state in this work is the 20 year mean sea state for RI shelf waters (south of Block Island), which has a modest expected wave power density on the order of 3.2 KW/m of wave crest, for a mean significant wave height on the order of H_s = 1.2 m and a mean peak spectral period on the order of T_p =4.5 s.

Several buoy design alternatives were evaluated, through a combination of theoretical analyses and numerical simulations for periodic or irregular waves. This led to selecting two buoy designs (referred to as DC2 and DC3). In both systems, wave mechanical energy induces buoy motion, which then produce electricity by way of induced coupled oscillations of a Linear Electric Generator (LEG) located in a central spar buoy/canister. The LEG is simply made of a permanent magnet, suspended to a spring, oscillating within a two-phase coil. In all cases, the main mode of wave energy harvesting is heave motion, with secondary roll oscillations. DC2 is a non-resonating wave compliant system, while DC3, which is the main object of the present work, is a multi-spar buoy tuned to resonate in heave at the peak frequency of the targeted sea state (Fig. 1).

For both designs, 1:10 scale models were built and tested in URI's wavetank (Fig. 1a); numerical models simulating the buoys' mechanical motion in waves, as well as electrical power generation, were developed and calibrated based on experimental results. These were then used to design 1:4 scale ruggedized mini-prototypes of each design, to be field tested (Fig. 1b). Such field tests were conducted in Narragansett Bay, RI for the DC3 design, under properly scaled

wave climates (Fig. 1c). As part of another ongoing project, similar field tests should soon be conducted for DC2.

(a) (b) (c)

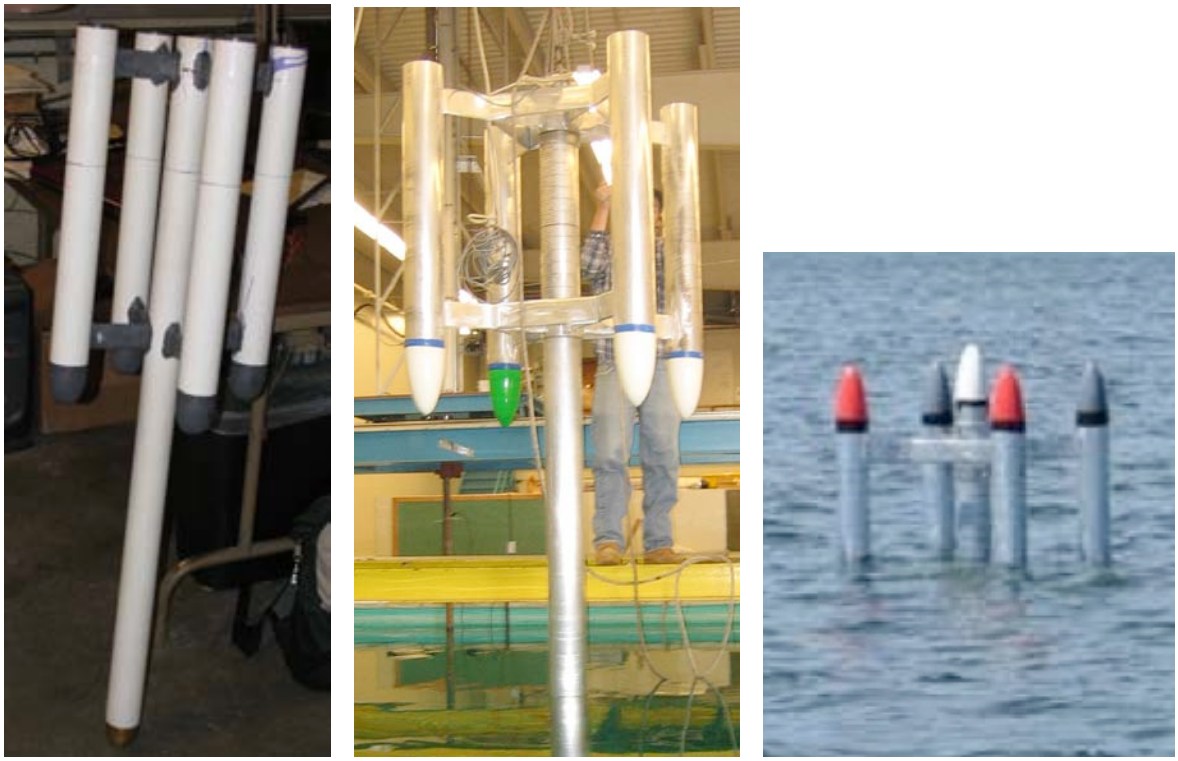

Figure 1 : Wave energy buoy DC3: (a) 1:4 scale model; (b) static testing of 1/4 scale mini-prototype partial assembly; (c) ocean testing of the latter.

In this work, an interactive tool was developed to optimize design parameters of wave energy buoys such as DC2 and DC3. The tool was developed and tested for the DC3 design and, although similar in principle, further work would be necessary to extend it to the DC2 design. Earlier work conducted on a multiple spar design, precursor of DC3, was reported by Grilli et al. (2007) (this work also includes a short literature review and background on point-absorber types of wave energy buoy systems; see also Previsic et al., 2004), and work on the LEG and its specific circuits for optimizing electricity production and storage was presented by Bastien et al. (2009). The most recent testing and numerical simulation results for both designs are presented in (Grilli et al, 2011).

Three major, linked sub-systems, are considered in each buoy design such as DC3, the: (i) *floating buoy dynamics* under wave action; (ii) *LEG dynamics* resulting from buoy motions; and (iii) *LEG electrical dynamics*. In the most general case, feedback between sub-systems must be considered to optimize the buoy system's overall performance. As an example, the movement of the armature will result in a change of the weight distribution and hence impact the buoy motion. Similarly the electro-magnetic force from the armature-coil system will alter the mechanical response of the generator. In this analysis, the focus has been restricted to the buoy and mechanical LEG dynamics portions of the problem (i.e., subsystems (i) and (ii)), and the electrical system (iii) is simply represented here as a two-phase resistive circuit. More advanced considerations and details of our proposed electric circuit/system can be found in Bastien et al. (2009).

The general aim of the tool is to adjust buoy design parameters to maximize power production, especially, tuning the sub-systems (i) and (ii) response to wave forcing. The goal is therefore to select parameter values, so that the mechanical responses of the buoy and the LEG are maximized for the most prevalent wave conditions. Ideally, in accordance with typical ocean wave energy spectra, the buoy systems should have broadband response, such as to optimize wave energy capture over a range of wave frequencies, and not just at or near one fixed frequency. DC3, by design, is tuned to resonate at/or near a specific wave period. Such resonant systems, however, could be further tuned to improve their response through fixed, slow, or fast tuning. Fixed tuning refers to non-changeable properties of the device (i.e., size, shape, and mass). Slow tuning refers to changes in the response on time scales of minutes to hours and typically is focused on changing the system's buoyancy and hence its mass and effective stiffness. This can be achieved for instance by active ballast control. Fast tuning actively controls system dynamics on the time scales of variation of individual waves or wave groups. The latter tuning is typically very difficult to implement because device characteristics must be changed quickly enough to alter system response. Also, for typical irregular sea states, one cannot exactly predict waves that are about to reach the system (and thus dynamically tune it for such waves), and hence one can only make a forecast and iteratively correct it over a number of wave periods (e.g., Babarit and Clement, 2006). In the present work, we only explored fixed tuning.

2 THE WAVE CLIMATE

The wave climate in a specific area is generally described by a wave spectrum, representing the power density of each spectral wave component. At each point, the spectrum thus represents the accumulated wave power, transmitted from the wind to the sea surface, and propagated over the ocean from all directions. When local spectra are not available, wave climate is described by semi-empirical wave-spectra using locally measured wave parameters, generally, the significant wave height (H_s) and the peak wave period (T_p) or frequency ($\omega_p = 2\pi/T_p$).

Table 1: Rhode Island average wave climate (Source WIS data)

Rhode Island Average Wave climates based on WIS data 1980-1999		
Wave Parameters	Station WIS 79	Station WIS 78
Hs(m)	1.04	1.11
T(s)	5.5	6.3

2.1 Wave spectra

The most widely used semi-empirical wave spectra are the Pierson-Moskowitz spectrum (PM), representing a fully developed sea (state reached when the waves cannot grow any larger for a given wind speed), and the JONSWAP (JS) spectrum used to represent developing sea (Fig. 2). The Pierson-Moskowitz spectrum is expressed as:

$$S_{PM}(\omega) = \frac{\alpha g^2}{\omega^5} e^{-1.25\left(\frac{\omega_p}{\omega}\right)^4} \tag{1}$$

with α =0.0081 and g the gravitational acceleration, and the JONSWAP spectrum as,

$$S_{JS}(\omega) = S_{PM}\gamma^{\exp\left[-\frac{(\omega-\omega_p)^2}{2\sigma^2\omega_p^2}\right]} \tag{2}$$

with, γ=3.3, typically; σ=[0.07-0.09] for [$\omega<=\omega_p$;$\omega>\omega_{pj}$, respectively], and,

$$\alpha = 0.57\left(\frac{gF}{U_{10}^2}\right)^{-\frac{1}{2}} \tag{3}$$

with ω_p, the peak spectral frequency, γ a shape parameter and F (m) , the fetch or distance over which the wind has been blowing.

For a fully developed sea, the PM spectrum directly relates the wind peak spectral frequency to the mean local wind speed, U_{10} (m/s; 10 meters above the sea surface) by the empirical relationship:

$$\omega_p = 0.797 \frac{g}{U_{10}} \tag{4}$$

For the JS spectrum, the wind peak spectral frequency is function of the mean local wind speed at 10 m and of the fetch :

$$\omega_p = \frac{22g}{U_{10}} \left(\frac{gF}{U_{10}^{\ 2}} \right)^{-1/3} \tag{5}$$

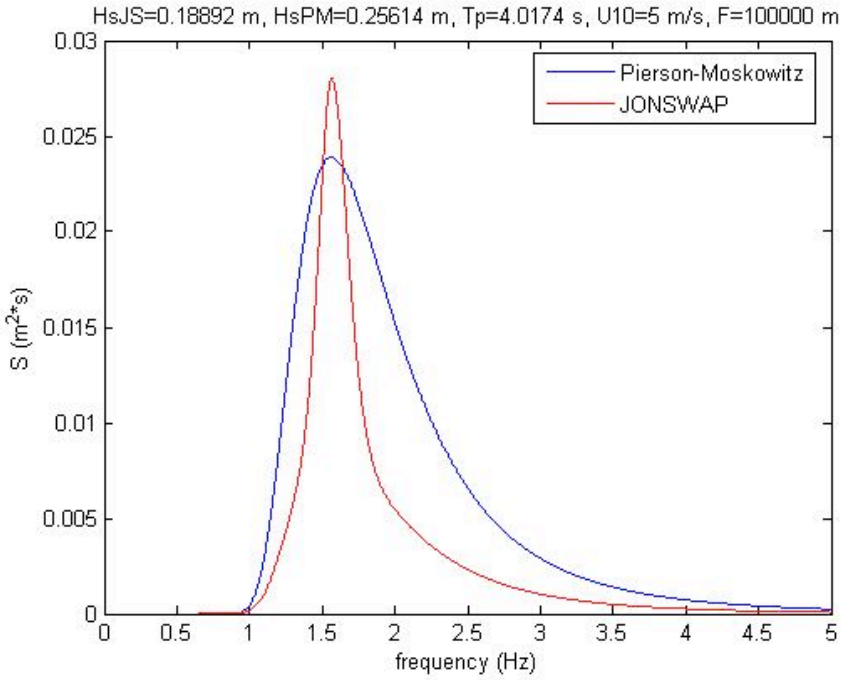

Figure 2: Examples of Pierson-Moskowitz (PM) and JONSWAP (JS) wave spectra

The significant wave height, H_s is related to the the zeroth-moment of the spectrum by,

$$H_s = H_{m0} = 4\sqrt{m_0} \tag{6}$$

with,

$$m_0 = \int_0^\infty S(\omega)d\omega \tag{7}$$

Based on one of these spectra, the sea state can be reconstructed assuming linear wave theory and, therefore, linear superposition of each spectral component, using he random phase method (Dean and Dalrymple 1984). Assuming a dominant direction, this results in a surface elevation time series η, function of space x and time t, expressed as,

$$\eta(x,t) = \sum_i A_i \cos(k_i x - \omega_i t + \psi_i) \tag{8}$$

$$\frac{\omega_i^2}{g} = k_i \tanh k_i h \tag{9}$$

$$\psi_i = 2\pi R_i \tag{10}$$

with A_i , the amplitude of each spectral wave component i, of frequency ω_i, phase ψ_i (with R_i a random number between 0 and 1), $\Delta\omega$ is a small frequency interval, and wave number k_i.

Fig. 3 shows some of the main properties of waves based on linear theory, with implications as far as water particle trajectories.

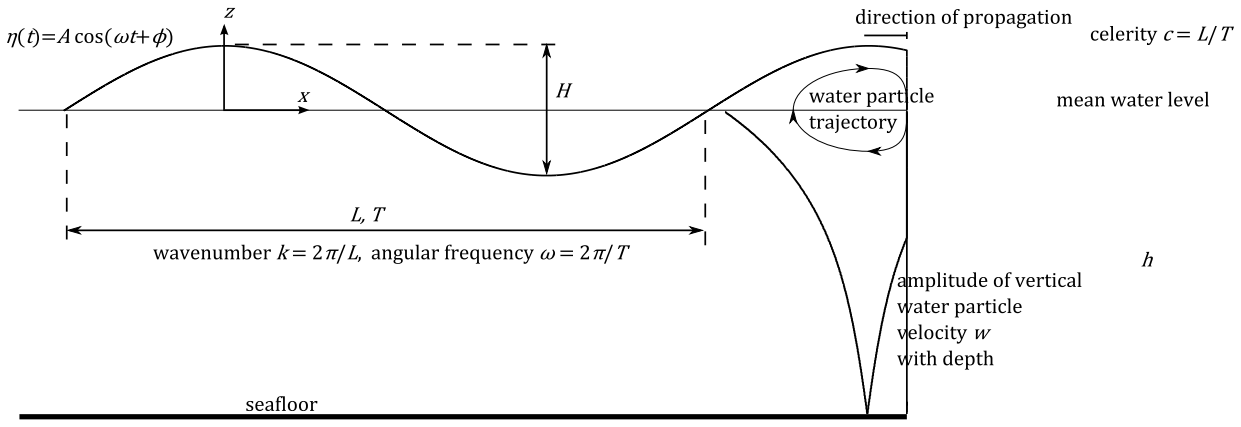

Figure 3: Definition sketch of a linear (sinusoidal) ocean wave.

2.2 Wave power resource

According to linear wave theory, the available wave power can be estimated in terms of power density, per meter of wave crest, as (Dean and Dalrymple, 1984; Previsic et al., 2004),

$$J \cong \frac{1}{64\pi}\rho g^2 H_s^2 T_p \cong 0.48\rho H_s^2 T_p (W/m) \tag{11}$$

with ρ the water density.

2.3 Technical power and capture width ratio

Only a fraction of the available power is technically recoverable, assuming a given site and a given device. Some empirical parameters have been developed to describe the power extractability specific to each conceptual design. The *Capture Width Ratio* (*CWR*) is one of those, which was developed for point absorber ocean energy conversion devices (Hagermann and Bedard, 2003). It represents the fraction of the incident power J captured by a wave extraction device of width W, and is formally expressed as:

$$CWR = \frac{P_{abs}}{J * W} \tag{12}$$

with P_{abs}, the power absorbed by the wave energy buoy. The device width is defined as the intersection between the wave propagation plane and the buoy vertical cross section. For instance, for a DC3 design with four (uniformly distributed) satellite spars of diameter D_2 and a central spar of diameter D_1, we would have,

$$W = D_1 + 2\,D_2 \tag{13}$$

3 SPAR BUOY DESIGN

The so-called *multispar* design (DC3) is based on the basic principle that wave mechanical energy induces buoy motion, which then produce electricity by way of the coupled oscillations of a Linear Electric Generator (LEG) located in a central spar buoy/canister. The LEG is simply made of a permanent magnet, suspended to a spring, oscillating within a two-phase coil and with a massive ballast suspended to the bottom of its magnetic armature (Fig. 4). For this design, the main mode of wave energy harvesting is heave motion, with secondary roll oscillations.

It seems reasonable to anticipate that larger buoy motions will create larger induced currents and, therefore, resonance effects should be favored. To achieve a resonant situation, the buoy's natural heave frequency should be near the wave climate's peak spectral frequency. Additionally, for optimal motion, the LEG's natural frequency of oscillation should also be near both the buoy's heave and the peak spectral frequencies. One can therefore specifically design the buoy system to achieve this triple resonance matching.

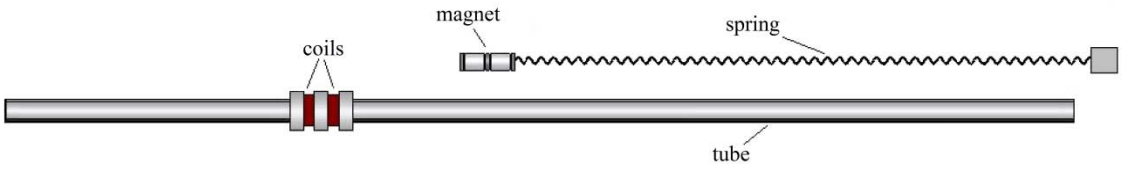

Figure 4: Linear Electric Generator (LEG) made of a spring-magnet system placed inside a guiding Teflon tube. The LEG is housed in DC3's central spar.

For a slender spar buoy (i.e., one whose draft d is at least ten times its diameter D), one can show that he natural heave period T_H depends solely on draft (Berteaux 1991),

$$T_H \cong 2\pi\sqrt{\frac{d}{g}} \tag{14}$$

The resonant period of the LEG spring/mass system T_S, can similarly be approximated as,

$$T_S \cong 2\pi\sqrt{\frac{M_g}{K_s}} \cong 2\pi\sqrt{\frac{l_s}{g}} \tag{15}$$

$$l_s = \frac{M_g g}{K_s} \tag{16}$$

where M_g is the mass of the LEG magnetic armature, K_s the LEG spring stiffness, and l_s the initial static extension of the spring.

In order to maximize the LEG electricity production from the buoy's heave motion, it is desirable to match the buoy and generator resonance periods, which requires,

$$2\pi\sqrt{\frac{d}{g}} = 2\pi\sqrt{\frac{l_s}{g}} \tag{17}$$

which yields that the buoy draft should be equal to the spring length of the spring, $d = l_s$.

Now, if a single spar buoy of draft d housing the LEG were used, to allow for unconstrained generator oscillations, the buoy draft should be on the order of,

$$d \approx 2l_s \tag{18}$$

which prevents achieving the resonance matching with a single spar buoy.

The concept of a multi-spar buoy was developed in large part to solve this problem (Fig. 5). By using shallower satellite spar buoys and a deeper central spar, the equivalent buoy draft for resonance purpose (this will be detailed later), to be used in Eq. (14), can be reduced to match the spring length l_s, and achieve resonance. In addition, the satellite spars increase the buoy roll/pitch stability, by increasing the water-plane inertia and reducing roll motion. Such "parasitic" motion places the buoy sideways with respect to the desirable heaving motion and increases buoy damping through viscous drag.

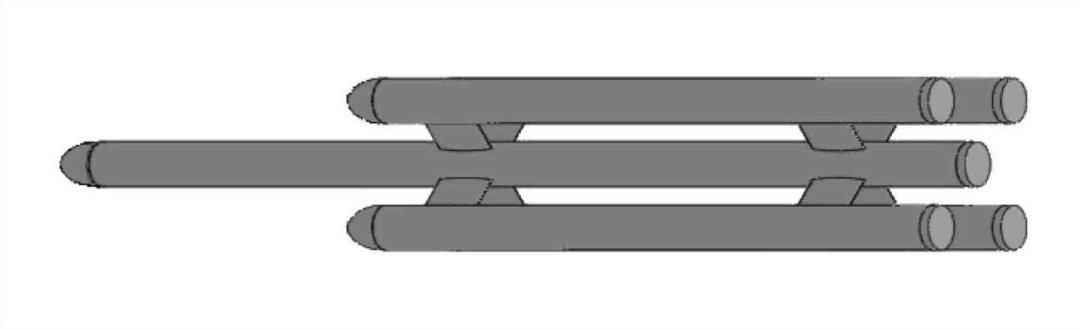

Figure 5: Star-spar buoy concept

Accordingly, this work focuses on the development and refinement of the DC3 buoy system design optimization (i.e., both buoy and LEG parameters), to maximize the "captured" power and the LEG's electricity production. As defined above, DC3's design is made of three major linked sub-systems:

(i) The *floating buoy dynamics* under wave action;

(ii) The *LEG dynamics* resulting from buoy motions;

(iii) The *LEG electric circuits* dynamics.

(a) (b)

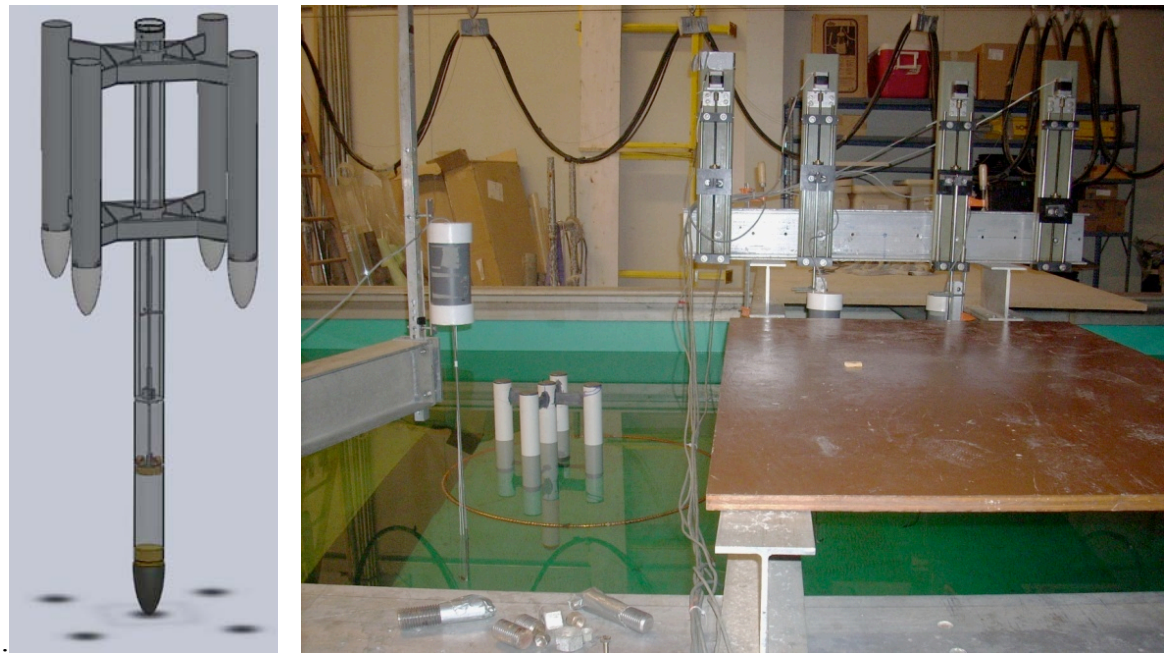

Figure 6: (a) Star-spar buoy concept, and (b) testing of 1:10 scale model in wavetank.

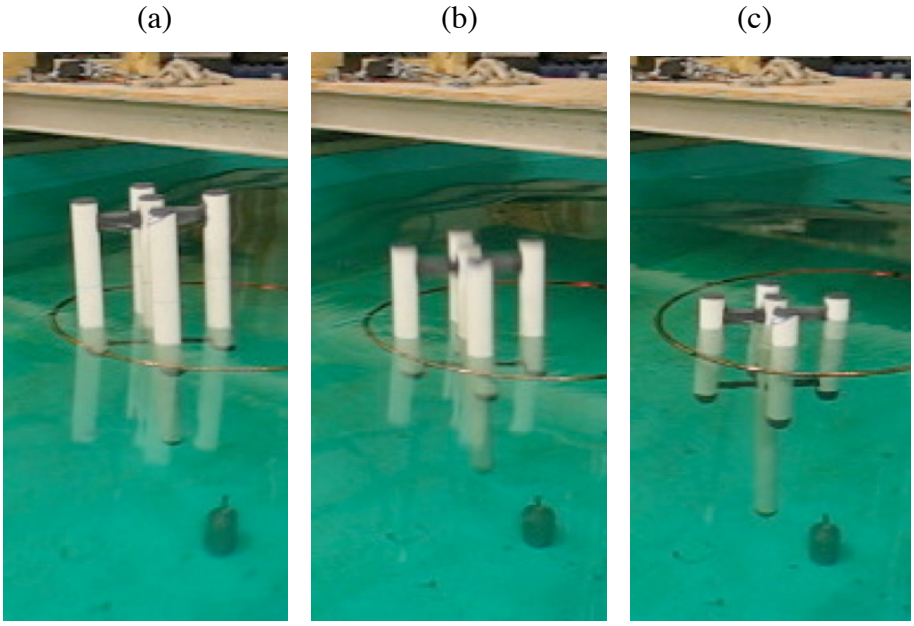

Figure 7 : DC3 buoy 1/10 scale model testing in wavetank. (a-c): three phases of heave resonance motion in regular waves. The buoy's maximum heave amplitude is much larger than the wave amplitude (seen in the background). We note that the main mode of motion is heave and there is very little roll motion.

Feedback between each sub-system must be considered, in order to optimize the buoy

system's overall performance. As a main example, the movement of the magnetic armature inside the coil in the LEG (i.e., a closed electric circuit), will induce an electromagnetic reaction force on the buoy, and also as a secondary effect will cause a change of the buoy weight distribution; both of these will impact buoy motion.

In fact, the electromagnetic reaction force, whose work per unit time is equal to the generated electric power in the LEG (as both actual current and heat losses), is the main energy extraction mechanism from the buoy mechanical motion and, hence, is the primary damping mechanism for the buoy, in addition to surface wave radiation and viscous drag.

In this project, the focus has been restricted to the buoy and mechanical LEG dynamics portions of the problem, i.e., subsystems (i) and (ii), which are detailed in the next sub-sections; the electric system (iii) is simply represented as a two-phase resistive circuit. More advanced considerations and details of our proposed electric circuit/system can be found in Bastien et al. (2009). Fig. 6a shows a more complete sketch of a typical DC3 buoy design, which is the basis for the construction of the 1:10 scale model shown in Fig. 1a, that was tested in both regular and irregular waves in URI's wavetank (see Fig. 6b), as part of other work. Figure 7 illustrates the principle of heave resonance matching, in periodic waves, where we see that the buoy maximum heave amplitude is much larger than the wave amplitude (seen in the background).

3.1 LEG Mechanical Design and Dynamics

The motion of the LEG spring-magnet, expressed by the axial displacement $z_a(t)$ of the magnetic armature relative to the coil/stator (attached to the buoy) from its initial static equilibrium position, is classically described by a 2nd-order Ordinary Differential Equation (ODE). For an armature of mass M_g suspended to a spring of stiffness K_s, this equation has inertia, damping proportional to armature speed, and spring restoring terms in the left-hand-side, and is forced in the right hand side by the inertia force induced by the buoy acceleration. We have (upper dots are time derivatives),

$$M_g \ddot{z}_a + \mu \dot{z}_a + K_s z_a = -M_g \ddot{z}_b \tag{19}$$

with $\mu = \mu_g + \mu_f$, the LEG damping coefficient, combining an electromagnetic resistance

coefficient, which depends on the LEG circuits and magnetic characteristics, and a friction coefficient (subscripts *g* and *f* respectively).

In static equilibrium the LEG spring has an initial extension:

$$l_{s0} = \frac{M_g g - T_0}{K_s} \tag{20}$$

assuming a spring preconstraint T_0 (i.e., the threshold force before the spring starts deforming). Solving Eq. (19), with $z_a = \dot{z}_a = 0 \quad at \quad t = 0$, for a harmonic forcing with acceleration $a_{0,}$ per unit wave amplitude, of frequency ω, the LEG Response Amplitude Operator (RAO) reads:

$$R = \frac{|z_a|}{A} = a_0 \left[\left(K_s - \omega^2 M_g \right)^2 + \omega^2 \mu^2 \right]^{-1/2} \tag{21}$$

where A denotes the actual wave amplitude. For this simple harmonic oscillator, the maximum response:

$$R^{\max} = \frac{a_0}{\omega \mu} \tag{22}$$

occurs at the system's natural frequency:

$$\omega = \sqrt{\frac{K_s}{M_g}} = \sqrt{\frac{g}{l_{s0} + \frac{T_0}{K_s}}} = \omega_s \tag{23}$$

Hence, the longer the spring initial extension, the lower the LEG natural frequency.

The mechanical power extracted from the buoy motion is due to the induced magnet motion, and corresponds to the work per unit time of the magnet damping force, $\mu \dot{z}_a$, such that,

$$P_\mu(t) = \mu \dot{z}_a^2 \tag{24}$$

The fraction of this power P_e used to produce electricity is c_e (ignoring magnetic and heat (Joule)

losses),

$$c_e = \frac{\mu_g}{\mu}$$
$$P_e(t) = c_e P_\mu(t) \tag{25}$$

3.2 Floating Buoy Dynamics

Assuming linearized floating body dynamics theory in transient waves, the buoy heave motion can be expressed from the conservation of linear momentum, as a balance of inertia, radiative wave damping, viscous damping, gravity, and buoyancy forces. This yields a 2nd-order nonlinear ODE (Newman, 1977),

$$(M_b + a_{33}(\infty))\ddot{\xi}_3 + \int_0^t \kappa_{b3}(t-\tau)\dot{\xi}_3 d\tau + b_{f,33}\left|\dot{\xi}'\right|\dot{\xi}' + F_{bs} = F_3 + F_g - F_{35} \tag{26}$$

in water of density ρ_w and depth h, with M_b the buoy mass, equal to the mass of the water volume statically displaced by the buoy,

$$M_b = \rho_w * \forall_{b0} \tag{27}$$

$a_{33}(\infty)$ is the instantaneous added mass (for very large frequency); $b_{f,33}$, the buoy heave viscous damping coefficient such that,

$$b_{f,33} = \frac{1}{2}\rho_w S_0 C_{dh} \tag{28}$$

with C_{dh} the buoy heave drag coefficient; $\xi_3(t)$, the buoy heave motion, $\dot{\xi}_3(t)$, the buoy heave velocity and,

$$\dot{\xi}'_3 = \dot{\xi}_3 - \tilde{w} \tag{29}$$

with $\tilde{w}$, the wave vertical particle velocity at the buoy equivalent draft d, $F_{bs}(t)$, the heave buoyancy restoring force such that,

$$F_{bs}(t) = \rho_w g\left\{\forall_b(\xi_3(t)) - \forall_{b0}\right\} \cong \rho_w g S_0 \xi_3(t) \tag{30}$$

with S_0, the total buoy horizontal cross-section; $F_3(t)$, the wave heave excitation force; $F_g(t)$, the LEG reaction force on the buoy, function of the armature oscillator motion, and,

$$F_g(t) = \mu \dot{z}_a + \kappa_s z_a \tag{31}$$

F_{35} is a change in heave excitation and/or viscous damping due to the buoy roll/pitch oscillations.

Assuming that the sea-state is made of the superposition of N linear periodic waves of amplitude A_n and frequency ω_n, with energy density represented by the frequency spectrum $S(\omega)$ (e.g.,JONSWAP; JS), the incident wave elevation and vertical particle velocity at the equivalent draft, can be expressed as,

$$\begin{aligned}
&\eta(t) = \sum_{n=1}^{N} A_n \cos(\omega_n t + \psi_n) \\
&\frac{\omega_n}{g} = k_n \tanh k_n h \\
&\tilde{w}(t) = \sum_{n=1}^{N} -A_n \omega_n \frac{\sinh k_n (h - \tilde{d})}{\sinh k_n h} \sin(\omega_n t + \psi_n)
\end{aligned} \tag{32}$$

with, $A_n = \sqrt{2S(\omega_n)\Delta\omega}$ and $\Delta\omega$, a small frequency interval; $\psi\,[0,2\pi]$ a specified set of random phases. The linear dispersion relationship expresses the wavenumber k_n for each wave components.

The total wave exciting force is expressed as,

$$F_3(t) = \rho_w g \sum_{n=1}^{N} A_n r_{3n} \cos(\omega_n t + \phi_{3n} + \psi_n) \tag{33}$$

with, $r_{3n}(\omega_n), \psi_n(\omega_n)$, the module and phase, respectively of the heave exciting force caused on

the buoy by a wave of unit amplitude and frequency ω_n (including diffraction effects induced by the buoy).

3.2.1 Heave Memory Term

The integral in Eq. (25) is a memory term (e.g., Babarit et al., 2006) expressing radiative wave damping, in which the heave impulse response function, $\kappa_{b3}(t)$, can be calculated as a function of the buoy frequency response by either of the inverse Fourier transforms,

$$\kappa_{b3}(t) = -\frac{2}{\pi}\int_0^\infty (a_{33}(\omega) - a_{33}(\infty))\omega \sin\omega t d\omega$$
$$\kappa_{b3}(t) = -\frac{2}{\pi}\int_0^\infty b_{33}(\omega)\cos\omega t d\omega \tag{34}$$

as a function of $a_{33}(\omega)$ and $b_{33}(\omega)$, the buoy frequency dependent linear heave added mass and wave radiative damping coefficients, respectively. The memory term, expressed as a time convolution, is both costly and difficult to accurately evaluate at each time. This difficulty can be overcome by representing $\kappa_{b3}(t)$ by way of the Prony method, which transforms the convolution into a system of additional ODEs for the Prony coefficient (e.g., Babarit and Clement, 2006) as,

$$\kappa_{b3}(t) = \sum_{p=1}^{Np} \beta_{3p}\exp(S_{3p}t)$$
$$\int_0^t \kappa_{b3}(t-\tau)\dot{\xi}_3(\tau)d\tau = \sum_{p=1}^{Np}\beta_{3p}I_{3p}(\dot{\xi}_3,t) \tag{35}$$
$$\dot{I}_{3p} = S_{3p}I_{3p} + \dot{\xi}_3 \qquad p = 1,.....,N_p$$

with (β_{3p},S_{3p}), N_p complex coefficients found through Prony's "curve fitting".

3.2.2 Linearized Heave Solution for Periodic Waves

Frequency dependent wave coefficients $\left[a_{33},b_{33},r_3,\phi_3\right]$ are calculated using the standard Floating

Body Dynamics Dynamic Boundary Element code WAMIT (Lee, 1995; Newman, 1977), in which *linearized* free surface boundary conditions are specified. Thus, for given buoy geometry and mass distribution, WAMIT computes the wave coefficients for N equally spaced periods T_n (or frequencies $\omega_n=2\pi/T_n$), in a specified interval [T_{min}, T_{max}].

For a periodic incident wave of amplitude A and frequency ω, the *linearized* (complex) equations governing the buoy motion for each of 6 degrees of freedom can be expressed using these coefficients (e.g., Newman, 1977) as (assuming tensor notation's summation convention),

$$\left\{-\omega^2\left(M_{ml}+a_{ml}\right)+i\omega\left(b_{ml}+b^l_{f,ml}\right)+c_{ml}\right\}\varsigma_l = Ar_l e^{i\psi_l} \tag{36}$$

with ζ_l the complex buoy amplitude in direction l. In this equation, $b^l_{f,ml}$ denotes the *linearized* friction coefficient obtained by applying the principle of "equivalent average dissipated power" over one wave period (e.g., Berteaux, 1994).

For the linearized heave motion (l =3) of multiple symmetric bodies ($a_{m3} = b_{m3} =0$, for $m \neq 3$) with $M = M_{33} = M_b + M_g$ and $b^l_{f,33} = \left\{\frac{8|\varsigma_3|\omega}{3\pi}\right\}b_{f,33}$, we find the heave frequency dependent Response Amplitude Operator (RAO),

$$Z_3 = \frac{|\varsigma_3|}{A} = r_3\left\{c_{33}-\omega^2\left(M+a_{33}\right)^2+\omega^2\left(b_{33}+b^l_{f,33}\right)^2\right\}^{-1/2} \tag{37}$$

This equation predicts maximum heave response,

$$Z_3^{maz} = \frac{r3}{\left\{\omega\left(b_{33}+b^l_{f,33}\right)\right\}} \tag{38}$$

when incident waves occur at the *heave* natural frequency,

$$\omega = \sqrt{\frac{c_{33}}{M+a_{33}(\omega)}} = \omega_H = \frac{2\pi}{T_H} \tag{39}$$

In the absence of viscous damping (such as assumed in WAMIT) and for a very small value of the linear wave damping coefficient (as, e.g., for the star-spar buoy DC3), maximum heave response will be significantly over-predicted near resonance. Hence, when solving Eqs. (26) to (35) one needs to use a properly calibrated drag coefficient for the buoy, which can be obtained through a comparison of model predictions with laboratory measurements performed on a scale model.

3.2.3 Multiple spar buoy heave dynamic

For slender spar buoys, such as the components of the star-spar DC3, the heave added mass, a_{33}, is small and varies little over any useful frequency interval around the buoy's heave resonance frequency, while the radiative damping, b_{33}, is very small, reflecting the fact that such buoys generate little waves in heaving motion (Grilli et al., 2007). Therefore $K_{b3}(t) \approx 0$, and hence the memory/radiative wave damping term in Eq. (25) is negligible, particularly as compared to the viscous damping term.

Additionally, the star-spar is made of multiple (N_s + 1) rigidly connected vertical spar buoys of cylindrical shape, with draft d_i, external diameter D_i, and total length l_i (i=1,.., N_s + 1) (Figs. 6 and 7). These individual buoys are set sufficiently far apart (typically a couple of diameters) not to interact hydrodynamically in heave. Additionally, the submerged extremity of each buoy is streamlined to reduce friction drag generated during motion. Due to the small added mass of spar buoys, Eq. (39) can be simplified to predict the star-spar natural heave period as,

$$T_H \cong 2\pi\sqrt{\frac{M}{c_{33}}} = 2\pi\sqrt{\frac{\tilde{d}}{g}} \qquad \text{with} \quad \tilde{d} = \frac{\sum_{i=1}^{N_s+1} S_i d_i}{\sum_{i=1}^{N_s+1} S_i} \tag{40}$$

the buoy equivalent draft.

Let us emphasize that the heave period of resonance in a multi-spar system is now

controlled by the *equivalent* draft, which combines the draft and cross-section of each spar. Hence, adjusting buoy geometry (i.e., the shape and draft of satellite and central spar buoys) allows to change the equivalent draft and thus gives a mean of solving the problem of the spring-spar matching frequency, that was discussed in more details in Section 2.3.

3.2.4 Multispar buoy roll/pitch dynamics

The buoy roll (or pitch, identical for buoys with two axes of symmetry) angular motion, $\xi_5 = \alpha(t)$, is modeled, similarly to the heave motion as,

$$\begin{aligned}
&\left(I_{55} + a_{55}(\infty)\right)\ddot{\alpha} + \sum_{p=1}^{N_p} \beta_{5p} I_{5p}(\dot{\alpha}, t) + M_{f,53} + c_{55}\sin\alpha = M_5 \\
&\dot{I}_{5p} = S_{5p} I_{5p} + \dot{\alpha} \quad ; \quad p = 1,\ldots N_p \qquad (41,\text{a,b,c}) \\
&M_5(t) = \rho_w g \sum_{n=1}^{N} A_n r_{5n} \cos(\omega_n t + \phi_{5n} + \psi_n)
\end{aligned}$$

where I_{55} and a_{55} are the mass moment of inertia and added inertia, respectively; the second term expresses the wave (linear) radiative wave damping; $M_{f,53}$ is the viscous damping moment resulting from heave-roll interactions; $c_{55} = M_b g\,\overline{GM}$ is the roll (or pitch) restoring moment, with $\overline{GM}$ the metacentric distance; M_5 is the wave roll excitation moment calculated by superposition of wave forcing, as for heave.

Similarly to the heave calculations, the frequency dependent coefficients for roll motion $\{a_{55}, b_{55}, r_5, \phi_5\}$ are calculated as before using the WAMIT. The roll excitation moment is then calculated using Eq. (41c); the radiative damping term is calculated by applying the Prony method to the roll impulse response function $K_{b5}(t)$, calculated as described by Eqs. (34) and (35) for heave motion, and leading to the complex Prony coefficient β_{5p} and S_{5p}, for $p=1,\ldots, N_p$.

3.3 Buoy Design Optimization

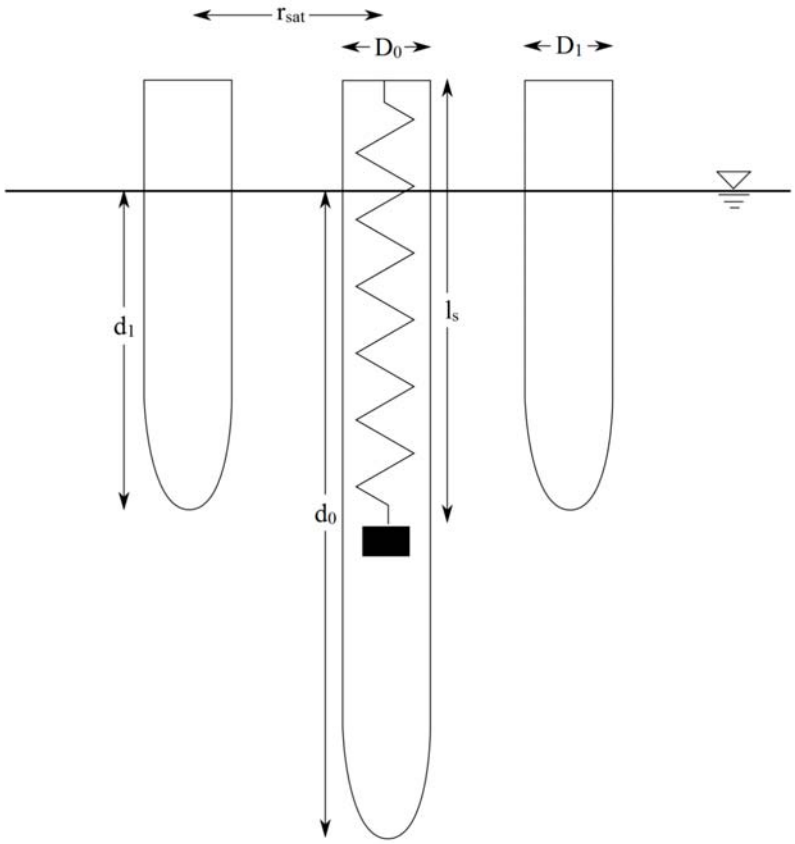

Figure 8: Sketch of cross section through 2 satellite spars and central spar of the multi-spar buoy.

Assuming a multi-spar with a longer central spar of draft, d_1 and diameter and D_1, hosting the generator, and a number n_{sat} of satellite spars, of identical draft d_2 and diameter and D_2, connected to the central spar by small, lightweight, rigid connectors. A parametric study of buoy parameters was performed in order to quantify how parameters interplay, to set a series of bounds for reasonable buoy dimensions, and to help converging to a final, optimized buoy design, for a given wave climate.

The objective function to optimize is maximizing the capture width ratio (i.e., how much of the incident wave energy is capture into buoy mechanical motion).

3.3.1 Shape parameters

From Eqs. (39, 40), assuming non-interacting slender spars, the resonance period of a multi-spar system can be expressed as a function of its geometric characteristics, draft and diameter of each spars as,

$$T_H = 2\pi\sqrt{\frac{\rho\sum_{i=1}^{nsat}\forall_i}{\rho g\sum_{i=1}^{nsat}S_i}} = 2\pi\sqrt{\frac{d_1D_1^2 + n_{sat}d_2D_2^2}{g\left(D_1^2 + n_{sat}D_2^2\right)}} \tag{42}$$

where $\forall_i$ is the volume of water displaced by an individual spar, i, and S_i its circular cross-sectional area. Defining the dimensionless parameters, the draft ratio $s = d_2/d_1$, and the diameter ratio $r = D_2/D_1$, then, the heave resonance period can be written as,

$$T_H = 2\pi\left\{\frac{d_1}{g}\frac{1+n_{sat}r^2s}{1+n_{sat}r^2}\right\}^{\frac{1}{2}} = T_{H1}\left\{\frac{1+n_{sat}r^2s}{1+n_{sat}r^2}\right\}^{\frac{1}{2}} \quad \text{or} \quad d_1 = \left(\frac{T_H}{2\pi}\right)^2\frac{g\left(1+n_{sat}r^2\right)}{1+n_{sat}r^2s} \tag{43}$$

with T_{H1} the central spar heave frequency. For instance, if $n_{sat} = 4$, $r = 1.5$, and $s = 0.25$, we find $T_H = 0.57\ T_{H1}$, which shows that we can significantly reduce the heave resonance frequency of the multiple spar, to be closer to, or even actually match that T_g of the LEG spring-armature system installed in the longer central spar.

In fact, for such a buoy's heave resonance frequency to exactly match the generator resonance frequency, we combine Eqs. (15) and (43) while specifying $T_H = T_g$, which yields,

$$d_1 = l_s\frac{1+n_{sat}r^2}{1+n_{sat}r^2s} \tag{44}$$

Additionally, the magnet range condition Eq. (18) imposes that $d_1 \approx 2l_s$, which yields, for given n_{sat} and r values,

$$s = \frac{\alpha(1 + n_{sat} r^2) - 1}{n_{sat} r^2} \tag{45}$$

with $\alpha = l_s/d_1$ for generality. Hence, using the same values as above, n_{sat} = 4 and r = 1.5, we find, s = 0.444 for α = 0.5. Combining Eqs. (43-45), we then find a simple expression for the *multiple* spar sea state, buoy and LEG period matching condition,

$$T_p = T_H = 2\pi \sqrt{\frac{d_1}{2g}} = \frac{T_{H1}}{\sqrt{2}} \tag{46}$$

or for a general α value, combining solving Eq. (46) for d_1 we find,

$$d_1 = \frac{L_p}{2\pi\alpha} \quad \text{with} \quad L_p = \frac{g T_p^2}{2\pi} \tag{47}$$

which can be used to find d_1 for given T_p and α values. Eq. (45) can then be used to find *s(r)*, and then $d_2 = s\, d_1$ for given n_{sat} and r values.

Now, as a practical example, if one designed a *starspar* buoy, such as in Fig. 1, to resonate in heave for New England shelf conditions, with T_p = 5 s, and using n_{sat} = 4, r = 1.5, and s = 0.444, which achieves $d_1 \approx 2l_s$, we would find d_1 = 12.42 m and $d_2 = s\, d_1$ = 5.52 m. One could also use the ratio $\alpha = l_s / d_1$ as a variable in Eqs. (47).

Additional considerations, related to the buoy roll/pitch stability, can be used to constrain the value of the buoy diameter ratio *r*. First, the *multispar* buoyancy center vertical distance below mean water level (MWL), $\overline{OB}$, is obtained as,

$$\overline{OB}(S_1 d_1 + n_{sat} S_2 d_2) = \overline{OB_1} S_1 d_1 + n_{sat} \overline{OB_2} S_2 d_2 \tag{48}$$

with $\overline{OB_1} \approx d_1/2$ and $\overline{OB_2} \approx d_2/2$ the buoyancy distances for the central and satellite buoys, respectively, or,

$$\overline{OB} = \overline{OB_1}\left\{\frac{1+n_{sat}r^2s^2}{1+n_{sat}r^2s}\right\} \tag{49}$$

Similarly the *multispar* center of mass vertical distance below MWL, $\overline{OG}$, is obtained as,

$$\overline{OG}\ \rho(S_1d_1 + n_{sat}S_2d_2) = \overline{OG_1}\ m_1 + n_{sat}\overline{OG_2}\ m_2 \tag{50}$$

with $\overline{OG_1} \approx \beta d_1$ and $\overline{OG_2} \approx \gamma d_2$ the center of gravity distances below the water surface for the central and satellite buoys, respectively, or,

$$\overline{OG} = \overline{OG_1}\left\{\delta\frac{1-\frac{\gamma}{\beta}s}{1+nr^2s} + \frac{\gamma}{\beta}s\right\} \tag{51}$$

with the total buoy mass, $M_b = m_1 + n_{sat}\, m_2 = \rho\forall_{b0} = \rho V_1\,(1 + n_{sat}\, r^2 s)$ and,

$$m_1 = \delta\,\rho V_1 \quad \text{and,} \qquad m_2 = \rho V_2\left\{1+\frac{1-\delta}{n_{sat}r^2s}\right\} \tag{52}$$

the central and satellite buoy masses, respectively.

While for individual spar buoys, the buoy mass and displaced water mass must balance each other, due to buoyancy static equilibrium (i.e., $\delta = 1$), for a *multiple* spar, one can unevenly distribute mass (i.e., through ballast), between the central and satellite buoys. Specifically, making the central buoy negatively buoyant, i.e., specifying $\delta > 1$, and using the lateral spars more as floats providing buoyancy, will lower both the central buoy's $\overline{OG_1}$ (due to increased ballast mass) and the overall center of mass $\overline{OG}$, hence increasing the *multispar* buoy's weight stability in roll/pitch.

Additionally, floating bodies benefit from a form stability depending upon the inertia of the water plane with respect to the axis of rotation, $I_{x,y}$ which controls the metacentric distance $\overline{BM}$ as,

$$\overline{BM} = \frac{I_{x,y}}{\forall_{b0}} = \frac{I_{x,y}}{V_1(1+n_{sat}r^2 s)} \tag{53}$$

The computation of $I_{x,y}$ depends upon the *multispar* configuration. Specifically, for a *starspar* with $n_{sat} = 4$, such as shown in Fig. 1, one can show that the inertia of the water plane is identical for rotations around the *x*-axis, *y*-axis or a bisecting axis at 45 degrees in between those, to,

$$I_{x,y} = \frac{\pi}{64}(D_1^4 + 4D_2^4) + 2w^2 S_2 \tag{54}$$

where *w* is the distance between the centers of the central and satellite spars, and the last term represents the transport inertia contribution of satellite buoys. Further developing this equation, we get,

$$I_{x,y} = I_1\left(1 + 4r^2\left(r^2 + 8\varepsilon^2\right)\right) \tag{55}$$

with $I_1 = \pi(D_1)^4/64$, and $\varepsilon = w/D_1$. Hence, combining Eqs. (53,55), one finds for a *starspar* with $n_{sat} = 4$,

$$\overline{BM} = \overline{BM_1}\left(\frac{1 + 4r^2\left(r^2 + 8\varepsilon^2\right)}{1 + 4r^2 s}\right) \tag{56}$$

where $\overline{BM_1} = I_1/V_1 = D_1^2/(16d_1)$, the central buoy metacentric distance. In dynamic roll/pitch analyses, one calculates the restoring buoyancy moment as, $\overline{GM}\, m\, g \sin\phi$ with,

$$\overline{GM} = \overline{OG} - \overline{OB} + \overline{BM} \tag{57}$$

and the different terms given by Eqs. (52), (54) and (56).

For selected n_{sat}, α and T_p, once the *multispar* diameter ratio *r* is set, the heave frequency matching condition yields d_1, *s,* and d_2; *t*hen $\overline{OB}$ is set, since it depends upon n_{sat}, *r,* and *s.* Hence, achieving a specific value of the distance $\overline{GM}$, or as large a value as possible can be

done by increasing $\overline{OG}$ (i.e., lowering G which may require a negative buoyancy of the central buoy and low ballast akin to a ship keel, with the proper selection of β, γ, and δ) and increasing $\overline{BM}$ by increasing ε, for given r and s, thus moving waterplane area away from the *multispar* center.

Using the example from above, with $n_{sat} = 4$, $r = 1.5$, $s = 0.444$, $d_1 = 12.42$ m, $d_2 = 5.52$ m, $T_p = 5$ s, and assuming $\beta = \gamma = 0.8$ and $\varepsilon = 3$, $\delta = 1.2$, we find $\overline{OB} = 3.448$ m, $\overline{OG}_1 = 9.936$ m, and $\overline{OG} = 5.739$ m. Assuming $D_1 = 0.75$ m and $D_2 = r\,D_1 = 1.125$ m, we find $\overline{BM}_1$=2.83 mm (i.e., negligible for the single central spar) and $\overline{BM} = 0.379$ m (i.e., 133 times the form stability of the single spar). Overall, $\overline{GM} = 2.67$ m, which could be further increased by increasing w and/or β and δ.

An upper limit for the δ can be found from Eq. (52), by specifying the minimum fraction $\kappa = m_2/(\rho V_2)$ denoting the satellite buoy mass over the displaced water mass, as

$$\delta^1_{\max} = 1 + nr^2 s(1-\kappa) \tag{58}$$

Using the above data and assuming $\kappa = 0.2$ for the satellite buoys, we would find $\delta_{max} = 4.2$, i.e., the central buoy mass could reach over 4 times that of the displaced water. Assuming that the buoy casing, equipment and linear motor, also make up about $\kappa = 0.2$ (20%) of the central buoy displacement, even using lead as ballast (density 11.34), achieving such a high δ^1_{max} would end-up taking up too much useful space in the buoy. One could instead assume that the emerged part of the central buoy would be a fraction f of the draft d_1, which could be filled with lead ballast at the bottom of the buoy, i.e., in a volume (neglecting buoy casing thickness) about $S_1 f\, d_1$. Hence, for the central buoy,

$$m_1 = \delta\rho V_1 = 0.2\rho V_1 + \frac{\rho_l}{\rho} f V_1 = \rho V_1 \left(0.2 + \frac{\rho_l}{\rho} f\right) \tag{59}$$

where the last parenthesis denotes the acceptable maximum value of δ,

$$\delta^2_{\max} = 0.2 + \frac{\rho_l}{\rho} f \tag{60}$$

Using f = 0.2 and assuming a lead ballast and fresh water, one would find $\delta^2_{max} = 2.47 < \delta^1_{max}$. With this value and the above data, we find $\overline{OG}$ = 7.143 m and hence a much better $\overline{GM}$ = 4.074 m. This value could still be improved by increasing *w*. Finally, using the δ^2_{max} value from Eq. (18) in Eq. (16), one finds the fraction,

$$\kappa = 1 - \frac{\delta^2_{\max} - 1}{nr^2 s} \tag{61}$$

With the above data, we would find $\kappa = 0.63$, which seems to be on the high side but could easily be achieved as a small lead ballast. Clearly, however, some more fine tuning of the weight distribution is required.

Note, in addition to the main generator located in the central buoy, smaller generators of length $l'_s = \alpha d_2 = \alpha\, s d_1$ could also be located in the external buoys, thus capturing energy from secondary resonance periods. In the latter case, assuming the same fraction α, we have $l'_s = 0.5 d_2$ = 2.76 m, which corresponds to a secondary resonance period T'_g = 3.33 s. Hence the secondary generators could resonate for shorter waves, thus widening the buoy response.

3.3.2 Frequency dependent parameters

In an order to have an interactive code and Graphical User Interface for buoy parameter optimization, we should be free of the use of a complex model such as WAMIT, to calculate the frequency dependent coefficients r_3, ϕ_3, a_{33}, b_{33}, r_5, ϕ_5, a_{55}, and b_{55}. In an attempt to do so, we developed semi-empirical summation and scaling formulas, in the frequency/period domain, for *j* spars of diameter $D_{sj} = D_j$ and draft $d_{sj} = d_j$ as a function of corresponding coefficients calculated with WAMIT, for a reference single spar buoy of diameter D_{ref} and draft d_{ref}.

Specifically, for multiple spars buoys made of a central buoy of diameter D_1 , and draft d_1 and N_s satellite buoys of diameter D_{sj} and draft d_{sj} , the WAMIT coefficients were calculated for each individual buoy, and then they were summed up, assuming independent contributions from individual spar buoys. Doing so, it was assumed that, if satellite buoys were located far enough away (in terms of number of diameters) from the central buoy, interactions of wave fields created by each buoy in diffraction (i.e., buoy fixed under the action of incident waves) or radiation (i.e., buoy in forced unitary motion along one degree of freedom, heave, roll, pitch,…) would be negligible. The relevance of this summation was verified by comparing the coefficients thus calculated with those computed for an entire multi-spar buoy with WAMIT.

Additionally, we developed semi-empirical scaling formula relating WAMIT coefficients for a spar buoy of diameter D and draft d, to those of a spar buoy of diameter D_{ref} and draft d_{ref}.

These scaling and summation formulas were independently verified for the scale model recently built and tested at URI. This model is made of one central spar and 4 satellite buoys, all of identical diameter $D = D_{\text{sj}} = 0.0603$ m, and draft $d_1 = 1$ m and $d_{\text{si}} = 0.3781$ m, respectively. The shortest horizontal distance on axis between satellites and the central buoy was $h_{\text{s}} = 0.156$ m.

a. Verification of scaling formulas

WAMIT simulations were performed for the complete assembled star-spar, and then separately for single satellite and central spars. The latter single spar simulations will be used to verify scaling with respect to draft. Additionally, to verify scaling with respect to diameter, WAMIT simulations were also performed for a central spar (Nb. # 2) with a diameter 50% larger than the original central spar (Nb. #1) or $D_{12} = 0.09045$ m.

Scaling formulas were first verified, by trying to predict frequency parameters of a satellite spar buoy, as a function of those of central spar buoys.

1. Heave equations:

After scaling verification we obtain the following equation for the *heave excitation force*, on a single spar j:

$$F_{3j}(t) = \rho \cdot g \cdot \sum_{i=1}^{N_w} A_i \cdot \left(\frac{D_{sj}}{D_{ref}}\right)^2 \cdot \hat{r}_3(\omega_i) \cdot \cos\left(\omega_i \cdot t + \hat{\phi}_3(\omega_i) + \psi_i\right) \frac{\cosh\left(k_i \cdot (h - d_{sj})\right)}{\cosh\left(k_i \cdot (h - d_{ref})\right)} \tag{62}$$

with, $$r'_{3j}(\omega_i) = \hat{r}_3(\omega_i) \cdot \left(\frac{D_{sj}}{D_{ref}}\right)^2 \frac{\cosh(k_i \cdot (h - d_{sj}))}{\cosh(k_i \cdot (h - d_{ref}))} \quad \text{and} \quad \phi_{3j}(\omega_i) = \hat{\phi}_3(\omega_i) \tag{63}$$

Figure 9 shows the comparison of various forces. The force on the satellite buoy is almost perfectly predicted by scaling from either reference buoy. Diameter scaling between central spar buoys 1 and 2 has the exponent 2, and draft scaling is captured by the pressure scaling factor in the equation. Almost no difference is found on phase angles.

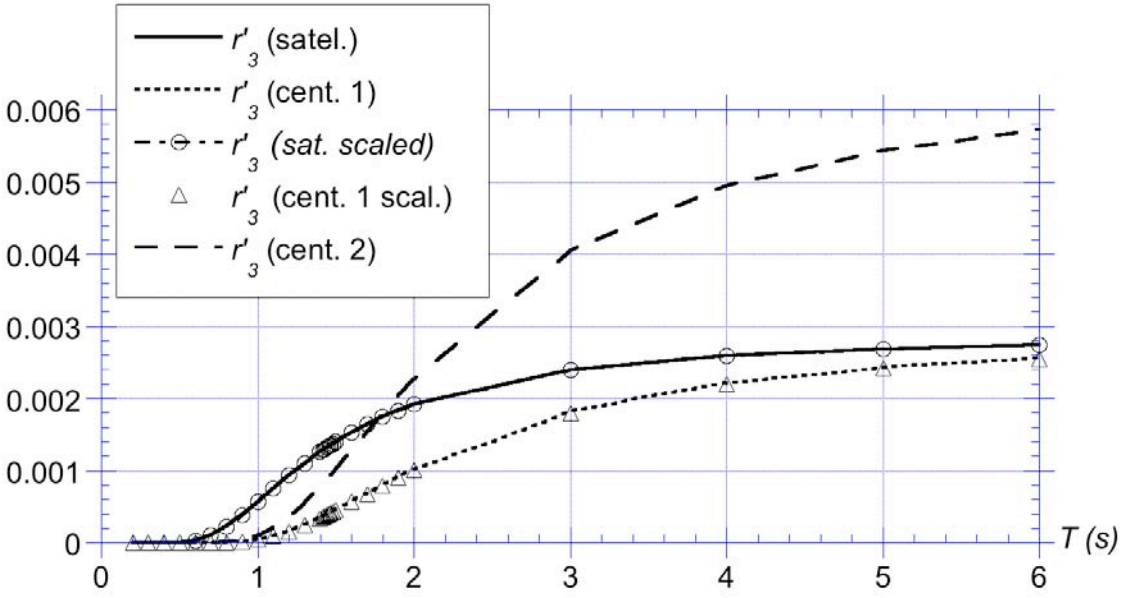

Figure 9: Non-dimensional heave excitation force module computed for satellite and central spar reference buoys (1 and 2). Prediction of force on central spar buoy 1 by scaling of central spar buoy 2 (Δ). Prediction of force of satellite buoy by scaling of central spar buoys 1 or 2 (o).

After scaling verification we obtain the following equation for the *heave added mass* at the peak frequency, on a multiple spar.

$$a_{33\,j}(\omega_p) = \hat{a}_{33\,j}\left(\omega_p \cdot \sqrt{\frac{d_{ref}}{d_{sj}}}\right) \cdot \left(\frac{D_{sj}}{D_{ref}}\right)^3 \tag{64}$$

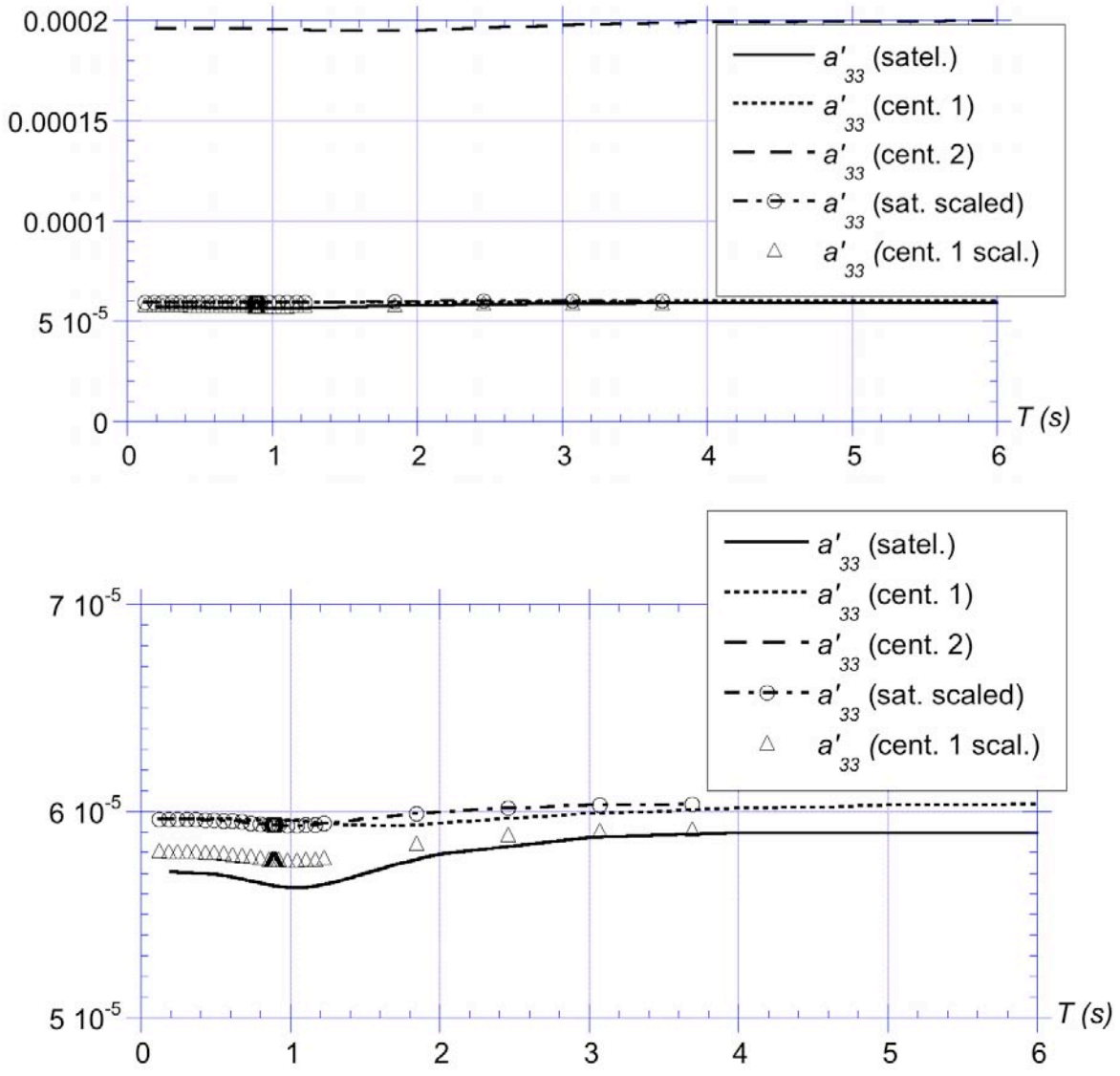

Figure 10: Non-dimensional heave added mass coefficient computed for satellite and central spar reference buoys (1 and 2). Prediction of added mass on central spar buoy 1 by scaling of central spar buoy 2 (Δ). Prediction of added mass of satellite buoy by scaling of central spar buoys 1 or 2 (o). The two figures show identical data, but have different scales.

Figure 10 shows the comparison of various added mass curves, as a function of period. The added mass on the satellite buoy is accurately predicted by scaling from either reference buoy. To capture the added mass minimum, a shift of the frequency/period axis is needed but scaling is found proportional to draft rather than diameter. Diameter scaling between central spar buoys 1 and 2 has the exponent 3, and no effect of draft scaling is found.

After scaling verification, the equation for the *radiative damping coefficients* of individual spars is expressed as follows:

$$b_{33\,j}(\omega_p) = \hat{b}_{33\,j}\left(\omega_p \cdot \sqrt{\frac{d_{ref}}{d_{sj}}}\right) \cdot \left(\frac{D_{sj}}{D_{ref}}\right)^4 \cdot \frac{d_{ref}}{d_{sj}} \tag{65}$$

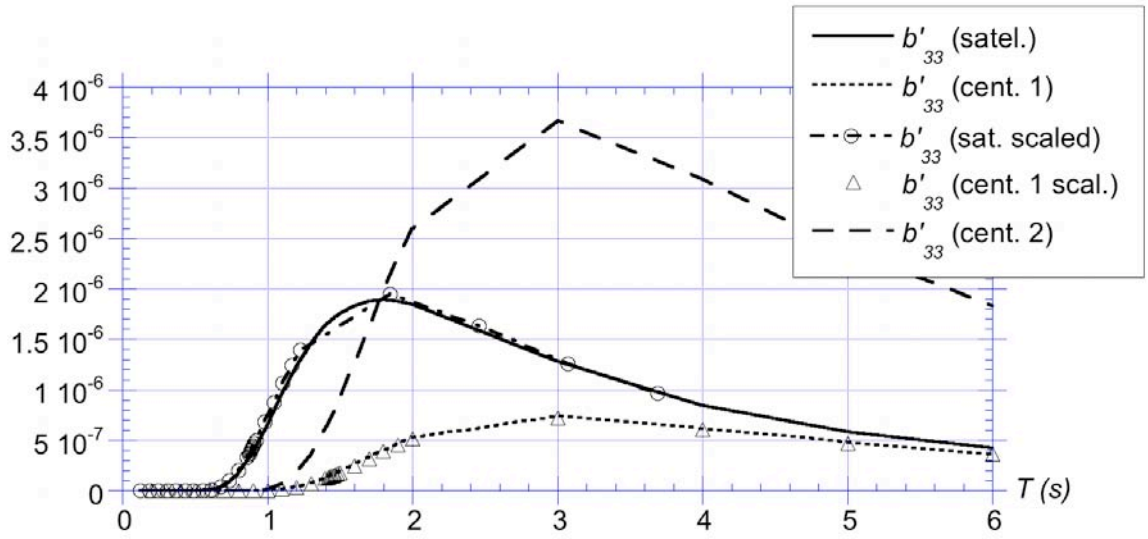

Figure 11: Non-dimensional heave radiative damping coefficient computed for satellite and central spar reference buoys (1 and 2). Prediction of radiative damping on central spar buoy 1 by scaling of central spar buoy 2 (Δ). Prediction of radiative damping of satellite buoy by scaling of central spar buoys 1 or 2 (o).

Figure 11 shows the comparison of various radiative damping coefficient curves as a function of period. The radiative damping coefficient of the satellite buoy is very accurately predicted by scaling from either reference buoy. To capture the radiative damping maximum, a shift of the frequency/period axis is needed but scaling is found proportional to draft rather than diameter. Diameter scaling between central spar buoys 1 and 2 has the exponent 4 (not 2.5), and

the effect of draft scaling is found proportional to the inverse of the draft ratio, rather than the pressure coefficient.

2. Roll (or pitch) equations:

The verified equation, including scaling, for the *roll excitation moment*, on a single spar j is,

$$M_{5j}(t,x_b) = \rho \cdot g \cdot \sum_{i=1}^{N_w} A_i \cdot \left(\frac{D_{sj}}{D_{ref}}\right)^2 \cdot \left(\frac{d_{sj}}{d_{ref}}\right)^1 \cdot \hat{r}_5\left(\omega_i \cdot \sqrt{\frac{d_{ref}}{d_{sj}}}\right) \cdot \cos\left(\omega_i \cdot t + \hat{\phi}_5\left(\omega_i \cdot \sqrt{\frac{d_{ref}}{d_{sj}}}\right) + \psi_i\right) \qquad (66)$$

$$\text{with,} \quad r'_{5j}(\omega_i) = \hat{r}_5\left(\omega_i \cdot \sqrt{\frac{d_{ref}}{d_{sj}}}\right) \cdot \left(\frac{D_{sj}}{D_{ref}}\right)^2 \cdot \left(\frac{d_{sj}}{d_{ref}}\right)^1 \quad \text{and} \quad \phi_{5j}(\omega_i) = \hat{\phi}_5(\omega_i) \qquad (67)$$

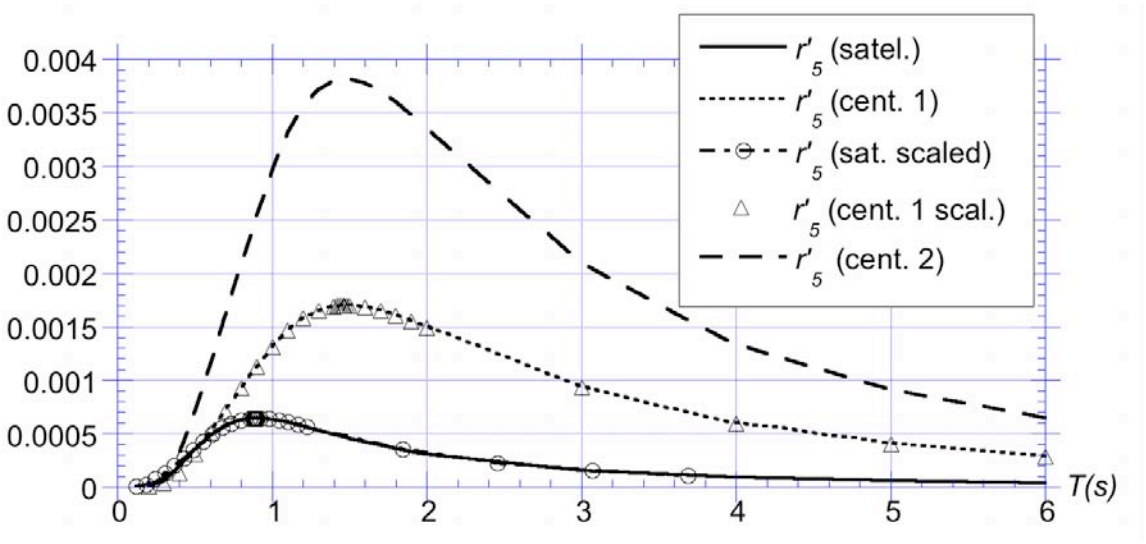

Figure 12: Non-dimensional roll excitation moment module computed for satellite and central spar reference buoys (1 and 2). Prediction of moment on central spar buoy 1 by scaling of central spar buoy 2 (Δ). Prediction of moment of satellite buoy by scaling of central spar buoys 1 or 2 (o).

Figure 12 shows the comparison of various moments. The moment on the satellite buoy is almost perfectly predicted by scaling from either reference buoy. A shift of the frequency/period axis is needed, but scaling is proportional to diameter ratios. Diameter scaling

between central spar buoys 1 and 2 has the expected exponent 2, and draft scaling has the expected exponent 1. Almost no difference is found on phase angles (not shown).

The verified equation, including scaling for the *roll added inertia* at the peak frequency, on a multiple spar is :

$$a_{55p} = \sum_{j=0}^{N_s} a_{55\,j}(\omega_p) \quad \text{with} \quad a_{55\,j}(\omega_p) = \hat{a}_{55\,j}\left(\omega_p \cdot \sqrt{\frac{d_{ref}}{d_{sj}}}\right) \cdot \left(\frac{D_{sj}}{D_{ref}}\right)^2 \cdot \left(\frac{d_{sj}}{d_{ref}}\right)^3 \tag{68}$$

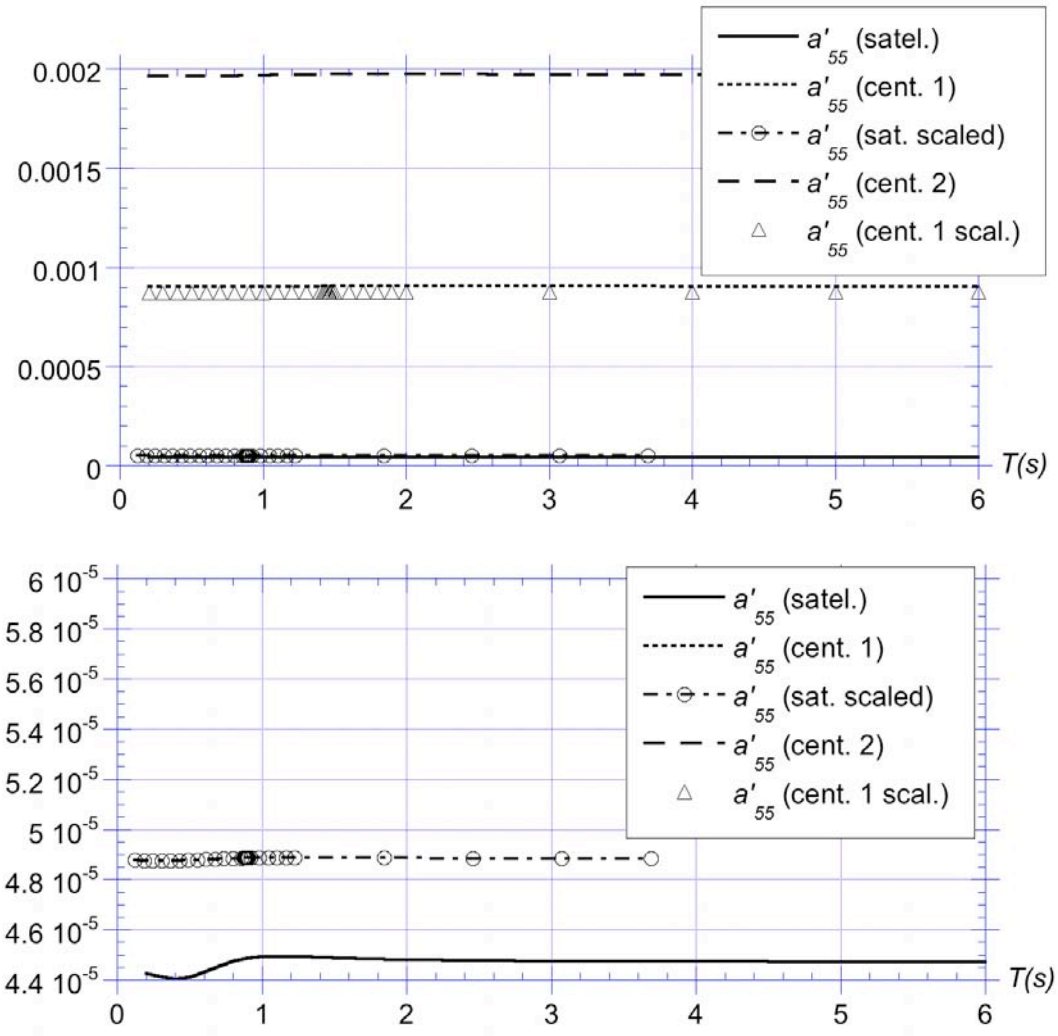

Figure 13: Non-dimensional roll added inertia coefficient computed for satellite and central spar reference buoys (1 and 2). Prediction of added inertia on central spar buoy 1 by scaling of central spar buoy 2 (Δ). Prediction of added inertia of satellite buoy by scaling of central spar buoys 1 or 2 (o). The two figures show identical data, but have different scale.

Figure 13 shows the comparison of various added inertia curves as a function of period. The added inertia on the satellite buoy is accurately predicted by scaling from either reference buoy. To capture the added inertia minimum, a shift of the frequency/period axis is needed but scaling is found proportional to draft rather than diameter. Diameter scaling between central spar buoys 1 and 2 has the exponent 2, and draft scaling between central spar buoys 1 and 2 has the exponent 3. No transport term is necessary in the summation equation. In fact, a more careful theoretical development indicates that such transport terms disappear for any multiple spar configuration.

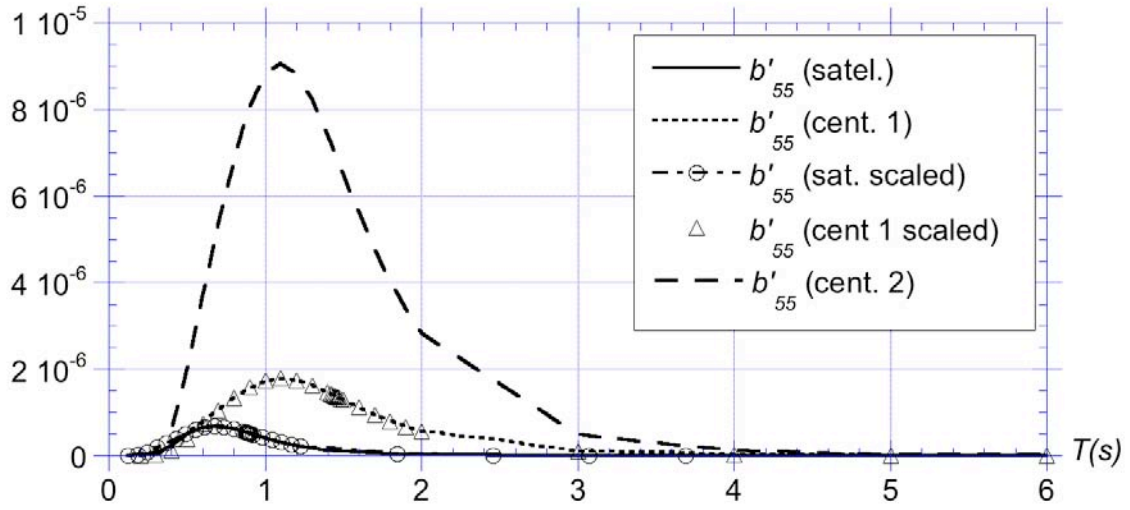

Figure 14: Non-dimensional roll radiative damping coefficient computed for satellite and central spar reference buoys (1 and 2). Prediction of radiative damping on central spar buoy 1 by scaling of central spar buoy 2 (Δ). Prediction of radiative damping of satellite buoy by scaling of central spar buoys 1 or 2 (o).

The verified equation for the *roll radiative damping* coefficient at the peak frequency, on a multiple spar, including scaling is:

$$b_{55p} = \sum_{j=0}^{N_s} \hat{b}_{55}\left(\omega_p \cdot \sqrt{\frac{d_{ref}}{d_{sj}}}\right) \cdot \left(\frac{D_{sj}}{D_{ref}}\right)^4 \cdot \left(\frac{d_{sj}}{d_{ref}}\right)^1 \tag{69}$$

Figure 14 shows the comparison of various radiative damping coefficient curves as a function of period. The radiative damping coefficient of the satellite buoy is very accurately predicted by scaling from either reference buoy. To capture the radiative damping maximum, a shift of the frequency/period axis is needed but scaling is found proportional to draft. Diameter scaling between central spar buoys 1 and 2 has the exponent 4, and the effect of draft scaling is found proportional to draft ratio.

b. Verification of summation formulas

Summation formulas are validated below. For each WAMIT coefficient, buoy parameters computed for the star-spar are compared to the summation of coefficients computed for the 5 individual spars ($N_s = 4$) of the buoy. As shown above, the latter are essentially identical to the coefficients scaled from a reference spar. Hence, the present comparison is just aimed at validating the summation over the spars. Accordingly, to better estimate effects of the distance of satellites to the central spar, WAMIT coefficients are computed for a second star-spar with a larger distance $h_s = 0.2401$ m or 4 diameters, on axis, between the satellites and the central buoy; this is referred to hereafter as the "wide" star-spar.

We will see that, for all coefficients but the radiative damping coefficients b_{33} and b_{55}, the summation formulas work very well. For the radiative damping coefficients, however, discrepancies in magnitude are significant (factor 2 to 5 for b_{33} and 50-70% for b_{55}), likely due to wave reflection and interactions between wave patterns generated by various spar buoys. However, in the dynamic buoy equations, because of the use of spar buoys, radiative damping forces and related coefficients are very small as compared to other forces and particularly viscous damping. Hence, the poor agreement of the summation formulas for these terms is considered acceptable. Details are given in the following.

1. Heave equations:

The original equation for the *heave excitation force* on a multiple-spar was:

$$F_3(t) = \sum_{j=0}^{N_s} F_{3j}(t) \tag{70}$$

with F_{3j} now given by Eqs. (62). The summation is performed by first switching to complex notations and thus calculating the real and imaginary parts of each force, using modules r'_{3j} and angles ϕ_{3j}, module, given by Eq. (63), then recalculating the summation heave force module r'_3 and angle ϕ_3. The latter is very close to that calculated by WAMIT for the complete star-spars. Figure 15 shows the various computed heave force modules, for the complete star-spar, the summation, and the wide complete star-spar. All three-force modules are nearly identical as a function of period.

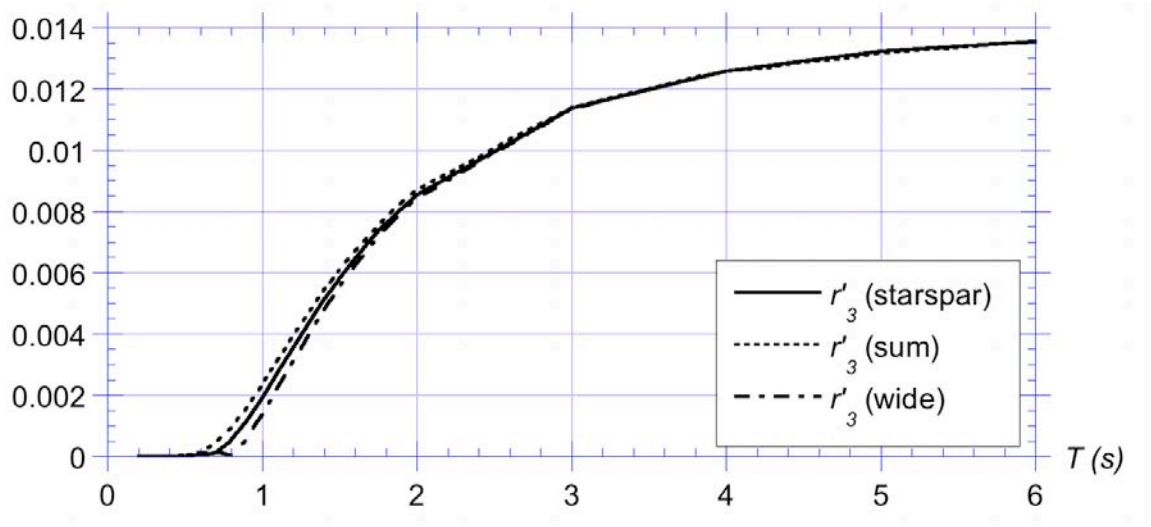

Figure 15: Non-dimensional heave excitation force module computed for the complete starspar, from the summation of satellite and central buoy, and for the complete wide starspar.

The original equation for the *heave added mass*, on a multiple spar, was:

$$a_{33}(\omega_p) = \sum_{j=0}^{N_s} a_{33\,j}(\omega_p) \tag{71}$$

with a_{33j} (now) given by Eq. (64). Figure 16 shows the comparison of various added mass curves as a function of period. The added mass computed as a summation is about 7-20% smaller than that of the complete starspar, with the smaller relative errors occurring in the more useful period range below 2 s. Although relative differences with the summation formula are slightly smaller for the wide spar, these are still significant.

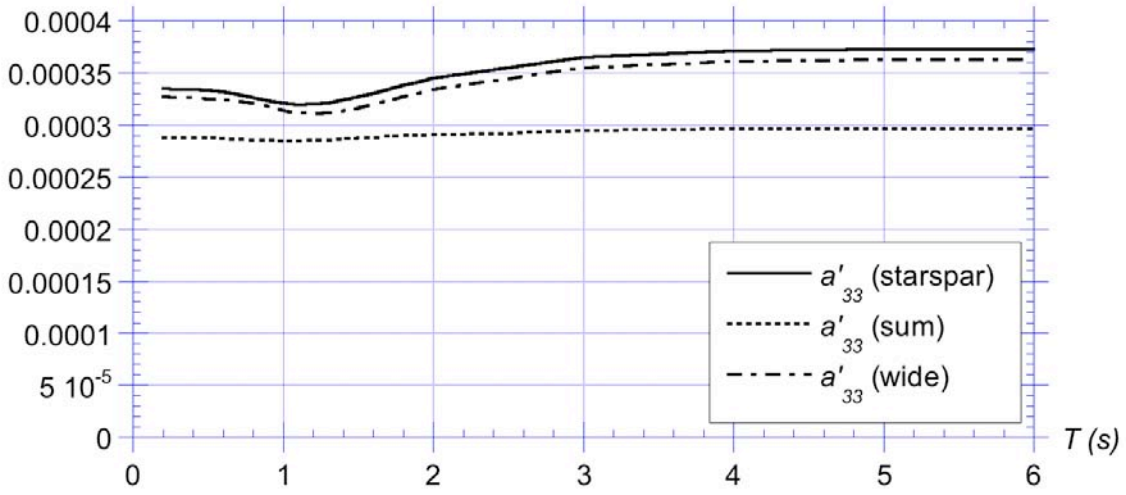

Figure 16: Non-dimensional heave added mass coefficient computed for the complete starspar, from the summation of satellite and central buoy, and for the complete wide starspar.

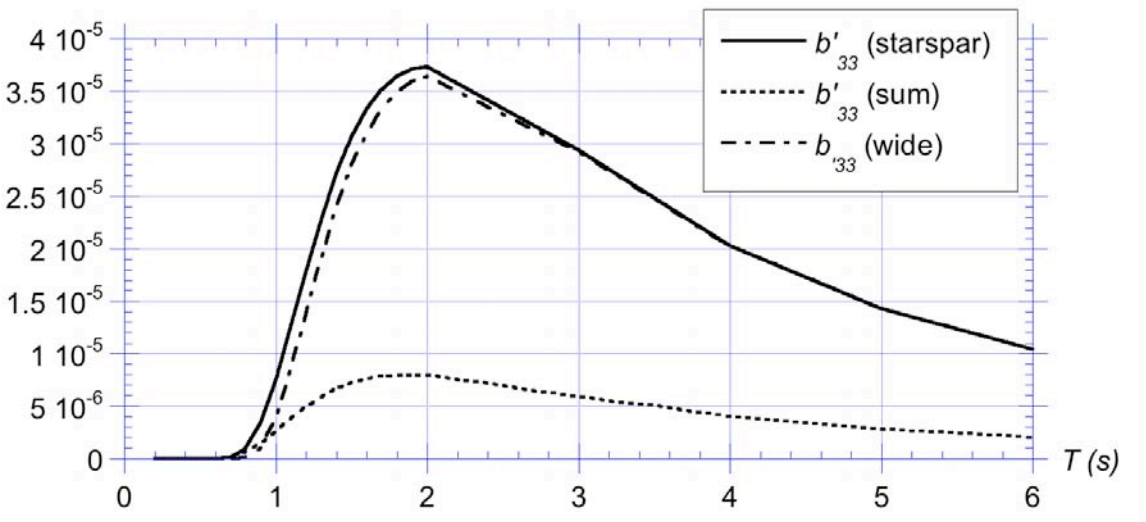

Figure 17: Non-dimensional heave radiative damping coefficient computed for the complete starspar, from the summation of satellite and central buoy, and for the complete wide starspar.

The original equation for the *heave radiative damping* coefficient, on a multiple spar, was:

$$b_{33}(\omega_p) = \sum_{j=0}^{N_s} b_{33\,j}(\omega_p) \tag{72}$$

with b_{33j} (now) given by Eq . (65).

Figure 17 shows the comparison of various radiative damping curves as a function of period. The radiative damping coefficient computed as a summation is about 4.5-5 times smaller than that of the complete star-spar. Relative differences with the summation formula are barely slightly smaller for the wide complete spar, indicating those large differences are likely not primarily due to satellite spacing but to reflections and interactions between spars that may still occur at large distance. One should note, however, that the magnitude of the non-dimensional radiative damping coefficient is about 100 times less than that of added mass coefficient in fig. 16.

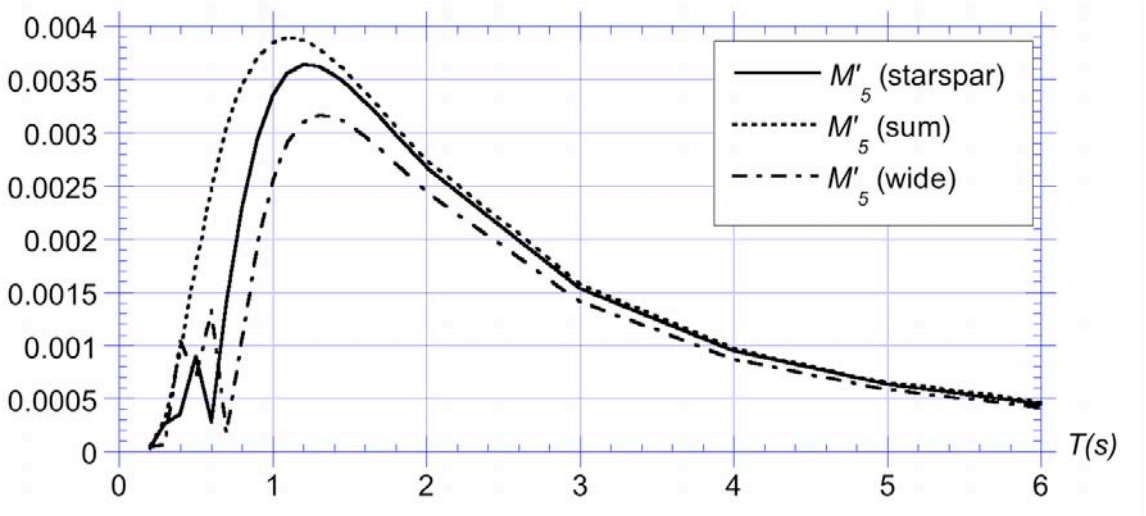

Figure 18: Non-dimensional roll excitation moment module computed for the complete starspar, from the summation of satellite and central buoy, and for the complete wide starspar.

3. Roll equations:

The original equation for the *roll excitation moment* on a multiple-spar was:

$$M_5(t) = \sum_{j=0}^{N_s} \left(M_{5j}(t) + r_{sj} \cdot \sin(\theta_{sj}) \cdot F_{3j}(t) \right) \tag{73}$$

with M_{5j} (now) given by Eqs. (66, 67). A detailed and careful theoretical derivation, however, showed that for multiple spar buoys, unlike initially thought, the transport term always vanishes.

Hence, this equation can be expressed as,

$$M_5(t) = \sum_{j=0}^{N_s} M_{5j}(t) \tag{74}$$

The summation in Eq. (74) is performed by first switching to complex notations and thus calculating the real and imaginary parts of each force, using modules r'_{5j} and angles ϕ_{5j}, module, given by Eq. (67), then recalculating the summation heave force module r'_5 and angle ϕ_5. The latter is found to be very close to that calculated by WAMIT for the complete starspars and hence not shown.

Figure 18 shows the various roll excitation moment modules computed, for the complete starspar, the summation, and the wide complete starspar. All three moment modules are quite close to each other, as a function of period, with mostly the summation curve showing a slight shift in period for periods less than 1 s.

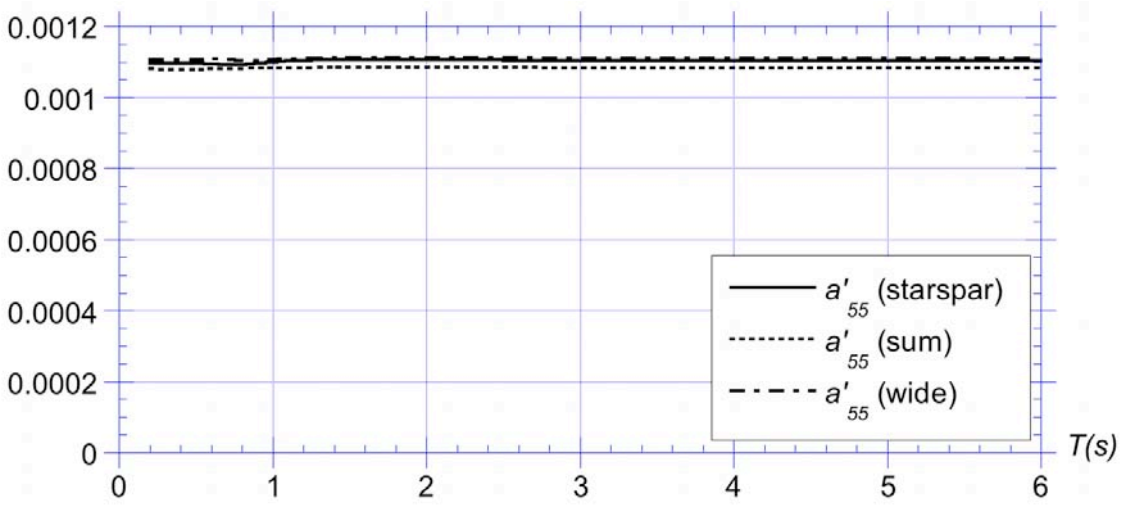

Figure 19: Non-dimensional roll added inertia coefficient computed for the complete starspar, from the summation of satellite and central buoy, and for the complete wide starspar.

The original equation for the *roll added inertia*, on a multiple spar, was:

$$a_{55}(\omega_p) = \sum_{j=0}^{N_s} \left(a_{55\,j}(\omega_p) + a_{25\,j}(\omega_p) \sqrt{\left(z_M - \frac{d_{sj}}{2} \right)^2 + r_{sj}^2 \cdot \sin^2 \theta_{sj}} \right) \tag{75}$$

with a_{55j} (now) given by Eq. (68). A detailed and careful theoretical derivation, however, showed that for multiple spar buoys, unlike initially thought, the transport term in Eq. (75) always vanishes. Hence, this equation can be expressed as given in Eq. (68).

Figure 19 shows the comparison of various added inertia curves as a function of period. The added inertia computed as a summation is nearly identical to that of the complete starspar, with the smaller relative errors occurring in the more useful period range below 2 s. Similarly small differences are found with the wider complete spar.

The original equation for the *roll radiative damping* coefficient, on a multiple spar, was :

$$b_{55}(\omega_p) = \sum_{j=0}^{N_s} b_{55\,j}(\omega_p) \tag{76}$$

with b_{55j} (now) given by Eq. (69).

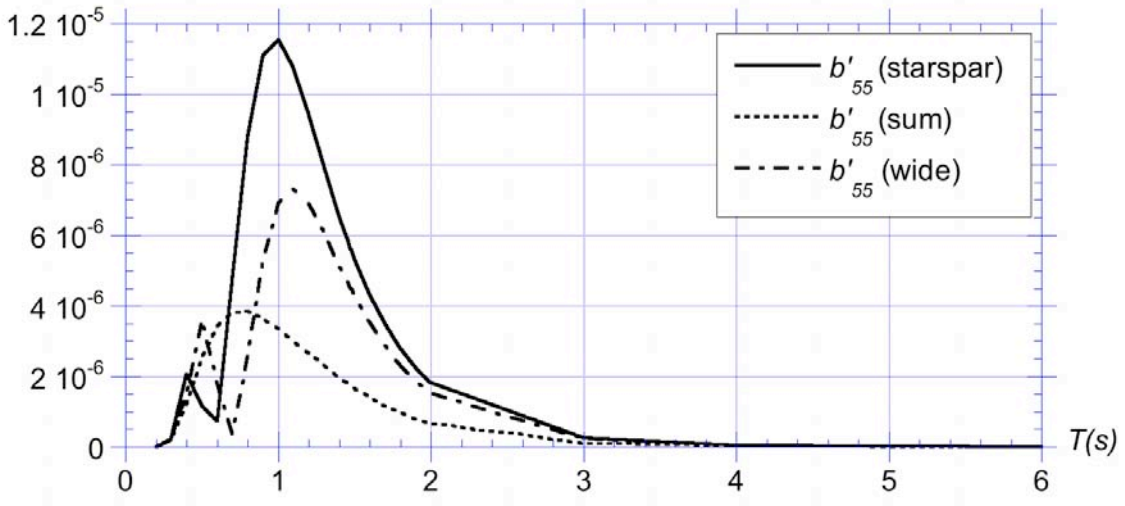

Figure 20: Non-dimensional roll radiative damping coefficient computed for the complete starspar, from the summation of satellite and central buoy, and for the complete wide starspar.

Figure 20 shows the comparison of various radiative damping curves as a function of period. The roll radiative damping coefficient computed as a summation is about 50-60% smaller than that of the complete starspar. Relative differences with the summation formula are much smaller for the wide complete spar, indicating differences are partly due to satellite spacing and partly to reflections and interactions between spars that may still occur at large distance. One should note, however, that the magnitude of the non-dimensional radiative damping coefficient is about 100 times less than that of added inertia coefficient in Fig. 19.

3.4 Interactive user interface

We coupled a linear sea state model, function of local wave parameters, and the numerical model for the multi-spar buoy and LEG dynamics, to perform interactive optimization of the buoy parameters, in order to maximize wave energy harvesting. In the buoy dynamic heave and roll equations, the frequency dependent parameters are estimated using scaling and summation formula, as detailed above, to allow the program to perform as a stand alone tool, without the use of a separate model (such as WAMIT).

A graphical/interactive user interface was developed, to provide the user with the flexibility to specify sea surface and buoy design parameters, with realistic degrees of freedom. The user can adjust the sea state parameters to simulate specific wave climate as well as geometric buoy parameters to optimize the capture width ratio, and therefore the wave power extracted.

The flowchart of the conceptual approach and the model flowchart are presented in Figures 21 and 22. Besides power production, the interactive tool output produces a movie of the actual buoy, moving in the given sea–state. An example of a still frame is shown in Figure 23.

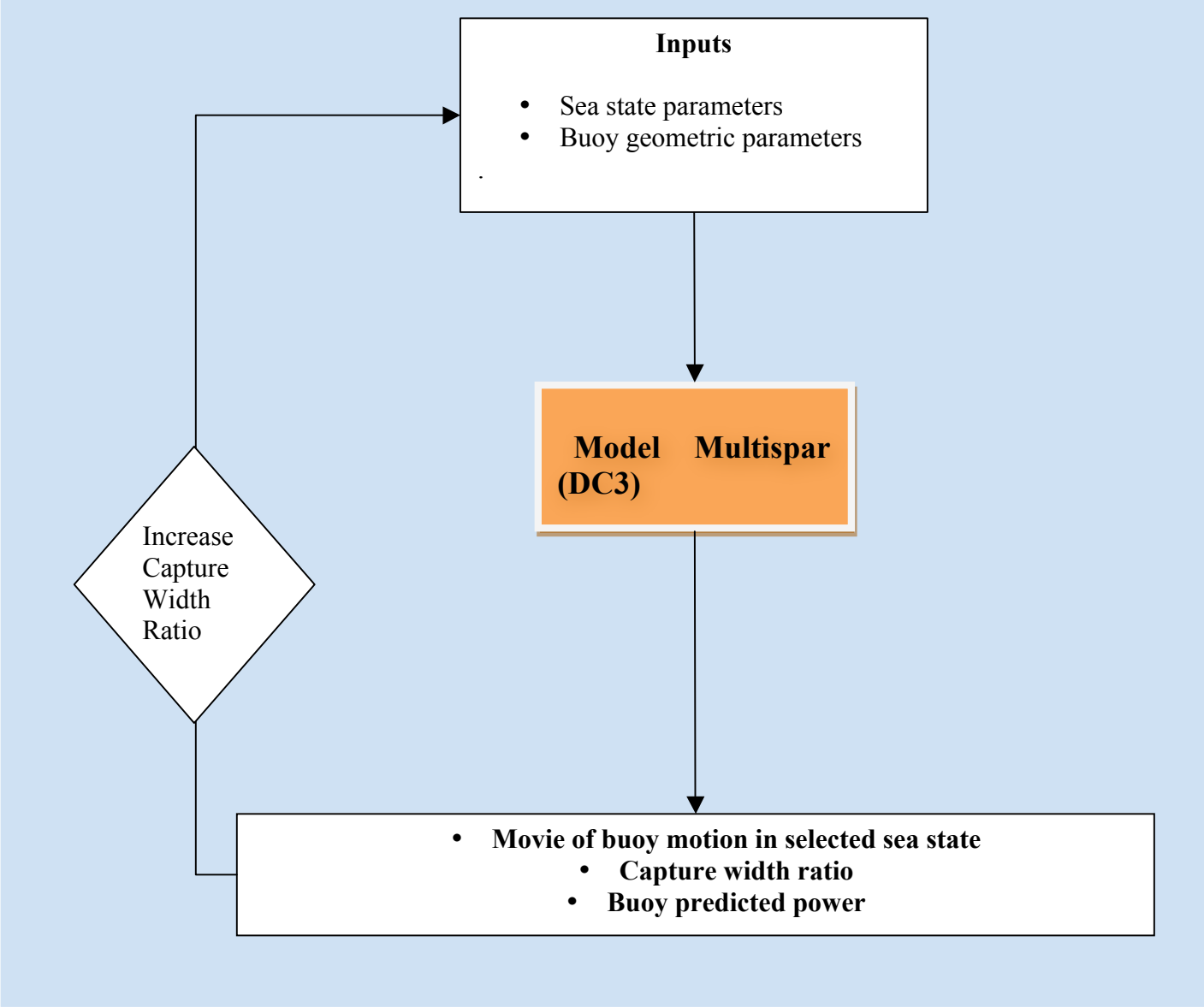

Figure 21: Flow chart of interactive tool conceptual approach

Multispar interactive algorithm

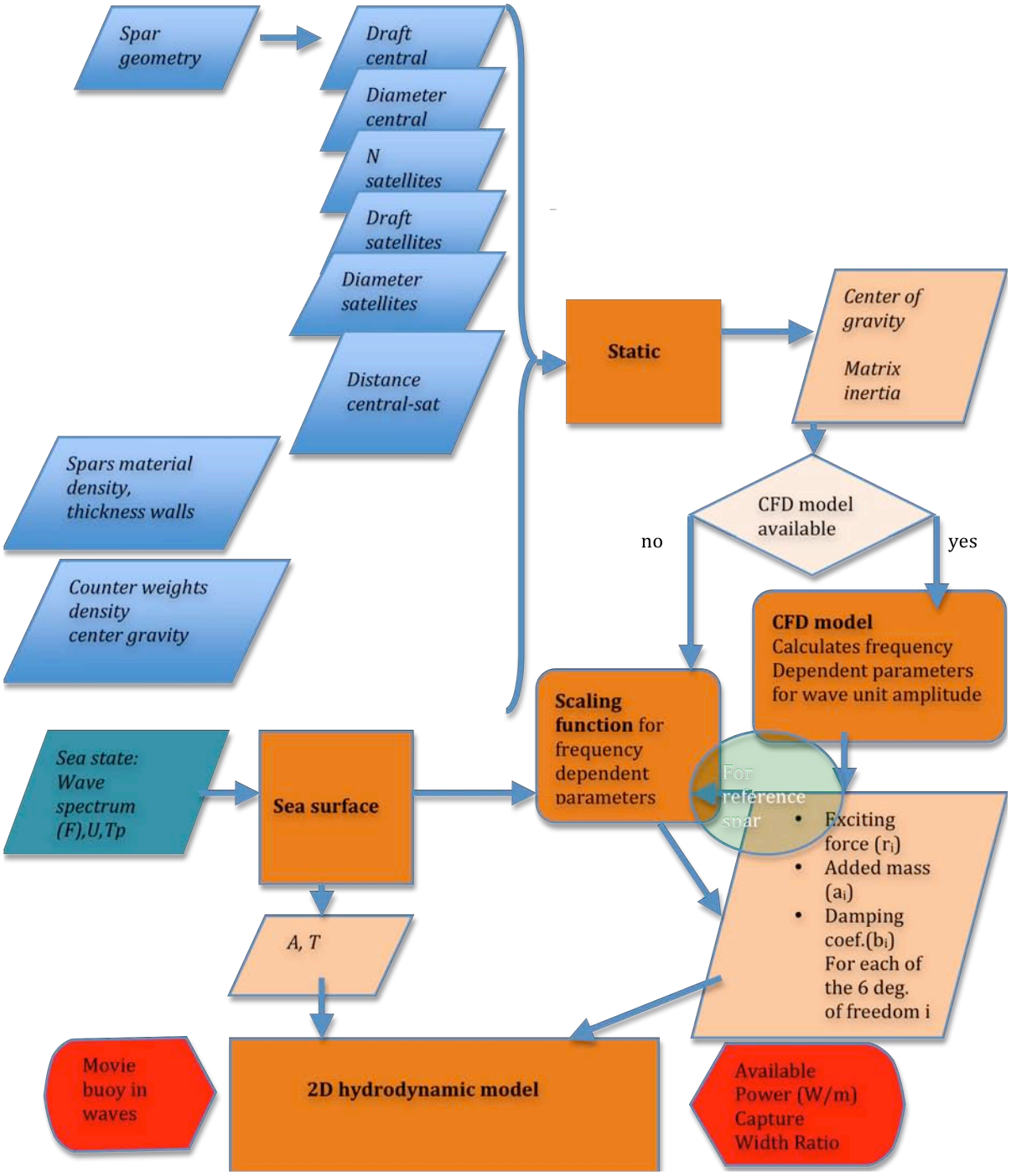

Figure 22: Interactive tool model flowchart

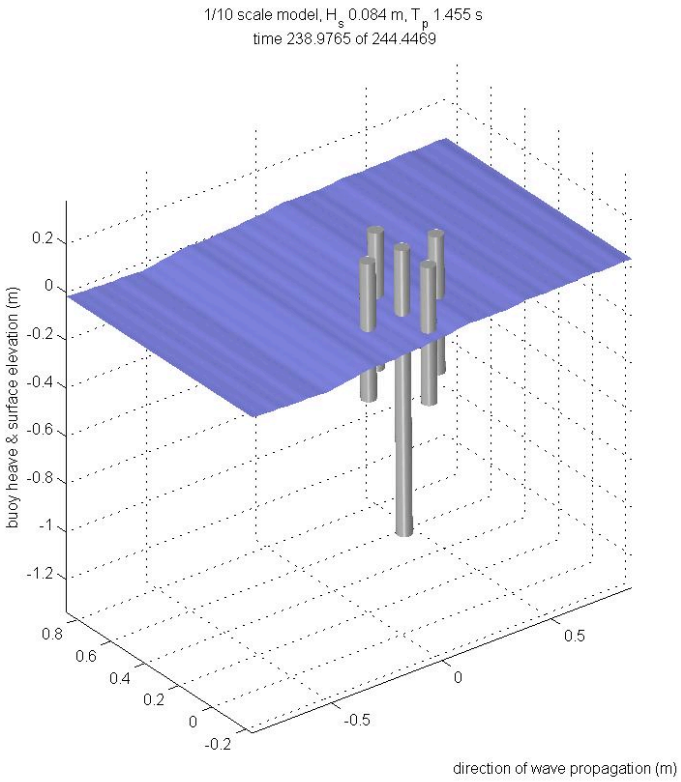

Figure 23: Still frame of output movie of optimized buoy design using the interactive design tool model.

Exemples of output in movie format can be found using the following links:

http://www.oce.uri.edu/~grilli/meanseastate_5.avi

http://www.oce.uri.edu/~grilli/extremeseastate_10.avi

http://www.oce.uri.edu/~grilli/meanseastate_10.avi

4 REFERENCES

Bastien, S., and A.R. Grilli. "Small Buoy for Energy Harvesting." Final Technical Report for SBIR Phase I base period (Grant N00039-07-C-0076), 2008, 97 pps.

Bastien, S.P., A.R. Grilli, S.T. Grili, R.B. Jr. Sepe, and M.L. Spaulding. "Ocean Energy Extraction for Sensor Applications." Final Technical Report for STTR Phase I base period (Grant N00014-08-M-0277), 2009, 164 pps.

Bastien, S.P., Sepe R.B., Grilli A.R., Grilli S.T., and M.L. Spaulding (2009). Ocean Wave Energy Harvesting Buoy for Sensors. In *Proc. IEEE Energy Conversion Congress and Exposition* (ECCE09, San Jose CA, September, 2009), pps 3718-3725, doi: 978-1-4244-2893-9/09/.

Berteaux, H.O. *Coastal and Oceanic Buoy Engineering.* Woods Hole, MA: H.O. Berteaux, 1991.

Borsay, K., A. Sanguinetti, and M. Ziolkowski. "Experimental Testing of Starspar Buoy for Wave Power Generation." Internal Document: Senior Design Report, Ocean Engineering, University of Rhode Island, Narragansett, RI, 2009.

Dean, R.G., and R.A. Dalrymple. *Water Wave Mechanics For Engineers and Scientists.* New Jersey: Prentice Hall Inc., 1984.

Grilli, A.R., J. Merrill, S.T. Grilli, M.L. Spaulding, and J.T. Cheung. "Experimental and numerical study of spar buoy-magnet/spring oscillators used as wave energy absorbers." *17th International Offshore and Polar Engineering Conference.* Lisbon, Portugal: International Society of Offshore and Polar Engineers, 2007. 489-496.

Grilli, S.T. "StarSpar parametric study." Internal Document, Ocean Engineering, University of Rhode Island, Narragansett, RI, 2008.

Hagerman, G., and R. Bedard. *Guidelines forPreliminary Estimation of Power Production by Offshore Wave Energy Conversion Devices.* EPRI 297213, 2003.

Merrill, J.S. "Experimental Testing of Spar Buoy for Wave Power Generation." MS Thesis, Ocean Engineering, University of Rhode Island, Narragansett, RI, 2007.

Newman, J.N. *Marine Hydrodynamics.* Cambridge, Massachusetts: Massachusetts Institute of Technology Press, 1977.

Spaulding, M.L., A.R. Grilli, S.T. Grilli, and J. Merrill. "Design and Evaluation of Wave Energy Conversion Device to Power Ocean Surveillance Systems." Technical Report for Teledyne Scientific & Imaging LLC, Ocean Engineering, University of Rhode Island, Narragansett, RI, 2007.

White, F.M. *Fluid Mechanics.* Boston, Massachusetts: McGraw-Hill, 2003.